

Studies in Systems, Decision and Control 75

Jacek Kabziński *Editor*

Advanced Control of Electrical Drives and Power Electronic Converters

 Springer

Studies in Systems, Decision and Control

Volume 75

Series editor

Janusz Kacprzyk, Polish Academy of Sciences, Warsaw, Poland
e-mail: kacprzyk@ibspan.waw.pl

About this Series

The series “Studies in Systems, Decision and Control” (SSDC) covers both new developments and advances, as well as the state of the art, in the various areas of broadly perceived systems, decision making and control- quickly, up to date and with a high quality. The intent is to cover the theory, applications, and perspectives on the state of the art and future developments relevant to systems, decision making, control, complex processes and related areas, as embedded in the fields of engineering, computer science, physics, economics, social and life sciences, as well as the paradigms and methodologies behind them. The series contains monographs, textbooks, lecture notes and edited volumes in systems, decision making and control spanning the areas of Cyber-Physical Systems, Autonomous Systems, Sensor Networks, Control Systems, Energy Systems, Automotive Systems, Biological Systems, Vehicular Networking and Connected Vehicles, Aerospace Systems, Automation, Manufacturing, Smart Grids, Nonlinear Systems, Power Systems, Robotics, Social Systems, Economic Systems and other. Of particular value to both the contributors and the readership are the short publication timeframe and the world-wide distribution and exposure which enable both a wide and rapid dissemination of research output.

More information about this series at <http://www.springer.com/series/13304>

Jacek Kabziński
Editor

Advanced Control of Electrical Drives and Power Electronic Converters

 Springer

Editor

Jacek Kabziński
Institute of Automatic Control
Lodz University of Technology
Łódź
Poland

ISSN 2198-4182 ISSN 2198-4190 (electronic)
Studies in Systems, Decision and Control
ISBN 978-3-319-45734-5 ISBN 978-3-319-45735-2 (eBook)
DOI 10.1007/978-3-319-45735-2

Library of Congress Control Number: 2016950385

© Springer International Publishing Switzerland 2017

This work is subject to copyright. All rights are reserved by the Publisher, whether the whole or part of the material is concerned, specifically the rights of translation, reprinting, reuse of illustrations, recitation, broadcasting, reproduction on microfilms or in any other physical way, and transmission or information storage and retrieval, electronic adaptation, computer software, or by similar or dissimilar methodology now known or hereafter developed.

The use of general descriptive names, registered names, trademarks, service marks, etc. in this publication does not imply, even in the absence of a specific statement, that such names are exempt from the relevant protective laws and regulations and therefore free for general use.

The publisher, the authors and the editors are safe to assume that the advice and information in this book are believed to be true and accurate at the date of publication. Neither the publisher nor the authors or the editors give a warranty, express or implied, with respect to the material contained herein or for any errors or omissions that may have been made.

Printed on acid-free paper

This Springer imprint is published by Springer Nature
The registered company is Springer International Publishing AG
The registered company address is: Gewerbestrasse 11, 6330 Cham, Switzerland

*Oh, I get by with a little help from my friends.
Mmm, I get high with a little help from my
friends. Mmm, gonna try with a little help
from my friends.*

—John Lennon and Paul McCartney,
released on the Beatles album Sgt. Pepper's
Lonely Hearts Club Band in 1967

Foreword

Advanced Control of Electrical Drives and Power Electronic Converters is state-of-the-art monograph which includes expanded contributions selected from numerous research topics discussed during the XII Conference on Control in Power Electronics and Electrical Drives (SENE) organized by the Institute of Automatic Control, Lodz University of Technology under the auspices of the Committee of Electrical Engineering Polish Academy of Sciences, November 18–20, 2015. This conference has a long tradition in Poland and is organized biannually since 1991 attracting usually over 150 participants, mostly Ph.D. students, young assistants, and professors working on the area of power electronics and drives.

Based on a strict peer-review process, the editor has selected 15 chapters describing new research results and offering strong monographic impact. The material is presented in three parts: electric drives and motion control, (Chapters “[Sensorless Control of Polyphase Induction Machines](#)” through “[Selected Methods for a Robust Control of Direct Drive with a Multi-mass Mechanical Load](#)”), electric drives and fault-tolerant control (Chapters “[Fault-Diagnosis and Fault-Tolerant Control in Industrial Processes and Electrical Drives](#)” through “[Detection and Compensation of Transistor and Position Sensors Faults in PM BLDCM Drives](#)”), and design and control of power converters (Chapters “[Advanced Control Methods of DC/AC and AC/DC Power Converters—Look-up Table and Predictive Algorithms](#)” through “[Switched Capacitor-Based Power Electronic Converter—Optimization of High Frequency Resonant Circuit Components](#)”). The Part I of the book begins with a chapter providing a highly interesting and important topic of sensorless control of polyphase induction machines authored by Prof. Zbigniew Krzemiński (Chapter “[Sensorless Control of Polyphase Induction Machines](#)”) and followed by three chapters devoted to position control and tracking, especially for two- and multi-mass drives, drives with flexible shaft and friction co-authored by professors: Jacek Kabziński (Chapter “[Adaptive Position Tracking with Hard Constraints—Barrier Lyapunov Functions Approach](#)”), Krzysztof Szabat (Chapter “[Predictive Position Control of a Two-Mass System with an Induction Motor in a Wide Range of Speed Changes](#)”), and Stefan Brock (Chapter “[Selected Methods for](#)

a Robust Control of Direct Drive with a Multi-mass Mechanical Load”). The Part II of the book is dedicated to research activities of the group headed by Profs. Teresa Orłowska-Kowalska and Czesław T. Kowalski and is devoted to current topic of fault-diagnosis and fault-tolerant control of VSI-fed induction motor drives (Chapters “Fault-Diagnosis and Fault-Tolerant-Control in Industrial Processes and Electrical Drives”—“Stator Faults Monitoring and Detection in Vector Controlled Induction Motor Drives—Comparative Study”) as well as PM BLDC drives (Chapter “Detection and Compensation of Transistor and Position Sensors Faults in PM BLDCM Drives”). The first chapter of Part III co-authored by Prof. Andrzej Sikorski is devoted to analysis and comparative study of table-based and model predictive control of back-to-back AC-DC-AC converters (Chapter “Advanced Control Methods of DC/AC and AC/DC Power Converters—Look-up Table and Predictive Algorithms”). The two other chapters (“Active Power Filter Based on a Dual Converter Topology” and “Power Electronics Inverter with a Modified Sigma-Delta Modulator and an Output Stage Based on GaN E-HEMTs”) in the Part III, co-authored by Prof. Michał Gwóźdź, are dealing with novel single-phase active filters and sigma-delta modulator for GaN-based converter. Also, chapters presenting follow-up reactive power compensator (Chapter “FC+TCR-type Symmetrical Follow-up Compensator of the Fundamental Harmonic Reactive Power—Analysis and Experiment”), AC-DC-AC converter with current modulator in DC link (Chapter “AC/DC/AC Converter with Power Electronics Current Modulator Used in DC Circuit for Renewable Energy Systems”), and switched capacitor-based power electronic converters (Chapter “Switched Capacitor-Based Power Electronic Converter—Optimization of High Frequency Resonant Circuit Components”) are included.

This book gives a highly valuable view on several problems of power electronics and AC drives discussing several aspects of the authors’ current research containing innovative and original concepts.

I would like to congratulate the editors for the initiative taken in this timely book to publish an impressive collection of reports belonging to the edge of research in power electronics and drives, and I wish the book great success being accepted by the professional community.

Warsaw
September 2016

Marian P. Kaźmierkowski

Preface

“There is nothing so practical as a good theory”—Kurt Lewin claimed,¹ taking part in the ongoing debate between practitioners and scientists about their relationship and the desirability of applied research as opposed to basic research. Any engineer working in the field of power electronics and drives has to support this statement strongly, having in mind control theory, artificial and computational intelligence, or signal processing. On the other hand, there is nothing more stimulating for the development of a theory as a strong need for practical applications and the influence of smart, practical solutions that may be generalized and become a part of the general approach. Power electronics and variable frequency drives are continuously developing multidisciplinary fields which require applications of the recently developed techniques of modern control theory and provide an important impulse for the development of new predictive, nonlinear and robust control methods. That is why the book concerning recent solutions in control of power electronics and drives appears in the series “Studies in Systems, Decisions and Control.”

The presented contributed volume is written by key specialists working in multidisciplinary fields in electrical engineering, linking control theory, power electronics, artificial neural networks, embedded controllers, and signal processing. The authors of each chapter report the state of the art of the various topics addressed and present results of their own research, laboratory experiments, and successful applications. The presented solutions concentrate on three main areas of interest: motion control in complex electromechanical systems, including sensorless control; fault-diagnosis and fault-tolerant control of electric drives; and new control algorithms for power electronics converters.

I believe that particular chapters and the complete book possess strong monograph attributes. Important practical and theoretical problems are deeply and accurately presented on the background of an exhaustive state-of-the-art review.

¹Lewin, K. (1951). Problems of research in social psychology. In D. Cartwright (Ed.), *Field theory in social science: Selected theoretical papers* (pp. 155–169). New York: Harper & Row. (p. 169), although the same quotation is sometimes attributed to James Clerk Maxwell, Ludwig Boltzmann, or even Leonid Brezhnev.

Many results are completely new and were never published before. Therefore, this book will be interesting for a wide audience:

- researchers working in control, especially nonlinear control, model predictive control, and fault-tolerant control, who are interested in challenges caused by practical applications;
- experts in power electronics, electrical machines, motion control, and drives, who are involved in the use of advanced control methods;
- creative industry engineers and constructors faced with new challenging applications; and
- graduate and Ph.D. students of control, electrical engineering, power conversion, robotics, or mechatronics.

The idea of this book originated among the research community gathered around the conference Control in Power Electronics and Electric Drives. It is a leading Polish Conference devoted to power electronics, motion control, electric drives automation, and control theory application. It is a regular biennial event with a very long tradition—the 13th edition will be organized in November 2017. The conference is organized by the Institute of Automatic Control, Lodz University of Technology, always in Lodz, under auspices of the Committee on Electrical Engineering, Polish Academy of Sciences, and in cooperation with IEEE (Polish section). The event is the main meeting forum for researchers, developers, and specialists from the industry. I cordially invite the readers of the presented book to participate in future editions of our conference.

I would like to express my sincere gratitude to numerous persons, who contributed to the edition of this book:

- the authors, who worked hard to make their chapters perfect and in time; apologies if I made you be under a pressure from time to time;
- numerous anonymous researchers, who helped to review the chapters, to eliminate mistakes, and to improve the final result;
- Prof. Janusz Kacprzyk, the Editor of Springer Book Series, for his enthusiasm, encouragement, and support to publish this book;
- the editorial team of Springer Applied Sciences and Engineering, for professional support during implementation of this project; and
- last but not least, Prof. Marian P. Kaźmierkowski, one of the greatest scientists specializing in power electronics and electrical drives, who was the first person to mention the idea of writing this book and supported the editorial process.

Łódź, Poland
September 2016

Jacek Kabziński

Contents

Part I Electric Drives and Motion Control

Sensorless Control of Polyphase Induction Machines	3
Zbigniew Krzeminski	
Adaptive Position Tracking with Hard Constraints—Barrier Lyapunov Functions Approach	27
Jacek Kabziński, Przemysław Mosiołek and Marcin Jastrzębski	
Predictive Position Control of a Two-Mass System with an Induction Motor in a Wide Range of Speed Changes	53
Piotr Serkies and Krzysztof Szabat	
Selected Methods for a Robust Control of Direct Drive with a Multi-mass Mechanical Load	75
Stefan Brock, Dominik Łuczak, Tomasz Pajchrowski and Krzysztof Zawirski	

Part II Electric Drives and Fault-Tolerant Control

Fault-Diagnosis and Fault-Tolerant-Control in Industrial Processes and Electrical Drives	101
Teresa Orłowska-Kowalska, Czesław T. Kowalski and Mateusz Dybkowski	
IGBT Open-Circuit Fault Diagnostic Methods for SVM-VSI Vector-Controlled Induction Motor Drives	121
Piotr Sobański and Teresa Orłowska-Kowalska	
Speed and Current Sensor Fault-Tolerant-Control of the Induction Motor Drive	141
Mateusz Dybkowski, Kamil Klimkowski and Teresa Orłowska-Kowalska	

Stator Faults Monitoring and Detection in Vector Controlled Induction Motor Drives—Comparative Study	169
Marcin Wolkiewicz, Grzegorz Tarchała, Czesław T. Kowalski and Teresa Orłowska-Kowalska	
Detection and Compensation of Transistor and Position Sensors Faults in PM BLDCM Drives.	193
Marcin Skóra and Czesław T. Kowalski	
Part III Design and Control of Power Converters	
Advanced Control Methods of DC/AC and AC/DC Power Converters—Look-Up Table and Predictive Algorithms	221
A. Godlewska, R. Grodzki, P. Falkowski, M. Korzeniewski, K. Kulikowski and A. Sikorski	
Active Power Filter Based on a Dual Converter Topology	303
Michał Gwóźdź	
AC/DC/AC Converter with Power Electronics Current Modulator Used in DC Circuit for Renewable Energy Systems.	317
Michał Krystkowiak and Adam Gulczyński	
Power Electronics Inverter with a Modified Sigma-Delta Modulator and an Output Stage Based on GaN E-HEMTs.	327
Michał Gwóźdź and Dominik Matecki	
FC + TCR-Type Symmetrical Follow-Up Compensator of the Fundamental Harmonic Reactive Power—Analysis and Experiment.	339
Małgorzata Latka	
Switched Capacitor-Based Power Electronic Converter—Optimization of High Frequency Resonant Circuit Components	361
Zbigniew Waradzyn, Robert Stala, Andrzej Mondzik and Stanisław Piróg	

Introduction

The main function of any electric drive operating in motoring mode is to convert electrical energy into mechanical form. In generation mode, the drive is able to convert mechanical energy into electrical form and transfer it back to the network. Electrical power is nowadays supplied from the alternative current (AC) grid in a “raw” form with fixed voltage frequency and amplitude. At times, a power source is a direct current (DC) source like an accumulator or a battery. The resulting mechanical power is used to generate rotational or linear motion of the working machinery (the load). In modern industrial applications, this motion, i.e., position and velocity, must be controlled precisely according to variable reference signals, in spite of numerous disturbances. The structure of a typical drive is shown in Fig. 1, and the components are shortly described below.

The **load** represents the dynamics of the working machinery that is usually described by nonlinear ordinary differential equations (ODEs) with unknown or imprecisely known parameters, including such nonlinear phenomena as friction or backlash. Several parameters of the load such as inertia may change during the operation, and several external disturbances may affect the motion.

The **torque transmission** system consists of shafts (that may be flexible) or belts, gears, and clutches and is also described by nonlinear differential or algebraic equations with some unknown parameters.

The **electric machine** may be an induction motor (IM), a direct current motor (DCM), a permanent magnet synchronous motor (PMSM), a brushless direct current motor (BLDCM), or any other rotational or linear electric motor. The electrical energy and the mechanical energy are interconverted via the magnetic field. Therefore, the motor model may be represented by partial differential equations (PDEs). Although such models are commonly used for electrical machines design and analysis, simplified models represented by nonlinear ODEs with unknown parameters are used for control purposes. Some of these parameters, such as winding resistance, may change during the drive operation.

The **power electronic converter** can be thought of as a network of semiconductor power switches. Most of the existing power switches are fully controlled; that is, they can be turned on and off by appropriate voltage or current signals.

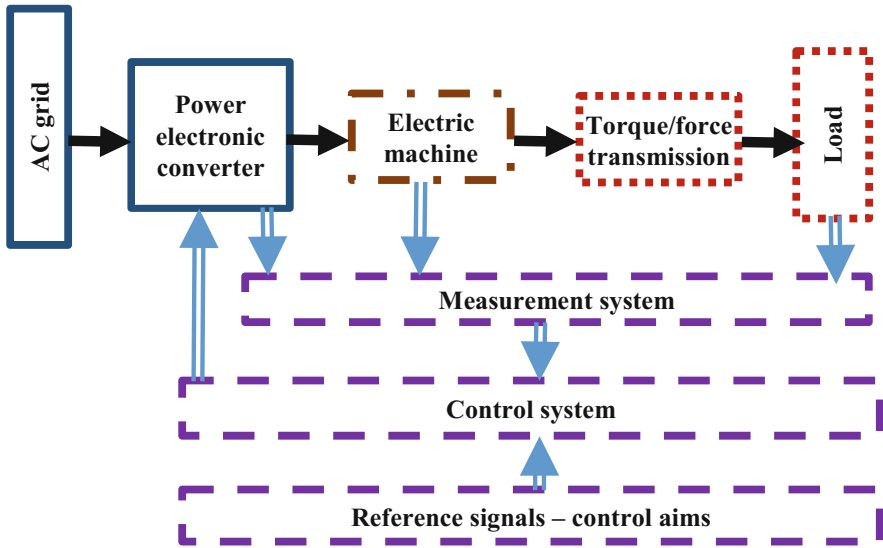


Fig. 1 Electrical drive operating in motoring mode. *Solid arrows* represent the flow of energy; *double arrows*—the flow of information; *dotted lines*—mechanical parts of the system; *solid lines*—electrical parts; and *dashed lines*—measurement and control subsystem

These signals are generated by the control system as a result of control algorithm operation. The same technology is applied to any type of power electronic converters—not only applied in electric drives but also generally used for electric power conditioning. Therefore, many types of AC to DC, DC to AC, AC to AC, or DC to DC converters may be controlled by similar methods. An electronic power converter may be modeled as a variable structure, periodic systems, whose state is determined by logic signals.

The **measurement system** is in charge of collecting all necessary information from the plant. Theoretically, all mechanical and electrical quantities (position, velocity, currents, and voltages) may be measured. However, measurement of all or some mechanical signals is impossible in many systems, and this originates the so-called sensorless control techniques, i.e., application of observers.

The **control system** is nowadays a digital controller. Electric drives or power converters are fast plants, and therefore, the increasing availability of low-cost, high-performance microcontrollers, digital signal processors, and FPGA devices was the main factor opening new possibilities of implementing sophisticated control laws, taking care of nonlinearities and parameter variations by means of adaptive control, self-analysis, and autotuning strategies. Another important advantage is the flexibility inherent in any digital controller, which allows the designer to modify the control strategy, or even to totally reprogram it, without the need for significant hardware modifications.

The **reference signals** provide information about the control aims. Usually, the drive is supposed to track a smooth position or speed reference or to stabilize constant position or speed in the presence of external disturbances. Sometimes, the drive works as a part of a complex system; for example, a valve drive is used to control pressure or flow rate. Numerous constraints of input, output, or state variables must be considered to assure proper drive operation.

This short characteristic of the drive components shown in Fig. 1 explains why electric drive control is a complex, multidisciplinary problem involving modern control techniques. The scenery becomes even more complex if we consider that any industrial plant degrades as a result of aging and wear, which decreases performance reliability and increases the probability of various faults. Therefore, fault modeling, fault-diagnosis, and fault-tolerant control are important problems concerning electric drives and power converter control. Several faults of a drive may be classified as follows:

- power converter faults: open or short circuit semiconductor faults and DC bus faults;
- motor faults: windings short circuit or disconnection, insulation deterioration, broken rotor bars or rings, and mechanical faults (eccentricity and bearing faults); and
- electrical and mechanical sensor faults: total failure, noise, offset, and periodic miss operation.

The goal of the fault-tolerant system is to recognize the fault occurrence, to continue stable operation of the drive maintaining its partial functionality, or to stop it safely.

Considering any possible model complexity, any possible disturbance, any parameter variation, and any fault possibility will lead to an unsolvable task. The researcher has to distinguish the main problem of the particular application, to propose a suitable model (as simple as possible and as accurate as necessary), and to derive an efficient, implementable control algorithm. That is why in some chapters of this book the authors concentrate on the mechanical part of the system, assuming that the torque is the control input, and in others, they discuss mainly the converter control, but in any case, the final control is tested in a complex, real drive or a power conversion system.

This book presents some new solutions for motion control, fault-tolerant control, and power converter control. Well-known control methods such as field-oriented control (FOC) or direct torque control (DTC) are referred as a starting point for modifications or are used for comparison. Among numerous control theories used to solve particular problems are as follows: nonlinear control, robust control, adaptive control, Lyapunov techniques, observer design, model predictive control, neural control, sliding mode control, signal filtration and processing, fault-diagnosis, and fault-tolerant control.

The important social and technological impact of the problems discussed in the book is obvious. Motion control, drives, and power conditioning are ubiquitous in industry, transport, removable energy systems, household appliances, and many

other branches of modern life. The effective use of electrical energy is a key technique for achieving global energy efficiency, and power electronics technologies that can convert electrical power into the optimum characteristics for each application are essential to this way of development. Power electronics systems are key components for building a sustainable society by reducing CO₂ emissions. The use of effective adjustable-speed drives improves energy efficiency, and the power conditioning systems provide stable connections to the power grid for unstable DC or AC electric power generated from removable sources such as solar or wind energy.

The material of this book is presented in the following three parts: electric drives and motion control (Chapters “[Sensorless Control of Polyphase Induction Machines](#)”–“[Selected Methods for a Robust Control of Direct Drive with a Multi-mass Mechanical Load](#)”), electric drives and fault-tolerant control (Chapters “[Fault-Diagnosis and Fault-Tolerant-Control in Industrial Processes and Electrical Drives](#)”–“[Detection and Compensation of Transistor and Position Sensors Faults in PM BLDCM Drives](#)”), and design and control of power converters (Chapters “[Advanced Control Methods of DC/AC and AC/DC Power Converters—Look-Up Table and Predictive Algorithms](#)”–“[Switched Capacitor-Based Power Electronic Converter—Optimization of High Frequency Resonant Circuit Components](#)”).

In Chapter “[Sensorless Control of Polyphase Induction Machines](#),” new solutions for control of polyphase machines are presented. The nonlinear transformation of state variables is proposed. Nonlinear decoupling is used to generate a linear model of the virtual machine, and a simple torque controller can be applied. Details of the torque and flux control are explained. This chapter is written by the founder of the so-called multiscalar approach to induction motor control.

In Chapter “[Adaptive Position Tracking with Hard Constraints—Barrier Lyapunov Functions Approach](#),” a servo control with unknown system parameters and constraints imposed on the maximal tracking error is considered. The barrier Lyapunov function approach is applied to assure the preservation of hard constraints in any condition. The system’s performance is examined for three methods of controller design based on quadratic Lyapunov functions; on barrier Lyapunov functions if only position constraints are imposed; and on barrier Lyapunov functions if both position and velocity constraints are present. The tuning rules are discussed, and several experiments demonstrating features of the proposed control and the influence of the parameters are presented. This chapter forms a kind of monographic tutorial on the application of barrier Lyapunov functions.

Next two chapters discuss control problems resulting from a complicated mechanical structure of the plant. In Chapter “[Predictive Position Control of a Two-Mass System with an Induction Motor in a Wide Range of Speed Changes](#),” model predictive control (MPC) of the shaft position is applied to an induction motor (IM) coupled to a load machine through a long, flexible shaft. Contrary to the classical cascade structure with independent position and speed control loops, a common MPC controller, which regulates those two variables, is designed. An additional fuzzy block, allowing adaptation of MPC parameters, is successfully used.

Chapter “[Selected Methods for a Robust Control of Direct Drive with a Multi-mass Mechanical Load](#)” is also devoted to drives with complex mechanical structure, i.e., with a non-stiff connection between motor and driven mechanism and with a variable moment of inertia. As it is difficult to damp high resonance frequencies by the control system, an original solution is proposed, which is based on damping of the highest resonance frequencies by a specially selected and tuned filter, leaving damping of the lowest frequencies for the control system. The identification method is presented, and robust notch filters are tuned for the whole range of the parameter variability. Two robust control methods are proposed: one based on an adaptive neural speed controller with the resilient backpropagation (RPROP) learning algorithm and other using terminal sliding mode control for systems with delays and unmodeled dynamics.

The next part of this book is devoted to fault identification and fault-tolerant control of electric drives, including a power electronic converter and a motor. Exhaustive discussion of general methods applied in the fault-diagnosis and fault-tolerant control is presented in Chapter “[Fault-Diagnosis and Fault-Tolerant-Control in Industrial Processes and Electrical Drives.](#)” The data-driven methods and model-based schemes are addressed, and the main fault-detection and fault-diagnosis methods for control systems are characterized. Fault-tolerant-control methods, using passive and active concepts, are described and evaluated. All the methods are discussed from the point of view of electric drives.

In Chapter “[IGBT Open-Circuit Fault Diagnostic Methods for SVM-VSI Vector-Controlled Induction Motor Drives,](#)” a two-level three-phase voltage inverter fed induction motor drive is considered and IGBTs open-circuit faults diagnostic methods based on voltage and flux vector hodographs analysis are presented and validated for induction motor drives with direct torque control and direct rotor field-oriented control strategies.

Speed and current sensor fault-tolerant control of the induction motor drive are presented in Chapter “[Speed and Current Sensor Fault-Tolerant-Control of the Induction Motor Drive.](#)” Several active algorithms are discussed, and their advantages and disadvantages are demonstrated. The fault-detection time and the safety of the drive operation are compared.

Chapter “[Stator Faults Monitoring and Detection in Vector Controlled Induction Motor Drives—Comparative Study](#)” deals with the stator winding fault detection in the induction motor drives working in the closed speed control loops, with the direct field-oriented control—DFOC or with the direct torque control—DTC. The analysis of the characteristic components of the stator currents spectra, as well as the control signals of the DFOC structure, is used for diagnostic purposes.

New methods of detection and compensation of transistor and position sensors faults in permanent magnet brushless direct current motor drives are presented in Chapter “[Detection and Compensation of Transistor and Position Sensors Faults in PM BLDCM Drives.](#)” Simple diagnostic and localization methods to identify a faulty part of the drive system are proposed using the analysis of the waveforms and FFT spectra of the stator currents and hodographs of the stator current space vector in the stationary reference frame. The post-fault control has been analyzed as well,

and it enables the drive system to continue its operation despite the diagnosed faults.

Finally, the last part of this book presents new solutions and advanced control methods of power converters used in electrical drives and power transmission systems. It starts with a monographic Chapter “[Advanced Control Methods of DC/AC and AC/DC Power Converters—Look-Up Table and Predictive Algorithms](#)”, devoted to a modern look-up table and predictive control methods of three-phase power electronic converters. The authors consider voltage source converters in two- and three-level configurations as well as a two-level current source rectifier. Some of the methods concern DC/AC inverter fed induction and PMSM motors, and the others are dedicated to the control of the AC/DC rectifier working as an active front end of an AC/DC/AC converter. The authors focus on the methods with a nonlinear look-up table and predictive control due to their excellent dynamic properties (limited only by the physical parameters of controlled systems such as the value of the DC voltage, grid inductance, or AC motor leakage inductance). Moreover, nonlinear methods, especially the predictive ones, provide very good quality of control in steady states, i.e., lack of active and reactive power steady-state error in AC/DC converters or torque error—in the case of DC/AC converters.

Subsequent chapters describe innovative solutions determined by the converter topology and applied switching components. The active power filter based on dual converter topology is presented in Chapter “[Active Power Filter Based on a Dual Converter Topology](#).” The voltage-controlled current source (VCCS), a fundamental component of such a filter, is based on two converters connected in parallel. The advantage of this arrangement is the potential for accurate mapping of the VCCS output current in the reference signal. Thanks to the continuous manner of the operation of the auxiliary converter pulse modulation components in the current, the total harmonic distortion (THD) is minimized. Therefore, it is expected that energy transmission loss can be reduced.

In Chapter “[AC/DC/AC Converter with Power Electronics Current Modulator Used in DC Circuit for Renewable Energy Systems](#),” the structures of the main circuit and control system of a power electronic AC/DC/AC converter, dedicated to high power systems, working as a coupling between the energy grid and a water turbine with an electric machine, are described. In aiming to ensure the high efficiency of this system, input and output converters with sinusoidal current were implemented. The input AC/DC converter is based on a diode rectifier with a power electronics current modulator in the DC circuit, while the output circuit is based on a transistor inverter. Maximum power point tracking algorithm is elaborated and used to control the DC/DC converter.

Chapter “[Power Electronics Inverter with a Modified Sigma-Delta Modulator and an Output Stage Based on GaN E-HEMTs](#)” presents a new control method of power electronic inverter, based on a modified sigma-delta modulator (SDM) approach. The proposed modulator includes a comparator with dynamic hysteresis instead of a latched comparator, which is typically used in single-bit SDMs. Thanks to this feature, the resolution of the SDM output bit stream is, theoretically, unlimited. As a result, the value of the THD of an inverter output

voltage (or current) is much lower than that of a typical SDM solution. The control system is simpler than in the case of a conventional inverter. Due to the very high frequency of an SDM output bit stream, in a power stage of the inverter, the gallium-nitride (GaN)-based E-HEMTs (enhancement mode high-speed mobility transistors) are implemented.

In Chapter “[FC + TCR-type Symmetrical Follow-Up Compensator of the Fundamental Harmonic Reactive Power—Analysis and Experiment](#),” application of thyristors as switching components is considered. This chapter presents results of analyses, simulations, and experiments concerning the so-called symmetrical follow-up compensator of the fundamental harmonic reactive power in which a three-phase bridge rectifier with two additional thyristors (6T + 2T) was used as the adjustable inductive component. Proper selection and application of the appropriately developed thyristor controlling algorithm enables current flow outside supply source phases in those instants of time when output voltages of the star rectifiers have instantaneous negative values. This effect in minimization of rms and the reactive power component of the fundamental harmonic of source currents. To obtain a lower content of harmonics in the power grid current, it has been proposed to couple a 5th and 3rd harmonics filter on the converter.

The last Chapter “[Switched Capacitor-Based Power Electronic Converter—Optimization of High Frequency Resonant Circuit Components](#)” concerns the important problem of optimization of converters components selection. The volume of resonant circuit components in a special electronic converter called switched capacitor voltage multiplier (SCVM) is optimized. The SCVM is derived from chip-scale technology, but can effectively operate as a power electronic converter in a zero-current switching mode when recharging of switched capacitors occurs in a resonant circuit supported by an inductance. Selection of the passive LC components is not strictly determined and depends on the optimization strategy, according to volume, efficiency, or cost of the converter. Optimization of the volume of LC components is limited by the energy transfer ability via switched capacitors, thus by the rated power of the converter and switching frequency. Depending on the LC values the converter operates in some specific states which determine the efficiency of the converter and voltage stress on semiconductor switches and diodes. All these issues are analyzed in the context of optimization of the resonant circuit components’ value.

Each chapter presented in the book is self-consistent and may be readied separately. It contains a necessary background, theoretical analysis of the problem, derivation of the proposed solution, and the results of simulations or experiments demonstrating the features of the applied approach.

Jacek Kabziński

Part I
Electric Drives and Motion Control

Sensorless Control of Polyphase Induction Machines

Zbigniew Krzeminski

Abstract The basics of transformations of polyphase systems into orthogonal systems are explained. Vector models of induction machines in orthogonal planes are analysed and multiscalar models for rotor flux and main flux together with stator current are presented. A speed observer based on an extended model of the induction machine for selected variables is applied in the control system for the induction machine. On the basis of the model developed for a three phase machine, a multiscalar model for a five phase machine is presented. The control system acts on the basis of the model for the first sequence of phases achieving speed control. The model for the second sequence of phases is used to synchronize the fluxes in orthogonal planes. Near trapezoidal flux distribution in the air gap is achieved independently of the machine load. All variables used in the control system are estimated using the speed observer for the first sequence and the Luenberger observer for the second sequence. The properties of the control systems are explained using examples of transients generated by simulations.

Keywords Polyphase machine · Induction machine · Multiscalar model · Observer · Control system

1 Introduction

Three phase induction machines are widely used in variable speed drives because of the low cost and the good properties resulting from the application of inverters with control systems. In the case of the drive with an induction motor, a polyphase machine may be more economical than the usual three phase machine [1–3]. For example the inverter for a five phase machine consists of five legs. However the switching elements are rated on a lower current than for three legs of the same

Z. Krzeminski (✉)

Faculty of Electrical and Control Engineering, Gdansk University
of Technology, Gdansk, Poland
e-mail: zbigniew.krzeminski@pg.gda.pl

power which have the same cost. Additional costs are caused by drivers for transistors and current sensors for five phase systems. On the other hand, it is possible to achieve higher torque from a five phase motor than from a three phase motor in the same frame [4]. As a result the representative cost of the drive may be the same for three and five phases.

Control of polyphase machines is based on the Fortescue transformation of variables defined in a phase system into variables defined in an orthogonal system [5]. In the case of a three phase machine the variables defined in the orthogonal system are transformed to dq coordinates aligned with the rotor flux vector. Decoupling and application of PI controllers for variables determined in field oriented coordinates is a well-known method for controlling the induction motor. A drawback of field oriented control is that flux control is coupled with rotor speed and torque control when the rotor flux is changing. The other well-known method for the induction machine is direct torque control. In fact this method is based on control of amplitude of the stator flux vector and the angle between the stator and rotor flux vector without using an exact mathematical model.

Both of these methods for the control of the induction machine variables are inconvenient in the case of polyphase machines. The torque of a polyphase machine is the sum of torques generated in at least two virtual machines. This gives rise to coupling between virtual machines and complicates the otherwise well-known, simple control methods for the induction machine.

Using a rotating frame of references oriented with the rotor flux vector for variables in an orthogonal system is complicated because the angular velocity of the third harmonic of the flux depends on the generated torque. The q components of the stator current vector in virtual machines are difficult to calculate [6].

The coupling between the torques generated in virtual machines complicates the use of the direct torque control method.

The nonlinear transformation of variables proposed in [7] for three phase machines can be applied to polyphase machines. The variables of virtual machines arising from the application of the Fortescue transformation are nonlinearly transformed to multiscalar model variables. Nonlinear decoupling is used to generate a linear model of the virtual machine and a simple torque controller can be applied. The torque of the virtual machine is one of the multiscalar model variables and can be controlled without the need for complicated calculations. Details of the torque and flux control are explained in this work.

2 Transformation of Phase Variables to Orthogonal Coordinates

Control of AC electric machines is based on the transformation of phase variables to orthogonal coordinates. While transformation is commonly used, explanation and interpretation are not readily available in the current literature. Control of

polyphase machines is possible if the proper interpretation of transformation is applied and the properties of the machine models are determined in orthogonal planes. For polyphase machines a modified Fortescue transformation is an appropriate approach. In its general form the modified Fortescue transformation is as follows [5]:

$$\mathbf{x}_n = x_{\alpha n} + jx_{\beta n} = C_n \sum_{k=1}^m x_k(t) e^{j\frac{2\pi n}{m}(k-1)}, \quad (1)$$

where $x_k(t)$ is a phase variable, \mathbf{x}_n is a transformed complex variable, $x_{\alpha n}$, $x_{\beta n}$ are real and imaginary components of the transformed complex variable, m is the number of phases and n is number of transformed variables, where:

- $n = 0, 1, 2, \dots, \frac{m-1}{2}$ for odd numbers of phases,
- $n = 0, 1, 2, \dots, \frac{m-1}{2}, \frac{m}{2}$ for even numbers of phases,
- and C_n is the scale coefficient equal to

$$C_n = \begin{cases} \sqrt{\frac{2}{m}} & \text{for } \mathbf{x}_n \neq \mathbf{x}_{\alpha n} \\ \sqrt{\frac{1}{m}} & \text{for } \mathbf{x}_n = \mathbf{x}_{\alpha n} \end{cases}, \quad (2)$$

assuming transformation with invariant power.

Further analysis will be made on the assumption that the number of phases of induction machine is odd.

Inverse transformation has the following form:

$$x_k = \sum_{n=0}^q C_n \mathbf{x}_n e^{-j\frac{2\pi n}{m}(k-1)}, \quad (3)$$

where $k = 1, 2, \dots, m$.

Transformation (1) converts a polyphase system into orthogonal coordinates. The coordinate number 0 only has a real part. The complex variables of numbers 1, ..., n are presented on independent planes using rotating space vectors. For even numbers of phases the complex variable number 0 only has a real part and in this case is called 0^- while the coordinate number $\frac{m}{2}$ is called 0^+ .

Transformation of the phase variables to an orthogonal system may be written in matrix form:

$$\mathbf{x}_{\text{ort}} = \mathbf{A} \mathbf{x}_{\text{ph}}, \quad (4)$$

where \mathbf{x}_{ort} is the vector of transformed variables, \mathbf{x}_{ph} is the vector of phase variables and \mathbf{A} is the transformation matrix defined by (1).

Matrices of coefficients, for example inductances, appearing in the differential equations forming the mathematical model of the induction motor for phase variables, are transformed into matrices of coefficients in differential equations for variables in orthogonal coordinates in accordance with the following equation:

$$\mathbf{L}_{\text{ort}} = \mathbf{A}\mathbf{L}_{\text{ph}}\mathbf{A}^{-1} \quad (5)$$

where \mathbf{L}_{ph} is the matrix of phase inductances and \mathbf{L}_{orth} is the matrix of inductances for orthogonal systems.

Stator windings of the induction motor may be constructed as distributed or concentrated. In the case of a distributed winding of a polyphase machine a matrix of self and mutual inductances has the following form:

$$\mathbf{L}_{\text{ph}} = \begin{bmatrix} L & L \cos\left(\frac{2\pi}{m}\right) & \dots & L \cos\left(\frac{2(m-1)\pi}{m}\right) \\ L \cos\left(\frac{2(m-1)\pi}{m}\right) & L & L \cos\left(\frac{2\pi}{m}\right) & \dots \\ \dots & \dots & \dots & \dots \\ L \cos\left(\frac{2\pi}{m}\right) & \dots & L \cos\left(\frac{2(m-1)\pi}{m}\right) & L \end{bmatrix} \quad (6)$$

where L is the phase inductance.

Independently of the number of phases, the matrix defined by (6) is transformed into matrix \mathbf{L}_{orth} with the following form:

$$\mathbf{L}_{\text{orth}} = \begin{bmatrix} 0 & 0 & 0 & 0 & \dots & 0 \\ 0 & \frac{m}{2}L & 0 & 0 & \dots & 0 \\ 0 & 0 & \frac{m}{2}L & 0 & \dots & 0 \\ 0 & 0 & 0 & 0 & \dots & 0 \\ \dots & \dots & \dots & \dots & \dots & \dots \\ 0 & 0 & 0 & 0 & \dots & 0 \end{bmatrix}. \quad (7)$$

The form of the matrix (7) means that in the case of distributed windings of the stator the inductances appear only for the first complex plane. The inductances for other planes are equal to 0 and the variables appearing in these planes do not take part in the transformation of energy.

In the case of concentrated windings the magnetic field of one phase is distributed along the air gap with rectangular shape described by the following equation:

$$L_{\text{ph}} = L \cos(\rho) + \frac{1}{3}L \cos(3\rho) + \frac{1}{5}L \cos(5\rho) + \frac{1}{7}L \cos(7\rho) + \dots, \quad (8)$$

where ρ is the angle along the air gap and L_{ph} is the inductance of the phase containing fundamental and higher harmonics.

Only harmonics with numbers less than the number of phases should be taken into account. Harmonics of higher numbers than m should not be used because of the inaccuracy of high frequency fields generated in m -phase system.

Application of L_{ph} , defined by (8), instead of L in the elements of the matrix (6), leads, after transformation, to the orthogonal system of the following form:

$$\mathbf{L}_{orth} = \begin{bmatrix} 0 & 0 & 0 & 0 & 0 & \dots & 0 & 0 \\ 0 & L_1 & 0 & 0 & & \dots & 0 & 0 \\ 0 & 0 & L_1 & 0 & & \dots & 0 & 0 \\ 0 & 0 & 0 & L_2 & & \dots & 0 & 0 \\ 0 & 0 & 0 & 0 & L_2 & \dots & 0 & 0 \\ \dots & \dots & \dots & \dots & \dots & \dots & \dots & \dots \\ 0 & 0 & 0 & 0 & 0 & \dots & L_N & 0 \\ 0 & 0 & 0 & 0 & 0 & \dots & 0 & L_N \end{bmatrix}, \quad (9)$$

where L_1, L_2, \dots, L_N are the inductances appearing in the complex planes of consecutive numbers and

$$N = \begin{cases} \frac{m-1}{2} & \text{for odd number of phases} \\ \frac{m}{2} - 1 & \text{for even number of phases} \end{cases}. \quad (10)$$

The fundamental harmonic of the inductance always appears in the first complex plane. Higher harmonics result in inductances in planes defined by the following equation:

$$n = \begin{cases} v & \text{if } v \leq N \\ m - v & \text{if } v > N \end{cases}, \quad (11)$$

where n is number of complex plane and v is the number of inductance harmonics.

Harmonics of inductance forms virtual poles, the number of which is connected to the number of fundamental poles by the equation:

$$p_v = vp, \quad (12)$$

where p is the number of fundamental poles and p_v is the number of poles for the harmonic of number v .

The rotor of the induction motor rotates in the stator with angular velocity ω_r which differs from the synchronous angular velocity by the slip. Mechanical angular velocity of the rotor in the virtual machine has the same value as the angular velocity in the physical stator. On the other hand the electrical angular velocity of the rotor in the virtual machine is given by:

$$\omega_{r(v)} = z_{(v)} v \omega_{r(1)}, \quad (13)$$

where $\omega_{r(v)}$ is the electrical angular velocity for inductance harmonic v in the complex plane n and z is the sign of the angular velocity.

If $v = n$ the rotor rotation in the virtual machine for the n -th complex plane is in the same direction as the plane for the fundamental harmonic and $z_{(v)} = 1$.

If $v \neq n$ the rotor rotation in the virtual machine for the n -th complex plane is in the opposite direction to the plane for the fundamental harmonic and $z_{(v)} = -1$.

The principle of operation of a polyphase machine is based on the generation of a rotating field in natural phase system. Such a rotating field is the sum of the harmonic fields generated in all phases. The conventional approach is the generation of the fundamental harmonic in the three phase machine. In machines with more than four phases higher harmonic fields may be additionally generated to deform the field distribution in the air gap. Using higher harmonics has some benefits such as increased torque from the same dimensions of the machine or increased efficiency.

The number of time harmonics appearing in complex planes is as follows:

$$v^{(n)} = k_v m + d_v n, \quad (k_v = 0, 1, 2, \dots; d_v = 1, -1), \quad (14)$$

where $v^{(n)}$ is the number of harmonics appearing in plane n , k_v are consecutive numbers and d_v is equal 1 if the space vector of the harmonic rotates on the plane in a counter clockwise direction, and is equal to -1 if the space vector of the harmonic rotates in a clockwise direction.

For example for a five phase machine the number of time harmonics rotating in the counter clockwise direction in the first plane are 1, 6, 11, etc., and in the clockwise direction are 4, 9, 14 etc. Rotating in the counter clockwise direction in the second plane are 2, 7, 12 etc., in the clockwise direction are 3, 8, 13 etc. Of course, all harmonics may rotate in the opposite direction as mentioned above.

For the same reason as for harmonics of inductances, only one time harmonic should be generated in one complex plane.

Higher time harmonics of the currents generated in the stator give rise to virtual machines with higher harmonics of the field formed by the same numbers of harmonics of inductances. In general, the fields of virtual and fundamental machines may rotate with arbitrary angular velocity. In certain cases amplitude of the fundamental harmonic or selected higher harmonics may be equal to zero.

The space vector of the variable on each complex plane is formed from the α and β components of the phase vector whose position is determined by the angle:

$$\alpha = \frac{2\pi n}{m} (k - 1), \quad (15)$$

where α is the position of the phase.

The positions of phases and the phase components of the space vector are shown in Fig. 1 and Fig. 2.

Each virtual machine determined in each complex plane should be controlled taking into account the general properties of the induction machines, mainly efficiency. In any case, all virtual machines have the same rotor which connects them into one system of energy conversion. This means that if in one machine field and torque are generated, then in the remaining machines fields and torques cannot be arbitrary.

Higher harmonics appearing in physical phases should be synchronized with the fundamental one. The generation of higher harmonics in the phases results in the appearance of harmonics in the complex planes. The synchronized angular velocity of the field in the virtual machine defined in the complex plane of number n is connected with the angular velocity of the fundamental harmonic by the expression:

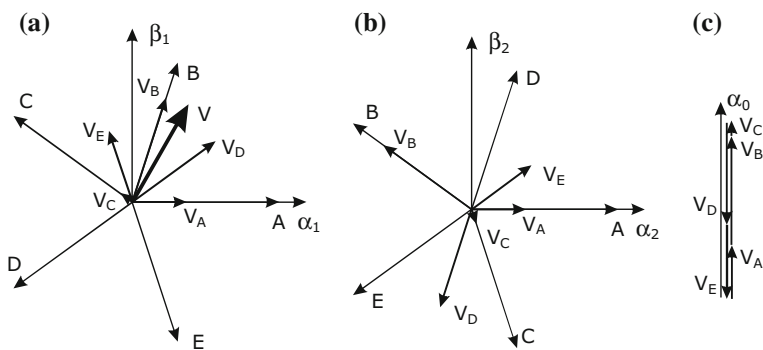


Fig. 1 a Components of the voltage vector defined in the first plane b components of the same vector in the second plane and c in the zero plane

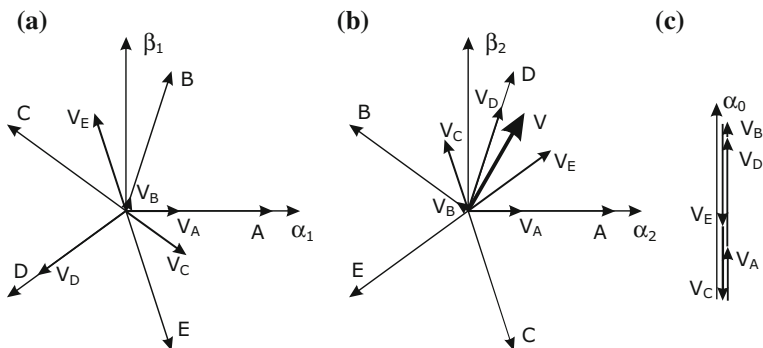


Fig. 2 a Components of the voltage vector defined in the second plane shown in the first plane b Components of the voltage vector defined in the second plane shown in the second plane and c the same voltage vector in the zero plane

$$\omega_{fv} = v\omega_f, \quad (16)$$

where ω_{fv} is the angular velocity of the field for v harmonic and ω_f is the angular velocity of the field for the fundamental harmonic.

The transformed variable number 0 does not take part in conversion of electrical energy into mechanical energy and will be not considered further. However there are some technical applications where the zero component plays an important role. For example disturbances caused by supplying the machine from an inverter create problems which may be solved taking the parameters of the resultant circuit with the transformed coordinate number 0.

3 Vector Models of a Polyphase Induction Machine

A vector model of the induction machine is a useful basis for further development. There are various possibilities in selecting the variables for the machine model but the stator current and the rotor flux vectors are usually used in the differential equations as follows:

$$\frac{d\mathbf{i}_{s(n)}}{d\tau} = a_{1(n)}\mathbf{i}_{s(n)} + a_{2(n)}\boldsymbol{\Psi}_{r(n)} + ja_{3(n)}\omega_{r(n)}\boldsymbol{\Psi}_{r(n)} + a_{4(n)}\mathbf{u}_{s(n)}, \quad (17)$$

$$\frac{d\boldsymbol{\Psi}_{r(n)}}{d\tau} = a_{5(n)}\mathbf{i}_{s(n)} + a_{6(n)}\boldsymbol{\Psi}_{r(n)} + j\omega_{r(n)}\boldsymbol{\Psi}_{r(n)}, \quad (18)$$

$$\frac{d\omega_{r(n)}}{d\tau} = \frac{1}{J} \left(\sum_{n=1}^N T_{e(n)} - T_L \right), \quad (19)$$

where \mathbf{u}_s , \mathbf{i}_s and $\boldsymbol{\Psi}_r$ are the vectors of stator voltage, stator current and rotor flux, $T_{e(n)}$ is torque generated in n -th plane, T_L is the load torque, τ is time, $\omega_{r(n)}$ is the angular velocity of the rotor in the n -th plane and a_1, \dots, a_6 are coefficients defined as:

$$\begin{aligned} a_{1(n)} &= -\frac{R_{s(n)}L_{r(n)}^2 + R_{r(n)}L_{m(n)}^2}{w_{(n)}L_{r(n)}}; & a_{2(n)} &= \frac{R_{r(n)}L_{m(n)}}{w_{(n)}L_{r(n)}}; & a_{3(n)} &= -\frac{L_{m(n)}}{w_{(n)}}; \\ a_{4(n)} &= \frac{L_{r(n)}}{w_{(n)}}; & a_{5(n)} &= \frac{R_{r(n)}L_{m(n)}}{L_{r(n)}}; & a_{6(n)} &= -\frac{R_{r(n)}}{L_{r(n)}}; & w_{(n)} &= L_{s(n)}L_{r(n)} - L_{m(n)}^2; \end{aligned}$$

where $R_{s(n)}$ and $R_{r(n)}$ are the stator and rotor resistances and $L_{s(n)}$, $L_{r(n)}$, $L_{m(n)}$ are the stator, rotor and mutual inductances defined in n -th plane. $n = 1, \dots, N$ is, as

denoted already, the number of complex planes and the equations are written for each n . All variables and parameters are expressed in per unit system.

The resistances and inductances in particular phases depend on the construction of machine.

The torque generated by the virtual machine in n -th plane is expressed as:

$$T_{e(n)} = \frac{L_{m(n)}}{L_{r(n)}} \left(\Psi_{r\alpha(n)} i_{s\beta(n)} - \Psi_{r\beta(n)} i_{s\alpha(n)} \right). \quad (20)$$

The angular velocity of the rotor in the n -th complex plane is defined by (16).

Equations (17)–(19) are used in the synthesis of control systems based on the orientation of coordinates with respect to the rotor flux vector. In polyphase machines the fluxes generated in the air gap by the magnetizing current should be synchronized. Application of the vector model with the rotor flux vector selected as a state variable is not suitable for synchronizing fields. Some corrections of angles needs to be introduced to the positions of the rotor flux vectors to ensure proper synchronization of the main flux vectors. These angles depend on torques generated by the virtual machines defined in complex planes. This complicates the control system and is not convenient.

A more suitable model for the control of a polyphase machine is obtained if the main flux vector is selected as the state variable instead of the rotor flux vector. The main flux vector depends on the stator current and the rotor flux vectors as follows:

$$\Psi_{m(n)} = \frac{L_{\sigma r(n)} L_{m(n)}}{L_{r(n)}} i_{s(n)} + \frac{L_{m(n)}}{L_{r(n)}} \Psi_{r(n)}, \quad (21)$$

where $\Psi_{m(n)}$ is the main flux vector in plane n .

For the stator current and main flux vectors the following equations are obtained:

$$\frac{d\mathbf{i}_{s(n)}}{d\tau} = d_{1(n)} \mathbf{i}_{s(n)} + d_{2(n)} \Psi_{m(n)} + j d_{3(n)} \omega_{r(n)} \mathbf{i}_{s(n)} + j d_{4(n)} \omega_{r(n)} \Psi_{m(n)} + d_{5(n)} \mathbf{u}_{s(n)}, \quad (22)$$

$$\frac{d\Psi_{m(n)}}{d\tau} = d_{6(n)} \mathbf{i}_{s(n)} + d_{7(n)} \Psi_{m(n)} + j d_{8(n)} \omega_{r(n)} \mathbf{i}_{s(n)} + j d_{9(n)} \omega_{r(n)} \Psi_{m(n)} + d_{10(n)} \mathbf{u}_{s(n)}, \quad (23)$$

where

$$\begin{aligned} d_{1(n)} &= -\frac{R_{s(n)} L_{r(n)} + R_{r(n)} L_{m(n)}}{W_{(n)}}; & d_{2(n)} &= \frac{R_{r(n)}}{W_{(n)}}; \\ d_{3(n)} &= \frac{L_{\sigma r(n)} L_{m(n)}}{W_{(n)}}; & d_{4(n)} &= -\frac{L_{r(n)}}{W_{(n)}}; & d_{5(n)} &= \frac{L_{r(n)}}{W_{(n)}}; \\ d_{6(n)} &= -\frac{L_{m(n)} (R_{s(n)} L_{\sigma r(n)} + R_{r(n)} L_{\sigma s(n)})}{W_{(n)}}; & d_{7(n)} &= -\frac{L_{\sigma s(n)} R_{r(n)}}{W_{(n)}}; \\ d_{8(n)} &= \frac{L_{\sigma s(n)} L_{\sigma r(n)} L_{m(n)}}{W_{(n)}}; & d_{9(n)} &= -\frac{L_{\sigma s(n)} L_{r(n)}}{W_{(n)}}; & d_{10(n)} &= \frac{L_{\sigma r(n)} L_{m(n)}}{W_{(n)}}. \end{aligned}$$

The machine torque is expressed as follows:

$$\mathbf{T}_{e(n)} = \Psi_{m\alpha(n)} \mathbf{i}_{s\beta(n)} - \Psi_{m\beta(n)} \mathbf{i}_{s\alpha(n)}. \quad (24)$$

Equations (22) and (23) are applied for all virtual machines and Eq. (19) remains in the same form.

It should be noted that the above models are valid only for the unsaturated machine. The machine models with saturation effect taken into account are complicated as shown in [8] and magnetizing current in one plane may influence the parameters in other planes.

4 Multiscalar Models of a Polyphase Induction Machine

Nonlinear transformation of vector components results in the multiscalar variables proposed in [7]. For each virtual machine the set of multiscalar variables obtained for stator current and rotor flux vectors has the following form:

$$x_{11(n)} = \omega_{r(n)}, \quad (25)$$

$$x_{12(n)} = \Psi_{r\alpha(n)} \mathbf{i}_{s\beta(n)} - \Psi_{r\beta(n)} \mathbf{i}_{s\alpha(n)}, \quad (26)$$

$$x_{21(n)} = \Psi_{r\alpha(n)}^2 + \Psi_{r\beta(n)}^2, \quad (27)$$

$$x_{22(n)} = \Psi_{r\alpha(n)} \mathbf{i}_{s\alpha(n)} + \Psi_{r\beta(n)} \mathbf{i}_{s\beta(n)}. \quad (28)$$

A multiscalar model of a machine has differential equations for variables (25)–(28) of the following form:

$$\frac{dx_{11(n)}}{d\tau} = \frac{1}{J_r} \sum_1^n \frac{L_{m(n)}}{L_{r(n)}} x_{12(n)} - \frac{1}{J} m_0, \quad (29)$$

$$\frac{dx_{12(n)}}{d\tau} = -\frac{1}{T_{x(n)}} x_{12(n)} - x_{11(n)} (x_{22(n)} - a_{3(n)} x_{21(n)}) + a_{4(n)} u_{1(n)}, \quad (30)$$

$$\frac{dx_{21(n)}}{d\tau} = 2a_{5(n)} x_{22(n)} + 2a_{6(n)} x_{21(n)}, \quad (31)$$

$$\frac{dx_{22(n)}}{d\tau} = -\frac{1}{T_{x(n)}} x_{22(n)} + x_{11(n)} x_{12(n)} + a_{2(n)} x_{21(n)} + a_{5(n)} i_s^2(n) + a_{4(n)} u_{2(n)}, \quad (32)$$

where

$$i_{s(n)}^2 = \frac{x_{12(n)}^2 + x_{22(n)}^2}{x_{21(n)}}, \quad (33)$$

$$T_{x(n)} = \frac{w_{\sigma(n)}}{R_{r(n)}L_{s(n)} + R_{s(n)}L_{r(n)}}, \quad (34)$$

$$u_{1(n)} = \Psi_{r\alpha(n)}u_{s\beta(n)} - \Psi_{r\beta(n)}u_{s\alpha(n)}, \quad (35)$$

$$u_{2(n)} = \Psi_{r\alpha(n)}u_{s\alpha(n)} + \Psi_{r\beta(n)}u_{s\beta(n)}. \quad (36)$$

The control variables $u_{1(n)}$ and $u_{2(n)}$ are determined in the control system and the voltage vector components for control of an inverter are calculated as follows:

$$u_{s\alpha(n)} = \frac{\Psi_{r\alpha(n)}u_{2(n)} - \Psi_{r\beta(n)}u_{1(n)}}{\Psi_{r(n)}^2}, \quad (37)$$

$$u_{s\beta(n)} = \frac{\Psi_{r\alpha(n)}u_{1(n)} + \Psi_{r\alpha(n)}u_{2(n)}}{\Psi_{r(n)}^2}. \quad (38)$$

The multiscalar model of the induction machine contains a few additional terms in Eqs. (30) and (32) compared to the vector model. On the other hand Eq. (31) is simpler than general equation for the vector model. The multiscalar variables are scalars and vector notation is not applicable. This may look inconvenient but no additional transformations are needed for synthesis of the control system. In particular the controllers in the system based on the multiscalar model act on stationary variables. Nonlinear transformation leading to multiscalar variables is similar to the rotation of the coordinate system but the result does not depend on the frames of reference in which vectors are defined.

The main benefit of the multiscalar model is the selection of the variable proportional to the machine torque. The control system obtained after application of linearization by feedback is simple and the rotor torque is controlled independently of changes in the rotor flux.

Nonlinear feedback of the form:

$$u_{1(n)} = \frac{1}{a_{4(n)}} \left(\frac{1}{T_{x(n)}} m_{12(n)} + x_{11(n)} (x_{22(n)} - a_{3(n)} x_{21(n)}) \right), \quad (39)$$

$$u_{2(n)} = \frac{1}{a_{4(n)}} \left(\frac{1}{T_{x(n)}} m_{2(n)} - x_{11(n)} x_{12(n)} - a_{2(n)} x_{21(n)} - a_{5(n)} i_{s(n)}^2 \right).$$

applied to Eqs. (29)–(32) results in the following linear equations:

$$\frac{dx_{11(n)}}{d\tau} = \frac{1}{J} \sum_1^n \frac{L_{m(n)}}{L_{r(n)}} x_{12(n)} - \frac{1}{J} m_0, \quad (40)$$

$$\frac{dx_{12(n)}}{d\tau} = \frac{1}{T_{v(n)}} (-x_{12(n)} + m_{1(n)}), \quad (41)$$

$$\frac{dx_{21(n)}}{d\tau} = 2a_{5(n)}x_{22(n)} + 2a_{6(n)}x_{21(n)}, \quad (42)$$

$$\frac{dx_{22(n)}}{d\tau} = \frac{1}{T_{v(n)}} (-x_{22(n)} + m_{2(n)}) \quad (43)$$

for all n .

Equations (40) and (41) describe the mechanical subsystem and consist of the common equation for the rotor speed for all virtual machines and separate equations for the torques. This causes some difficulties in the synthesis of control system. Only the torque of one virtual machine can be set by a controller of the rotor angular velocity. The other torques are lower and, of course, act on the rotor angular velocity. In any case, the variables which are controlled by the other torques are angular velocities of the rotor flux vector. In this way the rotor fluxes appearing in the remaining virtual machines may be synchronized with the rotor flux of the main virtual machine.

Equations (42) and (43) forms models of linearized electromagnetic subsystems.

The rotor flux vectors are controlled indirectly, which means that that the control variable acts on the derivative of variable x_{22} and this variable acts on the derivative of the square of the rotor flux. This is a property of the induction motor model based on stator current and rotor flux. In particular, the model of the ‘squirrel cage’ induction motor contains one differential equation for the rotor flux without a control variable on the right hand side.

It is possible to change the induction model variables using liner transformation. Different vectors may be used in the mathematical model even without a known physical meaning. If the rotor flux vector does not appear in the motor model, the control variable is present on the right hand side of all of the differential equations.

The selection of certain vectors for developing models of the induction motor may results in particular benefits. The induction motor model with a main flux vector is especially convenient because this makes it possible to control the saturation of main magnetic path.

The application of nonlinear transformation to the stator current and main flux vectors makes it possible to define following variables:

$$q_{11(n)} = \omega_{r(n)}, \quad (44)$$

$$q_{12(n)} = \Psi_{m\alpha(n)} i_{s\beta(n)} - \Psi_{m\beta(n)} i_{s\alpha(n)}, \quad (45)$$

$$q_{21(n)} = \psi_{m\alpha(n)}^2 + \psi_{m\beta(n)}^2, \quad (46)$$

$$q_{22(n)} = \psi_{m\alpha(n)} i_{s\alpha(n)} + \psi_{m\beta(n)} i_{s\beta(n)}. \quad (47)$$

The differential equation for the multiscalar model variables defined by formulae (44)–(47) are as follows:

$$\frac{dq_{11(1)}}{d\tau} = \frac{1}{J} \sum_1^n q_{12(n)} - \frac{1}{J} m_0, \quad (48)$$

$$\begin{aligned} \frac{dq_{12(n)}}{d\tau} = & -\frac{1}{T_{m1(n)}} q_{12(n)} - d_{8(n)} i_s^2 q_{11(n)} \\ & + \left(d_{11(n)} q_{22(n)} + d_{4(n)} q_{21(n)} \right) q_{11(n)} + d_{12(n)} u_{12(n)}. \end{aligned} \quad (49)$$

$$\frac{dq_{21(n)}}{d\tau} = 2d_{7(n)} q_{21(n)} + 2d_{6(n)} q_{22(n)} + 2d_{10(n)} u_{21(n)}. \quad (50)$$

$$\frac{dq_{22(n)}}{d\tau} = -\frac{1}{T_{m1(n)}} z_{22(n)} + d_{2(n)} q_{21(n)} + d_{6(n)} i_s^2 - d_{11(n)} q_{12(n)} q_{11(n)} + d_{12(n)} u_{22(n)}, \quad (51)$$

where

$$i_s^2 = \frac{q_{12(n)}^2 + q_{22(n)}^2}{q_{21(n)}}, \quad (52)$$

$$T_{m1(n)} = \frac{w(n)}{R_{s(n)} L_r(n) + R_r(n) L_s(n)}, \quad (53)$$

$$d_{11(n)} = \frac{L_{\sigma r(n)} L_m(n) + L_{\sigma s(n)} L_r(n)}{w(n)}, \quad (54)$$

$$d_{12(n)} = \frac{L_m(n)}{w(n)}. \quad (55)$$

$$u_{12(n)} = \psi_{r\alpha(n)} u_{s\beta(n)} - \psi_{r\beta(n)} u_{s\alpha(n)}, \quad (56)$$

$$u_{21(n)} = \psi_{m\alpha(n)} u_{s\alpha(n)} + \psi_{m\beta(n)} u_{s\beta(n)}, \quad (57)$$

$$u_{22(n)} = \psi_{r\alpha(n)} u_{s\alpha(n)} + \psi_{r\beta(n)} u_{s\beta(n)}. \quad (58)$$

The control variables $u_{12(n)}$ and $u_{21(n)}$ are determined in the control system and the voltage vector components for the control of an inverter are calculated as follows:

$$\mathbf{u}_{s\alpha(n)} = \frac{\Psi_{r\alpha(n)}\mathbf{u}_{21(n)} - \Psi_{m\beta(n)}\mathbf{u}_{12(n)}}{w}, \quad (59)$$

$$\mathbf{u}_{s\beta(n)} = \frac{\Psi_{m\alpha(n)}\mathbf{u}_{12(n)} + \Psi_{r\beta(n)}\mathbf{u}_{21(n)}}{w}, \quad (60)$$

$$w = \Psi_{r\alpha(n)}\Psi_{m\alpha(n)} + \Psi_{r\beta(n)}\Psi_{m\beta(n)}.$$

The model described in (48)–(51) differs from the model obtained for the stator current vector and rotor flux vector because control variables appear in three equations for the virtual machine. There are two stator vector components so only two output variables can be controlled using these variables. If two electromagnetic variables are controlled the third one remains uncontrolled. However it simple to verify that if two controlled variables are stabilized, the third is stable, too.

The multiscalar model for the stator current and main flux vectors is similar to the vector model used in the so-called direct torque control method. From comparison of the differential equation for the machine torque in the multiscalar model and differential equation for the torque in the known field oriented and direct torque control it is clear that the torque is controlled by acting on its derivative through the control variable. All of these systems are equivalent taking a way of control of the machine torque into consideration.

It is convenient to control the square of the main flux and the motor torque. The main flux may be directly controlled as the control variable acts on its derivative. Such a system is referred to here as direct flux control.

Nonlinear feedback applied to Eqs. (49) and (50) has the following form:

$$\mathbf{u}_{12(n)} = \frac{1}{d_{12(n)}} \left(\frac{1}{T_{m1(n)}} m_{12(n)} + d_{8(n)} i_{s(n)}^2 q_{11(n)} - (d_{11(n)} q_{22(n)} + d_{4(n)} q_{21(n)}) q_{11(n)} \right), \quad (61)$$

$$\mathbf{u}_{21(n)} = \frac{1}{d_{10(n)}} \left(-d_{7(n)} m_{21(n)} - d_{6(n)} q_{22(n)} \right). \quad (62)$$

After application of (61) and (62) the linearized model has the following form:

$$\frac{dq_{11(1)}}{d\tau} = \frac{1}{J} \sum_1^n q_{12(n)} - \frac{1}{J} m_0, \quad (63)$$

$$\frac{dq_{12(n)}}{d\tau} = \frac{1}{T_{m1(n)}} \left(-q_{12(n)} + m_{12(n)} \right), \quad (64)$$

$$\frac{dq_{21(n)}}{d\tau} = -2d_{7(n)} \left(-q_{21(n)} + m_{21(n)} \right), \quad (65)$$

for all n .

Similarly to the system based on stator current and rotor flux vectors, Eqs. (63) and (64) describe the mechanical subsystem consisting of the common equation for the rotor speed for all virtual machines and separate equations for the torques. The main fluxes appearing in the virtual machines in the planes of number higher than one may be synchronized with the main flux of the main virtual machine.

Equation (65) forms the linearized model of electromechanical subsystems.

5 Speed Observer for the Virtual Induction Machine in the First Plane

Sensorless control of the polyphase induction machine is the same as for the three phase machine and means that no mechanical sensor is applied. Instead, the rotor angular velocity is estimated in different way. One of the most precise methods of estimation is a speed observer as proposed in [9]. The structure of the speed observer is based on an extended model of the induction machine. Extension means the addition of variables determined as components of the rotor flux vector multiplied by the rotor angular velocity. In this way the number of variables is greater than minimum needed to determine the model in state space. The extended model requires the introduction of stabilizing feedback. Together with the error of the stator current, the extended model forms the speed observer for the virtual machine in the first plane as follows:

$$\dot{\hat{\mathbf{x}}}_{(1)} = \mathbf{A}_{(1)}\hat{\mathbf{x}}_{(1)} + \mathbf{B}_{(1)}\mathbf{u}_{(1)} + \mathbf{K}_{(1)}\mathbf{e}_{(1)}, \quad (66)$$

where $\hat{\mathbf{x}}$ denotes observer variables and

$$\hat{\mathbf{x}}_{(1)}^T = \left[\hat{\mathbf{i}}_{s(1)} \quad \hat{\Psi}_{r(1)} \quad \hat{\zeta}_{(1)} \right], \quad (67)$$

$$\mathbf{u}_{(1)} = \mathbf{u}_{s(1)}, \quad (68)$$

$$\mathbf{e}_{(1)}^T = \left[\tilde{\mathbf{i}}_{s(1)} \quad \tilde{\zeta}_{(1)} \right], \quad (69)$$

$$\mathbf{A}_{(1)} = \begin{bmatrix} a_{1(1)} & a_{2(1)} & ja_{3(n)} \\ a_{5(1)} & a_{6(1)} & j \\ a_{5(1)}\hat{\omega}_{r(1)} & \Delta\hat{\omega}_{r(1)}/\Delta\tau & a_{6(1)} + j\hat{\omega}_{r(1)} \end{bmatrix} \quad (70)$$

$$\mathbf{B}_{(1)} = \begin{bmatrix} a_{4(1)} \\ 0 \\ 0 \end{bmatrix}, \quad (71)$$

$$\mathbf{K}_{(1)+} = \begin{bmatrix} \mathbf{k}_{11(1)} + \mathbf{jk}_{12(1)} & \mathbf{k}_{13(1)} + \mathbf{jk}_{14(1)} \\ \mathbf{k}_{21(1)} + \mathbf{jk}_{22(1)} & \mathbf{k}_{23(1)} + \mathbf{jk}_{24(1)} \\ \mathbf{k}_{31(1)} + \mathbf{jk}_{32(1)} & \mathbf{k}_{33(1)} + \mathbf{jk}_{34(1)} \end{bmatrix}. \quad (72)$$

Detailed analysis of the properties of the speed observer shows that if the matrix (72) is defined for the positive direction of the rotor speed, the matrix for the negative direction has the form:

$$\mathbf{K}_{(1)-} = \begin{bmatrix} \mathbf{k}_{11(1)} - \mathbf{jk}_{12(1)} & -\mathbf{k}_{13(1)} + \mathbf{jk}_{14(1)} \\ \mathbf{k}_{21(1)} - \mathbf{jk}_{22(1)} & -\mathbf{k}_{23(1)} + \mathbf{jk}_{24(1)} \\ -\mathbf{k}_{31(1)} + \mathbf{jk}_{32(1)} & \mathbf{k}_{33(1)} - \mathbf{jk}_{34(1)} \end{bmatrix}. \quad (73)$$

The error of stator current vector is defined as:

$$\tilde{\mathbf{i}}_{s(1)} = \mathbf{i}_{s(1)} - \hat{\mathbf{i}}_{s(1)}. \quad (74)$$

The variable ζ is introduced to extend the model of the induction machine and is defined as follows:

$$\zeta_{(1)} = \omega_{r(1)} \Psi_{r(1)}. \quad (75)$$

The dependence (75) should appear in the extended model which means that the following stabilizing error has to be reduced to zero by the action of the observer:

$$\tilde{\zeta}_{f(1)} = \hat{\omega}_{r(1)} \hat{\Psi}_{r(1)} - \hat{\zeta}_{(1)}, \quad (76)$$

where $\tilde{\zeta}_{f(1)}$ is the full stabilizing error of the variable $\hat{\zeta}_{(1)}$.

Simple transformations lead to the following expression for the rotor speed taking the components of the vectors in (75) into account:

$$\omega_{r(1)} = \left(\Psi_{r\alpha(1)} \zeta_{\alpha(1)} + \Psi_{r\beta(1)} \zeta_{\beta(1)} \right) / \Psi_{r(1)}^2. \quad (77)$$

Equation (77) is used for the calculation of the rotor speed in the observer of the variables of the first machine.

The square of the rotor flux amplitude appearing in (77) changes slowly and this variable may be included in the gain coefficients of the speed observer. Taking into account (76) and (77) the stabilizing error takes the simplified form:

$$\tilde{\zeta}_{(1)} = -\mathbf{j} \hat{\Psi}_{r(1)} \left(\hat{\zeta}_{\alpha(1)} \hat{\Psi}_{r\beta(1)} - \hat{\zeta}_{\beta(1)} \hat{\Psi}_{r\alpha(1)} \right), \quad (78)$$

where $\tilde{\zeta}_{(1)}$ is a simplified error of variable $\hat{\zeta}_{(1)}$.

The expression in parenthesis in (78) represents the value of the vector product of $\hat{\zeta}_{(1)}$ and the rotor flux vector. In stable steady states this vector product is equal to 0 which results from the definition expressed in (75).

The derivative of the estimated rotor speed $\hat{\omega}_{r(1)}$ in the observer equations is replaced by an approximated value calculated by a digital method. It may be omitted for slow transients of the rotor speed.

It is possible to design the speed observer for other vectors such as the stator current and the main flux. Such an observer will contain terms defined by (75) and the rotor speed will be calculated in the same way. No special benefits result from using any other pair of vectors.

The case where the mutual inductance is calculated on the basis of estimated variables requires a mention. The main flux or magnetizing current vector is very convenient for calculating the main inductance in such a case. The other method is based on using the virtual flux vector with the same direction as the main flux and arbitrary vectors may be selected as state variables for the machine.

The rotor angular velocity may be estimated in the first plane but situations can arise where the rotor flux is equal to zero in this plane. In such cases the rotor angular velocity may be estimated for the virtual machine in another plane.

6 The Luenberger Observer for the Virtual Induction Machine with Known Rotor Speed

The rotor speed estimated in the first plane may be used in the other planes taking the relationship (13) into account. For a known rotor speed the Luenberger observer may be used to estimate the variables of the virtual machine. The differential equations of the Luenberger observer for the stator current and rotor flux vectors are as follows:

$$\dot{\hat{\mathbf{x}}}_{(n)} = \mathbf{A}_{(n)}\hat{\mathbf{x}}_{(n)} + \mathbf{B}_{(n)}\mathbf{u}_{(n)} + \mathbf{K}_{(n)}\mathbf{e}_{(n)}, \quad (79)$$

where

$$\hat{\mathbf{x}}_{(n)}^T = \left[\hat{\mathbf{i}}_{s(n)} \quad \hat{\boldsymbol{\psi}}_{r(n)} \right], \quad (80)$$

$$\mathbf{u}_{(n)} = \mathbf{u}_{s(n)}$$

$$\mathbf{e}_{(n)} = \mathbf{i}_{s(n)} - \hat{\mathbf{i}}_{s(n)}, \quad (81)$$

$$\mathbf{A}_{(n)} = \begin{bmatrix} \mathbf{a}_{1(n)} & \mathbf{a}_{2(n)} + \mathbf{j}\mathbf{a}_{3(n)}\omega_{r(n)} \\ \mathbf{a}_{5(n)} & \mathbf{a}_{6(n)} + \mathbf{j}\omega_{r(n)} \end{bmatrix} \quad (82)$$

$$\mathbf{B} = \begin{bmatrix} \mathbf{a}_{4(n)} \\ \mathbf{0} \end{bmatrix}, \quad (83)$$

$$\mathbf{K}_{(n)} = \begin{bmatrix} \mathbf{k}_{11(n)} + \mathbf{j}\mathbf{k}_{12(n)} \\ \mathbf{k}_{21(n)} + \mathbf{j}\mathbf{k}_{22(n)} \end{bmatrix} \quad (84)$$

The angular velocity of the rotor in (82) and (84) is defined by (13).

7 The Control System for the Polyphase Machine

The control system for the polyphase machine is presented in Figs. 3 and 4. The amplitude of the rotor or main flux vector for the virtual machine in the first plane is stabilized on a value dependent on the actual optimum condition. The rotor or main flux vectors in the remaining planes are synchronized with the flux vector in the first plane. All of the planes are independent and the variables defined in them may be controlled arbitrarily. The virtual machine in the first plane generates the fundamental harmonic of the field in phase coordinates and the virtual machines in the remaining planes generate higher harmonics. The number of harmonics is defined by (14). To synchronize the harmonics generated in planes of number greater than 1 with the fundamental harmonic, the actual fundamental position angle is multiplied by the number of the synchronized harmonic and reduced to the range $0-2\pi$. The angle of the same frequency as the synchronized harmonic is obtained as a reference for a phase locked loop.

Synchronization of harmonics differs for each kind of multiscalar model. The angular velocity of the rotor flux expressed in terms of multiscalar variables is as follows:

$$\omega_{\psi r(n)} = \omega_{r(n)} + \frac{R_{r(n)}L_{m(n)}x_{12(n)}}{L_{r(n)}x_{21(n)}}. \quad (85)$$

The angular velocity of the rotor flux vector depends on the value of the variable $x_{12(n)}$ which is proportional to the torque of the virtual machine. The machine torque is controlled by the variable $u_{12(n)}$ or by the variable $m_{12(n)}$ if nonlinear

Fig. 3 Control system for variables of the virtual machine

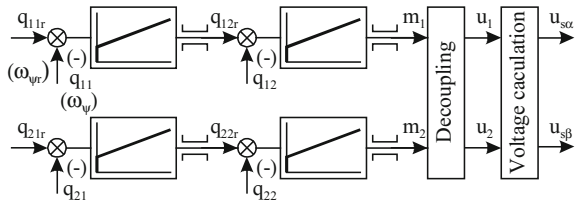
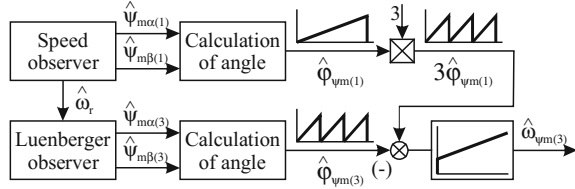


Fig. 4 Synchronizing system for angles of main fluxes determined in virtual machines



feedback is applied. In this way some inertia appears in the control loop for angular velocity of the rotor flux.

Synchronization of the main flux is realized in a different way. The angular velocity of the main flux vector is expressed as follows:

$$\omega_{\psi m(n)} = \omega_{r(n)} + \frac{(\mathbf{R}_{s(n)}\mathbf{L}_{\sigma r(n)} + \mathbf{L}_{\sigma s(n)}\mathbf{R}_{r(n)})\mathbf{q}_{12(n)} + \mathbf{L}_{\sigma r(n)}\mathbf{u}_{12(n)}}{\mathbf{L}_{\sigma s(n)}\left(-\mathbf{L}_{\sigma r(n)}\mathbf{q}_{22(n)} + \frac{\mathbf{L}_{r(n)}}{\mathbf{L}_{m(n)}}\mathbf{q}_{21(n)}\right)}. \quad (86)$$

The variable $\mathbf{u}_{12(n)}$ changes the angular velocity of the main flux vector directly. After the application of nonlinear feedback the variable $\mathbf{m}_{12(n)}$ may be used to directly set the main flux angular velocity. Some correction of the variable $\mathbf{m}_{12(n)}$ is needed in transient states. In this way the synchronization of the main flux is faster than that of the rotor flux vector.

The value of torques generated by virtual machines are strongly dependent if the harmonics of the flux vector are synchronized with the fundamental. A slip of flux in the virtual machine defined as:

$$\mathbf{s}(n) = \omega_{\psi r(n)} - \omega_{r(n)} \quad (87)$$

depends on the slip in the first plane machine as follows:

$$\mathbf{s}(n) = \mathbf{z}_{(v)}\mathbf{v}_{(n)}\mathbf{s}_{(1)}, \quad (88)$$

which results in the dependence:

$$\mathbf{x}_{12(n)} = \mathbf{z}_{(v)}\mathbf{v} \frac{\mathbf{R}_{r(1)}\mathbf{L}_{r(n)}\mathbf{L}_{m(1)}\mathbf{x}_{12(1)}\mathbf{x}_{21(n)}}{\mathbf{R}_{r(n)}\mathbf{L}_{r(1)}\mathbf{L}_{m(n)}\mathbf{x}_{21(1)}}, \quad (89)$$

where $\mathbf{z}_{(v)}$ and \mathbf{v} are as defined in (13).

For the main flux vector selected for control, the dependence (89) takes the form:

$$\mathbf{q}_{12(n)} = \mathbf{z}_{(v)}\mathbf{v} \frac{\mathbf{R}_{r(1)}\mathbf{q}_{12(n)}\mathbf{x}_{21(n)}}{\mathbf{R}_{r(n)}\mathbf{x}_{21(1)}}, \quad (90)$$

where

$$x_{21(n)} = \frac{L_{r(n)}^2}{L_{m(n)}^2} q_{21(n)} - 2 \frac{L_{\sigma r(n)} L_{r(n)}}{L_{m(n)}} q_{22(n)} + L_{\sigma r(n)}^2 i_{s(n)}^2. \quad (91)$$

The control system for a polyphase machine with concentrated windings makes it possible to generate a near trapezoidal flux shape by adding the third harmonic to the fundamental. The amplitude of the third harmonic should be equal 0.15 and the fundamental harmonic is increased to 1.15 to achieve the condition that the instantaneous value of the flux vector is not greater than 1. The square of the third harmonic of the flux is equal to 0.0225 and the resulting coefficient in (89) and (90) is equal about 0.06, depending on the machine parameters.

A higher value of the fundamental harmonic of flux gives rise to a lower active current component for the same torque. On the other hand, the torque generated by the machine with the third harmonic added is equal about 115 % of the torque generated by fundamental only for the same rated rms value of stator current. Additionally, taking the rotor current into consideration, the losses in the machine with the third harmonic of flux added are lower than in the machine with the fundamental only.

Control of the machine torque for systems based on the rotor and main flux are similar to each other. Nonlinear feedback is applied and the variables are controlled using PI controllers for each virtual machine. If the square of the rotor flux is a controlled variable then the control system has the structure presented in Fig. 3. The control system for the main flux does not contain an inner loop and only one PI controller is applied. The variable m_2 is obtained directly from the output of the main flux controller.

The rotor angular velocity is controlled only for the virtual machine determined in the first plane. For the virtual machine determined in the second plane the angular velocity of the main flux is controlled.

A PI controller is used to control the rotor angular velocity and from its output the reference value for the motor torque is obtained. From the set value of the motor torque the reference value for the variable $x_{12(1)}$ is calculated. The reference value of $x_{12(1)}$ without the third harmonic is given by:

$$x_{12(1)}^* = \frac{L_{r(1)}}{L_{m(1)}} T_e^*, \quad (92)$$

where * denotes the reference value.

If the third harmonic is taken into account, the value $x_{12(1)}^*$ is calculated as follows:

$$x_{12(1)}^* = C T_e^*, \quad (93)$$

where the coefficient C is given by:

$$C = \frac{R_{r(n)}L_{r(1)}^2 x_{21(1)}}{R_{r(n)}L_{r(1)}L_{m(n)}x_{21(1)} + z_{(v)}vR_{r(1)}L_{r(n)}L_{m(1)}x_{21(n)}} \quad (94)$$

and depends on the motor parameters and value of the third flux harmonic.

In the first plane only part of torque is generated. The remaining part is generated in plane n with a small inertia resulting from the action of the synchronization loop.

The synchronization loop for the third harmonic in the case of a five phase machine is shown in Fig. 4. The rotor flux vector components obtained from the speed observer for the first plane and the Luenberger observer for the second plane are used to calculate the angles of the fundamental and third components of the flux. The angle of the fundamental is multiplied by -3 and reduced to the range $0-2\pi$. The PI controller controls the angle between the positions of the fundamental and third harmonic.

8 Simulation Results

Properties of the drive with five phase machine are shown on the base of simulation results presented in Figs. 5 and 6. Ideal voltage source has been assumed and control system based on the variables available from the model has been applied. Such idealized system makes it possible to show all transients clearly.

All variables are expressed in per unit system. Base values for the voltage and current are equal to:

$$U_b = \sqrt{5}U_N; I_b = \sqrt{5}I_N,$$

where U_N, I_N are rated phase voltage and current.

The base values for remaining variables are defined similarly.

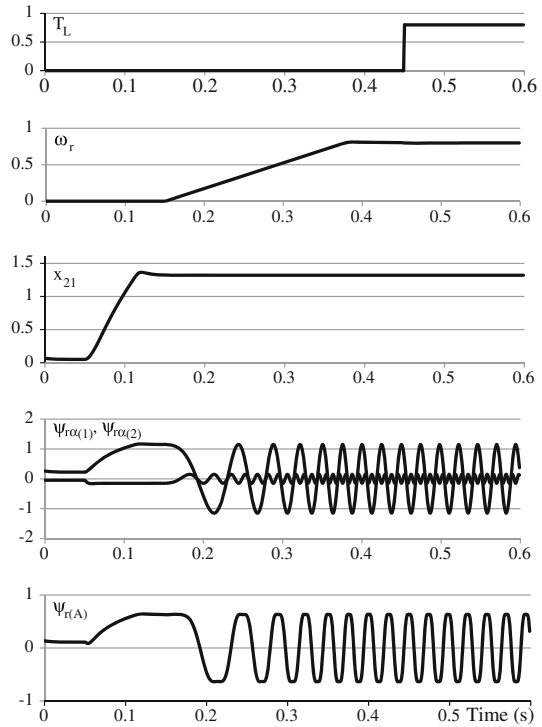
The amplitude of the rated phase variable is equal to 0.63. Taking into account the power invariance transformation of variables provides the value of rated phase amplitude equal to 1.

The transient shown in Figs. 5 and 6 consists of consecutive starting, short time without load and final interval of work with load. The transient of load torque is shown in Fig. 5.

In the simulation investigation at first the machine is excited with the speed near zero. The reference value of variable x_{21} is set to 1.32 and after time less than 50 ms this variable is stabilized.

The rotor speed is next set on 0.8. The fluxes $\psi_{r\alpha(1)}$ and $\psi_{r\alpha(2)}$ are synchronized as can be seen in Fig. 5. The amplitude of the flux $\psi_{r\alpha(1)}$ is equal to 1.15. At the same time the amplitude of phase rotor flux ψ_{rA} is equal to 0.63 which is rated value. This means that the rotor flux is reduced in the phase system and do not

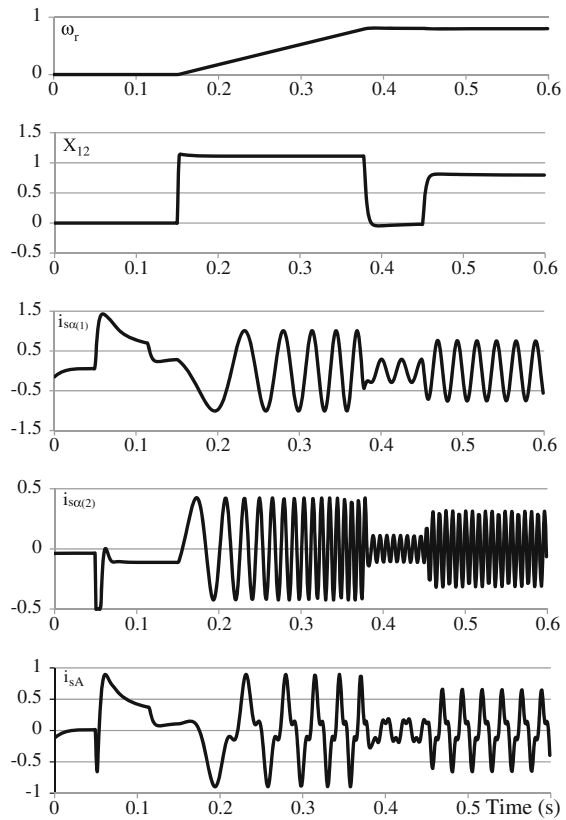
Fig. 5 Transients of the speed and the electromagnetic variables during starting and loading of machine



exceeds the rated value. The rotor flux is always kept on the value which assures operation of the machine in an unsaturated region.

As it can be seen in the last chart of Fig. 6 the third harmonic of the stator current appearing in the second plane has a different angle in relation to the fundamental in consecutive time intervals. The angle depends on the machine torque. For the very low torque only the magnetizing current components appear in the phase current. For high values of the torque the active current is great and the third harmonic generated in second plane is synchronized with such the angle that the maximum value of the phase current is increased. This effect should be taken into account in designing of the machine and inverter.

Fig. 6 Transients of the speed and the electromagnetic variables during starting and loading of machine



9 Summary

Properly controlled polyphase machines with concentrated windings generate higher torques than three phase machines designed in the same frame. This is obtained by applying the third harmonic of the field in the air gap, making the virtual machines more efficient. The explanation of the operation principle of the polyphase machine based on Fortescue transformation makes it possible to determine the virtual machines which are separately controlled. The variables of the virtual machines are expressed in orthogonal coordinates. The planes obtained after the Fortescue transformation are stationary in relation to the stator phase system. The rotor speed is the common variable for virtual machines. The rotor speed in a virtual machine in which a high harmonic of the field is generated is equal to the rotor speed in a machine with the fundamental multiplied by the number of harmonic. The sign of the rotor speed in the virtual machine is determined on the basis of analysis of possibility to generate harmonic in the sequence of phases in accordance with (13).

The variables of each virtual machine are controlled separately by synchronizing the fluxes in phase coordinates. Transformation of the variables expressed in orthogonal planes to multiscalar variables and application of nonlinear decoupling results in a simple control system.

The space variables of each virtual machine may be separately estimated using observers. The speed observer should be applied in the first plane to estimate the rotor flux vector and the rotor speed. In the remaining planes the rotor speed from the first plane may be used in the full order Luenberger observer.

Acknowledgments The work was financially supported by NCN grant no 2011/01/B/ST7.

References

1. Levi E (2008) Multiphase electric machines for variable-speed applications. *IEEE Trans Ind Electron* 55(5):1893–1909
2. Abdel-Khalik AS, Masoud MI, Williams BW (2012) Improved flux pattern with third harmonic injection for multiphase induction machines. *IEEE Trans Power Electron* 27(3):1563–1578
3. Mengoni M, Zarri L, Tani A, Parsa L, Serra G, Casadei D (2015) High-torque-density control of multiphase induction motor drives operating over a wide speed range. *IEEE Trans Ind Electron* 62(2):814–825
4. Xu H, Toliyat HA, Petersen LJ (2001) Rotor field oriented control of five-phase induction motor with the combined fundamental and third harmonic currents. In: *Proceedings of the IEEE 16th annual applied power electronics conference and exposition*, 4–8 Mar 2001, Vol 1, pp 392–398
5. Imecs M, Kelemen A (1995) Comparison between multiphase servo drives using the polyphase space-phasor theory. In: *Proceedings of PCIM'95, Nurnberg*
6. Zheng L, Fletcher JE, Williams BW, He X (2008) Dual-plane vector control of a five-phase induction machine for an improved flux pattern. *IEEE Trans Ind Electron* 55(5):1996–2005
7. Krzeminski Z (1987) Nonlinear control of induction motor. In: *10th IFAC congress on automatic control*, vol 3, pp 349–354
8. Krzeminski Z (1988) Differential equations of induction motor with nonlinear control synthesis with regard to saturation of main magnetic path. In: *Rozprawy Elektrotechniczne*, no. 1
9. Krzeminski Z, Lewicki A, Morawiec M (2010) Speed observer based on extended model of induction machine. In: *IEEE international symposium on industrial electronics*

Adaptive Position Tracking with Hard Constraints—Barrier Lyapunov Functions Approach

Jacek Kabziński, Przemysław Mosiołek and Marcin Jastrzębski

Abstract A servo control with unknown system parameters and constraints imposed on the maximal tracking error is considered. The barrier Lyapunov functions approach is applied to assure the preservation of constraints in any condition. The system's performance is examined for three methods of controller design based on: quadratic Lyapunov functions; on barrier Lyapunov functions if only position constraints are imposed; and on barrier Lyapunov functions if both position and velocity constraints are present. The tuning rules are discussed and several experiments demonstrating features of the proposed control and the influence of the parameters are presented.

Keywords Nonlinear control · Adaptive control · Servo control · Barrier Lyapunov functions

1 Introduction

Servo systems are commonly used in various branches of industrial automation and robotics. The basic aim of a servo system or a robot manipulator is to track the desired motion trajectory with sufficient precision. For numerous servo systems rigorous handling of constraints imposed on a position and/or speed during any dynamic transient is a necessary condition of safe operation. Any violation of the constraints can lead to damage or destruction of the drive system or destroy any objects that happen to be in collision with the actuator. For plentiful robot manipulators, such as medical robots, automatic welding machines, microelectromechanical systems and many others, operation inside constraints is a matter of safety. It is reasonable to assume that the desired trajectories are planned with sufficient security margins and hence rigorous constraints must be imposed on the

J. Kabziński (✉) · P. Mosiołek · M. Jastrzębski
Institute of Automatic Control, Lodz University of Technology,
Stefanowskiego 18/22, 90-924 Łódź, Poland
e-mail: jacek.kabzinski@p.lodz.pl

tracking errors. In such cases any control method that assumes the constraints are ‘soft’ and that it is possible to neglect constraints in control design and circumvent the problem through adequate control-parameter selection must be rejected.

Several approaches to control nonlinear systems with constraints were reported. Among them, the nonlinear model predictive control seems to be promising [1]. From the recent reports the diffeomorphism-based control may be mentioned [2]. As the literature on nonlinear, constrained control is rich, it is out of the scope of this chapter to provide an exhaustive review.

Nonlinear adaptive control is widely applied to designing high-performance servo systems in the presence of unknown plant parameters. Usually the controller derivation is based on control Lyapunov functions (CLF) and backstepping techniques [3]. Quadratic Lyapunov functions (QLF) are commonly used to assure the stability of the system, but unfortunately with this approach the designer is not able to impose the hard constraints a priori and to guarantee the constraints are fulfilled during any transient conditions.

Recently, use of the so-called barrier Lyapunov functions (BLF) in control synthesis has been proposed for constraint handling in Brunovsky type systems [4], nonlinear systems in the strict feedback form [5] and with adaptive control [6, 7]. The BLF approach applies the backstepping technique and allows the system output (or all state variables) to be kept inside the predefined constraints. Although the theory of stability investigation by BLF is well established, only a few practical applications are reported [8, 9].

The aim of the presented chapter is to demonstrate the possibility of applications of BLF in servo systems design to provide a systematic description of the design procedure and to formulate some rules for the selection of the design parameters. Particular attention is given to illustrating the problem of interactions among position and velocity constraints. To present clear and compact derivation we concentrate on the simplest motion model with one degree of freedom, but generalizations to many more complex applications are straightforward.

2 Plant Model and Control Objectives

A linear servo is considered and its very simple model is described by:

$$\frac{d}{dt}x = v \quad (1)$$

$$m \frac{d}{dt}v = \varphi i - F_o, \quad (2)$$

where x , v are the forcer position and velocity, m is the forcer mass, φ represents the coefficient converting the motor current i into the thrust force and F_o is an external load force, acting against the motion. The motor current i is supplied by a PWM

inverter working in a current control mode and it is assumed that this control loop is much faster than mechanical dynamics, so the motor current i is considered as the control input. The same approach and the analogous model may be used for the rotational motors, therefore the linear motion supposition is carried out without the loss of generality.

It is assumed that the parameters $m > 0$, $\varphi > 0$, are unknown, constant or slowly varying. Although the constant φ is usually provided by the motor manufacturer, this information is not accurate. This constant may vary with the motor temperature, PWM conduction mode or, for some tubular linear motors with permanent magnets built in the inner part, it may be noticeably lower if the forcer operates near the edge of the inner part. It is assumed that the load may be modelled as a nonlinear, memoryless function of the position and the velocity and that this model may be represented as a linear combination of known nonlinear functions ζ with unknown parameters A :

$$F_o(x, v) = A^T \zeta(x, v). \quad (3)$$

Such models are natural if the load is approximated using any approximation technique: artificial neural networks, fuzzy modelling, polynomial approximation and so on. The number of unknown parameters and the approximation basis ζ may be chosen for the particular application.

Remark 1 For the sake of brevity, it is assumed that model (3) is accurate, but it is also possible to consider an inaccurate approximation with a bounded approximation error ε :

$$F_o(x, v) = A^T \zeta(x, v) + \varepsilon. \quad (4)$$

The main consequence of using model (4) or (3) is that under assumption (3) it is possible to prove the asymptotic stability of the tracking errors system. In case of the load model (4), one has to introduce a switching control component to obtain the asymptotic stability, or to accept the stability in the sense of the uniform ultimate boundedness [10].

To remove the difficulties caused by the unknown control gain φ , the motion Eq. (2) is transferred into:

$$\mu \frac{d}{dt} v = i - A_o^T \zeta(x, v), \quad (5)$$

where:

$$\mu = \frac{m}{\varphi}, \quad A_o = \frac{1}{\varphi} A. \quad (6)$$

The control objective is that the motor position has to follow a smooth, bounded reference $x_d(t)$:

$$|x_d(t)| \leq x_{max}. \quad (7)$$

It is assumed that the derivatives of the reference are bounded as well. It is required that the tracking error denoted by:

$$e_x = x_d - x \quad (8)$$

is constrained for any t by a pre-defined, rigorous inequality:

$$|e_x(t)| < \Delta_{ex}, \quad (9)$$

for any initial conditions that assure $|e_x(0)| < \Delta_{ex}$. It follows from (9) that the position trajectory will be bounded by a hard constraint:

$$|x(t)| < \Delta_x \quad \Delta_x := \Delta_{ex} + x_{max}. \quad (10)$$

3 Quadratic and Barrier Lyapunov Functions

Lyapunov stability theory will be used to construct the stabilizing control for the discussed problem. For the sake of completeness, some preliminaries are given in this section.

Definition 1 Let $V : R^n \rightarrow R$ be a continuously differentiable, proper, and positive definite function defined with respect to the nonlinear system $\dot{x} = f(x, u)$. Let us denote $\dot{V}(x, u) = V_x^T f(x, u)$. $V(x)$ is a control Lyapunov function (CLF) for the system $\dot{x} = f(x, u)$ if, for all $x \neq 0$, there exists such u that $\dot{V}(x, u) < 0$. If $V(x) = x^T P x$ for some positive definite P , it is called a quadratic Lyapunov function (QLF).

Definition 2 [5] A Barrier Lyapunov Function (BLF) is a scalar function $V(x)$, defined with respect to the system $\dot{x} = f(x)$ on an open region D containing the origin; that is continuous, positive definite, has continuous first-order partial derivatives at every point of D , has the property $V(x) \rightarrow \infty$ as x approaches the boundary of D , and satisfies condition: $\exists M, \forall t > 0 V(x(t)) < M$ along any system trajectory starting inside D .

Usually it is assumed that D is a hyper-rectangle defined by $D = \{x : |x_i| \leq \Delta_{xi}\}$.

Lemma 1 [5] Consider a smooth dynamical system $\dot{z} = f(t, x, w)$, with the state variables $z = [x, w]^T$. Let $V_i(x_i)$ be a BLF satisfying $V_i(x_i) \rightarrow \infty$ if $x_i \rightarrow \pm \Delta_{xi}$, let $Q(w)$ be a QLF. Let $V = \sum_{i=1}^{\dim(x)} V_i(x_i) + Q(w)$. If the inequality $\dot{V} = \frac{\partial V^T}{\partial z} f \leq 0$ holds anywhere in the set $S = \{(x, w) : |x_i| < \Delta_{xi}\}$, then any trajectory that fulfils the initial constraints $\forall i |x_i(0)| < \Delta_{xi}$ remains in S for any t .

In Lemma 1 the state is split into the constrained variables x and the unconstrained variables w . For each x_i a BLF is constructed, while a QLF may be used for w .

It is well known that the selected Lyapunov function heavily influences the features of the resulting closed loop system. The commonly accepted form of a single variable BLF corresponding to the interval $D = (-\Delta, \Delta)$ is a logarithmic BLF [4–7]:

$$V(x) = \frac{1}{2} \log \left(\frac{1}{1 - \left(\frac{x}{\Delta}\right)^2} \right). \quad (11)$$

The motion control with application of such BLFs was investigated in [11]. As the function (11) does not possess any parameters that may change the shape of the plot and therefore the resulting system properties, it is interesting and informative to investigate other possibilities of barrier function selection. In this chapter we consider BLFs based on trigonometric functions:

$$V(x) = \frac{\Delta}{\pi} \tan^2 \frac{\pi x}{2\Delta} \quad (12)$$

and

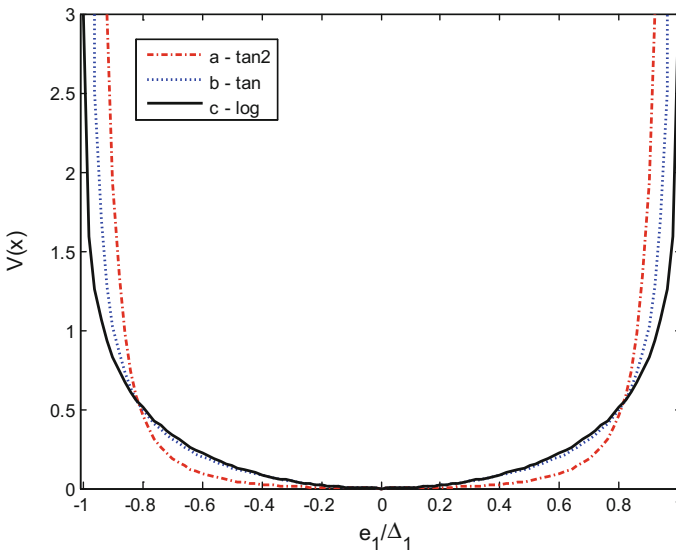


Fig. 1 Plots of **a** $\frac{\Delta}{\pi} \tan^2 \frac{\pi x}{2\Delta}$, **b** $\frac{\Delta^2}{\pi} \tan \left(\frac{\pi}{2} \left(\frac{x}{\Delta} \right)^2 \right)$, **c** $\frac{1}{2} \log \left(\frac{1}{1 - \left(\frac{x}{\Delta}\right)^2} \right)$

$$V(x) = \frac{\Delta^2}{\pi} \tan\left(\frac{\pi}{2} \left(\frac{x}{\Delta}\right)^2\right). \quad (13)$$

The main difference between these Lyapunov functions is their behaviour near the constraint boundary. As it is shown in Fig. 1, if the scaling factors are ignored, the function (12) grows up most rapidly, (11) slowly, (13) is the moderate one. Therefore in the subsequent derivation we concentrate on BLF (13).

4 QLF Control Design

Let us forget for a moment about constraints (9) and design the controller using QLFs. The adaptive back-stepping scheme [12] will be used to design the controller. The velocity will be the ‘virtual control’ for position tracking. Let us consider the error equation:

$$\dot{e}_x = \dot{x}_d - v \quad (14)$$

and the desired ‘virtual control’ trajectory v_d with the tracking error defined as:

$$e_v = v_d - v. \quad (15)$$

The desired ‘virtual control’ v_d will be designed to guarantee the required convergence of the error e_x . Considering the following QLF:

$$V_1 = \frac{1}{2} e_x^2 \quad (16)$$

allows one to conclude that the desired ‘virtual control’ v_d :

$$v_d = \dot{x}_d + k_x e_x, \quad (17)$$

where $k_x > 0$ is a design parameter, will generate the tracking error dynamics:

$$\dot{e}_x = \dot{x}_d - \dot{x}_d - k_x e_x + e_v = -k_x e_x + e_v \quad (18)$$

and:

$$\dot{V}_1 = -k_x e_x^2 + e_x e_v \quad (19)$$

and so will assure stability if $v = v_d$.

During the second stage of the backstepping procedure the velocity error e_v is considered:

$$\mu \dot{e}_v = \mu \dot{v}_d - \mu \dot{v} = \mu \dot{v}_d - i + A_o^T \xi = -i + A_1^T \xi_1, \quad (20)$$

where the new variables are defined as:

$$A_1^T = [\mu, A_o^T], \quad \xi_1^T = [\dot{v}_d, \xi^T]. \quad (21)$$

The derivative of the reference speed is given by:

$$\dot{v}_d = \ddot{x}_d + k_x(-k_x e_x + e_v), \quad (22)$$

so, fortunately, it is available for the control algorithm, and hence ξ_1 in (21) is a known function. Parameters A_1 in (21) are not known, therefore they will be replaced by adaptive parameters $\hat{A}_1^T = [\hat{\mu}, \hat{A}_o^T]$.

The control variable i will be designed using the QLF:

$$V_2 = V_1 + \frac{1}{2} \mu e_v^2 + \frac{1}{2} \tilde{A}_1^T \Gamma^{-1} \tilde{A}_1, \quad (23)$$

where:

$$\tilde{A}_1 = A_1 - \hat{A}_1 \quad (24)$$

denotes the adaptation error and positive definite Γ is the matrix of the design parameters of appropriate dimensions.

Plugging in (19) and (20) into:

$$\dot{V}_2 = \dot{V}_1 + e_v \mu \dot{e}_v + \tilde{A}_1^T \Gamma^{-1} \dot{\tilde{A}}_1 \quad (25)$$

Allows calculation of the Lyapunov function derivative:

$$\dot{V}_2 = -k_x e_x^2 + e_x e_v + e_v(-i + A_1^T \xi_1) + \tilde{A}_1^T \Gamma^{-1} \dot{\tilde{A}}_1. \quad (26)$$

The control variable i will be designed to compensate the unnecessary components in (26) and to introduce the stabilizing component, so:

$$i = e_x + \hat{A}_1^T \xi_1 + k_v e_v, \quad (27)$$

where $k_v > 0$ is a design parameter. Such control allows the tracking error to be described by:

$$\mu \dot{e}_v = -k_v e_v - e_x - \tilde{A}_1^T \xi_1 \quad (28)$$

and to represent the Lyapunov function derivative as:

$$\dot{V}_2 = -k_x e_x^2 - k_v e_v^2 + \tilde{A}_1^T \left(e_v \zeta_1 + \Gamma^{-1} \dot{\tilde{A}}_1 \right). \quad (29)$$

As $\dot{\tilde{A}}_1 = -\dot{\tilde{A}}_1$, the differential rule describing the adaptation may be used to guarantee that (29) is non-positive for any, unknown \tilde{A}_1 . The simplest way is to cancel the last component in (29) by imposing:

$$\dot{\tilde{A}}_1 = e_v \Gamma \zeta_1. \quad (30)$$

By using the LaSalle-Yoshizawa theorem [12], (29, 30) guarantees that all errors e_x, e_v, \tilde{A}_1 are uniformly bounded and e_v, e_x are regulated to zero. Since the reference x_d is bounded, x is bounded as well. The boundedness of v_d follows from the boundedness of \dot{x}_d and e_x in (17). Combining this with (27), we find that the control is also bounded. Although the boundedness of state variables is proven using QLF, it is impossible to define the constraints a priori. The maximal value of each state variable depends on the design parameters and initial conditions.

Remark 2 It is well known that similar results may be obtained with some other adaptation rules. For example:

$$\dot{\tilde{A}}_1 = \text{proj}_\rho \left(\hat{A}_1, e_v \Gamma \zeta_1 \right), \quad (31)$$

where $\text{proj}_\rho(\cdot, \cdot)$ is a projection operator assuring that $\|\cdot\| \leq \rho$ [12]. Although (31) allows the maximal values of adaptive parameters to be influenced, it will not provide a priori constraints for the state variables.

Remark 3 The design parameter k_x influences not just the values of e_x , but also the ‘virtual control’ v_d in (17), and so the error e_v in (28). Therefore, the maximal value of the current (27) depends on both design parameters k_x and k_v , although only k_v is explicitly visible in (27).

Remark 4 State variables may be constrained by the initial value of the Lyapunov function. As $\dot{V}_2 \leq 0, V_2(t) \leq V_2(0)$ along any trajectory of the system (18, 28). Therefore, $\frac{1}{2} e_x^2 \leq V_2(0)$, so $|e_x| \leq \sqrt{2V_2(0)}$. Unfortunately, $V_2(0) = \left[\frac{1}{2} e_x^2 + \frac{1}{2} \mu e_v^2 + \frac{1}{2} \tilde{A}_1^T \Gamma^{-1} \tilde{A}_1 \right]_{t=0}$ depends on the initial guess of the unknown parameters and the obtained constraint is not informative.

Although QLF design allows the influence of the error system dynamics by a proper selection of design parameters, it will not provide any tool to impose hard constraints for position or velocity a priori.

5 BLF Design with Position Constraints

To satisfy the position error constraint (9), the BLF will be applied during the first stage of back-stepping:

$$V_1 = \frac{1}{2k} \tan(ke_x^2), k = \frac{\pi}{2\Delta_{ex}^2}. \quad (32)$$

The derivative of the BLF is given by:

$$\dot{V}_1 = e_x \dot{e}_x (1 + \tan^2(ke_x^2)), \quad (33)$$

hence plugging (18) into (33) gives:

$$\dot{V}_1 = e_x (\dot{x}_d - v_d + e_v) (1 + \tan^2(ke_x^2)). \quad (34)$$

At this moment of the design procedure we have two possibilities to select the desired velocity v_d : the nonlinear v_d , which makes the Lyapunov function derivative a quadratic function of the tracking error:

$$v_d = \dot{x}_d + \frac{k_x e_x}{1 + \tan^2(ke_x^2)} \Rightarrow \dot{V}_1 = -k_x e_x^2 + e_x e_v (1 + \tan^2(ke_x^2)), \quad (35)$$

or linear v_d , as in (17), which gives nonlinear \dot{V}_1 :

$$v_d = \dot{x}_d + k_x e_x \Rightarrow \dot{V}_1 = -k_x e_x^2 (1 + \tan^2(ke_x^2)) + e_v e_x (1 + \tan^2(ke_x^2)). \quad (36)$$

Both approaches give a theoretical possibility to derive stable control systems, but it must be noticed that in case of nonlinear v_d (35) the negative gain $Q(e_x) = \frac{k_v}{1 + \tan^2(ke_x^2)}$, which is responsible for the stability of the tracking error dynamics:

$$\dot{e}_x = \dot{x}_d - v_d + e_v = -Q(e_x) e_x + e_v, \quad (37)$$

tends to zero if $|e_x| \rightarrow \Delta_{ex}$. Therefore, the linear form (36) of v_d is selected.

As the constraints are imposed only on the first state variable (the position tracking error), the control variable i will be designed using the Lyapunov function:

$$V_2 = V_1 + \frac{1}{2} \mu e_v^2 + \frac{1}{2} \tilde{A}_1^T \Gamma^{-1} \tilde{A}_1, \quad (38)$$

where V_1 defined in (32) is a BLF. Substitution of (20, 34) allows the calculation of the Lyapunov function derivative as:

$$\begin{aligned} \dot{V}_2 = & -k_x e_x^2 (1 + \tan^2(k e_x^2)) + e_v e_x (1 + \tan^2(k e_x^2)) \\ & + e_v (-i + A_1^T \xi_1) + \tilde{A}_1^T \Gamma^{-1} \dot{\tilde{A}}_1. \end{aligned} \quad (39)$$

The control variable i will be designed to compensate the unnecessary components in (39) and to introduce the stabilizing component, so:

$$i = \tilde{A}_1^T \xi_1 + e_x (1 + \tan^2(k e_x^2)) + k_v e_v, \quad (40)$$

where $k_v > 0$ is a design parameter. This control gives the velocity tracking error:

$$\mu \dot{e}_v = -k_v e_v + \tilde{A}_1^T \xi_1 - e_x (1 + \tan^2(k e_x^2)) \quad (41)$$

and the Lyapunov function derivative fulfils:

$$\dot{V}_2 = -k_x e_x^2 (1 + \tan^2(k e_x^2)) - k_v e_v^2 + \tilde{A}_1^T (e_v \xi_1 + \Gamma^{-1} \dot{\tilde{A}}_1). \quad (42)$$

Either of the adaptation rules (30) or (31) assures that:

$$\dot{V}_2 \leq -k_x e_x^2 (1 + \tan^2(k e_x^2)) - k_v e_v^2 \leq 0. \quad (43)$$

The following corollary abstracts the main features of the obtained system.

Corollary 1 Consider the closed loop system (18), (41) with any of the adaptation laws (30) or (31) and the reference position trajectory, under all assumptions formulated above. Consider any trajectory with initial conditions fulfilling $|e_x(0)| < \Delta_{ex}$. Then the following properties hold along this trajectory:

1. The variables e_x, e_v, \tilde{A}_1^T remain inside a compact set and the tracking error e_x fulfils the constraint $|e_x(t)| < \Delta_{ex}$.
2. All closed loop signals are bounded.
3. The tracking errors e_x, e_v converge to zero asymptotically.

Sketch of the proof:

1. $V_2(0)$ is bounded and as $\dot{V}_2 \leq 0$, $V_2(t) \leq V_2(0)$ along the considered trajectory. Lemma 1 yields that $|e_x(t)| < \Delta_{ex}$. Another constraint for the tracking error may be obtained noticing that $\frac{1}{2k} \tan(k e_x^2) \leq V_2(0)$ and thus $|e_x| \leq \Delta_{ex} \sqrt{\frac{2 \operatorname{atan}(2k V_2(0))}{\pi}}$.

Similarly, we may derive that $|e_v| \leq \sqrt{\frac{2}{\mu} V_2(0)}$ and $\|\tilde{A}_1\| \leq \sqrt{\frac{2 V_2(0)}{\lambda_{\min}(\Gamma^{-1})}}$, where

$\lambda_{\min}(\ast)$ denotes the smallest eigenvalue of the symmetric matrix \ast .

2. As e_x, e_v, \tilde{A}_1^T are bounded, \tilde{A}_1 are bounded also. From (17), (22), the desired ‘virtual control’ and its derivative are bounded as well. Therefore, the functions ξ_1 are bounded and from (40) the control is bounded.

3. The tracking error asymptotic convergence may be obtained by demonstrating that \ddot{V}_2 is bounded and making use of Barbalat's lemma [2].

Remark 5 The component $\tan^2(ke_x^2)$ in (40) suggests the control variable increases if $e_x \rightarrow \pm\Delta_{ex}$. Although the inequality $|e_x| < \Delta_{ex}$ is always fulfilled and the control is bounded, the maximal value of the control variable depends on all design parameters (similarly as it was explained in Remark 3) and initial conditions and requires careful investigation.

6 BLF Design with Position and Velocity Constraints

The hard constraint imposed on the position tracking may cause rapid variations of the trajectory near the constraint boundary and unacceptable velocity values. The maximal velocity may be restricted if (a) the tracking error of the desired velocity e_v will be limited by a hard constraint, and (b) the desired velocity v_d will be moderate. The constraints imposed on the velocity tracking error e_v may be preserved if a BLF will be used also during the second stage of the back-stepping design. Therefore, instead of (38), the Lyapunov function:

$$V_2 = V_1 + \frac{\mu}{2K} \tan(Ke_v^2) + \frac{1}{2} \tilde{A}_1^T \Gamma^{-1} \tilde{A}_1, \quad K = \frac{\pi}{2\Delta_{ev}^2} \quad (44)$$

will be used, where V_1 defined in (32) is a BLF and Δ_{ev} is a constraint imposed on the tracking error e_v . The Lyapunov function derivative may be represented as:

$$\dot{V}_2 = \dot{V}_1 + \mu e_v (1 + \tan^2(Ke_v^2)) \dot{e}_v + \tilde{A}_1^T \Gamma^{-1} \dot{\tilde{A}}_1 \quad (45)$$

and plugging in (36) and (20) results in:

$$\begin{aligned} \dot{V}_2 = & -k_x e_x^2 (1 + \tan^2(ke_x^2)) + e_v e_x (1 + \tan^2(ke_x^2)) \\ & + e_v (1 + \tan^2(Ke_v^2)) (-i + A_1^T \xi_1) + \tilde{A}_1^T \Gamma^{-1} \dot{\tilde{A}}_1. \end{aligned} \quad (46)$$

Once again, the control variable i will be designed to compensate the unnecessary components in (46) and to introduce the stabilizing component, so:

$$i = \hat{A}_1^T \xi_1 + e_x \frac{1 + \tan^2(ke_x^2)}{1 + \tan^2(Ke_v^2)} + k_v e_v, \quad (47)$$

where $k_v > 0$ is a design parameter. This control gives the velocity tracking error:

$$\mu \dot{e}_v = -k_v e_v + \tilde{A}_1^T \zeta_1 - e_x \frac{1 + \tan^2(ke_x^2)}{1 + \tan^2(Ke_v^2)} \quad (48)$$

and the Lyapunov function derivative fulfils:

$$\begin{aligned} \dot{V}_2 &= -k_x e_x^2 (1 + \tan^2(ke_x^2)) - k_v e_v^2 (1 + \tan^2(Ke_v^2)) \\ &\quad + \tilde{A}_1^T \left(e_v (1 + \tan^2(Ke_v^2)) \zeta_1 + \Gamma^{-1} \dot{\tilde{A}}_1 \right). \end{aligned} \quad (49)$$

As $\dot{\tilde{A}}_1 = -\dot{\hat{A}}_1$, the differential rule describing the adaptation may be used to guarantee that (49) is non-positive for any, unknown \tilde{A}_1 . The simplest way is to cancel the last component in (49) by selecting:

$$\dot{\hat{A}}_1 = e_v (1 + \tan^2(Ke_v^2)) \Gamma \zeta_1, \quad (50)$$

which results in:

$$\dot{V}_2 = -k_x e_x^2 (1 + \tan^2(ke_x^2)) - k_v e_v^2 (1 + \tan^2(Ke_v^2)). \quad (51)$$

Therefore:

$$\dot{V}_2 \leq 0 \text{ in } S = \left\{ (e_x, e_v, \tilde{A}_1) : |e_x| < \Delta_{ex}, |e_v| < \Delta_{ev} \right\}. \quad (52)$$

The following corollary summarizes the main features of the obtained system.

Corollary 2 Consider the closed loop system (18), (48) with adaptation laws (50). Assume there is a trajectory with initial conditions fulfilling $|e_x(0)| < \Delta_{ex}$, $|e_v(0)| < \Delta_{ev}$. Then the following properties hold along this trajectory:

1. The variables e_x, e_v, \tilde{A}_1^T remain inside a compact set and state variables fulfil the constraints $|e_x(t)| < \Delta_{ex}$, $|e_v(t)| < \Delta_{ev}$.
2. All closed loop signals are bounded.
3. The tracking errors e_x, e_v converge to zero asymptotically.

Sketch of the proof:

1. $V_2(0)$ is bounded and as $\dot{V}_2 \leq 0$, hence $V_2(t) < V_2(0)$ along the considered trajectory. Lemma 1 yields that $|e_x(t)| < \Delta_{ex}$ and $|e_v(t)| < \Delta_{ev}$. Another constraint for the tracking error may be obtained noticing that $\frac{1}{2k} \tan(ke_x^2) \leq V_2(0)$ and thus $|e_x| \leq \Delta_{ex} \sqrt{\frac{2 \operatorname{atan}(2kV_2(0))}{\pi}}$. Similarly, $\frac{\mu}{2k} \tan(Ke_v^2) \leq V_2(0)$ and so $|e_v| \leq \Delta_{ev} \sqrt{\frac{2 \operatorname{atan}(2kV_2(0)/\mu)}{\pi}}$. Using analogical reasoning, it can be derived that

$\tilde{A}_1 \leq \sqrt{\frac{2V_2(0)}{\lambda_{\min}(\Gamma^{-1})}}$, where $\lambda_{\min}(\ast)$ denotes the smallest eigenvalue of the symmetric matrix \ast .

2. As e_x, e_v, \tilde{A}_1^T are bounded, \hat{A}_1 are also bounded. The desired ‘virtual control’ and its derivative are bounded as well. Therefore the functions ξ_1 are bounded and from (47) the control is bounded.
3. The tracking error asymptotic convergence may be obtained by demonstrating that \dot{V}_2 is bounded and making use of the Barbalat’s lemma [2].

Remark 6 The property (52), and therefore Corollary 2 will hold with other adaptation rules, corresponding to (31), for example:

$$\dot{\hat{A}}_1 = \text{proj}_\rho \left(\hat{A}_1, e_v (1 + \tan^2(K e_v^2)) \Gamma \xi_1 \right), \quad (53)$$

where $\text{proj}_\rho(\ast, \cdot)$ is a projection operator assuring that $\|\ast\| \leq \rho$.

7 Feasibility Conditions

The set of design parameters that must be selected by the designer consists of $\Delta_{ex}, \Delta_{ev}, k_x, k_v, \Gamma$ and initial conditions for adaptive parameters \hat{A}_1 . The constraints Δ_{ex}, Δ_{ev} are imposed by the designer to limit the tracking errors, the gains k_x, k_v are responsible for tracking error convergence and Γ is in charge of the adaptation speed. The Corollary 2 is derived under the feasibility condition that ‘there exists a trajectory with initial conditions fulfilling $|e_x(0)| < \Delta_{ex}, |e_v(0)| < \Delta_{ev}$ ’. This condition implies that k_x and Δ_{ev} cannot be selected independently. As:

$$e_v(0) = \dot{x}_d(0) + k_x e_x(0) - v(0), \quad (54)$$

Δ_{ev} must be chosen according to the inequality:

$$|\dot{x}_d(0) + k_x e_x(0) - v(0)| \leq |\dot{x}_d(0) - v(0)| + k_x \Delta_{ex} < \Delta_{ev}. \quad (55)$$

Similarly, as imposing Δ_{ex} allows $|x(t)|$ to be constrained by the inequality (10), the choice of Δ_{ev} provides constraints for the maximal velocity:

$$|v(t)| \leq |\dot{x}_d(t) + k_x e_x(t)| + |e_v(t)| \leq \max_{t > 0} |\dot{x}_d(t)| + k_x \Delta_{ex} + \Delta_{ev} := \Delta_v. \quad (56)$$

The designer may be interested in constraining the gap between the desired position derivative and the actual velocity:

$$E(t) = \dot{x}_d(t) - v(t). \quad (57)$$

As:

$$|E| = |\dot{x}_d - v| = |v_d - v - k_x e_x| = |e_v - k_x e_x|, \quad (58)$$

it may be bounded by a proper choice of Δ_{ex} and Δ_{ev} :

$$|E| \leq \Delta_{ev} + k_x \Delta_{ex}. \quad (59)$$

Therefore it is evident that a larger k_x , which allows the faster convergence of the tracking error, requires greater maximal velocity and a bigger gap between the desired position derivative and the actual velocity. Also the maximal value of the control variable (47) depends on the selected design parameters and must be checked carefully before implementation in a real drive.

8 Numerical Experiments

The linear actuator with the parameters $m = 8$ kg, and $\varphi = 39$ N/A is supposed to track the desired position provided by the filtered sinusoid:

$$x_d(t) = \mathcal{L}^{-1} \left\{ \frac{1}{T^2 s^2 + 2Ts + 1} \mathcal{L}\{0.3 \sin(3t)\} \right\} \quad [\text{m}], \quad (60)$$

where $T = 0.1$ s and \mathcal{L} denotes the Laplace transform. The desired trajectory is presented in Fig. 2.

It is assumed that the actuator works against the load described by:

$$F_o(x, v) = Av^2 \text{sign}(v) + B|v| \sin(2\pi x) \quad [\text{N}]. \quad (61)$$

with unknown coefficients A and B , hence, according to (21):

$$\begin{aligned} A_1^T &= \frac{1}{\varphi} [m, A, B] \\ \zeta_1^T &= [\dot{v}_d, v^2 \text{sign}(v), |v| \sin(2\pi x)]. \end{aligned} \quad (62)$$

If it is assumed that none of the motor or load parameters are known, the initial values of adaptive parameters are selected as:

$$\widehat{A}_1^T = \frac{1}{\varphi} [0.5 \text{ m}, 0, 0], \quad (63)$$

while the real values are $\widehat{A}_1^T = \frac{1}{\varphi} [m, A, B] = \frac{1}{39} [8, 10, 6]$.

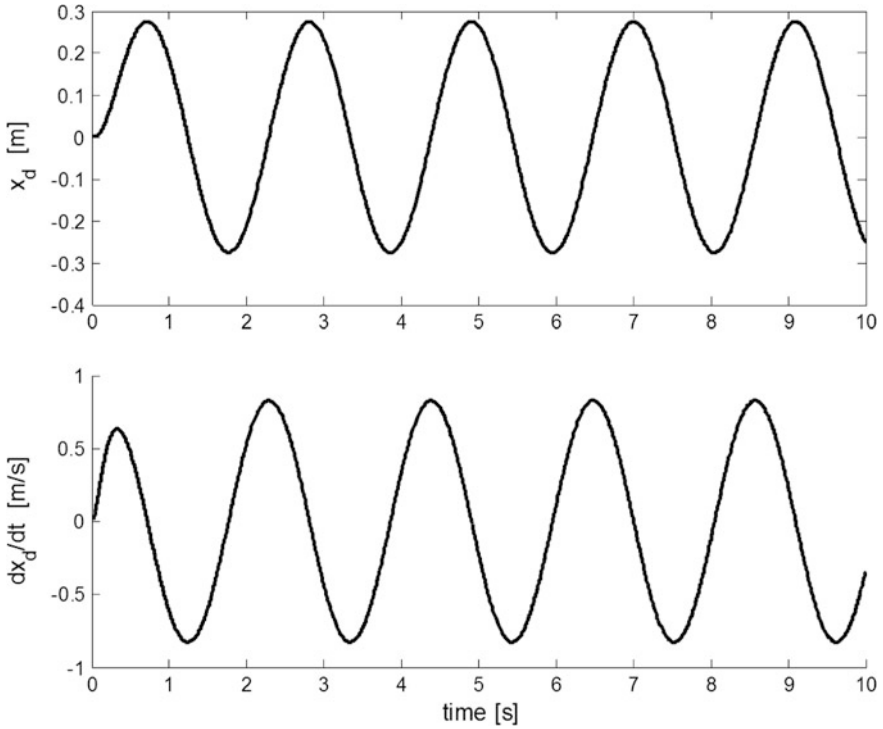


Fig. 2 Desired position trajectory \bar{x}_d and its derivative \dot{x}_d

8.1 Known-Parameter Case

If all parameters A_1 are known exactly, the problem is simplified by taking $\widehat{A}_1 = A_1$ and $\Gamma^{-1} = 0$. The adaptive loop is inactive. The two-dimensional state-space allows simple comparisons of the system behaviour under all discussed control strategies. The final Lyapunov functions for the non-adaptive case are:

$$V_2 = \frac{1}{2}e_x^2 + \frac{1}{2}\mu e_v^2 \quad (64)$$

for the QLF approach;

$$V_2 = \frac{1}{2k} \tan(k e_x^2) + \frac{1}{2}\mu e_v^2, \quad k = \frac{\pi}{2\Delta_{ex}^2} \quad (65)$$

for the position constrained BLF approach; and

$$V_2 = \frac{1}{2k} \tan(ke_x^2) + \frac{\mu}{2K} \tan(Ke_v^2), \quad k = \frac{\pi}{2\Delta_{ex}^2}, \quad K = \frac{\pi}{2\Delta_{ev}^2} \quad (66)$$

for the position and velocity constrained BLF approach.

The control signal is given by:

$$i = A_1^T \xi_1 + e_x + k_v e_v \quad (67)$$

$$i = A_1^T \xi_1 + e_x (1 + \tan^2(ke_x^2)) + k_v e_v \quad (68)$$

$$i = A_1^T \xi_1 + e_x \frac{1 + \tan^2(ke_x^2)}{1 + \tan^2(Ke_v^2)} + k_v e_v \quad (69)$$

for the discussed strategies respectively, where $e_v = \dot{x}_d + k_x e_x - v$. The main difference between the approaches (67–69) lies in the coefficient of e_x . The ‘gain’ of e_x equals $K_{QLF} = 1$, $K_x = 1 + \tan^2(ke_x^2)$ and $K_{xv} = \frac{1 + \tan^2(ke_x^2)}{1 + \tan^2(Ke_v^2)}$ respectively. The gains are plotted in Fig. 3.

If the position tracking error is the only constrained variable, the control effort increases illimitably if the error approaches the constraint boundary. If both errors are restricted, the current increase is moderated if the velocity error is large.

In Fig. 4 the state trajectories of the tracking error system under all discussed control strategies are compared for the same control gains k_x, k_v . The trajectories are plotted on the background of constant-level curves of the Lyapunov function. The plots illustrate how the barrier Lyapunov function acts to preserve the constraints.

Figure 5 demonstrates the time history under QLF and BLF control starting with the same initial conditions $e_x(0) = -0.018$, $e_v(0) = -0.04$, lying inside the constraints $|e_x| < 0.02$, $|e_v| < 0.05$. It is visible that even in the non-adaptive case the

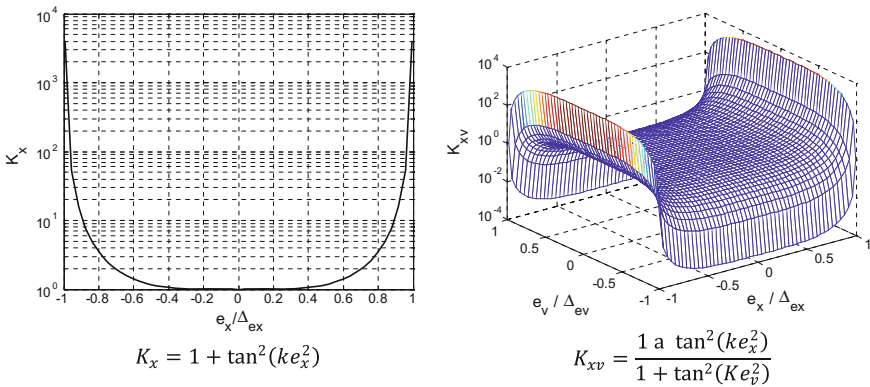


Fig. 3 The ‘gain’ of e_x for BLF strategies

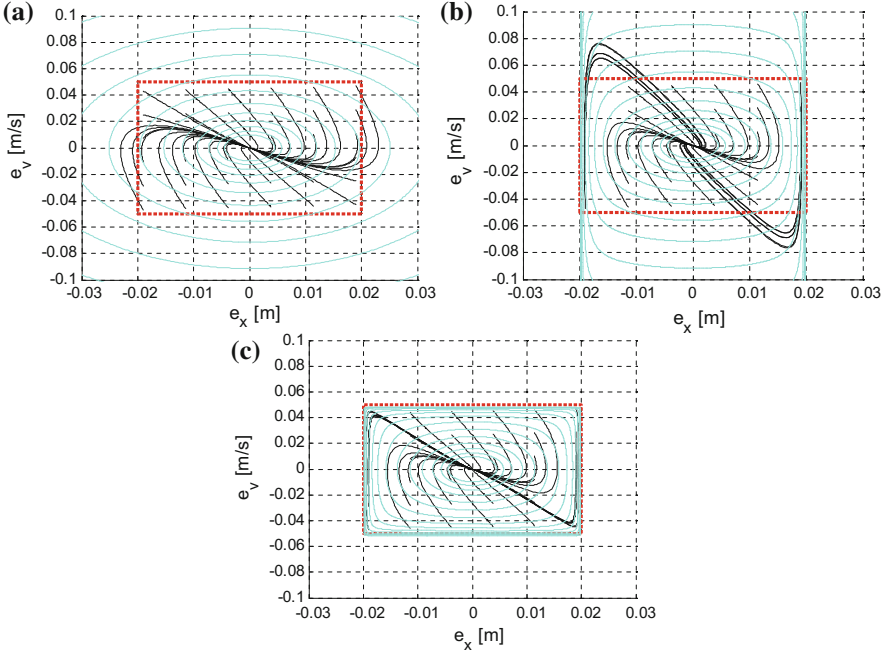


Fig. 4 State trajectories of the tracking error: **a** the QLF design, **b** position constrained BLF design and **c** position and velocity constrained BLF approach

QLF-based control does not guarantee that the position tracking error will remain inside the predefined bounds. Therefore the BLF approaches will be investigated for the adaptive case.

8.2 BLF-Based Adaptive Control with Position Constraints

The command (67) is presented under initial conditions $x(0) = -0.019$ [m] and $v(0) = -0.09$ [m/s], so $e_x(0) = 0.019$, $E(0) = 0.09$, $e_v(0) = 0.019k_x + 0.09$ according to (54). The control (40) and the adaptive law (30) with $\Gamma = \text{diag}(1, 10, 1000)$ were applied with design coefficients $k_x = 0.1$, $k_v = 1$. The influence of the imposed constraint on the system performance was tested in three cases: $\Delta_{ex} = 0.04$, $\Delta_{ex} = 0.03$ and $\Delta_{ex} = 0.02$, close to the initial condition $e_x(0) = 0.019$ (Fig. 6). The asymptotic stability of all errors is observed. The imposed constraint is preserved in all cases with a sufficient, save distant between the extremal value and the barrier.

If the constraint gets tighter more rapid movements near the boundary are observed and thus the maximal ‘virtual control’ tracking error and the ‘velocity gap’

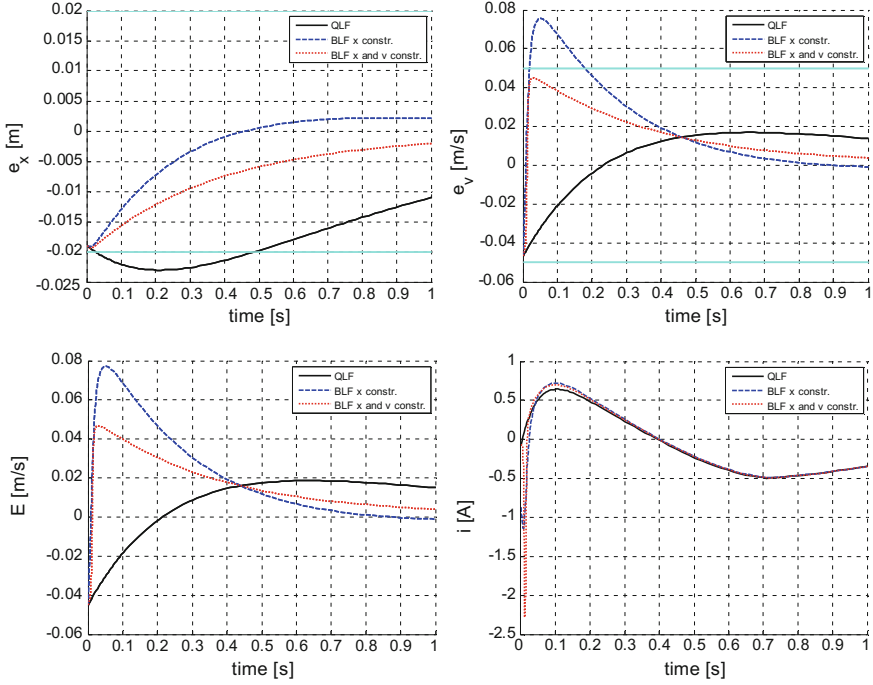


Fig. 5 Time history under QLF and BLF control

increase. The maximal current increases significantly, which is not surprising. Because large oscillations of e_v are observed, this system requires a careful tuning of adaptation gains in (30). Therefore, considering all the above, the application of a velocity constraint that will contribute to current restriction and will damp the oscillations is highly recommended.

8.3 BLF-Based Adaptive Control with Position and Velocity Constraints

The control (47) and the adaptive law (50) were applied with design coefficients $k_x = 0.1$, $k_v = 1$. For the initial conditions we can select any $\Delta_{ex} > e_x(0) = 0.019$ and $\Delta_{ev} > e_v(0) = 0.019k_x - (-0.09) = 0.0919$. We select $\Delta_{ex} = 0.02$ [m] and $\Delta_{ev} = 0.2; 0.15; 0.1$ [m/s]. As demonstrated in Fig. 7, in all the cases the imposed bounds are preserved during the transient. Tightening the bound Δ_{ev} allows to decrease the ‘velocity gap’ and the maximal current as well.

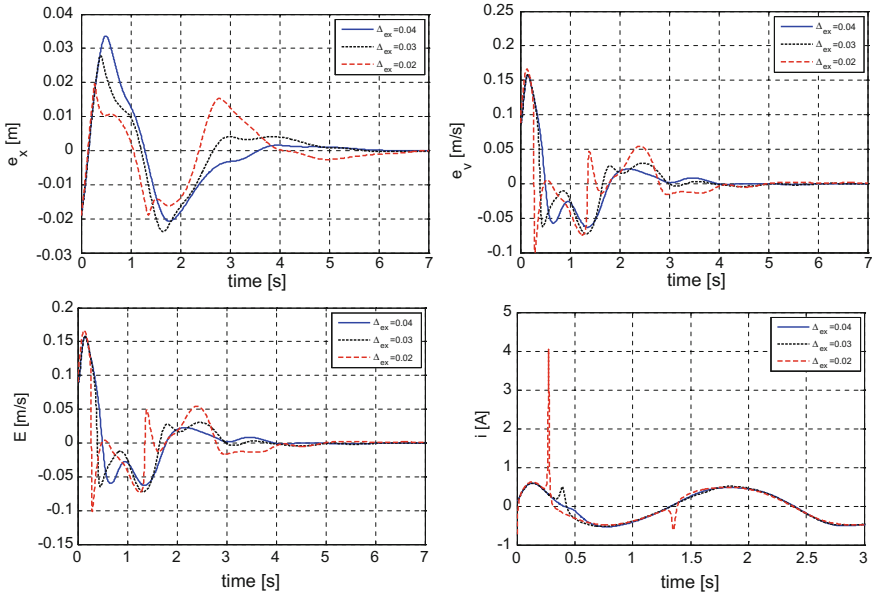


Fig. 6 Position tracking error e_x , ‘virtual control’ tracking error e_v , ‘velocity gap’ E and control i for different constraints Δ_{ex} ($k_x = 0.1, k_v = 1$)

8.4 System Performance with Bounded Adaptive Parameters

All systems tested above demonstrate robustness against imperfect reconstruction of the load. Selection of the adaptive gains Γ in (30) was not difficult and the maximal values of adaptive parameters were reasonable. In spite of this, the system performance with a priori constraints imposed on adaptive parameters was tested. The control strategies (27), (40), (47) were applied with constraints $\Delta_{ex} = 0.02$ [m] and $\Delta_{ev} = 0.1$ [m/s] with appropriate adaptive laws (30), (50). The adaptive loop coefficients were $\Gamma = \text{diag}(1, 10, 1000)$ as previously, also the design coefficients k_v and k_x remained unchanged. Estimated parameters were bounded to be larger than 0 and smaller than 300 % of their exact value. The results are plotted in Figs. 8, 9 and 10. The adaptive parameters’ bounds are respected and the tracking errors are asymptotically stable for any applied controller. As in the non-adaptive case, the QLF design does not assure the position tracking error respects the constraint. The BLF designed system with position constraints demonstrates rapid changes of velocity near the constraint boundary accompanied by high values of the current. To sum up, the worse transient of the position error is observed for the QLF-designed system and the best transient is obtained for the BLF-designed system with position and velocity constraints.

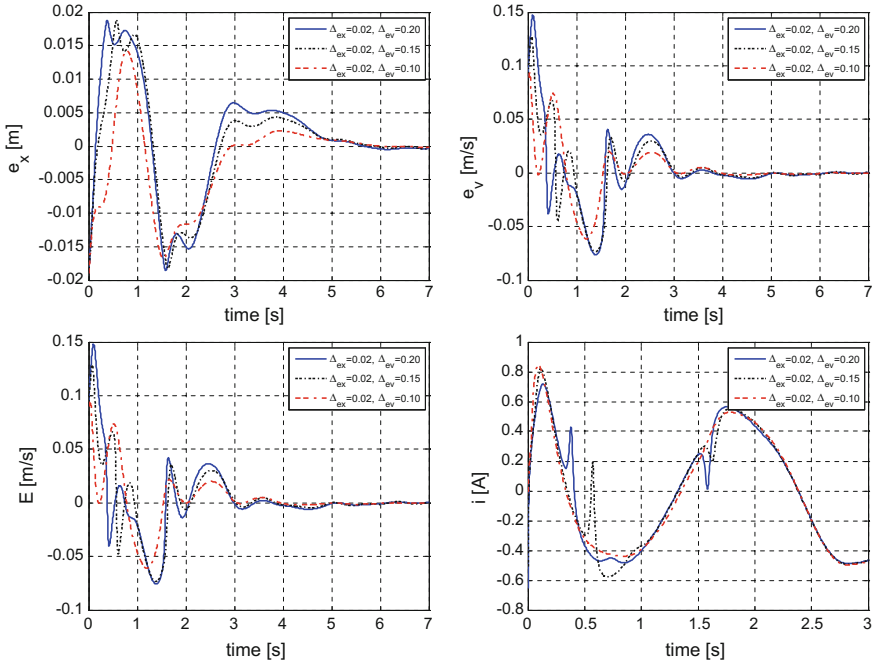


Fig. 7 Position tracking error e_x , 'virtual control' tracking error e_v , 'velocity gap' E and control i for different constraints Δ_{ex} ($k_x = 0.1, k_v = 1, \Delta_{ex} = 0.02$)

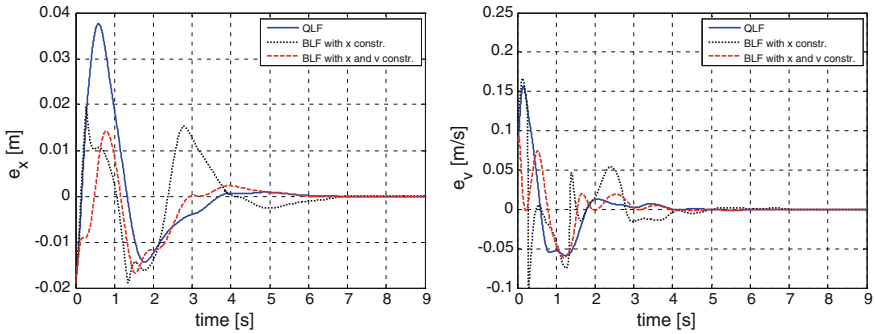


Fig. 8 Position tracking error e_x and 'virtual control' tracking error e_v

9 Real Plant Experiment

The application of the proposed controller design to a real plant allows the checking of the robustness against several phenomena that were not consider during the theoretical derivation. The effects of discrete in time controller implementation,

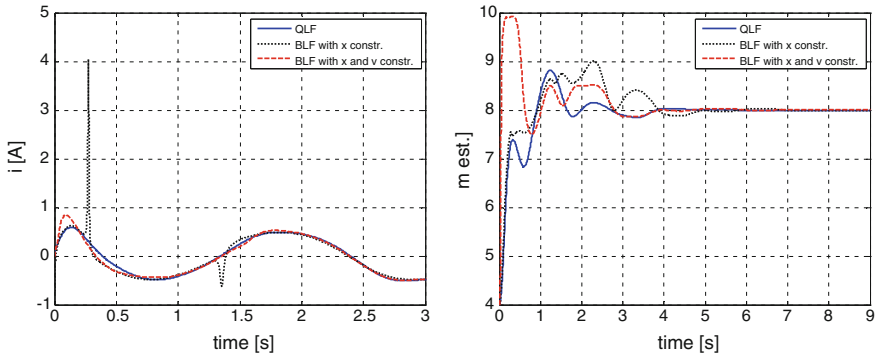


Fig. 9 Control i and estimate of parameter m (the first component of \hat{A}_1 multiplied by 39)

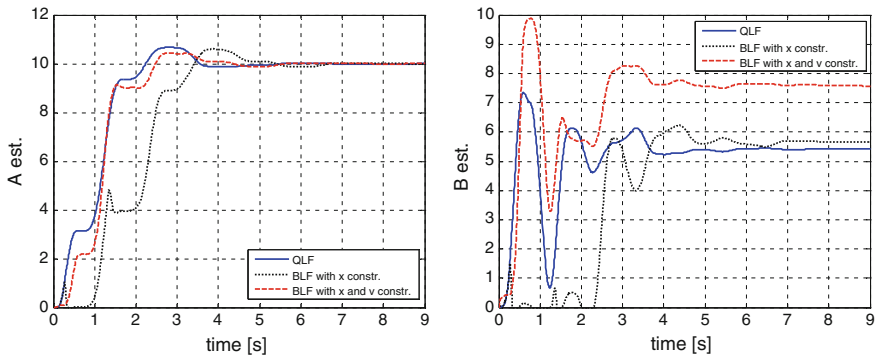


Fig. 10 Estimates of load parameters A, B (the second and the third component of \hat{A}_1 multiplied by 39)

error of quantization during any digital measurement of an analogous signal, measurement noise and outliers are present in any real drive. The fast part of the drive dynamics—the current generation—was neglected during the derivation, but, most importantly, the load model (3) is idealized. Therefore the BLF design was tested with a real drive.

The electric linear drive (Fig. 11) system includes: TB2510 linear motor, total weight: $m = 8$ kg, long-term force 104 N, current-force coefficient $\varphi = 39$ N/A, 1 μ m resolution encoder, XTL-230-18 Xenus PWM inverter with built-in current controller, modular set based on DS1006 dSpace processor card for control and data acquisition.

Fig. 11 Linear drive

The load is mostly the friction and pulling forces from the cables. It is very difficult to propose a realistic model for such resistance force, hence it will be described by the simplest possible friction model:

$$F_o(v) = A^T \zeta(v) = S \cdot \text{sign}(v) + b \cdot v \quad (70)$$

with unknown parameters S, b for static and Coulomb friction respectively. A very rough guess for these parameters is 5 N and 25Ns/m respectively. The desired position trajectory is:

$$x_d(t) = \mathcal{L}^{-1} \left\{ \frac{1}{0.1^2 s^2 + 0.2s + 1} \mathcal{L}\{0.3 \sin(2t)\} \right\} \quad [\text{m}]. \quad (71)$$

The control strategies (27), (40), (47) with appropriate adaptive laws (30), (49) were applied with the design coefficients $k_x = 1$; $k_v = 1$, constraints $\Delta_{e_x} = 0.01$ [m] and $\Delta_{e_v} = 0.05$ [m/s]. The initial conditions for the presented plots were $e_x(0) = 0.008$ and $e_v(0) = 0.008k_x = 0.008$. The adaptive loop gains were $\Gamma = \text{diag}(1, 10, 1000)$. Estimated parameters \hat{A} were constrained to be positive and smaller than 300 % of their initial value. The results of experiments are plotted in Figs. 12, 13, 14, 15, 16 and 17.

As is visible in Figs. 12, 13 and 14, the constraints are violated under the QLF design and respected if the BLF approach is used. If the position tracking constraint is applied alone, the system requires high control effort (high motor current), while

Fig. 12 The error system state-space trajectories: 'virtual control' tracking error e_v versus position tracking error e_x , is the initial condition

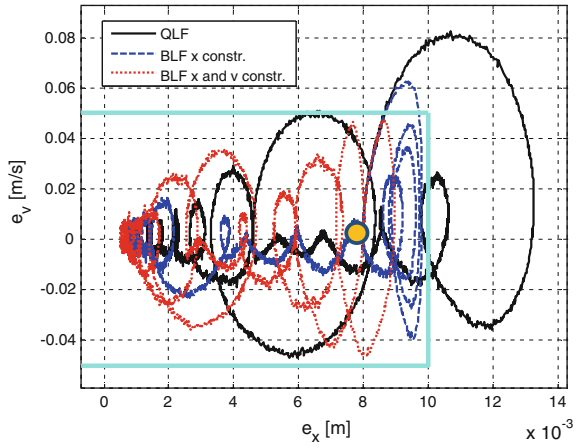


Fig. 13 The position tracking error e_x time history

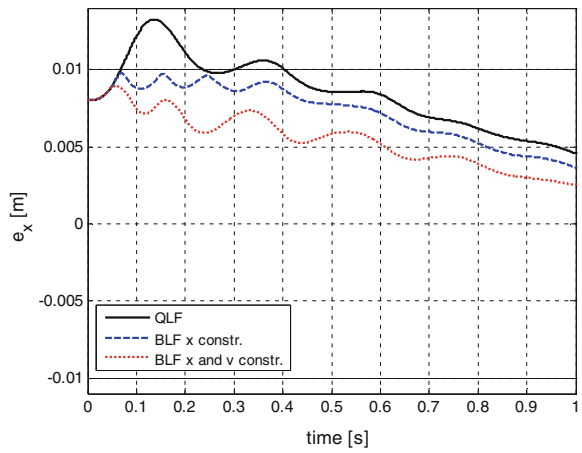


Fig. 14 The 'virtual control' tracking error e_v time history

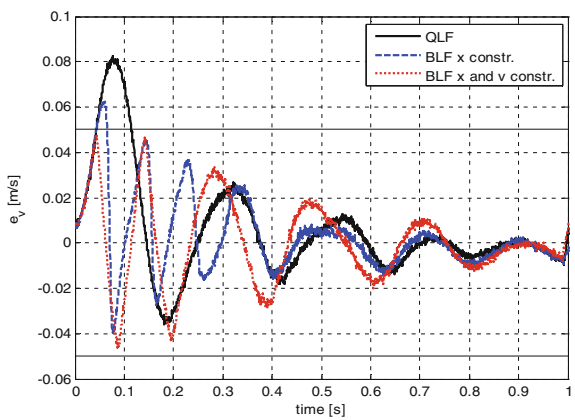


Fig. 15 The control i (motor current) time history

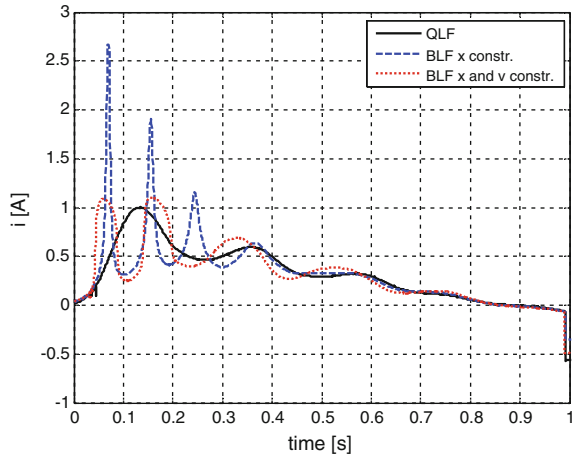
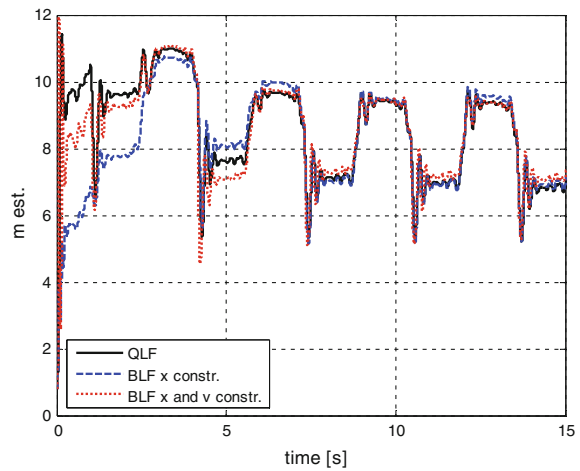


Fig. 16 Estimate of parameter m (the first component of \hat{A}_1 multiplied by 39)



changing the direction of movement near the constraint boundary (see Fig. 15). Position and velocity constraints applied together assure the best performance. The resistance force is changing (because of movement of cables mostly), so no steady state of the entire system is achieved. The adaptive parameters are continuously trying to fit to the inexact model (70) (Figs. 16, 17) and this is visible in the oscillations in the tracking errors (Fig. 13). As a matter of fact, the uniform ultimate boundedness is achieved (see Remark 1) rather than the asymptotic stability.

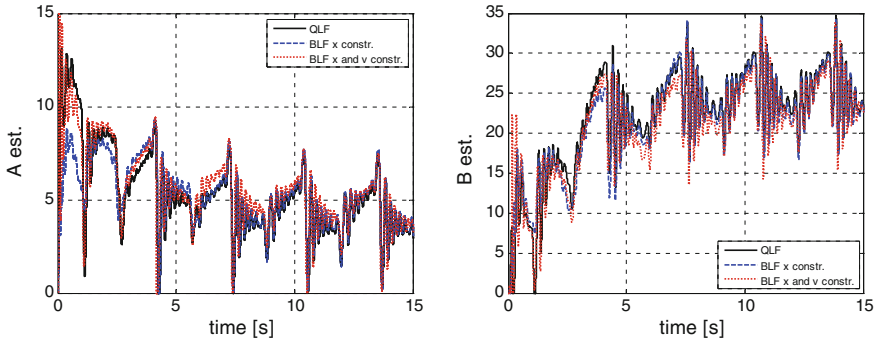


Fig. 17 Estimates of friction parameters A , B (the second and the third component of \hat{A}_1 multiplied by 39)

10 Conclusions

A systematic motion controller design procedure based on barrier Lyapunov functions was described. The method ensures the tracking errors remain inside the predefined constraints in spite of unknown system parameters and along any trajectory starting inside the constraints. Even if preliminary requirements impose the bounds for the position tracking error only, it is advantageous to constrain the velocity tracking error as well. This provides a smoother trajectory and allows the avoidance of rapid movements near the position-constraint boundary, requiring high values of the control. Proper choice of control system parameters is easier in the case of coexisting position and velocity constraints.

The experiment with real linear drives demonstrates that the application of the proposed approach in real servos is possible and all expected features of the control system are preserved.

The proposed approach may be easily generalized to include inexact models like in (4) and cover motion control with many degrees of freedom, particularly control of robotic manipulators.

References

1. Grüne L, Pannek J (2011) Nonlinear model predictive control theory and algorithms. Springer, London
2. Dòria-Cerezo A, Acosta JA, Castaño ÁR, Fossas E (2014) Nonlinear state-constrained control. Application to the dynamic positioning of ships, In: IEEE conference on control applications (CCA), Juan Les Antibes, pp 911–916
3. Krstic M, Kanellakopoulos I, Kokotovic P (1995) Nonlinear and adaptive control design. Wiley, New York

4. Ngo K, Jiang Z (2005) Integrator backstepping using barrier functions for systems with multiple state constraints, In: Proceedings of the 44th IEEE conference on decision and control European control conference, pp 8306–8312
5. Tee KP, Ge SS, Tay EH (2009) Barrier Lyapunov functions for the output-constrained nonlinear systems. *Automatica* 45(4):918–927
6. Ren BB, Ge SS, Tee KP, Lee TH (2010) Adaptive neural control for output feedback nonlinear systems using a barrier Lyapunov function. *IEEE Trans Neural Netw* 21(8):1339–1345
7. Tee KP, Ge SS (2010) Control of nonlinear systems with partial state constraints using a barrier Lyapunov function. *Int J Control* 84(12):2009–2023
8. Ren BB, Ge SS, Tee KP, Lee TH (2009) Adaptive control of electrostatic microactuator with bidirectional drive. *IEEE Trans Contr Syst Technol* 17(2):340–352
9. How BVE, Ge SS, Choo YS (2011) Control of coupled vessel, crane, cable, and payload dynamics for subsea installation operation. *IEEE Trans Contr Sys Tech* 19(1):208–220
10. Ioannou P, Fidan B (2006) Adaptive control tutorial. Society for industrial and applied mathematics, Philadelphia
11. Jastrzębski M, Kabziński J, Mosiołek P (2016) Adaptive motion control with state constraints using barrier Lyapunov functions. *Przegląd Elektrotechniczny (Electr Rev)* 92(4):112–116
12. Slotine JE, Li W (1991) Applied nonlinear control. Prentice-Hall, Englewood Cliff

Predictive Position Control of a Two-Mass System with an Induction Motor in a Wide Range of Speed Changes

Piotr Serkies and Krzysztof Szabat

Abstract In the chapter issues related to the application of the Model Predictive Control (MPC) to position control of a drive system with an induction motor (IM) coupled to a load machine through a long shaft are presented. After a short introduction the mathematical model of IM is demonstrated. Then, the standard MPC algorithm is described in detail. Next, the proposed MPC-based position control structure is introduced. Contrary to the classical cascade structure with independent position and speed control loops, one MPC controller which regulates those two variables is designed. An additional fuzzy block allowing adaptation of MPC parameters is used. The tested MPC controller cooperates with DTC-SVM (direct torque control—space vector modulation) strategy of electromagnetic torque regulation including operation in the field weakening regions. The theoretical considerations are supported by a variety of simulation and experimental tests.

Keywords Two-mass system · Torsional vibration · Model predictive control · Induction motor

Nomenclature

Symbols

u_s	Vector of stator voltage,
i_s, i_r	Vectors of stator and rotor currents,
Ψ_s, Ψ_r	Vectors of stator and rotor flux,
ψ_s	Amplitude of stator flux,
ω_r	Slip pulsation,
ω_1, ω_2	Speed of the motor and load,
m_e, m_s, m_L	Electromagnetic, shaft and load torque,

P. Serkies · K. Szabat (✉)

Department of Electrical Machines, Drives and Measurements, Wrocław University of Science and Technology, Wybrzeże Wyspiańskiego 27, Wrocław, Poland
e-mail: krzysztof.szabat@pwr.edu.pl

P. Serkies
e-mail: piotr.serkies@pwr.edu.pl

f_r	Resonant frequency of the system,
f_{ar}	Antiresonant frequency of the system,
ψ_s^{nom}	Nominal value of the stator flux,
ω_s	Synchronous speed,
$u_{s,max}$	Supplied voltage,
m_e^{max}	The limitation value of the electromagnetic torque,
m_s^{max}	The limitation value of the shaft torque,
ω^{max}	The limitation value of the speed.

Parameters

T_N	Reference time constant,
r_s, r_r	Stator and rotor resistance,
x_s, x_r, x_M	Reactance of stator, rotor and magnetising,
p_b	Pair of poles,
T_1, T_2	Time constant of the motor and load,
T_c	Stiffness time constant,
T_x	Positioning time constant,
J_1, J_2	Inertia of the motor and load,
Ω_b	Base speed of the system,
M_b	Nominal electromagnetic torque,
K_c	Stiffness time constant,
N	The prediction horizon,
N_c	Denotes the control action horizon,
\mathbf{Q}, \mathbf{R}	Weighting coefficients matrix, $\mathbf{Q} = \text{diag}(q_1, q_2, \dots, q_n)$,
$q_1 \dots q_n$	Values of the main diagonal of the matrix.

1 Introduction

One of the main aims of modern drive systems is positioning of industrial actuators. In order to cope with common requirements, such as precision of control, safety, response time etc., characteristics of the whole system should be taken into consideration during control structure design. The most popular control scheme for an electrical drive is a cascade control structure with linear PI controllers [1]. The torque, speed and position controllers can be clearly distinguished in this scheme. In such a case controllers can be tuned separately, which simplifies the design procedure. Also the limitation of the state variables is quite simple. Drawbacks of the cascade structure are as follows. Firstly, it can be used for a system where dynamics of the inner loop is fast and position loop is slow—which is not always fulfilled in electrical drives. Secondly, it is relatively slow to changes of reference input or rejecting disturbances—this hindrance can be partially eliminated by application of

additional techniques such as a reference generator. Thirdly, the robustness of cascade scheme is limited [1].

The structure of the torque control loop strictly depends on the type of the driving motor. For IM the following methodologies can be used: field-oriented control, direct torque control, predictive control, sliding-mode control and others [1–5]. The flux control ensures the possibility of faster speed response in some specific cases (operation in the so-called field weakening region without full load). If fast and accurate electromagnetic torque control is assured the dynamics of this loop can be represented by a first-order lag with a small time constant.

The speed control loop includes the following parts: optimized torque control loop, mechanical part of the drive, speed sensor and speed controller. For the special drive system with an extended mechanical part including not only a driving motor but also the characteristic of the shaft and inertia of the load machine (two-mass system) the classical structure should be modified. Neglecting the shaft characteristic can lead to torsional vibrations, which substantially deteriorate the speed/positioning precision. In extreme cases, they can cause a damage of the drive and immobilize the machine [6–11]. Different techniques can be used to eliminate torsional vibrations. The most popular approach relies on inserting additional state variables to the PI speed controller [6]. Usually, the coefficients of this loop (speed) can be adjusted based on the poles-placement methodology. Among the popular approaches there is also RRC (resonance ratio control). Instead of the linear controller a more advanced concept can be applied: sliding-mode, fuzzy, forced dynamic, adaptive-control or other. It should be stressed that all of the above-mentioned control methodologies require feedbacks from additional variables of the two-mass system. The difficulty of limitation of internal state variables is a general drawback of those schemes.

The outer control loop encompasses the position controller, optimized speed control loop and position sensor. The following papers provide examples of position control schemes for the two-mass system: [12–14]. In [14] two control structures are proposed. One is based on the Forced Dynamic Control methodology and the second on Sliding-Mode Control. The authors report good dynamics of both structures, although the SMC ensures a slightly better properties of the drive. As a disadvantage of those structures lack of direct limitation of the system state variables can be mentioned. Papers which describe regulators based on the nominal reference trajectories have appeared in recent years [15]. They require the application of digital filters in order to eliminate the torsional vibrations of the shaft. However, the results of such approach can be effective only for systems with high frequency oscillations. Otherwise the decrease of the system dynamics can be expected. These position control structures are of cascade form, so their disadvantages are clearly visible. Thus, other solutions are sought after.

The applications of *MPC* in electrical drives and power electronics can be divided into two main frameworks: finite set *MPC* and continuous *MPC* [16–22]. In

the first approach only one or two samples ahead are used in the predictive windows [18, 19, 22]. There are many examples of applying this method to electromagnetic torque control. Its applications to speed/position control of drive systems are rare. In the second approach so-called continuous *MPC* can be distinguished. This methodology is usually applied to control of speed/position of electrical drives. The length of the predictive horizon can be even 30 samples, hence sometimes this approach is also called long-horizon *MPC* [16, 17]. One of the main advantages of *MPC* is the fact that the limitation of the internal state variable can be directly incorporated in the control algorithm. Also the dynamics of the system depends on the operation point and it is changeable. In the literature there are examples of applications of *MPC* to two-mass systems. In [16] the speed control using *MPC* is demonstrated in simulation and experimental studies. Besides, the possibilities of limitation of the internal state variables are shown. In [23] the *CNC* tools are controlled. The application of the *MPC* to position control of a drive system with an elastic joint is reported in [17]. Different aspects are investigated, for instance: the length of the prediction horizon, robustness etc. For experimental realization an off-line version of the *MPC*, which requires less computational effort, is selected.

In the presented chapter a control structure based on the long horizon *MPC* dedicated for position control of a two mass system with an induction motor is considered. Contrary to the classical cascade scheme, one *MPC* controller substitutes for two control loops: speed and position. The on-line *MPC* algorithm allows to change the controller parameters during work. The presented position *MPC* controller is connected with the field weakening algorithm of the *IM* motor. Operation in the field weakening region allows to shorten the response time of the drive system in some cases. Furthermore, an additional fuzzy system is changing the *MPC* parameter on-line which improves the property of control structure.

The application of the *MPC* approach to control the position of *IM*, considering the possibility of the flux weakening operation is the main contribution of the presented chapter. Furthermore, application aspects of the on-line *MPC* algorithm are investigated. A critical review showing the properties of such implementations is included in the paper.

The chapter is divided into 5 sections. After an introduction the mathematical model of the drive system and description of the control structure are provided. Then, in the third section the *MPC* design methodology is presented in detail. In the fourth section a brief description of the laboratory stand and the experimental and simulation results are presented. Finally, the conclusions are formulated.

2 Mathematical Model of the Drive

First, the mathematical model of the induction motor using the space vector in per unit system (in α - β coordinates) is introduced. The *IM* is described by the following equations based on the commonly-used simplifications [1, 24]:

$$\begin{aligned}
 \vec{u}_s &= r_s \vec{i}_s + T_N \frac{d}{dt} \vec{\Psi}_s \\
 \vec{\Psi}_s &= x_s \vec{i}_s + x_M \vec{i}_r \\
 0 &= r_r \vec{i}_r + T_N \frac{d}{dt} \vec{\Psi}_r - j\omega_r \vec{\Psi}_r \\
 \vec{\Psi}_r &= x_r \vec{i}_r + x_M \vec{i}_s \\
 \frac{d}{dt} \omega &= \frac{3 p_b x_M}{2 T_1 x_r} \left(\text{Im} \left\{ \vec{\Psi}_r * \vec{i}_s \right\} \right).
 \end{aligned}
 \tag{1}$$

The two-mass inertia-shaft-free model is described by the following equations in per unit values [6]:

$$\begin{cases}
 \frac{d}{dt} \omega_1 = \frac{1}{T_1} (m_e - m_s) \\
 \frac{d}{dt} \omega_2 = \frac{1}{T_2} (m_s - m_L) \\
 \frac{d}{dt} m_s = \frac{1}{T_c} (\omega_1 - \omega_2) \\
 \frac{d}{dt} \alpha = \frac{1}{T_x} \omega_2
 \end{cases}
 \tag{2}$$

The above-mentioned time constants T_1 , T_2 , T_c and T_x can be determined on the basis of the nominal values of the drive system [6]:

$$T_1 = \frac{\Omega_b J_1}{M_b}; \quad T_2 = \frac{\Omega_b J_2}{M_b}; \quad T_c = \frac{M_b}{\Omega_b K_c}.
 \tag{3}$$

The resonant and anti-resonant frequency of the system (2) can be calculated using the following equations:

$$f_r = \frac{1}{2\pi} \sqrt{\frac{T_1 + T_2}{T_1 T_2 T_c}},
 \tag{4}$$

$$f_{ar} = \frac{1}{2\pi} \sqrt{\frac{1}{T_2 T_c}}.
 \tag{5}$$

The schematic diagram of a two-mass system is shown in Fig. 1.

The value of the resonant frequency depends on the type of the drive and can vary from a few hertz in a paper machine section, through dozens of hertz in a rolling-mill drive, and can exceed a few hundred hertz in a modern servo-drive.

Fig. 1 The ideal diagram of the two-mass system

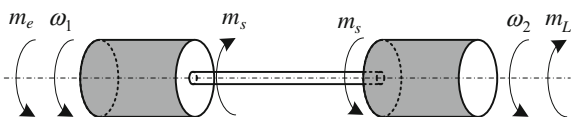


Table 1 Mechanical parameters

$T1$ [s]	$T2$ [s]	Tc [s]	f_r [Hz]	f_{ar} [Hz]
0.085	0.095	0.0022	16.02	11.01

The value of the antiresonant frequency can be even ten times lower than the resonant one in a dryer, but usually the difference is much smaller (smaller than two) [6, 25]. The main parameters of the analyzed system are presented in Table 1.

3 Control Structure

3.1 General Structure

The block diagram of the considered control structure is presented in Fig. 2. It consists of a predictive position controller, Kalman filter which estimates mechanical variables, optimized torque control loop, fuzzy system, field-weakening algorithm and electrical drive system. The predictive controller generates a reference value for the electromagnetic torque controlled in the direct torque control structure with a space vector modulator. The values of the constraints of the electromagnetic and shaft torques depend on the current value of the flux. Additionally, on the basis of the selected state variables the fuzzy system returns the limitation of the load speed.

The proposed control structure requires information about mechanical state variables of the system (motor speed, shaft torque) as well as disturbance (load torque). In a typical drive system only the motor speed is measured, whereas the rest of the states have to be estimated. There are different methods which can be used to reconstruct the variables of the system, such as Luenberger observer, Kalman filter, neural networks or fuzzy systems [26–28]. In this chapter the Kalman filter is applied according to [17] (the estimated variables are indicated by the dash sign $\hat{}$ in Fig. 2).

3.2 Torque Control Structure with Field Weakening Algorithm

Direct Torque Control with Space Vector Modulation *DTC-SVM* (Fig. 3), used for the induction motor drive control, can be classified as a constant flux control method [1]. In this case stator flux amplitude estimated on the basis on (6) is stabilized.

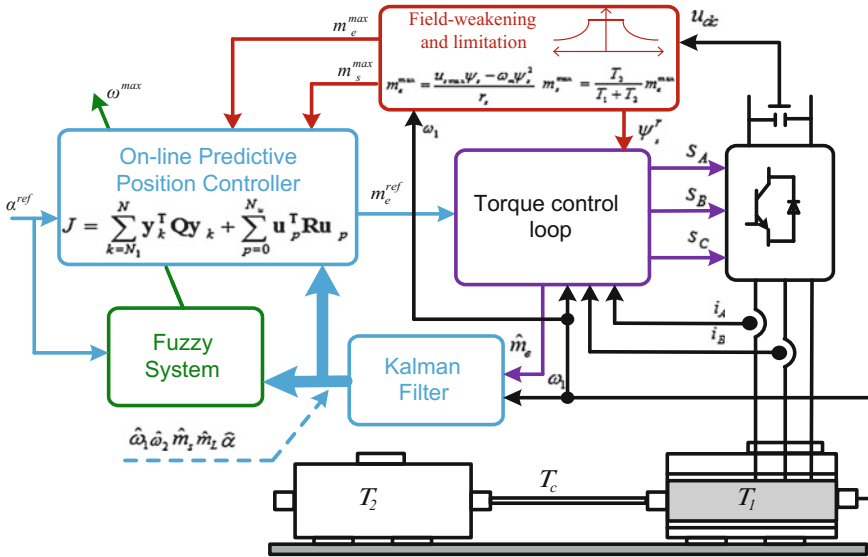
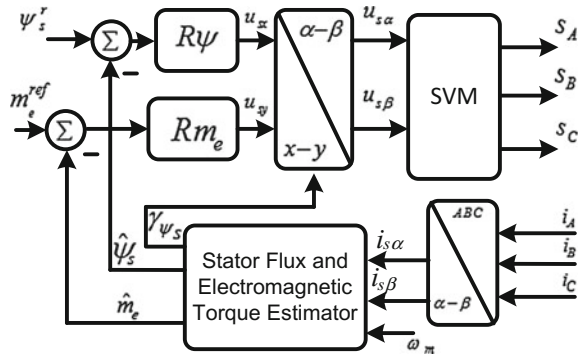


Fig. 2 The block diagram of the analyzed control structure with MPC position controller

Fig. 3 Direct torque control with space vector modulator structure



$$\hat{\Psi}_s = \frac{x_M}{x_r \hat{\Psi}_r + x_s \sigma \mathbf{i}_s} \tag{6}$$

where: the dash sign ^—estimated value, $\sigma = 1 - x_M^2 / (x_s x_r)$.

Rotor flux can be reconstructed using one of the different estimators [1, 29, 30]. Motor torque is usually estimated using (7) defined in the stationary reference frame:

$$\hat{m}_e = \hat{\psi}_{s\beta} i_{sz} - \hat{\psi}_{sz} i_{s\beta}. \quad (7)$$

The principle of the operation of the described control method is based on the analysis of the induction motor equations written in the coordinate system rotating with the stator flux vector velocity ($\omega_k = \omega_{\psi_s}$, $\Psi_{sx} = \Psi_s$, $\Psi_{sy} = 0$), i.e.

$$u_{sx} = r_s i_{sx} + T_N \frac{d\psi_s}{dt}. \quad (8)$$

$$u_{sy} = r_s i_{sy} + \omega_{\psi_s} \psi_s. \quad (9)$$

The torque Eq. (7) in this coordinate system can be written as follows:

$$m_e = \psi_{sx} i_{sy} - \psi_{sy} i_{sx} \xrightarrow{\psi_{sx}=\psi_s, \psi_{sy}=0, \omega_{\psi_s}, \psi_s \text{ decup.}} m_e = \frac{1}{r_s} \psi_s u_{sy}. \quad (10)$$

A possibility of the stator flux amplitude control using u_{sx} component results from Eq. (8). A factor $\omega_{\psi_s} \Psi_{sx}$ appears in (9) allows decoupling of the electromagnetic torque loop (10) using u_{sy} component.

The field-weakening algorithm changes the flux reference value according to:

$$\psi_s^{ref} = \begin{cases} \psi_s^{nom} & \text{if } \omega_1 \leq \omega_s \\ \frac{\psi_s^{nom}}{\omega_1} & \text{if } \omega_1 > \omega_s \end{cases}. \quad (11)$$

In the field-weakening region the maximal available torque of induction motor is decreasing. For that reason, there is a need to apply adaptation of the limitation of the electromagnetic torque. In present work a simple limitation algorithm which includes reduction of system currents and voltages [31, 32] is applied.

$$m_e^{\max} \leq \frac{3}{2} p_b \frac{u_{s\max} \psi_s - p_b \omega_1 \psi_s^2}{r_s}. \quad (12)$$

The limitation value of the shaft torque results from the geometry and material of the mechanical connection. Usually, it is much bigger than the maximal value of the electromagnetic torque. However, the ratio of the limitation of the shaft to electromagnetic torques influences the system property significantly. Better dynamics can be achieved when the value of this ratio is smaller than one. The optimal value of limitations of the shaft torque can be set using the following formula:

$$m_s^{\max} \leq \frac{T_2}{T_1 + T_2} m_e^{\max} \quad (13)$$

3.3 Fuzzy Adaptation System

In the control structure a simple mechanism for the system speed limitation can be implemented in order to improve the quality of the positioning system:

$$\omega^{\max} = \begin{cases} 1 & \text{if } |\alpha^{ref} - \alpha| \leq 0.3 \\ 1.5 & \text{if } |\alpha^{ref} - \alpha| > 0.3 \end{cases} \quad (14)$$

This adaptation mechanism operates in the field-weakening region where the available value of the electromagnetic torque is limited. To ensure the proper operation of the drive, formula (14) should be active when the estimated value of the load torque is smaller than available electromagnetic torque of the system.

As an alternative solution to (14), a fuzzy Mamdani-type system is proposed. The block diagram of fuzzy system is shown in Fig. 4a.

The used fuzzy system has two inputs and is based on fifteen rules. In order to decrease the computational complexity the singleton defuzzification strategy is utilised. The position error has the most significant influence on the properties of the system. Therefore, this input is divided into five trapezoidal-type fuzzy membership functions (Fig. 4b). The second input is an estimated load torque. The universe of discourse of this variable is divided into three fuzzy sets. The location of the output singletons is shown in Fig. 4d. The main goal of the system is to constrain the speed in the meaner (manner?) to minimise the settling time as well as overshoot of the position transients. In Fig. 5 the resulting surface of the fuzzy system is presented.

The application of the fuzzy logic allows to change the limitation value in a sophisticated non-linear way which improves the performance of the drive.

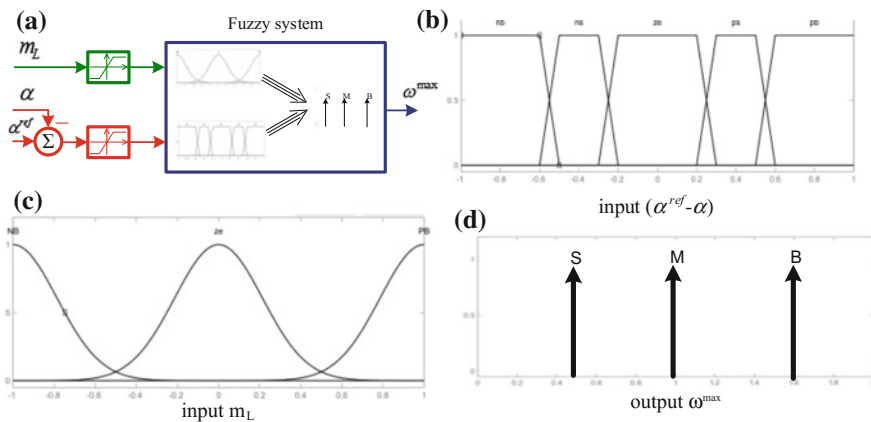


Fig. 4 Proposed fuzzy system: **a** block diagram, **b, c** input membership functions, **d** output membership function

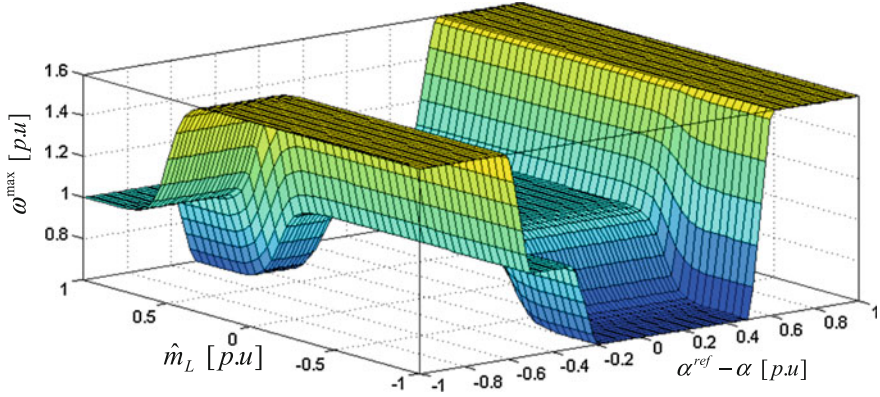


Fig. 5 Resulting relationship between load torque, difference of position and limitation of speed

3.4 Predictive Control

In the linear model predictive control, an explicit model of the plant is used to predict the effect of future actions of the manipulated variables on the process output. In the recent literature, the following linear discrete-time state-space model is typically employed:

$$\begin{aligned} \mathbf{x}(k+1) &= \mathbf{A}\mathbf{x}(k) + \mathbf{B}\mathbf{u}(k) \\ \mathbf{y}(k) &= \mathbf{C}\mathbf{x}(k) \end{aligned} \quad (15)$$

where $\mathbf{x}(t) \in \mathfrak{R}^n$, $\mathbf{u}(t) \in \mathfrak{R}^m$, $\mathbf{y}(t) \in \mathfrak{R}^p$ denote the system state, input and output vectors, respectively. $\mathbf{A} \in \mathfrak{R}^{n \times n}$, $\mathbf{B} \in \mathfrak{R}^{n \times m}$, $\mathbf{C} \in \mathfrak{R}^{p \times n}$ are matrices describing the dynamics of the plant, k —is a discrete time constant.

At each time step k , the MPC algorithm solves the following optimization problem [33]:

$$\min_{\mathbf{u}_0^T, \dots, \mathbf{u}_{N_c-1}^T} \left\{ \sum_{i=0}^N \mathbf{y}_{\mathbf{k}+i|k}^{ref} \mathbf{Q} \mathbf{y}_{\mathbf{k}+i|k}^T + \sum_{i=0}^{N_c-1} \mathbf{u}_{\mathbf{k}+i|k}^T \mathbf{R} \mathbf{u}_{\mathbf{k}+i|k} \right\} \quad (16)$$

$$\begin{aligned} \mathbf{u}_{\min} &\leq \mathbf{u}_{\mathbf{k}+i|k} \leq \mathbf{u}_{\max} & i = 0, 1, \dots, N_c-1 \\ \mathbf{x}_{\min} &\leq \mathbf{x}_{\mathbf{k}+i|k} \leq \mathbf{x}_{\max} & i = 0, 1, \dots, N \\ \mathbf{y}_{\min} &\leq \mathbf{y}_{\mathbf{k}+i|k} \leq \mathbf{y}_{\max} & i = 0, 1, \dots, N \\ \mathbf{x}_{\mathbf{k}+i+1|k} &= \mathbf{A}\mathbf{x}_{\mathbf{k}+i|k} + \mathbf{B}\mathbf{u}_{\mathbf{k}+i|k}, & i \geq 0, \\ \mathbf{y}_{\mathbf{k}+i|k} &= \mathbf{C}\mathbf{x}_{\mathbf{k}+i|k} & i \geq 0, \\ \mathbf{x}_{k|k} &= \mathbf{x}(k), \end{aligned} \quad (17)$$

where $\mathbf{Q} \geq 0$ and $\mathbf{R} > 0$ are the weighting matrices, N , N_c denote the prediction and control horizon, respectively, and \mathbf{u}_{\min} , \mathbf{u}_{\max} , \mathbf{y}_{\min} , and \mathbf{y}_{\max} are the input and output constraints of the system. The following inequality holds in the system $N_c \leq N$.

Equations (16) and (17) can be written in the matrix form using quadratic programming notation (QP) [33]:

$$J(U, y(k)) = \mathbf{Y}^T \tilde{\mathbf{Q}} \mathbf{Y} + \mathbf{U}^T \tilde{\mathbf{R}} \mathbf{U} \quad (18)$$

where \mathbf{X} and \mathbf{U} are the predictive vectors of the state variables and controls:

$$\mathbf{Y}(k) = \begin{bmatrix} y(k|k) \\ \vdots \\ y(k+N|k) \end{bmatrix}, \quad \mathbf{U}(k) = \begin{bmatrix} \Delta u(k|k) \\ \vdots \\ \Delta u(k+N_u-1|k) \end{bmatrix} \quad (19)$$

The matrices $\tilde{\mathbf{Q}}$ and $\tilde{\mathbf{R}}$ have the following form:

$$\tilde{\mathbf{Q}} = \begin{bmatrix} \mathbf{Q} & \mathbf{0} & \mathbf{0} \\ \mathbf{0} & \ddots & \mathbf{0} \\ \mathbf{0} & \mathbf{0} & \mathbf{Q} \end{bmatrix}; \quad \tilde{\mathbf{R}} = \begin{bmatrix} \mathbf{R} & \mathbf{0} & \mathbf{0} \\ \mathbf{0} & \ddots & \mathbf{0} \\ \mathbf{0} & \mathbf{0} & \mathbf{R} \end{bmatrix} \quad (20)$$

Finally, the problem of optimal control using quadratic programming is formulated (QP):

$$\begin{aligned} V(x(k)) = x(k)^T \mathbf{T} x(k) + \min_U \left(\frac{1}{2} \mathbf{U}^T \mathbf{H} \mathbf{U} + 2x^T(k) \mathbf{F} \mathbf{U} \right) \\ \text{subject to} \\ \mathbf{G} \mathbf{U} \leq \mathbf{W} + \mathbf{E} x(k) \end{aligned} \quad (21)$$

where: $\mathbf{U} = [\mathbf{u}'(k), \dots, \mathbf{u}'(k+N_u+1)]' \in \mathbf{R}^s$, $s = mN_u$ is the control vector (for the optimization process). Matrices of and \mathbf{H} , \mathbf{F} , \mathbf{T} , $\tilde{\mathbf{A}}$ and $\tilde{\mathbf{B}}$ are defined as follows:

$$\mathbf{H} = \tilde{\mathbf{B}}^T \tilde{\mathbf{Q}} \tilde{\mathbf{B}} + \tilde{\mathbf{R}} \quad (22)$$

$$\mathbf{F} = \tilde{\mathbf{A}}^T \tilde{\mathbf{Q}} \tilde{\mathbf{B}} \quad (23)$$

$$\mathbf{T} = \tilde{\mathbf{A}}^T \tilde{\mathbf{Q}} \tilde{\mathbf{A}} \quad (24)$$

$$\tilde{\mathbf{A}} = [\mathbf{C} \mathbf{A} \quad \mathbf{C} \mathbf{A}^2 \quad \dots \quad \mathbf{C} \mathbf{A}^{N_c} \quad \dots \quad \mathbf{C} \mathbf{A}^N]^T \quad (25)$$

$$\tilde{\mathbf{B}} = \begin{bmatrix} 0 & \cdots & 0 \\ \mathbf{CB} & \cdots & 0 \\ \vdots & \ddots & \vdots \\ \mathbf{CA}^{N_c} & \cdots & \mathbf{CB} \\ \vdots & \vdots & \vdots \\ \mathbf{CA}^{N-1}\mathbf{B} & \cdots & \sum_{i=0}^{N-N_c} \mathbf{CA}^i\mathbf{B} \end{bmatrix}^T \quad (26)$$

The implementation of an MPC controller requires solving (16) and (17) on-line for a given \mathbf{x}_0 in a receding horizon fashion. This means that, at time k , only the first element \mathbf{u}_0^* of the optimal input sequence is applied to the plant and the remaining future control actions $\mathbf{u}_1^*, \dots, \mathbf{u}_{N_c-1}^*$ are discarded. At the next time step the whole procedure is repeated for the new measured or estimated output $y(k+1)$. Let ΔU^* be the sequence minimizing (18). The on-line MPC algorithm can be implemented in a few steps as presented below:

On-line MPC algorithm Consider the optimization problem:

1. At time k , measure (or estimate) the current system output $y(k)$
2. Solve (18) to obtain $\Delta U^* = [\Delta u_k^{*T}, \dots, \Delta u_{k+N_c}^{*T}]^T$.
3. Apply $u_k^* = \Delta u_k^* - u_{k-1}^*$ to the plant
4. Update $k \leftarrow k+1$ and return to step 1.

3.5 Design of MPC Strategy for Two-Mass Drive System

The model of the mechanical system described by (2) can be presented in the following state equation:

$$\underbrace{\frac{d}{dt} \begin{bmatrix} \omega_1 \\ \omega_2 \\ m_s \\ \alpha \end{bmatrix}}_{\mathbf{x}} = \underbrace{\begin{bmatrix} 0 & 0 & \frac{-1}{T_1} & 0 \\ 0 & 0 & \frac{1}{T_2} & 0 \\ \frac{1}{T_c} & \frac{-1}{T_c} & 0 & 0 \\ 0 & \frac{1}{T_s} & 0 & 0 \end{bmatrix}}_{\mathbf{A}} \cdot \underbrace{\begin{bmatrix} \omega_1 \\ \omega_2 \\ m_s \\ \alpha \end{bmatrix}}_{\mathbf{x}} + \underbrace{\begin{bmatrix} \frac{1}{T_1} \\ 0 \\ 0 \\ 0 \end{bmatrix}}_{\mathbf{B}} \cdot m_e + \underbrace{\begin{bmatrix} 0 \\ \frac{-1}{T_2} \\ 0 \\ 0 \end{bmatrix}}_{\mathbf{B}_d} \cdot m_L \quad (27)$$

$$\underbrace{\begin{bmatrix} \omega_1 \\ \omega_2 \\ m_s \\ \alpha \end{bmatrix}}_{\mathbf{y}} = \underbrace{\begin{bmatrix} 1 & 0 & 0 & 0 \\ 0 & 1 & 0 & 0 \\ 0 & 0 & 1 & 0 \\ 0 & 0 & 0 & 1 \end{bmatrix}}_{\mathbf{C}} \cdot \underbrace{\begin{bmatrix} \omega_1 \\ \omega_2 \\ m_s \\ \alpha \end{bmatrix}}_{\mathbf{x}}$$

In (27) the vector of reference values y^{ref} is specified for the given input:

$$\mathbf{y}^{ref} = [0 \quad 0 \quad m_L \quad \alpha^r]^T \quad (28)$$

For the input vector defined as above the *MPC* algorithm minimizes the difference between the reference and the motor and load speed as well as the difference between the shaft and load torque. The specified cost function relies on the limitation of the control signal, which is a reference value of the electromagnetic torque as well as the selected internal state variables (shaft torque in the considered case). Finally, bearing in mind the above-mentioned remarks, the cost function can be represented in its detailed form:

$$\min_{\substack{m_{e1}^{ref}, \\ m_{e2}^{ref}, \\ m_{e3}^{ref}}} \left\{ \sum_{p=1}^N \left(q_1(\omega_1(p|k))^2 + q_2(\omega_2(p|k))^2 \right) + \sum_{p=0}^{N_c-1} R(m_e^{ref}(p|k))^2 \right\} \quad (29)$$

$$\begin{aligned} |m_e^{ref}(p|k)| &\leq m_e^{ref \max} & p = 0, 1, \dots, N_c \\ |m_s(p|k)| &\leq m_s^{\max} & p = 1, \dots, N \\ |\omega_1(p|k)| &\leq \omega^{\max} & p = 1, \dots, N \end{aligned}$$

where $(p|k)$, are the predicted variables of the drive system at a future time p based on the k samples.

4 Results

In order to illustrate the operation and advantages of the presented predictive regulator the laboratory tests were conducted. The influence of the reference position value and the position time constant on the ability of the operation in the field-weakening region were analysed. Parameters of the chosen regulator are shown in Table 2.

A schematic block diagram of the laboratory set-up is shown in Fig. 6. The set-up is composed of two induction motors with nominal power of 1.1 and 1.5 kW respectively. The long shaft which connects two motors has the following parameters: length of 600 mm and a diameter of 6 mm. In order to change the moment of inertia of the drive additional flywheels can be installed on both sides. This allows to increase the moment of inertia from 2 to 4 times of its nominal values. The driving motor is powered by a voltage inverter with direct access to the switches of the power module.

Table 2 Parameters of the proposed regulator

N	N_u	m_e^{\max}	ω^{\max}	q_1	q_2	q_3	q_4	r	\mathbf{T}_s
21	3	1.50	1.5	420	15	5	5	1	2.5

\mathbf{T}_s is a sampling period of position controller in ms

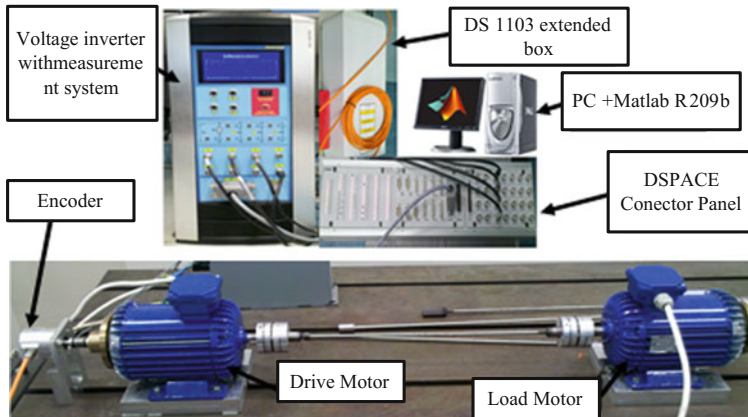


Fig. 6 The block diagram of the experimental set-up with IM drives

The speed of the motor is measured by an incremental encoder with a resolution of 36,000 pulses per/rotation. The current in each phase is measured by *LEM* transducers. Additionally, the inverter is equipped with a system that allows to measure the voltage in the *DC* buffer. The control algorithm is implemented using rapid prototyping system—*DS1103* based on the digital signal processor. In order to ensure optimal performance of the control circuit currents (structure *DTC + SVM*) the sampling period is set to 100 μ s. The Kalman filter is working with the sampling time equal to 1 ms while the position controller is implemented with a step of 2.5 ms.

First a comparative study of the predictive position controller as well as the classical control structure (described in the appendix) are presented. Two values of the reference position are selected for the tests: 0.5 and 0.001. First the system with bigger reference value is tested. The obtained transients are shown in Fig. 7.

As can be concluded from transients presented in Fig. 7 both structures ensure stable operation of the two-mass system. However, there is no direct possibility to limit the shaft torque in the classical control structure. Therefore, this variable reaches the level of 1.2 of its nominal value. Contrary to this, the proposed MPC structure keeps the value of shaft torque within its set limit (0.75). In this particular case the rising times of both structures are similar. It should be mentioned that rising time of speed/position in classical structure depends directly on the limitation of electromagnetic torque.

Then both structures are tested for the small value of reference position. The transients of the system are shown in Fig. 8.

As can be seen from the presented transients both systems operate correctly also for a small value of reference position. The torsional vibrations are not evident in the transients. However, the responses of the system are different. The settling time of the position in the classical control structure is evidently bigger than in MPC structure. It results from constant gains of the control structure. The MPC controller

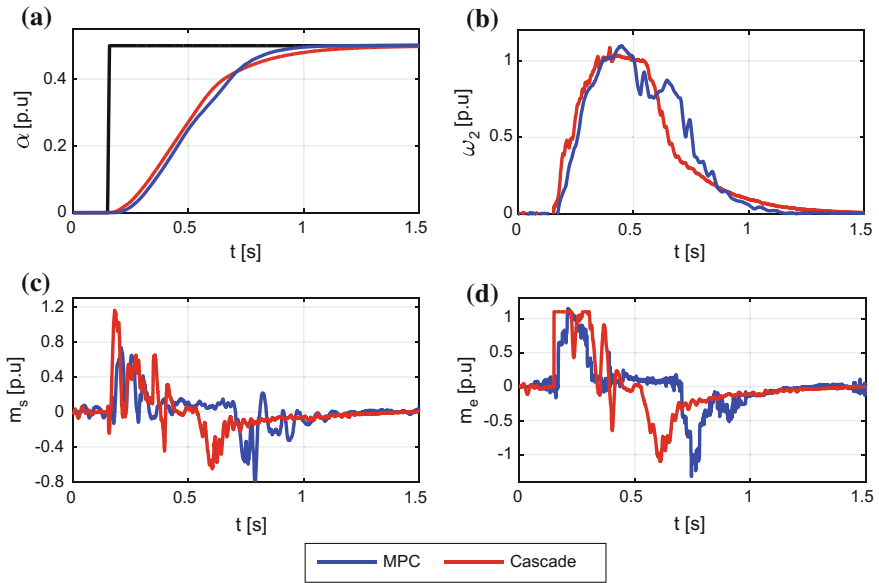


Fig. 7 Transients of the classical and MPC control structures for big reference value: positions of the load (a), load speeds (b), shaft torques (c), electromagnetic torques (d)

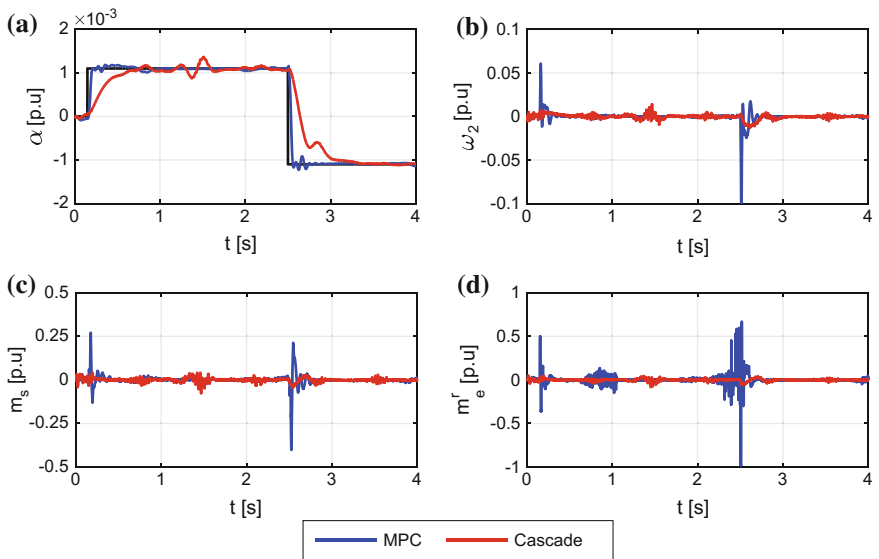


Fig. 8 Transients of the classical and MPC control structures for small reference value: positions of the load (a), load speeds (b), shaft torques (c), electromagnetic torques (d)

generates the control signal according to specify the cost function and ensure faster responses. The dynamics of the system is also visible into transients of electromagnetic and shaft torques. In the MPC structure they reach bigger values than in the classical structure.

The main drawbacks of the classical control structure are as follows: there is no possibility to limit the internal state variables directly (e.g. shaft torque) and oscillations in steady state are bigger. Also the classical structure ensures constant dynamics resulting from the location of the system closed-loop poles. Contrary to this, the MPC methodology has changeable dynamics.

Then the MPC based control structure is investigated in detail. First the influence of the speed limitation on the drive performance is investigated. Two following values of the limitations of the speeds are tested: $\omega^{\max} = 1$, $\omega^{\max} = 1.5$. The limitation value of the shaft torque is set to 0.75 of its nominal value and is constant during this test. The selected transients of the system are shown in Fig. 9.

As can be seen in Fig. 9, the system with the nominal value of the limitation of the speed has the biggest rising time of the position without overshoot

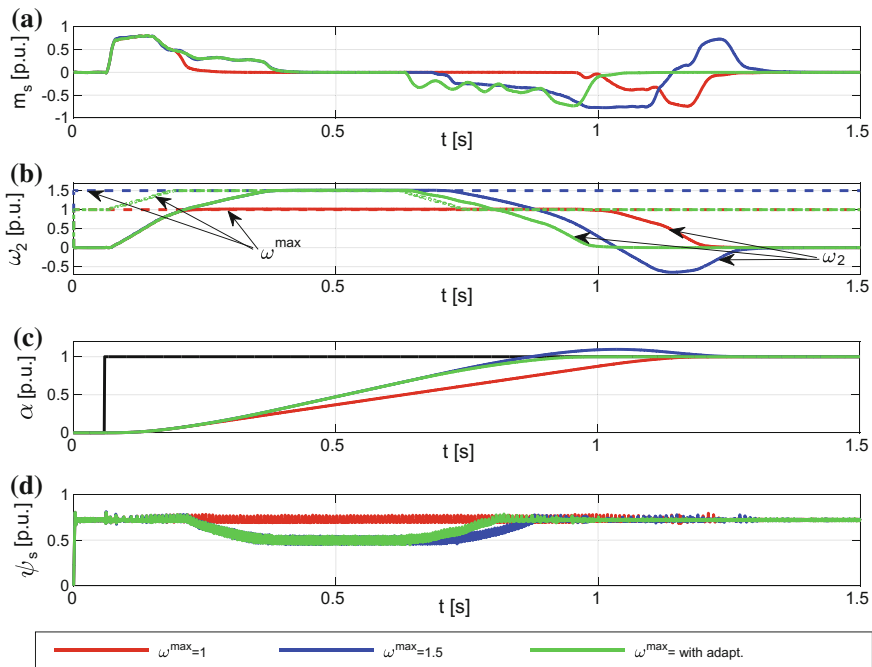


Fig. 9 Transients of the system with different value of the limitation of the speed: shaft torques (a), load speeds and its limitation value—dotted lines (b), position of the drive (c), flux of the IM (d)

(Fig. 9c—red line). The speed and shaft torque are kept within the specified boundary (Fig. 9b). The flux of the *IM* is constant in this case (Fig. 9d).

Next, the performance of the system with $\omega^{\max} = 1.5$ is analyzed (indicated by blue line in Fig. 9). As can be expected, in this case the position has the smallest rising time. However, the resulting overshoot cannot be accepted in most industrial applications (Fig. 9c). This property can be eliminated by extending the value of the prediction horizon, but this will increase the computational requirements of the algorithm significantly. The shaft torque and speed constraints are fulfilled. The flux of the *IM* is decreasing dynamically (Fig. 9d) during the work with the speed over nominal value.

The overshoot of the position can be eliminated by applying the fuzzy system ensuring changeable value of the speed limitation. The transients of this system are indicated by a green line in Fig. 9. This system possesses the shortest settling time. There is no overshoot in the position of the drive. The flux of the *IM* is changeable as presented in Fig. 9d.

In order to show the advantages of the control structure with the fuzzy adaptation system the subsequent tests are planned. The system with different values of the load torque is considered, namely with zero, positive and negative load torque. The

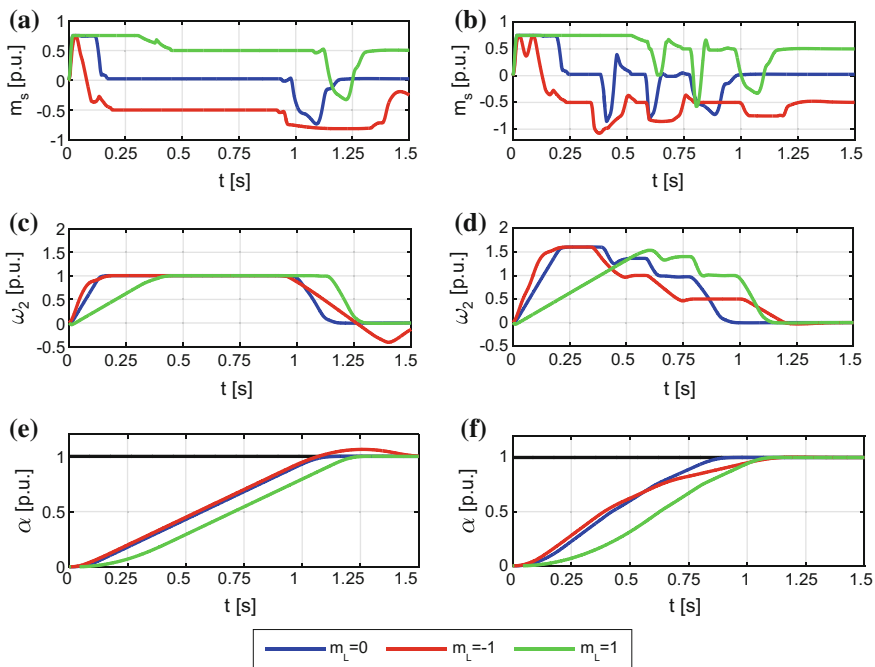


Fig. 10 The transients of the system without (a, c, e) and with (b, d, f) fuzzy adaptation for different value of the load torque: a, b shaft torque; c, d speeds of the system; e, f transients of the load machine

system without adaptation is also tested as a reference point. The transients of the system are demonstrated in Fig. 10.

As can be concluded from the transients demonstrated in Fig. 10 both systems are working correctly. Still, the control structure with the fuzzy block ensures better dynamics. It has the shortest rising time of the position in all analysed cases. Also there is no overshoot in the position transients. Contrary to it, the system without adaptation block cannot ensure zero overshoot for the negative load torque.

Then the computational complexity of the considered on-line algorithm is investigated. In this case the levels of the speed limitation are set as follows: $\omega^{\max} = 0.6$, $\omega^{\max} = 1$, and the case where ω^{\max} depends on the fuzzy adaptation system. The system transients are shown in Fig. 11.

As can be concluded from the presented transients, the drive system is working correctly. The limitations of the state variables are kept in every case. The flux of the *IM* is regulated dynamically in the system with changeable limitation of the speed (Fig. 11c). As can be expected, this system ensures the shortest settling time of the speed. The realization time of each control algorithm is presented in Fig. 11e. The application of the changeable limitation does not increase the computational

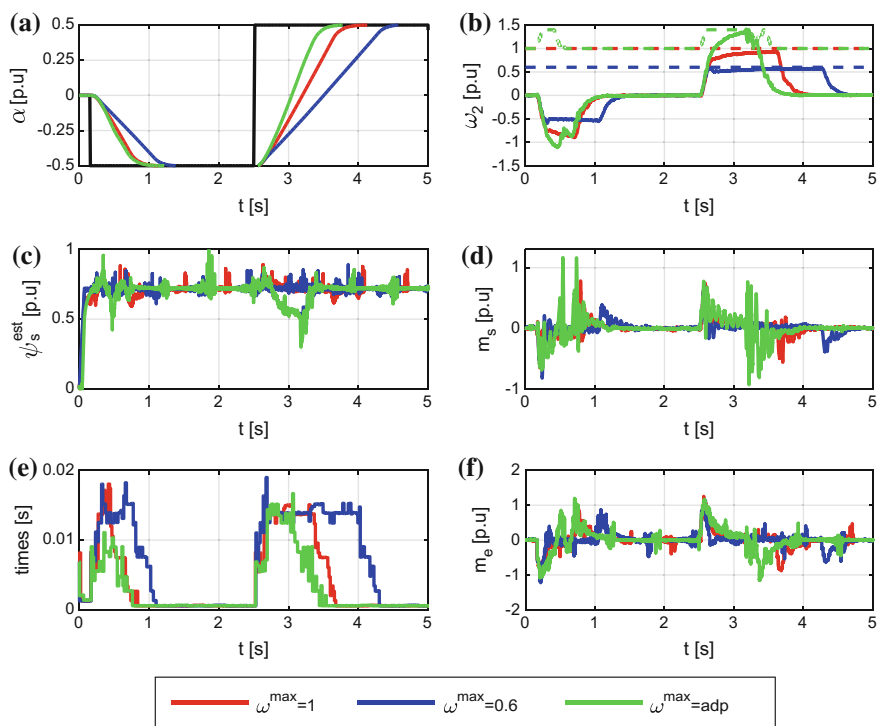


Fig. 11 The transients of the system with different values of the limitation of the speed: position (a), load speeds and its limitation value—dotted lines (b), flux of *IM* (c), shaft torque (d), execution time (e) and electromagnetic torque (f)

complexity of the algorithm in the analyzed cases. The realization time is even smaller than in other cases.

5 Conclusions

In the chapter an MPC-based position control structure of the drive system with an induction motor and a flexible connection is presented. The proposed control structure allows to operate in the field-weakening region. An additional fuzzy system is proposed to ensure the optimal value of the limitation of the system state variables. The following concluding remarks can be formulated on the basis on the presented tests:

- Contrary to the classical cascade control structure with speed and position controllers in the proposed MPC algorithm only one controller is applied.
- The MPC allows to limit not only the control signal but also all state variables of the system. This feature is not directly evident in the classical control structure.
- The torsional vibrations of the two-mass system are suppressed. The limitations of the system state variables are kept in the control structure with MPC algorithm.
- The operation in field-weakening region increases the dynamics of the drive in all considered cases.
- Application of the fuzzy adaptation system enables to regulate the limitation of the system speed in a non-linear way which further improves the properties of the drive—the overshoot is eliminated from the load position.
- The computational complexity of the fuzzy system is not significant compared to MPC algorithm.

The future works will be devoted to the design of an MPC position controller which directly controls the switches of the inverter.

Acknowledgments This research work is supported by National Science Centre (Poland) under grant Adaptive fuzzy control of the complex drive system with changeable parameters UMO-2011/03/B/ST7/02517 (2012–2015).

Appendix

The classical structure consists of the optimized torque control loop and two additional controllers: a *PI* speed controller supported by two additional feedbacks used in order to suppress torsional vibrations effectively [6] and a supervisory *P* position controller. The parameters of the *PI* controller and additional feedbacks are set with the help of the methodology presented in [6] using the following equations:

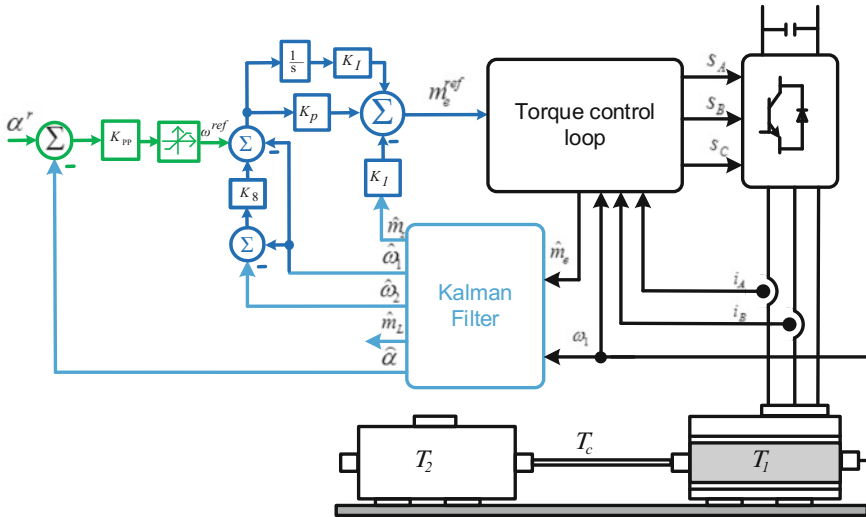


Fig. 12 Block diagram of classical control structure

$$\begin{aligned} k_8^\omega &= \frac{1}{\omega_{rez}^2 T_2 T_C} - 1, & k_1^\omega &= \frac{T_1(4\zeta^2 - k_8)}{T_2(1 + k_8)} \\ K_I^\omega &= \omega_{rez}^4 T_1 T_2 T_C & K_P^\omega &= 4\zeta \omega_{rez}^3 T_1 T_2 T_C \end{aligned} \quad (30)$$

The gain of the position controller is set according to the following equation:

$$K_{PP} = \frac{T_z}{2T_{0\omega}} \quad (31)$$

where: $T_{0\omega}$ —equivalent time constant of the speed control loop.

The block diagram of the considered control structure is shown in Fig. 12.

References

- Leonard W (2001) Control of electrical drives, third edition. Springer, Berlin
- Kaźmierkowski MP, Krishnan R, Blaabjerg F (2002) Control in power electronics: selected problems. Academic Press, San Diego
- Sutikno T, Idris NRN, Jidin A, Cirstea MN (2013) An improved FPGA implementation of direct torque control for induction machines. IEEE Trans Ind Inform 9(3):1280–1290
- Preindl M, Bolognani S (2013) Model predictive direct torque control with finite control set for PMSM drive systems, part 2: field weakening operation. IEEE Trans Ind Inform 9(2): 648–657
- Orłowska-Kowalska T, Tarchala G (2013) Unified approach to the sliding-mode control and state estimation—application to the induction motor drive. Bull Pol Acad Tech Sci 61(4): 837–846

6. Szabat K, Orłowska-Kowalska T (2007) Vibration suppression in two-mass drive system using PI speed controller and additional feedbacks—comparative study. *IEEE Trans Ind Electron* 54(2):1193–1206
7. Muszynski R, Deskur J (2010) Damping of torsional vibrations in high-dynamic industrial drives. *IEEE Trans Ind Electron* 57(2):544–552
8. Hori Y, Sawada H, Chun Y (1999) Slow resonance ratio control for vibration suppression and disturbance rejection in torsional system. *IEEE Trans Ind Electron* 46(1):162–168
9. Vašák M, Baotić M, Petrović I, Perić N (2007) Hybrid theory-based time-optimal control of an electronic throttle. *IEEE Trans Ind Electron* 54(3):1483–1494
10. Bang JS, Shim H, Park SK, Seo JH (2010) Robust tracking and vibration suppression for a two-inertia system by combining backstepping approach with disturbance observer. *IEEE Trans Ind Electron* 57(9):3197–3206
11. Thomsen S, Hoffmann N, Fuchs FW (2011) PI control, PI-based state space control, and model-based predictive control for drive systems with elastically coupled loads—a comparative study. *IEEE Trans Ind Electron* 58(8):3647–3657
12. Schutte E, Beineke S, Rolfsmeier A, Grotstollen H (1997) Online identification of mechanical parameters using extended Kalman filters. In: *Industry applications conference IAS'97*, New Orleans
13. Hashimoto S, Hara K, Funato H, Kamiyama K (2001) AR-based identification and control approach in vibration suppression. *IEEE Trans Ind Appl* 37(3):806–811
14. Vittek J, Makys P, Stulrajter M, Dodds SJ, Perryman R (2008) Comparison of sliding mode and forced dynamics control of electric drive with a flexible coupling employing PMSM. In: *International conference on industrial technology, ICIT'08*
15. Fitri M, Yakub M, Martono W, Akmeliawati R (2010) Vibration control of two-mass rotary system using improved NCTF controller for positioning systems. *Control and System Graduate Research Colloquium, ICSGRC*
16. Cychowski M, Szabat K, Orłowska-Kowalska T (2009) Constrained model predictive control of the drive system with mechanical elasticity. *IEEE Trans Ind Electron* 56(6):1963–1973
17. Serkies P, Szabat K (2013) Application of the MPC controller to the position control of the two-mass drive system. *IEEE Trans Ind Electron* 60(9):3679–3688
18. Wang Fengxiang, Che Zhe, Stolze P, Stumper JF, Rodriguez J, Kennel R (2014) Encoderless finite-state predictive torque control for induction machine with a compensated MRAS. *IEEE Trans Ind Inform* 10(2):1097–1106
19. Fuentes E, Kennel R (2011) Finite-set model predictive control of the two-mass-system. *Workshop on predictive control of electrical drives and power electron (PRECEDE)*, pp 82–87
20. Fuentes EJ, Silva C, Yuz JI (2012) Predictive speed control of a two-mass system driven by a permanent magnet synchronous motor. *IEEE Trans Ind Electron* 59(7):2840–2848
21. Ma Zhixun, Saeidi Saeid, Kennel R (2014) FPGA implementation of model predictive control with constant switching frequency for PMSM drives. *IEEE Trans Ind Inform* 10(4):2055–2063
22. Rodriguez J, Kazmierkowski M, Espinoza J, Zanchetta Abu-Rub PH, Young H, Rojas C (2013) State of the art of finite control set model predictive control in power electronics. *IEEE Trans Ind Inform* 9(2):1003–1016
23. Stephens M, Manzie C, Good M (2013) Model predictive control for reference tracking on an industrial machine tool servo drive. *IEEE Trans Ind Inform* 9(2):808–816
24. Orłowska-Kowalska T, Dybkowski M (2012) Performance analysis of the sensorless adaptive sliding-mode neuro-fuzzy control of the induction motor drive with MRAS-type speed estimator. *Bull Pol Acad Tech* 60(1):61–70
25. Valenzuela MA, Bentley JM, Lorenz RD (2005) Evaluation of torsional oscillations in paper machine sections. *IEEE Trans Ind Inform Appl* 41(2):493–501
26. Serkies P, Szabat K (2013) Fuzzy adaptive Kalman filter for the drive system with an elastic coupling. *Arch Electr Eng* 62(2):251–265

27. Szabat K, Orłowska-Kowalska T (2012) Application of the Kalman filters to the high-performance drive system with elastic coupling. *IEEE Trans Ind Electr* 59(11): 4226–4235
28. Zawirski K, Janiszewski D, Muszynski R (2013) Unscented and extended Kalman filters study for sensorless control of PM synchronous motors with load torque estimation. *Bull Pol Acad Tech* 61(4):793–801
29. Buja GS, Kaźmierkowski MP (2004) Direct torque control of PWM inverter-fed AC motors—a survey. *IEEE Trans Ind Electron* 51(4):744–757
30. Orłowska-Kowalska T, Dybkowski M (2010) Stator-current-based MRAS estimator for a wide range speed-sensorless induction-motor drive. *IEEE Trans Ind Electron* 57(4): 1296–1308
31. Xu X, Novotny D (1992) Selection of the flux reference for induction machine drives in the field weakening region. *IEEE Trans Ind Appl* 28(6):1353–1358
32. Shin Myoung-Ho, Hyun Dong-seok, Cho Soon-Bong (2002) Maximum torque control of stator-flux-oriented induction machine drive in the field-weakening region. *IEEE Trans Ind Appl* 38(1):117–122
33. Maciejowski JM (2002) Predictive control with constraints. Prentice-Hall, Harlow

Selected Methods for a Robust Control of Direct Drive with a Multi-mass Mechanical Load

Stefan Brock, Dominik Łuczak, Tomasz Pajchrowski
and Krzysztof Zawirski

Abstract Mechanical vibrations represent one of the key issues in the development of direct drives with a complex mechanical structure, i.e., with non-stiff connections between motor and driven mechanisms and with variable moments of inertia. A solution for motion control in relation to a direct drive, with highly dynamic performance, coupled with multi-mass mechanical load is proposed in the chapter. Due to high resonance frequencies that are difficult to be actively damped by the control system, an original solution is proposed, which is based on damping the highest resonance frequencies with a specially selected and tuned filter, leaving the damping of the lowest frequencies to the control system. In the first part of this chapter, the identification method is presented, along with robust notch filters, which are tuned for the whole range of parameter variability. Due to variable moment of inertia, two robust control methods are proposed in the second and third parts of this chapter: one is based on an adaptive neural speed controller, while the other is based on a terminal sliding mode control (SMC). The online learning neural speed controller is based on the resilient back propagation (RPROP) algorithm. A modified terminal sliding control law is proposed for a system with delays and unmodelled dynamics. The advantages of both solutions are verified on the basis of experiment investigations.

Keywords Vibration damping · Tunable filter · Neural controller · Online learning · Terminal sliding mode · Direct drive

S. Brock (✉) · D. Łuczak · T. Pajchrowski · K. Zawirski
Institute of Control and Information Engineering,
Poznan University of Technology, Poznan, Poland
e-mail: Stefan.Brock@put.poznan.pl

D. Łuczak
e-mail: Dominik.Luczak@put.poznan.pl

T. Pajchrowski
e-mail: Tomasz.Pajchrowski@put.poznan.pl

K. Zawirski
e-mail: Krzysztof.Zawirski@put.poznan.pl

1 Introduction

The direct drive is a mechanical solution, in which an electric motor is connected with the operating machine without any mechanical gear. A special construction of the motor is required, which enables the drive system operation with a low rotational speed of about 100 rpm, in general, and often even less. The increase in industrial requirements, which can be observed over many years, has required the application of more and more precise solutions, especially in the industrial drives of robots and technological machines, e.g., paper machines, rolling machines or other servo drives. The lack of mechanical gear offers numerous advantages, e.g., an elimination of backlashes introduced by the gear, which improves the static accuracy of the operation and dynamic properties of the drive, as well as increases drive system efficiency (an elimination of losses in the gear) and reliability (a smaller amount of mechanical elements). The aforementioned advantages in direct drives require the application of proper regulation algorithms in the control system.

Mechanical systems with reduced rigidity are characterized by undesired vibrations, which are associated with mechanical resonance phenomena. These unwanted oscillations represent one of the major problems within the control of mechanical systems with limited stiffness [1, 2]. The degradation of parts' parameters and breakdowns, as well as machine and equipment faults, may be caused by the occurrence of oscillations. The elimination of vibration in the system may significantly extend the lifespan of the mechanical system, resulting in an avoidance of the problems associated with accidents and damage. One of the ways of eliminating vibrations is the application of a properly tuned digital filter in the control system, whose role is to prevent the excitation of oscillations [3]. The proper selection of the structure of digital filters allows for minimizing the influence of the limited stiffness in the mechanical system, such that the dynamic and static properties of the drive remain excellent. The task of properly avoiding vibration is particularly challenging for systems with variable parameters, where the oscillation frequency is also variable. In these situations, it is necessary to identify the parameters of the operating machine.

In the direct drive, the moment of inertia in an operating machine is many times higher than the moment of inertia in the motor itself; therefore, large changes in the moment of inertia in the machine can have a significant influence on operating conditions in the drive system. Robustness and adaptability to parameter variation and load disturbances in a highly dynamic and accurate trajectory tracking system are prerequisites for fulfilment of the application requirements.

Methods of computational intelligence, artificial neural networks (ANNs) in particular, are utilized in the implementation of adaptive control structures.

Different concepts of the adaptive neural controller are presented. Both offline learning, based on data from simulations, and online learning during system operation are used. Recently, controllers with online learned neural networks have especially been the focus of many studies [4, 5].

One of the methods to achieve robustness is sliding mode control (SMC) [6, 7]. However, SMC creates some problems in practical applications due to chattering effects, such as high frequency oscillation of the motor torque, additional mechanical stresses and noise during an operation [8, 9]. An interesting solution is terminal SMC, ensuring a finite duration of transient processes [10]. Unfortunately, such an approach cannot be directly used in the real drive system [11].

This chapter is divided into six sections. In Sect. 2, an example of a direct drive, with emphasis upon the general structure the control system, is presented. The study in Sect. 3 shows that the application of a digital signals analysis to the frequency domain allows for the correct identification of the frequency of vibrations in the drive systems, which contain a complex mechanical structure for various parameters of the machine. As a result of the single identification procedure, the amplitude of frequency response is obtained for the mechanical part of the drive for the selected moment of inertia in the machine. In Sect. 4, an improved solution of the neural speed controller and proposed ANN structure are discussed. The modified RPROP algorithm of the online ANN training is presented. The theoretical analysis is validated by the experiment results. The modified algorithm of a terminal sliding mode controller is discussed in Sect. 5. The modifications of the sliding surface and the control laws, which allow the implementation in a real system, are presented. Proper operation of the controller is tested by a simulation exercise. Section 6 contains the conclusions summarizing the presented studies.

2 Laboratory Stand

The structure of the laboratory stand is presented in Fig. 1. The system consists of three main parts: a motor with a load construction, a pulse-width modulation (PWM) converter and a control algorithm, which is implemented in a digital signal processor (DSP). The data of the investigated drive are presented in the appendix. The set of metal plates fixed to the arm, which are mounted on the motor shaft, enables change to the moment of inertia. The disc brake, with four adjustable brake pads, is fixed to the motor shaft. This adjustable brake may be used to model dry friction, typically for cutting processes [12].

The sampling time of the control algorithm, which runs in the floating point DSP, is set to 100 μ s. An incremental optical encoder provides information about the rotor position. Drive speed is calculated by the differentiation of the rotor position with respect to time. It is very important to filter the speed signal adequately in order to exclude the mechanical resonance amplification. A digital biquadratic multi-band filter is designed and tested [3].

Field-oriented control of currents along the d -axis and q -axis is performed by applying a robust proportional-integral control algorithm. The closed current control loop is much faster than mechanical dynamics.

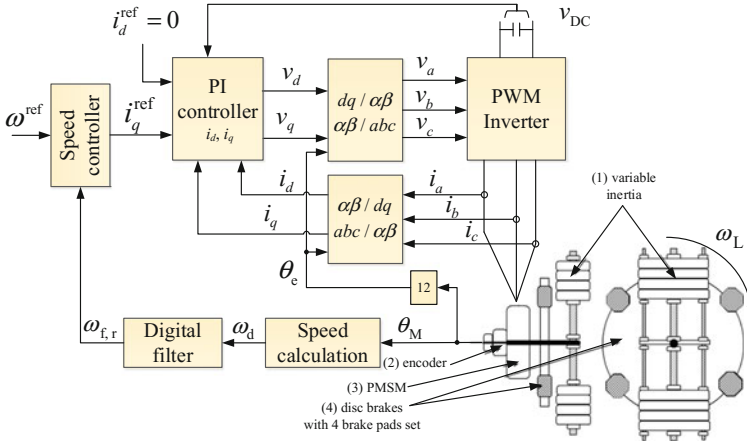


Fig. 1 Block diagram of a laboratory stand with a vector-controlled PMSM direct drive

3 Filter Tuned to Several System Frequency Responses

3.1 Model of an Electrical Drive Control System

A block diagram of the drive with the control system is presented in Fig. 2. The structure of the control system consists of a cascade connection between the current controller and the speed controller. The mechanism is driven by a low-speed permanent-magnet synchronous motor (PMSM) (up to 2.5 rev/s), which is designed to operate with no mechanical gear. The motor is powered by a PWM transistor inverter. A typical vector control structure for the PMSM is assumed, with appropriate transformations of phase currents from a three-phase A - B - C coordinate frame to a d - q system, with inverse transformation of the reference voltages.

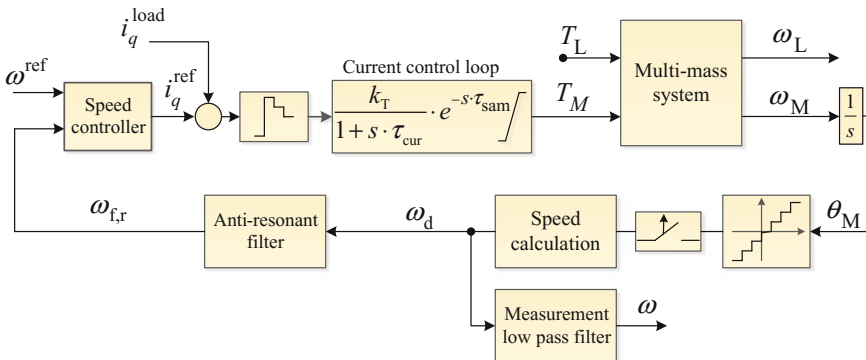


Fig. 2 Drive control scheme

According to the most common control strategy for a PMSM, the reference current along the d -axis is equal to zero ($i_d^{\text{ref}} = 0$), while the q -axis reference current (i_q^{ref}) is fed by the speed controller. The operating machine is presented as a multi-mass system with flexible connections. Such a system is characterized by many mechanical resonance frequencies, which negatively affect the quality of regulation, or may lead to an unstable operation of the system. The high mechanical resonance frequency signal components are transmitted by the control system. Therefore, the application of an appropriately tuned anti-resonance filter allows for attenuating the selected frequency components [3]. As a result, the feedback signal is filtered ($\omega_{f,r}$) and does not excite the system into oscillation. The filter is tuned after an identification procedure of the system. The sampling time is equal to $\tau_s = 100 \mu\text{s}$. The position sensor (512,000 pulses/rev) is installed on the motor shaft. Due to the lack of direct measurement, the speed signal is substituted with a differentiated and digitally filtered measurement signal from the shaft rotation angle. In the control system, an Analog Devices' SHARC signal processor is utilized, equipped with a motion coprocessor and an appropriate set of 14-bit digital-analogue converters. A low-pass measurement filter with a cut-off frequency equal to 100 Hz and damping at 40 dB/dec is utilized only for the measurements' registration.

The current control loop may be depicted as a first-order inertial element with time constant $\tau_{\text{cur}} = 0.3 \text{ ms}$, combined with transport delay $\tau_{\text{sam}} = 0.2 \text{ ms}$. The torque constant is equal to $k_T = 17.5 \text{ Nm/A}$. The end of the bandpass of the current/torque control system is approximately equal to 530 Hz. Therefore, identification of the system is performed in the range of 50–500 Hz.

3.2 Model of the Mechanical Part

The mechanical part of the drive can be described by an MIMO system in the form of state space equations [2] or an equivalent matrix of transfer functions (Fig. 3) [13]. State space representation can be derived from the knowledge of the system's exact mechanical construction and equations of motion. When the mechanical system is complex and hard to describe by equations of motion, the use of transfer functions can be sufficient for the synthesis of the control system.

It is assumed that the poles are equal for each of the transfer functions. If the poles of the transfer functions $H_{1,1}(s)$, $H_{1,2}(s)$, $H_{2,1}(s)$ and $H_{2,2}(s)$ are the same, then

Fig. 3 MIMO scheme of the mechanical part with a transfer function description

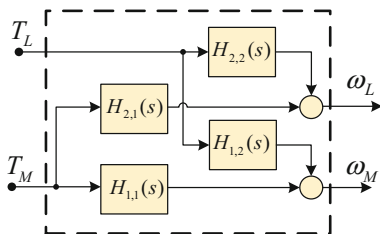
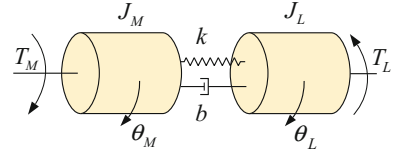


Fig. 4 Kinematic elastic and damped two-mass system



the resonance frequencies are also identical. From the point of view of the anti-resonance filter synthesis, information about the parameters of one of four transfer functions is sufficient for proper filter synthesis. Transfer function $H_{1,1}(s)$ is chosen due to the availability of measurement signals (motor torque and motor speed), allowing identification of its parameters.

For example, let us consider the two-mass system presented in Fig. 4. This example justifies the poles' equality in the four remaining transfer functions. The system is described by motion equations in matrix notation

$$\begin{bmatrix} J_M & 0 \\ 0 & J_L \end{bmatrix} \begin{bmatrix} \ddot{\theta}_M \\ \ddot{\theta}_L \end{bmatrix} + \begin{bmatrix} b & -b \\ -b & b \end{bmatrix} \begin{bmatrix} \dot{\theta}_M \\ \dot{\theta}_L \end{bmatrix} + \begin{bmatrix} k & -k \\ -k & k \end{bmatrix} \begin{bmatrix} \theta_M \\ \theta_L \end{bmatrix} = \begin{bmatrix} T_M \\ T_L \end{bmatrix}, \quad (3.1)$$

where the torsional torque equal to $T_s = k(\theta_M - \theta_L)$ is assumed, while k is the elasticity constant, θ_M and θ_L are the respective positions on the motor and load side, and b is the damping constant. The general mathematical notation of the system in the state space is presented by:

$$\begin{aligned} \dot{\mathbf{x}}(t) &= \mathbf{A}\mathbf{x}(t) + \mathbf{B}\mathbf{u}(t) \\ \mathbf{y}(t) &= \mathbf{C}\mathbf{x}(t) + \mathbf{D}\mathbf{u}(t), \end{aligned} \quad (3.2)$$

where \mathbf{x} is the state variables vector, \mathbf{u} is the input vector, \mathbf{y} is the output vector, \mathbf{A} is the state matrix, \mathbf{B} is the input matrix, \mathbf{C} is the output matrix and \mathbf{D} is the feed-forward matrix.

For the described case, the following state variables are assumed to be $\omega_M = \dot{\theta}_M$, $\omega_L = \dot{\theta}_L$, T_s ; as a result, the description in the state space assumes the formula (\mathbf{D} is the zero matrix):

$$\begin{aligned} \underbrace{\begin{bmatrix} \dot{\omega}_M \\ \dot{\omega}_L \\ \dot{T}_s \end{bmatrix}}_{\dot{\mathbf{x}}} &= \underbrace{\begin{bmatrix} -\frac{b}{J_M} & \frac{b}{J_M} & -\frac{1}{J_M} \\ \frac{b}{J_L} & -\frac{b}{J_L} & \frac{1}{J_L} \\ k & -k & 0 \end{bmatrix}}_{\mathbf{A}} \underbrace{\begin{bmatrix} \omega_M \\ \omega_L \\ T_s \end{bmatrix}}_{\mathbf{x}} + \underbrace{\begin{bmatrix} \frac{1}{J_M} & 0 \\ 0 & -\frac{1}{J_L} \\ 0 & 0 \end{bmatrix}}_{\mathbf{B}} \underbrace{\begin{bmatrix} T_M \\ T_L \end{bmatrix}}_{\mathbf{u}} \\ \mathbf{y} &= \underbrace{\begin{bmatrix} 1 & 0 & 0 \\ 0 & 1 & 0 \end{bmatrix}}_{\mathbf{C}} \begin{bmatrix} \omega_M \\ \omega_L \\ T_s \end{bmatrix}. \end{aligned} \quad (3.3)$$

The derivatives of subsequent state variables are defined by the formula:

$$\begin{cases} \dot{\omega}_M = \frac{T_M - b(\omega_M - \omega_L) - T_S}{J_M} \\ \dot{\omega}_L = \frac{T_S + b(\omega_M - \omega_L) - T_L}{J_L} \\ \dot{T}_S = k(\omega_M - \omega_L) \end{cases} \quad (3.4)$$

It is possible to pass from the MIMO system, as defined in the state space, to the system description by using the transfer function matrix, with the application of the relation $\mathbf{H}(s) = \mathbf{C}(s\mathbf{I} - \mathbf{A})^{-1}\mathbf{B} + \mathbf{D}$. Interconnections between subsequent inputs and outputs of the system are presented in Fig. 3. Taking into account formula (3.3) and the conversion relationship, the following transfer function matrix is obtained:

$$\begin{aligned} \mathbf{H}(s) &= \mathbf{C}(s\mathbf{I} - \mathbf{A})^{-1}\mathbf{B} + \mathbf{D} = \begin{bmatrix} \frac{\mathcal{L}\{\omega_M\}}{\mathcal{L}\{T_M\}} & \frac{\mathcal{L}\{\omega_M\}}{\mathcal{L}\{T_L\}} \\ \frac{\mathcal{L}\{\omega_L\}}{\mathcal{L}\{T_M\}} & \frac{\mathcal{L}\{\omega_L\}}{\mathcal{L}\{T_L\}} \end{bmatrix} = \begin{bmatrix} H_{1,1}(s) & H_{1,2}(s) \\ H_{2,1}(s) & H_{2,2}(s) \end{bmatrix} \\ &= \begin{bmatrix} \frac{J_I s^2 + bs + k}{s((J_M + J_L)k + (J_M + J_L)bs + J_M J_L s^2)} & \frac{k + bs}{s((J_M + J_L)k + (J_M + J_L)bs + J_M J_L s^2)} \\ \frac{k + bs}{s((J_M + J_L)k + (J_M + J_L)bs + J_M J_L s^2)} & \frac{J_M s^2 + bs + k}{s((J_M + J_L)k + (J_M + J_L)bs + J_M J_L s^2)} \end{bmatrix}. \end{aligned} \quad (3.5)$$

The denominator is identical in each of the four functions. The transfer function matrix (3.5) is then transformed to:

$$\mathbf{H}(s) = \begin{bmatrix} \frac{1}{(J_M + J_L)s} \frac{s^2 + 2\zeta_{ar}\omega_{ar}s + \omega_{ar}^2}{s^2 + 2\zeta_r\omega_r s + \omega_r^2} \frac{\omega_r^2}{\omega_{ar}^2} - \frac{1}{(J_M + J_L)s} \frac{2\zeta_{ar}\omega_{ar}s + \omega_{ar}^2}{s^2 + 2\zeta_r\omega_r s + \omega_r^2} \frac{\omega_r^2}{\omega_{ar}^2} \\ \frac{1}{(J_M + J_L)s} \frac{2\zeta_{ar}\omega_{ar}s + \omega_{ar}^2}{s^2 + 2\zeta_r\omega_r s + \omega_r^2} \frac{\omega_r^2}{\omega_{ar}^2} - \frac{1}{(J_M + J_L)s} \frac{R^{-1}s^2 + 2\zeta_{ar}\omega_{ar}s + \omega_{ar}^2}{s^2 + 2\zeta_r\omega_r s + \omega_r^2} \frac{\omega_r^2}{\omega_{ar}^2} \end{bmatrix} \quad (3.6)$$

using the relations:

$$\begin{cases} \omega_r = \sqrt{\frac{J_M + J_L}{J_M J_L}} k, & \omega_{ar} = \sqrt{\frac{k}{J_L}}, \\ \zeta_r = \frac{J_M + J_L}{J_M J_L} \frac{b}{2\omega_r}, & \zeta_{ar} = \frac{b}{2J_L \omega_{ar}}, \\ R = J_L / J_M \end{cases} \quad (3.7)$$

where ω_r and ω_{ar} are respectively angular resonance and anti-resonance frequencies, ζ_r and ζ_{ar} are respectively the damping coefficient for resonance and anti-resonance frequencies, and R is the inertia ratio. Formula (3.6) allows for proper synthesis of the anti-resonance filter.

3.3 Synthesis of a Fixed Anti-resonance Filter Based on the Identification of the Mechanical Part of Drive

The identification of $H_{1,1}(s)$ is performed due to the measurement accessibility of the motor torque (proportional to the reference current along the q -axis) and motor speed (sensor on the motor side). Generally, all identification methods are divided

into two main groups of identification algorithms: parametric [14] and non-parametric. The selection of model structure and fitting algorithm is required for the application of the parametric approach. However, a parametric model is not necessary for the proper tuning of the digital anti-resonance filter used in the control system shown in Fig. 2. Therefore, non-parametric identification in the frequency domain is applied. The system is identified in open loop. Additionally, the dynamic of the current closed loop is neglected because it has no influence on resonance frequency components in the range of identification frequencies. The reference current along the q -axis is used as the excitation input using a chirp signal. A chirp signal is a cosine wave with linear frequency modulation. The frequency is linearly changed from f_{\min} to f_{\max} in the time equal to τ_{inc} (see the top of Fig. 5).

Therefore, this signal allows for the excitation of resonance components in the required range of frequencies. Excitation and response signals in the time and frequency domain is shown in Fig. 5. The frequency amplitude response of drive G_{ident} is calculated on the basis of a discrete Fourier transform of the input and output signal. The number of filter sections and their parameters is determined after the identification procedure, which is equal to the number of frequencies recognized as resonant. The location of the filter in the control system is presented in Fig. 2. The filter is marked as an anti-resonant filter, whose input is, in this particular case, ω_d , while the output is $\omega_{f,r}$. In this case, both the structure and parameters of the

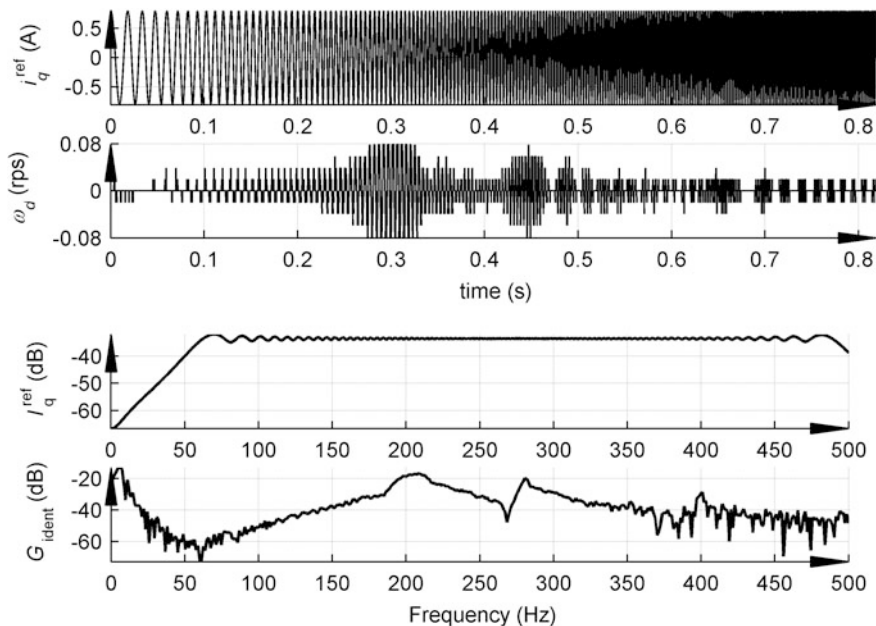


Fig. 5 Drive response to the excitation with a chirp signal: time response (*top*) and frequency response (*bottom*)

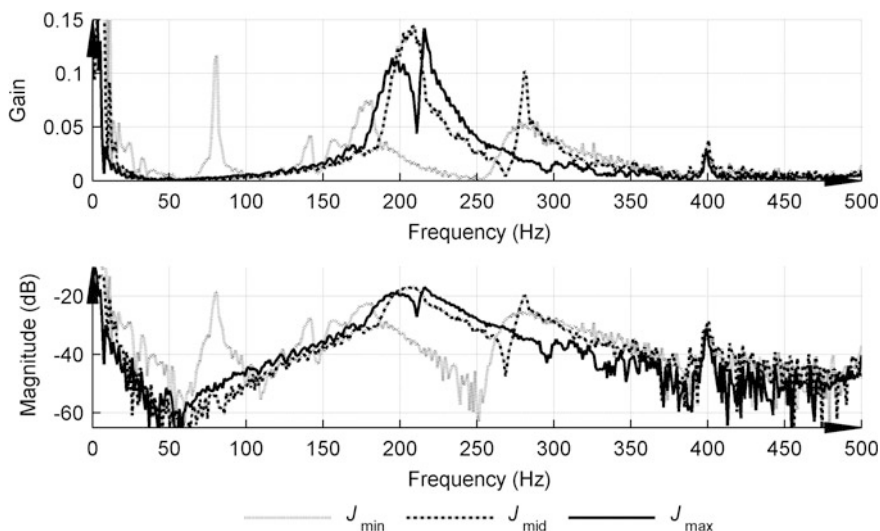


Fig. 6 Frequency response family: gain (*top*) and magnitude (*bottom*)

filter are determined by human intervention on the basis of data obtained during the identification procedure.

Separate identification is performed for three configurations of load machine. Each modification of the mechanical part of the drive results in a change of system frequency response. The amplitude frequency response family of the drive in different cases is shown in Fig. 6. Therefore, for each case, a separate anti-resonance filter is required. Instead of preparing three filters, only one fixed anti-resonance filter is prepared (Fig. 7) for the whole family of frequency responses. The filter consists of four sections: (1) a low-pass filter approximation of inverse Chebyshev parameters [15]: $a_p = 3$ dB, $a_z = 3.8$ dB, $f_p = 76$ Hz, $f_z = 80.88$ Hz, $f_0 = f_z$; (2) a notch filter [15]: $f_z = 200$ Hz, $f_{width} = 180$ Hz; (3) another notch filter: $f_z = 280$ Hz, $f_{width} = 200$ Hz; and (4) another low pass filter: $a_p = 3$ dB, $a_z = 20$ dB, $f_p = 200$ Hz, $f_z = 200$ Hz, $f_0 = 400$ Hz.

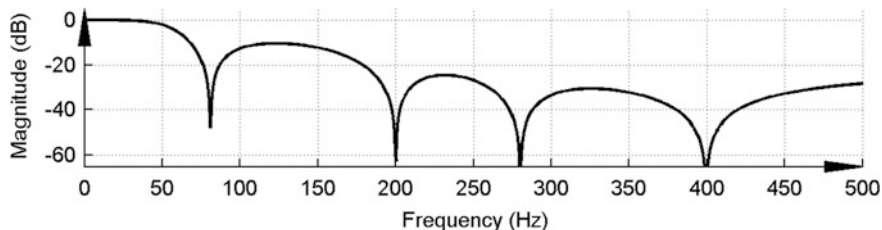


Fig. 7 Frequency response of the fixed anti-resonance filter tuned on the basis of the frequency response family of the drive

4 Online Trained Neural Speed Controller

4.1 Structure and Training Algorithm

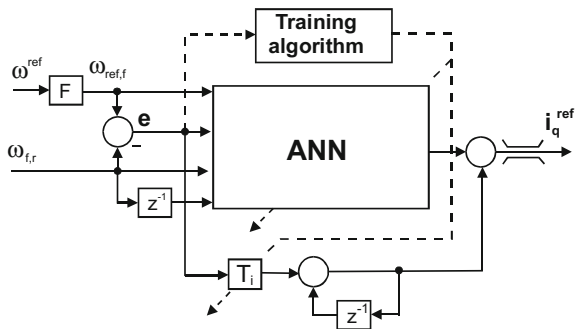
The changes in the moment of inertia influence the parameters of the mechanical resonance frequencies, which essentially complicates their damping. In such cases, the adaptive controllers, based on ANNs that are trained online, can be good solutions. In order to solve this issue an anti-resonance filter with fixed, properly tuned frequency characteristics is proposed and an adaptive neural controller is applied. Such an approach provides a compromise effect of higher frequency torsional vibration damping at changing values of these frequencies. The neural controller structure is shown in Fig. 8. The following signals have been chosen as network inputs: the reference speed value, the present and previous samples of filtered speed signals, and the current value of the control error. These input signals are delivered to the three-neuron hidden layer with a non-linear activation function. The output signal i_q^{ref} is computed by one output neuron with a linear activation function.

Besides the selection of the ANN structure, there are two different issues during neural controller synthesis: the determination of the network error signal and the training rule. For the ANN speed controller, the network error value is related to the speed control error according to the following formula [5]:

$$E = \frac{1}{2} (\omega_{\text{ref},f} - \omega_{f,r})^2 = \frac{1}{2} e^2. \quad (4.1)$$

Due to the assumed “online” training mode of the ANN, the selection of an appropriately fast and efficient training method becomes an important issue. The chosen method is the RPROP algorithm, described in [16]. Its basic advantage, in comparison to the widely applied error backpropagation method, is the fact that, instead of the accurate value of the error function gradient, only its sign is required.

Fig. 8 Structure of non-linear PID-2DOF controller



The value of weight w_{ij} of the connection between i -th neuron, in a given layer, and j -th neuron, in the preceding layer, is modified in each step of the ANN training, according to equation [16]:

$$\Delta w_{ij}(k) = -\eta_{ij}(k) \cdot \operatorname{sgn}\left(\frac{\partial E(w(k))}{\partial w_{ij}}\right) = -\eta_{ij}(k) \cdot \operatorname{sgn}(S_{ij}(k)). \quad (4.2)$$

In the RPROP method, for each weight coefficient, corresponding training factors η_{ij} is defined. The training factors are also updated in every algorithm step:

$$\eta_{ij}(k) = \begin{cases} \min(a \cdot \eta_{ij}(k-1), \eta_{\max}) & \text{if } S_{ij}(k) \cdot S_{ij}(k-1) > 0 \\ \max(b \cdot \eta_{ij}(k-1), \eta_{\min}) & \text{if } S_{ij}(k) \cdot S_{ij}(k-1) < 0 \\ \eta_{ij}(k-1) & \text{other cases} \end{cases}. \quad (4.3)$$

An analysis of the results of many simulations and experimental tests for different conditions of the controller and the drive system operation leads to the conclusion that formula (4.3), in the original RPROP algorithm, should be redefined. A stable online training process, under conditions of measured real feedback signals with some disturbances, is obtained when a tolerant band ΔS is used instead of a zero value, under the conditions of the training factors' update (4.4) [5].

$$\eta_{ij}(k) = \begin{cases} \min(a \cdot \eta_{ij}(k-1), \eta_{\max}) & \text{if } S_{ij}(k) \cdot S_{ij}(k-1) > \Delta S \\ \max(b \cdot \eta_{ij}(k-1), \eta_{\min}) & \text{if } S_{ij}(k) \cdot S_{ij}(k-1) < -\Delta S \\ \eta_{ij}(k-1) & \text{if } -\Delta S \leq S_{ij}(k) \cdot S_{ij}(k-1) \leq \Delta S \end{cases}. \quad (4.4)$$

One of the RPROP algorithm advantages is eliminated by the modification resulting from the introduction of a "tolerant band" into formula (4.4), since the value of the error function gradient is required when considering the non-zero value of ΔS , which is present in the inequalities. This modification implies the substitution of the comparator, described by Eq. (4.3), with a comparator with hysteresis, according to (4.4), where the hysteresis width is the value of ΔS .

In such a comparator, it is necessary to determine not only the sign of the error function gradient, but also to calculate its value. Fortunately, the value of ΔS is selected empirically on the basis of tests, which allows the use of roughly estimated gradient values in (4.4) only. In [17], a modified and improved ANN training algorithm is applied, assuring the improvement of the control properties. For this purpose, the formula's error backpropagation method is utilized.

In order to avoid neural network overtraining, a particularly small limit value of the error $e_x(k)$ should be assumed so that the network weights are not modified when $|e_k(k)| < e_x(k)$ (when the training process is stopped). The training is continued when $|e_k(k)| > e_x(k)$. This modified training rule is defined as:

$$\Delta w_{ij}(k) = \begin{cases} -\eta_{ij}(k) \cdot \text{sgn}(S_{ij}(k)) & \text{if } |e_k(k)| > e_x(k) \\ 0 & \text{if } |e_k(k)| \leq e_x(k) \end{cases} \quad (4.5)$$

4.2 Experiment Results

Efficiency of the applied fixed filter may be evaluated by comparison of step response waveforms in the speed control system with and without an anti-resonance filter, as presented in Figs. 9 and 10. Unacceptable oscillations in the rotational speed, leading to stability loss, are displayed by the system without a filter (Fig. 9). These oscillations are eliminated by the introduction of an anti-resonance filter, which can be observed in the waveform in Fig. 10. Nevertheless, a small pulsation in the motor speed is still observed after a step change in load signal i_q . The process of controller adaptation, i.e., the ANN training process, which, after two periods of reference, changes to provide a successful effect, is well-depicted in Fig. 10.

The basic goal of the adaptive neural speed controller application is obtaining good and invariable control properties despite changes in the mechanism moment of inertia. This property may be noticed by an analysis of waveforms in the

Fig. 9 Reference and measured (ω) rotational speed and current (i_q) of the speed control system during the step response without an anti-resonance filter

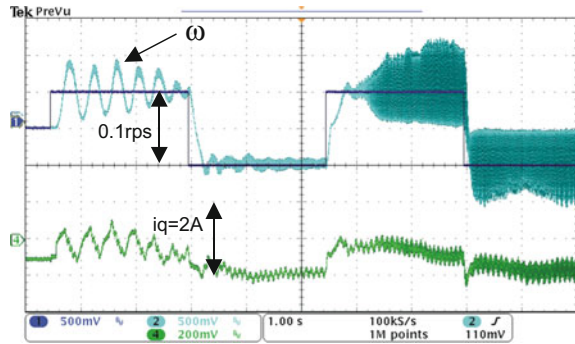


Fig. 10 Reference and measured (ω) rotational speed and current (i_q) of speed control system during the step response with an anti-resonance filter

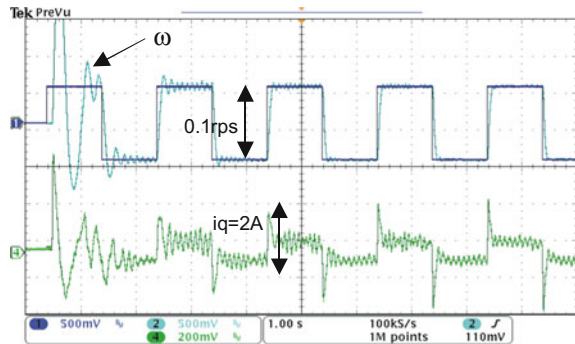


Fig. 11 Reference (ω_{ref}) and measured (ω) rotational speed and current (i_q) of the speed control system during the step response and step change of the load torque for the largest value in the moment of inertia (J_{max})

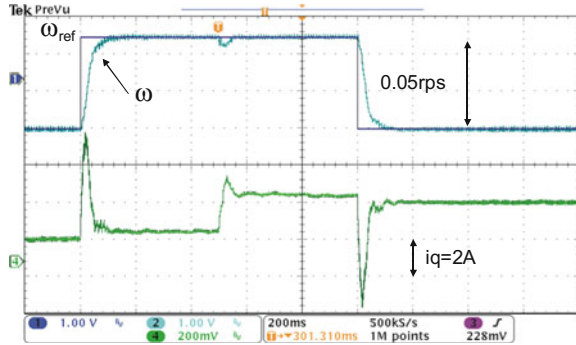


Fig. 12 Reference (ω_{ref}) and measured (ω) rotational speed and current (i_q) of the speed control system during the step response and step change of the load torque for the smallest value in the moment of inertia (J_{min})

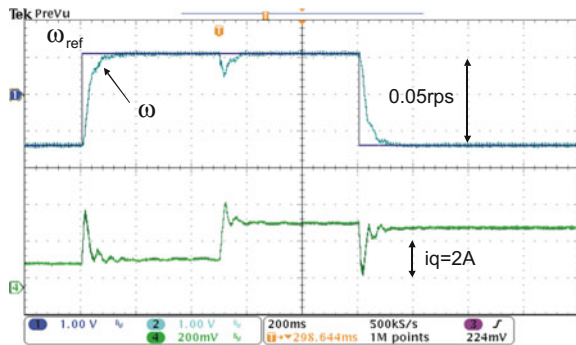


Table 1 Quality indexes for the neural network controller

Quality index	Unit	J_{min}	J_{max}
Response time (10–90 %)	ms	56.4	59.5
Settling time (5 %)	ms	97.4	94.2
Settling time after step change of load (5 %)	ms	109.3	68.4

reference speed, measured speed and q -axis current during controller responses, which lead to a step change in the reference speed and load torque step changes, as presented in Figs. 11 and 12. The experimental waveforms are registered for the largest (Fig. 11) and the smallest (Fig. 12) value in the moment of inertia, demonstrating almost identical properties, which are confirmed by the quality indexes collected in Table 1. These quality indexes should be read as follows: response time (10–90 %), settling time (5 %), and settling time after a step change in load (5 %). The speed signal during the reference speed step change increases rapidly, while the reference value is achieved with no overshoot from either value of inertia; whereas, after load torque step changes, the small dynamic error in speed control is quickly removed, as are the extreme values in the moment of inertia. The application of this controller is fully substantiated by the obtained results.

5 Terminal SMC of a Direct Drive with a Multi-mass Mechanical Load

5.1 Concept of the Terminal SMC

Let us assume that a second order system, described by Eq. (5.1), is considered:

$$\begin{aligned}\frac{dx_1}{dt} &= x_2 \\ \frac{dx_2}{dt} &= f(\mathbf{x}) + b(\mathbf{x}) \cdot u + d(\mathbf{x}, t),\end{aligned}\tag{5.1}$$

where $\mathbf{x} = [x_1 \ x_2]^T$ is the system state vector and u is the scalar control input. Functions $f(\mathbf{x})$, $b(\mathbf{x})$ are smooth and known, while component $d(\mathbf{x}, t)$ represent uncertainties and disturbances, thereby satisfying:

$$|d(\mathbf{x}, t)| \leq D.\tag{5.2}$$

In the case of the classical SMC, the control signal switching surface is defined as:

$$\sigma = x_2 + \lambda \cdot x_1 = 0,\tag{5.3}$$

where $\lambda > 0$ defines the decay rate of generalized error σ .

The control task is to bring the state vector to the origin. If the initial value of the state vector is $\mathbf{x}(0) = [x_1(0) \ 0]^T$, then, in the sliding mode, the system will tend to a steady state, according to the equation:

$$x_1 = x_1(0) \cdot e^{-\lambda t}.\tag{5.4}$$

The system, therefore, tends asymptotically to a steady state with a time constant of $1/\lambda$ and reaches it after an infinitely long time.

In [10], a new formula for switching surface is proposed:

$$\sigma = x_2 + \lambda \cdot x_1^{q/p} = 0,\tag{5.5}$$

where p and q are positive odd integers, which satisfy the following condition: $q < p$. Considering the acceptable range of values of the state variables, Eq. (5.5) may be written in a modified form:

$$\sigma = x_2 + \lambda \cdot |x_1|^{q/p} \cdot \text{sgn}(x_1) = 0.\tag{5.6}$$

A sufficient condition of the sliding mode is to ensure that, for the full variation range for parameters and possible disturbances, the derivative of the Lyapunov function $V(\mathbf{x}) = \frac{1}{2}\sigma^2$ satisfies the relationship:

$$\frac{d}{dt}V(\mathbf{x}) = \frac{1}{2} \cdot \frac{d}{dt}\sigma^2 = \frac{d\sigma}{dt} \cdot \sigma < -\eta \cdot |\sigma|, \quad (5.7)$$

where $\eta > 0$ is a constant.

The proposed control law is expressed by the formula:

$$u = -b^{-1}(\mathbf{x}) \cdot \left(f(\mathbf{x}) + \lambda \cdot \frac{q}{p} \cdot |x_1|^{\frac{q}{p}-1} \cdot x_2 \cdot \operatorname{sgn}(x_1) + L \cdot \operatorname{sgn}(\sigma) \right). \quad (5.8)$$

Let $x_1 \geq 0$. After substituting control law (5.8) in the equations of object (5.1), the derivative of the generalized error (5.6) can be written as:

$$\begin{aligned} \frac{d\sigma}{dt} &= \frac{dx_2}{dt} + \lambda \cdot \frac{q}{p} \cdot x_1^{\frac{q}{p}-1} \cdot x_2 \\ &= f(\mathbf{x}) + b(\mathbf{x}) \cdot u + d(\mathbf{x}, t) + \lambda \cdot \frac{q}{p} \cdot x_1^{\frac{q}{p}-1} \cdot x_2 \\ &= d(\mathbf{x}, t) - L \cdot \operatorname{sgn}(\sigma). \end{aligned} \quad (5.9)$$

Condition (5.7) is thus fulfilled when the amplitude of the switching part is selected, such that:

$$L > |d(\mathbf{x}, t)| + \eta. \quad (5.10)$$

In the sliding mode, the system will tend to a steady state according to equation:

$$x_2 = -\lambda \cdot x_1^{q/p}. \quad (5.11)$$

Finite time t_s is taken to travel $\mathbf{x}(0)$ to origin (0, 0) as follows:

$$t_s = \frac{p}{\lambda \cdot (p - q)} \cdot |x_1(0)|^{1-\frac{q}{p}}. \quad (5.12)$$

5.2 Elimination of Singularities in the Control Law

In a real control system, it is possible that $x_2 \neq 0$ and $x_1 = 0$. This condition does not occur in an ideal sliding mode, described by Eq. (5.6), but can occur in the phase of reaching the sliding surface or during the sliding motion, which is a result of discretization errors associated with the measurements of variables. In this case, the value of the control law component $\lambda \cdot \frac{q}{p} \cdot |x_1|^{\frac{q}{p}-1} \cdot x_2$ tends to infinity. This may cause oscillations and instability in the control system. To eliminate this singularity, a modified switching surface is proposed [11]

$$\sigma = \frac{1}{\lambda^{p/q}} \cdot |x_2|^{p/q} \cdot \text{sgn}(x_2) + x_1 = 0. \quad (5.13)$$

During the sliding mode, Eq. (5.13) is equivalent to Eq. (5.6). The modification used in (5.13), however, allows for the introduction of control law:

$$u = -b^{-1}(\mathbf{x}) \cdot \left(f(\mathbf{x}) + \lambda^{\frac{p}{q}} \cdot \frac{q}{p} \cdot |x_2|^{2-\frac{p}{q}} \cdot \text{sgn}(x_2) + L \cdot \text{sgn}(\sigma) \right). \quad (5.14)$$

A similar analysis of the stability of the sliding mode, as in (5.9), leads to the equation:

$$\begin{aligned} \frac{d\sigma}{dt} &= \frac{1}{\lambda^{p/q}} \cdot \frac{p}{q} \cdot x_2^{p/q-1} \cdot \frac{dx_2}{dt} + x_2 \\ &= \frac{1}{\lambda^{p/q}} \cdot \frac{p}{q} \cdot x_2^{p/q-1} \cdot (f(\mathbf{x}) + b(\mathbf{x}) \cdot u + d(\mathbf{x}, t)) + x_2 \\ &= \frac{1}{\lambda^{p/q}} \cdot \frac{p}{q} \cdot x_2^{p/q-1} \cdot (d(\mathbf{x}, t) - L \cdot \text{sgn}(\sigma)). \end{aligned} \quad (5.15)$$

When $q < p < 2q$ and L is selected in accordance with formula (5.10), condition (5.15) is satisfied. Control law (5.14) eliminates the singularity that occurs in control law (5.8), thereby offering the same sliding trajectory.

5.3 Modification of the Sliding Surface

The sliding surface described by Eqs. (5.6) or (5.13) does not limit the scope of the state variables. However, in practical drive applications, it is necessary, for example, to limit the speed by which the actuator system accelerates. Therefore, it is proposed to modify the sliding surface according to the relationship:

$$\sigma = \begin{cases} x_2 + x_2^{\max} \cdot \text{sgn}(x_1) & \text{if } \lambda \cdot |x_1|^{q/p} \geq x_2^{\max} \\ \frac{1}{\lambda^{p/q}} \cdot |x_2|^{p/q} \cdot \text{sgn}(x_2) + x_1 & \text{if } \lambda \cdot |x_1|^{q/p} < x_2^{\max} \end{cases}. \quad (5.16)$$

The fulfilment of the condition for sliding mode $\sigma = 0$ on the sliding surface, as defined by Eq. (5.16), provides the motion with speed $\pm x_2^{\max}$ away from the origin. The switching point is determined at the intersection of characteristics. When moving at constant speed $x_2^{\max} \cdot \text{sgn}(x_1)$, control law (5.14) is reduced to the following formula:

$$u = -b^{-1}(\mathbf{x}) \cdot (f(\mathbf{x}) + L \cdot \text{sgn}(\sigma)). \quad (5.17)$$

In the control systems of the electric drive, it is necessary to take into account the delay introduced by the blocks of discrete control algorithms, whose delay is caused by the filtering of measurement signals, with an equivalent delay in the force or torque closed-loop control. This delay in the control loop limits the allowable gain.

For the sliding motion along the surface, as defined by Eq. (5.6), the speed gain can be determined according to the following formula:

$$\frac{\partial x_2}{\partial x_1} = -\lambda \cdot \frac{q}{p} \cdot \frac{|x_1|^{q/p}}{|x_1|}. \tag{5.18}$$

For x_1 values close to zero, expression (5.18) tends to infinity. In a closed control loop with delays, such a large speed gain leads to vibrations. Therefore, it is proposed to limit the velocity gain for small values of x_1 . The modified sliding surface, therefore, has the following formula:

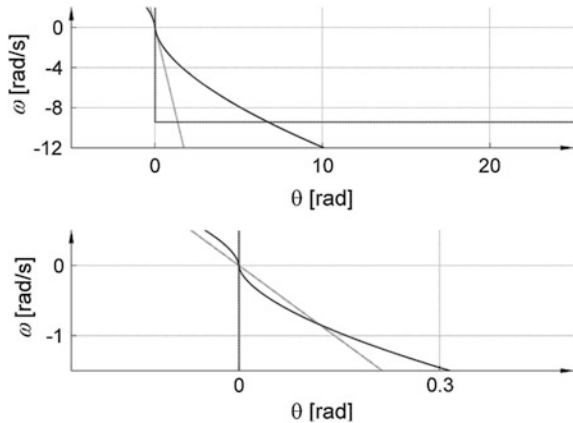
$$\sigma = \begin{cases} x_2 + x_2^{\max} \cdot \text{sgn}(x_1) & \text{if } x_2^{\max} \leq \min(\lambda_l \cdot |x_1|, \lambda \cdot |x_1|^{q/p}) \\ \frac{1}{\lambda^{p/q}} \cdot |x_2|^{p/q} \cdot \text{sgn}(x_2) + x_1 & \text{if } \lambda \cdot |x_1|^{q/p} < \min(\lambda_l \cdot |x_1|, x_2^{\max}) \\ x_2 + \lambda_l \cdot x_1 & \text{if } \lambda \cdot |x_1| \leq \min(\lambda_l \cdot |x_1|^{q/p}, x_2^{\max}) \end{cases}. \tag{5.19}$$

The value of the slope of the linear part of sliding surface λ_l is chosen in order to eliminate vibration for small values of variable x_1 . In this interval, the control law has the formula:

$$u = -b^{-1}(\mathbf{x}) \cdot (f(\mathbf{x}) + \lambda_l \cdot x_2 + L \cdot \text{sgn}(\sigma)). \tag{5.20}$$

Figure 13 presents the components of the sliding surface described by Eq. (5.19). The top part of Fig. 13 illustrates the surfaces for the range of motion in the drive from 25 rad to 0, while the bottom shows the zoom in the vicinity of the origin.

Fig. 13 Components of the sliding surface: non-linear surface (solid line), speed limit (dotted line) and rectilinear final part (grey line)



5.4 Elimination of Chattering in the Control Signal

The control law described by Eqs. (5.14, 5.17, 5.20) comprises the component, which is dependent on the sign of generalized error σ . During the sliding motion, this component switches with a infinitely high frequency, ensuring the movement of the state vector object along the sliding surface. In any real system, the frequency of these switches is limited by the delays that occur in objects, which may lead to the loss of the possibility to keep the state vector at the given surface [18]. The application of a fast alternating control signal also stimulates unmodelled vibration modes of the object, which is disadvantageous from the viewpoint of motion accuracy and durability of the device. When implementing the sliding mode control, the discontinuous control law is often replaced by a continuous approximation. For example, a saturation function is defined according to the following equation:

$$\text{sat}(\sigma) = \begin{cases} \frac{\sigma}{\Phi} & \text{if } |\sigma| \leq \Phi \\ \text{sgn}(\sigma) & \text{if } |\sigma| > \Phi \end{cases} \quad (5.21)$$

Function $\text{sat}()$ defines the band of width Φ on both switching surfaces sides, wherein the discrete component control law is replaced by the component proportional to the generalized error. The studies presented in [18] do not show any significant advantages, which are suggested in the literature on non-linear approximation function $\text{sgn}()$ in comparison to function $\text{sat}()$. It should be noted that, when replacing $\text{sgn}()$ with function $\text{sat}()$, a finite gain is introduced into the control system. From the point of view of stability, it is important that the cumulative gain in the closed-loop control is defined by the width of band approximation Φ and sliding surface slope λ_l [18].

Conditions for switching between different segments of the sliding surface (5.19) and corresponding control laws (5.14, 5.17, 5.20) provide a bumpless change in the structure of the control system, but only if there is a perfect sliding motion when the state vector is on the defined sliding surface. However, replacing relay function $\text{sgn}()$ in the control law with continuous approximation $\text{sat}()$ causes the state vector to move at distance $0 \leq \delta \leq \Phi$ from the sliding surface. In this case, the switching control structures involves large step change in the control signal, which is undesirable in practice. Therefore, a partial reduction of this effect, by dynamically changing the width of the approximation of the maximum value from Φ^{\max} to minimum Φ^{\min} is proposed.

The maximum value of width Φ is taken when changing the sliding surface (5.19), after which it is exponentially reduced, according to Eq. (5.22), to the minimum value, thereby guaranteeing the proper elimination of chattering in the control signal:

$$\Phi = \Phi^{\min} + (\Phi^{\max} - \Phi^{\min}) \cdot e^{-t/T_\Phi} \quad (5.22)$$

The rate of change in width approximation, determined by T_Φ , is selected experimentally.

5.5 Simulation Tests

Identified parameters of the laboratory stand were used for the synthesis of the simulation model of the drive. This model takes into account the following phenomena: the discrete character of the speed and position controllers, the equivalent model of a torque control loop, which includes delay and inertia, the complex multi-mass structure of the mechanical load, and the quantized measurement of the angular position of the motor shaft. The speed, calculated on the basis of a discrete measurement position, was subjected to digital filtering to eliminate the influence of the mechanical load resonances.

To verify the appropriateness of the presented theoretical analysis, a set of simulation tests was carried out. A sliding mode position controller for direct drive was designed. Position θ and drive speed ω were assumed as state vectors of the object, as described by Eq. (5.23)

$$\begin{aligned}\frac{d\theta}{dt} &= \omega \\ \frac{d\omega}{dt} &= -\frac{\hat{k}_f}{\hat{J}} \cdot \omega + \frac{k_T}{\hat{J}} \cdot i_q^{\text{ref}} + d,\end{aligned}\tag{5.23}$$

where the estimated moment in system inertia \hat{J} is the geometric mean of the variation range of the moment of inertia in the drive:

$$\hat{J} = \sqrt{J_{\max} \cdot J_{\min}}\tag{5.24}$$

and \hat{k}_f is the estimated viscous friction coefficient, equal to half of the maximum coefficient of friction in the drive. Component d describes the influence of load torque, as well as the equivalent effect of the variability moment of inertia and friction in the assumed range. The method of determining D variability of component d is presented in [12]. The control signal is the reference current in q -axis i_q^{ref} , which is proportional to torque command T_m^{ref} .

All tests were carried out using the same scenario: a step change in position from the specified initial value $8 \cdot \pi$ radians to zero. Speed limitation during the drive operation was assumed as equal to ± 10 rad/s.

In the first stage of the study, the case of the smallest moment of inertia was analysed. Due to the largest gain in the object, this case determined the range of the stable operation of the drive. Control law was implemented according to Eq. (5.8). Saturation function $\text{sat}()$ was applied and the selected sliding surface was described in a similar way to formula (5.16). The test results are shown in Fig. 14.

Given that, in the real implementation of the sliding mode controller, there are cases in which the measured position is equal to zero, while the speed is non-zero, control law (5.8) introduces the control signals of a large amplitude and high switching frequency. This status is unacceptable in practice. It should be noted that increasing the width of function $\text{sat}()$ leads to a deterioration in the quality of

Fig. 14 Base terminal SMC

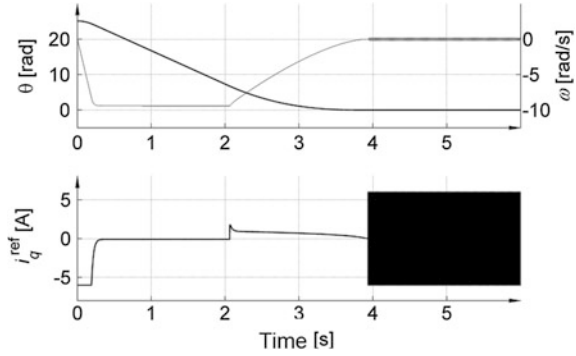
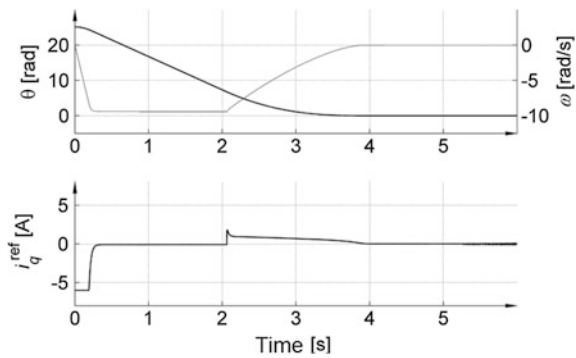


Fig. 15 Non-singular terminal SMC



tracking the sliding surface, while chattering occurs during the standstill of the drive.

In the second stage of the research, modified control law (5.14) was applied, which eliminated the mathematical singularity points. Satisfactory results were obtained for this case, whose waveforms are shown in Fig. 15. However, closer analysis revealed the appearance of oscillations around the origin. They were caused by a velocity gain that was too high near the location of the error, which was equal to zero. Due to the delays in the object, such a gain led to a loss of stability. In a direct drive system with a complex, multi-mass mechanical structure, such oscillations of the torque command may lead to the excitation of high frequency vibrations, which will adversely affect the quality of control and stability of the mechanism. Therefore, it is advised to eliminate them. In the third stage of the study, modified sliding surface (5.19) was applied, along with appropriately switching the control law in the different phases of motion (5.14, 5.17, 5.20). The test results for the lowest assumed inertia drive are shown in Fig. 16.

For such designed control systems, there are no vibrations in the reference current, while the settling time is only slightly longer in relation to the basic terminal sliding motion.

Fig. 16 Non-singular terminal SMC with a rectilinear final part

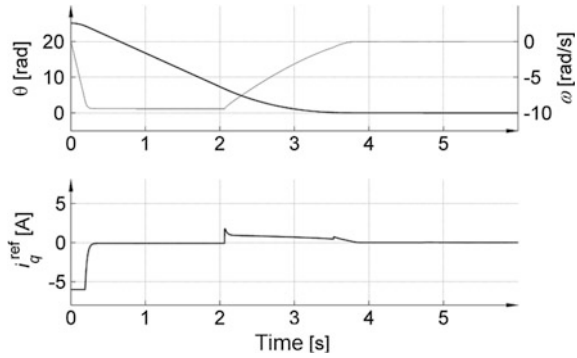
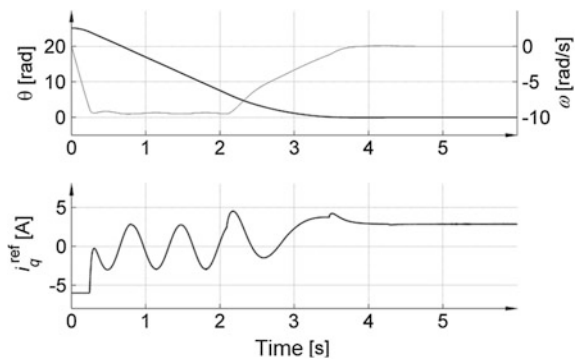


Fig. 17 Medium inertia and high-load torque case



In the second part of the simulation study, the robustness of the designed control system was tested. Tests were carried out for the unbalanced load and the maximum moment of inertia.

Unbalanced load carried the gravity load torque in the case of medium inertia. The test results are given in Fig. 17. The system behaved properly, while the speed and position waveforms were similar to those in the case of low inertia, as shown in Fig. 16. The apparent difference only occurred during the phase of constant speed movement, since function $\text{sat}()$ was applied to the motion control law instead of the function of $\text{sgn}()$, meaning that the state vector did not exactly slip on the set sliding surface.

The last presented tests were made for the case of the maximum moment of inertia; the waveforms are shown in Fig. 18.

For comparison, aggregated phase trajectories of all tests are plotted in Fig. 19. Significant differences only appeared in the phase of acceleration, which was not covered by a sliding motion. The motion phase with constant speed deviations were visible due to a gravity torque in the case of medium inertia.

The braking phase is clearly visible: the trajectory was initially non-linear, then rectilinear in the final part. In the course of the motion phase with constant speed, it

Fig. 18 Maximum inertia case

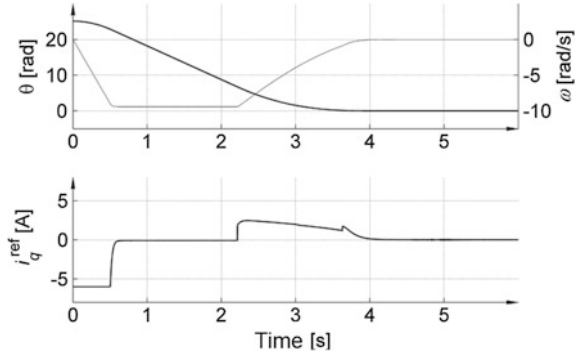
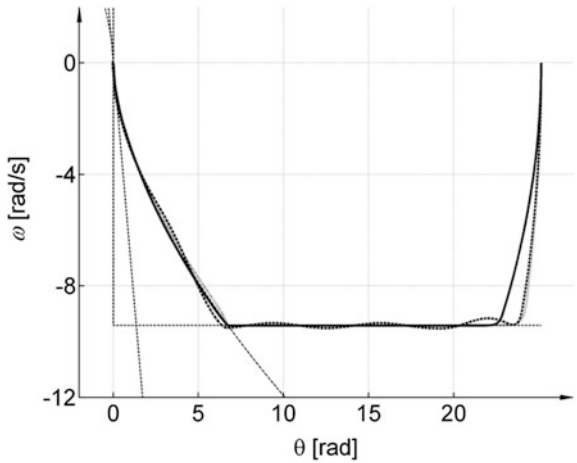


Fig. 19 Aggregated phase trajectories for minimum inertia (*grey line*), medium inertia (*dotted line*) and maximum inertia (*solid line*) cases



can be seen that the deviation from the set speed decreased. This was the result of modifying the applied width of linear function $\text{sat}()$ according to Eq. (5.22).

6 Conclusions

As a result of the proposed synthesis of a fixed anti-resonance filter, a family of frequency characteristics was gathered for a range of possible changes in the moment of inertia. Further analysis of the characteristics family allowed for the definition of a set of common resonant frequencies and their changes for different operation parameters of the drive. In the final stage, a filter with a fixed structure and fixed parameters was derived, taking into account all identified mechanical resonance frequencies.

The advantages of the proposed concept of a neural speed controller trained online, which are automatic tuning and the ability to adapt to the variable parameters of the object, have been confirmed. It transpired that the controller was not only tuned to the changes of the object parameters, but also influenced by the reference signal or load torque during all transient processes, in order to minimize the speed control error. The pointed modifications of the original RPROP training algorithm are essential for the operation of a proper system. The proposed original modifications may demonstrate its usefulness in different ANN applications as well. Very good static and dynamic properties of the speed controller may be successfully implemented using the presented ANN in industrial drive systems.

The chapter presents the implementation of a modified terminal sliding mode control method, which is applied to a direct drive. Given the conditions for the stable operation of the control system of an object with delays, it was necessary to apply a continuous approximation of a discontinuous component control law, while replacing the non-linear sliding surface of the rectilinear segment of constant slope in the vicinity of the zero position error.

The presented conclusions are based on the critical evaluation of the terminal sliding control method and its application in drives with a complex mechanical structure. From the scope of the sliding control methods, better properties can be found, for example, with a variable sliding surface method [6] and a method with a reference model [18]. However, it is noted that, in the scope of the terminal sliding control, further work should be published that is focused, for example, on eliminating the chattering without the need for a continuous approximation of discontinuous functions in the control law [7].

The useful properties of the presented methods have allowed for the consideration of their implementation in industrial drives.

Appendix

Data of investigated drive

Parameters of PMSM	Unit	Value
Minimum moment of inertia	kg m ²	0.75
Maximum moment of inertia	kg m ²	5.83
Torque constant	Nm/A	17.5
Rated load torque	Nm	50
Rated value of speed	rev/s	2.41
Rated current in q axis	A	2.85
Rated voltage	V	310

References

1. Janiszewski D (2011) Real-time control of drive with elastic coupling based on motor position measured only. In: IEEE international symposium on industrial electronics (ISIE), pp 1931–1936
2. Szabat K, Than T-V, Kaminski M (2015) A modified fuzzy luenberger observer for a two-mass drive system. *IEEE Trans Ind Inform* 11(2):531–539
3. Brock S, Łuczak D (2011) Speed control in direct drive with non-stiff load. In: Proceedings IEEE international symposium on industrial electronics (ISIE), Gdańsk, Poland, pp 1937–1942
4. Kazmierkowski MP, Orłowska-Kowalska T (2002) NN state estimation and control in converter-fed induction motor drives. In: *Soft computing in industrial electronics*, vol 110. Springer International Publishing, Heidelberg, pp 45–94 (ch 2)
5. Pajchrowski T, Zawirski K, Nowopolski K (2014) A neural speed controller trained on-line by means of modified RPROP algorithm. *IEEE Trans Ind Inform* PP(99):1
6. Bartoszewicz A, Nowacka-Leverton A (2009) *Time-varying sliding modes for second and third order systems*. Springer International Publishing, New York
7. Liu J, Wang X (2011) *Advanced sliding mode control for mechanical systems*. Springer International Publishing, Beijing
8. Utkin V, Lee H (2006) Chattering problem in sliding mode control systems. *IEEE international workshop on variable structure systems, VSS 2006*, pp 346–350
9. Sabanovic A (2011) Variable structure systems with sliding modes in motion control—a survey. *IEEE Trans Ind Inform* 7(2):212–223
10. Yu X, Man Z (1996) On finite time mechanism: terminal sliding modes. In: *Proceedings of variable structure systems, VSS '96*, pp 164–167
11. Feng Y, Yu X, Man Z (2002) Non-singular terminal sliding mode control of rigid manipulators. *Automatica* 38(12):2159–2167
12. Brock S (2011) Sliding mode control of a permanent magnet direct drive under non-linear friction. *COMPEL Int J Comput Math Electr Electron Eng* 30(3):853–863
13. Luczak D (2014) Mathematical model of multi-mass electric drive system with flexible connection. In: *19th international conference on methods and models in automation and robotics (MMAR)*, pp 590–595
14. Saarakkala SE, Hinkkanen M (2015) Identification of two-mass mechanical systems using torque excitation: design and experimental evaluation. *IEEE Trans Ind Appl* 51(5):4180–4189
15. Luczak D (2012) Tunable digital filter structures for resonant frequency effect reduction in direct drive. In: *8th international symposium on communication systems, networks digital signal processing (CSNDSP)*, Poznan, Poland, pp 1–6
16. Riedmiller M, Braun H (1993) A direct adaptive method for faster backpropagation learning: the RPROP algorithm. In: *IEEE international conference on neural networks*, vol 1. 28 March–1 April, pp 586–591
17. Pajchrowski T, Zawirski K, Nowopolski K (2015) Application of adaptive neural controller for drive with elastic shaft and variable moment of inertia. In: *17th conference on power electronics and applications, EPE'15-ECCE Europe*, Geneva, Switzerland, 8–10 Sept
18. Brock S (2013) Hybrid PI sliding mode position and speed controller for direct drive. In: *Mechatronics*. Springer International Publishing, Switzerland, pp 741–748

Part II
Electric Drives and Fault-Tolerant Control

Fault-Diagnosis and Fault-Tolerant-Control in Industrial Processes and Electrical Drives

Teresa Orłowska-Kowalska, Czesław T. Kowalski
and Mateusz Dybkowski

Abstract This chapter presents a discussion of general methods applied in fault-diagnosis and fault-tolerant control systems. First the data-driven methods and model-based schemes are shortly addressed. Next the main fault-detection and fault-diagnosis methods for controlled plants are characterized. In the following part of the chapter fault-tolerant-control methods, using passive and active concepts, are described and evaluated. At the end, the above methods are discussed from the point of view of electric drives. The main faults occurring in AC motor drives are listed and characterized. Some issues related to fault-tolerant-control of electrical drives are illustrated and discussed.

Keywords Fault diagnosis · Fault-tolerant-control · Industrial process · Electrical drives

1 Introduction

The performance of machines and equipment of technological systems degrades as a result of aging and wear, which decreases performance reliability and increases the potential for different faults. Actuator faults reduce the performance of control systems and may even cause a complete breakdown of the system. Erroneous sensor readings are the reason for operating points that are far from the optimal ones. Wear reduces the efficiency and quality of a production line. In many fault situations, the system operation has to be stopped to avoid damage to machinery

T. Orłowska-Kowalska (✉) · C.T. Kowalski · M. Dybkowski
Department of Electrical Machines, Drives and Measurements, Wrocław University of
Science and Technology, Wybrzeże Wyspiańskiego 27, Wrocław, Poland
e-mail: teresa.orłowska-kowalska@pwr.edu.pl

C.T. Kowalski
e-mail: czeslaw.t.kowalski@pwr.edu.pl

M. Dybkowski
e-mail: mateusz.dybkowski@pwr.edu.pl

and humans. As a consequence, the detection and the handling of faults play an increasing role in modern technology, where many highly automated components interact in a complex way such that a fault in a single component may cause the malfunction of the whole system. Due to the simultaneously increasing economic demands and the requirements of the system safety and reliability, the correct diagnosis or prognosis of abnormal condition plays an important role in the maintenance of industrial systems. Early detection and diagnosis of process faults while the plant is still operating in a controllable region can help avoid abnormal event progression and reduce productivity loss. Thus recently the process monitoring and diagnostic methods have been receiving considerably increasing attention.

Two types of process monitoring and fault diagnosis methods have been developed during the past several decades, namely data-driven methods [1] and model-based schemes [2, 3].

In the data-driven approach the necessary process information can be extracted directly from huge amounts of the recorded process data. Thus the multivariate statistical process monitoring methods, which utilize input and output information of the process, are very popular nowadays in process monitoring and fault diagnosis, particularly principal component analysis and partial least squares [1, 4].

On the contrary, the model-based schemes require a priori physical and mathematical knowledge of the process. After the development of the process model based on the physical principles, the well-established model-based techniques can be successfully applied. Due to various operational requirements and constraints of particular industrial processes, the design of model-based process monitoring and fault diagnosis systems has been a remarkable research topic during the past several decades. Methods of modern systems theory show the systematic use of mathematical process and signal models, identification and estimation methods and methods of computational intelligence. With these methods it is possible to develop advanced tools of fault detection and diagnosis. The goals of these methods are, for example:

- early detection of small faults with abrupt or incipient behavior;
- diagnosis of faults in actuators, processes, components and sensors; fault detection in closed loops;
- supervision of processes in transient states;
- process condition-based maintenance and repair;
- deep quality control of assembled products in manufacturing;
- teleservices like remote fault detection and diagnosis;
- basis for fault management;
- basis for fault-tolerant and reconfigurable systems.

Based on the physical and mathematical knowledge of different industrial processes, the model-based techniques have been successfully applied on plenty of processes for automatic control systems, industrial electronics, etc. [3, 5, 6]. Thanks to well established model-based fault diagnosis techniques, numerous approaches

with successful industrial applications have been also developed in last two decades in power electronics and AC motor drives [7–10].

2 Fault Detection and Fault Diagnosis Methods

2.1 General Ideas

Damage preventing can be realized using different actions, like: protection, equipment redundancy or analytical redundancy and technical diagnosis methods. The protection systems belong to classical methods of automatic supervision and monitoring of industrial processes. They consist in limit (or threshold) checking of some important variables. The alarms raised due to limit values crossing cause an automatic action of protection systems. In many cases this is sufficient to prevent larger failures or damages. This method works well in steady state of the process or if the monitored variables does not depend on the operating point. However, faults are detected rather late and a detailed fault diagnosis is mostly not possible with this simple method. The advantage of the classical limit-value-based supervision methods is their simplicity and reliability for steady-state operation. However, these methods are effective only for a rather large sudden fault or a long-lasting gradually increasing fault [6]. The general view of such system is illustrated in Fig. 1.

The reliability of the industrial processes can be also obtained using the equipment redundancy which, however, raises significant costs and requires extension of control, measuring and supervising equipment. Such solutions are applied only in critical industrial processes or installations. The other method of system reliability increasing is application of analytic redundancy, which is based on an additional diagnostic information obtained (calculated) using plants' mathematical models and methods of control theory, signal processing and mathematical modeling.

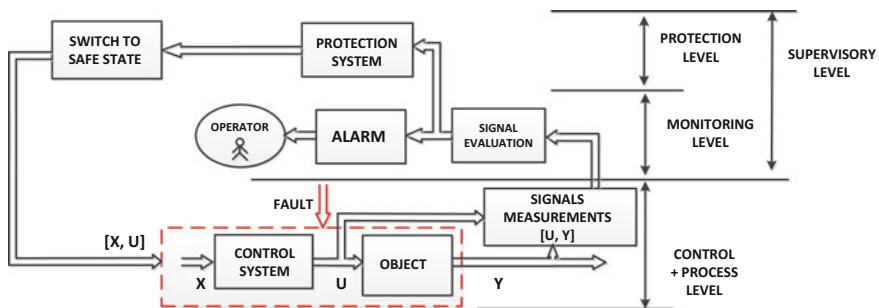


Fig. 1 A classical automatic supervision and monitoring system [6]

As it is seen from Fig. 2, analytical redundancy methods can be divided into different categories, depending on the method of obtaining information on the state variables [5, 6]:

- methods based on expert (heuristic) knowledge,
- methods based on mathematical models,
- methods based on data analysis.

Fault management and damage preventing can be realized nowadays using advanced methods of automatic supervision and technical diagnostics, e.g. fault detection and fault diagnosis methods, which use modern systems theory methods, control theory, mathematical models and signal models of the processes, identification, estimation methods, computational intelligence and informatics. Technical diagnostics is nowadays widely developed in different research centers and consists in technical state recognition of the objects (equipment, machinery, processes) based on actually accessible information [3, 5, 6].

The main tasks of the diagnostics are [5]:

- diagnosis, e.g. actions designed to specify the actual technical conditions of the object;
- genesis, e.g. recognition of previous (past) states of the object (seeking for failure reason);
- prognosis (prediction) of future states of the object (elaboration of failure predicted development).

According to [6], three stages of object technical state testing can be determined:

- fault detection, e.g. detection of the failure in the controlled plant and time of the detection;
- fault isolation, e.g. determination of the type, location and time of the failure;
- fault identification, e.g. determination of the fault size and its evolution in time.

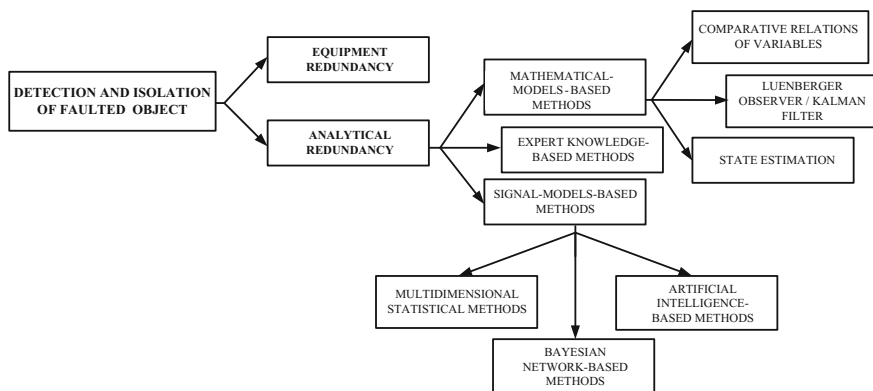


Fig. 2 General classification of fault detection and isolation methods [6]

All these advanced methods of fault detection and diagnosis, used to detect the already incipient faults and to diagnose their origins are also called condition monitoring. Monitoring of the system operation is realized in real-time and consists in diagnostic signals (process variables) acquisition and processing as well as recognition of abnormal behavior of the system (alarm signaling). Condition monitoring is realized on-line by a computer-based diagnosis system. If the monitoring is extended to the whole object (process) operation and includes actions designed to assure a proper state of the object after fault occurrence, such functionality is called supervision. In Fig. 3 a general scheme of the system realizing supervision, fault detection and diagnostics is presented. This system enables the performance of the following tasks:

- early detection of incipient or abrupt faults,
- diagnosis of faults in the processes or process parts and their manipulating devices (actuators) and measurement equipment (sensors),
- detection of faults in closed-loops of the control systems,
- supervision of processes in transient states.

Such a condition monitoring and supervision system has three levels of action:

- monitoring of the object operation (set of alarms),
- protection of the plant in critical states (automatic protection system),
- fault diagnosis.

In Fig. 3 additional types of action, called fault management, are presented, they can be activated by the supervision system depending on the fault kind, e.g. stopping of the object, change of operation mode, reconfiguration of the structure, maintenance or repair [6].

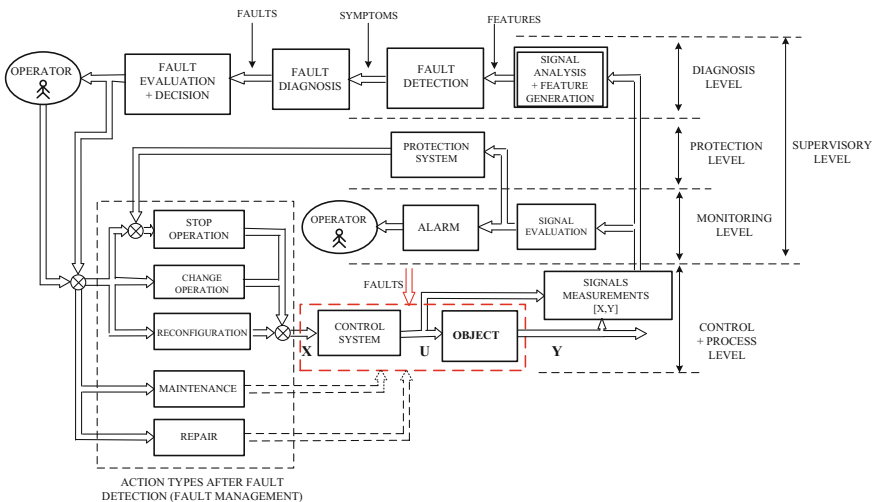


Fig. 3 The general scheme of the supervising, fault detection and diagnosis system [6]

2.2 Basic Fault Detection Methods

Fault detection and fault diagnosis, in general, are based on diagnostic signals measured by sensors or on process variables and states observed by a human operator. The automatic processing of measured signals requires analytical knowledge, while the evaluation of observed variables needs human expert knowledge, which is called heuristic knowledge [3, 5, 6].

Analytical knowledge consists of different methods, from simple rules defining limit values of measured signals to complex methods of signal analysis, such as: spectral analysis, filtration, state and parameter estimation, mathematical models, etc.

Heuristic knowledge includes human observation and inspection, heuristic specific values in the form of noises, vibration, colors, smells, temperature, wear and tear, etc. Also the process history (e.g. previous failures), experience with maintenance and repair operations, statistical data achieved from similar processes or objects, constitutes additional sources of heuristic information.

Thus signals and variables measured and observed together with analytical and heuristic knowledge enable the isolation of fault symptoms and next the proper fault diagnosis. This diagnosis process is illustrated in Fig. 4.

Taking into account the way of generating symptoms, two main fault detection methods can be distinguished:

- process-model-based fault detection methods (comparative methods);
- signal-model-based fault detection methods (direct methods).

Process-model-based methods, called sometimes comparative methods, are based on dependencies between different measurable signals, e.g. on mathematical models of the process which operates in parallel with the diagnosed object. The basic structure of the process-model-based fault-detection system is illustrated in Fig. 5 [6].

Based on the measured input signals \mathbf{U} and output signals \mathbf{Y} , the detection methods generate residuals \mathbf{r} , parameter estimates $\hat{\Theta}$ or state estimate $\hat{\mathbf{x}}$, which are called features. By comparison with normal features (nominal values), changes of features are detected, leading to analytical symptoms \mathbf{s} . In the simplest solution, the diagnostic signal is calculated as a difference between output signals measured in the object and those obtained from the model (residuum \mathbf{r}). If the object operates normally (“healthy” object), this value oscillates around zero. For a faulted object this value is much greater, which confirms the fault. However, the best results are obtained for dynamic process models and diagnostic signals generated based on state or parameter estimation methods, which could contain fault symptoms.

Different mathematical models can be applied in process-mode-based methods, such as: state estimators or observers, Kalman filters, parity equations [2, 3, 5, 6]. Comparative methods are closely connected with redundancy methods, and because mathematical models have an analytical form, this type of redundancy is called analytical redundancy. When residuum is obtained by comparison of the measured

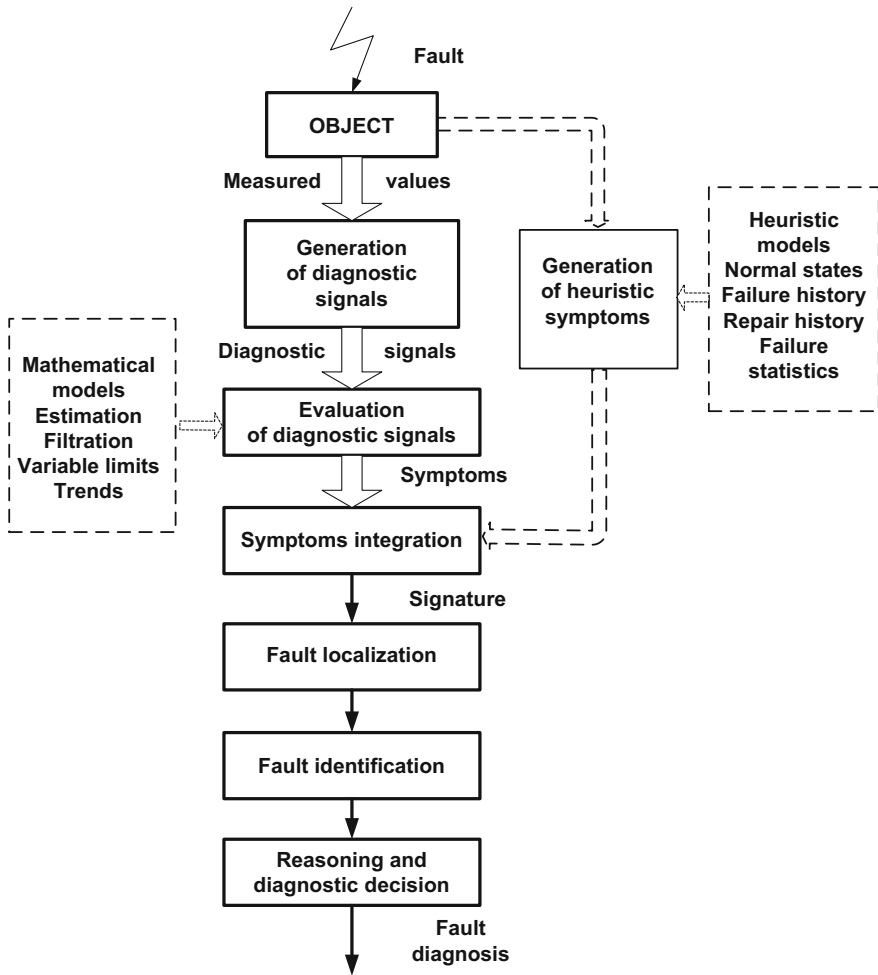


Fig. 4 The main idea of the diagnostic process

signals with those obtained from neural or fuzzy models, which are qualitative or qualitative-quantitative models, the informatics redundancy is used, which is considered as a special type of analytical redundancy [2, 3, 6].

Process-model-based fault diagnosis methods are very sensitive to the adequacy of the used models and to measurement noises. Under on-line implementation they also require high computing power. Complexity of different objects, such as electrical machines, drives for tools machinery and industrial robots, etc., the need for knowledge of many parameters, difficulty in identification, are the reason for serious problems with the credibility of analytical models. Inaccurate models would provide false diagnostic information and patterns, which would result in false alarms generation.

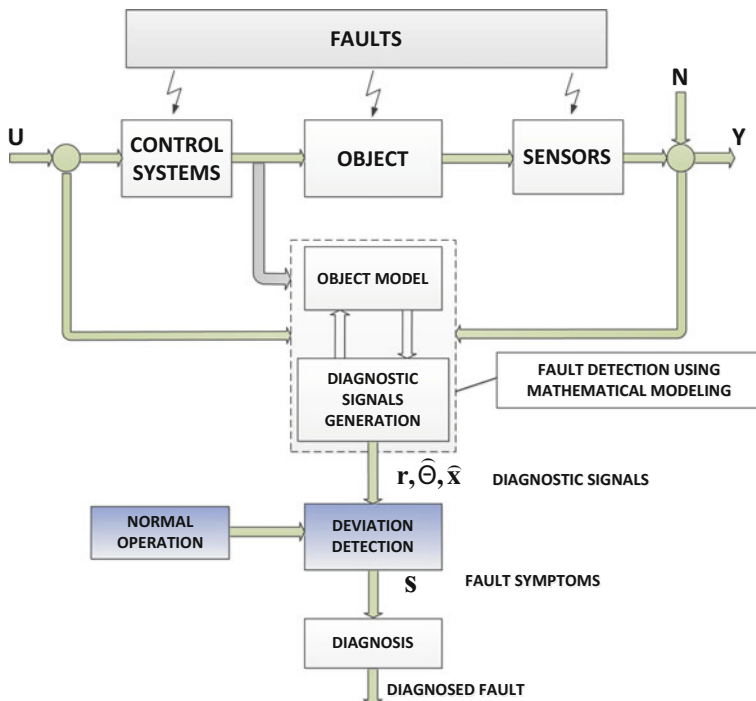


Fig. 5 The general scheme of process-model-based fault detection system [6]

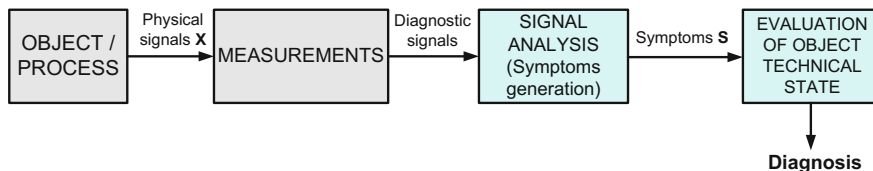


Fig. 6 An illustration of signal-model-based fault detection methods

Signal-model-based fault detection methods rely on the analysis and inspection of selected physical variables which are characteristic for a given object and thus are sometimes called direct methods. In the simplest solutions the limits of credibility or limit values (thresholds) are checked. In other solutions more advanced signal analysis methods, such as: Fourier analysis, correlation analysis, spectral analysis, stochastic parameter analysis, wavelet analysis, HOS analysis are applied, depending on the type of the analyzed signals (periodic, stochastic, non-stationary) [6, 7, 11, 12]. The general scheme of the diagnostic procedure conducted with signal-model-based fault detection methods is presented in Fig. 6.

The above methods are relatively simple, as they do not need a mathematical model of the process. However, their drawbacks result from limited diagnostic information concluded in single signals and from ambiguity of signal parameters' change (e.g. for nonstationary signals), which significantly makes difficult to determine the relations between faults and their symptoms.

Therefore nowadays one can observe a growing interest in application of artificial intelligence methods (neural networks, fuzzy logic and neuro-fuzzy networks) is observed in fault monitoring and diagnosis [13–15]. These methods enable replacement of analytical models by qualitative or qualitative-quantitative models in the diagnosis of technological processes, however in case of such objects like machines and different equipment they are an interesting tool in diagnostic information processing.

3 Fault-Tolerant-Control Systems

About 20 years ago, together with the Fault Detection and Diagnosis (FDD) methods, also the Fault Tolerant Control (FTC) was developed [5, 16–18]. The FTC aims to ensure the continuous system functionality, even after fault occurrence. FTC systems possess the ability to detect component failures automatically, using suitable FDD methods. They are capable of maintaining overall system stability and acceptable performance as long as the controlled system can be safely stopped for maintenance or repair. In other words, a closed-loop control system which can tolerate component malfunctions, while maintaining desirable performance and stability properties is said to be a Fault Tolerant Control System (FTCS) [5, 16, 18]. The general scheme of the FTC system is presented in Fig. 7.

The FDD system constitutes a part of the FTC system (Fig. 7) and is responsible for providing the supervision system with information about the location and severity of any fault. The supervision system can take a suitable action and can reconfigure the sensor set and/or actuators to isolate the faults, and tune or adapt the

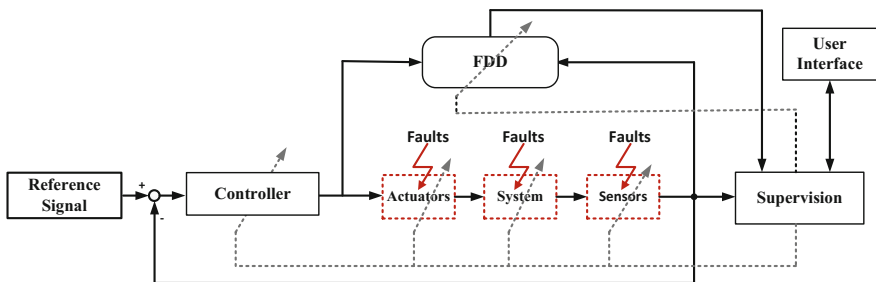


Fig. 7 The general scheme of FTC system with supervision subsystem

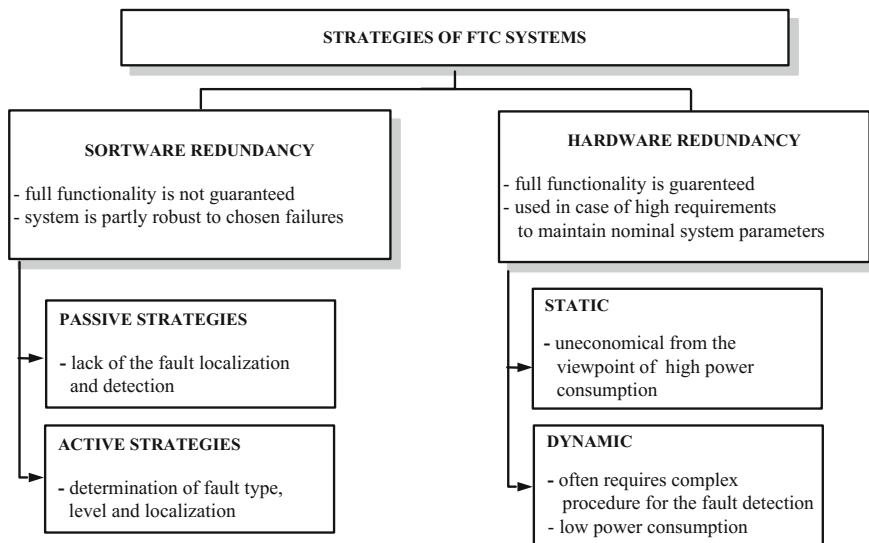


Fig. 8 A classification of the fault tolerant control strategies

controller to accommodate the fault effects [5, 16, 18], according to the possibilities and strategies listed in the scheme shown in Fig. 8.

As it was said in the previous section, the hardware (equipment) redundancy, is attractive from the viewpoint of full system functionality after fault occurrence, but it raises significant costs and requires duplication of control, measuring and even actuator equipment. Such solutions are applied only in critical industrial processes or installations.

FTC systems based on software (analytic) redundancy are generally divided into two classes: passive and active. Passive FTCs are based on robust controller design techniques and aim at designing a single, robust controller that makes the closed-loop system insensitive to unexpected faults. Under faulty conditions a process continues operation with the same structure and parameters of the controller [16–18]. The general scheme of passive FTC is presented in Fig. 9.

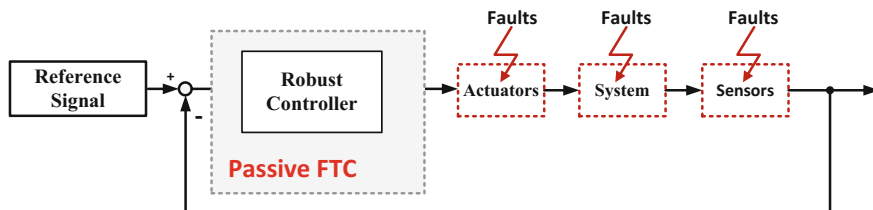


Fig. 9 The scheme of a passive FTC system

This approach does not require on-line faults detection and is therefore computationally more attractive. The controller design for passive FTC is based on advanced control techniques, such as: adaptive theory, predictive control concepts or artificial intelligence methods.

The applicability of passive FTC is very limited due to its serious disadvantages [17]:

- a very selective subset of possible faults can be considered in the design of a passive FTC system; usually those faults that do not have a significant effect on the system operation of the system can be treated in this way, while only under such condition the controller robustness to faults can be achieved;
- an increased robustness to certain faults can be achieved at the expense of decreased nominal performance of the system. Since faults happen rather rarely, it is not reasonable to significantly degrade the fault-free performance of the system only to achieve some insensitivity to a restricted class of faults.

Still, passive FTCs have some advantages too. One of them is the fact that a fixed controller has relatively reasonable hardware and software requirements. Another advantage is lower complexity compared to active FTC systems [5, 17, 18].

In contrast to passive methods, the *active* FTC systems are based on controller reconfiguration or selection of a few predesigned controllers. This technique requires a fault detection and diagnosis (FDD) system that realizes the task of detecting and localizing the faults if they occur in the system. The structure of an active FTC system with a FDD unit is presented in Fig. 10.

The FDD part uses input-output measurement from the system to detect and localize the faults. The estimated faults are subsequently passed to a reconfiguration mechanism that changes the parameters and/or the structure of the controller in order to achieve an acceptable post-fault system performance. Active FTC systems use dedicated detectors or special state or parameter observers [5, 16–18] to identify failure condition. The choice of the proper topology and fault tolerant control algorithm depends on the system requirements and used components.

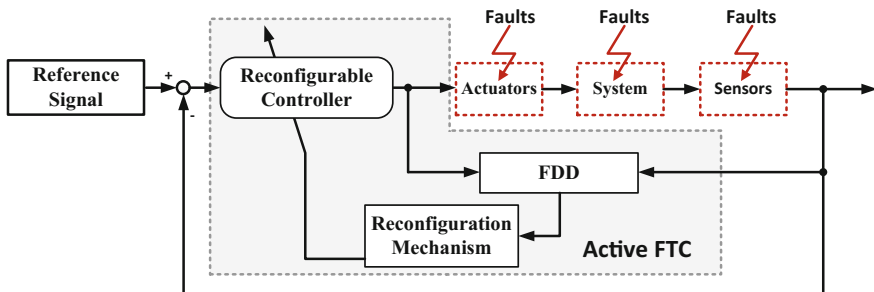


Fig. 10 The scheme of active FTCS

Designing such a system is a complicated and complex issue because of the need to ensure its stable operation after a component failure, while maintaining full or partial functionality at the required performance level of the whole process. To ensure the proper work of complex systems, it is necessary to take into account the diagnostic techniques, which within a reasonable period of time will allow to detect a failure and to ensure appropriate reaction of the control structure.

Depending on the way the post-fault controller is formed, active FTC methods are further subdivided into projection-based methods and on-line redesign methods [17]. In the projection based methods, the post-fault controller is selected from a set of the off-line predesigned controllers. Each controller from the set is designed for a particular failure situation and is switched on by the reconfiguration mechanism when the corresponding fault pattern has been diagnosed by the FDD system. Thus, in this solution only a limited class of the system faults can be taken into account. On the contrary, the on-line redesign methods require the on-line computation of the controller parameters, which can be treated as a reconfigurable control, or recalculation of both the structure and the parameters of the controller, which is called as a restructurable control. Comparing the obtainable post-fault system performances, the on-line redesign methods are superior to the passive methods and the off-line projection-based methods. However, computationally they are the most complicated and expensive methods, as they often require on-line optimization.

One of the most important issues when designing active FTC systems is the integration between the FDD part and the FTC part. Most approaches are based on an independent design of these two parts, with the assumption that the other one is perfect. It means that many FDD algorithms do not consider the closed-loop operation of the system and, vice versa, many FTC methods assume that fault estimates realized by the FDD scheme are perfect. In practice such assumptions do not guarantee proper post-fault performance or even can lead to instability of the system. For making the integration of FDD and FTC parts possible, one should first investigate what information from the FDD is needed by the FTC, as well as what information can actually be provided by the FDD scheme. Imprecise information from the FDD that is incorrectly interpreted by the FTC scheme might lead to a complete loss of the system stability. This last issue is especially important in high-dynamic systems, like drives, robots, aircrafts etc. [5, 16–18].

4 Fault Classification in Electrical Drives

Vector controlled AC motor drives are now widely used in industrial applications for speed and torque regulation due to their high performance [19]. In such systems AC motors are supplied from voltage-source inverters with pulse width modulation (PWM) or space vector modulation (SVM). These inverters mostly use power switches based on the insulated-gate bipolar transistors (IGBTs), due to their well-known advantages, such as high efficiency, high switching frequency and relatively short-circuit current handling ability. The modern AC motor drives,

operating in closed-loop speed or position system, are equipped with advanced digital control systems. In Fig. 11, the schematic diagram of such a modern electrical drive is presented, where besides chosen sensors of electrical and mechanical variables, state estimators or state observers were introduced, they illustrate the software redundancy in the system. So according to the previous sections, this drive can be analyzed as a type of FTC system.

Inverter-fed AC motors are sensitive to different faults occurring at the static converter, at the motor itself and at the control system stage. All these faults lead to the interruption of the drive system operation and unprogrammed maintenance brakes. Unplanned drive stops could lead to high financial losses, so the development of reliable monitoring and fast fault detection methods as well as fault-tolerant control strategies applied in the drive system are a current demand of the industry [13, 19].

Electrical drive systems are subject to different faults whose consequences significantly depend on the fault location [13, 20]. In Fig. 12 basic faults occurring in the drive system are listed and illustrated.

Among various types of failures in electric motor drive applications, power converter faults make up about 80 % [21, 22]. There are many kinds of faults in power converters such as a power semiconductor device (21 %), solder (13 %), DC-link capacitor (30 %), printed circuit boards (PCB) (26 %), sensor, etc. [21]. Thus power device modules failures compose 34 % of power converter faults. All these faults result in a drive performance deterioration or even an unplanned stoppage of the drive system.

The power device faults can be divided into two cases: short-circuit faults and open-switch faults. A short-circuit fault can occur due to several reasons, such as the wrong gate voltage, overvoltage, avalanche stress, or temperature overshoot. Short-circuit faults are difficult to handle because of an abnormal over-current which can cause serious damage to other parts is produced within a very short time. In addition, the period between the fault initiation and failure is very short. Therefore, most diagnostic methods of a short-circuit fault are based on hardware circuits which use high integrated transistor drivers turning off an affected transistor

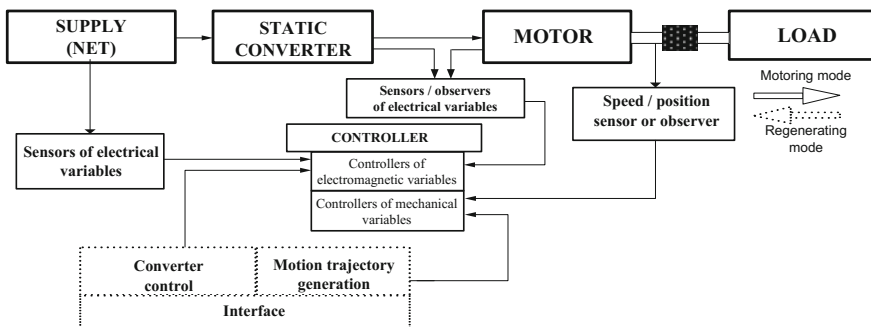


Fig. 11 The schematic diagram of the modern electrical drive robust to sensor faults

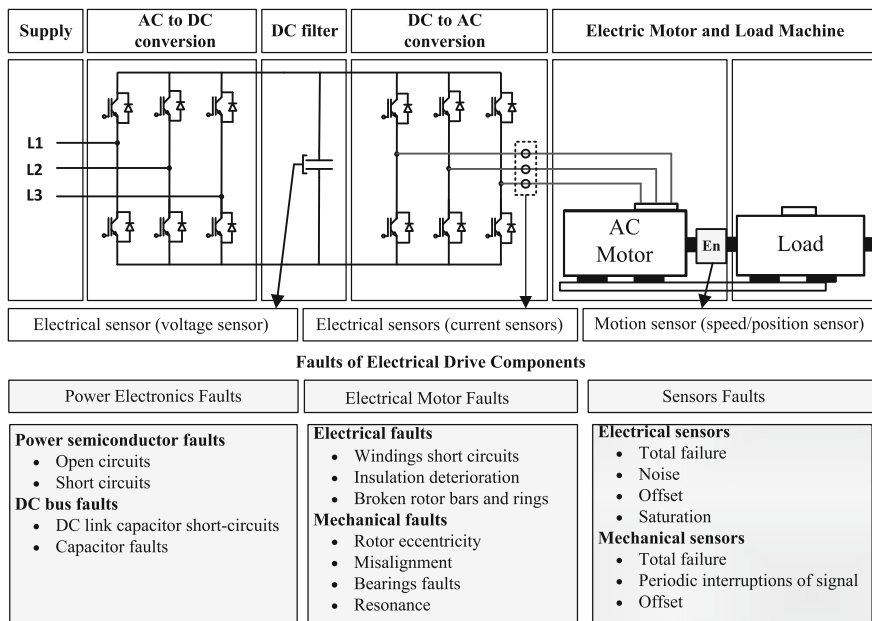


Fig. 12 Faults classification in the voltage-fed AC motor drive

before its permanent damage. Indeed, a drive performance is significantly reduced after turning off the switch, but a high current does not flow through a converter and therefore further rapidly progressive inverter faults can be avoided.

An open-switch fault occurs due to the lifting of a bonding wire caused by thermal cycling. An extremely high collector current may also cause open-switch faults. The open-switch fault leads to a current distortion. It can cause secondary problems in other components through induced noise and vibrations. The open-switch fault does not cause serious damages, compared to short-circuit faults, but it does degrade the performance of overall converter systems. This type of switch failure should be detected and compensated, as it causes big stator current values and high transients in electromagnetic torque which could damage the drive [21, 23]. Therefore, the diagnostic methods of power device faults are needed to improve the reliability of the converter system. Hence, fault-tolerant control (FTC) techniques, which combine transistor fault diagnostic methods, hardware redundancy and post-fault control algorithms that allow simultaneous electric drive operation, are developed, recently [23–26].

The most frequently used approaches are based on the analysis of easily accessible signals, like current or voltage, thus the methods of an open-circuit fault detection can be classified as current- or voltage-based ones [28, 30, 32]. In accordance with these techniques, a fault diagnosis is carried out in order to conduct a remedial action, which is normally based on a power converter circuits reconfiguration as well as changes in a main drive control algorithm. Correct failure

detection and its localization, robustness against false alarms and the fast failure diagnosis allow to perform an appropriate remedial action that brings back a partial or full drive functionality. A detailed survey of methods that are dedicated to transistor failures diagnosis has been presented in many works [23–26].

The second group of damages, which occur in electric drive, are AC/DC rectifier semiconductor faults and a DC bus link failures. The problems connected with the faults of AC/DC rectifier are similar to those in DC/AC voltage inverters, so the methods of detection are similar. However, there are only few works that deal with power switch fault diagnosis in the AC/DC rectifiers [27]. Moreover, most of the fault diagnostic methods, which are known from literature, are not validated in the vector-controlled sensorless control structures.

In most power converter applications, the electrolytic capacitors are predominantly used in DC-links because of their low cost. However, they have some undesirable properties such as sensitivity to temperature, frequency and low reliability resulting in their finite lifetime and high failure rate due to a wear-out degradation failure. In [21] a brief overview of the condition monitoring methods for electrolytic capacitors is given, such as: on-line estimation of equivalent series resistance method or off-line method based on capacitor model.

Among different failures of drive systems, electrical and mechanical faults of AC motors constitute a significant part [20]. Electrical faults are connected with the stator windings of the induction motor and permanent-magnet motors, and with rotor squirrel-cage of the induction motor (broken rotor bars or rings). The stator winding failures occur due to insulation stresses, inter-turn short circuits or even short-circuits of phase windings. In the case of PMSM rotor faults are connected mainly with deterioration of permanent magnets performance or their mechanical displacements or vibrations. Mechanical faults in the electrical motors are connected with the quality of mechanical connection between the driving motor and a load machine. It could be: rotor eccentricity, misalignment or bearings, clutch or gear failures. The statistical research realized by different research centers show that bearings faults are close to 40 % of all IM faults, while stator winding faults constitutes about 38 % and rotor faults—about 10 %.

The faults detection of AC motors rely on the analysis of two easily measured signals: phase current and mechanical vibrations [7, 28–32]. They can be preprocessed to obtain other diagnostic signals, such as: magnitude of the stator current space vector, estimated electromagnetic torque, transient active or reactive power, internal variables in closed-loop control structures [28, 30, 31]. The extension of the diagnostic signals number enables more accurate fault isolation, using different signal analysis methods, such as: Fast Fourier Transform (FFT), Short Time Fourier Transform (STFT), wavelet analysis, Higher Order Transforms (HOTs), etc. [7, 28, 32]. The fault diagnostics and fault differentiation based on extracted fault symptoms is done using different methods, such as: multidimensional statistical methods, state estimators and observers, artificial intelligence methods (see Fig. 2) [13–15, 29, 33].

The last source of failures in drive systems are sensors faults. In the electrical drive systems the current and voltage sensors are necessary for the proper work of the control algorithms [19]. Those sensors are very sensitive to various damages [5, 34]. A drive system and estimation techniques can work stably without information from a stator voltage sensor, but cannot work properly without signals from stator current sensors [19, 34, 35]. This signal is used to the non-measurable state variable reconstruction (like stator or rotor fluxes in AC motor drives) and in the internal current control loops. Similarly, the measurement of the rotor speed is required for external speed or position control loops in adjustable drive systems. The speed is measured using mechanical sensors (mainly encoders), which are also very sensitive to the actual drive and environment conditions and can be destroyed. The topology of the drive must be changed if the speed sensor is broken [10, 34–36]. In most cases a speed sensorless operation, which requires suitable speed estimators or observers, is applied [10, 36, 37].

In the case of electrical drives monitoring, the fast fault detection and isolation is very important, as different failures, described above, usually cause high current asymmetry and overshoots as well as electromagnetic torque oscillations. Thus not only localization but also compensation of the failure should be realized immediately. It is illustrated in Fig. 13.

The electromagnetic time constants of the drive system are much smaller than the mechanical time constant, thus phase motor currents are generally used as diagnostic signals. Based on [6, 38] it can be stated, that the process of isolating the damaged element of the drive system, ($t_1 \div t_2$) is generally the longest of the three shown in Fig. 12. It results mainly from the need to take into account the phenomena of commutation in the electric circuits of the drive. Isolation of the faulted circuit at the wrong time can result not only in lengthening the time of the assumed functionality of the drive, but, moreover, the destruction of other elements of the system [38]. The time dedicated to fault localization ($t_1 \div t_2$) should not exceed one stator current period in case of power converter failures. Similarly the fault compensation time interval ($t_2 \div t_3$) should not take more than two stator current periods. In the time t_3 the drive operates with some functionality according to the assumed post-fault control strategy.

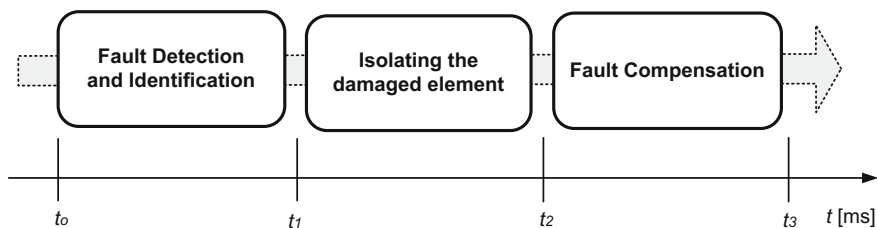


Fig. 13 The sequence of actions in FTC drives

Modern control strategies of the drive systems, like adaptive, predictive or sliding-mode control algorithms should ensure the reliable and safe operation in case of occurrence of the motor or even the power converter failures. However, usually under semiconductor faults the reorganization of the internal structure of the power converter and its control (modulation method). Faults of the sensors can have different effects in the complex drive system, however, their occurrence makes it necessary to amend the topology of the drive control structure completely. Thus, drive systems with the described functionalities, resulting from FTC concepts, recently are called safe systems or fault-tolerant drives (systems robust to failures) [6, 9, 10, 26, 35, 36, 38].

As it was said in the previous section, the goal of the fault-tolerant system is the continued stable operation of the drive (while maintaining its full or partial functionality) or its safe stoppage, depending on the failure type or guaranteed safety level. Depending on the solution chosen for the FTC of the adjustable electrical drive, different strategies can be distinguished, according those listed in Fig. 9. Due to the nature of adjustable drive systems, one should choose such a method of the failure compensation which maintains the basic characteristics of the functionality of the drive. Usually, the use of the software redundancy does not preserve the previous functionality of the drive. Software tools allow to specify the type, extent and location of the damage. Therefore, in most cases, because of the advantages of knowledge on the fault location, the active strategies of FTC are applied in drive systems. To restore functionality of the faulted drive is necessary to use the dynamic hardware redundancy.

To implement the above FTC strategies in electrical drives it is necessary to apply certain mathematical methods, like algorithmic ones (e.g. advanced analysis methods of diagnostic signals, state and parameter estimators and observers) or artificial intelligence methods (neural networks, fuzzy logic, neuro-fuzzy network etc.). For example, when the drive operates in the vector control structure with a speed sensor, in the event of its failure, the fault-tolerant structure should switch to the new control strategy based on the speed estimator or observer. Further, in the case of more than one current sensor failure, the vector controlled structure should be switched to the scalar control strategy (as lack of the current signals destroys the current control loops and simultaneously makes impossible the estimation of internal state variables of the AC motor). Obviously, changing the control strategy of the AC motor from vector to scalar control will result in a deterioration of the drive operation but guarantees the operation stability and security of users as well as the technological process.

Therefore, nowadays the advanced adjustable drive systems should be equipped with diagnostic features to prevent damages and sudden switch-offs of complex industrial installations. Thus, the incipient fault detection of all basic components of the modern converter-fed recently has become one of the basic requirements which will be addressed in the following chapters of this monograph.

5 Summary

Recently the rapid development of research in the diagnosis of industrial processes is observed, which is undoubtedly a consequence of the increasing interest in industrial applications of diagnostic systems. It results from potentially large economic benefits that can bring the implementation of such systems and the emergence of new solutions, industrial automation systems, enabling the use of advanced control and diagnostic techniques. Also in the field of electric drive systems issues of monitoring and fault diagnosis starts include not only the so-called critical high-power drives but also drives of low and medium power. This mainly concerns the converter-fed drives, with advanced control strategies.

In this chapter a discussion of the main faults occurred in AC motor drives and solutions of fault-tolerant control problems is presented from the viewpoint of general theory of fault diagnosis, fault detection and fault compensation methods developed for industrial processes applications.

Acknowledgment This work was supported by the National Science Centre Poland, under project 2013/09/B/ST7/04199 (2014–2017).

References

1. Shen Y, Ding SX, Xiaochen X, Hao L (2014) A review on basic data-driven approaches for industrial process monitoring. *IEEE Trans Ind Electron* 61(11):6418–6428
2. Ding SX (2008) *Model-based fault diagnosis techniques*. Springer, Berlin
3. Isermann R, Balle P (1997) Trends in the application of model-based fault detection and diagnosis of technical processes. *Control Eng Pract* 5(5):709–719
4. Hou ZS, Wang Z (2013) From model-based control to data-driven control: survey, classification and perspective. *Inf Sci* 235:3–35
5. Isermann R (2006) *Fault-diagnosis systems. An introduction from fault detection to fault tolerance*. Springer, Berlin
6. Isermann R (2011) *Fault-diagnosis applications, model-based condition monitoring: actuators, drives, machinery, plants, sensors, and fault-tolerant systems*. Springer, Berlin
7. Riera-Guasp M, Antonino-Daviu JA, Capolino GA (2015) Advances in electrical machine, power electronic, and drive condition monitoring and fault detection: state of the art. *IEEE Trans Ind Electron* 62(3):1746–1759
8. Campos-Delgado DU, Espinoza-Trejo DR (2011) An observer-based diagnosis scheme for single and simultaneous open-switch faults in induction motor drives. *IEEE Trans Ind Electron* 58(2):671–679
9. Akrad A, Hilairet A, Diallo D (2011) Design of a fault-tolerant controller based on observers for a PMSM drive. *IEEE Trans Ind Electron* 58(4):1416–1427
10. Najafabadi TA, Salmasi FR, Jabehdar-Maralani P (2011) Detection and isolation of speed-, DC-link voltage-, and current-sensor faults based on an adaptive observer in induction-motor drives. *IEEE Trans Ind Electron* 58(5):1662–1672
11. Singh GK, Ahmed SAKS (2004) Vibration signal analysis using wavelet transform for isolation and identification of electrical faults in induction machine. *Electr Power Syst Res* 68(2):119–136

12. Chow TWS, Tan H (2000) HOS—based nonparametric and parametric methodologies for machine fault detection. *IEEE Trans Ind Electron* 47(5):1051–1059
13. Vas P (1993) Parameter estimation, condition monitoring, and diagnosis of electrical machines. Oxford University Press, Oxford
14. Kowalski CT, Orłowska-Kowalska T (2003) Neural networks application for induction motor faults diagnosis. *Trans IMASC Math Comput Simul* 63(3–5):435–448
15. Kowalski CT, Kaminski M (2014) Rotor fault detector of the converter-fed induction motor based on RBF neural network. *Bull Pol Acad Sci Tech Sci* 62(1):69–76
16. Blanke M, Kinnaert M, Lunze J, Staroswiecki M (2003) *Diagnosis and fault-tolerant control*. Springer, Berlin
17. Verhaegen M, Kanev S, Hallouzi R, Jones C, Maciejowski J, Smail H (2010) Fault tolerant flight control—a survey. In: Edwards C, Lombaerts T, Smaili H (eds) *Fault tolerant flight control*. Springer, Berlin, pp 47–85
18. Jiang J, Xiang Y (2002) Fault-tolerant control systems: a comparative study between active and passive approaches. *Ann Rev Control* 36(1):60–72
19. Kazmierkowski MP, Blaabjerg F, Krishnan R (2001) *Control in power electronics—selected problems*. Academic Press, London
20. Thorsen OV, Dalva M (1995) A survey of faults on induction motors in offshore oil industry, petrochemical industry, gas terminals, and oil refineries. *IEEE Trans Ind Appl* 31(5):1186–1196
21. Lee K-B, Choi U-M (2014) Faults and diagnosis systems in power converters. In: Orłowska-Kowalska T, Blaabjerg F, Rodriguez J (eds) *Advanced and intelligent control in power electronics and drives*. Springer, Heidelberg, pp 143–178
22. Yang S, Xiang D, Bryant A, Mawby P, Ran L, Tavner P (2010) Condition monitoring for device reliability in power electronic converters: a review. *IEEE Trans Power Electron* 25(11):2734–2752
23. Lu B, Sharma SK (2009) A literature review of IGBT fault diagnostic and protection methods for power inverters. *IEEE Trans Ind Appl* 45(5):1770–1777
24. Espinoza-Trejo DR, Campos-Delgado DU, Bossio G et al (2013) Fault diagnosis scheme for open-circuit faults in field-oriented control induction motor drives. *IET Powder Electron* 6(5):869–877
25. Sobanski P, Orłowska-Kowalska T (2014) Low-cost fault-tolerant control scheme for SVM two-level voltage-inverter-fed induction motor drive. In: *Proceedings of the 11th international conference ElectriMACS, Valencia, 19–22 May 2014*
26. De Araujo Ribeiro RL, Jacobina CB, Da Silva ERC, Lima AMN (2004) Fault-tolerant voltage-fed PWM inverter AC motor drive systems. *IEEE Trans Ind Electron* 51(2):439–446
27. Rothenhagen K, Fuchs FW (2004) Performance of diagnosis methods for IGBT open circuit faults in voltage source active rectifiers. In: *Proceedings of the 35th annual IEEE power electronics specialists conference PESC, Aachen, 20–25 June 2004*
28. Tallam RM, Lee SB, Stone GC, Kliman GB et al (2007) A survey of methods for detection of stator-related faults in induction machines. *IEEE Trans Ind Appl* 43(4):920–933
29. Wolkiewicz M, Kowalski CT (2013) On-line neural network-based stator fault diagnosis system of the converter-fed induction motor drive. In: *Proceedings of the 39th annual conference IEEE industrial electronics society IECON, Vienna, 10–13 Nov 2013*
30. Drif M, Cardoso AJM (2014) Stator fault diagnostics in squirrel cage three-phase induction motor drives using the instantaneous active and reactive power signature analyses. *IEEE Trans Ind Inf* 10(2):1348–1360
31. Orłowska-Kowalska T, Dybkowski M, Kowalski CT (2010) Rotor fault analysis in the sensorless field oriented controlled induction motor drive. *Automatika* 51(2):149–156
32. Kowalski CT, Wierzbicki R, Wolkiewicz M (2013) Stator and rotor faults monitoring of the inverter-fed induction motor drive using state estimators. *Automatika* 54(3):348–355
33. Seshadrinath J, Singh B, Panigrahi BK (2014) Investigation of vibration signatures for multiple fault diagnosis in variable frequency drives using complex wavelets. *IEEE Trans Power Electron* 29(2):936–945

34. Fan S, Zou J (2012) Sensor fault detection and fault tolerant control of induction motor drivers for electric vehicles. In: Proceedings of the 7th international power electronics and motion control conference PEMC, Harbin, 2–5 June 2012
35. Berriri H, Naouar MW, Belkhouja IS (2012) Easy and fast sensor fault detection and isolation algorithm for electrical drives. *IEEE Trans Power Electron* 27(1):490–499
36. Klimkowski K, Dybkowski M (2015) A comparative analysis of the chosen speed sensor faults detectors for induction motor drives. In: Proceedings of the 18th international conference on electrical drives and power electronics EDPE, The High Tatras, 21–23 Sept 2015
37. Orłowska-Kowalska T, Dybkowski M (2007) Improved MRAS-type speed estimator for the sensorless induction motor drive. *Compel* 26(4):1161–1174
38. Rodrigues MA, Claudio A, Theilliol D, Vela LG, Hernandez L (2008) A strategy to replace the damaged element for fault-tolerant induction motor drive. In: Proceedings of the 5th international conference on electrical engineering, Computing Science and Automatic Control CCE, Mexico, 12–14 Nov 2008

IGBT Open-Circuit Fault Diagnostic Methods for SVM-VSI Vector-Controlled Induction Motor Drives

Piotr Sobański and Teresa Orłowska-Kowalska

Abstract In this chapter a two-level three-phase voltage inverter fed induction motor drive is considered and a discussion of IGBTs open-circuit faults diagnostic methods based on voltage and flux vector hodographs analysis is presented. These techniques have been validated for the drives with Direct Torque Control and Direct Rotor Field Oriented Control strategies. Additionally, a speed of the diagnosis has been considered and the post-fault strategy has been addressed.

Keywords Induction motor drives · Vector control · Transistor faults · Fault detection

1 Introduction

Faults of power electronics in electrical motor drives can significantly disturb a control process, resulting in drive functionality decrease. There are many kinds of faults in power converters such as: defects of a power semiconductor device, DC-link capacitor, printed circuit board (PCB), solder, sensor, etc. All these faults, which can lead to the interruption of the drive system operation and un-programmed maintenance brakes. Unplanned drive stops could lead to high financial losses, so the development of reliable monitoring and fast fault detection methods as well as fault-tolerant control strategies is a current demand of the industry. Therefore, diagnostic procedures and new control techniques, that allow a fault detection and localization as well as simultaneous electric drive operation after fault occurrences are developed recently. These techniques are known as fault-tolerant control methods, and integrate failures diagnosis algorithms and

P. Sobański (✉) · T. Orłowska-Kowalska
Department of Electrical Machines, Drives and Measurements, Wrocław University of Science and Technology, Wybrzeże Wyspiańskiego 27, Wrocław, Poland
e-mail: piotr.sobanski@pwr.edu.pl

T. Orłowska-Kowalska
e-mail: teresa.orlowska-kowalska@pwr.edu.pl

hardware or software redundancy that allows correct drive operation under its faulty condition. The effectiveness of fault detection and its localization techniques, robustness against false alarms as well as fast diagnosis have an important influence on applicability of an appropriate remedial action. Semiconductor and soldering failures in power device modules compose 34 % of power converter failures [1].

The power device fault can be divided into two cases: a short-circuit fault and an open-switch fault. A short-circuit fault can occur due to several reasons, such as the wrong gate voltage, overvoltage, avalanche stress, or temperature overshoot. The short-circuit faults are difficult to handle because an abnormal over-current which can cause serious damage to other parts is produced within a very short time. In addition, the period between the fault initiation and failure is very short. Therefore, most diagnostic methods of a short-circuit fault are based on hardware circuits.

An open-switch fault occurs due to lifting a bonding wire caused by thermal cycling. An extremely high collector current may also cause open-switch faults. The open-switch fault leads to a current distortion. It can cause secondary problems in other components through induced noise and vibrations. The open-switch fault does not cause serious damages, compared to short-circuit faults, but does degrade the performance of overall converter systems. Therefore, diagnostic methods of power device faults are needed to improve the reliability of the converter system.

This chapter deals with selected open-circuit IGBT fault diagnostic methods that are dedicated for three-phase two-level voltage-inverter-fed vector controlled induction motor drive systems. The presented techniques are based on transient analysis of stator voltage and stator flux space vector hodographs in a stationary reference frame and do not require application of extra sensors. The diagnostic algorithm is based on software solutions and ensures to detect and localize single and multiple IGBT failures in a time shorter than one period of a stator current fundamental harmonic, regardless a drive operation point. The presented schemes of the diagnostic systems can be easily applicable in the vector-controlled electric drives that use voltage space vector modulation (SVM) algorithms. To maintain high drive performance for a post-fault action, a reconfigurable inverter topology is applied. The selected experimental results are presented in this chapter.

2 A Short Overview of IGBT Diagnostic Methods

Due to the demand for the drive manufacturing cost reduction, a vast majority of the detection methods for the transistor open-circuit failures are designed so that their implementation does not require an additional hardware. The idea of the fault detection relies on calculation and standardization of errors between the reference and estimated or measured variables [2–7]. As a consequence of the switch open-circuit failures inverter voltages are incorrectly estimated which results in a wrong flux [7] and stator currents calculation [4]. In the case of these methods,

diagnostic variables are achieved calculating the average values of the errors. Further, they are compared with a “fault threshold” whose overstepping indicates the transistor defect. The faulted transistors are localized analyzing signs of the diagnostic variables.

A vast majority of the diagnostic techniques that concern the transistor open-circuit failures is based on the analysis of the estimated or measured variables in the stationary coordinate system α - β [8–16]. For this purpose, in most cases, the stator phase currents are processed, namely the Park’s transformation is used to obtain the current vector amplitude and phase. Further, the faulty transistor is identified by taking information about the position of the current vector in α - β system at the instant of immediately when the current vector stops its rotational movement [14]. To eliminate the load dependence, this approach has been improved by using stator or rotor flux signals for the faults diagnosis [16]. In accordance with the direct field oriented control or the direct torque control methods the flux is stabilized at a constant value and therefore as opposed to the faulty mode under the healthy drive operations its amplitude is not affected.

3 Analysis of IGBT Faults Influence on the Drive System Operation

Considering the three-phase two level voltage inverter, whose a circuit topology is presented in Fig. 1a, output voltages u_{AN} , u_{CN} , u_{CN} are produced using eight switching configurations, as shown in Fig. 2. A vector representation of the inverter voltages are presented in Fig. 1b.

Single transistor open-circuit failures cause unidirectional voltage in one of the inverter phases resulting in significant electromagnetic torque ripples because of the currents distortions. These deformations are characteristic for the faults of particular transistor. This fact is visible comparing current vector hodographs with a healthy and faulted drive. In steady states, under the healthy motor drive operations, the

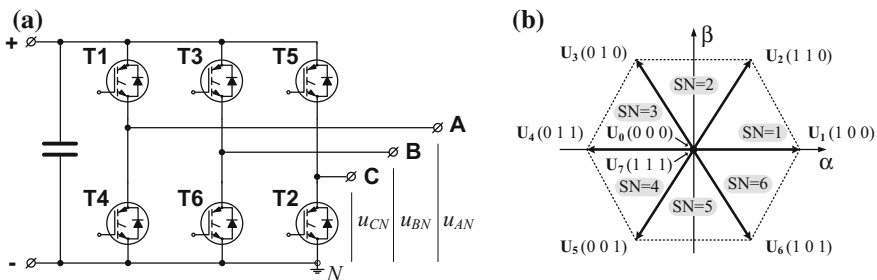


Fig. 1 Three-phase voltage source inverter: circuit topology (a) and voltage space vectors (b)

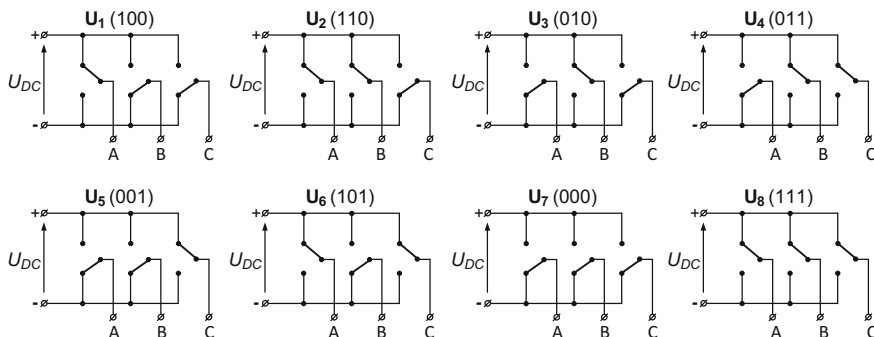


Fig. 2 Switching states for the voltage inverter healthy operating mode

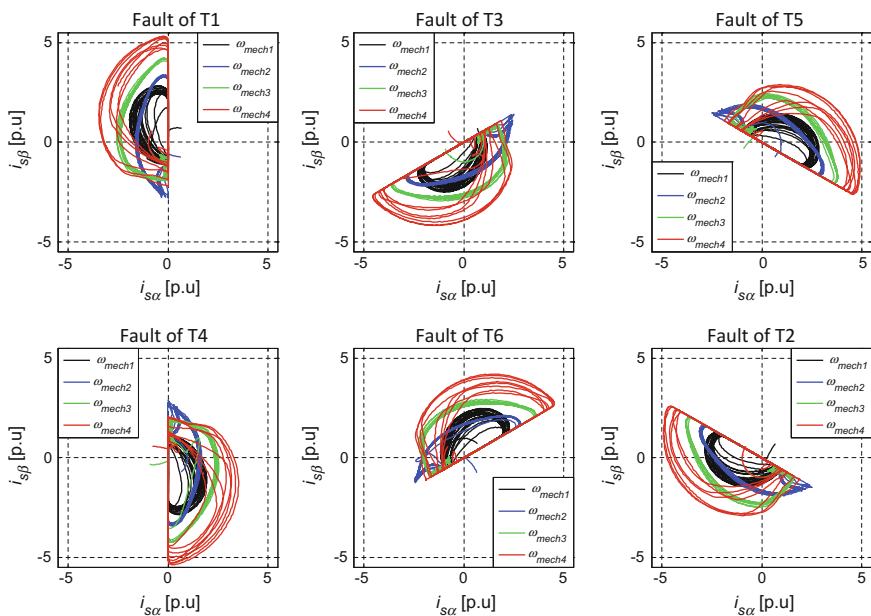


Fig. 3 Hodographs of the stator current vector for the transistor open-circuit faults in the inverter for the drive which operates at a different angular motor speed ($\omega_{mech1}, \dots, \omega_{mech4}$)

hodographs have a circular shape, whereas for the single open-circuit failure is semicircular, as shown in Fig. 3.

As a result of the fault, the drive performance is decreased. Compared to the healthy vectors $\mathbf{U}_0, \dots, \mathbf{U}_7$, the faulted ones $\mathbf{U}_0^F, \dots, \mathbf{U}_7^F$ are different in respect of their amplitudes and phases, as shown in Fig. 4 [17]. For instance, T1 open-circuit failure results in the magnitude of \mathbf{U}_2^F and \mathbf{U}_6^F reducing to $(1/\sqrt{3})U_{DC}$ but the vectors phase

is shifted by an angle $\pm\pi/6$, respectively. Additionally, the amplitude of $U1^F$ is equal to zero and that is the reason why the α component of the inverter reference voltage vector U_{ref} increases. Hence, this vector is located for a longer time in the first sector $SN = 1$ in α - β system. Further, the flux of the machine depends on the stator voltage and it cannot be controlled in the case when the faulty states of the inverter vectors are applied because of voltage malfunctions. As a result, the amplitude of the stator and rotor flux vector decreases in some part of the α - β system, which is shown in Fig. 5.

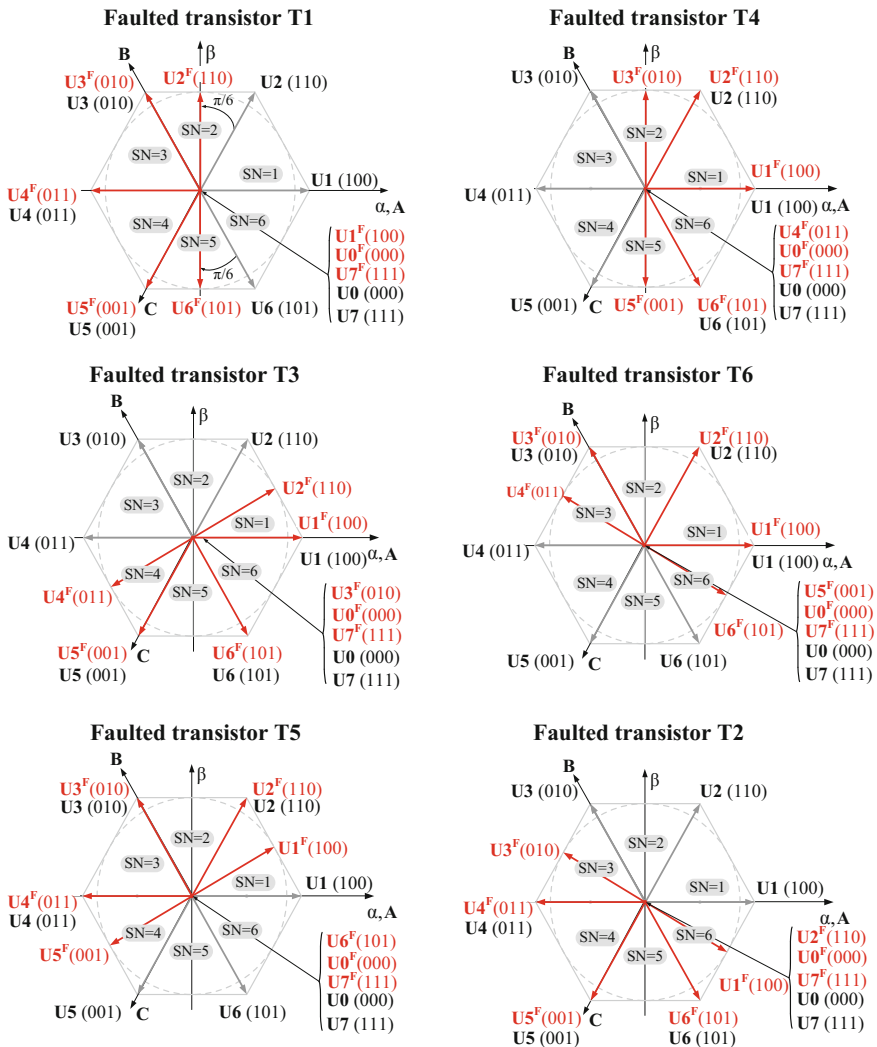


Fig. 4 Inverter voltage vectors during the single transistor open-circuit faults

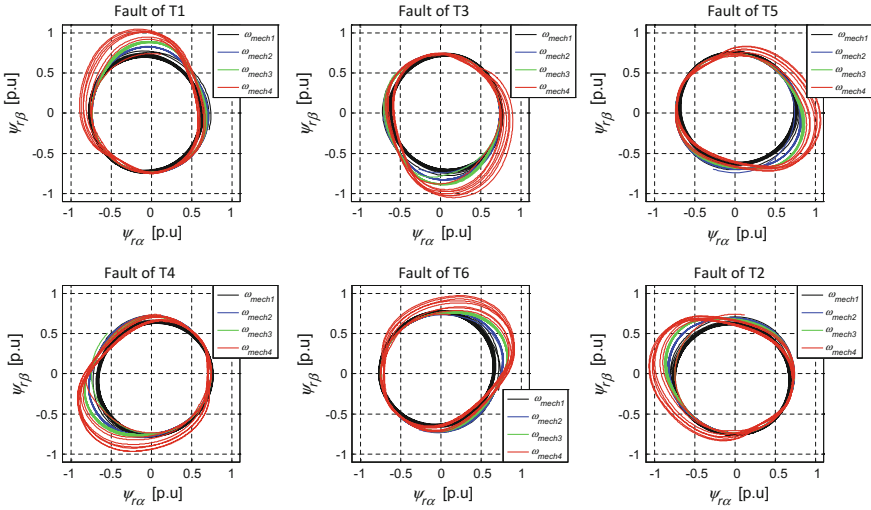


Fig. 5 Hodographs of the rotor flux vector for the transistor open-circuit faults in the inverter for the drive which operates with different angular motor speeds (ω_{mech1} , ..., ω_{mech4})

The specific behavior of the reference voltage as well as flux vector is used for the transistor open-circuit diagnosis.

In order to formulate the transistor failure diagnostic algorithms, the sectors of the α - β system are defined according to the following formula (1):

$$SN_{U,\psi} = E\left(\frac{\gamma_{U,\psi}}{\pi/3}\right). \quad (1)$$

where $SN_{U,\psi}$ means a number of the sector containing the reference voltage or estimated flux vector, which position in the α - β system is defined by an angle $\gamma_{U,\psi}$. A function $E(x)$ returns an integer value of x .

4 Description of Chosen Diagnostic Methods of Open-Circuit IGBT Faults in VSI-Fed Induction Motor Drive

4.1 A Method Based on the Analysis of Stator Voltage Vector Transient

In accordance with the first transistor open-circuit fault diagnostic method (M1) the presence time t_M of the reference voltage vector in the sectors of the α - β plane is calculated [8] as follows:

$$t_{Mnorm} = \frac{t_M}{a\omega^{-1}}, \tag{2}$$

where t_{Mnorm} means the normalized diagnostic signal, ω_m is an angular speed of the motor, T_{timer} is a period of the timer block used in a diagnostic system, which a block diagram is presented in Fig. 6, $a = 1/T_{timer}$.

The fault diagnostic system consists of the timer that is activated when the reference voltage vector moves to another sector on the α - β plane, so the value of the SN_U changes. Next, the value of timer output signal t_M is proportional to a duration when the reference voltage vector is located in each sector. In order to normalize the diagnostic variable a division of t_M by the signal proportional to the drive speed is applied resulting in t_{Mnorm} which is approximately equal to 1 during the drive healthy operation. Transistor faults are detected when the signal $|t_{Mnorm}|$ achieves a fault threshold $T_{TF} = 1.15$. For the faulted switch localization the rule base taking into account direction of the motor rotation is used, in accordance with Table 1. The output signals of comparators $k1$ and $k2$ carry the information about the rotation direction or speed sign as well as the fault threshold exceeding, respectively. For example, if the transistor fault occurs under motor operation with the positive speed ($k1 = 1$), the diagnostic signal $|t_{Mnorm}|$ value is greater than 1.15 ($k2 = 1$) and the reference voltage vector is located in the first sector of the α - β plane ($SN_U = 1$), then the fault of T1 switch is detected. Similarly, if the drive operates with the negative direction ($k1 = 0$) and the fault threshold is observed ($k2 = 1$) when the reference voltage vector is described in the sixth sector ($SN_U = 6$) of the stationary reference frame, the failure of T1 is established.

4.2 A Method Based on the Analysis of Stator Flux Vector Transient

In accordance with the widely used vector control algorithms, namely DRFOC or DTC, an amplitude of the rotor or stator flux is regulated so that it has an approximately constant value which is equal to the reference one. However, under

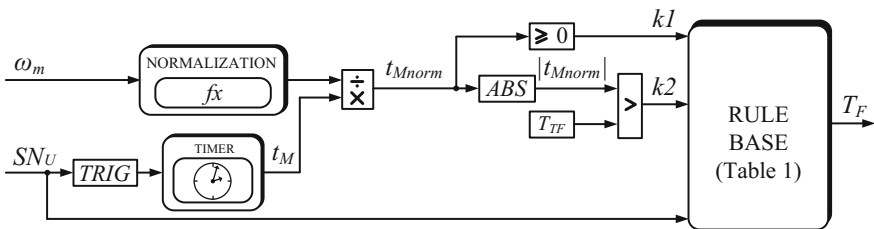


Fig. 6 Schematic diagram of the switch fault diagnostic system for the method M1

Table 1 Open-switch fault symptoms patterns for the first diagnosis technique M1

$k1$	$k2$	SN_U	Faulted transistor
1	1	1	T1
0	1	6	
1	1	2	T2
0	1	1	
1	1	3	T3
0	1	2	
1	1	4	T4
0	1	3	
1	1	5	T5
0	1	4	
1	1	6	T6
0	1	5	

the inverter faulty condition, in the period of the flux rotational movement in the α - β system, the absolute value of the estimated flux vector decreases below the nominal value ψ_{ref} when the reference inverter voltages cannot be obtained. This behavior is used to formulate the second transistor open-circuit fault diagnostic method (M2). In accordance with this method, the local minimums of the rotor or stator flux amplitude are monitored. If the flux amplitude is less than the fault threshold value ψ_{thr} in the case when the local minimum is observed, the information about the position of the flux vector, that is defined by the angle γ_ψ in the α - β system, allows to detect the faulty switch [16, 17].

The algorithm simplification follows from the definition of the flux vector location, using partition of the α - β plane into six sectors SN_ψ . The rule base of the fault diagnostic system, whose block diagram is shown in Fig. 7, is presented in Table 2. For example, if a value of the local minimum of the flux amplitude is less than the fault threshold ψ_{thr} , that means $k1 = 1$, the angular drive speed is positive ($k2 = 1$) and $SN_\psi = 1$, then the fault of T1 is detected ($d = 1$).

Fig. 7 Block diagram of the transistor failures diagnostic system for the method M2

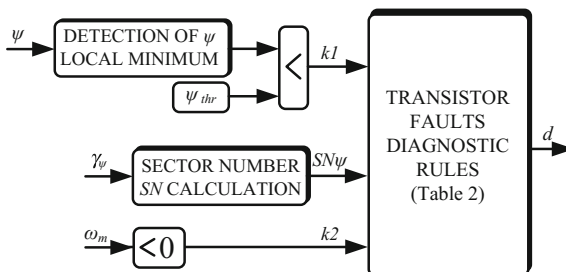


Table 2 Transistor open-circuit fault symptoms patterns for the second diagnosis method M2

$k1$	$k2$	Sector SN_{ψ} in which the local minimum of ψ is observed	Faulty switch
1	1	1	T1
1	0	6	
1	1	2	T2
1	0	1	
1	1	3	T3
1	0	2	
1	1	4	T4
1	0	3	
1	1	5	T5
1	0	4	
1	1	6	T6
1	0	5	

5 A Descriptive Analysis of Selected Diagnostic Methods of Open-Circuit IGBT Faults in VSI-Fed Induction Motor Drive

5.1 A Short Description of the Testing Methodology and the Laboratory Set-up

The analyzed transistor open-circuit fault diagnostic methods have been tested by experimental research, whose selected results are presented in this section. First, the robustness of these algorithms against the occurrence of false alarms during normal motor drive operations was proved. For this purpose, plenty of various tests under constant reference motor speed values and rapid load changes were carried out. Additionally, a similar research taking into account the drive performance under changeable motor speed as well as load variations was done. All these tests resulted in the fault threshold definition for each considered transistor open-circuit fault diagnostic algorithms. In order to prove the effectiveness of the diagnostic techniques the transistor defects were emulated during the constant reference motor speed. Next, the research was extended into the analysis of the diagnostic methods correctness under transistor faults occurring during the linear motor speed changes. Finally, the speed of the faults diagnosis was compared for each method, considering a failure instance referred to the phase of the current. In all figures, magenta dashed, vertical lines mark the instance of the single switch open-circuit faults and the moment of the faulted transistor detection is marked as a blue dotted line. For the rating diagnosis speed of the proposed algorithms a variable t_D was defined as a part of the stator current period T_i which is measured before the transistor defect

emulation. Additionally, the speed n of the drive, phase currents $i_{sA,B,C}$ and selected diagnostic variables, are presented in the figures with the respective analyzed method. In the case of M1, time-domain waveforms of the signal $|t_{Mnorm}|$ and the variable SN_U , which denotes the sector number, that described the position of the reference voltage vector in the stationary coordinate system, is shown. Supplementary, transients of the rotor ψ_r or stator ψ_s flux absolute value and the flux vector position that is described by the sector number $SN\psi$ are presented.

The research was conducted using a laboratory set-up (see Fig. 8) built of 2.2 kW induction machine connected by a stiff shaft to the DC motor which was used as a load machine controlled by changing armature current. Nominal parameters of the induction motor are shown in Appendix 1, Table 3. The drive control as well as diagnostic algorithm were implemented using the dSPACE DS1103 rapid prototyping system with the sampling period $T_s = 100 \mu s$. The phase currents and DC-link voltage measurements were made using LA 55-P and LV 25-P transducers, respectively. An incremental encoder (36,000 imp./rev.) was used for speed measurements. The switch open-circuit failures were emulated removing command transistor gate signals.

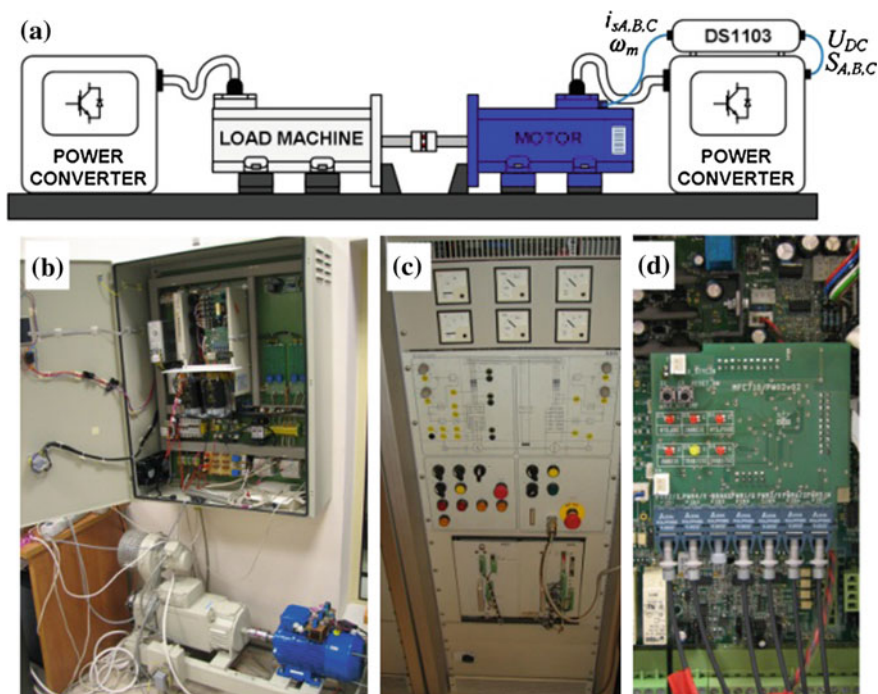


Fig. 8 Experimental set-up: a schematic diagram (a), a photo of the induction motor drive (b) DC motor supplier (c) the fiber-optic modules of the inverter (d)

5.2 Method Robustness Against the False Alarms

In Fig. 9 chosen experimental results that demonstrate the diagnostic methods robustness against the false alarms are presented. For this purpose, the drives were tested under various speed conditions and rapid load changes. These tests resulted in the determination of the transistor fault thresholds: $T_{TF} = 1.15$ for the M1 method (for both control structures: DRFOC and DTC), and $\psi_{sthr} = 0.86$ and $\psi_{rthr} = 0.95$ for the M2 method, for DRFOC and DTC strategies respectively. It means, that the values of the diagnostic variables do not exceed these thresholds during healthy drive operations. The main advantage of this approach is that it does not require any knowledge about diagnostic signals corresponding to the faulty inverter mode.

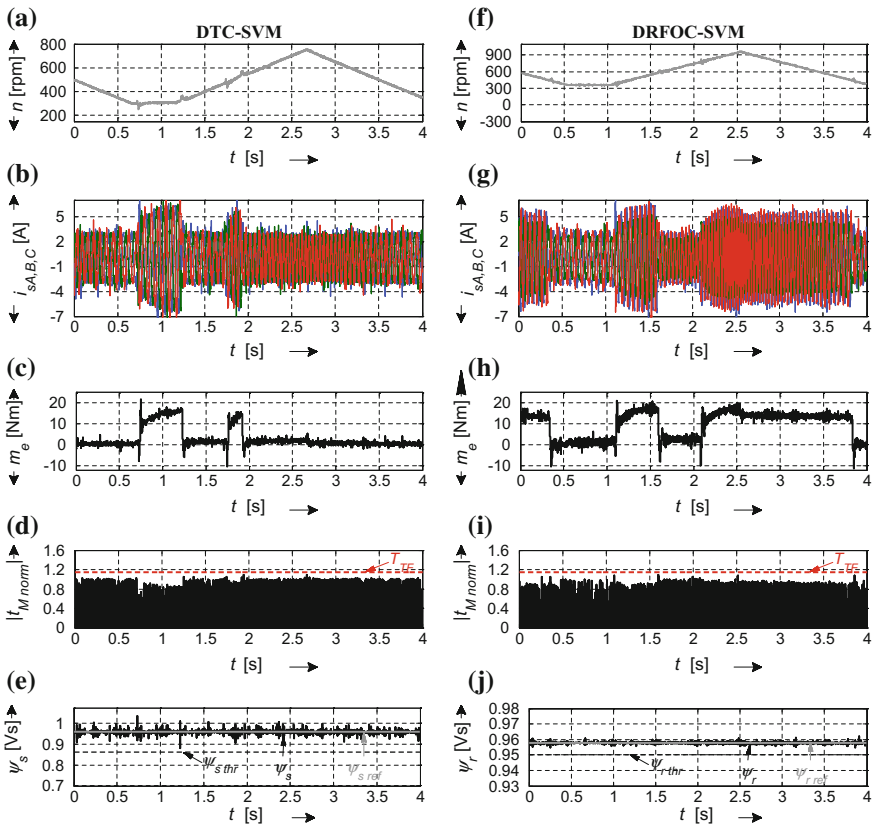


Fig. 9 Experimental results regarding the fault threshold adjusted to the time-domain waveforms of the speed n (a, f), stator currents $i_{sA,B,C}$ (b, g), electromagnetic torque m_e (c, h), diagnostic variables related to the 1st method $|t_{Mnorm}|$ (d, h) and the absolute value of the stator ψ_s or rotor ψ_r flux of the machine (e, i) for the DTC-SVM and DRFOC

5.3 Verification of the Transistor Open-Circuit Fault Diagnostic Methods

In Fig. 10a–e the experimental results related to the transistor T3 open-circuit failure, which occurred during the constant reference drive speed $n_{ref} = 720$ rpm and the load $m_L = 7.2$ Nm in the DTC-SVM controlled drive, are shown (Fig. 10a). At the instant of $t = 0.046$ s the fault was simulated and shortly after that, at time $t = 0.50$ s, the diagnostic signal, which corresponds to the method M1 crossed the fault threshold T_{TF} (Fig. 10c). At the same time, the reference voltage vector was located in the 3rd sector of the α - β plane, so the faulted switch was recognized correctly (Fig. 10e). The fault resulting in the stator flux disturbances, which were processed. Shortly after that, the local minimum of the time-domain waveform of the flux was observed when the estimated stator flux was in the 3rd sector of the stationary system (Fig. 10d, e). Taking into consideration the previously formulated diagnostic rules of the M2 method, the fault of T3 was detected. Similar results were obtained for the fault of transistor T6 in the drive with DRFOC (Fig. 10f–j). As can be seen, the diagnostic rules were fulfilled for the both diagnostic methods, the transistor T6 fault was detected, namely the method M1 gave the information about the fault at $t = 0.047$ s but the method M2 at the instant of $t = 0.053$ s. In the case of both electric drives (with DTC and DRFOC), the fault localization time was shorter than one period T_i of the current fundamental (Fig. 10b, g).

The presented results correspond to the drive operation with the constant speed and semi-loaded motor. Next results are obtained during the drive performance with the full load and the motor speed that was linearly changed, namely increased or decreased. It is reasonable to verify both diagnostic methods because they are based on the signals whose frequency is changing depending on the reference speed of the motor. First, the faults were simulated for the fully-loaded motor. The chosen results are presented in Figs. 11 and 12. These results correspond to the fault of T3 (Figs. 11 and 12f–j) and T6 (Fig. 12a–e). Due to the diagnostic signal normalization the method M1 is effective even when faults occur during the reference speed is changed. For the healthy motor drive operation the signal $|t_{Mnorm}|$ is approximately equal to one, despite the fact that the voltage frequency increases. The flux error does not depend significantly on the motor speed or load, therefore the diagnostic signal normalization is not necessary. The following examples proved that the diagnostic method M2 gives correct results for the drive with DTC or DRFOC as well.

Figure 13 shows experimental results that have been achieved under the fault of the transistor T6 and no-loaded motor drive operations. Alike as in the previously presented cases, the method based on reference voltage vector analysis is characterized by faster transistor failure diagnosis than the flux-based techniques. Furthermore, both algorithms allows to localize the faulted transistor in the time shorter than one current fundamental period which allows to change the control algorithm sufficiently fast to compensate the negative fault influence on the drive performance without interruption of the motor operation.

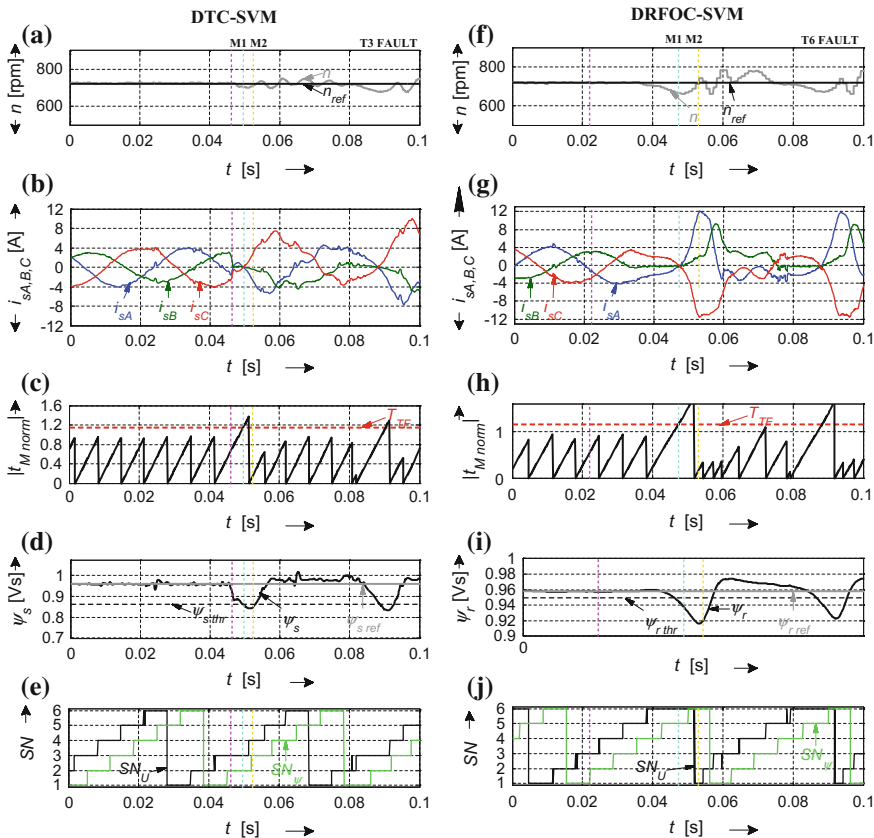


Fig. 10 Experimental results regarding the fault of transistor in the inverter phase B with the time-domain waveforms of the speed n (a, f), stator currents $i_{sA,B,C}$ (b, f), diagnostic variables related to the M1 method $|t_{Mnorm}|$ (c, g), and the absolute value of the stator ψ_s or rotor ψ_r flux of the machine (d, h) and position of the reference voltage SN_U or flux SN_ψ vector in the α - β system (e, i) for the DTC-SVM and DRFOC

Figure 14 presents summarized results of the test which shows the relationship between the failure instant, defined by the phase angle γ_i of the current i_{sA} , and the speed of the T1 open-circuit fault diagnosis. This research was conducted under constant reference speed $n_{ref} = 720$ rpm and the load $m_L = 7.2$ Nm. These conditions correspond to a half of the nominal values. The achieved results showed that the speed of the transistor fault diagnosis t_D depends on the fault instant described by γ_i . It is clear that depending on rotational speed direction of the reference voltage or flux vector the diagnosis speed increases after these vectors leave the sector of the α - β plane which is crucial for the failure diagnosis. When the vectors move in this sectors the time t_D decreases. Due to the phase shift between the voltage or flux and the current vector, in the case of T1 fault, the fastest fault diagnosis is observed around the angle $\gamma_i = \pi/3$.

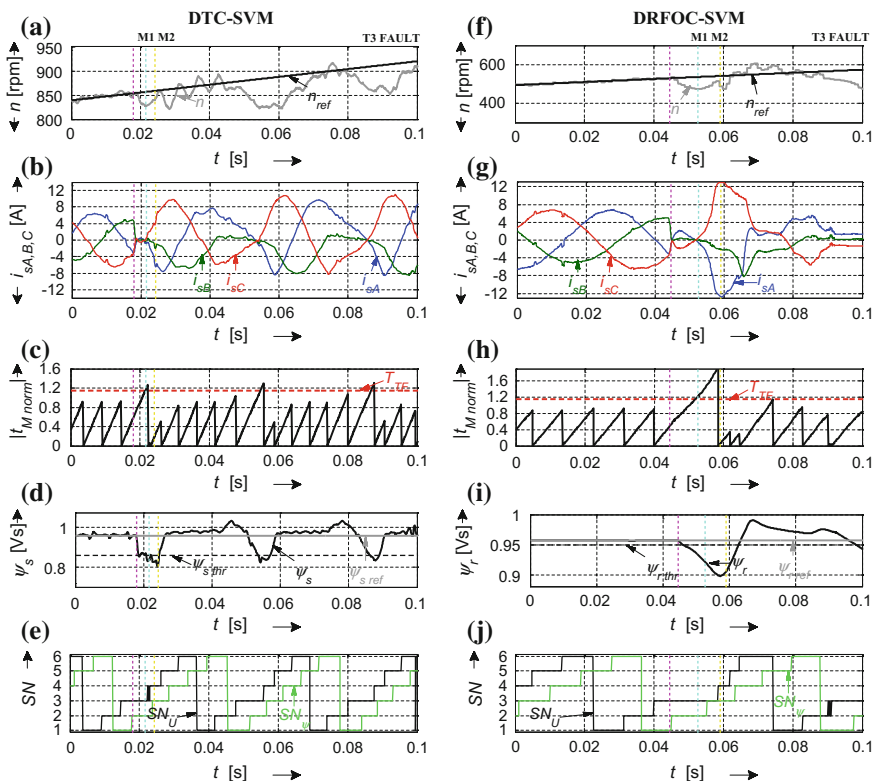


Fig. 11 Experimental results regarding the fault of transistors in the inverter phase B with the time-domain waveforms of the speed n , which is linearly increased (a, f), stator currents $i_{sA,B,C}$ (b, g), diagnostic variables related to the 1st method $|t_{Mnorm}|$ (c, h), and the absolute value of the stator ψ_s or rotor ψ_r flux of the machine (d, i) and position of the reference voltage SN_U or flux SN_ψ vector in the α - β system (e, j) for the DTC-SVM and DRFOC-SVM

The achieved results proved that for the both fault monitoring techniques the diagnostic time is shorter than one period of the current fundamental harmonic. Additionally, the first method (M1) is faster than the second one (M2) in every case.

6 Post-fault Control of the Drive System

The transistor open-circuit fault diagnostic methods are applied in the fault-tolerant control systems in order to carry out the remedial action, which brings back partial or full motor drive functionality. For this purpose, the redundant converter topologies, the survey of which was presented in [18], are developed. As a matter of fact, only full hardware redundancy, such as using an additional converter leg,

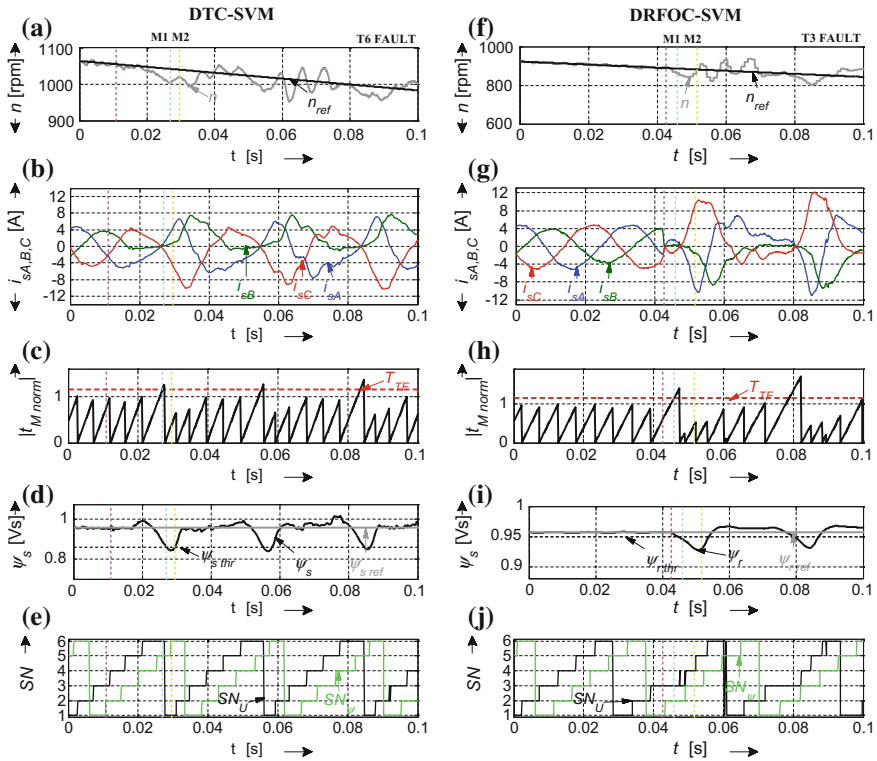


Fig. 12 Experimental results regarding the fault of transistors in the inverter phase B with the time-domain waveforms of the speed n , which is linearly decreased (**a**, **f**), stator currents $i_{sA,B,C}$ (**b**, **g**), diagnostic variables related to the 1st method $|I_{Mnorm}|$ (**c**, **h**), and the absolute value of the stator ψ_s or rotor ψ_r flux of the machine (**d**, **i**) and position of the reference voltage SN_U or flux SN_w vector in the α - β system (**e**, **j**) for the DTC-SVM and DRFOC-SVM

guarantees maintaining high drive performance. Nevertheless, in view of their high manufacturing cost, these solutions are recommended for use in safety-critical drive applications.

Another approach is based on four-switch three-phase inverter topologies. In accordance with this, a phase of the machine that is connected to the faulty inverter leg, is connected to a DC bus mid-point [19–23] or is separated from the inverter and the neutral point of the motor is connected to the mid-point of the capacitor input filter of the inverter [24–26]. The main drawback of the second solution is the requirement of access to a motor neutral point, that is not assured in most motor drives applications. Furthermore, a long post-fault drive operation has to be avoided because the current in the healthy phases significantly increases. In accordance with the first solution, a maximum speed of the drive, that operates with the nominal torque, is limited to a half of the nominal value. Additionally, flying capacitors problem occurs and must be considered in the voltage modulation strategy [12–14].

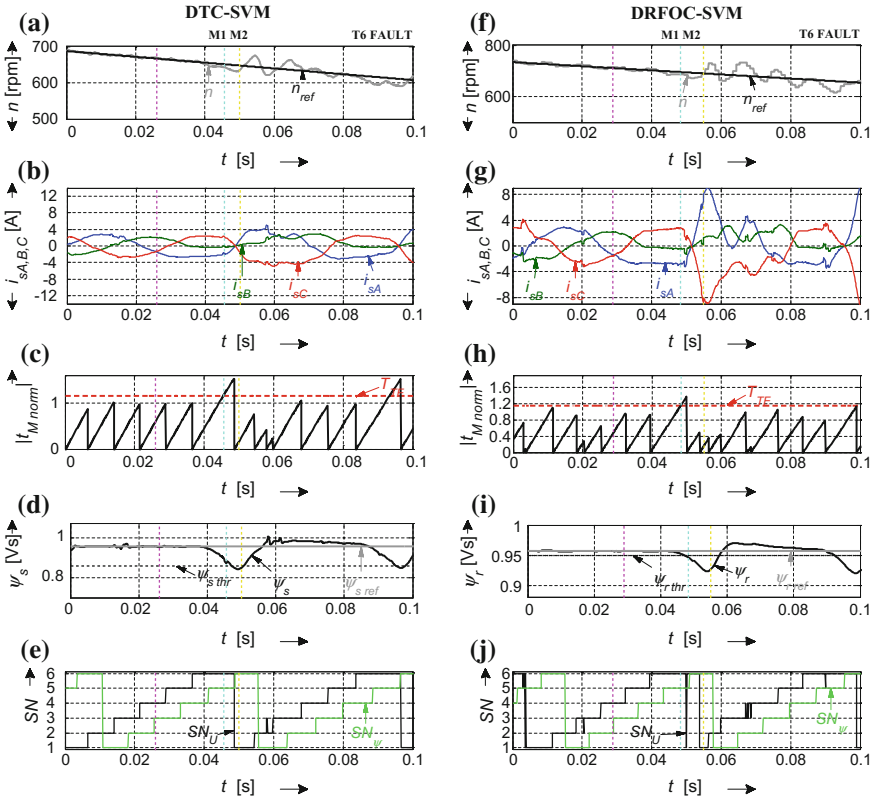
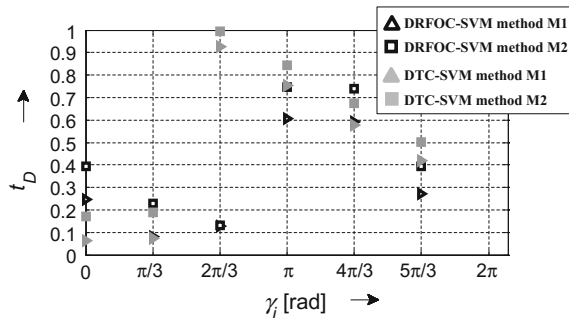


Fig. 13 Experimental results regarding the fault of transistors in the inverter phase B with the time-domain waveforms of the speed n , which is linearly decreased (a, f), stator currents $i_{sA,B,C}$ (b, g), diagnostic variables related to the 1st method $|t_{M^{norm}}|$ (c, h), and the absolute value of the stator ψ_s or rotor ψ_r flux of the machine (d, i) and position of the reference voltage SN_U or flux SN_ψ vector in the α - β system (e, j) for the DTC-SVM and DRFOC-SVM

Fig. 14 Speed t_D of the open-circuit fault diagnostic methods M1 and M2



A choice of the inverter topology for the post-fault operation should be justified by a required safety level of the motor drive applications and its acceptable manufacturing cost.

7 Summary

This chapter presents two simple transistor open-circuit fault diagnostic methods which have been applied in DTC-SVM as well as DRFOC-SVM induction motor drive systems. The concept of the fault diagnostic techniques consists in the analysis of the vector hodographs of easy assessable signals, so the additional hardware installation is not required for the methods implementation. The main advantage of the proposed schemes of diagnosis result from the accurate diagnostic signals selection which guaranties the methods load independence of the load. Both methods ensure the correct transistor open-circuit fault diagnosis in a time shorter than one period of the stator current fundamental harmonic regardless of the drive operation point. The great merit of the methods is their full robustness against false alarms and a simple hardware implementation. The presented techniques can be realized using microprocessor systems in the fault-tolerant motor drive systems.

Acknowledgment This work was supported by the National Science Centre Poland, under project 2013/09/B/ST7/04199 (2014–2017).

Appendix 1

See Table 3.

Table 3 Rated data of the tested induction motor

Quantity	Symbol	Value
Power	P_N	2.2 kW
Torque	m_N	14.6 Nm
Speed	n_N	1440 rpm
Voltage	u_N	400 V
Current	i_N	4.5 A

References

1. Yeh CC, Demerdash NAO (2007) Induction motor-drive systems with fault tolerant inverter-motor capabilities. In: IEEE international conference on electric machines & drives IEMDC, Antalya, 3–5 May 2007
2. Estima JO, Freire NMA, Cardoso AJM (2013) Recent advances in fault diagnosis by Park's vector approach. In: IEEE workshop on electrical machines design control and diagnosis WEMDCD, Paris, 11–12 Mar 2013
3. Sleszynski W, Nieznanski J, Cichowski A (2009) Open-transistor fault diagnostics in voltage-source inverters by analyzing the load currents. *IEEE Trans Ind Appl* 56(11):4681–4688
4. An Q, Sun L (2015) Current residual vector-based open-switch fault diagnosis of inverters in PMSM drive systems. *IEEE Trans Power Electron* 30(5):2814–2827
5. Estima JO, Cardoso AJM (2013) A new algorithm for real-time multiple open-circuit fault diagnosis in voltage-fed PWM motor drives by the reference current errors. *IEEE Trans Ind Electron* 60(8):3496–3505
6. Jlassi I, Estima JO, El Khil SK, Bellaj NM, Cardoso AJM et al (2015) Multiple open-circuit faults diagnosis in back-to-back converters of PMSG drives for wind turbine systems. *IEEE Trans Power Electron* 30(5):2689–2702
7. Freire NMA, Estima JO, Cardoso AJM (2012) A voltage-based approach for open-circuit fault diagnosis in voltage-fed SVM motor drives without extra hardware. In: XXth international conference on electrical machines ICEM, Marseille, 2–5 Sept 2012
8. Orłowska-Kowalska T, Sobanski P (2013) Simple sensorless diagnosis method for open-switch faults in SVM-VSI-fed induction motor drive. In: IEEE 39th annual conference on industrial electronics society IECON, Vienna, 10–13 Nov 2013
9. Peugeot R, Courtine S, Rognon JP (1998) Fault detection and isolation on a PWM inverter by knowledge-based model. *IEEE Trans Ind Appl* 34(6):1318–1326
10. Sleszynski W, Nieznanski J, Cichowski A (2005) Real-time fault detection and localization vector-controlled induction motor drives. In: European conference on power electronics and applications EPE, Dresden, 11–14 Sept 2005
11. Trabelsi M, Boussak M, Gossa M (2010) Multiple IGBTs open circuit faults diagnosis in voltage source inverter fed induction motor using modified slope method. In: 19th international conference on electrical machines ICEM, Rome, 6–8 Sept 2010
12. Espinoza-Trejo DR, Campos-Delgado DU, Bossio G et al (2013) Fault diagnosis scheme for open-circuit faults in field-oriented control induction motor drives. *IET Power Electron* 6(5):869–877
13. Campos-Delgado DU, Pecina-Sanchez JA, Espinoza-Trejo DR et al (2013) Diagnosis of open-switch faults in variable speed drives by stator current analysis and pattern recognition. *IET Electr Power Appl* 7(6):509–522
14. Orłowska-Kowalska T, Sobanski P (2015) Simple diagnostic technique of a single IGBT open-circuit faults for a SVM-VSI vector controlled induction motor drive. *Bull Pol Acad Sci Tech Sci* 63(1):281–288
15. Sobanski P (2014) Fuzzy-logic-based approach to voltage inverter fault diagnosis in induction motor drive. *Przeł Elektrotech* 90(6):149–153
16. Sobanski P (2014) IGBTs Open-circuit faults diagnostic methods for the voltage inverter fed induction motor drives. In: XII national conference on control in power electronics and electric drives SENE, Lodz, 18–20 Nov 2015
17. Orłowska-Kowalska T, Sobanski P (2014) Low-cost fault-tolerant control scheme for SVM two-level voltage-inverter-fed induction motor drive. In: Proceedings of the 11th international conference on modeling and simulation of electric machines, converters and systems ElectrIMACS, Valencia, 19–22 May 2014

18. Welchko BA, Lipo TA, Jahns TM, Schulz SE (2003) Fault tolerant three-phase AC motor drive topologies; a comparison of features, cost, and limitations. In: IEEE international conference on electric machines and drives IEMDC, Madison, 1–4 June 2003
19. Araujo Ribeiro RL, Jacobina CB, Da Silva ERC, Lima AMN (2004) Fault-tolerant voltage-fed PWM inverter AC motor drive systems. *IEEE Trans Ind Electron* 51(2):439–446
20. El Badsı B, Bouzidi B, Masmoudi A (2013) DTC Scheme for a four-switch inverter-fed induction motor emulating the six-switch inverter operation. *IEEE Trans Power Electron* 28(7):3528–3538
21. Lee HH, Dzung PQ, Khoa LD, Phuong LM (2009) Dynamic adaptive space vector PWM for four switch three phase inverter fed induction motor with compensation of DC—link voltage ripple. In: IEEE international conference on power electronics and drive systems PEDS, Taipei, 2–5 Sept 2009
22. Nacusse MA, Romero M, Haimovich H, Seron MM (2010) DTFC versus MPC for induction motor control reconfiguration after inverter faults. In: Conference on control and fault-tolerant systems SysTol, Nice, 6–8 Oct 2010
23. Nguyen TD, Nguyen HM, Lee H-H (2009) An adaptive carrier-based PWM method for four-switch three-phase inverter. In: IEEE international symposium on industrial electronics ISIE, Seoul, 5–8 July 2009
24. Fu J-R, Lipo TA (1993) A strategy to isolate the switching device fault of a current regulated motor drive. In: Proceedings of IEEE industrial applications society annual meeting IAS, Toronto, 2–8 October 1993
25. Bolognani S, Zordan M, Zigliotto M (2000) Experimental fault-tolerant control of a PMSM drive. *IEEE Trans Ind Electron* 47(5):1134–1141
26. Tabbache B, Benbouzid M, Kheloui A, Bourgeot JM, Mamoune A (2013) PWM inverter-fed induction motor-based electrical vehicles fault-tolerant control. In: IEEE 39th annual conference on industrial electronics society IECON, Vienna, 10–13 November 2013

Speed and Current Sensor Fault-Tolerant-Control of the Induction Motor Drive

Mateusz Dybkowski, Kamil Klimkowski
and Teresa Orłowska-Kowalska

Abstract In this chapter a rotor speed and stator current sensors faults detection systems for a vector controlled induction motor drive are described and tested. Different active algorithms are discussed, their advantages and disadvantages are demonstrated from the drive safety point of view. Another problem, presented in this chapter, is focused on the fault detection time. Simulation results show that the proposed detection systems can be used in fault tolerant control algorithms. The simulation studies are confirmed through a variety of experimental tests.

Keywords Induction motor drives · Speed sensor fault · Current sensor fault · Fault detection · Fault-tolerant-control

1 Introduction

For the proper work of the modern vector controlled induction motor drive system the mechanical and electrical variables sensors are necessary [1]. Some signals, used in the internal control structure of the drive system (such as stator and/or rotor flux, electromagnetic torque, rotor speed) can be estimated by different simulators [1], observers [2], Kalman Filters or neural networks [3, 4]. Those estimation systems and control algorithms cannot work stably when the sensors are broken. The advanced vector control structures of Induction Motor (IM) drives should be equipped with diagnostic features to prevent damages and sudden switch-offs of

M. Dybkowski (✉) · K. Klimkowski · T. Orłowska-Kowalska
Department of Electrical Machines, Drives and Measurements, Wrocław University
of Science and Technology, Wybrzeże Wyspiańskiego 27, Wrocław, Poland
e-mail: mateusz.dybkowski@pwr.edu.pl

K. Klimkowski
e-mail: kamil.klimkowski@pwr.edu.pl

T. Orłowska-Kowalska
e-mail: teresa.orlowska-kowalska@pwr.edu.pl

complex industrial installations. Thus the incipient fault detection has recently become one of the basic requirements for modern IM drive systems [1, 4].

During last few years, fault-tolerant control systems (FTC) [1] became a very active research field for many research groups [4, 5]. The FTC aims to ensure the continuous system functionality, even after fault occurrence. Therefore, the FTC should be able to detect and identify faults and to cancel their effects or to attenuate them to an acceptable level.

In this chapter the rotor speed and stator current sensors faults detection systems for vector controlled induction motor drive system are described and tested. Different active algorithms are discussed, their advantages and disadvantages are demonstrated from the safety point of view. Another problem, presented in this chapter, is focused on the fault detection time. Selected simulation and experimental results have been presented in this work.

2 A Short Review of Existing Diagnostic Methods of Sensor Faults in Induction Motor Drives

The fault tolerant control (FTC) has attracted lot of attention during the last 20 years in most industrial applications, such as: flight control, electric machines, power plants, computer networks and refineries. One of the most researched areas concerns fault diagnosis in induction motor drives. The main source of failure in these systems may be due to the machine, converter or faulty operation of measurement sensors. Studies show that proper and stable operation of the drive strongly relies on the efficiency of the measurement sensors. Measurements can be corrupted not only due to total sensor failure but also due to connection problems or some hardware or software malfunction [3, 6]. In vector-controlled drives, speed, current and voltage sensors are required to provide high performance and system efficiency. Therefore, sensor fault-tolerant control is an extremely important area of investigation for IM drives [7].

The proper choice of the fault tolerant control algorithm and topology depends on the drive system requirements and used components. To ensure the proper work of complex systems, it is necessary to take account of diagnostic techniques, that within a reasonable period of time will allow to detect a failure and an appropriate response of the control structure. There are several methods for sensor FDI (Fig. 1) that depend on hardware redundancy, analytical redundancy, or both of them [4, 5, 8, 9].

The general idea of methods based on the hardware redundancy, is based on continuous measurement of the respective state variable using two or more additional sensors. Any difference in compared readings from the other sensors indicates fault occurrence. These methods, because of their simplicity, are most commonly used in industrial applications [4, 5]. The main disadvantage of these solutions, presented in the papers [5, 8] is the high cost of this complex system with

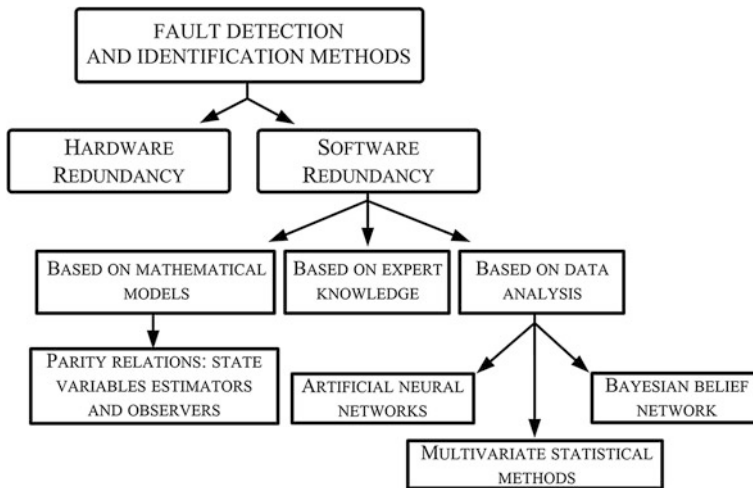


Fig. 1 Fault detection and identification methods [5]

additional redundant sensors. Hardware redundancy is a very expensive and cumbersome solution [7]. The use of additional components increases the complexity of the whole system and raises challenges in diagnosis. Also, the use of a hardware redundancy approach is limited due to cost constraints. Moreover, the additional components and sensing elements affect the design process of the mathematical model and introduce uncertainties into the system. In the case of the rotor speed sensor, the redundancy is not always acceptable because of lack of sufficient space (usually one sensor per mechanical shaft). A stator current sensor is very simple in practical implementation and can be mounted in each type of drive. In the case of voltage measurement there are two basic approaches to the calculation of the needed voltage of components: usage of one sensor in a DC-link of a frequency converter and the other solution is based on three (or even two) phase voltage sensors.

Methods based on the software redundancy do not use additional sensors, but are based on the relations between the measured and analytically calculated values of the state variables. The most commonly used fault detection and isolation (FDI) methods are knowledge-based fault-model methods [8], such as observer methods [6, 9] or parity space approach [6, 10]. Once the faulty sensor is detected, the FTC will try to accurately restore the readings from missing sensors using the remaining healthy sensor outputs. So reconfiguration strategies are generally developed using the redundancy of system state variables to restore missing data [1, 8, 11–14].

Residuals generated between the estimated and measured system outputs can be evaluated for fault detection using various methods. In [12], state variable observers are designed for this purpose and used to identify and isolate the faulty sensor. In [15], a bank of three rotor flux observers and a switching mechanism are presented

to identify the faulty sensor [16, 17]. Because three different observers are used in this method, the proposed solution demands more design efforts and is much more difficult in real-time implementation. In [9], to isolate all the sensor faults an adaptive current observer with rotor resistance estimation is used. This method is not robust to random system noise. In [18], a similar solution is presented and based on current and flux observer with estimation of stator and rotor resistances using a single current sensor.

In [3] and [10] an example of space parity approach is presented. The fault indicator generation is based on outputs of the sensor at the previous sampling acquisition periods. This approach was modified by [7]. The derived analytic algorithm is then enhanced against noise measurements [10]. The innovative FDI algorithm was proposed in [3], a parity space approach is used to identify and isolate the faulty sensor. The presented algorithm does not require the knowledge of the system model and is therefore independent of system model complexity. Reconfiguration of the control system is not possible as no estimation is performed. In [19], the fault diagnosis and reconfiguration strategy are based on the extended Kalman filter and a reduced number of adaptive observers. None of these methods work in the case of multiple sensor failures.

In [20–23], an additional decision block is used, which depending on the information about sensor faults (current and rotor speed) is able to change the control topology. In [20] and [23], the control reorganization is carried out by a fuzzy decision unit which ensures smooth transition from the encoder based to the sensorless control [7]. In [24], and [25], a neural network/fuzzy logic technique is used to identify and isolate the faulty sensor. The implementation of such a technique is difficult and also it cannot be used for non-complex applications. In [26], fuzzy logic is used to detect the faulty speed sensor. In [27] and [28], fault-tolerant control is based on maximum-likelihood voting (MLV) that uses the actual speed and estimated speed (obtained using the Extended Kalman Filter and Luenberger observer). The main problem connected with software redundancy approach is strong sensitivity to electric parameters characterizing the induction motor model variations. Basic difficulties may be caused by e.g. stator and rotor heating, magnetic saturation or the skin effect. Therefore, uncertainty and parameter variations can deteriorate the control algorithm and may accidentally enable the FDI unit in the healthy state of a drive.

In [12] an FDI unit that employs an adaptive fuzzy scheduling observer is proposed. Due to the used single observer structure, the proposed solution can easily be implemented in real-time systems. In [7] a new current and speed sensor fault detection, isolation, and compensation technique is proposed. A logic-based detection mechanism in the α - β reference frame is proposed to make the drive fault tolerant against current sensor failures. The speed sensor fault detection is based on MRAS type estimation technique. A survey on different types of faults in variable speed drives is reported in [29].

Despite these existing research efforts, the detection of sensors faults in an electric motor drives with induction motors remains a challenging problem [30, 31]. There is a strong necessity for continuous development of model and expert

knowledge based diagnostic system. The increasing requirements of real-time monitoring systems raise additional difficulties due to the limited computation power capabilities and memory. Therefore the further research of FTC systems should consider using less hardware demanding approaches while maintaining desirable results.

The goal of the presented research is to explore methods that utilize the embedded analytical algorithms for the detection and isolation of faulted sensors, even in the presence of failures in the monitored drive system. In order to accomplish the required level of safety and performance within a sensor network in induction motor drives, further research of fault identification methods is needed to overcome the following challenges:

- possibly the quickest or even instant detector response in the occurrence of faulted scenario,
- simple to implement algorithm,
- certain identification and localization of faulted sensor without mistaken isolation of a properly functioning component,
- identification of other sensors failures even in the case of already determined presence of failures in the monitored system,
- independent detection algorithm not affecting other diagnostic systems already installed in a drive (i.e. induction motor, frequency inverter or other measurement sensors FDI units),
- universal approaches which may be used in a wide range of motor drive types.

The main contribution of this chapter is designing and real-time validation of a different current and speed sensors faults detection systems for a vector controlled induction motor drive system. Contrary to the commonly used approach in power electronics and electrical drives, where only one type of the fault is analysed, in the chapter different faults scenarios are described. The proposed systems guarantee stable operation of the drive during faulted conditions. Those systems are based on simple signals from the internal control structure and estimated speed and rotor flux.

3 Analysis and Compensation of the Selected Speed and Current Sensor Faults in a Vector-Controlled Induction Motor Drive

3.1 A Short Description of the Analyzed Drive System

In the paper a well-known control structure of the induction motor was applied—the direct field-oriented control DFOC (Fig. 2). During the measurements an angular velocity the incremental encoder was used (5000 imp./rev.), the DC bus voltage and the switching states are observed to obtain the stator voltage components. Stator current in the course of unfaulty operation is measured using sensors

in the phases A and B, the third transducer may be used in a fault-tolerant control system.

In the rotor speed estimation, the MRAS^{CC} estimator is used in a vector control algorithm and in a diagnostic system. This system was presented in detail in [2]. This estimator is based on two well-known simulators (voltage model and current model of the rotor flux) transformed to the stator current estimator and to the rotor flux estimator based on a current model.

In the basis control structure the rotor flux can be calculated from the equation in [p. u.] system [2]:

$$\frac{d}{dt} \Psi_r^i = \left[\frac{r_r}{l_r} (l_m \mathbf{i}_s - \Psi_r^i) + j\omega_m \Psi_r^i \right] \frac{1}{T_N} \tag{1}$$

Current estimator used in MRAS^{CC} is obtained by the equation:

$$\frac{d}{dt} \mathbf{i}_s^e = -\frac{r_r l_m^2 + l_r^2 r_s}{\sigma T_N l_s l_r^2} \mathbf{i}_s^e + \frac{1}{\sigma T_N l_s} \mathbf{u}_s + \frac{l_m r_r}{\sigma T_N l_s l_r^2} \Psi_r^i - j\omega_m^e \frac{l_m}{\sigma T_N l_s l_r} \Psi_r^i \tag{2}$$

where ω_m^e —estimated rotor angular speed, r_s, r_r, l_s, l_r, l_m —stator and rotor resistances, stator and rotor leakage inductances, mutual inductance, $\mathbf{u}_s, \mathbf{i}_s^e, \Psi_r^i$ —stator

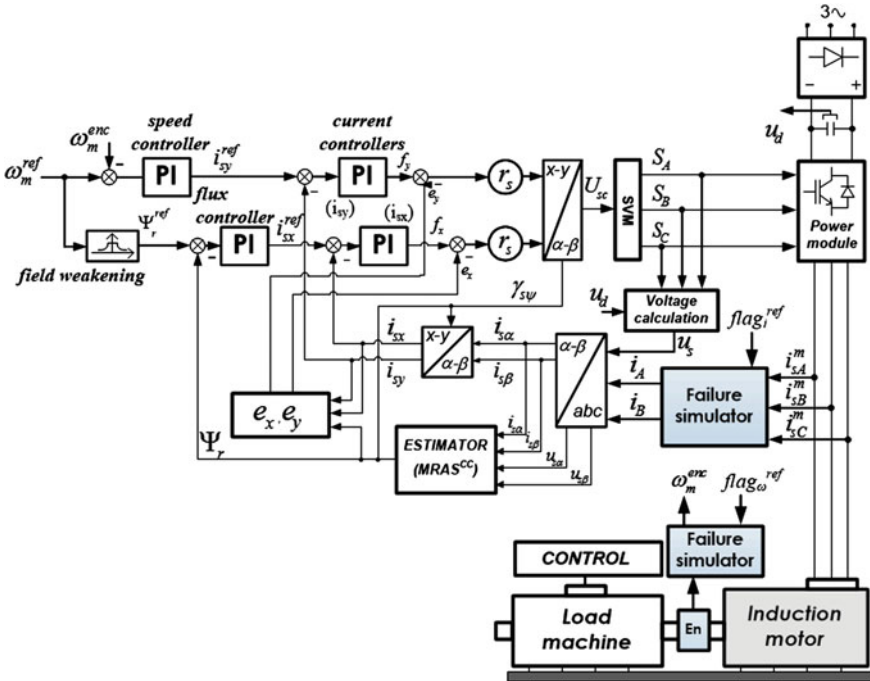


Fig. 2 A scheme of direct field oriented control structure for an induction motor drive

voltage, estimated stator current and rotor flux vectors respectively, $\sigma = 1 - l_m^2/l_s l_r$, $T_N = 1/2\pi f_{sN}$.

Both the stator current estimator (2) and the rotor flux model (1) are adjusted by the estimated rotor speed [2]:

$$\omega_m^e = K_P \left(e_{i_{s\alpha}} \Psi_{r\beta}^i - e_{i_{s\beta}} \Psi_{r\alpha}^i \right) + K_I \int \left(e_{i_{s\alpha}} \Psi_{r\beta}^i - e_{i_{s\beta}} \Psi_{r\alpha}^i \right) dt, \quad (3)$$

where $e_{i_{s\alpha,\beta}} = i_{s\alpha,\beta} - i_{s\alpha,\beta}^e$ —error between the estimated and measured stator current.

For some sensor faults, it is possible to guarantee the proper operation of the vector controlled drive. For this purpose, the whole control structure should be properly designed and adjusted. The control hardware redundancy should be installed in its structure. Fault accommodation strategies for electric motor drives can be divided into:

- state variable estimation,
- sensor redundancy,
- control accommodation—topology change.

3.2 The Influence of the Speed Sensor on the DRFOC Drive System Operation

On the basis of reports, it can be observed that the effects of speed sensor failure, in vector-controlled induction motor drives, are most visible in the error between measure and estimated speed and in the estimated electromagnetic torque (or stator current components) [3, 27, 29]. So monitoring those signals can be useful from the diagnostic point of view. The speed sensor faults can be obtained by the equation [3, 4]:

$$\omega^{enc} = (1 - \gamma)\omega_m, \quad (4)$$

where ω^{enc} —measured rotor speed, ω_m —real rotor speed, γ —constant coefficient.

For different values of the coefficient γ , the measured rotor speed can be:

- intermittent—partial damage of the speed sensor consisting in a partial failure of individual pulses from the encoder— $1 < \gamma < 1$;
- intermittent—partial damage of the speed sensor consisting in a cyclic interruption of specific pulses from the encoder— $\gamma = [0, 1]$;
- zero—total failure of the speed sensor— $\gamma = 1$, $\omega_m^m = 0$;
- with offset— $\gamma = const \in \langle -1, 1 \rangle$;

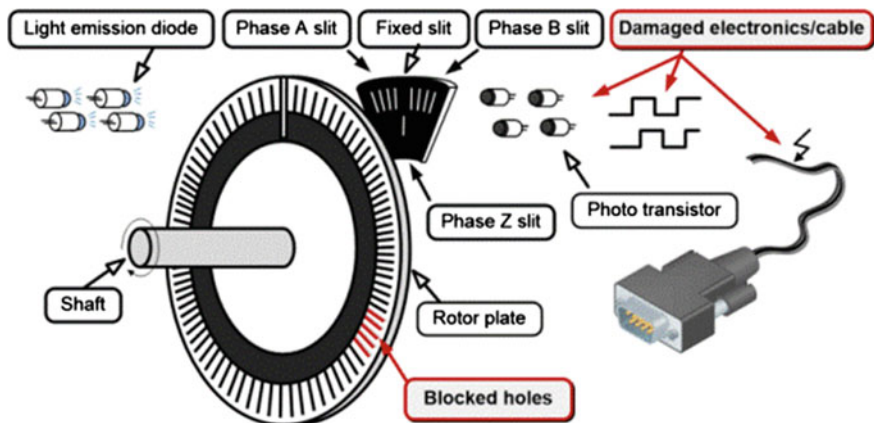


Fig. 3 A scheme of the simplified structure of the incremental encoder

The number of pulses of the sensor can be limited as a result of blocking holes in sensor’s ring and the periodic interruptions of the measurement signal occur due to the damage of the electronics or connecting cables (Fig. 3).

Drive is started from zero to the nominal speed (at $t = 3$ s drive is loaded $m_o = m_{oN}$). The speed sensor fault occurred at $t = 2$ s. It is visible that after the speed sensor faults in the DFOC algorithm abnormal behaviours of the system are

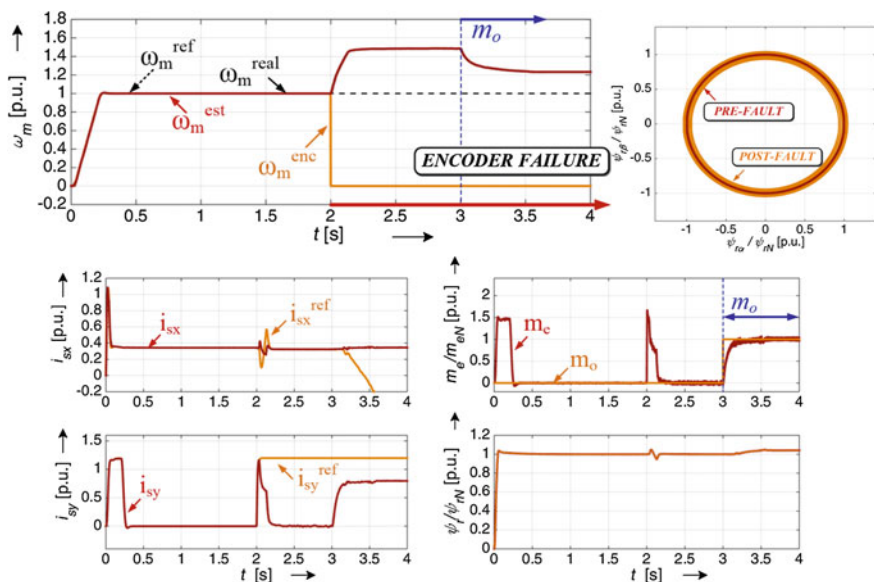


Fig. 4 Transients of measured and estimated speed, rotor flux hodograph, stator current components and electromagnetic torque for a total failure of the encoder in a vector control structure

observed. In this control algorithm, reference signals are limited [current i_{sy} limit is set to 1.2 in (p. u.)]. For the total failure of the speed sensor, the real and estimated speeds of the drive are increasing (Fig. 4).

The interruption in the speed control loop caused also the increase of the electromagnetic torque. For partial loss of individual pulses and for cyclic interruption of specific pulses of the speed sensor, speed oscillation is visible. In both cases drives are stable.

After the speed sensor faults, the stator current component i_{sy} is not constant. Oscillations on this variable are visible, the amplitude depends on fault types. Similar results can be obtained for the DTC-SVM algorithm [30, 31]. In this case, the symptoms are visible in the electromagnetic torque and stator flux vector (Figs. 5 and 6).

3.3 Detectors of Speed Sensor Faults in the DRFOC Structure

In the Fault Tolerant Control systems, abnormal behaviours of sensors must be detected and the system must be reconfigured [3, 4, 27, 29]. The main problem in

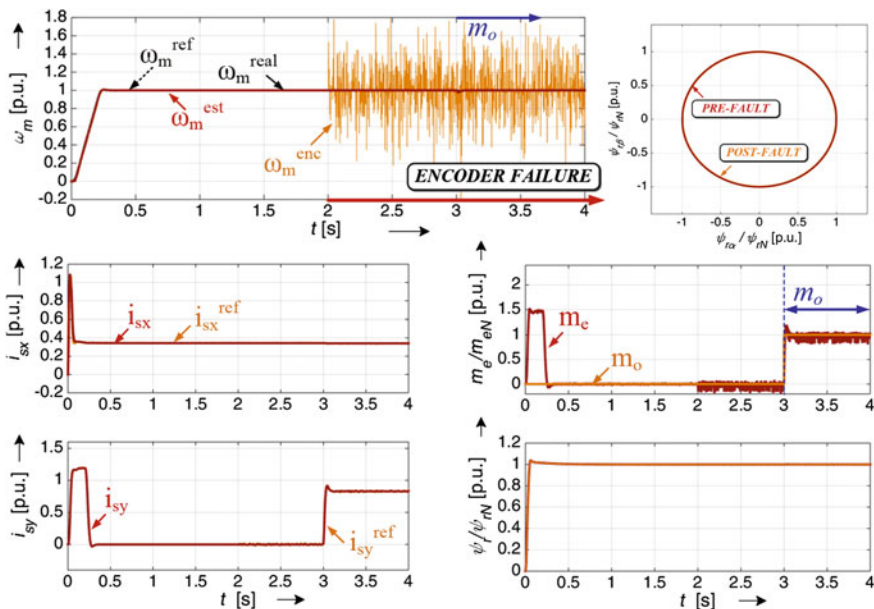


Fig. 5 Transients of measured and estimated speed, rotor flux hodograph, stator current components and electromagnetic torque for a partial loss of individual pulses of the encoder in a vector control structure

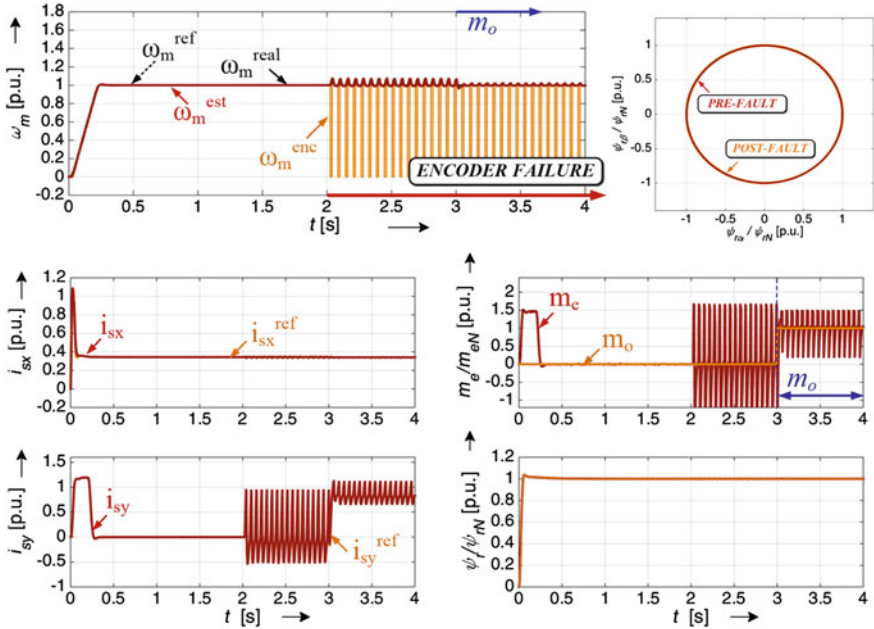


Fig. 6 Transients of measured and estimated speed, rotor flux hodograph, stator current components and electromagnetic torque for a cyclic interruption of specific pulses from the encoder in a vector control structure

this situation is connected with the proper identification of the broken sensor. In this chapter the chosen methods of the speed sensor fault detection for DRFOC algorithm are presented. Those methods are based on a signal taken from internal control loops.

For the Direct Field Oriented Control structure the stator current components (i_{sy} and i_{sy}^{ref}), and the rotor speed (measured and estimated) can be used. In the analysed detection systems, the estimated value of the rotor speed must be used. Different techniques can be applied in the reconstruction of this variable [2, 9, 32, 33]. In the presented systems, the MRAS type flux and speed estimator was used. This estimator was presented in detail in [2].

The rotor speed sensor fault detection algorithm consists of four stages (Fig. 7). In the first stage the measured and estimated (or reference and estimated) signals are compared and checked. In the second stage signals are compared with the limits.

If the differences between those signals are bigger than the assumed limit (chosen arbitrary), a simple logic algorithm (stage 3) can detect the speed sensor fault, in the following way:

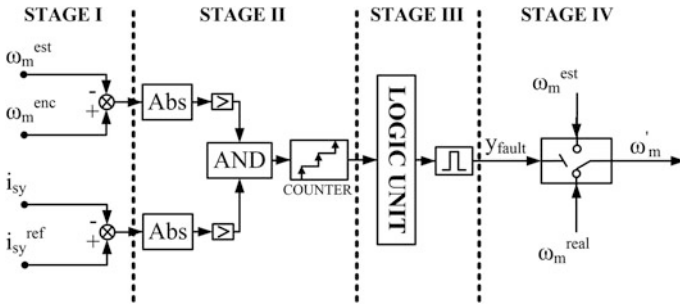


Fig. 7 A block diagram of the speed sensor fault detector for DRFOC algorithm

$$IF \left\{ \begin{array}{l} |\omega_m - \omega_m^{est}| \geq \varepsilon_{1DFOC} \\ |i_{sy}^{ref} - i_{sy}| \geq \varepsilon_{2DFOC} \end{array} \right. \quad THEN \omega_m^{est} \quad ELSE \omega_m, \quad (5)$$

where $\varepsilon_{1DFOC} = 0.02 + 0.1 \cdot |\omega_m^{ref}|$ —maximum speed error, $\varepsilon_{2DFOC} = 2.0 \cdot \omega_m^{ref}$ —maximum current error.

Limits of ε depend on the actual value of the reference speed. This solution provides stable operation of the detector during induction motor parameter variations and wrong speed and/or flux estimation.

The final stage (stage 4) of the detector consists in the isolation of the fault by switching to the speed estimator (MRAS^{CC} [2]) when a failure has been confirmed. When the failure is eliminated, the detector can switch the control back to the sensor mode if it is necessary. In the real system it is not possible.

The main problem in those algorithms is the correct choice of the maximum speed error and maximum stator current (or torque) error. It is well known, that all rotor speed observers are more or less sensitive to the induction motor parameters variations. In the case of an incorrect identification of those parameters, the rotor speed can be estimated with a steady state error. The first part of the detector (based on the speed error) cannot properly detect the speed sensor faults. The second part of this detector (based on the stator current error) guarantees proper operation for this situation.

As an alternative method for the rotor speed and stator current sensor faults detection, artificial intelligence can be used. A detector (for speed sensor faults detection) presented in Fig. 8 is based on an artificial neural network (NN) with three hidden layers in the configuration 5-11-4-2-1.

In this case the three hidden layers were used. Other solutions (with 2 hidden layers) can be proposed, but the numbers of neurons in each layer are much bigger and computation time is longer in this case. In the proposed systems the neurons with nonlinear activation functions were used. The hidden layer consists of 17 neurons and the output layer of 1 neuron.

On the output of the NN detector there is the signal connected with failures. Designed neural networks were trained by the Levenberg-Marquardt algorithm,

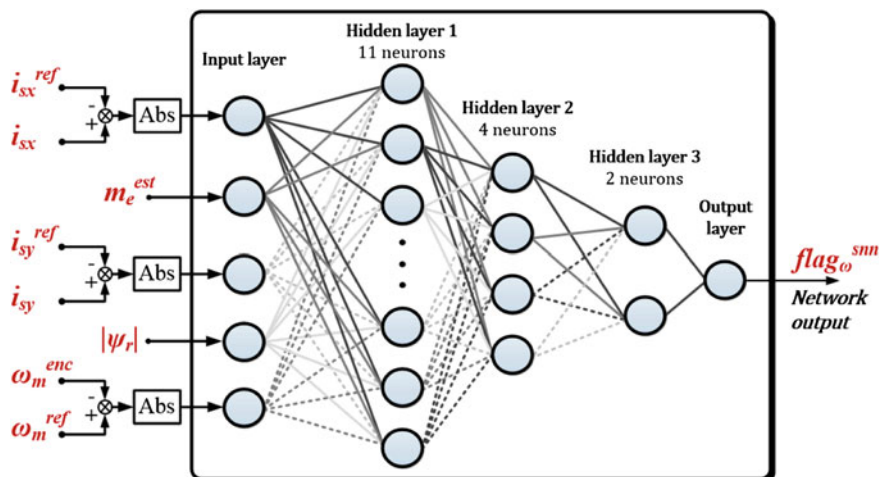


Fig. 8 Block diagrams of the speed sensor fault detectors based on the neural network for the DFOC algorithm

which is one of the most effective ways of learning used in one-way neural networks [24, 34]. It combines the convergence of the Gauss-Newton algorithm near minimum and the method of gradient descent for the greater distance from the minimum.

The Levenberg-Marquardt (L-M) algorithm performs compromise learning strategy between the linear model and gradient method approach in each iteration. Moving the point of seeking optimum weight is acceptable only if it leads to the reduction of the error [35].

During the learning process the reference speed was changed in the vector controlled systems. At first, the drive runs at rated speed, which at appropriate time points was reduced. During the drive operation a total interruption of the speed sensor loop occurred [34].

The main advantage of the NN detectors is the detection time. For the rotor speed sensor fault and stator current faults this time is much shorter than for other, algorithmic, detectors. The main disadvantage is connected with training procedure and some complications in real time applications. The analysis of the speed sensor fault detector based on the NN is presented in the next chapter.

3.4 The Compensation Method of Speed Sensor Faults in the DRFOC Structure

In this part of the chapter the experimental tests of the drive system chosen during faulted conditions are presented. It was assumed that two described detectors were

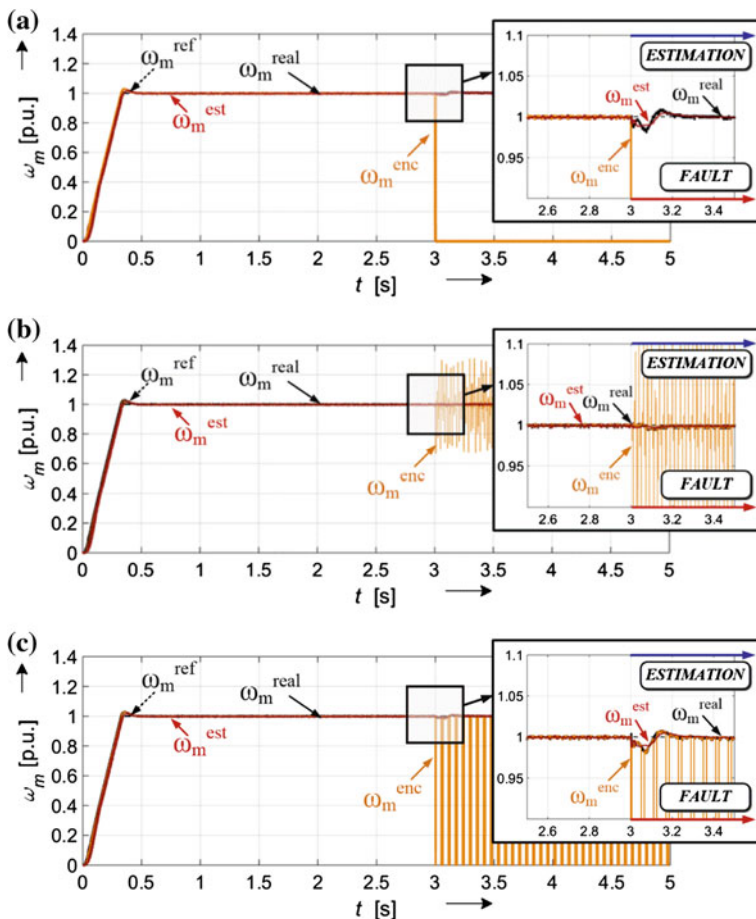


Fig. 9 Transients of the mechanical and estimated speed for a vector controlled drive with: **a** total failure of the speed sensor, **b** failure of individual pulses of the measurement signal, **c** cyclic interruption of specific pulses from the encoder

used. After fault detection the system was reconfigured to the sensorless mode with the MRAS^{CC} estimator. In Fig. 9 the Fault Tolerant Control structure during the faulted conditions is presented. The system presented in Fig. 7 is used for fault detection.

After the speed sensor fault, for $t = 3$ s, detection mechanism changed the topology of the drive for the sensorless mode. In all cases a fault is detected after ~ 0.01 s. In addition, short pulses are noticeable in the waveforms of the measured speed, but they do not significantly affect the performance of the entire control system. The results were obtained in the laboratory set-up.

Comparative results of the NN detector and algorithmic detector are presented in Fig. 10. In the sensorless mode the motor drive was able to operate stably. In the

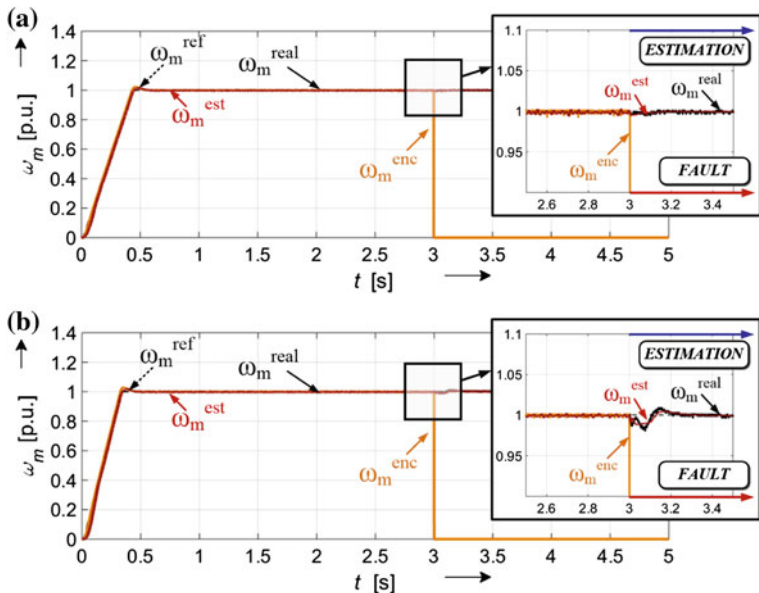


Fig. 10 Faulted operations of the FTDFOC algorithm for the total failure of the encoder: **a** neural based detector, **b** algorithmic detector, $\omega_m = \omega_{mN}$

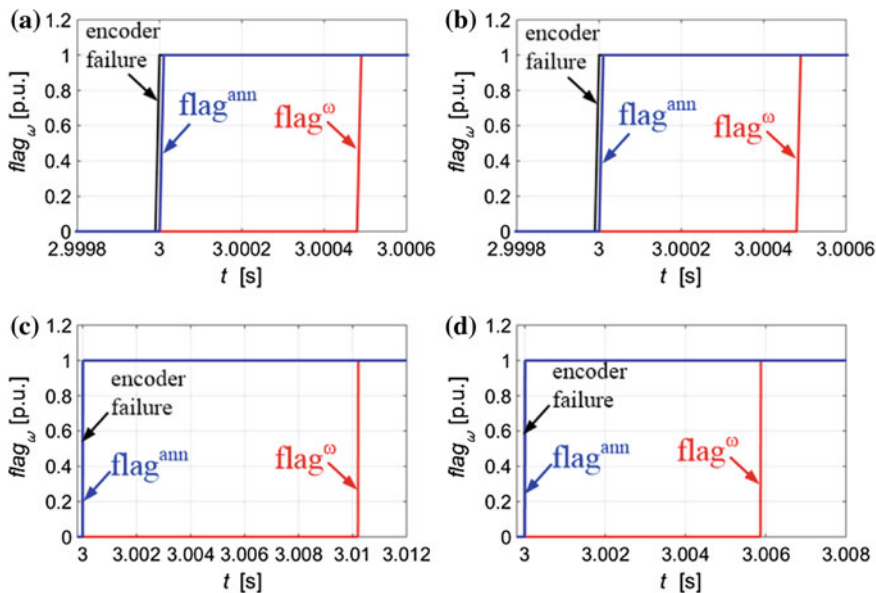


Fig. 11 Detection time of the NN and algorithmic detectors for the total failure of the encoder: **a** nominal speed value $\omega_m = \omega_{mN}$ with no load, **b** nominal speed value $\omega_m = \omega_{mN}$ and load $m_o = m_{oN}$, **c** low speed value $\omega_m = 0.05 \omega_{mN}$ with no load, **d** low speed value $\omega_m = 0.05 \omega_{mN}$ and load $m_o = m_{oN}$ (simulation results)

case of the neural detector, the identification of the sensor fault occurred in a much shorter period of time. During topology change fluctuations on the state variables are not visible. In Fig. 11 the comparison of detection time for each system, for two different speed values ($\omega_m = \omega_{mN}$ and $\omega_m = 0.05 \omega_{mN}$) in the occurrence of total interruption of control loop is presented.

After the sensor fault, the detection mechanism based on neural detector almost immediately changes the topology of the drive to the sensorless mode or switches the control structure to the redundant current sensor. The detector based on the algorithmic method was able to detect failure after 0.0005 s, which is also a very good result. However, the identification time, in this case, depends on drive operation conditions. The longest time duration occurred for the low speed value ($\omega_m = 0.05 \omega_{mN}$) with no load and was 0.01 s.

These differences, between the detection time for both algorithms, are very slight, however, as it was seen at previous transients, even a small discrepancy may lead to the interference of state variables. Such conditions in FTC drives are undesirable and should be eliminated or compensated. The computation time for a neural detector is much longer than for an algorithmic system.

4 An Analysis and Compensation of Current Sensor Faults in a Vector-Controlled Induction Motor Drive

4.1 The Influence of Current Sensor Faults on the DRFOC Drive System Operation

In the electrical drive systems the current and voltage sensors are necessary for the proper work of vector control algorithms [3, 4]. Those sensors are very sensitive and can be broken [3, 4, 8]. The drive system and estimation techniques can work stably without information from the stator voltage sensor, but cannot work properly without signals from stator current sensors [3, 4, 29]. This signal is used for state variable reconstruction [2, 36] and in the internal control loop. The general scheme of the closed—loop hall—effect current sensor is presented in Fig. 12.

The current sensor may indicate erroneous measurements due to saturation of the magnetic core or phase shift signal in the feedback loop. Basic types of damage current sensor are shown in Table 1.

In Fig. 13 the simulation results for the DRFOC drive system, with a totally broken current sensor in phase A, are presented. In Figs. 14 and 15 the stator current transients for the vector controlled induction motor drive system with a gain error of the current sensor and with noise on the output of the sensor are illustrated.

In those tests the three current sensors were used in a control system. Currents components i_{sx} and $i_{s\beta}$ were calculated from the Eq. (6):

Fig. 12 The closed—loop hall—effect current sensor scheme

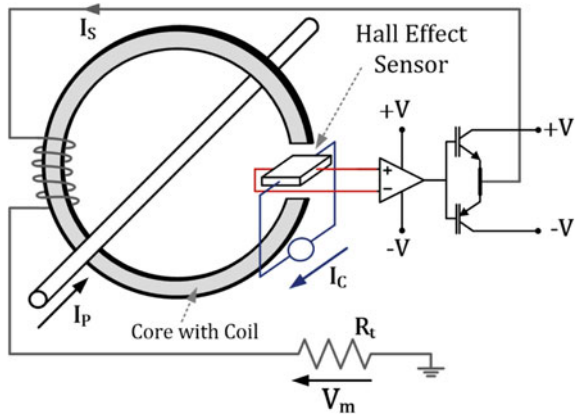


Table 1 Basic types of faults and the value of the output current sensor

Type of the fault	Current value
Variable gain	$i_s^m = (1 - \gamma)i_a$
Phase shift	$i_s^m = i_a + i_{offset}$
Signal limit	$i_s^m = i_{sat.}$
Noise	$i_s^m = i_a + n(t)$
Lack of signal	$i_s^m = 0$
Intermittent signal	$i_s^m = [0, 1]$

$$i_{sz} = \frac{2}{3} \left(i_{sA} - \frac{1}{2} (i_{sB} + i_{sC}) \right), \quad i_{s\beta} = \frac{\sqrt{3}}{3} (i_{sB} - i_{sC}). \quad (6)$$

The current sensor was broken for $t = 0.5$ s. The symptoms of the current sensor faults are visible on the current transients. The control structure compensates some behaviours of the drive after faults.

The total failure of the current sensor is most dangerous for the vector controlled induction motor drive. For the gain and offset error of the current sensor in phase B, some oscillations on the measure and estimated (by MRAS^{CC} estimator [2]) speed are visible. In both cases the drive is stable and can work with a broken sensor.

4.2 Detectors of Current Sensor Faults in the DRFOC Structure

An algorithm, based on the same idea as the previous one can be proposed for current sensor faults detection. The proposed stator current sensor fault detection system is based on observation of the estimated value of the rotor flux. In addition, a field oriented control structure uses information about the component i_{sx} of stator

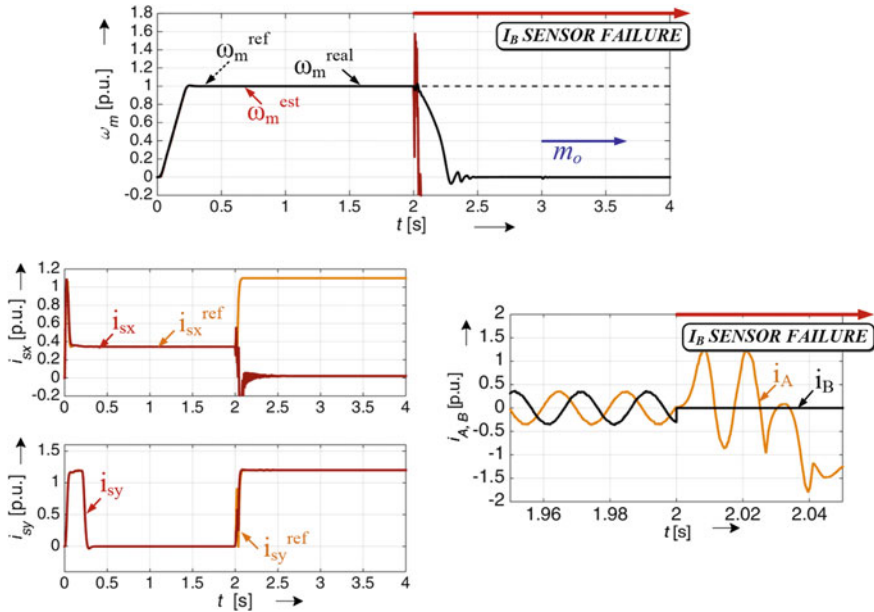


Fig. 13 Simulation results for the DRFOC drive system with a totally broken current sensor in phase B, $i'_B = 0$

current. Figure 16 presents a block diagram of the detector of a current sensor fault implemented in the structure of the DRFOC control.

These solutions are based on the analysis of the difference between the reference value of the rotor flux vector and actual (estimated) flux (for DRFOC). Additionally, in the DRFOC algorithm the difference between the reference and actual value of the stator current component in x axis is checked. This relationship can be written as:

$$if \begin{cases} |\Psi_r^{ref} - \Psi_r^{est}| \geq \varepsilon_1 \\ |i_{sx}^{ref} - i_{sx}| \geq \varepsilon_2 \end{cases} \quad then \ i_A = -(i_B + i_C) \ else \ i_A, \quad (7)$$

where $\varepsilon_1, \varepsilon_2$ —maximum error between rotor flux and stator current.

In stage II the signal is sampled and delayed to avoid accidental failure determination. The results are compared with the value of the permitted limit. If the value is bigger than threshold, the system generates a logic pulse indicating the occurrence of a damage. After fault detection, the system is switched to the additional sensor. Stator current in phase A is calculated according to Eq. (8):

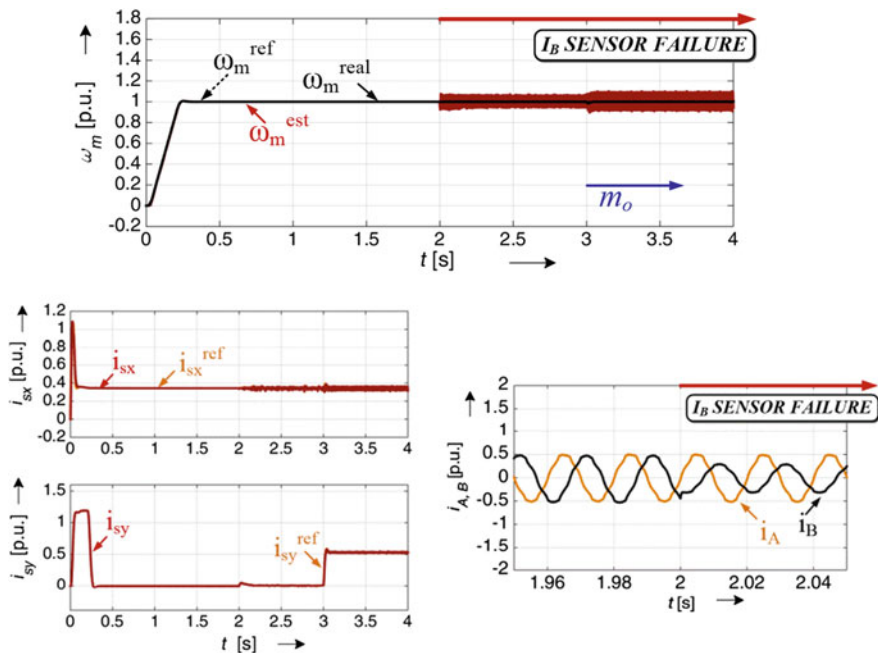


Fig. 14 Simulation results for the DRFOC drive system with a gain error of the current sensor $\pm 40\%$

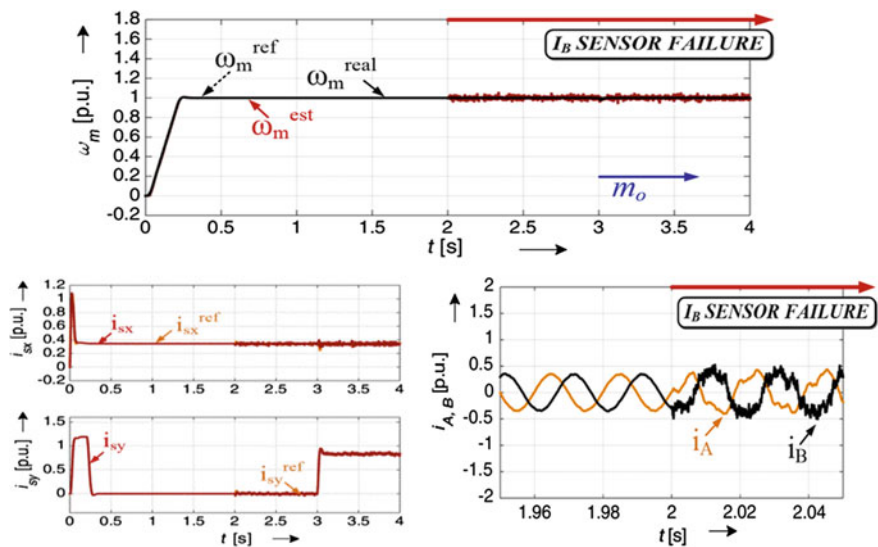


Fig. 15 Simulation results for the DRFOC drive system with a broken current sensor—signal with white noise 2×10^{-6}

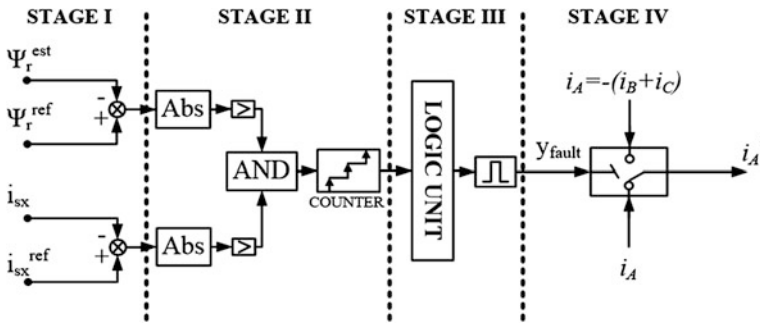


Fig. 16 A block diagram of a current sensor fault detector for DRFOC

$$i_A = -(i_B + i_C), \tag{8}$$

IF $y_{fault} = TRUE$ *AND* $i_{sx} = i'_{sA}$ *THEN* *Fault* i_{sB} *ELSE* *Fault* i_{sA}

As a result, proper operation of the drive is possible in the occurrence of a sensor fault.

For the current sensor fault detection, a similar idea, based on the NN theory, can be used. The general scheme of the neural network based detectors for DRFOC is presented in Fig. 17.

In an NN based detector the three hidden layers were used (as for speed sensor detection). In the algorithm presented in Fig. 17 the neurons with nonlinear

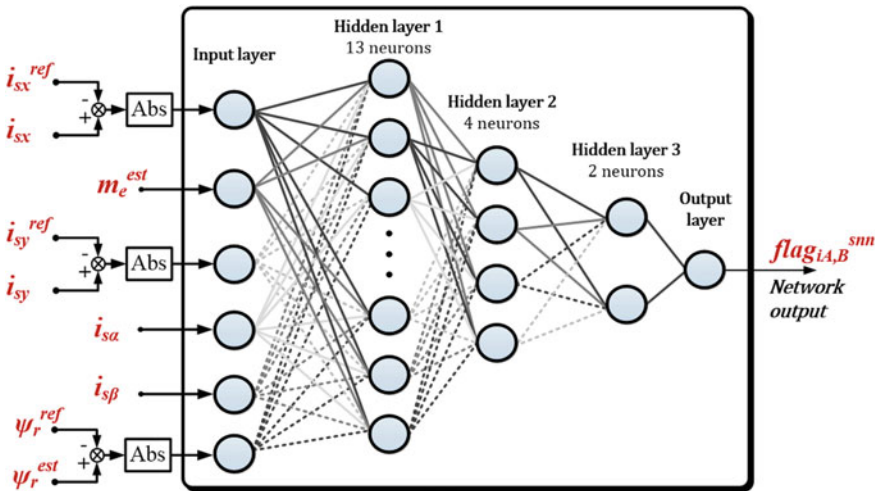


Fig. 17 Block diagrams of the current sensor fault detectors based on a neural network for: DFOC algorithm

activation functions were used. The hidden layers consist of 19 neurons and the output layer of 1 neuron (flag of the current fault). Designed neural networks were trained by Levenberg-Marquardt algorithm.

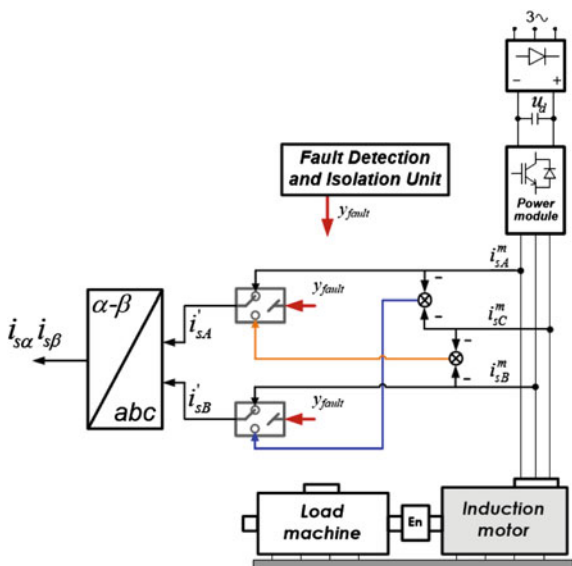
4.3 The Compensation Method of Current Sensor Faults in the DRFOC Structure

In this part of the paper selected experimental results of the detection algorithm of the stator current sensors for the DRFOC drive are presented. The general scheme of a complete Fault Tolerant Control system (for a current sensor fault) is presented in Fig. 18. Components α - β are obtained by measuring the currents in phases A and B. Thus, it is possible to determine which sensor has failed. If the component of the stator current α differs from the measuring signal from phase A, it means that the first sensor has a failure, otherwise the second sensor—phase B—is faulty.

A current sensor fault is detected in approximately ~ 0.01 s after a failure occurred (Fig. 19). The proposed solution for a fault tolerant system, based on the redundancy of the stator current measurement, allowed the detection of failures and thereby enabled further operation of the system and the correct estimation of the speed.

In Fig. 20 the comparative analysis of the two described detectors is presented. In Fig. 20a the results for an algorithmic detector are presented, while in Fig. 20b

Fig. 18 A block diagram of an FTC system with a current sensor fault detector



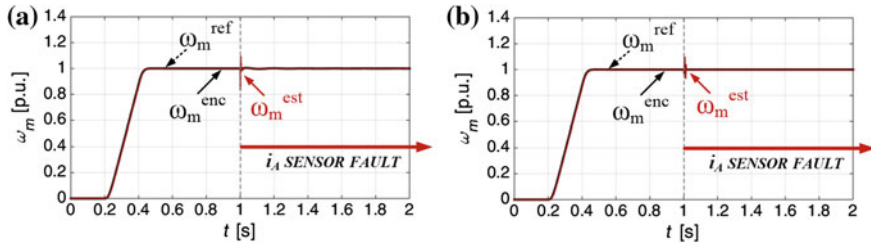


Fig. 19 Transients of the mechanical and estimated speed for faulted operation of phase A stator current sensor: **a** total failure of the sensor, **b** with gain error of the current sensor $\pm 40\%$

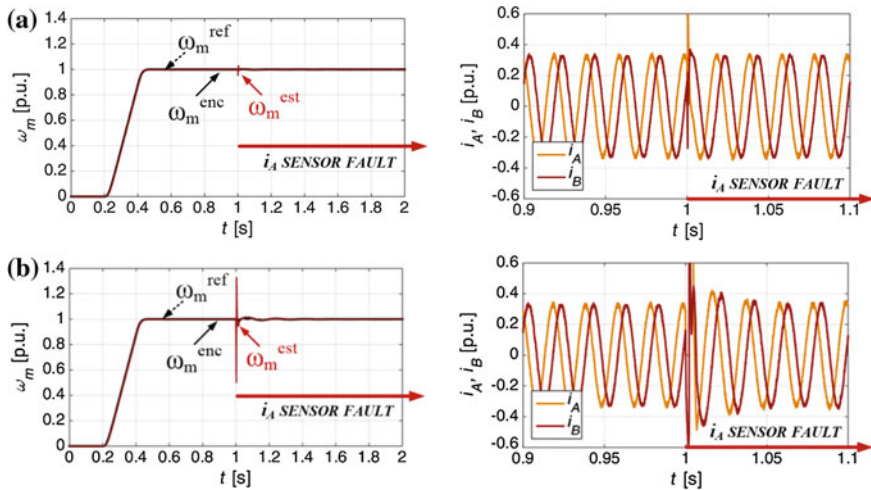


Fig. 20 Faulted operations of the DFOC algorithm for total failure of the current sensor in phase A: **a** neural based detector, **b** algorithmic detector, $\omega_m = \omega_{mN}$

for an NN based detector. In both cases the drive is stable. Faults are detected in a short period of time. For the NN based detector time detection is shorter, which is clearly visible on the transients.

5 The Fault Tolerant Control Algorithm with Current and Speed Sensor Fault Detectors

In this chapter, the selected experimental results of the full Fault Tolerant Control of the induction motor drive system are presented. It was assumed that algorithms must be robust to both (speed and current) sensors faults. A general scheme of the drive systems controlled by the FTDRFOC algorithm is presented in Fig. 22. Additionally, in the analysed control system, a typical scalar control structure was

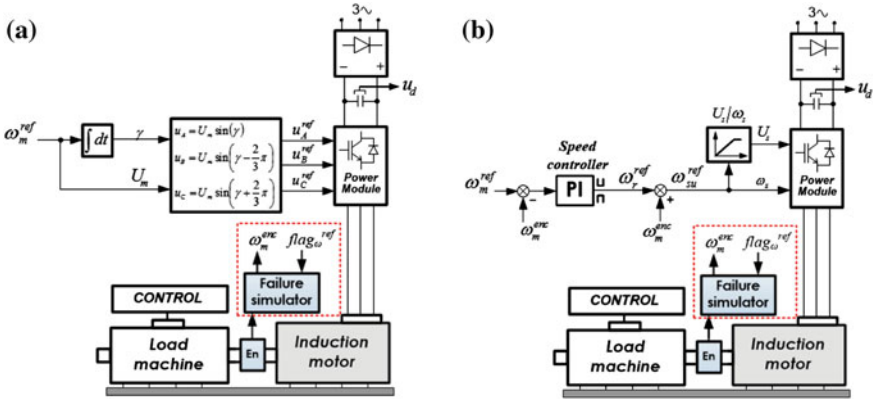


Fig. 21 A scheme of the scalar control algorithm: **a** open loop structure, **b** closed loop control structure

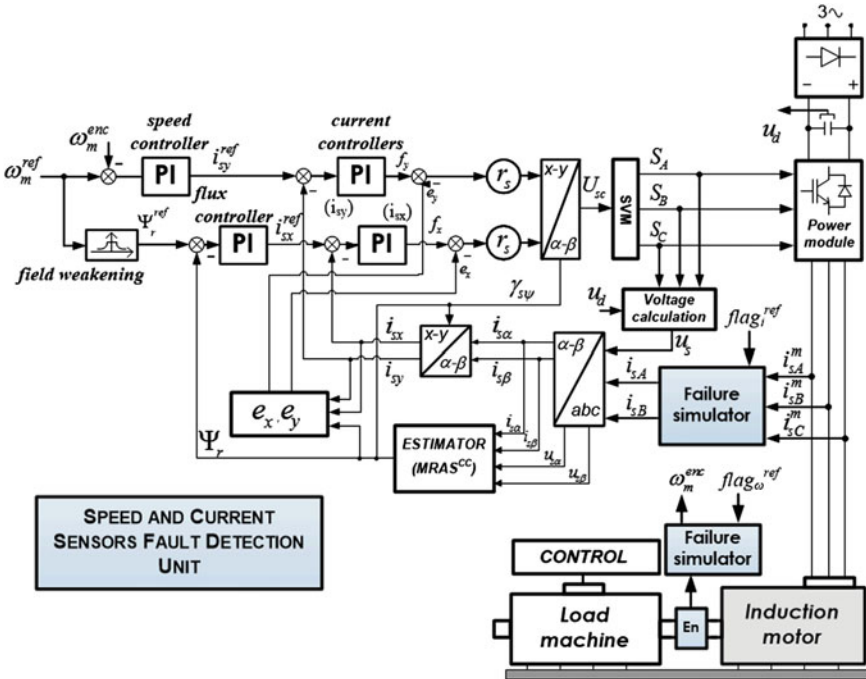


Fig. 22 A scheme of the FT-DFOC algorithm with a diagnostic system

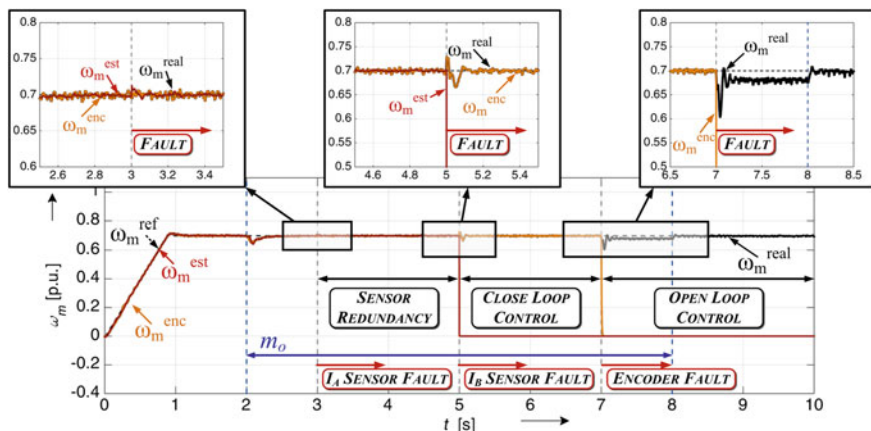


Fig. 23 The fault tolerant control system during faulted condition: scenario 1—fault of the current sensor in phase A, 2—fault of the current sensor in phase B, 3—speed sensor fault (experimental results, FT-DFOC)

used as a redundant algorithm. A scheme of this system was presented in Fig. 21. It is obvious that this structure can be applied in a closed loop (with speed feedback) or open loop.

The basic structure is always the vector control algorithm. In the case of the failure of some sensors, control structure topology can be changed to the scalar control system. The disadvantage of scalar control, presented in Fig. 21, is the lack of the motor control during dynamical states.

The main advantage of the scalar control algorithms is the fact, that they can work stably without information from the internal and external signals. This is very helpful in the safety drives.

Experimental tests were conducted using a laboratory set-up consisting of 1.1 kW induction motor, SVM voltage inverter and an incremental encoder to measure angular velocity (5000 imp./rev.). The control, detection and speed estimation algorithms were implemented using a Micro Lab Box DS1202 card. The Fault Tolerant Control (FT-DFOC) drives was tested for the different speeds.

The study involved faults of the speed sensor and the two current sensors during drive operation. It was assumed (Fig. 23) that after $t = 3$ s the first current sensor (in phase A) was broken, after 5 s from the start the second one was destroyed (phase B). After $t = 7$ s the rotor speed sensor was broken.

After the first fault detection the system was reconfigured. The redundant current sensor (in phase C) was used for the stator current components calculation (in the stationary reference frame). The second fault of the current sensor determined the change of the control structure. The topology is changed from the vector control algorithm to the scalar control with the speed control loop. It is obvious that without information from the current sensors the speed estimation is not possible, so after

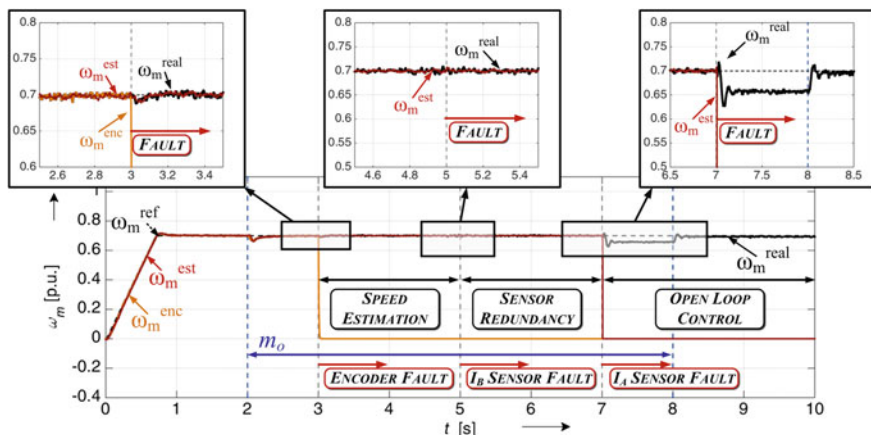


Fig. 24 The fault tolerant control system during faulted condition: scenario 1—speed sensor fault, 2—fault of the current sensor in phase B and 3—fault of the current sensor in phase A, $m_o = 0.5$ m_{oN} (experimental results, FT-DFOC)

the speed sensor fault, the control algorithm must be changed to the scalar control without feedback.

The second scenario, presented in Fig. 24 and analysed in this section, is based on the assumption that the rotor speed sensor was broken first. Afterwards the current sensors were faulted (for $t = 5$ s in phase B and for $t = 7$ s in phase A).

After the first fault (speed sensor) the topology of the drive is changed to the speed sensorless drive. For the rotor speed and flux estimation the MRAS [2] estimator was used (the same as in the diagnostic system). During the topology changes small oscillations are visible on the measure and estimated state variables. During this test the drive was loaded. After three seconds from the first fault, the current sensor was broken.

The detection system detected a failure and an additional sensor was used. During the current sensor changes abnormal behaviours are not observed. After the next fault the drive is switched to the scalar control with an open loop.

6 Summary

In the chapter some issues related to the application of the fault tolerant control system in the vector control structure of the induction motor drive are presented. The following remarks can be formulated on the basis of the presented study:

- it is possible to detect the rotor speed sensor using signals from the internal structure;

- algorithmic methods are simple in practical implementation but require selection of threshold coefficients;
- it is possible to use a similar solution for current sensor fault detection, these methods also depend on the proper choice of special coefficients;
- after detection of the speed sensor fault, the control algorithm could be switched to the sensorless mode or to the torque control structure (for DTC algorithm);
- two current sensors are necessary to the proper operation of the vector control system; after two sensor faults, the system must be changed to scalar control with or without a speed control loop;
- neural networks can be used for the sensor fault detection; the main advantage of this kind of detectors is the detection time;
- it is possible to detect different types of the selected sensor faults;
- the performance of the system depends on the quality of the state estimators;
- the system works correctly for very small as well as big values of the reference speed;
- the future works on the topic will be devoted to designing the universal detection system based on algorithmic or neural systems.

Acknowledgment This work was financed by the National Science Centre Poland under the project 2013/09/B/ST7/04199 (2014–2017).

Appendix

See Table 2.

Table 2 Motor rated data and parameters

P index N	U index N	I index N	n index N	f index N	T index M
1.1 kW	230/380 V	5.0/2.9 A	1380 rpm	50 Hz	0.188 s
R_s	R_r	X_s	X_r	X_m	Unit
5.9	4.559	131.1	131.1	123.3	[Ω]
0.0776	0.06	1.725	1.725	1.6232	[p.u.]

References

1. Gaeid K (2011) Fault tolerant control of induction motor. *Mod Appl Sci* 5(4)
2. Orłowska-Kowalska T, Dybkowski M (2010) Stator-current-based MRAS estimator for a wide range speed-sensorless induction-motor drive. *IEEE Trans Ind Electron* 57(4):1296–1308
3. Berriri H, Naouar M, Slama-Belkhodja I (2012) Easy and fast sensor fault detection and isolation algorithm for electrical drives. *IEEE Trans Power Electron* 27(2):490–499
4. Fan S, Zou J (2012) Sensor fault detection and fault tolerant control of induction motor drivers for electric vehicles. In: Proceedings of the 7th international power electronics and motion control conference IPEMC, Harbin, 2–5 June 2012

5. Jiang L (2011) Sensor fault detection and isolation using system dynamics identification techniques. PhD dissertation, University of Michigan
6. Rothenhagen K, Fuchs F (2009) Doubly fed induction generator model-based sensor fault detection and control loop reconfiguration. *IEEE Trans Ind Electron* 56(10):4229–4238
7. Chakraborty C, Verma V (2015) Speed and current sensor fault detection and isolation technique for induction motor drive using axes transformation. *IEEE Trans Ind Electron* 62(3):1943–1954
8. Isermann R (2006) *Fault-diagnosis systems*. Springer, Berlin
9. Najafabadi T, Salmasi F, Jabejdar-Maralani P (2011) Detection and isolation of speed-, DC-link voltage-, and current-sensor faults based on an adaptive observer in induction-motor drives. *IEEE Trans Ind Electron* 58(5):662–1672
10. Berriri H, Naouar M, Slama-Belkhdja I (2011) Parity space approach for current sensor fault detection and isolation in electrical systems. In: *Proceedings of the 2011 8th international multi-conference on systems, signals and devices EDD, Sousse, 22–25 Mar 2011*
11. Bahri I, Naouar M, Slama-Belkhdja I, Monmasson E (2007) FPGA-based FDI of faulty current sensor in current controlled PWM converters. In: *Proceedings of the international conference on computer as a tool EUROCON, Warsaw, 9–12 Sept 2007*
12. Lee K, Ryu J (2003) Instrument fault detection and compensation scheme for direct torque controlled induction motor drives. *IEE Proc Control Theory Appl* 150(4):376–382
13. Akrad A, Hilairat M, Diallo D (2011) Design of a fault-tolerant controller based on observers for a PMSM drive. *IEEE Trans Ind Electron* 58(4):1416–1427
14. Youssef A, El Khil S, Slama-Belkhdja I (2013) State observer-based sensor fault detection and isolation, and fault tolerant control of a single-phase PWM rectifier for electric railway traction. *IEEE Trans Power Electron* 28(12):5842–5853
15. Romero M, De Dona J, Seron M (2010) Sensor fault-tolerant vector control of induction motors. *IET Control Theory Appl* 4(9):1707–1724
16. Verma V, Chakraborty C, Maiti S, Hori Y (2013) Speed sensorless vector controlled induction motor drive using single current sensor. *IEEE Trans Energy Convers* 28(4):938–950
17. Meinguet F, Gyselinc J (2011) Fault detection, isolation and reconfiguration of three-phase AC drive with current sensor fault. In: *Proceedings of the 2011 IEEE international electric machines and drives conference IEMDC, Niagara Falls, 15–18 May 2011*
18. Salmasi F, Najafabadi T (2011) An adaptive observer with online rotor and stator resistance estimation for induction motors with one phase current sensor. *IEEE Trans Energy Convers* 26(3):959–966
19. Zhang X, Gajanayake C, Bhangu B et al (2013) Sensor fault detection, isolation and system reconfiguration based on extended Kalman filter for induction motor drives. *IET Electr Power Appl* 7(7):607–617
20. Diallo D, Benbouzid M, Makouf A (2004) A fault-tolerant control architecture for induction motor drives in automotive applications. *IEEE Trans Veh Technol* 53(6):1847–1855
21. Raisemche A, Boukhniher M, Larouci C, Diallo D (2014) Two active fault-tolerant control schemes of induction-motor drive in EV or HEV. *IEEE Trans Veh Technol* 63(1):19–29
22. Rothenhagen K, Fuchs F (2009) Model-based fault detection of gain and offset faults in doubly fed induction generators. In: *Proceedings of the 2009 IEEE international symposium on diagnostics for electric machines, power electronics and drives SDEMPED, Cargese, 31 Aug–3 Sept 2009*
23. Zidani F, Benbouzid M, Diallo D, Benchaib A (2003) Active fault-tolerant control of induction motor drives in EV and HEV against sensor failures using a fuzzy decision system. In: *Proceedings of the IEEE international electric machines and drives conference IEMDC, Madison, 1–4 June 2003*
24. Adouni A, Hamed MB, Flah A, Sbita L (2013) Sensor and actuator fault detection and isolation based on artificial neural networks and fuzzy logic applied on induction motor. In: *Proceedings of the 2013 international conference on control, decision and information technologies CoDIT, Hammamet, 6–8 May 2013*

25. Li H, Monti A, Ponci F (2012) A fuzzy-based sensor validation strategy for AC motor drives. *IEEE Trans Ind Inf* 8(4):839–848
26. Zidani F, Diallo D, Benbouzid M, Berthelot E (2007) Diagnosis of speed sensor failure in induction motor drive. In: *Proceedings of the 2007 IEEE international electric machines and drives conference IEMDC, Antalya, 3–5 May 2007*
27. Boukhniher M, Raisemche A, Diallo D, Larouci C (2013) Fault tolerant control to mechanical sensor failures for induction motor drive: a comparative study of voting algorithms. In: *Proceedings of the 39th annual conference of the IEEE industrial electronics society, Vienna, 10–13 Nov 2013*
28. Tabbache B, Benbouzid M, Kheloui A, Bourgeot J (2013) Virtual-sensor-based maximum-likelihood voting approach for fault-tolerant control of electric vehicle powertrains. *IEEE Trans Veh Technol* 62(3):1075–1083
29. Campos-Delgado D, Espinoza-Trejo D, Palacios E (2008) Fault-tolerant control in variable speed drives: a survey. *IET Electr Power Appl* 2(2):121–134
30. Dybkowski M, Klimkowski K, Orłowska-Kowalska T (2014) Speed sensor fault tolerant direct torque control of induction motor drive. In: *Proceedings of the 2014 16th international power electronics and motion control conference and exposition PEMC, Antalya, 22–24 Sept 2014*
31. Klimkowski K, Dybkowski M (2015) Adaptive fault tolerant direct torque control structure of the induction motor drive. In: *Proceedings of the 2015 international conference on electrical drives and power electronics EDPE, The High Tatras 21–23 Sept 2015*
32. Ohtani T, Takada N, Tanaka K (1992) Vector control of induction motor without shaft encoder. *IEEE Trans Ind Appl* 28(1):157–164
33. Lascu C, Boldea I, Blaabjerg F (2009) A class of speed-sensorless sliding-mode observers for high-performance induction motor drives. *IEEE Trans Ind Electron* 56(9):3394–3403
34. Klimkowski K, Dybkowski M (2015) A comparative analysis of the chosen speed sensor faults detectors for induction motor drives. In: *Proceedings of the 2015 international conference on electrical drives and power electronics EDPE, The High Tatras, 21–23 Sept 2015*
35. Vas P (1999) *Artificial-intelligence-based electrical machines and drives*. Oxford University Press, Oxford
36. Tan C, Edwards C (2002) Sliding mode observers for detection and reconstruction of sensor faults. *Automatica* 38(10):1815–1821

Stator Faults Monitoring and Detection in Vector Controlled Induction Motor Drives—Comparative Study

Marcin Wolkiewicz, Grzegorz Tarchała, Czesław T. Kowalski
and Teresa Orłowska-Kowalska

Abstract This chapter deals with the stator winding faults detection in the induction motor drives working in the closed speed control loops, with the direct field oriented control—DFOC or with the direct torque control—DTC. In order to detect the early stage of stator winding inter-turn short-circuits, the analysis of characteristic components of the stator currents spectra, as well as the control signals of the DFOC structure, are used for diagnostic purposes. Experimental results obtained from a specially prepared induction motor working under vector control are presented.

Keywords Induction motor drives · Stator faults · Fault diagnosis · Fault detection

1 Introduction

Modern technological processes are characterized by the application of more and more complicated equipment, also modern AC drives. The electrical motor together with the load machine as well as supply and control systems are prone to various failures, independently of the use of elements and materials characterized by high reliability. Among other failures, electrical faults of the induction motor (IM),

M. Wolkiewicz (✉) · G. Tarchała · C.T. Kowalski · T. Orłowska-Kowalska
Department of Electrical Machines, Drives and Measurements, Wrocław
University of Technology, Wybrzeże Wyspiańskiego 27, Wrocław, Poland
e-mail: marcin.wolkiewicz@pwr.edu.pl

G. Tarchała
e-mail: grzegorz.tarchala@pwr.edu.pl

C.T. Kowalski
e-mail: czeslaw.t.kowalski@pwr.edu.pl

T. Orłowska-Kowalska
e-mail: teresa.orlowska-kowalska@pwr.edu.pl

which is still the most popular electrical motor in industry, constitute close to 50 % of all motor faults which can be the reason for IM drives breakdowns.

Stator winding faults are one of the most common and comprise about 37 % of all failures [1–3]. The stator winding damage begins with unnoticeable inter-turn short circuit, that eventually spreads over the whole winding, causing the main short circuit. It leads to an emergency stop of the motor and necessity of its immediate upgrade or repair, that often generates large costs. Also the rotor bars and squirrel-cage rings constitute close to 13 % of the IM failures and should be monitored and detected, as disturbances continued for a long time in technological process cause big economical loses. For this reason the problem of fast fault detection and location as well as the problem of technical state evaluation is very significant in the industrial practice.

Nowadays, widely used vector control methods require the rotor or stator flux vector magnitude and angle to be precisely known, in order to make the proper state feedbacks and the transformation between stationary and synchronous reference frames [4]. When the stator or rotor winding damage occurs, the estimation of the flux vector is erroneous, due to the unsymmetrical resistance of the motor windings. As a consequence, the operation of the drive can become unstable when the damage process is uncontrolled and the proper action is not taken by the control system. According to the above, it is important to detect the early stage of the motor winding damage and to protect the drive system from abnormal operation.

2 A Short Review of Diagnostic Methods of Stator Winding Faults in Induction Motors

The stator winding failures of induction motors occur due to insulation stresses, inter-turn short circuits or even short-circuits of phase windings. Monitoring of the stator winding state is conducted at present mainly for medium and high-power drives and consists in periodical testing of an insulation, winding symmetry and temperature measurements. Online monitoring is applied only for the motors of high-importance industrial drives. It should be taken into account that even in the online monitoring procedures, the sensors' sensitivity is limited and they do not detect the stator winding failure at its initial stage.

In Fig. 1 the general classification of the methods applied for stator windings state monitoring is presented. The methods can be divided into two groups:

- insulation systems monitoring methods, which are used for important large high-voltage machines;
- signal analysis-based fault detection and diagnostic methods, used in low-voltage machines.

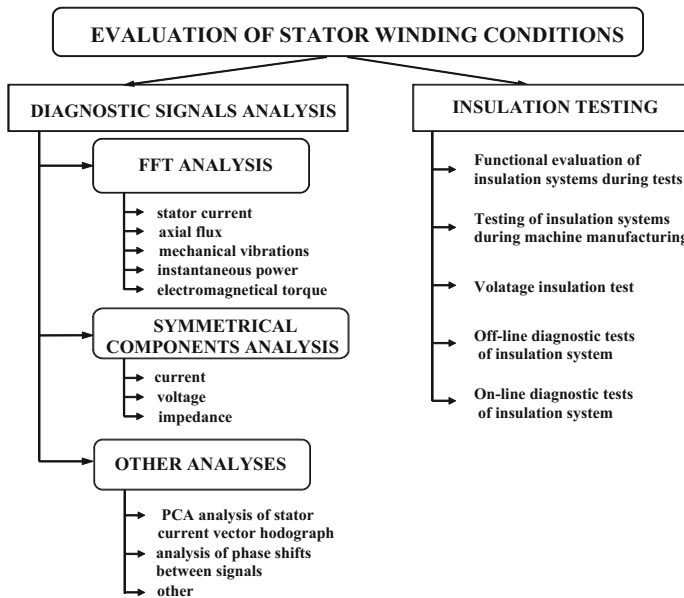


Fig. 1 Classification of the stator winding monitoring methods of the induction motors

Detection of the inter-turn short circuit under the motor operation is a difficult task and there are not typical industrial solutions, except for off-line and on-line methods based on the isolation testing, using the partial discharge analysis [2, 5]. However, these methods are out of the scope of this chapter.

In the case of low-voltage machines, the signal analysis-based methods do not provide information about insulation aging degree; they are used for the detection of inter-turn short-circuits in their early stage, before they spread out to a catastrophic damage [1].

Short circuits are recognized to be one of the most difficult failures to detect because the detection makes sense only at the initial stage of the damage; the so called incipient fault detection. Safety systems applied nowadays in industrial applications, do not react to the short-circuit of several shorted turns in one phase, since they cause too small quantitative changes in phase currents. Therefore, other solutions are searched for, based on measurement and digital diagnostic signal processing. It allows online monitoring of the machine condition and alarm the user at the initial stage of the damage [1, 2, 6, 7].

Faults monitoring and diagnosis in open-loop control structures with an induction motor is widely described in scientific literature, both for the net supply [8] and voltage-source inverter supply [6, 7, 9]. Most of them use the Motor Current Signature Analysis (MCSA) method [3, 6, 10]. A review of the MCSA techniques can be found in [3, 9, 11]. Spectral analysis use of instantaneous active and reactive

power for the damage diagnosis of net and inverter-fed drives is shown in [12]. In turn, the negative sequence currents analysis for the drives supplied from inverters and soft-starters is proposed in [6, 13].

The diagnosis of the stator winding inter-turn short circuits in a closed-loop system is the least explored topic—mainly because the application of the closed-loop control structure changes the effects of the damages in relation to the open-loop controlled motors [14]. In the case of the IM stator winding failures, working under a vector-controlled system, the change of the motor parameters, caused by this damage, results in operation disturbances of the whole control structure (e.g. improper value of estimated flux vector) [8, 9, 15]. Uncontrolled increase in the damage level can result in the instability of the drive system.

In [16] the detection of the short-circuits of IM operating under the classical Direct Torque Control with a switching table (DTC-ST) is presented. Two diagnostic methods are proposed—one of them uses the classical MCSA method, while the other one is based on the multiple reference frames theory. Detection of the short-circuits has also been applied in the Field Oriented Control (FOC) structures. In [14] a detection and localization method, based on the impedance identification for multiple motor system under the Indirect FOC (IFOC) structure is proposed. Neural networks use in the diagnostic process for FOC structure is presented in [17]. In [18] stator resistance estimation, using the Extended Kalman Filter (EKF) and the Luenberger observer, is applied in the short-circuits diagnosis. The use of the double fundamental harmonic frequency, $2f_s$, appearing in the flux component of the stator current vector, is introduced in [19]. Artificial neural networks and the extended wavelet analysis for field-oriented control structures can be found in [20] and [21]. In both publications the basic diagnostic signal comes from the vibration sensor. Recently the detection method of stator winding short-circuits of the induction motor operating in the vector control structure was reported in [22]. A novel detection algorithm was introduced, based on a spectral analysis of the internal signals from the control structure: controller outputs and control path decoupling variables. The superiority of the proposed detection algorithm over the classical Motor Current Signature Analysis method was described.

Although numerous solutions are presented in the technical literature, the field of research related to the monitoring of the stator windings failures is still an open issue, because many known methods are very sensitive to varying loads, machine manufacturing imperfections, environmental conditions as well as to the asymmetry in the motor supplying voltages and distortion of the stator voltages and currents associated with the PWM converter supply. Under certain operating conditions all these aspects could cause unreliable operation of the system monitoring the condition of the induction motor drive system.

3 Basic Vector Control Structures of the Induction Motor Drive

3.1 A Short Description of the Vector Control Structures

Vector control methods are currently commonly known and became a part of almost all modern industrial inverters. These methods have been described in detail in many scientific papers, e.g. in [4]. However, this section describes the two control structures, taken into account in this chapter: Direct Field Oriented Control and Direct Torque Control with Space Vector Modulation from the point of view of the diagnostic methods of the faulted stator windings.

Both control methods are similar and therefore their common block diagram is shown in Fig. 2. Both methods use PI regulators and in both cases the speed controller is the superior regulator. Its output is the reference i_{sy} component of the stator current in the case of the DFOC, and the reference motor torque m_e in the case of the DTC-SVM. Both methods define the reference values of the voltage components in synchronous frame and these value are then transformed to a stationary frame. In both methods the Space Vector PWM is used to control the voltage source inverter, supplying the tested induction motor. The main difference between the control structures is the type of the reference frame—the DFOC is oriented with respect to the rotor flux, while the DTC-SVM is oriented with respect to the stator flux. Therefore, the rotor flux amplitude is stabilized in the case of the DFOC and its angle is used to make the transformation between the coordinate frames. The opposite situation takes place in the case of the DTC-SVM—the stator flux amplitude is kept constant during the operation and the stator flux vector angle is taken for the transformation.

Both mentioned control structures require the information about non-measurable IM variables, such as: flux amplitude, its angle and electromagnetic torque. The type of the applied estimator influences the behavior of the drive system and the diagnostic algorithms effectiveness during the stator winding faults. In this research, the classical current-based simulator is used.

3.1.1 Direct Field Oriented Control Structure

Direct Field Oriented Control is a popular control method that allows to obtain very good dynamics and steady-state operation. It is based on the induction motor mathematical model expressed in the synchronous frame x - y , rotating with the rotor flux vector angular velocity ($\omega_k = \omega_{\psi_r}$, $\psi_{rx} = \psi_r$, $\psi_{ry} = 0$). In this reference frame, the stator voltage equations are as follows:

$$u_{sx} = r_s i_{sx} + l_s \sigma T_N \frac{di_{sx}}{dt} + \frac{l_m}{l_r} T_N \frac{d\psi_r}{dt} - l_s \sigma \omega_{\psi_r} i_{sy} \quad (1)$$

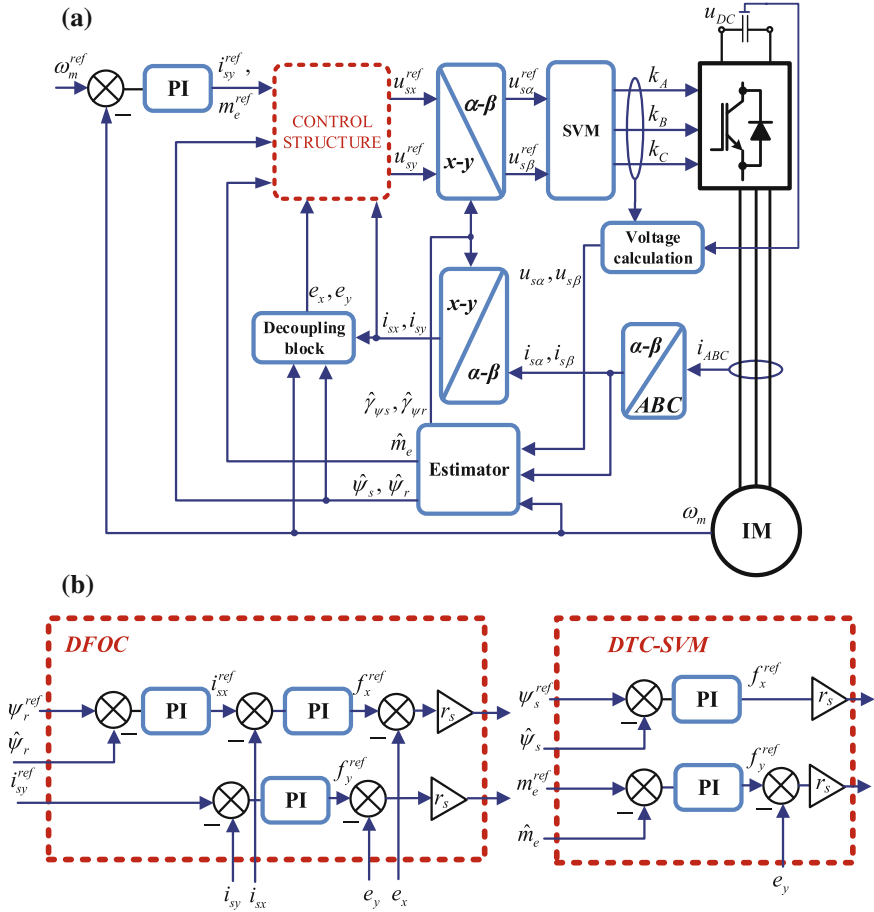


Fig. 2 Block diagram of vector control structures for induction motor: **a** common part of the control methods, **b** DFOC and DTC-SVM parts of the block diagram

$$u_{sy} = r_s i_{sy} + l_s \sigma T_N \frac{di_{sy}}{dt} + \frac{l_m}{l_r} \omega_{\psi r} \psi_r + l_s \sigma \omega_{\psi r} i_{sx}, \quad (2)$$

where: u_{sx}, u_{sy} —stator voltage vector components, i_{sx}, i_{sy} —stator current vector components, ψ_r —rotor flux vector amplitude, $\omega_{\psi r}$ —rotor flux vector angular velocity, r_s —stator winding resistance, $l_s = l_m + l_{s\sigma}$, $l_r = l_m + l_{r\sigma}$ —stator and rotor winding inductance, l_m —main inductance, $l_{s\sigma}$, $l_{r\sigma}$ —stator and rotor winding leakage inductance, σ —total leakage factor, $T_N = 1/(2\pi f_{sN})$ —nominal time constant, introduced by the per unit system, f_{sN} —nominal frequency.

The above Eqs. (1)–(2) prove that the current vector components can be controlled using their corresponding voltage components. However, this control is not

decoupled. In order to express the control path coupling, Eqs. (1) and (2) can be expressed in the following form:

$$\underbrace{i_{sx} + \frac{l_s \sigma}{r_s} T_N \frac{di_{sx}}{dt}}_{f_x} = \frac{1}{r_s} u_{sx} - \underbrace{\frac{l_m}{r_s l_r} T_N \frac{d\psi_r}{dt} + \frac{l_s \sigma}{r_s} \omega_{\psi_r} i_{sy}}_{e_x}, \quad (3)$$

$$\underbrace{i_{sy} + \frac{l_s \sigma}{r_s} T_N \frac{di_{sy}}{dt}}_{f_y} = \frac{1}{r_s} u_{sy} - \underbrace{\frac{l_m}{r_s l_r} \omega_{\psi_r} \psi_r - \frac{l_s \sigma}{r_s} \omega_{\psi_r} i_{sx}}_{e_y}. \quad (4)$$

Four signals appear in Eqs. (3) and (4): two control signals f_x , f_y and two decoupling signals e_x , e_y . These four signals will be used in the diagnostic algorithms, presented in next part of the chapter. The decoupling block, and the decoupling idea is shown in Fig. 2.

This idea for the first control path can be summarized in the following way—if signal e_x is added to the voltage u_{sx} in the mathematical model of the motor, its subtraction in the control structure should make the control paths ($f_x^{ref} - e_x$, r_s , $1/r_s$, $f_x + e_x$) independent. After this modification, the reference value of the f_x signal (taken as the output of the regulator) is equal to its real value and is not influenced by the e_x signal. Second control path is decoupled respectively. More details are presented in [22].

The decoupled control of the i_{sy} component is important since it is used to control motor torque, according to the expression:

$$m_e = \frac{l_m}{l_r} \psi_r i_{sy}. \quad (5)$$

In order to control the motor torque precisely, it is necessary to keep the amplitude of the rotor flux vector on the constant level. It is stabilized at its nominal value when the speed is lower than its nominal value. In order to control the rotor flux amplitude, the second component of the stator current i_{sx} is used, in accordance with the following equation:

$$\psi_r - \frac{l_r}{l_r} T_N \frac{d\psi_r}{dt} = l_m i_{sx}. \quad (6)$$

3.1.2 Direct Torque Control with Space Vector Modulation

As was mentioned above, the DTC-SVM algorithm is defined in the synchronous frame x - y , rotating with stator flux vector ($\omega_k = \omega_{\psi_s}$, $\psi_s = \psi_{sx}$, $\psi_{sy} = 0$) [23, 24]. In this control structure the stator voltage equations become:

$$u_{sx} = r_s i_{sx} + T_N \frac{d\psi_s}{dt}, \quad (7)$$

$$u_{sy} = r_s i_{sy} + \omega_{\psi_s} \psi_s, \quad (8)$$

where: ψ_s —stator flux amplitude, ω_{ψ_s} —stator flux velocity.

The motor torque in this coordinate frame is equal to:

$$m_e = \psi_s i_{sy}. \quad (9)$$

According to Eq. (7), stator flux amplitude can be controlled with the first component of the voltage vector u_{sx} , and is independent of the second control path. Therefore, there is no need to define the e_x signal. However, the second control path is coupled and is dependent on the stator flux amplitudes and its velocity changes. Therefore, this path can be also decoupled. Similarly, according to (4):

$$\underbrace{i_{sy}}_{f_y} = \frac{1}{r_s} u_{sy} - \underbrace{\frac{1}{r_s} \omega_{\psi_s} \psi_s}_{e_y}. \quad (10)$$

The idea of the decoupling is identical to the methodology given in the previous chapter. After the decoupling, the torque can be controlled using the u_{sy} component when the stator flux is stabilized (9)–(10). The block diagram, corresponding to the above description is presented in Fig. 2.

3.2 Experimental Setup Description

The experimental setup is shown in Fig. 3. The mechanical part of the setup consists of two induction motors (IMs), connected with a stiff shaft. The first induction motor is a specially prepared version of an industrial machine, allowing to model the short circuits of inter turns of each stator phase winding independently. It is possible to make a short circuit of minimum 1 to maximum 8 short turns in each phase. The rated data of the motor are given in Appendix, in the Table 1. The second motor is responsible for the load torque generation. Both induction motors, of nominal power 1.5 kW are supplied with voltage source inverters (VSI). The VSI that supplies the tested motor is controlled using the fiber optic wires, the second one uses its own program to generate the load torque and its reference value is defined using an analog signal.

There are several measurement devices present in the system: three phase currents transducers, DC-bus voltage sensor and two incremental encoders to measure the speed of the shaft (one with 36,000 imp./rev. is used in the control structure of the tested motor; the second one with 5000 imp./rev. is used by the VSI supplying the load machine).

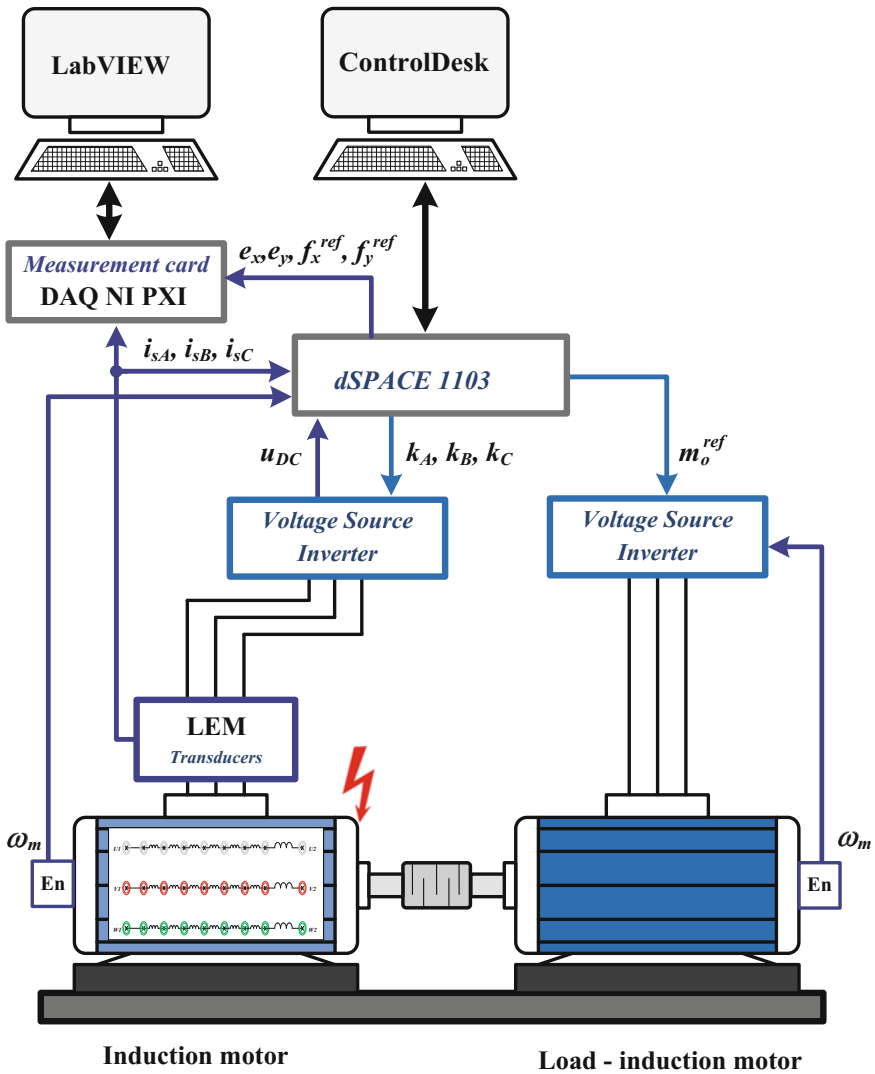


Fig. 3 Experimental setup

The whole control structure is implemented on the rapid prototyping system dSpace 1103. The program requires the knowledge of the three phase currents, DC-bus voltage (to calculate stator voltage) and the motor speed. The program defines the transistor control signals, while the specialized microprocessor based unit ensures the dead-time and transformation from electrical to fiber optics signals. The dSpace system defined the desired load torque value as well.

Fig. 4 Performance of the vector controlled induction motor drives during the stator winding fault: **a** speed, **b** stator and rotor flux amplitudes, **c** phase currents for the DFOC, **d** phase currents for the DTC-SVM, **e** electromagnetic torque and components of the stator current vector in synchronous frame

The diagnostic program is created using the LabView software environment. It uses three phase currents and the signals from the control structures, obtained from the dSpace systems: decoupling signals and the regulators outputs.

These two systems, from dSpace and National Instruments, are combined because of the cooperation and previous experience of the authors—it would not be difficult to create the whole control and diagnostic using only one system or the industrial available microprocessor.

4 Performance of the Vector Control Structures Under the Faulty Operation of the Induction Motor Drive

Performance of the vector control methods is shown as a comparative study in Figs. 4 and 5. The figures show the following steps: start-up of the machine, then the short circuit of 8 turns in phase A of the machine (after about 4.2 s for the DFOC and 4.65 s for the DTC-SVM) and finally the nominal load torque appears (after about 8.7 s for the DFOC and 9 s for the DTC-SVM). Reference values are disregarded in order to obtain better clarity of the figures—all of the controlled variables follow their reference values precisely.

The first subfigure (Fig. 4a) shows the speed of the drive—it is stabilized at 0.6 p.u. The speed response is almost the same in the case of both control structures. After the short circuit appears, the speed decreases slightly and the amplitude of the oscillations increases. However, this change of the oscillation level is too small to use it in the diagnostic process. The appearance of the nominal load torque causes higher fluctuation of the speed and then minor low frequency oscillations—the oscillations are connected with the operation of the load machine inverter.

The flux amplitude is stabilized on its nominal level (Fig. 4b)—rotor flux in the case of the DFOC and stator flux in the case of the DTC-SVM. When one of the fluxes is controlled, the remaining one is estimated closely to its nominal value. After the short circuit is introduced, quite visible oscillations appear in both controlled and estimated signals. The level of the oscillations is similar for the two control structures.

Stator currents almost do not change their amplitudes during the short circuit—it can be seen in Fig. 5c for the DFOC and Fig. 4d for the DTC-SVM. However, they become unsymmetrical and this phenomenon can be used in order to design the diagnostic method. After the load torque is generated, the three stator currents grow to 1 p.u., that means the nominal value.

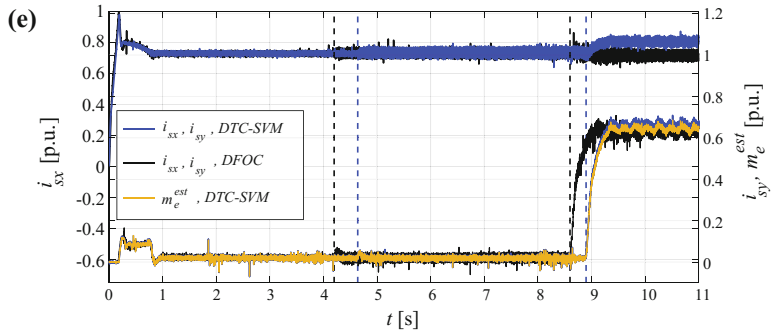
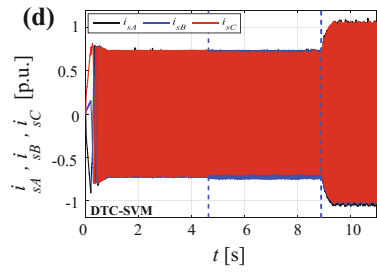
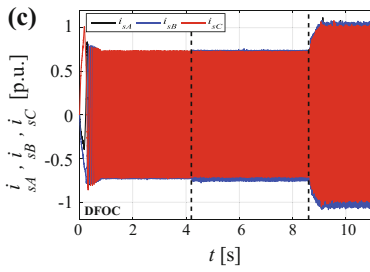
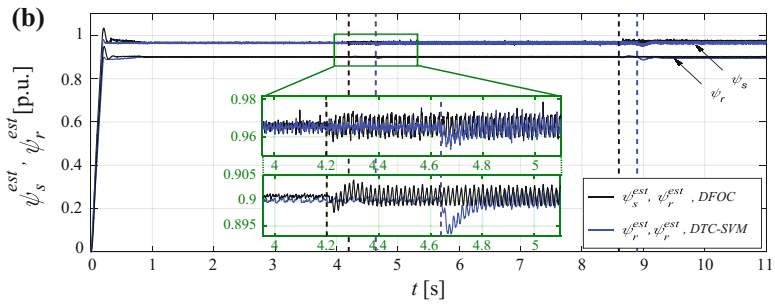
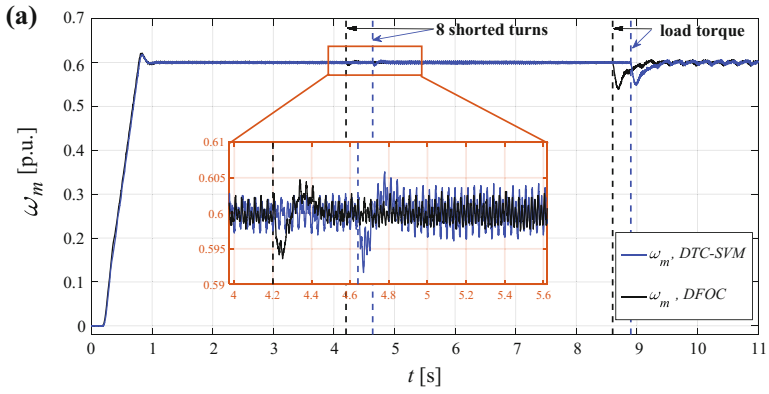


Fig. 5 Performance of the vector controlled induction motor drives during the stator winding fault: **a** outputs of the flux and torque regulators, **b** decoupling signals, **c** control signals in synchronous frame

Figure 4e shows the flux- and torque-components of the stator vector current in the synchronous frames (different for both control structures). In the case of the DFOC, the components follow their reference values, while in the case of the DTC-SVM the signals are calculated, and not utilized in the control structure. However, they can be still used in the diagnostic process. After the fault emerges, the oscillations in both components increase while their mean values remain constant. After the load torque appears, the i_{sx} components does not change significantly. However, the i_{sy} and electromagnetic torque change their values a lot after the load torque appears (nominal torque is equal to 0.67 in per unit system).

The oscillations of twice the fundamental frequency, that will be used in the diagnostic algorithm, can be seen mainly in the control and decoupling signals. They are shown in Fig. 5. The regulators' outputs, visible in Fig. 5a, change their mean values in a very similar way for both control structures, especially in the case of the f_x signal. After the short circuit occurs, large oscillations arise, slightly lower for the DTC-SVM method. The increase of the second harmonic of these signals can be one of the fault indicators—this will be described in the next section of the chapter. Similarly, the decoupling signals (Fig. 5b) have the same transients for both control structures (there is no e_x defined in case of the DTC-SVM).

Once more, the characteristic fluctuations are visible in the decoupling signals. As a consequence, the oscillations are present in the u_{sx}^{ref} and u_{sy}^{ref} control signals, as these signals are calculated directly from the mentioned signals: $e_x, e_y, f_x^{ref}, f_y^{ref}$. The reference voltage vector components are almost identical for both control structures in the case of the start-up and during the short circuit. However, they differ slightly when the load torque is generated. This phenomenon is connected with the fact that the position of the reference frames for the two control structures is the same when the load torque (slip speed) is equal to zero. The positions (velocities) of the x - y reference frames are different in the opposite situation.

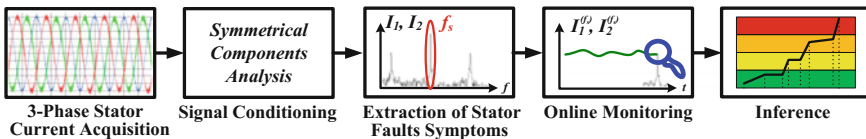
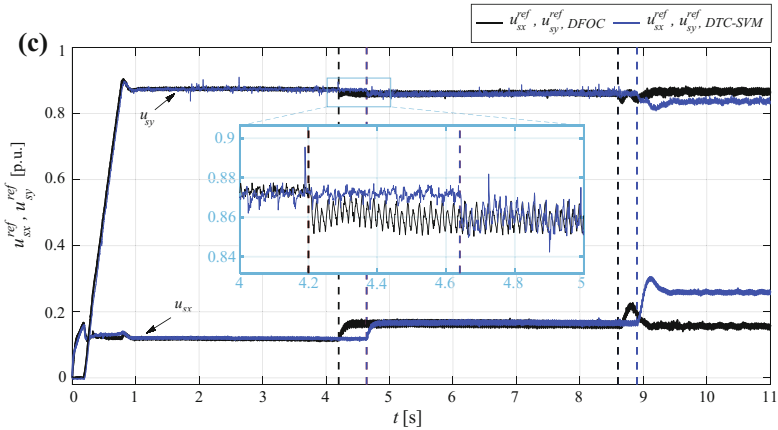
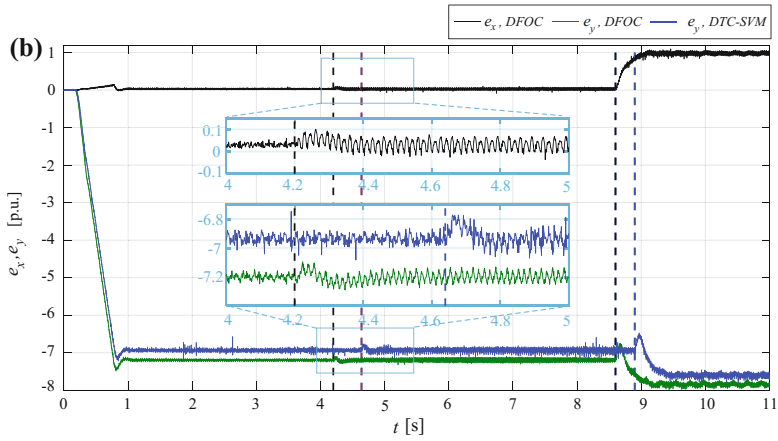
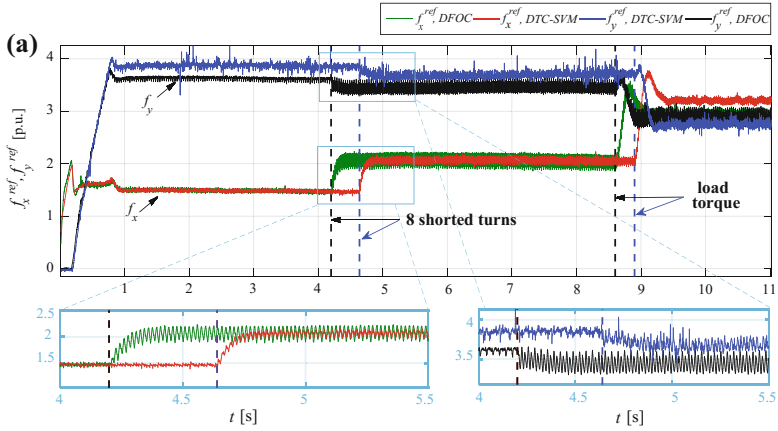


Fig. 6 Diagnostic signal processing using the symmetrical components analysis



5 Analysis of the Stator Winding Fault Diagnostic Methods in the Vector-Controlled Converter-Fed Induction Motor Drive

5.1 A Diagnostic Method Based on Stator Currents

In order to monitor the condition of the induction motor winding, the stator phase currents can be used, as easy-measurable signals. Analysis shown in previous sections proves that the quantitative changes of the phase currents are practically invisible in the case of the several shorted turns. Therefore, the symmetrical components analysis is proposed for the diagnostic purposes. It allows to extract the frequency component, in which the changes caused by the incorrect operation of the motor are visible.

The so-called instantaneous values of the symmetrical components are used in order to extract the fundamental frequency signals. These values are obtained replacing the complex variable j with the 90° angle displacement in the time domain. According to this it is possible to filter, for example using the Fast Fourier Transform (FFT), only the harmonic characteristic for a specific fault. In this case it is the fundamental frequency f_s of the signal, and the fault monitoring consists in the observation of this characteristic harmonics' amplitude changes.

In order to monitor changes of the f_s amplitude of the stator currents symmetrical components, a dedicated functional block has been created in the LabView environment. This block extracts the characteristic harmonics and monitors changes of their amplitudes based on the supply frequency. The diagnostic procedure stages, proposed for the symmetrical components analysis, are presented in Fig. 6.

The spectral analysis of the positive and negative sequence components is presented in Fig. 7, for no-load operation in case of 0, 3, 5, and 8 shorted turns in phase A of the motor working under the closed-loop control structures: DFOC (Fig. 7a, b) and DTC-SVM (Fig. 7b, d), respectively. In the case of the positive sequence component I_1 only the fundamental harmonic of the stator current is visible—it results from the actual speed of the motor. A short circuit of several turns in one coil of the motor's winding does not change the amplitude of the component in presented frequency range (0–100 Hz). On the other hand, it can be seen that the f_s frequency amplitude of negative sequence component I_2 increases significantly during the fault occurrence. A significant increase is visible especially for the DFOC control drive. However, in the case of the DTC-SVM structure it is also possible to extract the characteristic frequency after the short circuit of several turns.

A comparative study of the positive and negative sequence components is shown in Fig. 8 for both control structures and $\omega_m = \omega_n$. In case of the control structures, the short circuit of several turns does not cause changes of the positive sequence component $I_1^{(fs)}$ in the whole range of the load torque. An insignificant increase (during the short circuit of 5 and 8 turns) is visible for the nominal load operation. On the other hand, the negative sequence amplitude $I_2^{(fs)}$ grows even for 1 or 2

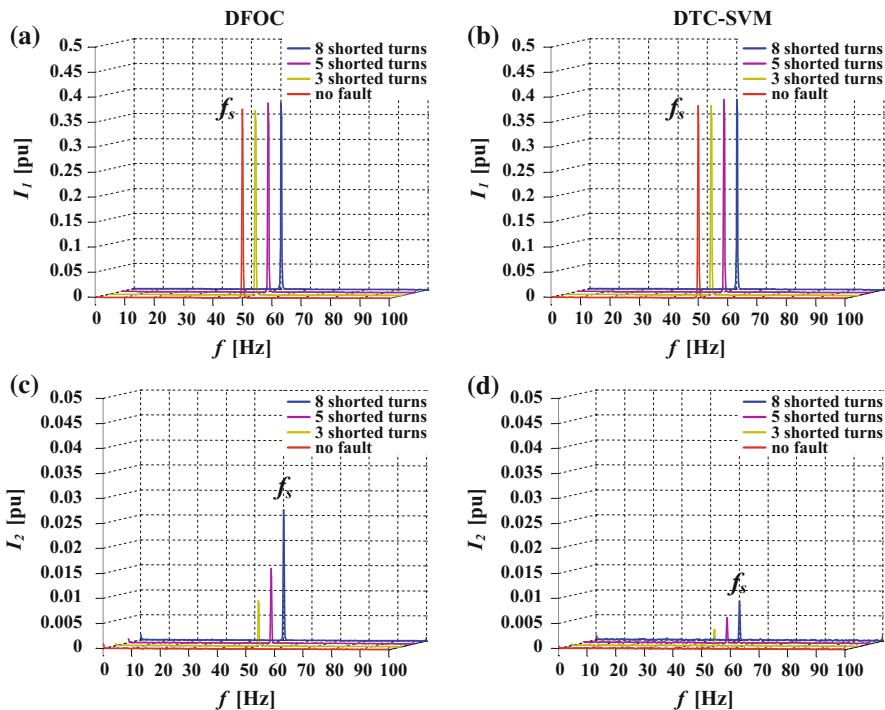


Fig. 7 Spectral analysis of: **a, b** positive sequence component I_1 and **c, d** negative sequence components I_2 of stator current, $\omega_m = 1$ [pu], no load operation

shorted turns. If this component is monitored, it is possible to detect the initial stage of the damage. Additionally, the load torque does not influence the $I_2^{(fs)}$ value in the case of the damage. The intensity of changes of the analysed component is much larger in case of the DFOC structure. However, it is also possible to detect several turns in the DTC-SVM structure as well.

Figure 9 shows changes of the positive $I_1^{(fs)}$ (Fig. 9a, b) and negative $I_2^{(fs)}$ (Fig. 9c, d) sequence components for the on-line operation of the drive system. After the start-up of the motor, the steady-state operation without the load torque is presented. After about 5–6 s the damage occurs—the short circuit of 8 turns. Large increase of the $I_2^{(fs)}$ amplitude is visible for both control structures. The component $I_1^{(fs)}$ is practically constant during the fault. After about 9–10 s the nominal load torque appears. In this case a rapid change of the positive sequence component can be seen, while the negative component amplitude $I_2^{(fs)}$ changes are negligible, which means that this fault symptom is load torque independent.

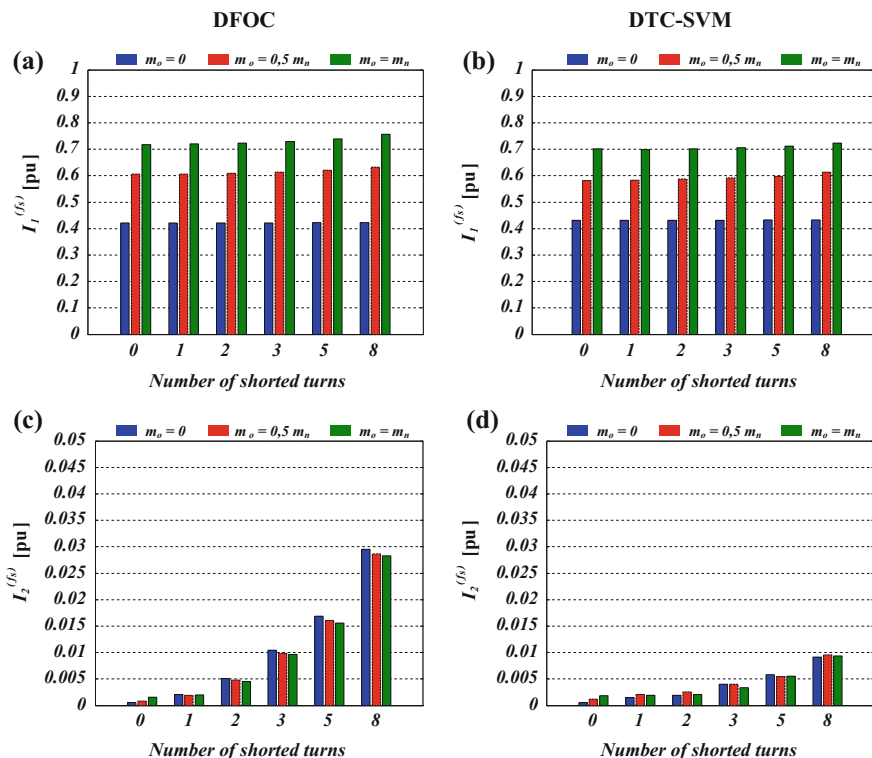


Fig. 8 Comparison of the fundamental frequency amplitudes of: **a, b** positive sequence component, **c, d** negative sequence component I_2 of stator current for $\omega_m = 1$ [pu] and different values of the load torque

5.2 A Diagnostic Method Based on Control Structure Signals

In order to extend the possibilities of the stator winding damage detection, it is proposed to use the signals that are available in both control structures. A detailed analysis is done in this paper for two additional signals—control signal f_y and the stator current vector component i_{sx} . The proposed additional signals are analysed first using the FFT, in order to extract the characteristic symptoms of the stator winding damage. In the case of the short circuit, some additional harmonics appear—second harmonic $2f_s$ of the supply voltage, in particular.

Figure 10 shows the consecutive steps of the diagnostic procedure, proposed for the control structure signals analysis.

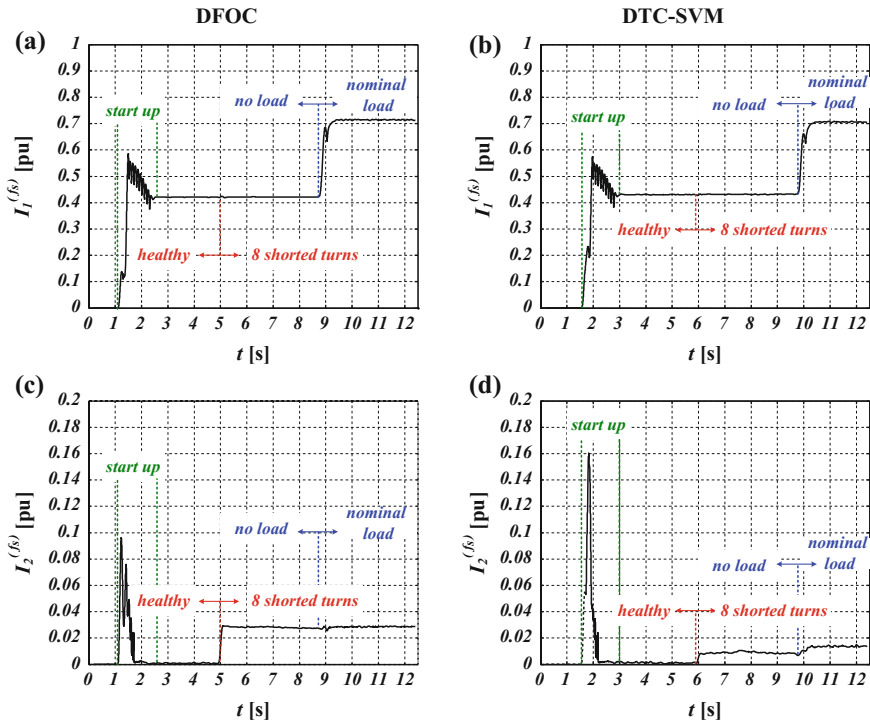


Fig. 9 On-line monitoring of the fundamental frequency components of: **a, b** positive sequence I_1 and **c, d** negative sequence I_2 stator current for $\omega_m = 1$ [pu]

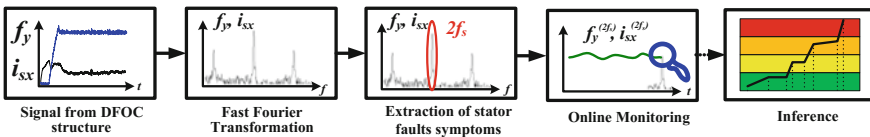


Fig. 10 Diagnostic signal processing using the internal drive structure signals

Spectra of the additional signals f_x and i_{sx} are presented in Fig. 11 for no-load operation and short circuit of 0, 3, 5 and 8 shorted turns for the drive operating under the vector control structures: DFOC (Fig. 11a, c) and the DTC-SVM (Fig. 11b, d), respectively, for $\omega_m = \omega_n$.

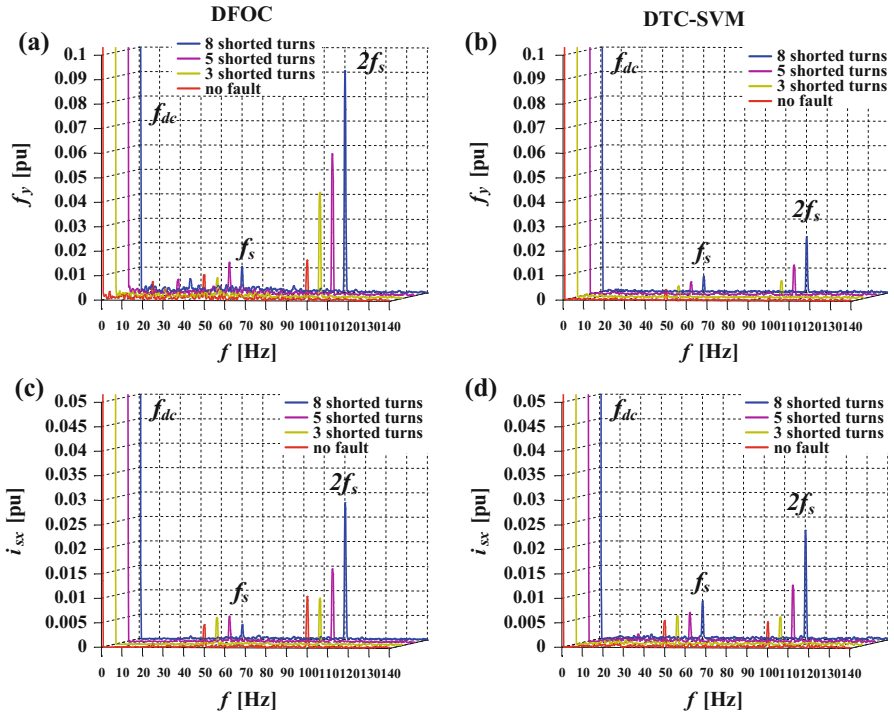


Fig. 11 Spectral analysis of: **a, b** control signal f_y and **c, d** stator current vector component i_{sx} for $\omega_m = 1$ [pu] and no load

If the stator winding is undamaged, in the analysed frequency range (0–140 Hz), only the following harmonics are visible: constant component f_{dc} and the fundamental component f_s . Short circuit of several turns in one coil of the motor winding causes the increase of the $2f_s$ amplitude. A significant change can be especially seen for the DFOC structure. However, in the case of the DTC-SVM it is also possible to detect even few shorted turns.

Figure 12 shows a comparative study of the proposed diagnostic signals from the DFOC and DTC-SVM structures. For both control structures, the stator winding damage causes the increase of the $2f_s$ component. Monitoring this component allows to detect the initial phase of the damage. Additionally, the load torque has almost no influence on the amplitudes of the analysed signals. Due to the larger intensity of the component changes, it is easier to detect the shorted turns in case of the DFOC.

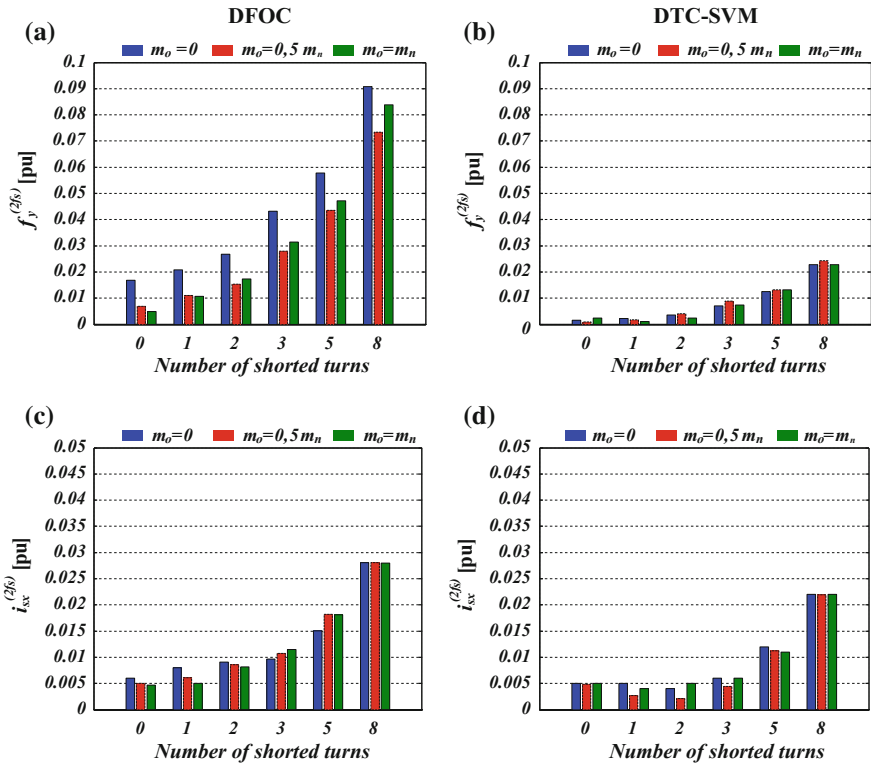


Fig. 12 Load torque influence on the second harmonic amplitude of: **a, b** control signal f_y and **c, d** stator current vector component i_{sx} for $\omega_m = 1$ [pu]

Figure 13 shows the experimental test results for on-line operation of the drive for 8 shorted turns and changing load torque. After the damage occurs, a sudden increase of the $2f_s$ component amplitude for both diagnostic signals is observed. Additionally, it can be observed, that the changes of the component are practically independent of the load torque. Thus, the changes of the $2f_s$ component are large enough to detect the damage even in case of changing load torque.

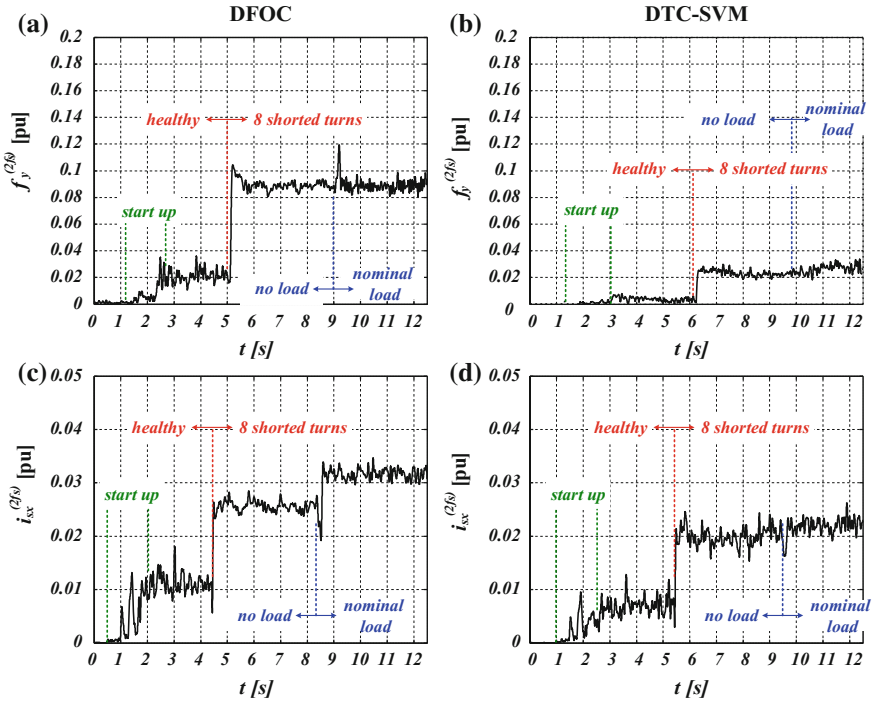


Fig. 13 The second harmonic amplitude of: **a, b** control signal f_y and **c, d** stator current vector component i_{sx} for $\omega_m = 1$ [pu]

6 Summary

This chapter deals with the inter-turn short-circuit diagnosis of the stator winding of the vector controlled induction motor. Two diagnostic methods have been analyzed: the first one based on the instantaneous values of the symmetrical components of the stator current, and the second one—based on signals available in the DFOC and DTC-SVM control structures.

On the basis of experimental tests, conducted for the special induction motor that allows the short-circuits introduction, working under the vector control, it was shown that it is possible to monitor this damage type even at its initial stage.

Despite the compensating operation of the closed-loop control structure on the damage symptoms, they are visible in the negative sequence component $I_2^{(fs)}$ of the stator current. Additionally, the load torque changes do not influence the value in case of the damage. Similarly, analyzing changes of the mean values of the amplitudes of the $2f_s$ component of the internal control signals f_y^{2fs} and i_{sx}^{2fs} of the DFOC and DTC-SVM structures, it can be stated that they significantly react to the stator winding damage. Additionally, their dependence on speed and load

torque values is low. Hence, by monitoring of this component it is possible to detect the initial phase of the stator winding fault at its to detect the early stage.

Practical realization of the stator winding monitoring requires introduction of some additional algorithms to the control software of the converted-fed induction motor drives. However, this implementation should not be a problem in the case of modern processors.

Acknowledgments This work was supported by the National Science Centre Poland, under project 2013/09/B/ST7/04199 (2014–2017).

Appendix

See Table 1.

Table 1 Rated parameters of the tested induction motor

Name	Symbol	SI units		Normalized units [p.u.]
Power	P_N	1500	[W]	0.621
Torque	M_N	10.16	[Nm]	0.661
Speed	N_N	1410	[r/min]	0.94
Stator phase voltage	U_{sN}	230	[V]	0.707
Stator current	I_{sN}	3.5	[A]	0.707
Frequency	f_{sN}	50	[Hz]	1
Stator flux	Ψ_{sN}	0.999	[Wb]	0.965
Rotor flux	Ψ_{rN}	0.933	[Wb]	0.901
Pole pairs	p_p	2	[-]	[-]
Number of rotor bars	N_r	26	[-]	[-]
Number of stator turns in each phase	N_s	312	[-]	[-]

References

1. Riera-Guas M, Antonino-Daviu JA, Capolino GA (2015) Advances in electrical machine, power electronic, and drive condition monitoring and fault detection: state of the art. *IEEE Trans Ind Electron* 62(3):1746–1759
2. Grubic S, Aller JM, Lu B, Habetler TG (2008) A survey on testing and monitoring methods for stator insulation systems of low-voltage induction machines focusing on turn insulation problems. *IEEE Trans Ind Electron* 55(12):4127–4136
3. Gandhi A, Corrigan T, Parsa L (2011) Recent advances in modeling and online detection of stator interturn faults in electrical motors. *IEEE Trans Ind Electron* 58(5):1564–1575
4. Casadei D, Profumo F, Serra G et al (2002) FOC and DTC: two viable schemes for induction motors torque control. *IEEE Trans Power Electron* 17(5):779–787
5. Cabanas MF, Normiella JG, Melero MG et al (2013) Detection of stator winding insulation failures: on-line and off-line tests. In: *Proceedings of IEEE workshop on electrical machines design, control and diagnosis WEMDCD, Paris, 11–12 Mar 2013*
6. Kowalski CT, Wolkiewicz M (2009) Stator faults diagnosis of the converter-fed induction motor using symmetrical components and neural networks. In: *Proceedings of 13th European conference on power electronics and applications EPE, Barcelona, 8–10 Sept 2009*
7. Wolkiewicz M, Kowalski CT (2013) On-line neural network-based stator fault diagnosis system of the converter-fed induction motor drive. In: *Proceedings of the 39th annual conference of the IEEE Industrial Electronics Society IECON, Vienna, 10–13 Nov 2013*
8. Cruz SMA, Cardoso AJM (2001) Stator winding fault diagnosis in three-phase synchronous and asynchronous motors, by the extended park's vector approach. *IEEE Trans Ind Appl* 37(5):1227–1233
9. Wolkiewicz M, Tarchała G, Kowalski CT (2015) Stator windings condition diagnosis of voltage inverter-fed induction motor in open and closed-loop control structures. *Archives Electr Eng* 64(1):67–79
10. Diallo D, Benbouzid MEH, Hamad D, Pierre X (2005) Fault detection and diagnosis in an induction machine drive: a pattern recognition approach based on concordia stator mean current vector. *IEEE Trans Energy Conv* 20(3):512–519
11. Bellini A, Filippetti F, Tassoni C, Capolino GA (2008) Advances in diagnostic techniques for induction machines. *IEEE Trans Ind Electron* 55(12):4109–4126
12. Drif M, Cardoso AJM (2014) Stator fault diagnostics in squirrel cage three-phase induction motor drives using the instantaneous active and reactive power signature analyses. *IEEE Trans Ind Informat* 10(2):1348–1360
13. Briz F, Degner MW, Guerrero JM, Garcia P (2009) Stator windings fault diagnostics of induction machines operated from inverters and soft-starters using high-frequency negative-sequence currents. *IEEE Trans Ind Appl* 45(5):1637–1646
14. Cheng S, Zhang P, Habetler TG (2011) An impedance identification approach to sensitive detection and location of stator turn-to-turn faults in a closed-loop multiple-motor drive. *IEEE Trans Ind Electron* 58(5):1545–1554
15. Orłowska-Kowalska T, Dybkowski M, Kowalski CT (2010) Rotor fault analysis in the sensorless field oriented controlled induction motor drive. *Automatika* 51(2):149–156
16. Cruz SMA, Cardoso AJM (2004) Diagnosis of stator inter-turn short circuits in DTC induction motor drives. *IEEE Trans Ind Appl* 40(5):1349–1360
17. Tallam RM, Habetler TG, Harley RG (2003) Stator winding turn-fault for closed-loop induction motor drives. *IEEE Trans Ind Appl* 39(3):720–724
18. Kowalski CT, Wierzbicki R, Wolkiewicz M (2013) Stator and rotor faults monitoring of the inverter-fed induction motor drive using state estimators. *Automatika* 54(3):348–355
19. Bellini A, Filippetti F, Franceschini G, Tassoni C (2000) Closed-loop control impact on the diagnosis of induction motors faults. *IEEE Trans Ind Appl* 36(5):1318–1329
20. Seshadrinath J, Singh B, Panigrahi BK (2014) Vibration analysis based interturn fault diagnosis in induction machines. *IEEE Trans Ind Informat* 10(1):340–350

21. Seshadrinath J, Singh B, Panigrahi BK (2014) Investigation of vibration signatures for multiple fault diagnosis in variable frequency drives using complex wavelets. *IEEE Trans Power Electron* 29(2):936–945
22. Wolkiewicz M, Tarchała G, Orłowska-Kowalska T, Kowalski CT (2016) Online stator interturn short circuits monitoring in the DFOC induction-motor drive. *IEEE Trans Ind Electron* 63(4):2517–2528
23. Żelechowski M (2005) Space vector modulated—direct torque controlled (DTC-SVM) inverter-fed induction motor drive. PhD thesis, Warsaw University of Technology
24. Buja GS, Kaźmierkowski MP (2004) Direct torque control of PWM inverter-fed AC motors—a survey. *IEEE Trans Ind Electron* 51(4):744–757

Detection and Compensation of Transistor and Position Sensors Faults in PM BLDCM Drives

Marcin Skóra and Czesław T. Kowalski

Abstract During normal operation of a permanent magnet brushless direct current motor (PM BLDCM) drive some faulty modes can occur as a result of the failures of the position sensors and transistors of a voltage inverter supplying the motor. In this chapter the impact of these faults on the PM BLDCM drive system has been presented. The waveforms and FFT spectra of the stator currents, hodographs of the stator current space vector in the stationary reference frame following transistor faults and waveforms of signals determining the actual position of the rotor have been analysed in the chapter. Simple diagnostic and localization methods to identify a faulty part of the drive system have been proposed. The post-fault control has been analysed as well, it enables the drive system to continue its operation despite the diagnosed faults, because additional hardware circuits are used. This chapter presents simulation results validated by experimental testes conducted in a laboratory set-up.

Keywords PM BLDC motor · Fault identification · Fault compensation

1 Introduction

Permanent magnet brushless direct current motors (PM BLDCM) are widely used in industry and in small-power electrical drives (e.g. electric bikes, wheelchairs). The reason for this are their advantages—low inertia rotors, good cooling and longer and longer life, resulting from the replacement of a mechanical commutator with an electronic one. The latter is responsible for appropriate supply of particular motor bands depending on the position of the rotor angle position. This position can

M. Skóra (✉) · C.T. Kowalski
Department of Electrical Machines, Drives and Measurements, Wrocław University of Science and Technology, Wybrzeże Wyspiańskiego 27, Wrocław, Poland
e-mail: marcin.skora@pwr.edu.pl

C.T. Kowalski
e-mail: czeslaw.t.kowalski@pwr.edu.pl

be determined in a number of ways—using discrete sensors of rotor position (optical or Hall effect ones), an encoder or sensorless methods. Abnormal operation of rotor position sensors and the lack of conductivity in the transistors of the supply system make motor operation impossible. This type of faults is especially inconvenient in mobile systems because they are stopped as a result. This is why, in accordance with general research trends newly developed systems are to be fault tolerant [1]. Hence, fast fault detection and compensation methods are sought after. In the case of PM BLDC drives, one cannot find numerous literature items devoted to simultaneous occurrence of both of these problems. Research is usually devoted to searching for and testing diagnostic methods offering credible and credible fault symptoms allowing to quickly identify and locate a fault as well as undertake compensation actions, such as hardware or software reconfiguration, transition to the sensorless mode or safe drive stoppage.

The consequences of commutation process disorder and transistor faults in the power electronic controllers as well as the presented detection and identification methods of faulty elements and fault compensation are discussed below. The considerations are illustrated with sequences recorded at the laboratory set-up.

2 Short Review of Diagnostic Methods Applied in PM BLDCM Drives

Detection of selected faults in a PM BLDCM drive can be conducted in a number of ways, depending on the current drive operation state. Most of the methods described in the literature focus on detection during drive operation. Another approach is used in the diagnostic tests conducted before start-up when the motor is stopped.

Usually detection algorithms are based on the analysis of time waveforms of phase currents [2] or DC-link current [3]. When the detection speed is not a key parameter, it is possible to use averaged waveforms from a few current periods [4–7]. In this case the operation of a detection system is based on an observation that after the occurrence of various faults a constant component appears in phase currents waveforms and their amplitude spectrum includes additional even components and the amplitude odd harmonics grows. Changes occur also near modulation frequency, in the case of the PWM regulated motors. In the analysis also the density of energy transferred by the fundamental wave of phase voltage is used [8, 9]. On the basis of available symptoms decisions can be made using the rule base [3, 6, 8] or artificial intelligence methods as in [10].

Another approach to overall detection of faults assumes that measurement signals can be used as input data for appropriately prepared observers [11] or online identification systems of drive parameters [12–14].

The above presented diagnostic methods belong to the group of methods which do not use additional sensors and systems, apart from the ones required in an

non-faulty system. Moreover, these methods are characterised by a uniform way of proceeding during detections regardless of fault type. However, sometimes it is worth changing the way of acting so as to detect a specific type of fault in a simple way. This refers to the faults of rotor position sensors. In an non-faulty drive such sensors code precisely defined states changing in a specified sequence. Disturbances in this order allow to detect an anomaly in a simple way [15–17].

During the identification of particular types of faults, one should bear in mind that symptoms (e.g. phase current waveforms) can be similar in the case of certain types of faults. Such a situation takes place when a position sensor is permanently faulty and when two transistors from different phases are faulty. In this case waveforms are different, e.g. for the reference phase current signals or signals directly controlling transistors. By contrast when there is no conductivity in both transistors in one phase the symptoms are similar to disrupted conductivity in one phase.

The faults considered so far are characterised by sudden occurrence and significant waveform changes. Apart from this, an operating drive, and especially a motor, undergoes exploitation wear. The issues related to e.g. bearing faults, eccentricity, coil short circuits, demagnetisation of magnets are discussed in separate publications [18, 19] in which the authors try to detect alarming signals in drive operation using the spectral analysis, online parameter identification and change trend setting, etc. It is also assumed that the considered system is properly made, i.e. the issues of irregular distribution of rotor position sensors, output signal disturbances of these sensors or the encoder are not considered. More information can be found in other publications, e.g. [20, 21].

The diagnostics of the drive system before starting operation (before start-up) should particularly encompass testing the proper operation of transistors and correct readings of the rotor position by discrete position sensors. Power stage can be checked by connection one after another all possible transistor pairs and checking the current flow. It is a simple method, however, it requires non-faulty current sensors. The time of such a test and the order of connected pairs must be adjusted to a particular application, depending if a possible rotor position change is admissible. Working power transistors and current sensors or voltage comparators allow to determine the initial rotor position, e.g. using the saturation effect of coil inductiveness [22, 23] to compare it with the position indicated by sensors.

3 Research Object and Laboratory Set-up

3.1 Operation of the PM BLDCM Control System

PM BLDC motors belong to the group of electrically commutated motors which cannot operate without an appropriate control system. Their topology and principle of operation have been extensively explained and described in numerous

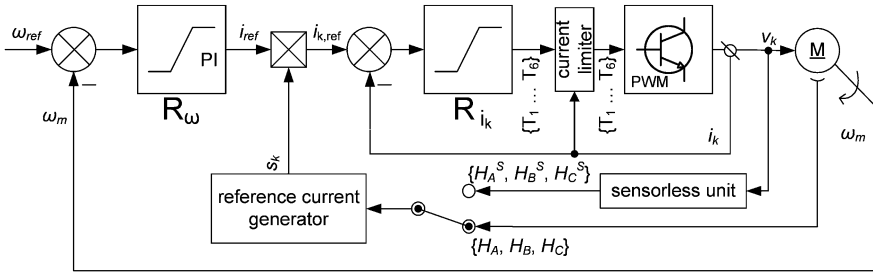


Fig. 1 Schematic diagram of the PM BLDCM control system

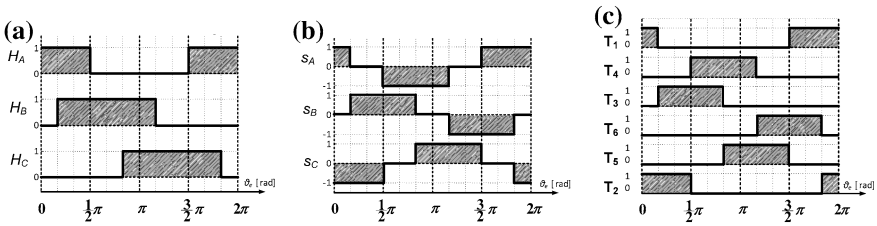


Fig. 2 Coding signals waveforms of rotor position (a), reference current shape (b) and transistor control signals for a positive direction of the rotational speed of motor operation (c)

publications, e.g. [24], this is why the description in this paper will be limited to minimum. Simulation and experimental research was conducted in a cascade control system (Fig. 1) with a PI superior speed control and inferior input currents controls, with P/PI or hysteresis controller. The transistors of the electronic commutator are switched on depending on the rotor position (coded by sensor signals H_A, H_B, H_C) and the reference current signal. The shape of the set current is determined by dependencies (1) and is shown in Fig. 2. Moreover, it is convenient to use on position signal of the rotor P , in accordance with (2).

$$\begin{aligned}
 s_A &= \bar{H}_B \cap H_A - H_B \cap \bar{H}_A \\
 s_B &= \bar{H}_C \cap H_B - H_C \cap \bar{H}_B \\
 s_C &= \bar{H}_A \cap H_C - H_A \cap \bar{H}_C
 \end{aligned} \tag{1}$$

$$P = 4H_A + 2H_B + H_C \tag{2}$$

where $s_k (k \in \{A, B, C\})$ —current flow direction (sign) in phase k , H_k —output signal from the rotor position sensor, treated as a logical value (0/1), P —number coding the rotor position.

3.2 Description of the Laboratory Set-up

At the first stage of the research of faulty states and diagnostic methods, simulations were conducted in the Matlab/Simulink package using the SimPowerSystems toolbox. Next the tests were repeated on a real object, a laboratory set-up adjusted to feed small power PM BLDC motors. The laboratory set-up consists of a voltage inverter made by the authors, measurement systems (phase currents, DC-link voltage and current), the investigated motor, a loading machine and its control system as well as a DSP processor. The voltage inverter is used as an electronic commutator and feeds the coils of the tested motor in a classical (block-type) way with a PWM voltage control on top transistors or a hysteresis control. The control system was developed in a signal processor DS1103, dSpace GmbH (PowerPC processor, 400 MHz and additional DSP TMS320F240 from Texas Instruments to generate PWM signals), and the control software was developed in the C programming language. The ControlDesk environment was used in the user control panel and for waveforms acquisition from the control system, apart from this an oscilloscope was used for acquisition of selected signals. The user graphic interface allows to choose a drive operation mode (operation in cascade, torque or open loop control systems, power stage test), coupling type and current regulator type (the use of phase currents or DC-link current, with linear P/PI or hysteresis controller), rotor position signal sources (embedded Hall effect sensors, external sensorless system, position reproduction in program), type of simulated faults and activation of defect compensation methods. Measurement transducers, rotor position sensors and the control system were galvanically isolated from power stage. The load torque is set using a separately excited DC machine configured for torque operation.

Drive operation during fault situations is obtained without physical destruction of elements, by a lack of control transistors or adoption of a constant value of the rotor position signal, independent of sensor indications.

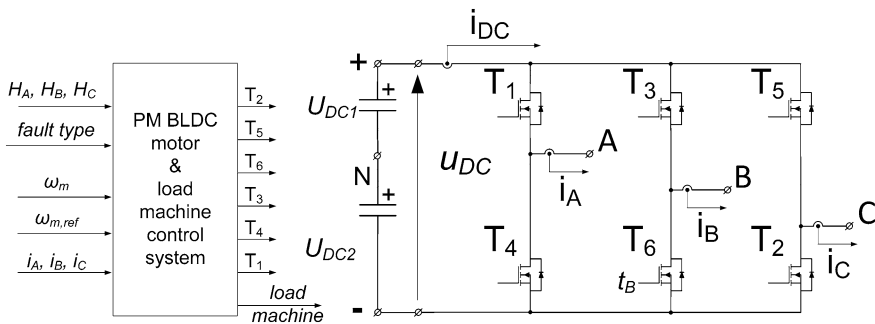


Fig. 3 Topology of the electronic commutator

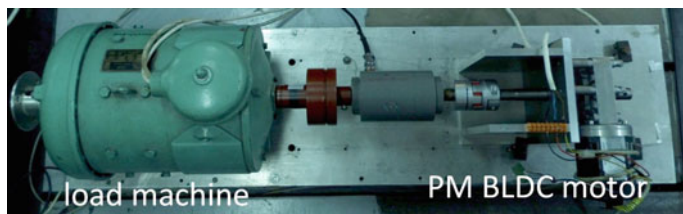


Fig. 4 The laboratory set-up

Table 1 Parameters of the tested motor PBL 86-118

Parameter	Value	Parameter	Value
Motor rated speed	$n_N = 3000$ rpm	Rated voltage	$u_{DC,N} = 48$ V
Rated electromagnetic torque	$t_{eN} = 1.1$ Nm	Rated current	$i_{DC,N} = 11$ A
Speed reduction gearbox ratio	$i = 30:1$	Pole pairs	$p_p = 4$

The topology of the voltage converter is presented in Fig. 3 and the experimental set-up in Fig. 4. The PM BLDC motor (with parameters shown in Table 1) is equipped with a gearbox reducing speed and an incremental encoder with 500 counts per revolution.

4 Analysis of Transistor Faults Diagnostic Methods in the PM BLDCM Drive

4.1 Symptoms of Transistor Faults

The lack of conductivity of one or more transistors of the PM BLDC motor drive with a block feeding scheme results in the occurrence of moments of time during one current period when the current does not flow through motor coils, hence the generated electromagnetic torque has zero value and the rotational speed decreases. At the next rotor position when efficient transistors conduct electric current, the control system can force maximum currents to compensate for the said speed decrease, in effect the rotor rotational speed can start to oscillate. Phase currents deformation can be conveniently observed in the form of the hodograph of the current space vector in the stationary coordinate system α - β (3) (examples are shown in Fig. 5) or they can undergo a frequency analysis. An example of analysis using the FFT is shown in Figs. 6 and 7. The basic frequency occurring in them related to input currents is defined by the (4), which for $n = 0.5 n_N = 1500$ rpm makes $f_s = 100$ Hz. It is possible to observe that although in an efficient system currents are not ideally rectangular (there is a relatively large share of even and triple multiplicities of the frequency f_s), after a fault their amplitude significantly

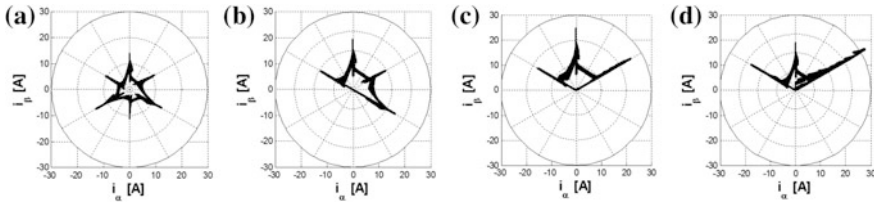


Fig. 5 Examples of hodographs of the phase current vector for a loaded drive operating at half rated speed at various operation states: non-faulty system (a), after a fault consisting in lack of conductivity at transistor T5 (b), simultaneous lack of conductivity of transistors T5 and T6 (c), damage of the sensor HC—it continues to return the value “0” regardless of the actual rotor position (d), for a positive direction of the rotational speed (experimental results)

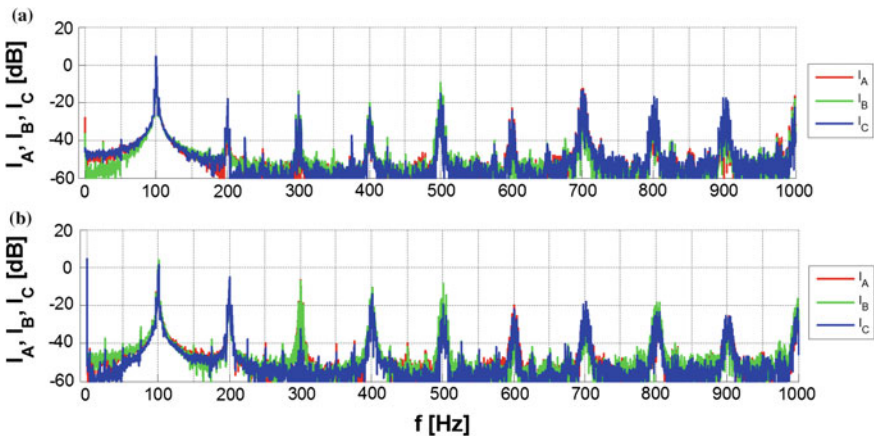


Fig. 6 Examples of the spectral analysis of phase currents in low frequency area: modules of amplitude spectra of input currents in an non-faulty system (a) and after fault occurrence—no conductivity at transistor T5 (b)

grows, the constant component appears (an increase for $f_{DC} = 0$ Hz) and amplitude increase for PWM frequency. The largest growths are observed in the phases in which faults occur. More details and explanations can be found in [5, 25]. In each case characteristic and significant changes in relation to a non-faulty system operation are visible. Current decays are visible also in the current feeding the converter [3, 25], which is the basis for one of the simplest detection methods and will be discussed in the further part of the paper.

$$\begin{bmatrix} q_\alpha \\ q_\beta \end{bmatrix} = \frac{2}{3} \begin{bmatrix} 1 & -1/2 & -1/2 \\ 0 & \sqrt{3}/2 & -\sqrt{3}/2 \end{bmatrix} [q_A \ q_B \ q_C]^T \quad (3)$$

where q_k is any arbitrary variable, in particular current i_k in phase k or rotor position signal H_k .

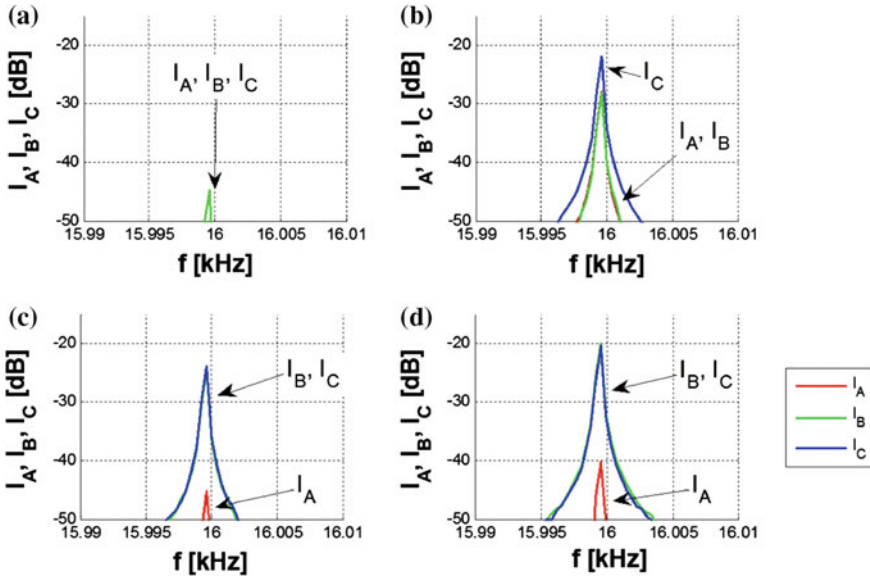


Fig. 7 Examples of the spectral analysis of phase currents surrounded by the PWM frequency (description of cases as in Fig. 5)

$$f_s = p_p \frac{n}{60} \tag{4}$$

where f_s [Hz] is feed frequency (the first harmonic of phase current), n [rpm]—rotational speed.

4.2 Transistor Faults Detection

While constructing the detection method one should first determine the symptoms accompanying the fault and adopt detection thresholds whose exceeding will mean the occurrence of fault. Additionally, to eliminate false alarms, the occurrences of exceeding thresholds should be permanent, it cannot result only from interferences. The method presented below is a modified approach of the one presented in [3]. The idea behind it is continuous controlling whether the sum of the measured phase currents is larger than a certain part of the reference current. If this condition is not met throughout a significant percentage of the time when the rotor is in a given position (a given sector) it is the first symptom of a fault. When the rotor turns to the next sector, one should check the relations between the reference and measured currents one more time. When the information about the previous and current rotor

Table 2 The selection of rules allowing to detect and identify faulty transistors

$P(n) \rightarrow P(n + 1)$ $\omega_m > 0$	F_I	Faulty transistor denotation	Detector output value	F_I	$P(n) \rightarrow P(n + 1)$ $\omega_m < 0$
4 → 6	0	T1	1	1	3 → 2
	1	T2	2	0	
6 → 2	0	T2	2	1	1 → 3
	1	T3	3	0	
2 → 3	0	T3	3	1	5 → 1
	1	T4	4	0	
3 → 1	0	T4	4	1	4 → 5
	1	T5	5	0	
1 → 5	0	T5	5	1	6 → 4
	1	T6	6	0	
5 → 4	0	T6	6	1	2 → 6
	1	T1	1	0	
Other cases: unrecognized problems			-1		
Presence of sensor fault symptoms rotor position (signal $FS = 1$)			-2		

position sector and the relation between currents in normal and faulty state is available, one can determine the number of a faulty transistor.

In the current rotor position $P(n)$ (2) the residuum signal r (5) is compared with the threshold i_{th} (6). If the relation $r < i_{th}$ is fulfilled by at least time T_{fault} (7), then the fault is detected and memorised by attaching tag F_D . In the next rotor position $P(n + 1)$ one should assess is the measured current is still below the value of the threshold i_{th} , set the level of tag F_I appropriately and following this choose the right case from a table such as Table 2. The reliability and speed of the described method can be established using two parameters: k_f (responsible for calculation time for a given sector P) and g_f (responsible for the level used for comparison). Figure 8 presents the waveforms of two phase currents and the rotational speed after the fault of transistor T_2 , and Fig. 9 shows a sample waveform of the described signals during detector operation.

$$r = |i_A| + |i_B| + |i_C|, \tag{5}$$

$$i_{th} = 2g_f i_{ref}, \tag{6}$$

$$T_{fault} = k_f \frac{2\pi}{p_p \omega_m} \frac{1}{N}, \tag{7}$$

where i_k ($k \in \{A, B, C\}$)—phase currents, i_{th} —switchover threshold, i_{ref} —reference current (the output of the superior speed controller in the cascade control structure), T_{fault} —limiting time for fault detection, g_f , k_f —parameters, $N = 6$ for a 3-phase

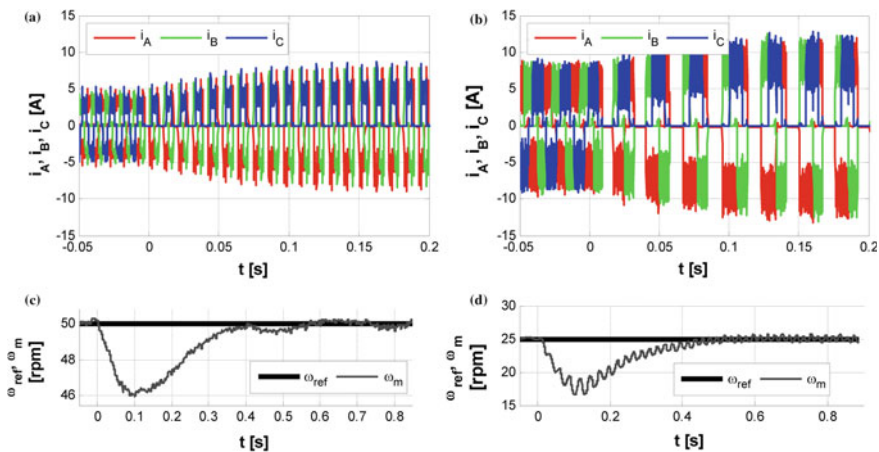


Fig. 8 Waveforms of phase currents (a, b) and the rotational speed of the gearbox shaft (c, d) after transistor T2 fault in the cascade speed control system, with phase currents PI type controllers (a, c) or with hysteresis ones (b, d)

motor—number of rotor position sectors per rotation, ω_m [rad/s]—mechanical angular speed.

The simplicity of this method is accompanied by some limitations as well. First of all it can be used in the detection of a single nonconductive transistor. In the case of a fault of at least two transistors (or a lack of control—the case of the fault of a rotor position sensor), the result will show only one of them or there will be information that this case does not match any of the models collected in Table 2. Another observed limitation of the detector operation is the fact that the motor must be loaded to some extent, i.e. the reference current must be larger than the idle run current. The time from fault occurrence to its identification depends on the adopted parameters k_f and g_f . However, sometimes detection and identification do not occur in the first possible rotor position P in which the fault becomes apparent, but in the subsequent ones. A remedy for this is a slight decrease in the time parameter k_f .

4.3 Checking the Transistor Conduction at the Standstill of the Drive System

Before starting operation transistor switches can be checked by connecting subsequent pairs of transistors to find out in which combinations there is no passage of current. Due to the low resistance of motor coils, one should use the PWM with a low filling factor and the test time for each pair should be selected in such a way that it would not be too long and at the same time it would allow to differentiate between forced currents and measurement interferences. The indication of

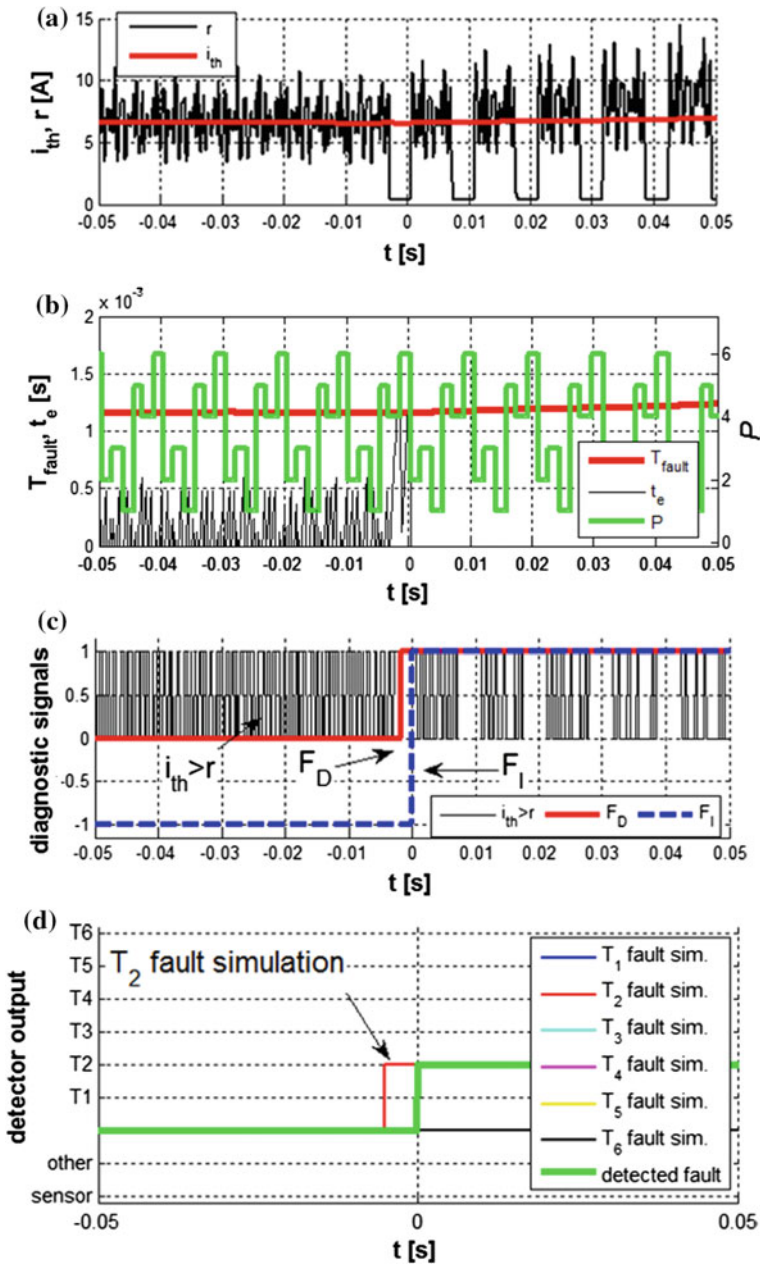


Fig. 9 The operation of the faulty transistors detection method—particular stages (a, b, c, d) for the current waveform as in Fig. 8a

nonconductive transistors takes place after the comparison of average current in each tested pair with the limiting value and relevant rules. The condition of successful testing is correct operation of current sensors. The detection of their various faults exceeds the range of this research and was widely described in e.g. [26, 27].

Assuming the order of connections as shown in Table 3 and acting in accordance with the scheme presented in Fig. 10, one can indicate suspicious transistor switches on the basis of rules collected in Table 4. A sample programme performance is presented in Fig. 11.

After this test the rotor can be turned by a certain angle. If there is short-circuit type of fault in power stage, then the emergency cut off of the power module should take place and fuses should blow, as a result this type of fault comes down to diagnosing such faults as lack of transistor conductivity. Another limitation of such a test are problems with selecting suspicious switches if physically the lack of conductivity occurs in more than 2–3 switches. This results from a lack of possibility of the passage of current through motor coils. Another inconvenience is a possible indication of a non-faulty switch as a faulty one in the case of multiple faults, e.g. if during a test the current does not flow though transistors T_1 and T_3 due

Table 3 Pairs of transistors connected during the test

Pair number	Transistor no	
	PWM	ON
1	T1	T6
2	T1	T2
3	T3	T2
4	T3	T4
5	T5	T4
6	T5	T6

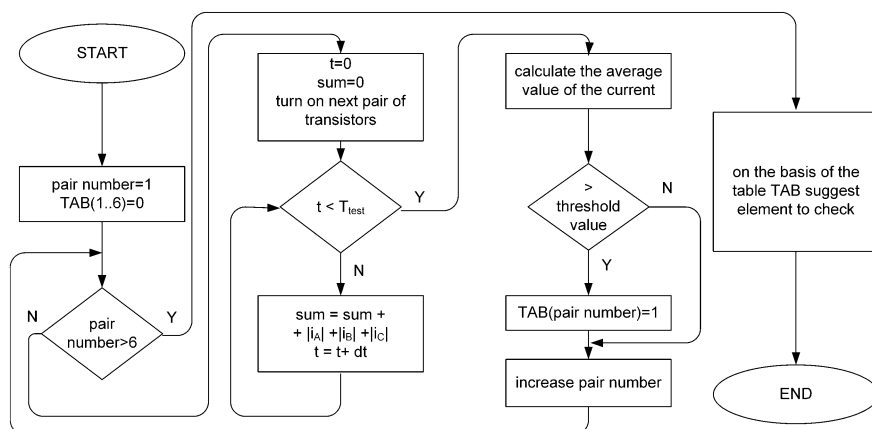


Fig. 10 The scheme of the testing method of transistor switch conductivity before activation

Table 4 Faulty transistor detection rules for testing power stage before activation, on the basis of Table TAB (Fig. 10)

Condition which when fulfilled indicates faulty transistor	Transistor no
TAB(1) == 0 AND TAB(2) == 0	T1
TAB(2) == 0 AND TAB(3) == 0	T2
TAB(3) == 0 AND TAB(4) == 0	T3
TAB(4) == 0 AND TAB(5) == 0	T4
TAB(5) == 0 AND TAB(6) == 0	T5
TAB(6) == 0 AND TAB(1) == 0	T6

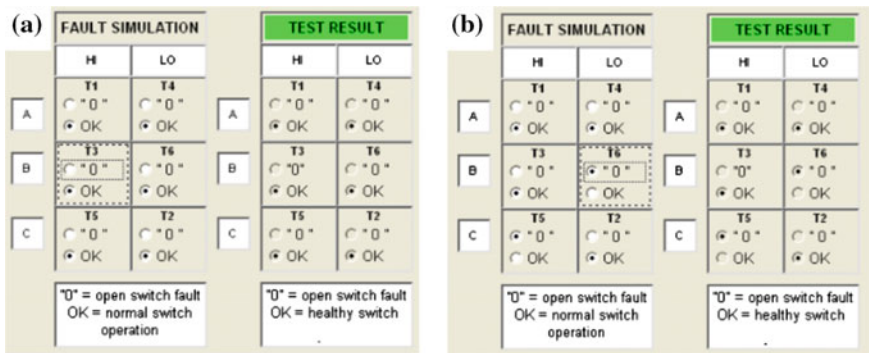


Fig. 11 An example faulty transistor detector performance at the standstill: none of transistors are faulty (a), simulation of lack of conductivity at transistors T5 and T6 (b)

to their faults, then transistor T2 will not conduct current either and hence will be suspected to be faulty, although it can be working one. The above mentioned limitations of this method do not seem to be significant because in each case a drive controller does not allow for further operation and should be repaired or replaced with working one. One should bear in mind that although a detector indicates potentially faulty switches, the problem of their lack of conductivity can be caused by another problem, e.g. no activity of the transistor gate driver.

5 Analysis of Position Sensors Faults Diagnostic Methods in PM BLDCM Drive

5.1 Symptoms of Position Sensors Faults

The rotor position, necessary for the control system to switch the fed motor phases, is frequently determined by discrete rotor position sensors which return digital information (0/1). Thanks to this using only three such sensors in a 3-phase

PM BLDC motor drive, one can determine the rotor position in increments of up to 60 electrical degrees, i.e. determine in which of the 6 sectors there is the rotor. The information about the rotor position can be treated as a word consisting of 3 bits assuming two states. It is important that only 6 out of 8 possible combinations of words make physical sense. The other two do not have a physical explanation and do not occur in an efficient drive (these will be different states depending on whether the sensors are distributed every 60 or 120 electrical degrees).

The sensors can be optical or Hall effect ones, their use slightly increases the cost of a finished motor and introduces the necessity of connecting additional cables. Drive performance is influenced by the precision of their location, presence of interferences in the form of magnetic field disturbances related to the passage of large, alternating currents round sensors and non-zero width of the hysteresis loop (Hall effect sensors), impurities (optical sensors) and also interferences influencing signal wires. Hence it is possible to distinguish accidental changes of signal coding the rotor position and permanent reading of one of the logical states (high or low), regardless of their position angle. The reasons for the latter, among others, encompass no connection or feeding of sensors, mechanical, magnetic or thermal sensor faults, sensor output damage/exceeding output current in the case of open collector outputs.

The use of rotor position sensors is not the only hardware solution applied to determine the rotor position. It is also possible to use absolute or incremental encoders, resolvers, however, these solutions will be more expensive and difficult to use in drives with typical parameters. On the other hand, in some types of drives rotor position sensors are not used, e.g. in PM BLDC high-speed motors in flying models.

The further part will present considerations related to permanent faults of sensors distributed every 120 electrical degrees, leading to incorrect indications of the rotor position. The performance of the rotor position signal (coded as a word) after fault

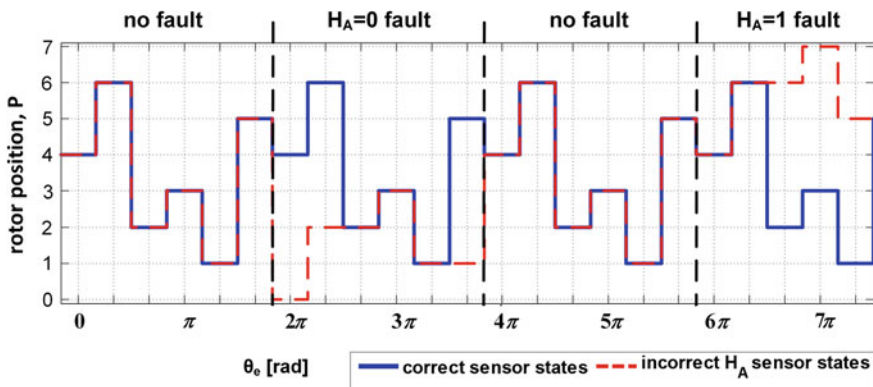


Fig. 12 Waveforms of signal P coding the rotor position, simulated for a non-faulty system in comparison with a system with hypothetical phase A sensors faults ($H_A = 0$, $H_A = 1$)

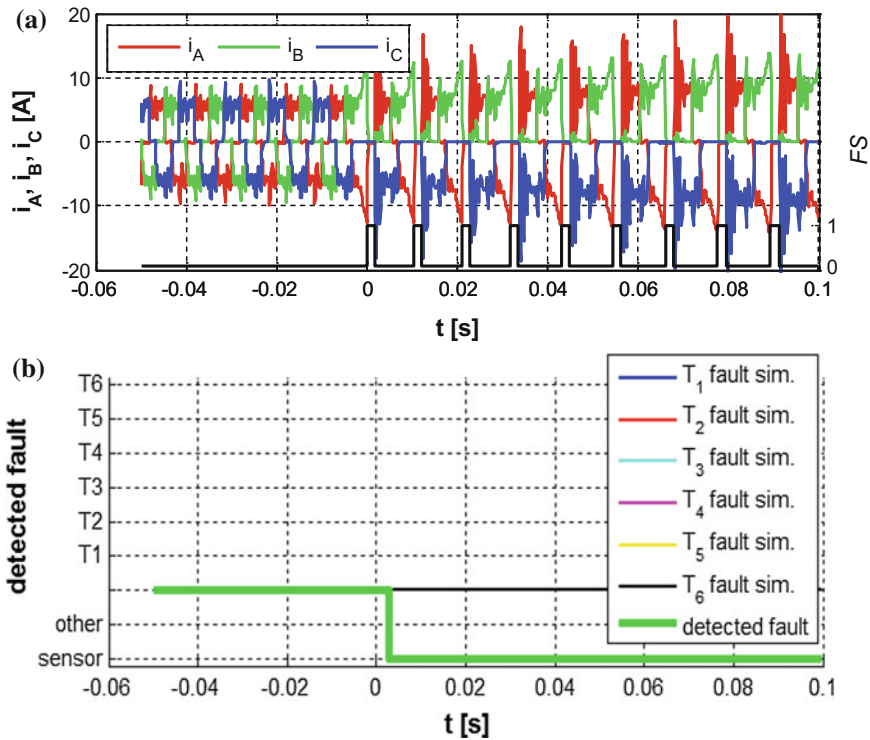


Fig. 13 The detection method of faulty transistors during the fault of the rotor position sensor $H_C = 0$: waveforms of phase currents and wrong combination signal FS (a) and detector reaction result (b)—experimental results

occurrence is presented in Fig. 12 while Fig. 13a shows the waveforms of input currents after the $H_C = 0$ fault occurrence.

5.2 Detection of the Position Sensors Faults

The detection of rotor sensor faults can be performed on the basis of two groups of symptoms. The first group is the direct control of the correctness of signal indications from sensors (whether either of the two positions of undefined significance occurs) and the order of these changes—sector changes cannot follow a random pattern skipping two intermediate positions. These activities do not require large calculation power and usually are simple to implement. The other group focuses on the analysis of the results of using incorrect signals in the controlled drive—the analysis of phase voltages or currents. An advantage of this approach is a uniform

way of acting in detection of various types of abnormal drive operation on the basis of the same set of signals.

The further part of the paper discusses the first approach more extensively [15, 28] due to its easy implementation. The basis of the method of detecting a single fault in the rotor position sensor is the occurrence of the word coding the rotor position which does not have any physical interpretation. For sensors distributed every 120 electrical degrees these are the words “000” and “111”. They are the indicator of abnormalities. They can be detected using a logical function, e.g. according to (8). The next content of the word depends on the number of sensor whose signal is faulty and the direction of the rotational speed, hence it is possible to develop a table of rules for faulty sensor identification [15, 28]. The faulty element is determined on the basis of the rotational speed direction and the subsequent coding word on the falling slope of the *FS* signal (Fig. 14). It should be noted that this method does not need any information about motor parameters to work, the only necessary information is the rotational speed direction and possibly another form of the (8) rule for sensors distributed every 60 electrical degrees. The method can be successfully applied during drive operation and at low rotational speed it has a relatively long identification time of the element. The rotational speed direction can be established on the basis of the actual speed determined using an encoder on the basis of the set speed or rotor position sensors. In the latter case one should make sure that the direction detection is correct also after a permanent fault of one of the sensors [28].

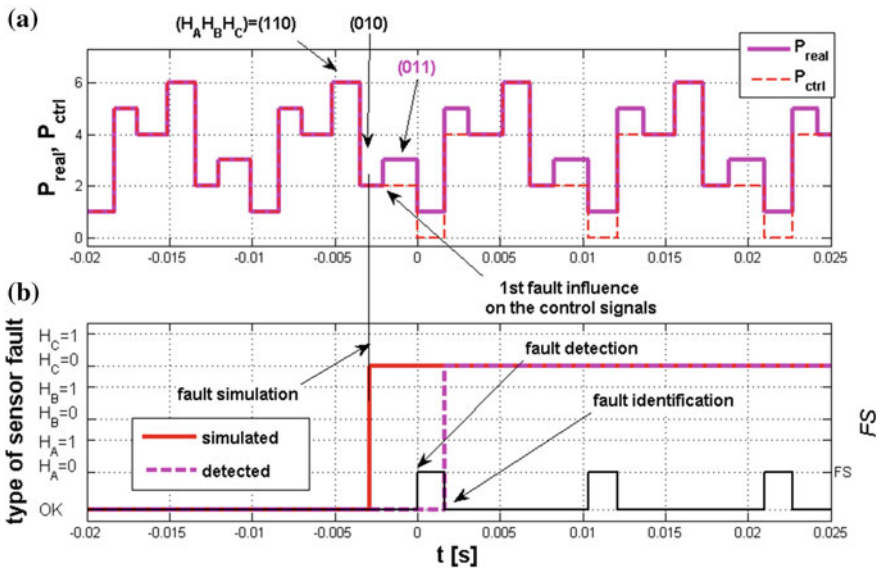


Fig. 14 Operation of the fault detector of the rotor position sensor (experiment—a, b)

$$FS = \left(\bigcap_{k \in \{A,B,C\}} \overline{H_k} \right) \cup \left(\bigcap_{k \in \{A,B,C\}} H_k \right) \quad (8)$$

Because faults in both power stage and information from the rotor position have a significant influence on the phase currents, each detector base on them should distinguish both fault types to avoid false alarms. For instance, the detector described in Sect. 4.2 has information about signal FS , hence should such a fault occur, it shows a special value (assumed value: -2 , in accordance with Fig. 13b) and as a result of detection the procedure of drive reconfiguration is not conducted.

It is possible to consider a justification for fault location because the occurrence of the FS signal is a sufficient premise to use an alternative way of rotor position determination. It is also beneficial that all coding signals of the rotor position are of the same origin to avoid situations in which a signal from a faulty sensor is replaced by another one, e.g. created by control program (however, without consideration for the state of the other non-faulty sensors) and then moments of time with the forbidden coding word ($FS = 1$) occur again.

6 Post-fault Operation of the Drive System

6.1 Drive Operation After Rotor Position Sensors Fault

A conducted fault detection is the first stage of the operation of a fault tolerant system [1]. The next stage is the identification of place and damage degree. It is an important point in situations when similar symptoms occur in various types of faults. Depending on the type of damaged element one should select a fault compensation method to maintain drive characteristics depending on the requirements related to operation length and quality after fault occurrence and detection. The best solution will be such software-hardware topology which will allow to use the drive without any additional limitations. Technically it is possible, however, it is not always economically justified, this is why various control algorithms, requiring the minimum number additional physical systems, are developed.

The identification of a faulty element, whenever possible, should be combined with the determination of the cause for the fault as this can be crucial for the fault compensation process. On the other hand limiting the number of additional hardware elements participating in the fault compensation process is important because each of them can become faulty, stop working and then it will not perform its role.

Another action after the detection and identification of a faulty sensor is software or hardware reconfiguration to ensure operation resistant to selected faults. The solutions described in the literature can be divided into the following groups:

- programmed generation of the missing signal on the basis of two correct signals and information about the time of transitions between particular states (ZOA algorithms [29], using FPGA in [16]),
- reproduction of rotor position with sensorless methods (by software) using available measurements and motor parameters (observers, estimators) [30, 31],
- determination of commutation torques using additional hardware systems (e.g. comparators) with a possible compensation for the delay time in methods based on voltage signals or the electromotive force [32],
- use of an incremental or absolute encoder [29].

When selecting a compensation method from the ones mentioned above, one should pay attention to two issues: the method must be insensitive to the faults of electronic commutator switching devices and it must allow to start the motor from the standstill and its operation at low rotational speeds if they are required.

At the beginning, to check the correctness of the concept, the sensorless method was selected, it determined the rotor position on the basis of filtered interphase voltages (Fig. 15) and the delay introduced by the filter and the method itself was compensated in the software. Figure 16 presents an example of drive operation after detecting abnormalities in the signals coding the rotor position and using an additional system shown in Fig. 15, in comparison with the operation of drive devoid of the possibility of fault tolerant operation (Fig. 13a).

It can be observed that the transition to operation in the sensorless system took place only after completing the detection and identification of the faulty sensor, however, it is possible to conduct this transition at the moment the *FS* signal occurrence (rising slope). Attaching the information about the *FS* signal occurrence (a premise for a sensor fault) to the transistor fault detector allows to distinguish between these two types of faults in a simple way and prevents false alarms as well as unnecessary transitions to the redundancy system. After a selected time period

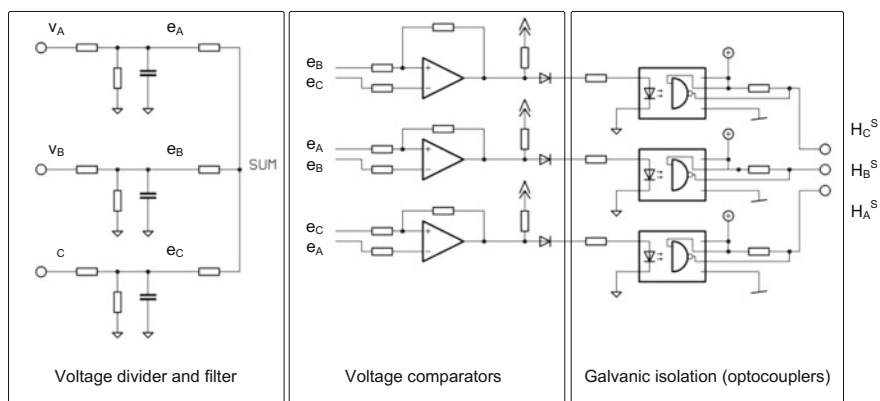


Fig. 15 The system determining substitute coding signals of the rotor position—the simplest form based on filtered phase-phase voltages—experimental version

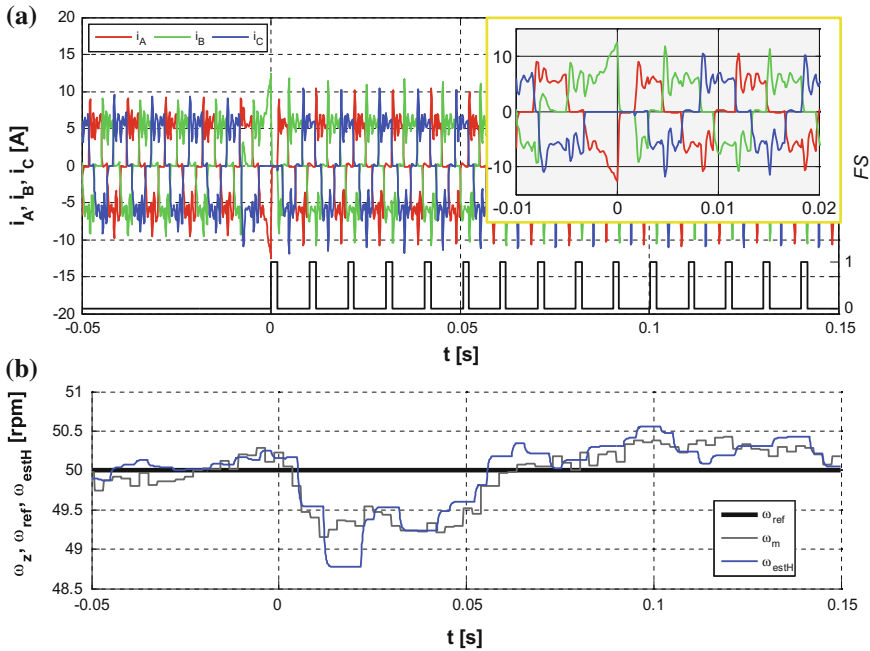


Fig. 16 Sample operation of the drive system after fault detection in the rotor position sensor $H_C = 0$ and using substitute rotor position signals: phase currents waveforms (a) and gearbox shaft speed: referenced, measured and estimated on the basis of H_A, H_B, H_C sensors

after the first occurrence of the FS signal it also seems beneficial to check if this signal still occurs or it only resulted from an accidental interference. Its disappearance then can be used as an opportunity for the determination of rotor position with sensors. The implementation details of the sensorless system can be found in [28].

Figure 16 additionally shows the waveform of the output shaft speed (with a gearbox), estimated on the basis of position sensor states. The correct identification of the faulty element and its elimination allows to continue using this way of rotational speed determination.

Another problem to be solved is the start-up procedure which should be changed after the detection of a faulty sensor. Incorrect indication of the rotor position can disable correct start-up as a result of the lack of coils feeding or in effect of alternate coils feeding making the rotor move in opposite directions (rotor vibration between two neighbouring position sectors). These cases are collated in Fig. 17. A solution to this would be, e.g. start-up in the sensorless system with an initial phase rebalancing the rotor to the set position and next feeding coils in an open loop without coupling until the minimum speed at which the used sensorless method brings positive results is achieved.

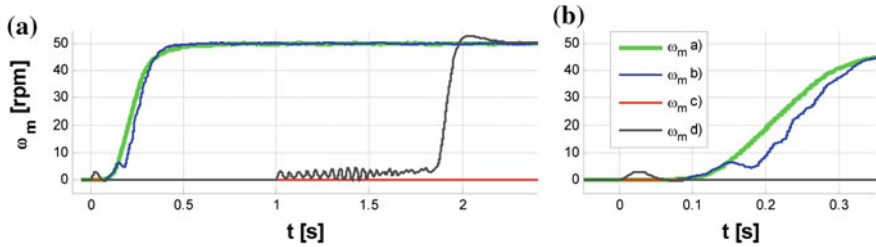


Fig. 17 Comparison of the transmission shaft rotational speeds for start-up cases: with non-faulty rotor position sensors (a), successful start-up regardless of a fault $H_C = 0$ (b), unsuccessful start-up with a fault $H_C = 0$ (c), start-up in the sensorless system d) (with a long rebalancing stage to the set position, as described in the text)

6.2 Drive Operation After Transistors Fault of the Electronic Commutator

After detecting and locating the fault—lack of conductivity of selected transistors—the following actions can be taken:

- ignoring the information about a fault: the simplest and least demanding approach. Depending on the set rotational speed, moments of inertia and drive duty, the rotor can still rotate, however, periodical disappearances of the electromagnetic torque lead to vibrations and in consequence faster wear of bearings. Such a way of acting can also have negative impact on the controlled manufacturing process or the comfort of vehicle use. It is also possible that the drive will not have sufficient spare power (torque) and as result of the duty, it will stop working in a predictable way and react to low value set signals. In the classical control it is also possible that the rotor will remain motionless regardless of attempts to start the motor from the standstill,
- change of the control algorithm without any hardware change in block commutation in a way which will ensure the generation of the electromagnetic torque free from periodical disappearances, with the use of the other non-faulty power commutator transistors. Such approach can also be used in the case of 3-phase motors [33], however, it has the best possible applications in the case of multiphase motors [14],
- hardware redundancy ensuring appropriate control signal redirection. It is necessary to have additional branch (or branches) in the converter or the whole converter module, and also additional switches (transistor, thyristor, relay) which will allow to reconfigure the hardware [34],
- hardware reconfiguration and changes in the control software: literature analysis indicates that this approach is very frequently used. In this approach the phase with a faulty element is disconnected and connected to the neutral power supply point. Such a structure, including its controlling system, was described, e.g. in [35, 36]. To develop this system it will be necessary to have additional

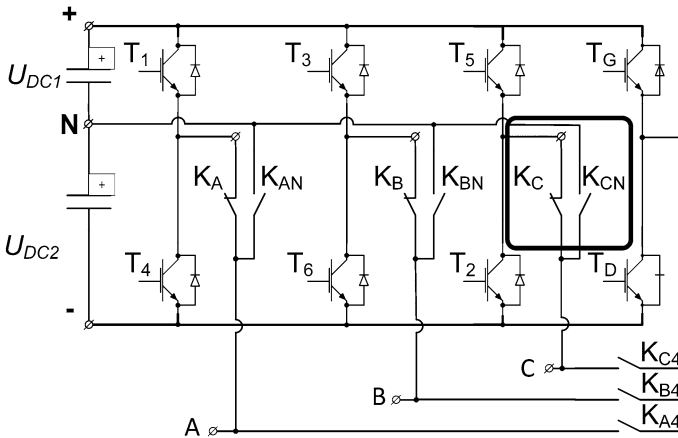


Fig. 18 The proposed topology of the electronic commutator resistant to faults

power-electronic switching devices and be prepared to situations in which some methods of sensorless commutation will require a special approach and small changes necessary to determine the rotor position, e.g. [37]. In this kind of controlling there is the problem of the occurrence of additional electromagnetic torque oscillations [38]. Another version of this solution assumes that an additional converter branch will be connected to the motor neutral point, which requires the introduction of the star coils point.

On the basis of the above analysis the topology of the electronic commutator and the control system (Fig. 18) was proposed, it is a combination of the two presented approaches. Thanks to such configuration it will be possible to compensate for faults occurring in two converter branches: using the redundant converter branch and connecting the motor phase with the neutral power supply point. This solution requires 9 auxiliary connecting devices with their own control system, an additional transistor half-bridge, which will increase the costs, dimensions and complexity level of the whole construction. The selection of additional switches (transistor, thyristor, relay) will depend on the requirements related to time of connection, possibilities of modulated operation of the switch and controlling.

The requirement of the power supply system with an introduced central point can be easy to meet in the case of battery powered drives with an even number of batteries which simultaneously will ensure high stiffness of the central point potential.

Now the experimental set-up has slightly limited abilities in comparison with the one proposed in Fig. 18—it is equipped with a switching relay with K_C and K_{CN} contacts, which allows to study faulty states with reconfiguration of connections in phase C. The selection of a switch was dictated by the simplicity of making the control system and its adjustment, apart from this such a systems seems interesting

from the scientific point of view. A disadvantage of this system is a relatively long time activating the used relay.

After the reconfiguration, although the topology of the power supply system is formally changed, the principle of operation of the PM BLDC motor remains unchanged. Hence it will still be necessary to appropriately feed coils depending on the rotor angular position. The difficulty is that the available voltage vectors have changed, i.e. using four switches one has to force currents in three phases. Moreover the available voltage vectors can change their length, because during the operation the equality of voltages U_{DC1} , U_{DC2} does not always occur on the condensers constituting the central point. Another problem in some applications can be additional oscillations of the electromagnetic torque occurring during commutation and in some sectors of the rotor position. It should be noted that the phase connected to the neutral point is fed by lower voltage, which results in decreasing the maximum rotational speed of the motor and limiting the electromagnetic torque.

If work in the reconfigured system is to last longer than the time necessary to ensure safe completion of the work by a machine/vehicle operator or the additional electromagnetic torque pulsation is not a critical problem, then it is enough to continue operation in the previous control system with regard for input currents regulation using the linear regulator P (PI) or with a hysteresis. Otherwise it is necessary to conduct a detailed analysis of the feeding conditions in various rotor positions and to adjust the control system to them [36, 38].

Sample waveforms of input currents during the diagnostic process are presented in Fig. 19. The use of regulators with a hysteresis allows for a more accurate control of currents, in particular during faulty states it does not allow to exceed the set limits by phase currents.

If the detection system finds lack of conductivity of the electronic commutator transistors in the standstill and there is a need to perform a start-up, then the controllers feeding system of the top transistors (i.e. T_1 , T_3 , T_5) can be limitation, it is built using bootstrap charged capacitors. The reason why is that in a particular case condensers will be unloaded or they will unload during the first motor feed stroke before the rotor shifts to the next position allowing recharging. Such a situation happens when one of the top transistors is connected for a (too) long time.

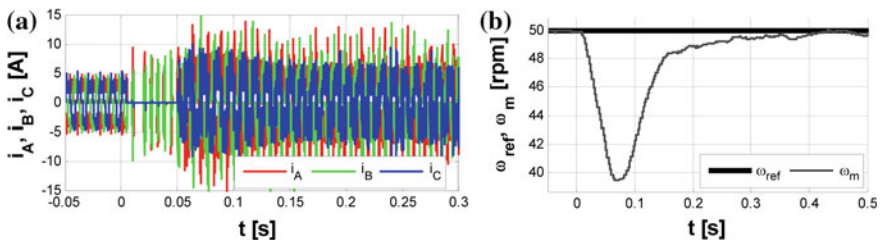


Fig. 19 Waveforms of phase currents (a) and the rotational speed of the gearbox shaft (b), after the occurrence and diagnosing the transistor T_2 fault and starting system reconfiguration activity combined with shifting to hysteresis current control

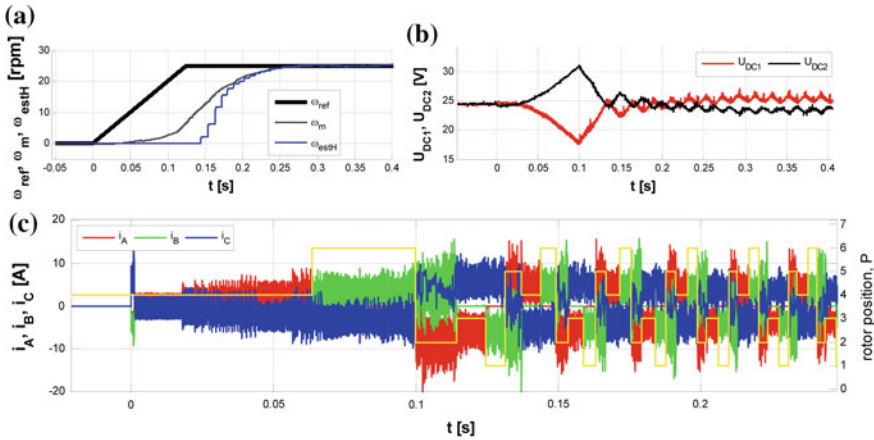


Fig. 20 Start-up procedure in the inverter system with reduced topology: measured and estimated rotational speed of the transmission shaft (a), voltages of condensers constituting the neutral power supply point (b), input currents waveforms and the coded rotor position (c)

Then a solution can be increasing the capacity of these capacitors, using an isolated feeder or programmed limitation of the signal duty cycle in PWM, e.g. up to 99 %, and in the hysteresis control connecting a different combination of transistors from time to time. Before the start-up one can prophylactically connect bottom transistors (at the set-up these are T_4 and T_6 , because T_2 was disconnected) to charge bootstrap condensers.

Sample waveforms registered during the start-up are presented in Fig. 20, in particular Fig. 20b presents voltage fluctuations of the condensers constituting the neutral power supply point, in some cases of the U_{DC1} , U_{DC2} voltage, they even reach the feeding level, while Fig. 20c shows the process of bootstrap capacitors charging when $t = 0$ s.

7 Summary

The use of PM BLDC motor drives in vehicles requires their control and feeding systems to be highly tolerant to faults. Quick detection, location and compensation for these faults allows to continue operation or smooth stopping of the vehicle in a safe place.

The chapter presents selected methods of fault detection on the basis of defined symptoms. The presented experimental research results showed that it is possible to efficiently detect the analysed faults and assess the technical condition of the PM BLDC motor power supply system. Fast identification and location of faults allows to undertake repairs and fault compensation actions (hardware or software reconfiguration or shifting to sensorless operation).

References

1. Isermann R (2006) *Fault-diagnosis systems. An introduction from fault detection to fault tolerance*. Springer, Berlin
2. Estima JO, Freire NMA, Cardoso AJM (2013) Recent advances in fault diagnosis by Park's vector approach. In: *Proceedings of the IEEE workshop on electrical machines design control and diagnosis WEMDCD*, Paris, 11–12 Mar 2013
3. Byoung-Gun P, Kui-Jun L, Rae-Young K, Tae-Sung K, Ji-Su R, Dong-Seok H (2011) Simple fault diagnosis based on operating characteristic of brushless direct-current motor drives. *IEEE Trans Ind Electr* 58(5):1586–1593
4. Song K, Liu W, Luo G, Zhou X (2007) Analysis of current waves and faults recognition in rare earth permanent magnet brushless DC motor. In: *Proceedings of the IEEE international conference on mechatronics and automation*, Harbin, 5–8 Aug 2007
5. Skóra M, Kowalski CT (2015) Influence of selected faults in PM BLDC motor driver on the phase currents spectrum. *Maszyny Elektryczne—Zeszyty Problemowe*, 108:7–13 (in Polish)
6. Benslimane T (2008) A new technique for simultaneous detection of one to two open-switch faults in three phase voltage-inverter-fed PM brushless DC motor drive. *J Electr Eng* 59(2):97–100
7. Fournier E, Picot A, Régnier J, Yamdeu MT, Andréjak JM, Maussion P (2015) Current-based detection of mechanical unbalance in an induction machine using spectral kurtosis with reference. *IEEE Trans Ind Electr* 62(3):1879–1887
8. Tashakori A, Ektesabi M (2013) A simple fault tolerant control system for hall effect sensors failure of BLDC motor. In: *Proceedings of the IEEE conference on industrial electronics and applications ICIEA*, Melbourne, 19–21 June 2013
9. Tashakori A, Ektesabi M (2013) Fault diagnosis of in-wheel BLDC motor drive for electric vehicle application. In: *Proceedings of the IV intelligent vehicles symposium, gold coast*, 23–26 June 2013
10. Awadallah MA, Morcos MM (2006) Automatic diagnosis and location of open-switch fault in brushless DC motor drives using wavelets and neuro-fuzzy systems. *IEEE Trans Energy Conv* 21(1):104–111
11. Eissa MA, Ahmed MS, Darwish RR, Bassiuny AM (2015) Model-based sensor fault detection to brushless DC motor using Luenberger observer. In: *Proceedings of the 7th international conference on modelling, identification and control ICMIC*, Sousse, 18–20 Dec 2015
12. Meagan M, Jayakumar JM, Jaleel A (2012) Fault detection in brushless DC motors using discrete square root filtering and fuzzy logic. In: *Proceedings of the international conference on computing, electronics and electrical technologies*, Kumaracoil, 21–22 Mar 2012
13. Salehifar M, Arashloo RS, Moreno-Equílaz M, Sala V, Romeral L (2014) Fault detection and fault tolerant operation of a five phase PM motor drive using adaptive model identification approach. *IEEE J Emer Select Top Power Electron* 2(2):212–223
14. Salehifar M, Arashloo RS, Moreno-Equílaz M, Sala V, Romeral L (2015) Observer-based open transistor fault diagnosis and fault-tolerant control of five-phase permanent magnet motor drive for application in electric vehicles. *IEEE Trans Power Electronics* 8(1):76–87
15. Scelba G, De Donato G, Pulvirenti M, Capponi FG, Scarcella G (2015) Hall-effect sensor fault detection, identification and compensation in brushless DC drives. In: *Proceedings of the IEEE energy conversion congress and exposition ECCE*, Montreal, 20–24 Sept 2015
16. Sova V, Chalupa J, Grepř R (2015) Fault tolerant BLDC motor control for hall sensors failure. In: *Proceedings of the 21st international conference on automation and computing ICAC*, Glasgow, 11–12 Sept 2015
17. Firmansyah E, Wijaya FD, Aditya WPR, Wicaksono R (2014) Six-step commutation with round robin state machine to alleviate error in hall-effect-sensor reading for BLDC motor control. In: *Proceedings of the international conference on electrical engineering and computer science ICEECS*, Kuta, 24–25 Nov 2014

18. Da Y, Shi X, Krishnamurthy M (2011) Health monitoring, fault diagnosis and failure prognosis techniques for Brushless Permanent Magnet Machines. In: Proceedings of the IEEE vehicle power and propulsion conference VPPC, Chicago, 6–9 Sept 2011
19. Rajagopalan S, Roux W, Habetler TG, Harley RG (2007) Dynamic eccentricity and demagnetized rotor magnet detection in trapezoidal flux (Brushless DC) motors operating under different load conditions. *IEEE Trans Power Electronics* 22(5):2061–2069
20. Tsooulidis S, Safacas A (2014) Side-effects of hall sensors misplacement on BLDC motor drive operation. In: Proceedings of the international conference on electrical machines, Berlin, 2–5 Sept 2014
21. Jun-Hyuk Choi J-H, Park J S, Gu B-G, Kim J-H, Won C-Y (2012) Position estimation and control of BLDC motor for VVA module with unbalanced hall sensors. In: Proceedings of the IEEE international conference on power and energy PECon, Kota Kinabalu, 2–5 Dec 2012
22. Ying M, Zaiping P (2010) A Novel Starting Method of Sensorless BLDC Motors for Electric Vehicles. In: Proceedings of the International Conference on Electrical and Control Engineering ICECE, Wuhan, 25–27 June 2010
23. Wisniewski J, Koczara W (2011) Poles position identification of the permanent magnet motor by the PIPCRM combined with zero voltage vector. In: Proceedings of the IEEE international symposium on industrial electronics ISIE, Gdansk, 27–30 June 2011
24. Boldea I, Nasar SA (2005) Electric drives. CR Press, New York
25. Skóra M (2015) Analysis of influence of selected faults on PM BLDC motor drive in supply system with external voltage regulator. Simulation research. *Scientific Papers of the Institute of Electrical Machines, Drives and Measurements of the Wrocław University of Technology. Stud Res* 35:127–139 (in Polish)
26. Meingue F (2012) Fault-tolerant permanent-magnet synchronous machine drives. Fault detection and isolation, control reconfiguration and design considerations. PhD dissertation, Université Libre de Bruxelles
27. Freire NMA, Estima JO, Cardoso AJM (2014) A new approach for current sensor fault diagnosis in PMSG drives for wind energy conversion systems. *IEEE Trans Ind Appl* 2(2):1206–1214
28. Skóra M, Kowalski CT (2015) The influence of sensor faults on PM BLDC motor drive. In: Proceedings of the 18th international conference on electrical drives and power electronics EDPE, The High Tatras, 21–23 Sept 2015
29. Harke MC, De Donato G, Capponi FG, Tesch TR, Lorenz RD (2008) Implementation issues and performance evaluation of sinusoidal, surface-mounted PM machine drives with hall-effect position sensors and a vector-tracking observer. *IEEE Trans Ind Appl* 44(1):161–173
30. Scelba G, Scarella G, De Donato G, Giulii Capponi F, Bonaccorso F (2014) Fault tolerant rotor position and velocity estimation using binary hall-effect sensors for low cost vector control drives. *IEEE Trans Ind Appl* 50(5):3403–3413
31. Kim Tae-Hyung, Ehsani M (2004) Sensorless control of the BLDC motors from near-zero to high speeds. *IEEE Trans Power Electronics* 19(6):1635–1645
32. Bist V, Singh B (2014) Power factor correction in sensorless BLDC motor drive. In: Proceedings of the 6th India international conference on power electronics IICPE, Kurukshetra, 8–10 Dec 2014
33. Aghili F (2011) Fault-tolerant torque control of BLDC motors. *IEEE Trans Power Electronics* 26(2):355–363
34. Errabelli RR, Mutschler P (2012) Fault-tolerant voltage source inverter for permanent magnet drives. *IEEE Trans Power Electronics* 27(2):500–508
35. Byoung-kuk L, Tae-Hyung K, Ehsani M (2003) On the feasibility of four-switch three-phase BLDC motor drives for low cost commercial applications: topology and control. *IEEE Trans Power Electronics* 18(1):164–172
36. Ozturk SB, Alexander WA, Toliyat HA (2010) Direct torque control of four-switch brushless DC motor with non-sinusoidal back EMF. *IEEE Trans Power Electronics* 25(2):263–271

37. Halvaei Niasar A, Moghbelli H, Vahedi A (2008) A low-cost sensorless control for reduced-parts, brushless DC motor drives. In: Proceedings of the IEEE international symposium on industrial electronics ISIE, Cambridge, 30 June–2 July 2008
38. Masmoudi M, Badi BE, Masmoudi A (2014) DTC of B4-inverter-fed BLDC motor drives with reduced torque ripple during sector-to-sector commutations. *IEEE Trans Power Electr* 29 (9):4855–4865

Part III
Design and Control of Power Converters

Advanced Control Methods of DC/AC and AC/DC Power Converters—Look-Up Table and Predictive Algorithms

A. Godlewska, R. Grodzki, P. Falkowski, M. Korzeniewski,
K. Kulikowski and A. Sikorski

Abstract This chapter is devoted to a modern look-up table and predictive control methods of three phase power electronic converters. The authors consider voltage source converters in two and three level configurations as well as a two level current source rectifier. Some of the methods concern DC/AC inverter fed induction and PMSM motors. The other methods described in this chapter are dedicated to the control of the AC/DC rectifier working as an Active Front End of an AC/DC/AC converter. The authors focus on the methods with a non-linear look-up table and predictive control due to their excellent dynamic properties (limited only by the physical parameters of controlled systems such as the value of the DC voltage, grid inductance or AC motor leakage inductance). Moreover, non-linear methods, especially the predictive ones, provide very good quality of control in steady states, i.e. lack of active and reactive power steady-state error (AC/DC) or torque error (in the case of DC/AC converters). Look-up table methods have been taken into consideration as they also ensure the above advantages in a relatively short calculation time. The selected look-up table and predictive methods are proposed for both 2-level and 3-level converters. All the described control methods have been illustrated by simulation results and laboratory tests confirming their characteristics.

Keywords DC/AC converters · AC/DC converters · Multilevel converters · Predictive control · Power control · Direct torque control

Abbreviation

CSI	Current source inverter
DPC	Direct power control
DPC-3V	Direct power control with 3-vectors modulation
DTC-3L-3A	Direct torque control—3 level 3 areas
DTC-3V	Direct torque control with 3-vectors modulation
DTC-SVM	Direct torque control with space vector modulation

A. Godlewska · R. Grodzki (✉) · P. Falkowski · M. Korzeniewski · K. Kulikowski · A. Sikorski
Białystok University of Technology, Wiejska 45D, 15-351 Białystok, Poland
e-mail: r.grodzki@we.pb.edu.pl

FCS-MPC	Finite control set model predictive control
FOC	Field oriented control
FS PPC	Finite set predictive power control
ICS-MPC	Infinite control set model predictive control
NPC Converter	Neutral point clamped converter
PCi ₂ u _c	Predictive current and capacitor voltage control
PCi-AD	Predictive current control of an AC/DC inverter with active damping
PWM	Pulse width modulation
SVM	Space vector modulation
THD	Total harmonic distortion
VOC	Voltage oriented control
VSR	Voltage source rectifier

1 Introduction

AC/DC/AC converters (back-to-back converters) constitute essential power electronics elements characterized by ever increasing application areas. AC/DC/AC converters, as a whole, connect induction motors with the grid and are used in adjustable drive systems and in renewable energy sources where they connect wind or water turbines to the grid. As separate units, AC/DC and DC/AC converters are used to connect the grid with other renewable energy sources or AC drives fed by a DC source, respectively. In recent years a growing interest has been observed in AC/DC converters connecting DC voltage systems to the grid. This is due to their advantages such as availability of bidirectional power flow and unity power factor. AC/DC converters are widely used especially to connect different types of renewable energy sources, such as photovoltaic cells, fuel cells, wind generators, etc. to the grid [1–4].

Depending on their applications, AC/DC converters are expected to perform numerous and specific functions. For renewable energy sources, the main requirement is to attain practically sinusoidal shape of currents, i.e. low THD values while, for active filters, the requirement involves capability of high dynamic current changes. The properties of AC/DC converters either in steady or transient states are determined by both power circuit components and the control method used. Principally, there are three groups of strategies used to control converters. They include: VOC (explanation of abbreviations used in this chapter in Appendix) methods with linear PI controllers and space vector modulation (SVM or PWM) [5–7]; DPC methods with linear (PI-VOC) [8] and nonlinear controllers [9] and finally predictive control methods [10–13].

Linear control methods, i.e. VOC [14, 15], DPC with SVM/PWM [16, 17] are characterized by good current quality (low THD_i for input currents [18–20]) and

constant switching frequency that makes it possible to apply LCL input filters. LCL filters, in comparison to L filters, have lower inductance, which makes them cheaper and smaller in size. Additional filtering capacities increase distortions in transient states, which, as a result, decreases the rate of current changes.

The control methods based on PWM/SVM modulators require the use of a dead time correction unit whose complexity has an influence on correction quality. Moreover, application of SVM/PWM modulators results in slower current changes after a step change of the current set value. This disadvantage is caused by PI controllers whose integral part produces delays resulting from the non-zero regulator time constant. The time delays in transient states also result from the fact that the modulator, during one sampling time T_s , always uses full switching sequence of three voltage vectors. However, in transient states the use of only one or two vectors is desirable. Yet, modulation rules impose the use of three-vector pattern, which lengthens the duration of transient response. The above is the main disadvantage of linear control methods (with SVM/PWM) in comparison to nonlinear algorithms. Both nonlinear and predictive control methods are characterized by the use of exclusively one converter voltage vector during a single sampling period.

Nonlinear controllers make use of direct control of converter transistors (without SVM/PWM) [21, 22]. Converter states in DPC methods are chosen from a look-up table based on an instantaneous error between set and real value of the active and reactive power or the real value of current vector components proportional to these powers. To achieve satisfactory current pulsations relatively short sampling times ($<25 \mu\text{s}$) are required. This, in turn, makes it necessary to apply faster and more expensive processor controllers. Moreover, nonlinear control is typically characterized by variable switching frequency that, in practice, prevents using LCL input filters effectively.

Predictive control based on Model Predictive Control (MPC) [11–13, 23] is a competitive solution to both linear and nonlinear control methods. There are a number of algorithms that have been known as finite control set model predictive control (FCS-MPC) [8, 24–26] and infinite control set model predictive control (ICS-MPC) [27–30]. The FCS-MPC involves calculations of expected current vector components (proportional to the active and reactive powers) depending on switched converter transistors and selection of such a configuration that fulfils the assumed optimization criterion. A limited number of available voltage vectors makes the control error minimization possible but not reduce it to zero. In order to improve the quality of input current (power) the authors have proposed modulation between selected two active and a zero voltage vectors during one sampling period [31, 32].

In the ICS-MPC method to calculate a set voltage vector uses a mathematical model and predicted current vector components that are proportional to active and reactive powers. The applied vector (reproduced by SVM/PWM modulator) ensures full compensation of the control error [27, 33–35]. However, this indirect current control causes inaccuracies that are typical of linear control methods. The accuracy of predictive methods is highly dependent on the model parameters.

In papers [9, 36] converter voltage vectors are defined in the table and chosen on the basis of the grid voltage vector angle or on the virtual flux vector. Thereafter, on the basis of a grid-converter model and predicted active and reactive powers for chosen voltage vectors in the next sampling step are calculated. The switching times are calculated on the basis of cost function derivative compared to zero. This solution enables minimal current (power) pulsations and constant average switching frequency of transistors. A certain constraint of the method is that the vector table has been optimized for steady states only, whereas during step change of the reference current value, the control algorithm does not use optimal (“dynamic”) vectors, which lengthens the response time during transient states.

The AC/DC converter control methods discussed above have their counterparts for DC/AC inverter control methods. There are three main groups of strategies used to control inverters, namely FOC methods with linear PI controllers and space vector modulation (SVM or PWM) [37]; direct torque and flux control methods with linear (DTC-SVM) [38–40] and nonlinear controllers (DTC) [41] and also predictive control methods [42–45]. The FOC method has similar advantages and disadvantages characteristic of the VOC method for controlling AC/DC converters. The method of direct flux and torque control with a switching table (DTC-ST) proposed by Takahashi and Noguchi [41] in 1985 has been used and developed up to now. In the literature on the subject the following problems are discussed:

- hexagonal flux vector trajectory and distorted stator current at low motor speed,
- motor start-up problems e.g. no possibility of motor “excitation” at the torque set value equal zero,
- variable switching frequency,
- variable torque ripples.

A characteristic feature of the conventional DTC-ST method is that in the steady state three vectors are used (two active and zero vectors) just as in the standard PWM. The only difference lies in the fact that in the standard PWM the switching processes occur in a determined sequence, while in the DTC-ST method, the sequence depends on torque and flux errors. As a result, the DTC method should ensure both the minimization of ripples as well as the switching frequency. These features are needed to improve the drive’s technical properties by decreasing speed pulsations/torque ripples and also operating cost by reducing switching frequency which affects power dissipation and inverter efficiency. The main way to improve the DTC method involves the torque pulsation decrease keeping the sampling time T_s and transistor switching frequency unchanged [46, 47]. Constant switching frequency is useful when passive filters are applied on the inverter output. The above is carried out in two ways. One method consists in the use of adequate torque and flux controller structures (using linear controllers) which, in the final stage, take advantage of space voltage modulation. These algorithms are called DTC-SVM, due to the fact that the used torque and flux PI controllers, have a longer response time to the torque step changes, although the complex controller systems [48] bring their properties closer to the DTC method, which applies the nonlinear controllers.

The other method involves improving the classical conception of the nonlinear (hysteresis) torque and flux controllers by an introduction of additional modulation algorithms at sampling time T_s [49–51]. For this purpose additional triangular signals modulating the torque and flux errors are used to decrease pulsations simultaneously increasing the inverter switching frequency. The most advanced algorithms use different complication levels of predictive controllers [52, 53]. Predictive algorithms require the knowledge of motor parameters that can be best identified on-line. The algorithms are sensitive to parameter changes. Prediction includes accurate calculations of controlled parameters (flux and torque) [54] as well as determination of their values in one or several steps ahead [55–57].

Greater possibilities of solving DTC-ST problems are offered by multi-level converters, in which a higher number of voltage vectors enable the implementation of various control algorithms [58].

In steady states and for low current frequencies, the main issue is the low content of AC/DC/AC current/voltage higher harmonics that arise from the industry standards and other requirements that must be met. The above applies to both linking high power renewable energy sources to the grid and the active power filtering (APF). Typically, in such cases, the converter construction requires the use of high voltage structures ranging from several to tens of kilovolts. Thus, the use of multi-level converters is essential [59–61]. Three level NPC converters due to their relatively low cost, simple structure and uncomplicated DC link voltage balancing methods [62–64] appear to be the most commonly used [59, 65, 66]. Replacing a two level converter by its three level equivalent enables us to reduce the du/dt voltage edges, decrease switching power losses and hence increase their efficiency [1]. On the other hand, the number of simultaneously conducting semiconductors is twice as large for three level converters as in the case of two level ones. This leads to an increase of conducting power losses. Therefore, it is difficult to state which converters exhibit lower power losses, as they generally depend on the operating conditions, switching frequency as well as the grid reactor parameters [67, 68].

The use of three level converters with FS PPC methods allow us to increase the control quality that results from a higher number of available converter voltage vectors. On the other hand, this solution requires a significantly larger number of calculations that impose the use of faster and more expensive processors. A compromise solution, especially for multilevel converters, is the use of nonlinear look up table methods (nonlinear DPC) [69, 70]. The DPC methods are modelled on the DTC methods, which are widely used in power drives.

Inverters fed by current source (CSI) are competitive to voltage source inverter (VSI). Three-phase current source rectifier (AC/DC converter) has many advantages, such as providing sinusoidal grid currents with unity power factor and enabling feeding energy back to the mains. Moreover, it produces DC output voltage that can be lower than AC input voltage, in contrast to more common voltage source rectifier (VSR). This is an important feature that makes it possible to

eliminate the buck converter or transformer in the case of low voltage load or variable speed drive. In addition, CSR ensures low electromagnetic interference (EMI) and offers better power density than VSR, caused by low dv/dt [71].

The advantages mentioned above are the reasons why CSR are becoming more and more popular in industry. The topology AC/DC current converter includes an LC filter (L represents grid inductance) on the input side. It can cause oscillations and enhance higher harmonics of grid currents. Harmonics damping is very complicated, but it is necessary because of the risk of low efficiency. Recent investigations have focused on developing alternative control strategies to improve the quality of waveforms or improve efficiency and power density.

First control algorithms designed for CSR were based on linear control with PWM modulators [72]. Obtaining waveforms with low THD became possible by adding linearization and decoupling [73]. Another solution is active damping that weakens higher harmonics influence of LC filter [74–77]. Moreover, good performance is provided by the algorithm with Selective Harmonic Elimination (SHE), which is a different type of modulation [78].

An alternative way of control is nonlinear control. Direct Power Control (DPC), originally designed for VSR, has been adapted for CSR [79]. The method has been developed to reduce resonance harmonics in the grid current [80, 81].

Predictive control for CSR is shown in [82] and [83]. Cost function has two components; the first one is instantaneous reactive power and the other is the error between load current and its reference. To reduce switching frequency an algorithm with active damping has been developed [84]. Another solution is based on different cost function [85], where the first component is a grid current error. An interesting method for a voltage source rectifier with LCL filter is presented in [86]. It provides error minimization for three variables, namely capacitor voltage, grid current and inverter current.

This chapter is devoted to a modern look-up table and predictive control methods of three phase AC/DC converters as well as DC/AC converters. Inverters supply induction (IM) and synchronous PMSM motors.

The introductory section describes advantages and disadvantages of various current (power) control methods of an AC/DC converter as well as the torque and flux control methods of a DC/AC converter. The authors focus on the methods with a non-linear look-up table and predictive control due to their excellent dynamic properties (limited only by the physical parameters of controlled systems such as the value of the DC voltage, grid inductance or AC motor leakage inductance). Moreover, non-linear methods, especially the predictive ones, provide very good quality of control in steady states, i.e. lack of active and reactive power steady-state error (AC/DC) or torque error (in the case of DC/AC converters). Look-up table methods are also taken into consideration due to providing the above advantages in a relatively short calculation time that results in lower hardware requirements (less

expensive microprocessors can be used in the control system). The selected look-up table and predictive methods are proposed for both 2-level and 3-level converters.

Section 2 presents basic mathematical models of voltage source converters (in both 2-level and 3-level configuration) and a 2-level current source rectifier cooperating with the grid and AC motors. In addition, there is an explanation of the dependences describing the direction and rate of current vector change (both the grid and IM stator current vector) caused by each voltage vector of the converter. This theory is used in all of the proposed advanced control methods.

Section 3 is concerned with analysis and synthesis of look-up table direct torque and flux control method of the DC/AC converter fed induction motor as well as the direct power control method for three level converter cooperating with the grid. DTC-3L-3A (Direct Torque Control—3 Level 3 Areas) is characterized by a novel division of the error area into three sectors, which makes it possible to control motor torque and flux with reduced switching frequency in comparison to the standard DTC method. The DTC-3L-3A control method has its counterpart for AC/DC rectifier called DPC-3L-3A (Direct Power Control 3 Level 3 areas). It is also described in this section. Finally, the section presents the DC-link voltage balancing algorithm for a 3-level converter.

Section 4 describes selected Model Predictive Control methods for 2-level AC/DC and DC/AC converters. DPC-3V and DTC-3V belong to ICS-MPC methods. They are based on current (torque and flux in the case of DTC-3V) error vector minimization criteria. Analysis of all the possible locations of the current (torque and flux) error vector in the next control step is the basis for the optimal voltage vector selection and application time calculation in order to compensate for the error vector. The converter output voltage vector is reproduced by SVM that provides all the advantages typical to linear methods, i.e. constant switching frequency, low grid current (torque) ripples. The proposed algorithms minimize the error vector for each and every state of the system. In transient states, they provide maximum dynamics comparable to the fastest nonlinear control methods.

In the next part of this section a modern FCS-MPC method of the voltage source rectifier with input LCL filter is presented. Equations describing voltages and currents are used to predict the direction and rate of changes of converter current and capacitor voltage vectors. Predicted values are used to define errors for every output voltage vector, which allows us to find the minimal value of the cost function. It results in choosing an optimal voltage vector and error minimization.

The last algorithm discussed in Sect. 4 is dedicated to the current source rectifier. It is based on the cost function minimization. Basing on the predicted values of the grid current and the capacitor voltage, the algorithm chooses a proper current vector. The great advantage of the method is grid current harmonics reduction combined with a low sample time.

All the described control methods are illustrated by the results of simulation and laboratory tests confirming their properties.

2 Basic Theory of 3-Phase Converters Fed AC Motors and 3-Phase Rectifiers Cooperating with the Grid

2.1 Mathematical Model of 3-Phase Voltage Source Converter

Figure 1 shows the main VSC circuit. The most commonly used topology of VSC is the three phase bridge. Each leg of the converter consists of two transistor switches with freewheeling diodes placed in parallel.

Converter output voltage can be described as a complex space vector. Active vectors correspond to phase voltage in relation 1/3 and 2/3 to the DC-link voltage U_{DC} . Zero vectors apply zero voltage at the AC-side of the converter because all three branches are connected to positive or negative DC-link bus. There are eight possible combinations of the switches. They can be described by the following equation:

$$u = \begin{cases} \frac{2}{3} U_{DC} e^{j(n-1)\frac{\pi}{3}} & \text{for } n = \{1, 2, 3, 4, 5, 6\} \\ "0" & \text{for } n = \{0, 7\} \end{cases} \quad (2.1)$$

In the three-level structure of VSC (Fig. 1b) one of the three electrical potentials (+ U_{DC} , 0 or $-U_{DC}$) may appear at each of the phase outputs. Owing to the choice of three possible states at each of the three independent outputs, the output voltages of the converter can be determined in $3^3 = 27$ valid combinations. Complex 3-level voltage vector can be expressed as:

$$u = \begin{cases} \frac{2}{3} U_{DC} \cdot e^{j(n-21)\frac{\pi}{3}}, & \text{for } n = \{21, 22, \dots, 26\} \\ \frac{\sqrt{3}}{3} U_{DC} \cdot e^{j(n-15)\frac{\pi}{3}}, & \text{for } n = \{15, 16, \dots, 20\} \\ \frac{1}{3} U_{DC} \cdot e^{j(n-3)\frac{\pi}{3}}, & \text{for } n = \{3, 4, \dots, 14\} \\ "0", & \text{for } n = \{0, 1, 2\} \end{cases} \quad (2.2)$$

Graphic representation of 2-level and 3-level converter output vectors is shown in Fig. 2.

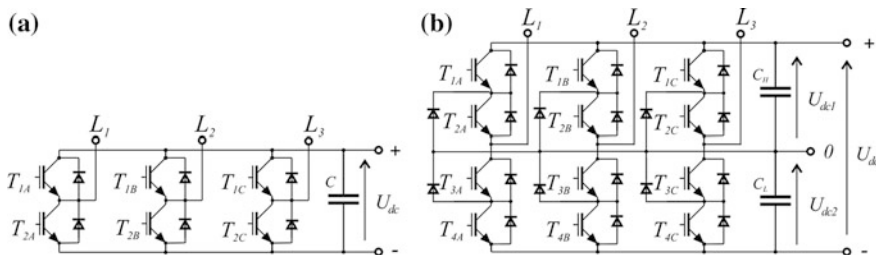


Fig. 1 Schematic diagrams of 2-level (a) and 3-level (b) VSC

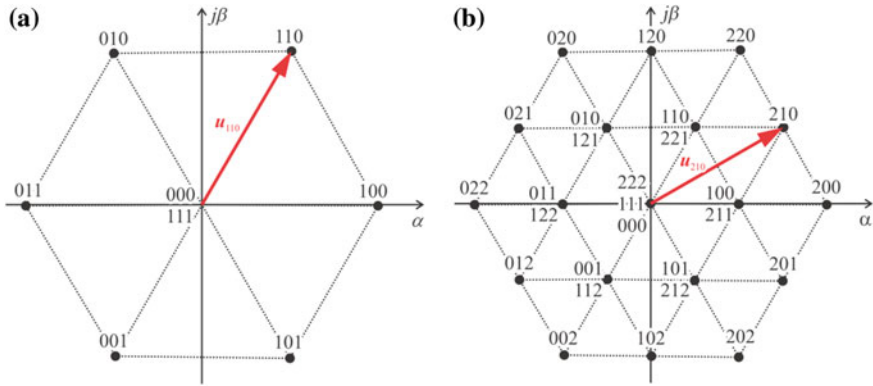


Fig. 2 Graphic representation of converter voltage vectors in $\alpha\beta$ reference frame for 2-level (a) and 3-level (b) converters

2.2 Mathematical Model of an AC/DC Converter Co-operating with the Supply Grid

2.2.1 Model with L Input Filter

A three-phase AC/DC converter circuit co-operating with a 3-phase supply grid is shown in Fig. 3.

The vector Eq. (2.3) in the stationary $\alpha\beta$ reference frame gives a clear description of the configuration in Fig. 3:

$$Ee^{j\omega_s t} = L \frac{d}{dt} \mathbf{i}_{\alpha\beta} + \mathbf{u}_{\alpha\beta} \tag{2.3}$$

where

- $\mathbf{i}_{\alpha\beta}$ grid current vector in $\alpha\beta$ rotating reference frame,
- L grid reactor inductance,
- $Ee^{j\omega_s t}$ grid voltage vector,
- $\mathbf{u}_{\alpha\beta}$ converter voltage vector given by (2.1) or (2.2) for 2-level and 3-level converter respectively.

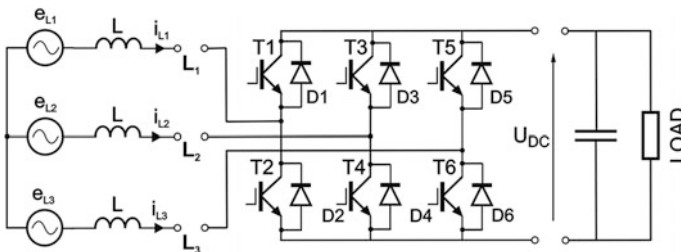


Fig. 3 Power configuration of AC/DC converter

Equation (2.3) can be transformed into an xy reference frame rotating with the grid voltage pulsation:

$$e_{xy} = L \frac{d}{dt} i_{xy} + j\omega_g L i_{xy} + u_{\alpha\beta} e^{-j\omega_g t} \tag{2.4}$$

From Eq. (2.4) it is possible to obtain both the vector proportional to the derivative vectors of the grid current (2.5) and the derivative vector of the grid current vector (2.6) [87]:

$$L \frac{d}{dt} i_{xy} = d_{guxxx} = e_{xy} - j\omega_g L i_{xy} - u_{xy} = u^* - u_{xy} \tag{2.5}$$

$$d_{gixxx} = \frac{d}{dt} i_{xy} = \frac{1}{L} d_{guxxx} \tag{2.6}$$

where the “xxx” index is the number of the converter voltage vector, for example, 110, 010, 010, etc.

Figure 4 shows a graphical form of Eqs. (2.5) and (2.6). The current derivative vectors d_{gixxx} describe both the direction and rate of change of the current vector caused by switching on an appropriate voltage vector of the converter.

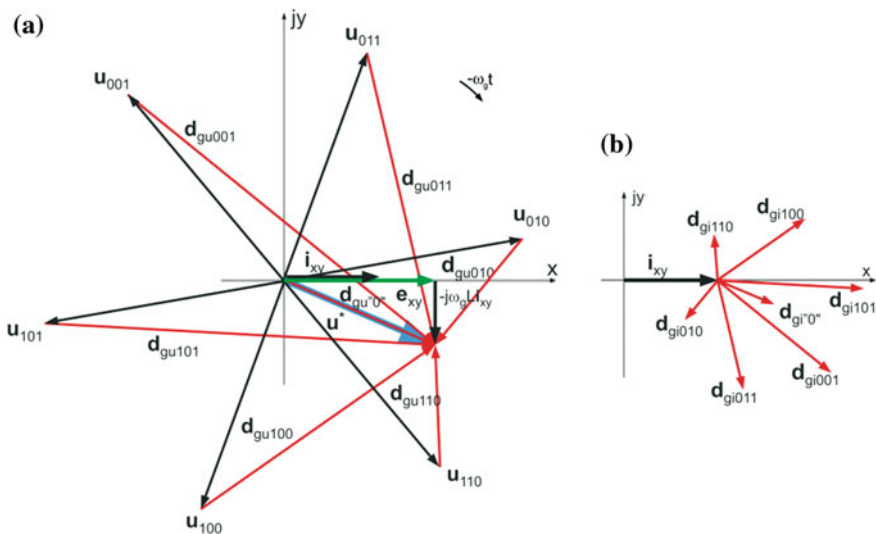


Fig. 4 Vectors proportional to vector derivatives of current (a) and their influence on current vector for 2-level converter (b)

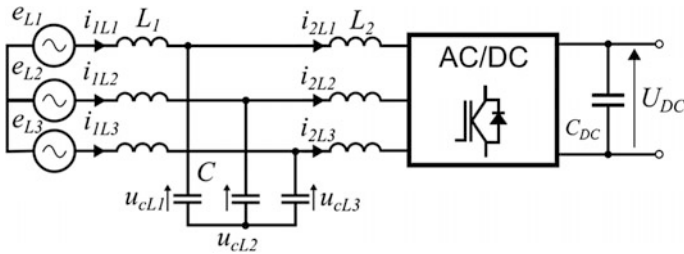


Fig. 5 Power configuration of AC/DC converter with LCL input filter

2.2.2 Model with LCL Input Filter

Figure 5 shows the power configuration of AC/DC converter with the LCL input filter.

Equation (2.7) in stationary $\alpha\beta$ reference frame give a clear description of the configuration from Fig. 5:

$$\begin{cases} \mathbf{e}_{\alpha\beta} = L_1 \frac{d}{dt} \mathbf{i}_{1\alpha\beta} + \mathbf{u}_{c\alpha\beta} \\ \mathbf{u}_{c\alpha\beta} = L_2 \frac{d}{dt} \mathbf{i}_{2\alpha\beta} + \mathbf{u}_{\alpha\beta} \\ C \frac{d}{dt} \mathbf{u}_{c\alpha\beta} = \mathbf{i}_{1\alpha\beta} - \mathbf{i}_{2\alpha\beta} \end{cases} \quad (2.7)$$

where

- $\mathbf{e}_{\alpha\beta}$ grid voltage vector in stationary $\alpha\beta$ reference frame,
- $\mathbf{i}_{1\alpha\beta}$ grid current vector,
- $\mathbf{i}_{2\alpha\beta}$ converter current vector,
- $\mathbf{u}_{c\alpha\beta}$ voltage vector on the capacitors of input LCL filter,
- $\mathbf{u}_{\alpha\beta}$ converter voltage vector,
- L_1 input filter inductance connected to the grid,
- L_2 input filter inductance connected to the converter,
- C capacitance of the input filter capacitors.

Equation (2.7) can be transformed into an xy reference frame rotating with grid voltage pulsation:

$$\mathbf{e}_{xy} = L_1 \frac{d}{dt} \mathbf{i}_{1xy} + j\omega_g L_1 \mathbf{i}_{1xy} + \mathbf{u}_{cxy} \quad (2.8)$$

$$\mathbf{u}_{cxy} = L_2 \frac{d}{dt} \mathbf{i}_{2xy} + j\omega_g L_2 \mathbf{i}_{2xy} + \mathbf{u}_{xy} \quad (2.9)$$

$$C \frac{d}{dt} \mathbf{u}_{cxy} = \mathbf{i}_{1xy} - \mathbf{i}_{2xy} - j\omega_g C \mathbf{u}_{cxy} \quad (2.10)$$

The equivalent circuit of the AC/DC converter with LCL input filter is shown in Fig. 6.

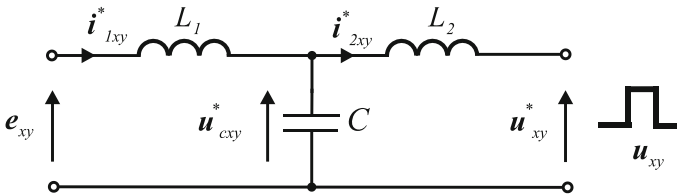


Fig. 6 Equivalent circuit of AC/DC converter with LCL input filter

Where u_{xy}^* is the set value of the converter voltage vector, u_{cxy}^* is the set value of the capacitor voltage vector. The “set value” means the 1st harmonic of u_{xy} and u_{cxy} respectively, which can be obtained from:

$$u_{xy}^* = u_{cxy}^* - j\omega_g L_2 i_{2xy}^* \tag{2.11}$$

$$u_{cxy}^* = e_{xy} - j\omega_g L_1 i_{1xy}^* \tag{2.12}$$

Graphical form of Eqs. (2.11) and (2.12) is shown in Fig. 7.

Vector d_{2u} is proportional to the derivative of converter current derivative $\frac{d}{dt}i_{2xy}$ and can be expressed by the following equation:

$$L_2 \frac{d}{dt}i_{2xy} = u_{xy}^* - u_{xy} = d_{2u} \tag{2.13}$$

where

u_{xy} is the converter voltage vector,

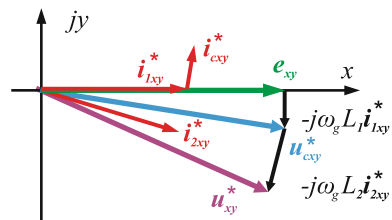
d_{2u} is the vector proportional to the current vector derivative.

Using Eq. (2.13) we can define the converter current derivative vector as:

$$d_{2i} = \frac{d}{dt}i_{2xy} = \frac{1}{L_2}d_{2u} \tag{2.14}$$

Graphical form of Eq. (2.14) is shown in Fig. 8.

Fig. 7 Graphical interpretation of the converter 1st harmonic voltage vector



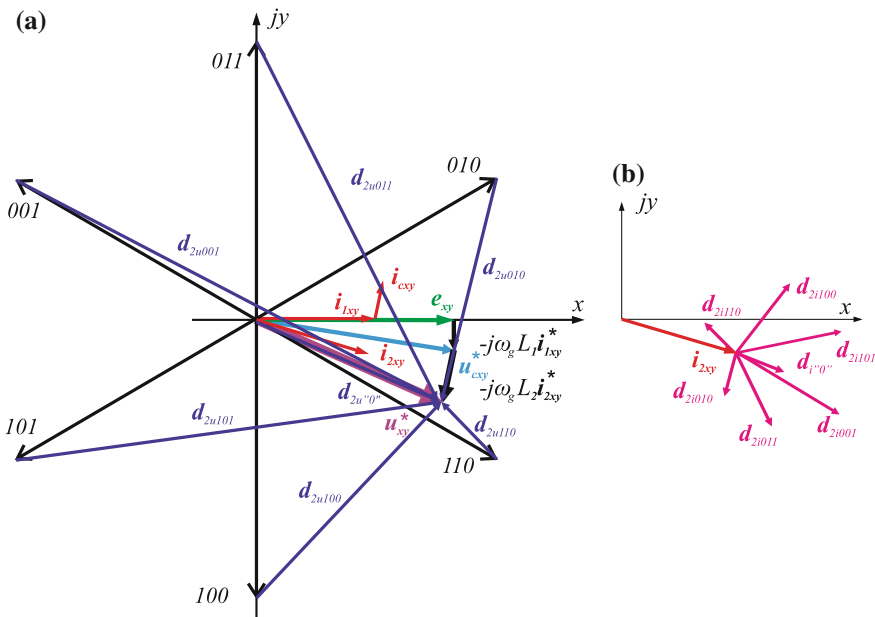


Fig. 8 Vectors proportional to vector derivatives of converter current and their influence on current vector (converter with LCL input filter)

2.3 Mathematical Model of a DC/AC Converter Fed Induction Motor

The induction motor can be described by the following equations in dq reference frame [88]:

$$\mathbf{u}_{sdq} = \mathbf{i}_{sdq}R_s + \frac{d}{dt}\Psi_{sdq} + j\omega_o\Psi_{sdq} \tag{2.15}$$

$$\mathbf{u}'_{rdq} = \mathbf{i}'_{rdq}R_r + \frac{d}{dt}\Psi'_{rdq} + j(\omega_o - p_b\omega_m)\Psi'_{rdq} \tag{2.16}$$

$$\Psi_{sdq} = L_s \cdot \mathbf{i}_{sdq} + L_m \cdot \mathbf{i}'_{rdq} \tag{2.17}$$

$$\Psi'_{rdq} = L'_r \cdot \mathbf{i}'_{rdq} + L_m \cdot \mathbf{i}_{sdq} \tag{2.18}$$

$$T = p_b \frac{3}{2} (\Psi_{sd}i_{sq} - \Psi_{sq}i_{sd}) \tag{2.19}$$

An induction motor supplied by an inverter (Fig. 9) in dq rotating reference frame can be described by the following formula (2.20) [88].

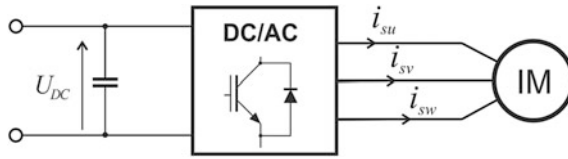


Fig. 9 Schematic diagram of an induction machine supplied by an inverter

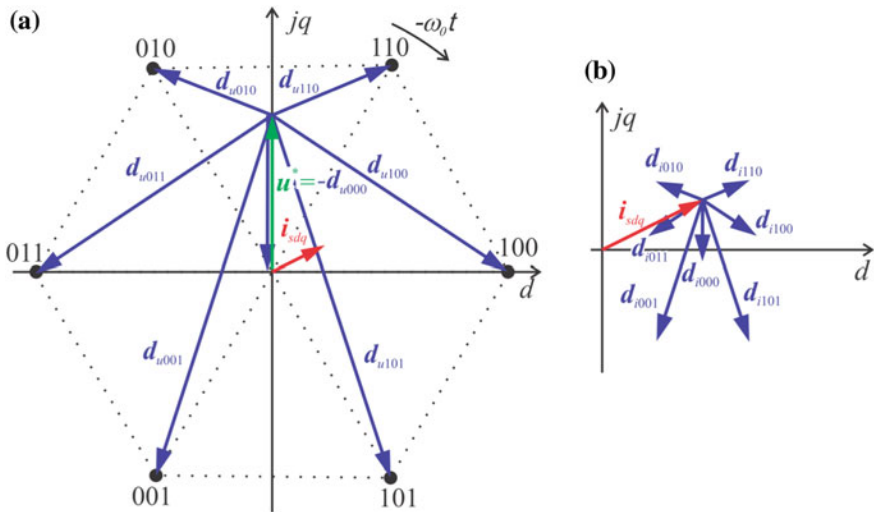


Fig. 10 Examples of voltage vectors proportional to current derivative vectors d_{uxxx} and corresponding current derivative vectors d_{ixxx}

$$\mathbf{u}_{sdq} = R_s \mathbf{i}_{sdq} + j\omega_o L_{\sigma s} \mathbf{i}_{sdq} + L_{\sigma s} \frac{d}{dt} \mathbf{i}_{sdq} + \mathbf{e}_m \tag{2.20}$$

Dependence (2.21) is obtained by the transformation of (2.20). The obtained voltage vector (Fig. 10a) is proportional to the vector of stator current derivative (2.22) (Fig. 10b) that determines both the direction and the speed of current changes:

$$L_{\sigma s} \frac{d}{dt} \mathbf{i}_{sdq} = -(\mathbf{e}_m + R_s \mathbf{i}_{sdq} + j\omega_o L_{\sigma s} \mathbf{i}_{sdq}) + \mathbf{u}_{sdq} = -\mathbf{u}^* + \mathbf{u}_{sdq} \tag{2.21}$$

$$L_{\sigma s} \frac{d}{dt} \mathbf{i}_{sdq} = \mathbf{d}_{uxxx} = \frac{1}{L_{\sigma s}} \mathbf{d}_{ixxx} \tag{2.22}$$

where

- \mathbf{u}^* stator voltage vector in dq reference frame,
- \mathbf{u}_{sdq} converter voltage vector given by (2.1) or (2.2) for 2-level and 3-level converter respectively,

- \mathbf{i}_s stator current vector,
 \mathbf{e}_m vector of electromotive force,
 ω_O angular speed of stator flux vector,
 R_s stator resistance,
 $L_{\sigma s}$ leakage inductance of windings.

2.4 Mathematical Model of a DC/AC Converter Fed Permanent Magnet Synchronous Machine

The equations used to model PMSM in the stator-flux-oriented rotating reference frame are as follows [89]:

$$\mathbf{u}_{sdq} = R_s \mathbf{i}_s + \frac{d\boldsymbol{\Psi}_s}{dt} + jp_b \omega_m \boldsymbol{\Psi}_s \quad (2.23)$$

$$\boldsymbol{\Psi}_s = L_s \mathbf{i}_s + \boldsymbol{\Psi}_{PM} \quad (2.24)$$

$$T = \frac{3}{2} p_b \text{Im}(\boldsymbol{\Psi}_s^* \cdot \mathbf{i}_s) \quad (2.25)$$

where

- \mathbf{u}_s and \mathbf{i}_s are stator voltage and current complex vectors,
 L_s ($L_q = L_d = L_s$) is synchronous inductance,
 $\boldsymbol{\Psi}_s$ is stator flux vector,
 $\boldsymbol{\Psi}_{PM}$ is permanent magnet rotor flux vector,
 p_b is the number of pole pairs, respectively.

After substituting (2.24) into (2.23), the current vector derivative can be expressed as:

$$L_s \frac{d\mathbf{i}_s}{dt} = -(\mathbf{R}\mathbf{i}_s + \frac{d\boldsymbol{\Psi}_{PM}}{dt} + jp_b \omega_m \boldsymbol{\Psi}_s) + \mathbf{u}_{sdq} \quad (2.26)$$

Assuming that the derivative of permanent magnet rotor flux vector $\boldsymbol{\Psi}_{PM}$ is equal to zero, we obtain the final Eq. (2.27) describing the derivatives of the PMSM stator current vector [90]. The derivatives are caused by the inverter voltage vectors.

$$L_s \frac{d\mathbf{i}_s}{dt} = -(\mathbf{R}\mathbf{i}_s + jp_b \omega_m L_s \mathbf{i}_s + \mathbf{e}_s) + \mathbf{u}_{sdq} \quad (2.27)$$

$$\mathbf{d}_{u_{xxx}} = L_s \mathbf{d}_{i_{xxx}} = L_s \frac{d\mathbf{i}_s}{dt} = -\mathbf{u}^* + \mathbf{u}_{sdq} \quad (2.28)$$

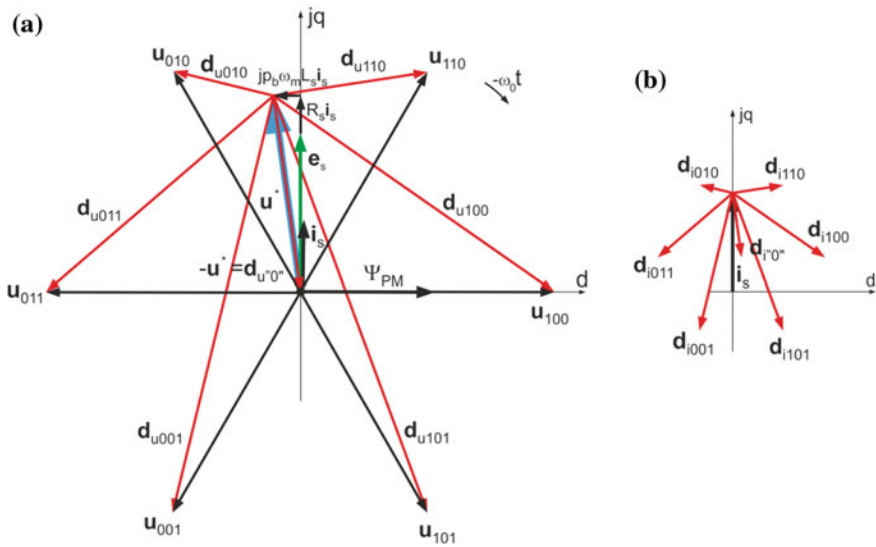


Fig. 11 Derivatives of current vectors corresponding to the voltage vectors of the 2-level inverter where

- $d_{u_{xxx}}$ Vector proportional to the stator current derivative vector caused by voltage vector u_{xxx} ,
- $d_{i_{xxx}}$ Stator current derivative vector caused by voltage vector u_{xxx} ,
- $e_s = jE_s$ Electromotive force described as $jp_b\omega_m\Psi_{PM}$,
- u^* Set voltage vector.

Graphical illustration of formula (2.28) is shown in Fig. 11. The derivatives of current vector $d_{i_{xxx}}$ determine the direction and rate of changes of current vector components and thus the direction and dynamics of torque and flux changes.

2.5 Mathematical Models of 3-Phase 2-Level AC/DC Current Source Converter

Three-phase two-level AC/DC current source converter has the topology shown in Fig. 12. It includes LC filter (L represents grid inductance) on the input side. The main constraint of proper converter control is the fact that at least one top and one bottom transistor must be closed at any time. There are nine valid states of transistors, three of them produce zero line currents [72, 73].

Line currents transformed to stationary reference frame $\alpha\beta$ are represented by current vector described by Eq. (2.29) and illustrated in Fig. 13.

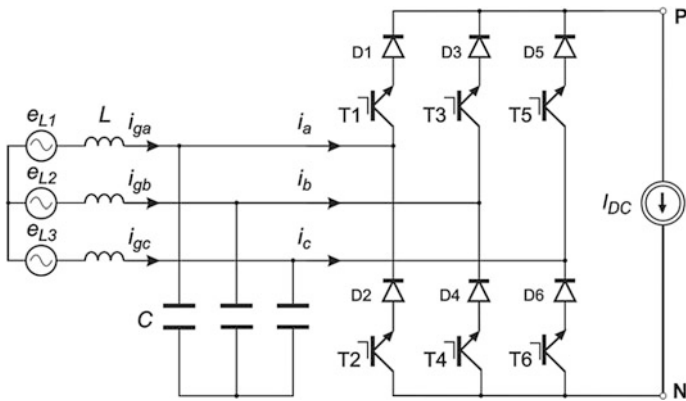


Fig. 12 Current source rectifier topology

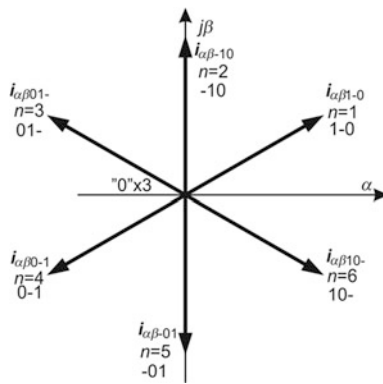


Fig. 13 Input current vectors

$$i_{\alpha\beta} = \frac{1}{\sqrt{3}} \begin{bmatrix} \mathbf{1} & \mathbf{a} & \mathbf{a}^2 \end{bmatrix} \begin{bmatrix} i_a \\ i_b \\ i_c \end{bmatrix} = \begin{cases} I_{DC} e^{j(n\frac{\pi}{3} - \frac{\pi}{6})} \\ 0 \end{cases} \quad (2.29)$$

where is

- $I_{DC} e^{j(n\frac{\pi}{3} - \frac{\pi}{6})}$ Active vectors in states $n = 1, 2, \dots, 6$;
- 0 Zero vectors, achieved by shortcut in one branch of the converter.

Analysis of the converter conducted in synchronous reference frame xy , which is rotating with angular speed $\omega_g = d\vartheta_g/dt$, allow us to define a model of the converter connected to the grid. Equation (2.30) presents current vectors of the rectifier in xy frame.

$$\mathbf{i}_{dq} = \begin{cases} I_{DC} e^{j(n\frac{\pi}{3} - \frac{\pi}{6} - \omega_g t)} \\ 0 \end{cases} \quad (2.30)$$

The filter model is described by Eqs. (2.31) and (2.32).

$$\mathbf{e}_{gxy} = \mathbf{u}_{cxy} + j\omega_g L \mathbf{i}_{gxy} + L \frac{d\mathbf{i}_{gxy}}{dt} \quad (2.31)$$

$$\mathbf{i}_{gxy} = \mathbf{i}_{xy} + j\omega_g C \mathbf{u}_{cxy} + C \frac{d\mathbf{u}_{cxy}}{dt} \quad (2.32)$$

where

\mathbf{e}_{gxy} grid voltage vector,

\mathbf{u}_{cxy} capacitor voltage vector,

\mathbf{i}_{gxy} grid current vector

The reference frame is oriented on the grid voltage vector, which means that $\mathbf{e}_{gxy} = e_{gx}$ [91]. To achieve unit power factor, the reference y component of the grid current vector has to be zero $i_{gy}^* = 0$.

In the steady state every derivative equals zero. Analyzing (2.31), the reference values of capacitor voltage components can be described by Eqs. (2.33) and (2.34) [92].

$$u_{cx}^* = e_{gx} \quad (2.33)$$

$$u_{cy}^* = -\omega_g L i_{gx}^* \quad (2.34)$$

Analyzing (2.32), the reference value of the rectifier current vector can be described by Eq. (2.35) [85].

$$\mathbf{i}_{xy}^* = \mathbf{i}_{gxy} - j\omega_g C \mathbf{u}_{cxy} \quad (2.35)$$

Space vectors of reference values are shown in Fig. 14. It presents the steady state with a unit power factor.

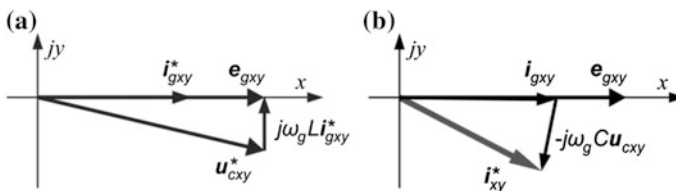


Fig. 14 Space vectors of reference values. Graphical explanation of u_{cxy}^* (a) and i_{xy}^* (b) in the steady state

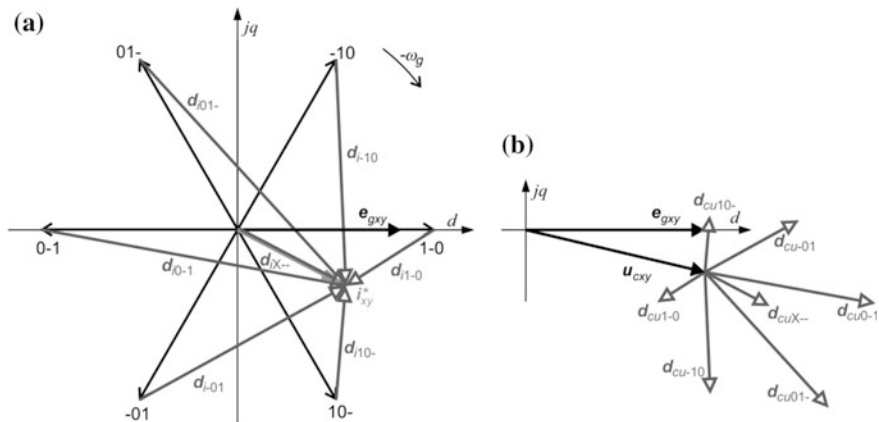


Fig. 15 Vectors proportional to capacitor voltage vector derivatives (a) and capacitor voltage vector derivatives (b)

The capacitor voltage vector derivative (2.36) taken from (2.32) allows us to find the relation between the selection of the rectifier current vector and the change in the capacitor voltage vector [82–84].

$$\frac{d\mathbf{u}_{cxy}}{dt} = \frac{1}{C} (\mathbf{i}_{gxy} - \mathbf{i}_{xy} - j\omega_g C \mathbf{u}_{cxy}) \tag{2.36}$$

Equations (2.35) and (2.36) make it possible to define variable \mathbf{d}_i which is proportional to capacitor voltage vector derivative (2.37), and variable \mathbf{d}_{cu} which describes the direction and the speed of the capacitor voltage vector change (2.38).

$$C \frac{d\mathbf{u}_{cxy}}{dt} = \mathbf{d}_i = \mathbf{i}_{xy}^* - \mathbf{i}_{xy} \tag{2.37}$$

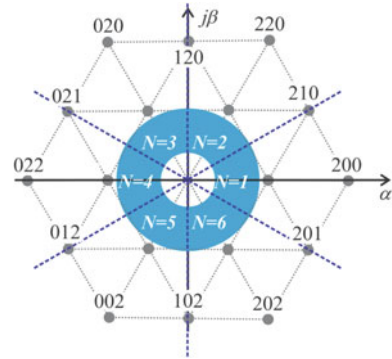
$$\mathbf{d}_{cu} = \frac{d\mathbf{u}_{cxy}}{dt} = \frac{1}{C} \mathbf{d}_i \tag{2.38}$$

Graphical illustrations for Eqs. (2.37) and (2.38) are given in Fig. 15a, b respectively.

3 Modern Look-Up Table Methods

The control methods described in this section make use of sector N division. The sectors divide $\alpha\beta$ plane into six areas (3.1), (3.3). The boundaries are made of six half-lines with common initial point that is placed at the origin. The half-lines are rotated with respect to each other by 60° (Fig. 16).

Fig. 16 The division of $\alpha\beta$ plane into 6 sectors N for three-level converters



The sector number in DTC 3L3A method depends on both the angle δ and the flux vector angle $\varphi_{\Psi_{sz\beta}}$ (3.1). The angle δ is defined as the \mathbf{u}^* vector angle shifted by $-\pi/2$ (3.2).

$$N = \begin{cases} 1, & \text{for } (\varphi_{\Psi_{sz\beta}} + \delta) \in \langle -\pi/6, \pi/6 \rangle \\ 2, & \text{for } (\varphi_{\Psi_{sz\beta}} + \delta) \in \langle \pi/6, \pi/2 \rangle \\ 3, & \text{for } (\varphi_{\Psi_{sz\beta}} + \delta) \in \langle \pi/6, 5\pi/6 \rangle \\ 4, & \text{for } (\varphi_{\Psi_{sz\beta}} + \delta) \in \langle 5\pi/6, \pi \rangle \vee \langle -\pi, -5\pi/6 \rangle \\ 5, & \text{for } (\varphi_{\Psi_{sz\beta}} + \delta) \in \langle -5\pi/6, -3\pi/6 \rangle \\ 6, & \text{for } (\varphi_{\Psi_{sz\beta}} + \delta) \in \langle -3\pi/6, -\pi/6 \rangle \end{cases} \quad (3.1)$$

$$\delta = \varphi_{\mathbf{u}^*} - \frac{\pi}{2} \quad (3.2)$$

The sector number in DPC 3L3A method depends on angle $\varphi_{\Psi_{vz\beta}}$ of the virtual flux vector, as shown in Eq. (3.3). The virtual flux vector does not have physical interpretation and has been introduced by analogy to the DTC method. Only the angle of the virtual flux vector is defined as \mathbf{u}^* vector angle shifted by $-\pi/2$ (3.4).

$$N = \begin{cases} 1, & \text{for } \varphi_{\Psi_{vz\beta}} \in \langle -\pi/6, \pi/6 \rangle \\ 2, & \text{for } \varphi_{\Psi_{vz\beta}} \in \langle \pi/6, \pi/2 \rangle \\ 3, & \text{for } \varphi_{\Psi_{vz\beta}} \in \langle \pi/2, 5\pi/6 \rangle \\ 4, & \text{for } \varphi_{\Psi_{vz\beta}} \in \langle 5\pi/6, \pi \rangle \vee \langle -\pi, -5\pi/6 \rangle \\ 5, & \text{for } \varphi_{\Psi_{vz\beta}} \in \langle -5\pi/6, -3\pi/6 \rangle \\ 6, & \text{for } \varphi_{\Psi_{vz\beta}} \in \langle -3\pi/6, -\pi/6 \rangle \end{cases} \quad (3.3)$$

$$\varphi_{\psi_{vz\beta}} = \varphi_{u_{z\beta}^*} - \frac{\pi}{2} \tag{3.4}$$

where

$\varphi_{\psi_{vz\beta}}$ virtual flux angle.

3.1 DPC-3L3A Method

Due to the fact that the y component of the grid voltage vector is equal zero ($e_{gy} = 0$), the active and reactive powers are proportional to the x and y grid current vector components respectively (3.5) [93].

$$\begin{aligned} p_g &= \frac{3}{2} (e_{gy} \cdot i_{gy} + e_{gx} \cdot i_{gx}) \\ q_g &= \frac{3}{2} (e_{gy} \cdot i_{gx} - e_{gx} \cdot i_{gy}) \end{aligned} \Big|_{e_{gy}=0} \Rightarrow \begin{aligned} p_g &= \frac{3}{2} e_{gx} \cdot i_{gx} \\ q_g &= -\frac{3}{2} e_{gx} \cdot i_{gy} \end{aligned} \tag{3.5}$$

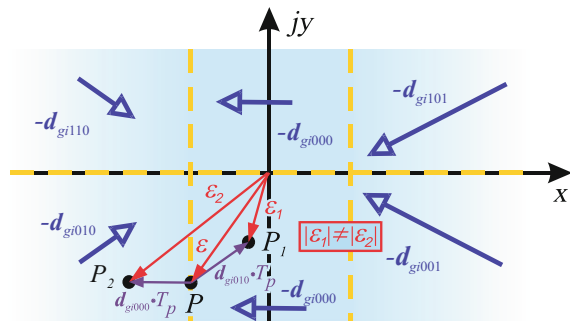
In order to simplify the description, the reference values of the powers are converted to reference values of current according to Eqs. (3.6).

$$i_{gx}^* = \frac{2}{3} \frac{p_g^*}{e_{gx}} \quad i_{gy}^* = -\frac{2}{3} \frac{q_g^*}{e_{gx}} \tag{3.6}$$

3.1.1 Method Description

It can be shown that the boundaries of the error plane division in the DPC method are suboptimally defined. In the DPC method the comparators divide the error plane into six areas (Fig. 16). In accordance with the switching table, converter voltage vectors u_{xxx} that correspond to current derivative vectors d_{gixxx} are assigned to individual areas. The error plane division as well as current derivative assignment in sector $N = 1$ for DPC method is shown in Fig. 17. If the error vector is located at

Fig. 17 Error plane division for the DPC method in sector $N = 1$



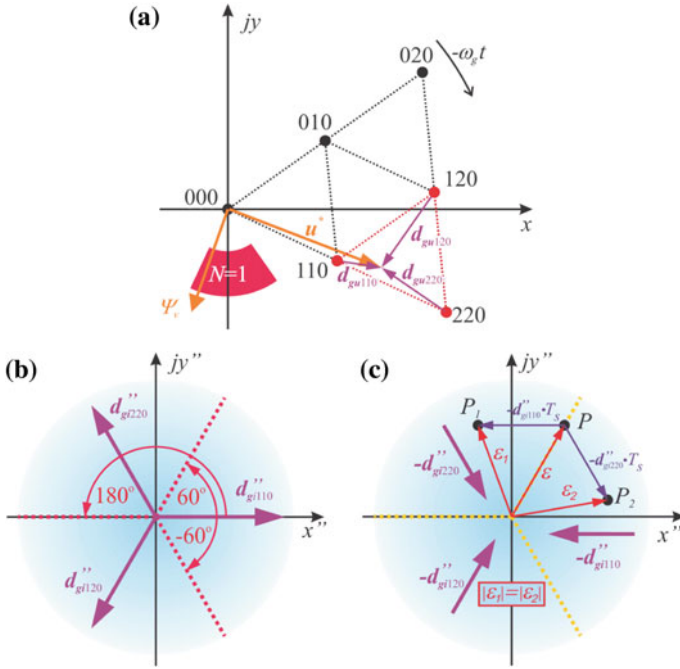


Fig. 18 Optimal error plane distribution in $x''y''$ reference frame (b) as referred to the arrangement shown in (a) as well as the equivalent impact of the adjacent converter voltage vectors on the error vector located on the division border (c)

point P , on the division boundary, the selection of u_{010} voltage vector will shift the error vector to point P_1 (ϵ_1). In contrast, the selection of u_{000} vector will shift the error vector to point P_2 (ϵ_2). Error vectors ϵ_1 and ϵ_2 have different lengths. This fact indicates that the boundaries of the error plane division are suboptimally defined. To determine an optimal division, it is required to establish such borders for which the impact of two adjacent voltage vectors is equivalent. In other words, the lengths of both error vectors ϵ_1 and ϵ_2 should be equal for optimal error plane division (Fig. 18c).

In order to determine the optimal error plane division in the DPC 3L3A method, it is assumed that one of the three converter voltage vectors u corresponding to the shortest current derivative vector (Fig. 18a) should be selected in the steady state. Also, the new $x''y''$ coordinate system has been introduced in which the current derivative vectors d_{gi} have equal lengths and are rotated with respect to each other by 120° (Fig. 18b). In such a specific reference system the boundary of an optimum error plane division are constructed with the three half-lines with a common origin and rotated with respect to each other by 120° (Fig. 18b).

In the DPC 3L3A method, if the error vector is located at point P on the division boundary (Fig. 18c), the selection of voltage vector u_{110} will shift the error vector to point P_1 (ϵ_1). In contrast, the selection of vector u_{220} will shift the error vector to

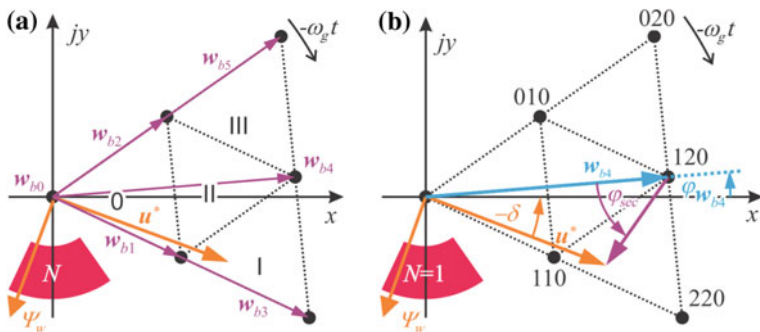


Fig. 19 Triangle numbers (a) and angle φ_{sec} construction (b)

Table 1 Triangle selection table

$\varphi_{sec} \in (\pi/6, \pi/2)$	Triangle I
$\varphi_{sec} \in (-\pi/6, \pi/6)$	Triangle II
$\varphi_{sec} \in \langle -\pi/2, -\pi/6 \rangle$	Triangle III

point P_2 (ε_2). Both ε_1 and ε_2 have equal lengths, which indicates that the boundaries of the error plane division have been optimally defined. It should be emphasized that in the DPC 3L3A method the selection of converter voltage vector \mathbf{u} is exclusively based on the error vector angle. This allows us to eliminate inconvenient hysteresis comparators in the control system.

Three converter voltage vectors \mathbf{u}_{xxx} , which correspond to the shortest current derivative vectors, always form an equilateral triangle inside which \mathbf{u}^* voltage vector is located. For three level converters, each N sector can be divided into four equilateral triangles (0, I, II, III) (Fig. 19a). The triangles are formed by \mathbf{u}_{xxx} vectors (in a general case by \mathbf{w}_{bx} vectors).

Selection of the triangle inside which \mathbf{u}^* vector is located is based on dependences (3.6) and (3.7). If inequality (3.6) is true, \mathbf{u}^* vector is located in triangle 0. Otherwise, the selection is based on φ_{sec} angle (3.7) (Fig. 19b) according to Table 1.

$$\frac{U_{dc} \sqrt{3}}{6} > |\mathbf{u}^*| \cdot \cos(\varphi_{w_{b4}} - \delta) \tag{3.6}$$

$$\varphi_{sec} = \arcsin\left(\frac{|\mathbf{u}^*|}{|\mathbf{w}_{b4} - \mathbf{u}^*|} \sin(\varphi_{w_{b4}} - \delta)\right) \tag{3.7}$$

In the arrangement shown in Fig. 20 the three converter voltage vectors that correspond to the shortest current derivative vectors \mathbf{d}_{gi} are \mathbf{u}_{110} , \mathbf{u}_{220} and \mathbf{u}_{120} . They correspond to vectors \mathbf{d}_{gu110} , \mathbf{d}_{gu220} and \mathbf{d}_{gu120} respectively (Fig. 20a, b).

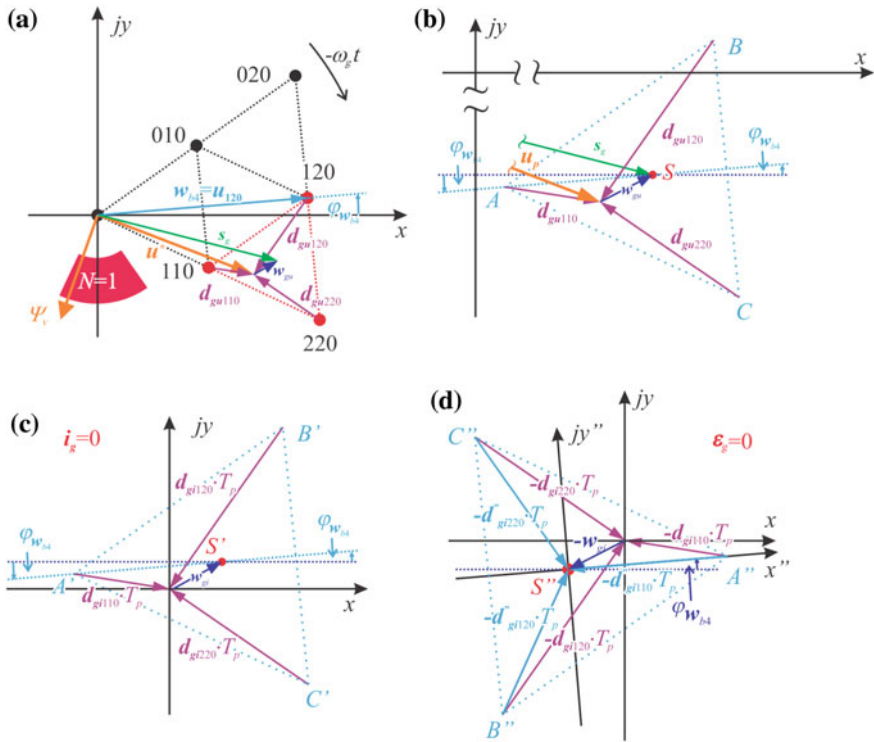


Fig. 20 Graphical interpretation of $x''y''$ coordinate system **(d)**; influence of d_{gi} vectors on current vector **(c)** and error vector **(d)** in the arrangement shown in **(a)** whose main part is expanded **(b)**

Vectors d_{gu} form equilateral triangle ABC with a center point S (Fig. 20b). Point S is shifted from vectors $d_{gu_{xxx}}$ by vector w_{gu} (3.8) (Fig. 24b) that is equal to the difference between the center of triangle vector s_g (3.9) and vector u^* (Fig. 20b).

$$w_{gu} = s_g - u_p \tag{3.8}$$

$$s_g = \begin{cases} 1/3(\mathbf{w}_{b0} + \mathbf{w}_{b1} + \mathbf{w}_{b2}), & \text{for triangle 0} \\ 1/3(\mathbf{w}_{b1} + \mathbf{w}_{b3} + \mathbf{w}_{b4}), & \text{for triangle I} \\ 1/3(\mathbf{w}_{b1} + \mathbf{w}_{b2} + \mathbf{w}_{b4}), & \text{for triangle II} \\ 1/3(\mathbf{w}_{b2} + \mathbf{w}_{b4} + \mathbf{w}_{b5}), & \text{for triangle III} \end{cases} \tag{3.9}$$

During one sampling period T_s vectors d_{gu110} , d_{gu220} and d_{gu120} exert influence on the current vector by vectors $d_{gi110} \cdot T_s$, $d_{gi220} \cdot T_s$ and $d_{gi120} \cdot T_s$ respectively. They form equilateral triangle $A'B'C'$ (Fig. 20c) that is similar to triangle ABC with T_s/L ratio. In Fig. 20c, in order to simplify the analysis, zero value of current ($i_g = 0$) has been assumed. Point S' is shifted from vectors d_{gi} by vector w_{gi} (3.10) (Fig. 20c) that is proportional to vector w_{gu} with T_s/L ratio.

$$\mathbf{w}_{gi} = \frac{T_s}{L} \mathbf{w}_{gu} \tag{3.10}$$

Due to the fact that current derivative vectors \mathbf{d}_{gixxx} shift error vector $\boldsymbol{\varepsilon}_g$ in the opposite direction during sampling period T_s vectors \mathbf{d}_{guxxx} affect error vector $\boldsymbol{\varepsilon}_g$ by $-\mathbf{d}_{gixxx} \cdot T_s$ (Fig. 20d). In Fig. 20d, in order to simplify the analysis, zero value of error ($\boldsymbol{\varepsilon}_g = 0$) has been assumed. Vectors $-\mathbf{d}_{gi110} \cdot T_s$, $-\mathbf{d}_{gi220} \cdot T_s$ and $-\mathbf{d}_{gi120} \cdot T_s$ also form equilateral triangle $A''B''C''$ that is proportional to ABC triangle with $-T_s/L$ ratio. The center of triangle S'' is shifted to vectors \mathbf{d}_{gixxx} by vector $-\mathbf{w}_{gi}$ (Fig. 20d). It can be seen that the origin of the reference frame $x''y''$ is located in the center of triangle $A''B''C''$ (point S'') and is oriented in accordance to point A'' (rotated at angle φ_{wb4}). Moreover, current derivative vectors in $x''y''$ coordinate system have the same lengths (Fig. 20d). The transfer of error vector $\boldsymbol{\varepsilon}_g$ to that reference frame is carried out using dependence (3.11).

$$\boldsymbol{\varepsilon}''_g = (\boldsymbol{\varepsilon}_g + \mathbf{w}_{gi}) \cdot e^{-j\varphi_{wb4}} \tag{3.11}$$

Due to the fact that the division of error plane in $x''y''$ reference frame are identical only for triangles 0, I and III (Fig. 21), it is recommended to standardize the angle of error vector used for the selection of the converter voltage vector. This can be carried out by performing additional calculations for triangle II (3.12).

$$\varphi_{\boldsymbol{\varepsilon}''_g} = \begin{cases} \varphi(\boldsymbol{\varepsilon}''_g), & \text{for triangles 0, I, III} \\ \varphi(-\text{Re}(\boldsymbol{\varepsilon}''_g) + j\text{Im}(\boldsymbol{\varepsilon}''_g)), & \text{for triangle II} \end{cases} \tag{3.12}$$

The behavior of DPC 3L3A depends on the converter state (Fig. 22). In steady states the method is optimized by selecting converter voltage vector \mathbf{u}_{xxx} that decreases the absolute value of the error vector by the use of the shortest current derivative vectors. That allows us to achieve both low switching frequency and high accuracy of control. In the steady state the selection of a converter voltage vector is determined by N sector number, triangle number (3.6), (3.7), (Table 1) as well as error vector angle $\varphi_{\boldsymbol{\varepsilon}''_g}$ (3.12) according to the vector selection table (Table 2).

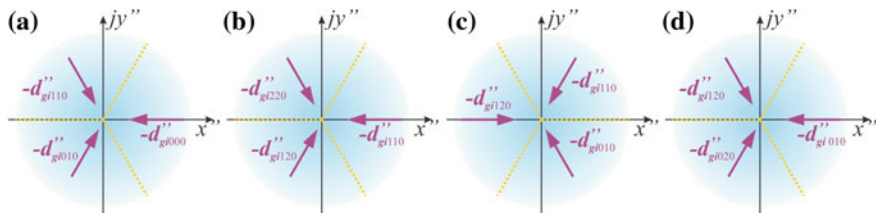


Fig. 21 Optimal division of error plane for 0 (a), I (b), II (c), III (d) triangles in sector $N = 1$

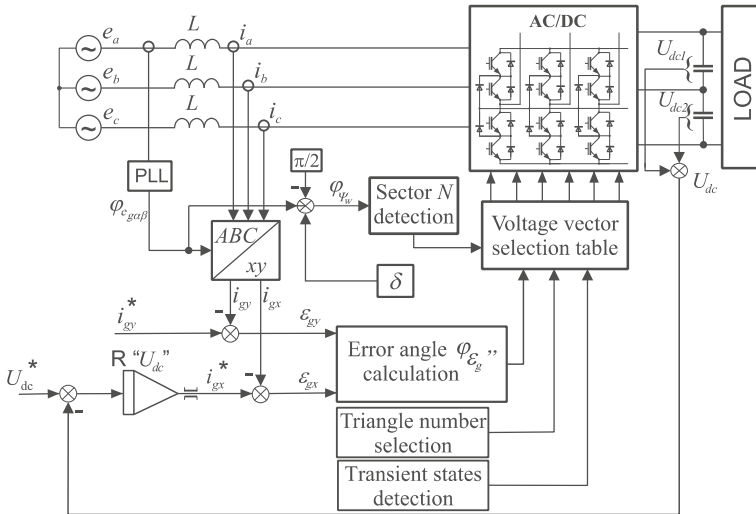


Fig. 22 Schematic diagram of the DPC 3L3A method

Table 2 Voltage vector selection table for DPC 3L3A method

$\varphi_{e_g''}$	Triangle	Sector N					
		$N = 1$	$N = 2$	$N = 3$	$N = 4$	$N = 5$	$N = 6$
$(-\pi; -\frac{\pi}{3})$	tr. 0	010	011	001	101	100	110
	tr. I	120	021	012	102	201	210
	tr. II	010	011	001	101	100	110
	tr. III	020	022	002	202	200	220
$(-\frac{\pi}{3}; \frac{\pi}{3})$	tr. 0	000	000	000	000	000	000
	tr. I	110	010	011	001	101	100
	tr. II	120	021	012	102	201	210
	tr. III	010	011	001	101	100	110
$(\frac{\pi}{3}; \pi)$	tr. 0	110	010	011	001	101	100
	tr. I	220	020	022	002	202	200
	tr. II	110	010	011	001	101	100
	tr. III	120	021	012	102	201	210

In transient states the selected voltage vectors decrease both components of the error vector by the use of the longest current vector derivatives. That enables fast response to dynamic changes of currents. The transient state in the DPC 3L3A is chosen in the case when component x of the error vector exceeds ϵ_{xdyn} value (3.13) corresponding to the maximum changes of error in the steady state during one sampling period. Due to the fact that the current vector in the DPC 3L3A method is formed by the converter voltage vectors that form an equilateral triangle, ϵ_{xdyn}

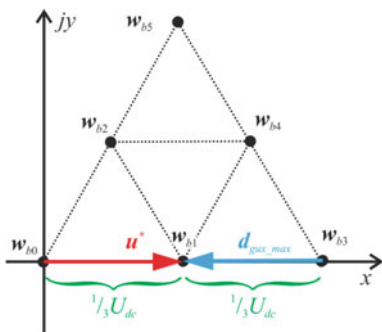


Fig. 23 Maximum value of vector d_{gux_max} proportional to current derivative vector

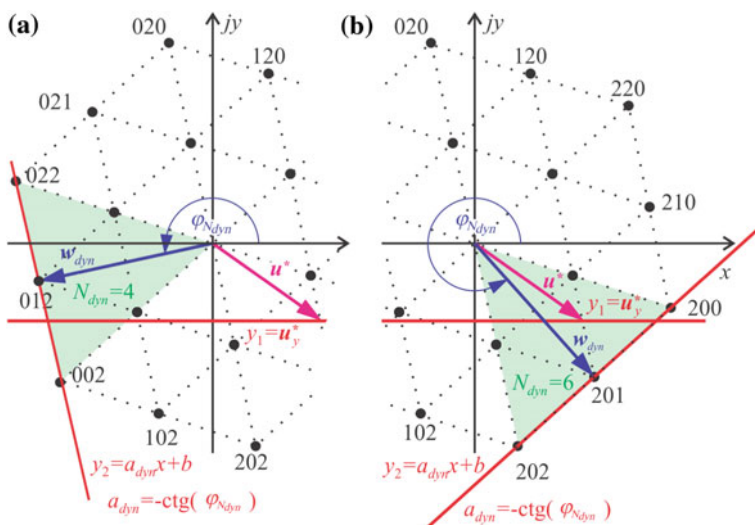


Fig. 24 Visualization of N_{dyn} sector, w_{dyn} vector and straight line y_2 for the ϵ_{gx} error vector component higher (a) and lower than (b) zero

value is defined as a length of the triangle side with the ratio of T_s/L (3.13) (Fig. 23).

$$\epsilon_{xdyn} = d_{gux_max} \cdot \frac{T_s}{L} = \frac{1}{3} U_{DC} \frac{T_s}{L} \tag{3.13}$$

In transient states, the sector N_{dyn} (3.15) is determined on the basis of angle $\varphi_{N_{dyn}}$ (3.14). In sector N_{dyn} , straight line $y_1 = u_{py}$ crosses the hexagon formed by converter voltage vectors u either on the left when ($\epsilon_{gx} > 0$) (Fig. 24a) or on the right when ($\epsilon_{gx} < 0$) (Fig. 24b). Vector w_{dyn} is calculated according to (3.16) (Fig. 24).

Table 3 Voltage vector selection table for DPC-3L-3am method in transient states

n_{dyn}	Sector N_{dyn}					
	$N_{dyn} = 1$	$N_{dyn} = 2$	$N_{dyn} = 3$	$N_{dyn} = 4$	$N_{dyn} = 5$	$N_{dyn} = 6$
-1	200	220	020	022	002	202
0	210	120	021	012	102	201
1	220	020	022	002	202	200

$$\varphi_{N_{dyn}} = \varphi(\mathbf{w}_{dyn}) = \begin{cases} \arcsin\left(\frac{3 \cdot u_y^*}{2 \cdot U_{dc}}\right) + \omega_g t, & \text{for } \varepsilon_{gx} \leq 0 \\ \pi + \arcsin\left(\frac{3 \cdot u_y^*}{2 \cdot U_{dc}}\right) + \omega_g t, & \text{for } \varepsilon_{gx} > 0 \end{cases} \quad (3.14)$$

$$N_{dyn} = \begin{cases} 1, & \text{for } \varphi_{N_{dyn}} \in (0; \pi/3) \\ 2, & \text{for } \varphi_{N_{dyn}} \in (\pi/3; 2\pi/3) \\ 3, & \text{for } \varphi_{N_{dyn}} \in (2\pi/3; \pi) \\ 4, & \text{for } \varphi_{N_{dyn}} \in (-\pi; -2\pi/3) \\ 5, & \text{for } \varphi_{N_{dyn}} \in (-2\pi/3; -\pi/3) \\ 6, & \text{for } \varphi_{N_{dyn}} \in (-\pi/3; 0) \end{cases} \quad (3.15)$$

$$\mathbf{w}_{dyn} = w_{dyn_d} + jw_{dyn_q} = \frac{\sqrt{3}}{3} U_{dc} \cdot e^{j((N_{dyn}-1)\frac{\pi}{3}) + \frac{\pi}{6}} \cdot e^{-j\omega_g t} \quad (3.16)$$

The number of voltage vector n_{dyn} (3.18) is calculated on the basis of the sign of slope a_{dyn} (3.17) of straight line y_2 (Fig. 24) as well as ε_g , \mathbf{w}_{dyn} and \mathbf{u}^* vectors.

$$\text{sgn}(a_{dyn}) = -\text{sgn}(w_{dyn_d}) \cdot \text{sgn}(w_{dyn_q}) \quad (3.17)$$

$$n_{dyn} = \begin{cases} \text{sgn}(\varepsilon_{gx} \cdot \varepsilon_{gy}), & \text{for } [\text{sgn}(a_{dyn}) = \text{sgn}(\varepsilon_{gx} \cdot \varepsilon_{gy}) \vee \\ & \text{sgn}(\varepsilon_{gy}) \neq \text{sgn}(u_{py} - w_{dyny})] \\ 0, & \text{for } [\text{sgn}(a_{dyn}) \neq \text{sgn}(\varepsilon_{gx} \cdot \varepsilon_{gy}) \wedge \\ & \text{sgn}(\varepsilon_{gy}) = \text{sgn}(u_{py} - w_{dyny})] \end{cases} \quad (3.18)$$

Sector N_{dyn} and vector number n_{dyn} are used in transient states to select the \mathbf{u}_{xxx} converter voltage vector according to Table 3.

3.1.2 Experimental Results

The experimental setup used for the comparison of DPC control methods consists of both a 3-level AC/DC converter and a DC/AC inverter. However, in order to carry out the experiments the DC/AC part was disconnected.

The experiments were performed both for two values of active power i.e. 3.5 and 10.5 kW and for two values of reactive power i.e. -2.5 and 10 kvar. The converter was supplied from 3×230 V phase voltage source by a grid reactor whose

inductance was equal to 20 mH. The value of DC link voltage U_{DC} amounted to 650 V. The main part of the control system was composed of ADSP21363—a 32bit floating point digital signal processor clocked at a frequency of 333 MHz made by Analog Devices. The sampling period T_s of the control system of the AC/DC converter amounted to 33 μ s.

The coefficient values of current ripples in xy rotating reference frame (3.19), (3.20) as well as THD values were determined for each analyzed case. It is worth noting that coefficients (3.19) and (3.20) are proportional to active and reactive power ripples respectively. The results of performed experiments are presented in Table 4, Figs. 25 and 26.

$$\Delta I_{gxRMS} = \sqrt{\frac{1}{T_o} \int_0^{T_o} (i_{gx} - I_{gxAV})^2 dt} \tag{3.19}$$

$$\Delta I_{gyRMS} = \sqrt{\frac{1}{T_o} \int_0^{T_o} (i_{gy} - I_{gyAV})^2 dt} \tag{3.20}$$

Table 4 Experimental results for DPC 3L3A method

Method	P (kW)	Q (kvar)	f_{1T} (kHz)	THD (%)	ΔI_{gxRMS} (A)	ΔI_{gyRMS} (A)
DPC 3L3Am	3.5	0	5.33	2.31	0.08	0.08
	10.5	0	4.65	1.49	0.15	0.13
	0	-2.5	4.38	3.39	0.08	0.09
	0	10	4.42	1.32	0.10	0.11

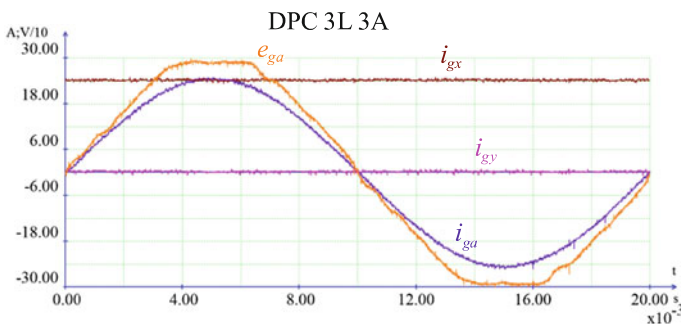


Fig. 25 Time courses of phase voltage (e_{ga}), phase current (i_{ga}) and current vector components (i_{gx} and i_{gy}) in the steady state for active and reactive powers amounting to 10.5 kW and 0 kvar respectively

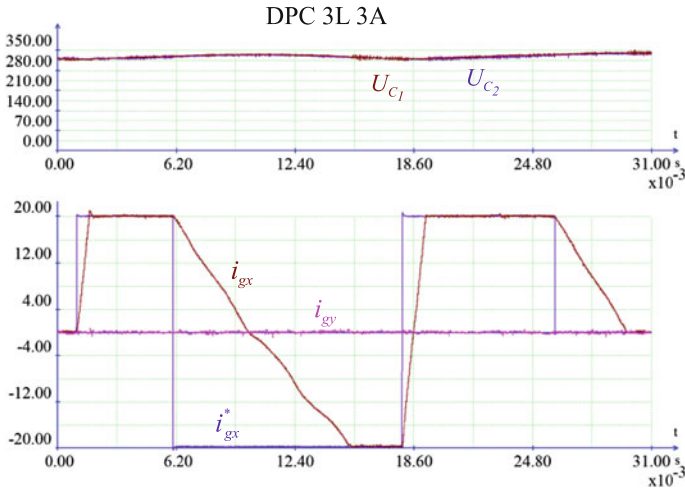


Fig. 26 Time courses of current vector components (i_{gx} and i_{gy}) as well as voltages of both capacitors (U_{C1} and U_{C2}) in the transient state for step changes of set x current vector component (i_{gx}^*) from 20 A to -20 A

where

ΔI_{gxRMS} , ΔI_{gyRMS} RMS values of current components in xy rotating reference frame after subtracting their average values.

In the transient state (Fig. 28) the DPC 3L3A method is able to properly recreate the y component of the current vector.

It is worth emphasizing here that a supplementary voltage balancing algorithm described in Sect. 3.3 was implemented in the control system to assure appropriate voltage balance for the both DC link capacitors (Fig. 28).

The DPC 3L3A look-up table method for a 3-level AC/DC converter cooperating with the 3-phase grid is proposed. The experimental results have shown excellent performance of the method in both steady and transient states. In the steady state the DPC 3L3A method is characterized by a close to sinusoidal shape of current, small values of THD and ΔI_{RMS} coefficients at a relatively small transistor switching frequency (Table 4). Additional balancing algorithms ensure the equality of the DC voltage on both capacitors (the differences are lower than 1 % of capacitor voltages). Similarly to all look-up table methods, the proposed algorithm is characterized by short processing time that makes it possible to implement the control algorithms on cheap standard processors. The algorithms' processing time (excluding measurements, etc.) for the DPC 3L3A method amounts to 4.05 μ s. In contrast, for the same setup, the processing time for the predictive control method described in [94] is as much as 16.39 μ s, i.e. over 4 times longer.

3.2 DTC-3L3A Method

Introduction of the DTC 3L3A method is required to perform analysis of the influence of inverter voltage vector \mathbf{u} on torque and flux changes.

Torque derivative $\frac{d}{dt}T$ (3.21) is described by transformation Eq. (2.19).

$$\frac{d}{dt}T = p_b \frac{3}{2} \cdot \frac{d}{dt} \text{Im}(\Psi_{sdq}^* \cdot \mathbf{i}_{sdq}) = p_b \frac{3}{2} \cdot \frac{d}{dt} (\Psi_{sd} \cdot i_{sq} - \Psi_{sq} \cdot i_{sd}) \quad (3.21)$$

Assuming that flux changes are much slower than current changes as well as component q of the stator flux vector is close to zero ($\Psi_{sq} \approx 0$), Eq. (3.21) can be simplified to (3.22).

$$\frac{d}{dt}T = p_b \frac{3}{2} \cdot \Psi_{sd} \cdot \frac{d}{dt} i_{sq} \quad (3.22)$$

By taking into account Eq. (2.22), which describe the impact of inverter voltage vector on stator current changes, the influence of inverter voltage vector on torque changes d_T takes the form of (3.23).

$$d_T = \frac{d}{dt}T = p_b \frac{3}{2} \cdot \Psi_{sd} \cdot d_{siq} = p_b \frac{3}{2} \cdot \Psi_{sd} \cdot \frac{d_{suq}}{L_{\sigma s}} \quad (3.23)$$

Flux derivative (3.24) is described by transformation Eq. (2.15) [88].

$$\frac{d}{dt} \Psi_{sdq} = \mathbf{u}_{sdq} - \mathbf{i}_{sdq} R_s - j\omega_o \Psi_{sdq} = \mathbf{u}_{sdq} - \mathbf{i}_{sdq} R - j\omega_o L_{\sigma s} \mathbf{i}_{sdq} - \mathbf{e}_{mdq} \quad (3.24)$$

where

\mathbf{e}_{mdq} —mutual electromotive force.

Due to the fact that the machine is supplied by the DC/AC inverter, Eq. (3.25) takes the shape of (3.26) by including dependence (2.22) on voltage vector \mathbf{u}^* .

$$\frac{d}{dt} \Psi_{sdq} = \mathbf{u} \cdot e^{-j\omega_o t} - \mathbf{u}^* = d_{su} \quad (3.25)$$

Since dq reference frame is oriented with respect to the mutual flux vector, which in most cases is shifted to the stator flux vector up to 2° , the impact of component q of the stator flux derivative vector on stator flux magnitude is neglected. Hence, for the computational simplicity sake, the omission of component q in Eq. (3.25) is justifiable. Thus, the influence of converter voltage vector \mathbf{u} is described by dependence (3.26).

$$d_{\psi} = \frac{d}{dt} \Psi_{sd} = d_{sud} \quad (3.26)$$

In order to analyze the behavior of the DTC method, error vector $\varepsilon_{\psi M}$ (3.27) is often introduced [88].

$$\varepsilon_{\psi T} = \varepsilon_{\psi} + j\varepsilon_T \quad (3.27)$$

where

$\varepsilon_{\psi T}$ vector of flux and torque errors,
 ε_{ψ} , ε_T flux and torque errors respectively.

The error vector $\varepsilon_{\psi T}$ is composed by two components in different scales and units. In order to standardize description the both components should have the same unit. Usually it is done by conversion both components to current unit. However better results and simplest subsequent calculations can be achieved by expression both error vector components in the flux unit (Wb). Hence, the torque component of the $\varepsilon_{\psi \psi T}$ (3.28) error vector is multiplied by scale factor $c_{\psi T}$ (3.29) that ensure that both error components are in the same scale and have the same unit.

$$\varepsilon_{\psi \psi T} = \varepsilon_{\psi} + jc_{\psi T} \varepsilon_T \quad (3.28)$$

$$c_{\psi T} = \frac{d_{suq}}{d_T} = \frac{2 \cdot L_{\sigma s}}{3 \cdot p_b \cdot \Psi_{sd}} \quad (3.29)$$

The impact of inverter voltage vectors \mathbf{u} on the error derivative vector in flux scale $\mathbf{d}_{\psi \psi T}$ (3.31) is described by transformation Eqs. (3.23), (3.26) and (3.29).

$$\begin{aligned} \mathbf{d}_{\psi \psi T} &= -d_{\psi} - jc_{\psi T} d_T = -d_{sud} - jc_{\psi T} \cdot p_b \frac{3}{2} \cdot \Psi_{sd} \cdot \frac{d_{suq}}{L_{\sigma s}} \\ &= -d_{sud} - j \frac{2 \cdot L_{\sigma s}}{3 \cdot p_b \cdot \Psi_{sd}} \cdot p_b \frac{3}{2} \cdot \Psi_{sd} \cdot \frac{d_{suq}}{L_{\sigma s}} = -d_{sud} - jd_{suq} = -\mathbf{d}_{su} \end{aligned} \quad (3.30)$$

3.2.1 Method Description

It can be shown that the boundaries of the error plane division in the DTC method are suboptimally defined. In the DTC method the comparators divide the error plane into six areas (Fig. 27). In accordance with the switching table, converter voltage vectors \mathbf{u}_{xxx} that correspond to current derivative vectors $\mathbf{d}_{\psi \psi T xxx}$ are assigned to individual areas. The error plane division as well as current derivative assignment in sector $N = 1$ for DTC method is shown in Fig. 27. If the error vector is located at point P , on the division boundary, the selection of \mathbf{u}_{000} voltage vector will shift the error vector to point P_1 (ε_1). In contrast, the selection of \mathbf{u}_{010} vector will shift the error vector to point P_2 (ε_2). Error vectors ε_1 and ε_2 have different lengths. This fact indicates that the boundaries of the error plane division are suboptimally defined. To determine an optimal division, it is required to establish such borders for which

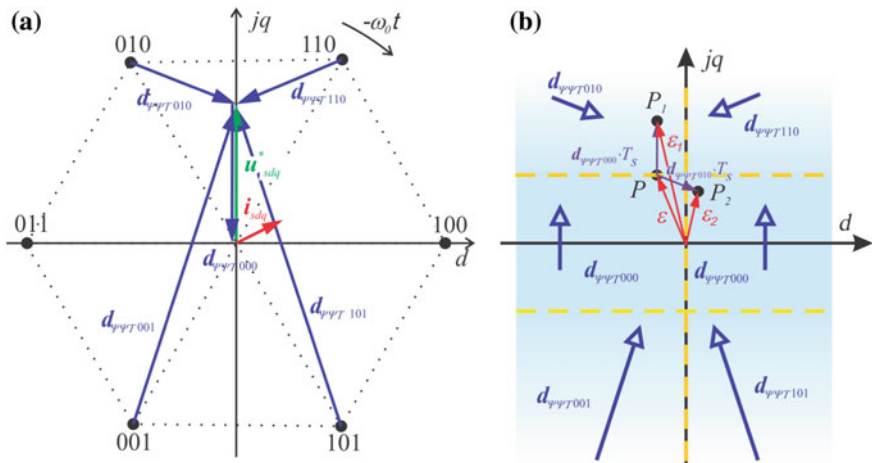


Fig. 27 Error plane division for the DTC method in sector $N = 1$

the impact of two adjacent voltage vectors is equivalent. In other words, the lengths of both error vectors ϵ_1 and ϵ_2 should be equal for optimal error plane division (Fig. 28c).

In order to determine the optimal error plane division in the DTC 3L3A method, it is assumed that one of the three converter voltage vectors \mathbf{u} corresponding to the shortest current derivative vector (Fig. 18a) should be selected in the steady state. Also, the new $d''q''$ coordinate system has been introduced in which the current derivative vectors $\mathbf{d}_{\psi/\psi T}$ have equal lengths and are rotated with respect to each other by 120° (Fig. 28b). In such a specific reference system the boundary of an optimum error plane division are constructed with the three half-lines with a common origin and rotated with respect to each other by 120° (Fig. 28b).

In the DTC 3L3A method, if the error vector is located at point P on the division boundary (Fig. 28c), the selection of voltage vector \mathbf{u}_{110} will shift the error vector to point P_1 (ϵ_1). In contrast, the selection of vector \mathbf{u}_{220} will shift the error vector to point P_2 (ϵ_2). Both ϵ_1 and ϵ_2 have equal lengths, which indicates that the boundaries of the error plane division have been optimally defined. It should be emphasized that in the DTC 3L3A method the selection of converter voltage vector \mathbf{u} is exclusively based on the error vector angle. This allows us to eliminate inconvenient hysteresis comparators in the control system.

The three converter voltage vectors \mathbf{u} , which correspond to the shortest current derivative vectors, always form an equilateral triangle inside which the \mathbf{u}^* voltage vector is located. The triangle is formed by \mathbf{u}_{xxx} vectors (in a general case by \mathbf{w}_{bx} vectors Fig. 29a).

Selection of the triangle inside which \mathbf{u}^* vector is located is based on dependences (3.31) and (3.32). If inequality (3.31) is true, \mathbf{u}^* vector is located in triangle 0. Otherwise, the selection is based on φ_{sec} angle (3.32) (Fig. 29b) according to Table 5.

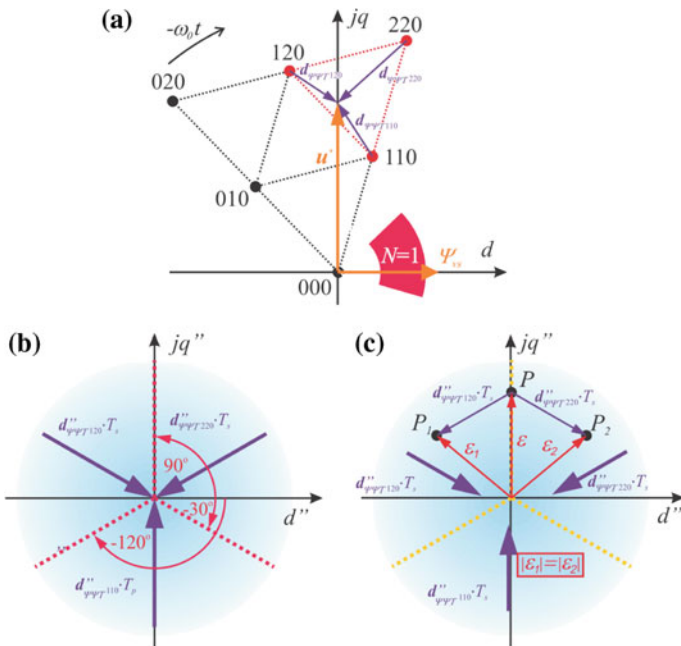


Fig. 28 Optimal error plane distribution in $d''q''$ reference frame (b) as referred to the arrangement shown in (a) as well as the equivalent impact of the adjacent converter voltage vectors on the error vector located on the division border (c)

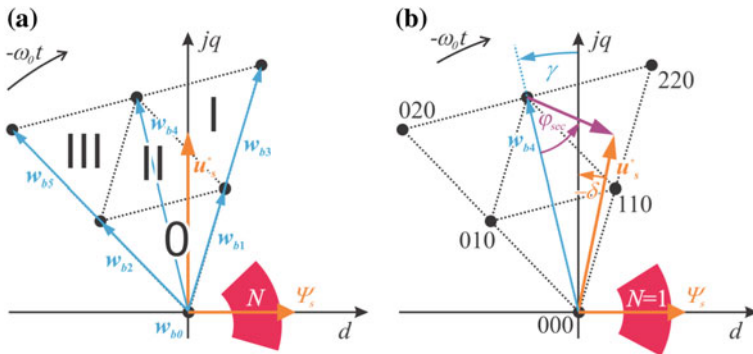


Fig. 29 Triangle numbers (a) and angle φ_{sec} construction (b)

$$\frac{U_{dc}\sqrt{3}}{6} > |\mathbf{u}^*| \cdot \cos(\gamma - \delta) \tag{3.31}$$

Table 5 Triangle selection table

$\varphi_{\text{sec}} \in (\pi/6, \pi/2)$	Triangle I
$\varphi_{\text{sec}} \in (-\pi/6, \pi/6)$	Triangle II
$\varphi_{\text{sec}} \in (-\pi/2, -\pi/6)$	Triangle III

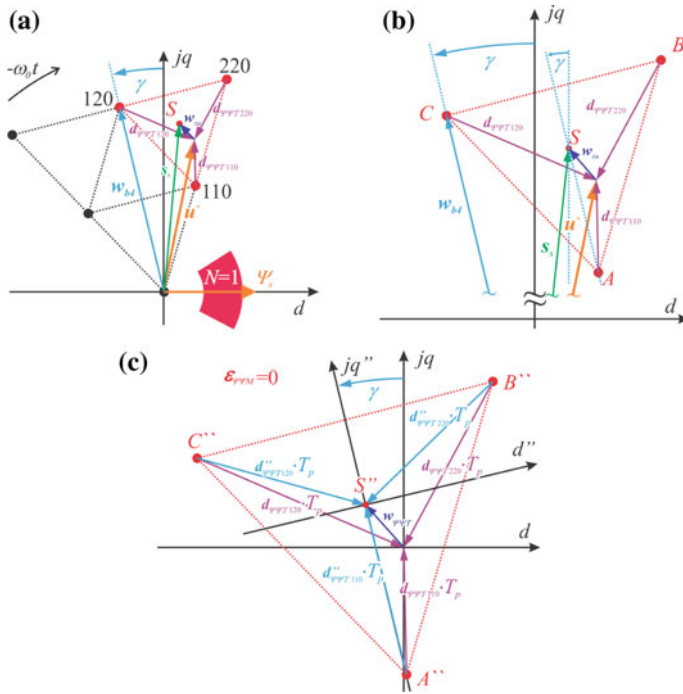


Fig. 30 Graphical interpretation of $x''y''$ coordinate system (c); influence of $d_{\psi/Txxx}$ vectors on error vector (c) in the arrangement shown in (a) whose main part is expanded (b)

$$\varphi_{\text{sec}} = \arcsin\left(\frac{|u^*|}{|w_{b4} - u^*|} \sin(\gamma - \delta)\right) \tag{3.32}$$

$$\gamma = \varphi_{w_{b4}} - \frac{\pi}{2} \tag{3.33}$$

In the arrangement shown in Fig. 30, the three converter voltage vectors that correspond to the shortest current derivative vectors $d_{\psi/Txxx}$ are u_{110} , u_{220} and u_{120} . They correspond to vectors $d_{\psi/T110}$, $d_{\psi/T220}$ and $d_{\psi/T120}$ respectively (Fig. 30a). The $d_{\psi/Txxx}$ vectors form the equilateral triangle ABC with a center point S (Fig. 30b).

Point S is shifted from $\mathbf{d}_{\psi/\psi T_{xxx}}$ vectors by vector \mathbf{w}_{su} (3.34) (Fig. 30b) that is equal to the difference between the center of triangle vector \mathbf{s}_s (3.35) and vector \mathbf{u}^* (Fig. 30b).

$$\mathbf{w}_{su} = \mathbf{s}_s - \mathbf{u}^* \tag{3.34}$$

$$\mathbf{s}_s = |\mathbf{s}_s| \cdot e^{j\phi_{s_s}} = 1/3(\mathbf{w}_{b0} + \mathbf{w}_{b1} + \mathbf{w}_{b2}) = 1/3(\mathbf{w}_{b1} + \mathbf{w}_{b2}) \tag{3.35}$$

During one sampling period T_s vectors $\mathbf{d}_{\psi/\psi T_{110}}$, $\mathbf{d}_{\psi/\psi T_{220}}$ and $\mathbf{d}_{\psi/\psi T_{120}}$ exert influence on the error vector by vectors $\mathbf{d}_{\psi/\psi T_{110}} \cdot T_s$, $\mathbf{d}_{\psi/\psi T_{220}} \cdot T_s$ and $\mathbf{d}_{\psi/\psi T_{120}} \cdot T_s$ respectively. They form equilateral triangle $A''B''C''$ (Fig. 19c) that is similar to triangle ABC with T_s ratio. In Fig. 30c, in order to simplify the analysis, zero value of error ($\varepsilon_{\psi/\psi T} = 0$) has been assumed. The center of triangle S'' is shifted to $\mathbf{d}_{\psi/\psi T_{xxx}}$ vectors by vector $\mathbf{w}_{\psi/\psi T}$ (Fig. 30c) (3.36).

$$\mathbf{w}_{\psi/\psi T} = T_s \mathbf{w}_{su} \tag{3.36}$$

It can be seen that the origin of the reference frame $d''q''$ is located in the center of triangle $A''B''C''$ (point S'') and is rotated at angle γ (3.33). Moreover, the vectors $\mathbf{d}_{\psi/\psi T_{xxx}}$ in $d''q''$ coordinate system have the same lengths (Fig. 30c). The transfer of error vector $\varepsilon_{\psi/\psi T}$ to that reference frame is carried out using dependence (3.38).

$$\varepsilon''_{\psi/\psi T} = |\varepsilon''_{\psi/\psi T}| \cdot e^{j\phi_{\varepsilon''_{\psi/\psi T}}} = (\varepsilon_{\psi/\psi T} - \mathbf{w}_{\psi/\psi T}) \cdot e^{-j\gamma} \tag{3.37}$$

Due to the fact that the division of error plane in $d''q''$ reference frame are identical only for triangles 0, I and III (Fig. 31), it is recommended to standardize the angle of error vector used for the selection of the converter voltage vector. This can be carried out by performing additional calculations for triangle II (3.38).

$$\varphi_{\varepsilon''_{\psi/\psi M}} = \begin{cases} \varphi(\varepsilon''_{\psi/\psi M}), & \text{for triangles 0, I, III} \\ \varphi(\text{Re}(\varepsilon''_{\psi/\psi M}) - j\text{Im}(\varepsilon''_{\psi/\psi M})), & \text{for triangle II} \end{cases} \tag{3.38}$$

The behavior of DTC 3L3A depends on the converter state. In steady states the method is optimized by selecting converter voltage vector \mathbf{u}_{xxx} that decreases the absolute value of the error vector by the use of the shortest error derivative vectors.

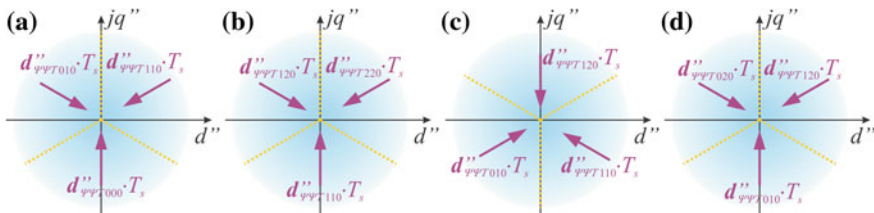


Fig. 31 Optimal division of error plane for 0 (a), I (b), II (c), III (d) triangles in sector $N = 1$

Table 6 Voltage vector selection table for DTC 3L3A method

φ_{e_g}	Sector N						
	Triangle	$N = 1$	$N = 2$	$N = 3$	$N = 4$	$N = 5$	$N = 6$
$(\frac{\pi}{6}; \frac{7\pi}{6})$	tr. 0	010	011	001	101	100	110
	tr. I	120	021	012	102	201	210
	tr. II	010	011	001	101	100	110
	tr. III	020	022	002	202	200	220
$(-\frac{5\pi}{6}; \frac{\pi}{6})$	tr. 0	000	000	000	000	000	000
	tr. I	110	010	011	001	101	100
	tr. II	120	021	012	102	201	210
	tr. III	010	011	001	101	100	110
$(-\frac{\pi}{6}; \frac{5\pi}{2})$	tr. 0	110	010	011	001	101	100
	tr. I	220	020	022	002	202	200
	tr. II	110	010	011	001	101	100
	tr. III	120	021	012	102	201	210

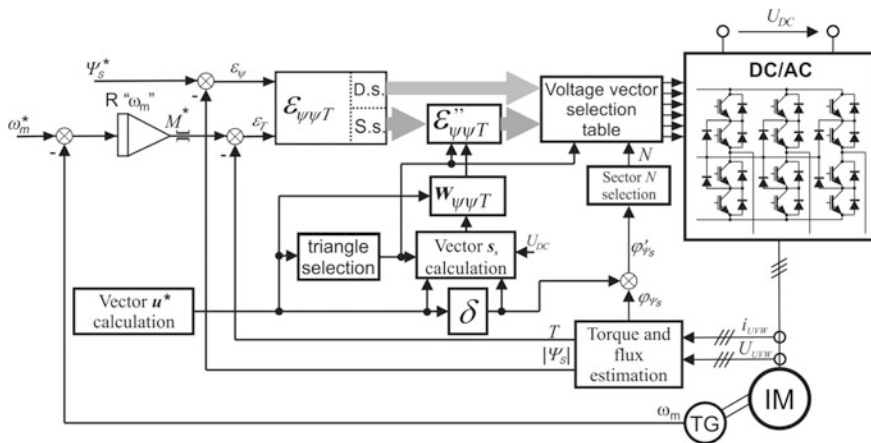


Fig. 32 Schematic diagram of the DTC 3L3A method

That allows us to achieve both low switching frequency and high accuracy of control. In the steady state selection of a converter voltage vector is determined by N sector number, triangle number (3.31), (3.32), (Table 5) as well as error vector angle φ_{e_g} (3.38) according to the vector selection table (Table 6) (Fig. 32).

In transient states the selected voltage vectors decrease both components of the error vector by the use of the longest error vector derivatives. That enables fast response to dynamic changes of torque. The transient state in the DTC 3L3A is chosen in the case when the component q of the error vector exceeds ε_{qdyn} value (3.39) corresponding to the maximum changes of error in the steady state during

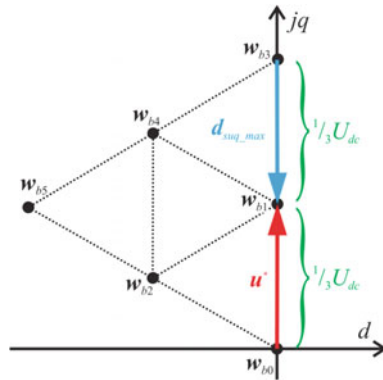


Fig. 33 Maximum value of vector d_{suq_max} proportional to current derivative vector

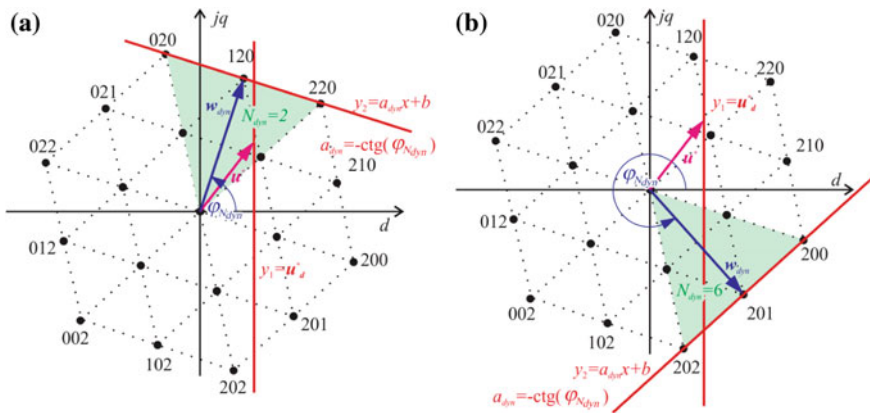


Fig. 34 Visualization of N_{dyn} sector, w_{dyn} vector and straight line y_2 for the ϵ_T error vector component higher (a) and lower (b) than zero

one sampling period. Due to the fact that the error vector in the DTC 3L3A method is formed by the converter voltage vectors that form an equilateral triangle, ϵ_{qdyn} value is defined as a length of the triangle side with the ratio of T_s (3.39) (Fig. 33).

$$\epsilon_{\psi/Tq_dyn} = d_{suq_max} \cdot T_s = \frac{1}{3} U_{DC} \cdot T_s \quad (3.39)$$

In transient states, the sector N_{dyn} (3.41) is determined on the basis of angle $\phi_{N_{dyn}}$ (3.40). In sector N_{dyn} , straight line $y_1 = u_d^*$ crosses the hexagon formed by converter voltage vectors u either on the top when ($\epsilon_T > 0$) (Fig. 34a) or on the bottom when ($\epsilon_T < 0$) (Fig. 34b). Vector w_{dyn} is calculated according to (3.42) (Fig. 34).

Table 7 Voltage vector selection table for DTC3L3A method in transient states

n_{dyn}	Sector N_{dyn}					
	$N_{dyn} = 1$	$N_{dyn} = 2$	$N_{dyn} = 3$	$N_{dyn} = 4$	$N_{dyn} = 5$	$N_{dyn} = 6$
-1	200	220	020	022	002	202
0	210	120	021	012	102	201
1	220	020	022	002	202	200

$$\varphi_{N_{dyn}} = \begin{cases} \arccos\left(\frac{3 \cdot u_d^*}{2 \cdot U_{dc}}\right) + \omega_0 t & , \text{ dla } \varepsilon_T \geq 0 \\ -\arccos\left(\frac{3 \cdot u_d^*}{2 \cdot U_{dc}}\right) + \omega_0 t & , \text{ dla } \varepsilon_T < 0 \end{cases} \quad (3.40)$$

$$N_{dyn} = \begin{cases} 1, & \text{for } \varphi_{N_{dyn}} \in (0; \pi/3) \\ 2, & \text{for } \varphi_{N_{dyn}} \in (\pi/3; 2\pi/3) \\ 3, & \text{for } \varphi_{N_{dyn}} \in (2\pi/3; \pi) \\ 4, & \text{for } \varphi_{N_{dyn}} \in (-\pi; -2\pi/3) \\ 5, & \text{for } \varphi_{N_{dyn}} \in (-2\pi/3; -\pi/3) \\ 6, & \text{for } \varphi_{N_{dyn}} \in (-\pi/3; 0) \end{cases} \quad (3.41)$$

$$\mathbf{w}_{dyn} = w_{dyn_d} + jw_{dyn_q} = \frac{\sqrt{3}}{3} U_{dc} \cdot e^{j\left(\left(N_{dyn}-1\right)\frac{\pi}{3}\right) + \frac{\pi}{6}} \cdot e^{-j\omega_g t} \quad (3.42)$$

The number of voltage vector n_{dyn} (3.44) is calculated on the basis of the sign of slope a_{dyn} (3.43) of straight line y_2 (Fig. 34) as well as ε_T , \mathbf{w}_{dyn} and \mathbf{u}^* vectors.

$$\text{sgn}(a_{dyn}) = -\text{sgn}(w_{dyn_d}) \cdot \text{sgn}(w_{dyn_q}) \quad (3.43)$$

$$n_{dyn} = \begin{cases} -\text{sgn}(\varepsilon_\psi \cdot \varepsilon_M), & \text{for } \text{sgn}(a_{dyn}) = \text{sgn}(\varepsilon_\psi \cdot \varepsilon_M) \vee \text{sgn}(a_{dyn}) \neq \text{sgn}(u_d^* - w_{dyn_d}) \\ 0, & \text{for } \text{sgn}(a_{dyn}) \neq \text{sgn}(\varepsilon_\psi \cdot \varepsilon_M) \wedge \text{sgn}(a_{dyn}) = \text{sgn}(u_d^* - w_{dyn_d}) \end{cases} \quad (3.44)$$

Sector N_{dyn} and vector number n_{dyn} are used in transient states to select the \mathbf{u} converter voltage vector according to Table 7.

3.2.2 Experimental Results

The investigations were performed for two values of load i.e. 10 and -7 N m, and for three set values of angular speed i.e. 10, 20 and 150 rad/s. The motor used in the investigations had the following nominal values: $P_n = 4$ kW, $U_n = 400$ V, $f_n = 50$ Hz, $I_n = 8.3$ A, $\omega_n = 150$ rad/s, $\cos\varphi_n = 0.82$. The sampling time of the control DC/AC converter amounted to 33 μ s.

Table 8 Experiment results for DPC and DPC 3L3A methods

Method	ω_m (rad/s)	M (N m)	f_{1T} (kHz)	THD (%)	ΔT_{RMS} (N m)
DTC	10	10	1.90	36.4	0.83
DTC 3L 3A			2.38	4.1	0.49
DTC	150	10	6.72	13.5	0.93
DTC 3L 3A			4.22	4.4	0.59
DTC	20	-7	1.98	11.5	0.97
DTC 3L 3A			2.01	7.3	0.53
DTC	150	-7	7.68	10.8	0.96
DTC 3L 3A			4.27	5.2	0.59

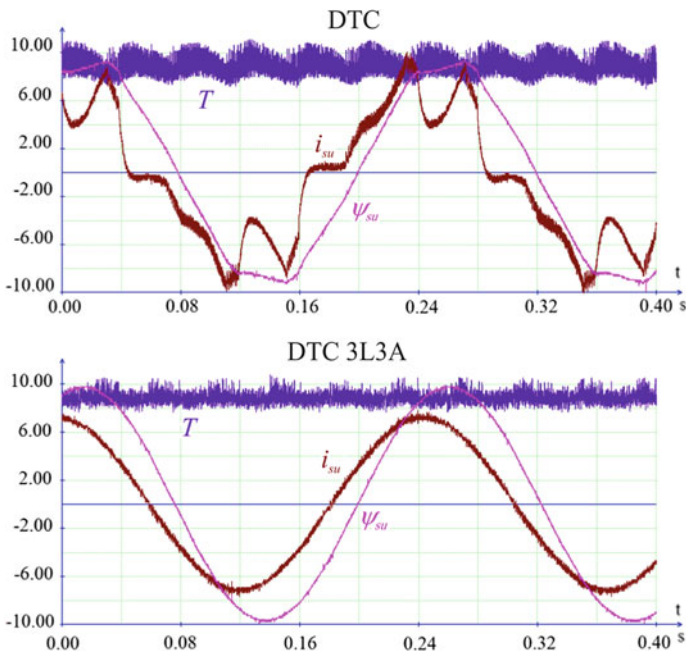


Fig. 35 Time courses of torque (T -scale 1:1), stator phase current (i_{su} -scale 1:1) and stator phase flux (ψ_{su} -scale 10:1) for 10 rad/s angular speed and 10 N m load for DTC3L3A and DTC methods

The basis for comparing the DTC 3L3A and DTC [41] methods were both the coefficient described by dependence (3.45) [88] as well as THD value. The results of the experiments are presented in Table 8, Figs. 35 and 36.

$$T_{(puls)RMS} = \sqrt{\frac{1}{T_o} \int_0^{T_o} (T - T_{AV})^2 dt} \tag{3.45}$$

where

- $T_{(plus)RMS}$ RMS value of all of torque harmonics for constant torque set value,
- T_0 period of phase current,
- T instantaneous value of electromagnetic torque,
- T_{AV} mean value of electromagnetic torque.

The investigation results have shown that the DTC 3L3A method is characterized by very good performance. The switching frequencies in almost the whole range of control are low, which means that they have very good efficiency. According to Table 8 the DTC 3L3A method shows low values of phase current distortions and torque ripples. The flux and current for DTC 3L3A method has almost a perfect sinusoidal shape (Fig. 35).

The DTC 3L3A method, in contrast to DTC method, makes it possible to generate nominal flux for a set zero angular speed with very good accuracy. As can be seen in Fig. 36 the real value of flux almost fully covers its set value. The above is desirable in order to achieve better performance at startup. As in the case shown in Fig. 36 when torque is not set until flux has achieved its nominal value by linear increase, large ripples of current during startup are eliminated.

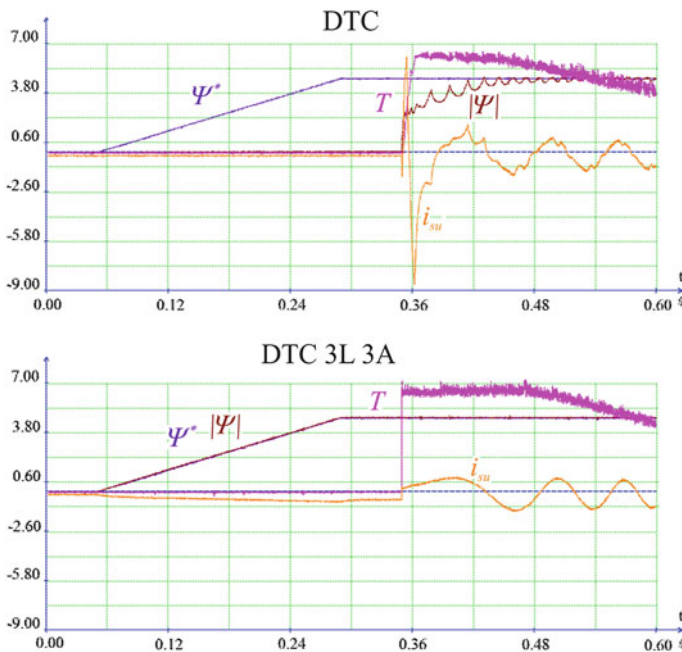


Fig. 36 Time courses of set and real stator flux absolute values (Ψ^* , $|\Psi|$ -scale 5:1), phase current (i_{su} -scale 1:10) and torque (T -scale 1:3) during startup for DTC 3L3A and DTC methods

3.3 Control Strategy of the DC-Link Voltage Balance in the Three-Level NPC DC/AC Inverter

Of all multilevel topologies, the three-phase three-level Neutral-Point-Clamped (NPC) DC/AC inverter is the most widely used and investigated. However, the neutral-point voltage-balancing problem, which is characteristic of the three-level NPC topology, limits the development and application of three-level NPC inverter [95–98]. In order to ensure proper operation of the inverter, it is essential to solve the balancing problem. In many cases, without NP voltage balancing control, the harmonic components greatly increase, or even, in some instances, DC-link capacitors and switching devices can be damaged.

The easiest solution that allows proper operation of the inverters the application presented in Fig. 37., i.e. the use of two independent three-pulse rectifiers and a connection point “0” in the DC-link of the neutral point N supply network.

The DC-link connection shown in Fig. 37 provides independent charging of capacitors C_H and C_L . This solution ensures proper balancing of DC-link capacitor voltages without the need to use additional control algorithms or systems. On the other hand, the solution requires the use of the grid neutral point “N”, which is not always available. Additionally, it can cause a number of problems, such as an increase of DC-link voltage ripples. Figures 38 and 39 show the differences during the drive start-up for two power supply systems: four-wire (neutral point “N” of supply network wired to point “0” in the DC-link) (Fig. 38a) and 3-wire supply system (Fig. 39a). In both cases, induction motor (IM) is controlled using the standard DTC method without DC-link voltage balancing algorithms.

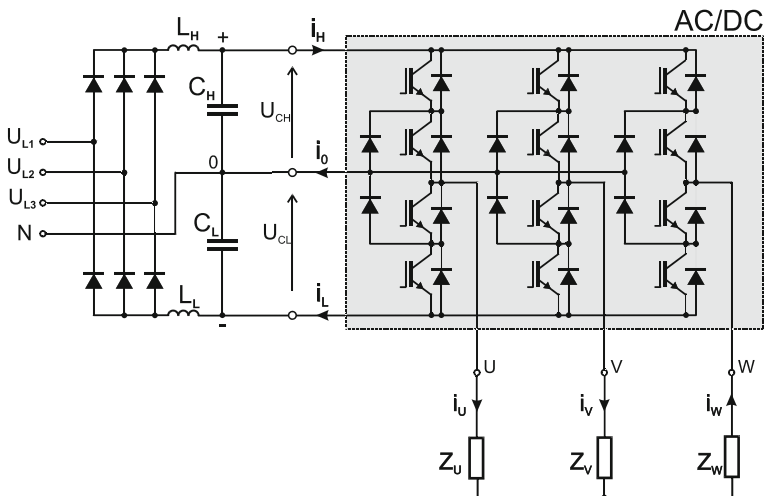


Fig. 37 Schematic diagram of three-level inverter supplied by two three-pulse rectifiers with grid neutral point “N” connected to “0” point of the DC-link

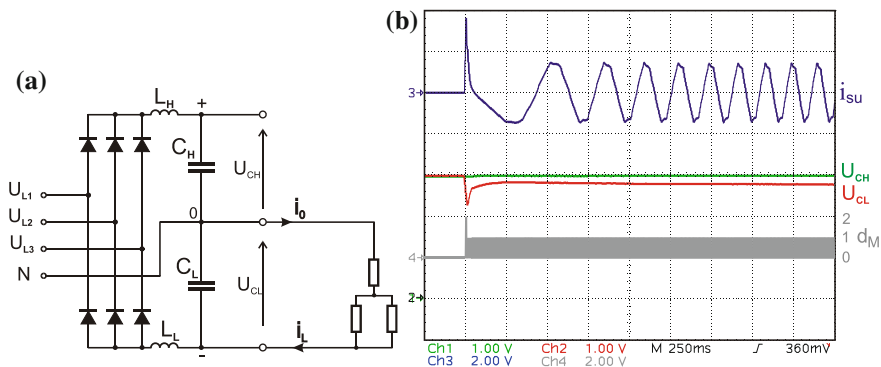


Fig. 38 Schematic diagram of three-phase, four-wire power supply system (a) as well as time courses of capacitor voltages— U_{CL} , U_{CH} (50 V/div) and stator current i_{su} (4 A/div)

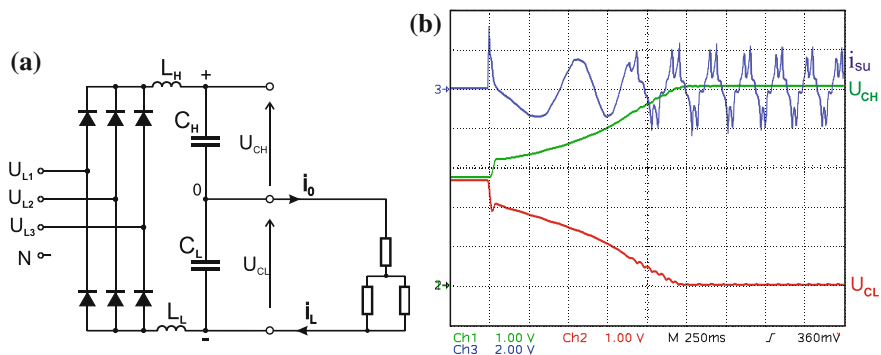
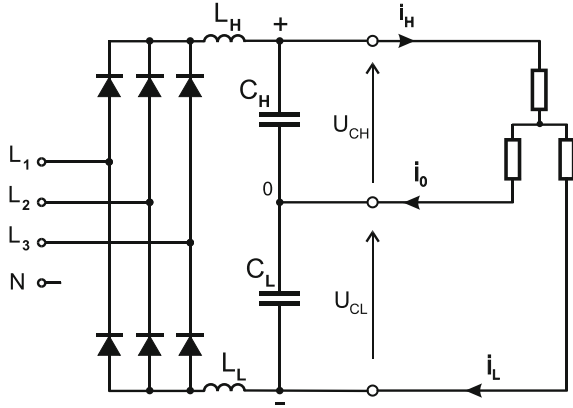


Fig. 39 Schematic diagram of three-phase, three-wire power supply system (a) as well as time courses of capacitor voltages— U_{CL} , U_{CH} (50 V/div) and stator current i_{su} (4 A/div) (b)

The above measurements of voltages in the DC circuit were carried out at reduced power grid voltage level (110 V) due to the voltage restrictions of capacitors. As follows from the above measurements, the control method without an additional balancing algorithm is not possible to use. The voltage levels on the capacitors depend mainly on the capacitor current directions. Thus selecting an appropriate sequence and type of inverter voltage vectors can directly affect capacitor voltage level control.

A three-level NPC inverter has 27 available switching states that correspond to 19 inverter voltage vectors. The vectors can be divided depending on their magnitude into four groups: “large/long”, “medium”, “small/short” and “zero” vectors. Zero vectors (000, 111 and 222) connect all the outputs of the inverter to the same DC-link voltage level, and therefore do not produce any current in the DC-link capacitors. As a result they do not affect neutral-point potential. The small voltage vector includes 12 switching states. Six of them make the current flow through the

Fig. 40 Schematic diagram illustrating the flow of the inverter and capacitor current for a medium voltage vector



lower capacitor (C_L), as illustrated in Fig. 39. The current flow can either charge or discharge capacitor C_L depending on the directions of currents i_0 and i_L . The other six states of the small voltage vectors make the current flow through the upper capacitor (C_H) and influences its voltage value. All these twelve vectors significantly affect the voltage balance of DC-link capacitors. In the case of the large vectors, the neutral-point does not participate in energy transmission since the current flows through both upper and lower capacitors. Therefore, large vectors have no impact on the voltage balance.

The medium voltage vectors have six switching states. When a load is powered by medium vector voltage (Fig. 40), capacitor voltage changes can be analyzed basing on the direction of current i_0 . When current i_0 flows through node “0” and there is a constant value of the DC-link voltage in one sample period T_p , as shown in (Fig. 40), we have a discharge of capacitor C_H , which, in turn, causes an increase of capacitor voltage C_L .

For a case in which current i_0 flows to a three-phase load, it causes voltage discharge on capacitor C_L , and at the same time, charges capacitor C_H . Assuming that the sum of the instantaneous values of three-phase load is equal to zero:

$$i_U + i_V + i_W = 0 \tag{3.46}$$

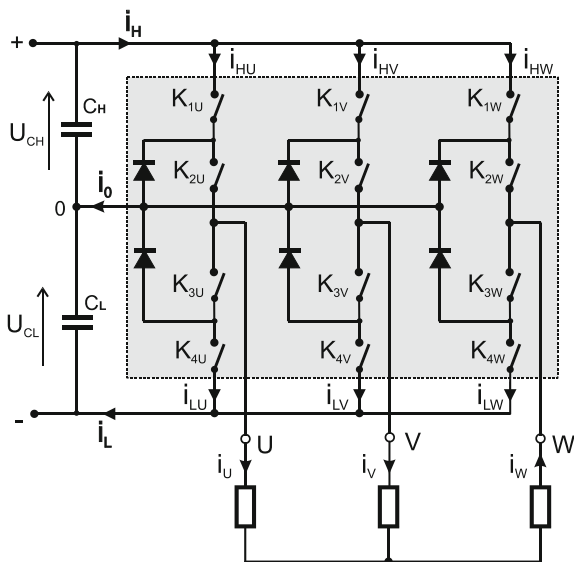
Basing on Fig. 40, it can be stated that:

$$i_H - i_0 - i_L = 0 \Rightarrow i_0 = i_H - i_L \tag{3.47}$$

Current values of “ i_H ” and “ i_L ” can be determined from the sum of the currents of each phase of the upper and lower connections of three-level inverter (Fig. 41):

$$i_H = i_{HU} + i_{HV} + i_{HW} \tag{3.48}$$

Fig. 41 Illustration of current directions in three-phase, three-level inverter



$$i_L = i_{LU} + i_{LV} + i_{LW} \tag{3.49}$$

Specific currents for each phase can be calculated knowing the configurations of switch states and the current value of each analyzed phase of the three-phase load.

For example, current values i_{LU} and i_{HU} are calculated as:

$$i_{HU} = (K_{1U} \cdot K_{2U}) \cdot i_U \tag{3.50}$$

$$i_{LU} = -(K_{3U} \cdot K_{4U}) \cdot i_U \tag{3.51}$$

Knowing that switching states K_{3X} and K_{4X} are always opposed to the states of switches K_{1X} and K_{2X} , Eq. (3.51) can be written as:

$$i_{LU} = -(\bar{K}_{1U} \cdot \bar{K}_{2U}) \cdot i_U \tag{3.52}$$

where the switching states K_{xxx} for each phase can take the values 0 or 1.

Substituting (3.50)–(3.52) into Eqs. 3.48 and 3.49, we obtain the following current dependencies in the upper and lower arm of the bridge:

$$i_H = (K_{1U} \cdot K_{2U}) \cdot i_U + (K_{1V} \cdot K_{2V}) \cdot i_V + (K_{1W} \cdot K_{2W}) \cdot i_W \tag{3.53}$$

$$i_L = -(\bar{K}_{1U} \cdot \bar{K}_{2U}) \cdot i_U - (\bar{K}_{1V} \cdot \bar{K}_{2V}) \cdot i_V - (\bar{K}_{1W} \cdot \bar{K}_{2W}) \cdot i_W \tag{3.54}$$

Current value i_0 can be calculated from currents i_H and i_L using Eq. 3.47. The knowledge of current value i_0 is required for proper operation of the balancing algorithm and division of voltage on the capacitors in the DC-link.

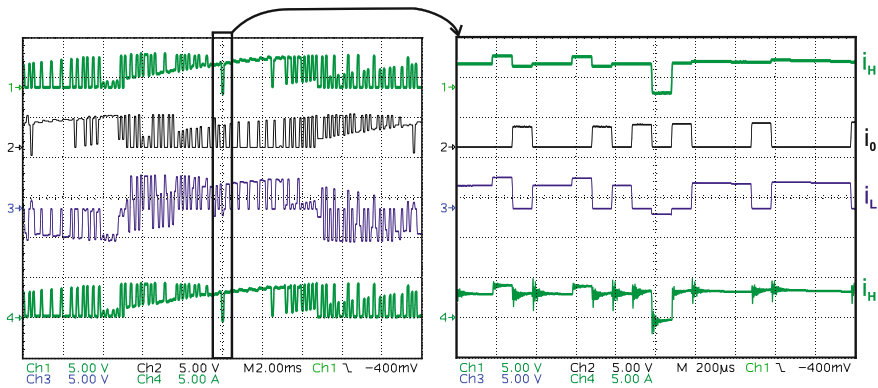


Fig. 42 Calculated current waveforms i_H , i_o and i_L (CH1-CH3) and actual current i_H (Ch-4) in real capacitor C_H of the inverter (scale: 5 A/div)

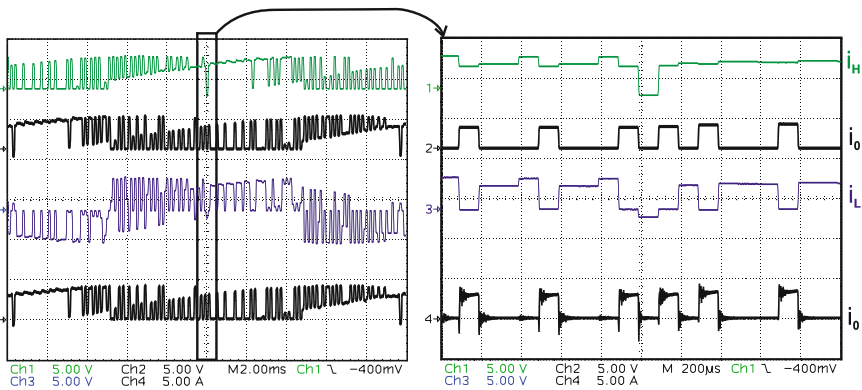


Fig. 43 Calculated current waveforms i_H , i_o and i_L (CH1-CH3) and actual current i_o (Ch-4) in the wire connected with middle point “0” of capacitors (scale: 5 A/div)

The correctness of the presented dependencies was verified by measurements on a real laboratory stand with at three-level DC/AC inverter (Figs. 42, 43 and 44). The waveforms were recorded in the inverter without connection to the neutral point using the DTC method divided into 12 sectors [99]. In the method both “small positive” and “small negative” vectors were used.

3.3.1 Operational Principle of Balanced Voltage Division Algorithm

Based on the calculated current and actual voltage values (U_{CH} and U_{CL}), an algorithm was created to provide balanced voltage division on the capacitors. Analyzing the input data, the algorithm replaces switch configurations of one “small

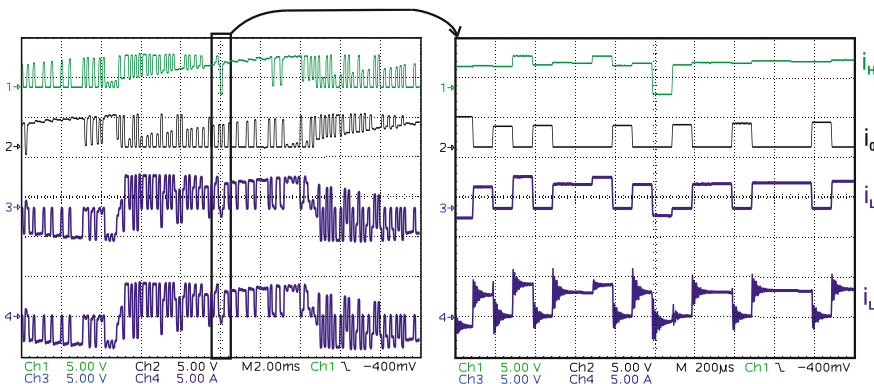


Fig. 44 Calculated current waveforms i_H , i_0 and i_L (CH1-CH3) and actual current i_L (Ch-4) in real capacitor C_L of the inverter (scale: 5 A/div)

vector” into another “small vector”. For example, it replaces an equivalent switch from vector u_{100} into its counterpart in u_{211} . In the control system, the replacements performed by the algorithm provide independent control of voltages in the DC and have no effect on the changes in the controlled torque and flux. For proper operation of the voltage balancing algorithm, it is required that the control system uses “small vectors” during normal operation. The necessary input signals are actual load values of the phase currents, the voltage on the capacitors in the DC-link and actual switching states of the control system.

Based on the calculated values of currents i_H , i_0 and i_L and also voltage values on the capacitors, it is possible to formulate instructions for the proper operation of the algorithm. There are four cases determining the final choice of the appropriate configuration of switches specifying the vector type: “small positive” or “small negative”. The drawings shown on Figs. 45 and 46 illustrate the dependencies used in the conditional statements of the algorithm.

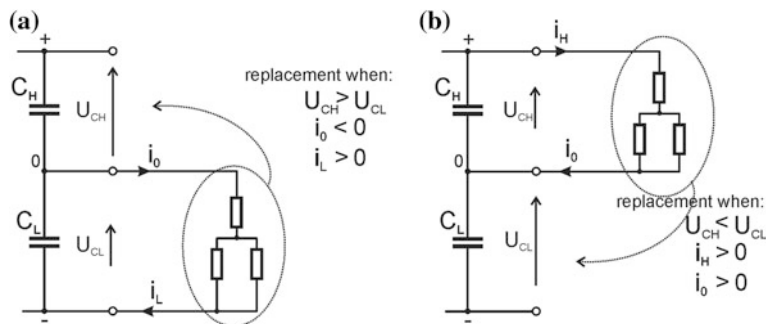


Fig. 45 Distribution of i_H , i_0 , i_L currents and U_{CH} , U_{CL} voltages during motor operation. For “small negative” vectors (a) and “small positive” vectors (b) with the recommended change load connection with fulfilled dependencies on voltage and current values

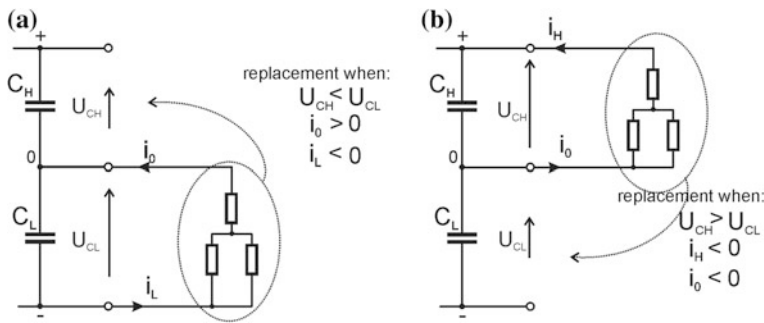


Fig. 46 Distribution of i_H , i_0 , i_L currents and U_{CH} , U_{CL} voltages during regenerative load for “small negative” (a) and “small positive” vectors (b) including the recommended changes with the fulfilled dependencies on voltage and current values

For motor operation, i.e. when energy flows from DC-link to the load, as shown in Fig. 45, two cases are considered. In each of these cases, depending on the presented conditions, there is a replacement of equivalent small voltage vectors.

Figure 45a illustrates the case where the control system “decided” to use a “small negative” vector while U_{CL} voltage is less than U_{CH} and $i_0 < 0$ and $i_L > 0$. It follows from the relations that for the small negative vector selected by the control system, the value of voltage U_{CL} will further decrease. In this case, the algorithm of balanced voltage division just before choosing the voltage vector changes the configuration of switches selected earlier by the control method. This vector replacement from a “small negative” into “small positive” results in current distributions, i.e. reduction of voltage U_{CH} , and increase of voltage U_{CL} , as shown in Fig. 45b. Similarly, the operation of the algorithm can be analyzed during the recovery of energy from the load to the DC-link circuit (Fig. 46), where switching between equivalent vectors results in a steady voltage increase on both capacitors.

Cyclic switching between “small vectors” of two-type switch the satisfied conditions, as in Figs. 45 and 46, makes it possible to maintain equal distribution of voltages on the capacitors in the DC-link circuit. The above algorithm works well in static and dynamic states, as well as during the return of power to the DC-link circuit. The main advantage of the algorithm is its ability to be applied to each control method with nonlinear controllers, where switch configurations in every T_s step of the control system are known. It is impossible to apply this algorithm for the PWM modulator control systems, in which explicit configuration of switches is not specified.

This algorithm analyzes the operating states of the inverter for “small” vectors only. If the control system chooses another type of voltage vector, the algorithm will not modify the switch configuration.

Figure 47 shows the waveforms during start-up and recurrence of the drive system in the DTC method control with the balanced algorithm of voltage division in DC-link. Both the operating statuses of steady and dynamic states as well of U_{CH} and U_{CL} voltage waveforms practically overlap.

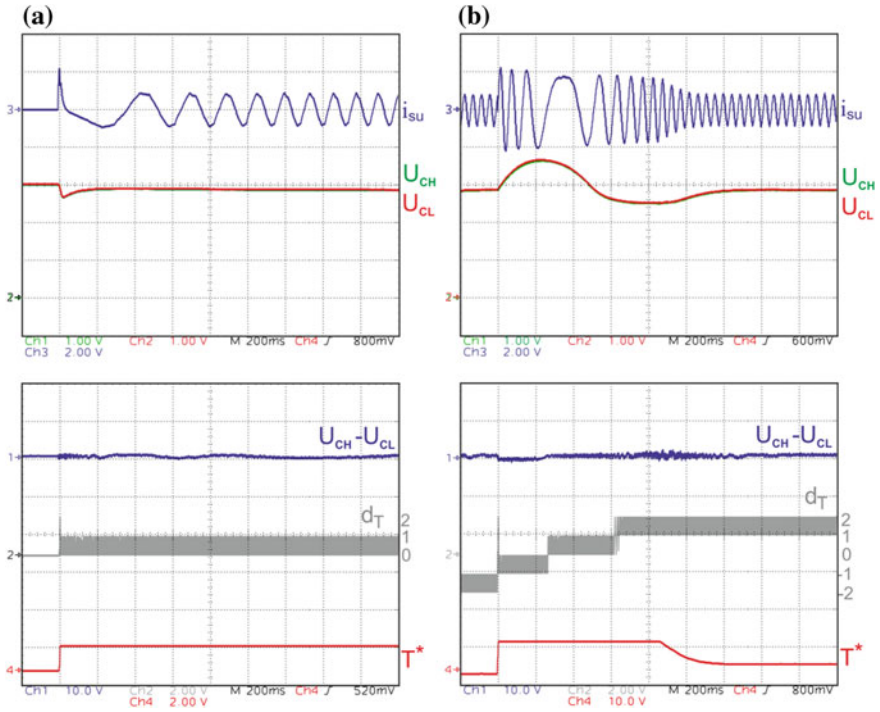


Fig. 47 Waveforms of voltages on the capacitors in the DC-link (50 V/div) and their difference $U_{CH} - U_{CL}$ (10 V/div) during start-up (a) and recurrence at a speed of ± 70 rad/s (b)

4 Predictive Control Methods

4.1 Constant Switching Frequency DPC-3V Method

The new predictive DPC-3V method is based on the analysis of the influence of the selected converter voltage vector on complex current error vector ϵ_{ixy} . Vector ϵ_{ixy} , expressed in the rotating xy reference frame, is defined as follow:

$$\epsilon_{ixy} = \epsilon_{ix} + j\epsilon_{iy} \tag{4.1}$$

In order to illustrate the impact of the choice of the selected voltage vector of the converter on the current error, it is necessary to define the error vector in the next sampling step $\epsilon_{ixy(k+1)}$. Assuming that the set current vector remains unchanged

during a short period of time T_s , the error vector after T_s time is expressed by the following dependence:

$$\boldsymbol{\varepsilon}_{ixy(k+1)} = \boldsymbol{i}_{xy}^* - \boldsymbol{i}_{xy(k+1)} \tag{4.2}$$

where \boldsymbol{i}_{xy}^* —set grid current vector, $\boldsymbol{i}_{xy(k+1)}$ —grid current vector in the next sampling step defined as:

$$\boldsymbol{i}_{xy(k+1)} = \boldsymbol{i}_{xy(k)} + T_s \boldsymbol{d}_{gixxx} \tag{4.3}$$

Taking into account (4.2) and (4.3), the predicted location of the current error vector in the successive sampling step can be rewritten as:

$$\boldsymbol{\varepsilon}_{ixy(k+1)} = \boldsymbol{i}_{xy}^* - (\boldsymbol{i}_{xy(k)} + T_s \boldsymbol{d}_{gixxx}) = \boldsymbol{\varepsilon}_n - T_s \boldsymbol{d}_{gixxx} \tag{4.4}$$

Equation (4.4) shows that the error vector changes are determined by the vector opposite to grid current derivative vector \boldsymbol{d}_{gixxx} . In order to simplify and increase the clarity of further analysis, the vector determining the changes of the error vector is defined and expressed as follows:

$$\boldsymbol{d}_{\varepsilon xxx} = -T_s \boldsymbol{d}_{gixxx} \tag{4.5}$$

Taking (4.5) into account (4.4) can be shaped as:

$$\boldsymbol{\varepsilon}_{ixy(k+1)} = \boldsymbol{\varepsilon}_{ixy(k)} + \boldsymbol{d}_{\varepsilon xxx} \tag{4.6}$$

In both the standard nonlinear DPC- δ and FCS-MPC methods only one voltage vector of the converter is used during one sampling step. As a result, possibilities of minimizing the current error are limited. This situation is shown in Fig. 48a.

The error vector after T_s sampling time can be moved in the steady state to one of the three points defined by appropriate vectors $\boldsymbol{d}_{\varepsilon xxx}$ (4.6). The length of these

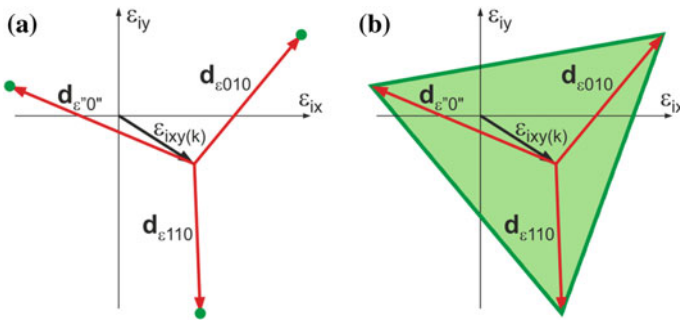


Fig. 48 Possibilities of error vector minimization using one (a) and three (b) voltage vectors of the converter during sampling time T_s

vectors depends on the value of sampling time T_s . As a result, in order to keep the required quality of current control, a short sampling time (below $25 \mu s$) is needed, which may require the use of a more expensive microprocessor of higher performance. Another significant disadvantage of DPC table-based methods is variable switching frequency of the converter's transistors.

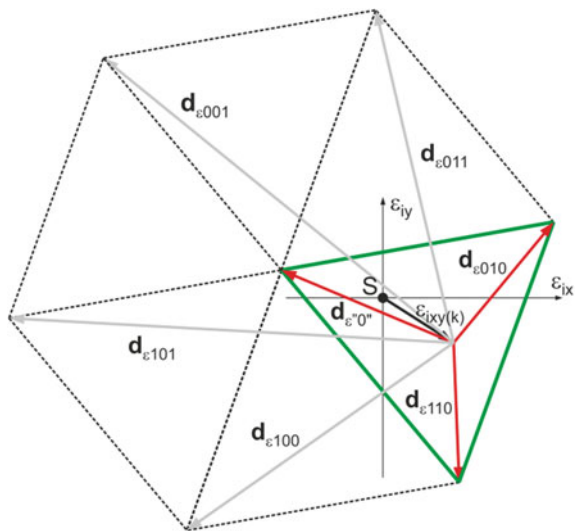
Figure 48b shows the possibilities of error vector minimization when three voltage vectors generating the shortest current derivatives (similar to the PWM-based methods) are selected during a single sample period. In this case, the predicted error vector $\mathbf{e}_{ixy(k+1)}$ can be placed at any point lying inside an equilateral triangle defined by direction vectors $\mathbf{d}_{e,xxx}$. It can be seen from Fig. 48b that, if the origin of the reference frame is situated inside the triangle, it is possible to achieve full compensation of the error vector components.

The situation shown in Fig. 48b relates to only one of the six sectors. In a general case, such a triangle can be created for each of the two adjacent active voltage vectors and zero vector. If we take this into account, full possibilities of error vector control provided by a two-level converter can be shown in Fig. 49. The current error vector during sampling period T_s can be directed to any point lying inside the hexagon.

The main goals of the DPC-3V algorithm are to:

- choose appropriate voltage vectors,
- calculate voltage vector application times.

Fig. 49 Full possibilities of error vector control in one sampling period provided by two-level converter



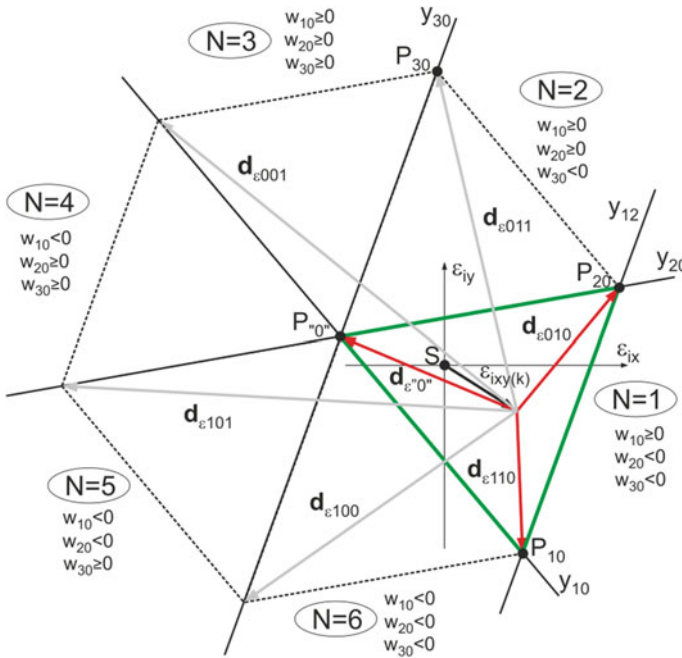


Fig. 50 Graphic illustration of voltage vector choice

4.1.1 Voltage Vectors Selection

Choice of voltage vectors is dependent on the position of S point relative to the hexagon from Fig. 49. There are six areas corresponding to six equilateral triangles. For each of them three voltage vectors (two active and “zero” vector) and the sector number N are assigned. To select appropriate voltage vectors we need to determine in which of these areas S point (the origin of the xy reference frame related to current error) is located.

The idea of voltage vector selection is shown in Fig. 50.

To choose the converter voltage vectors we should determine the equations of three straight lines (y_{10} , y_{20} and y_{30}) containing vertexes and the center of the hexagon. Knowing $d_{\epsilon 110}$, $d_{\epsilon 010}$ and $d_{\epsilon 011}$ (4.5) and the error vector, we can calculate the coordinates of P_{10} , P_{20} , P_{30} and $P_{0'}$ points, and hence obtain the straight line equations in a general form $Ax + By + C = 0$. After that coefficients w_{xx} are calculated from (4.7):

$$w_{xx} = A_{xx}x_p + B_{xx}y_p + C_{xx} \tag{4.7}$$

where: A_{xx} , B_{xx} and C_{xx} are the coefficients of straight line y_{10} , y_{20} and y_{30} equations respectively, x_p and y_p are coordinates of S point (in this case, S is the origin of the reference frame, so its coordinates are equal to zero).

Table 9 Voltage vectors used in corresponding sectors N

w_{10}	w_{20}	w_{30}	Sector N	Used voltage vectors
+	-	-	1	$\mathbf{u}_{110}, \mathbf{u}_{010}, \mathbf{u}_{00}$
+	+	-	2	$\mathbf{u}_{010}, \mathbf{u}_{011}, \mathbf{u}_{00}$
+	+	+	3	$\mathbf{u}_{011}, \mathbf{u}_{001}, \mathbf{u}_{00}$
-	+	+	4	$\mathbf{u}_{001}, \mathbf{u}_{101}, \mathbf{u}_{00}$
-	-	+	5	$\mathbf{u}_{101}, \mathbf{u}_{100}, \mathbf{u}_{00}$
-	-	-	6	$\mathbf{u}_{100}, \mathbf{u}_{110}, \mathbf{u}_{00}$

Knowing the signs of w_{xx} coefficients, we can choose from Table 9 sector number N and voltage vectors that provide error vector minimization.

4.1.2 Calculation of the Voltage Vectors Application Times

Basing on the equations of straight lines containing triangle sides, we should check if the origin of the reference frame lies inside the triangle (Fig. 51). If it does, then the whole procedure can be reduced to the calculation of relative switching-on times (a_{110} , a_{010} and a_{00}) of the chosen converter voltage vectors fulfilling the following equation:

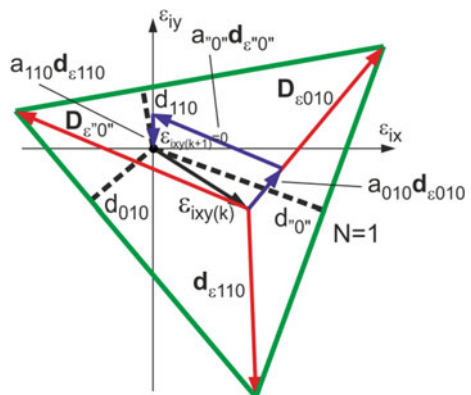
$$\boldsymbol{\varepsilon}_{ixy(k+1)} = \boldsymbol{\varepsilon}_{ixy(k)} + a_{110}\mathbf{d}_{\varepsilon 110} + a_{010}\mathbf{d}_{\varepsilon 010} + a_{00}\mathbf{d}_{\varepsilon 00} = 0 \tag{4.8}$$

The values of the switching-on times of the chosen vectors are described as follows:

$$t_{110} = a_{110} \cdot T_s, \quad t_{010} = a_{010} \cdot T_s, \quad t_{00} = a_{00} \cdot T_s \tag{4.9}$$

A graphical illustration of (4.8) is shown in Fig. 51. In this case (in the steady state, sector $N = 1$) zero vector (\mathbf{u}_{111} or \mathbf{u}_{000}) is used for time t_{00} , vector \mathbf{u}_{010} is

Fig. 51 Compensation concept of grid current error vector $\boldsymbol{\varepsilon}_{iy(k)}$ (steady state)



used for t_{010} and finally vector \mathbf{u}_{110} is used for t_{110} . The sum of the three time periods must be equal to sampling period T_s .

$$t_{110} + t_{010} + t_{v0v} = T_s \tag{4.10}$$

As can be seen from Fig. 51, after T_s sampling period, the current error vector is equal to zero, which means that the errors of both current components have been accurately compensated for. Analyzing Fig. 51, it can be theoretically proved by making use of the trigonometric dependences in an equilateral triangle that switching-on times of each voltage vector of the converter are clearly determined by individual lengths of d_{xxx} i.e. the distance of the origin of the reference frame from the straight lines containing triangle sides. These dependences are presented as follows:

$$a_{110} = \frac{d_{110}}{h}, \quad a_{010} = \frac{d_{010}}{h}, \quad a_{v0v} = \frac{d_{v0v}}{h} \tag{4.11}$$

where h is the height of an equilateral triangle and its value is defined as:

$$h = \frac{\sqrt{3}}{2} \frac{|\mathbf{u}_{\alpha\beta}|}{L} = \frac{1}{L} \frac{\sqrt{3}}{2} \frac{2U_{DC}}{3} = \frac{\sqrt{3}U_{DC}}{3L} \tag{4.12}$$

Making use of (4.11), the converter output spatial vector is calculated and reproduced using the SVM technique.

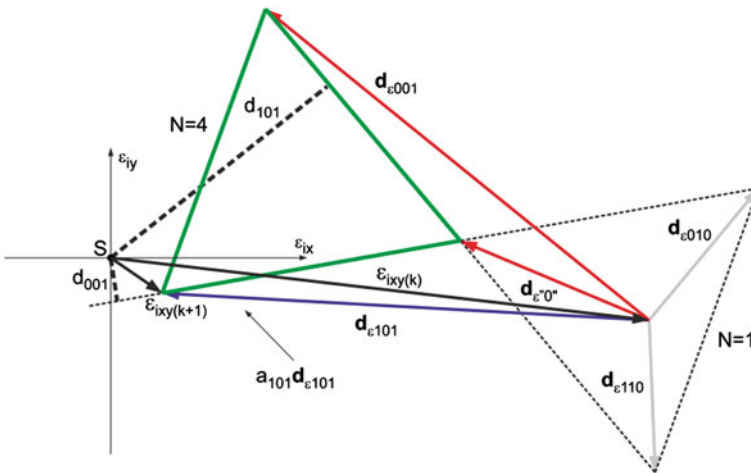


Fig. 52 Compensation concept of grid current error vector in transient states, for the origin of the reference frame lying outside the hexagon

Such an approach to grid converter control will ensure minimization of the current error vector, and thus reduce both the grid current pulsation and harmonics content.

In transient states the origin of the reference frame can be located outside the hexagon presented in Fig. 49, as shown in Fig. 52.

This time, a full compensation of error vector components in a single sampling period T_s is impossible, but even then the control algorithm should be able to minimize the error vector.

In the proposed DPC-3V method one of the active vectors (assigned to sector N from Table 9) remains switched on all the time T_s to ensure the fastest system response to dynamically changing values of the set grid current.

The choice of an appropriate vector is determined by the shortest distance of the reference frame origin from the straight lines containing active vectors used in the given sector N . For the presented case ($N = 4$):

$$d_{\min} = \min(d_{001}, d_{101}) \tag{4.13}$$

Two options are possible:

- (a) if $d_{\min} = d_{001}$, then $t_{001} = T_s, t_{101} = 0, t_{v'0'} = 0$
- (b) if $d_{\min} = d_{101}$, then $t_{001} = 0, t_{101} = T_s, t_{v'0'} = 0$

The final schematic diagram of the discussed control method is shown in Fig. 53.

The new DPC-3V algorithm minimizes the error vector of the grid current for each and every state of the system. In the steady state the control system uses the

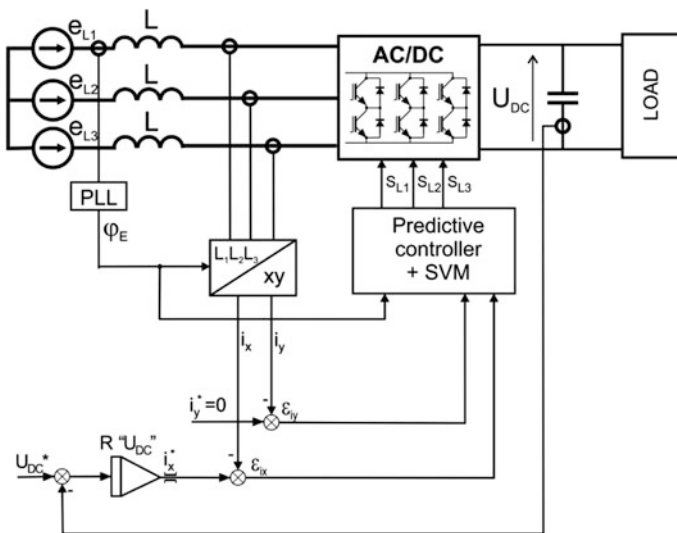


Fig. 53 Control structure of the DPC-3V

SVM modulation that provides all the advantages typical of linear methods, i.e. constant switching frequency, low grid current ripples. Moreover, it has no limitations arising from the use of linear controllers. In transient states, the proposed solution provides maximum dynamics, comparable to the fastest nonlinear control methods.

4.1.3 Experimental Results

The laboratory tests were performed on the set-up consisting of an AC/DC converter (6 kW of rated power), AC-side choke and digital control system with Analog Devices ADSP-21262 DSP processor. The converter was loaded by resistance. The parameters of the tested model are summarized in Table 10.

Sampling period T_s for DPC- δ is set to 200 μ s. Figure 54 shows phase current i_{L1} , voltage e_{L1} and x and y axis components of current vector i_{xy} during a steady state operation. The set values of xy current vector components are equal to 9 and 0 A for x and y axis component respectively. It can be seen that the proposed predictive DPC-3V method provides a sinusoidal current despite of the distorted grid voltage.

The behavior of the presented control method in transient states (during a step change of the reference value of current component ix from 9 to 3 A) has been also

Table 10 Main data of laboratory setup

Symbol	Quantity	Value
e_{L-L}	Grid voltage L-L	400 V
U_{DC}	DC-link voltage	700 V
L	Input filter inductance	50 mH
P_N	Converter rated power	6 kW

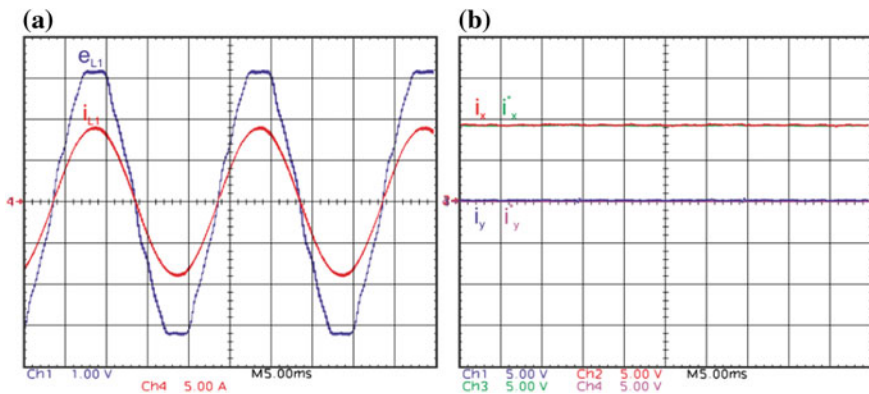


Fig. 54 Steady state operations using DPC-3V: grid phase voltage (100 V/div) and current (5 A/div) (a) and x- and y-axis current vector components (b)

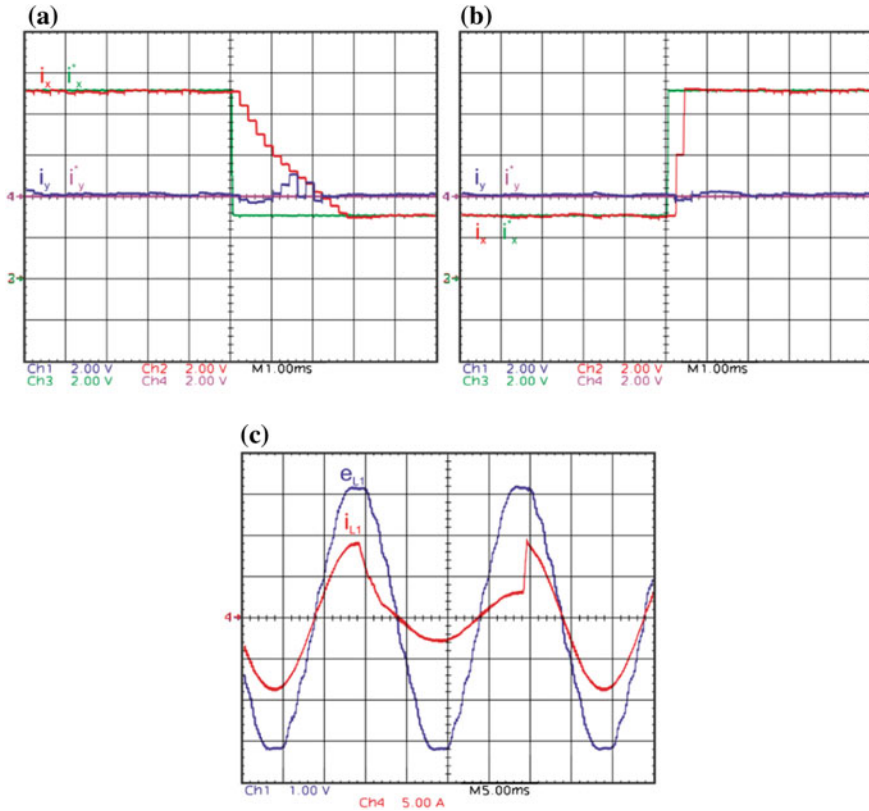


Fig. 55 Transient state operations with the DPC-3V method. **a, b** Components i_x and i_y (5 A/div) of the current vector and their reference values (i_x^* and i_y^*) during the step changes of i_x^* . **(c)** Grid phase voltage (100 V/div) and current (5 A/div) during the step changes of i_x^* .

investigated and shown in Fig. 55. The test was carried out with an open DC-link voltage control loop. Current response time in the DPC-3V method is comparable to the fastest nonlinear methods (such as DPC or VOC with nonlinear hysteresis current controllers). This is due to the fact that each of these control methods identifies a dynamic state during which voltage vectors giving the longest current derivatives are selected. This means that the transient response should be as fast as possible.

4.2 Constant Switching Frequency Predictive DTC-3V Method

The DTC-3V control algorithm ensures both the elimination of disadvantages of the standard DTC and very good dynamic properties of DTC, which are the major advantages of nonlinear control methods. The proposed method is based on torque and flux error vector minimization criteria. The control algorithm selects three voltage vectors per sampling time. The goal of the predictive control is to calculate optimal vector application times in order to minimize the torque and flux error vector.

In practice, this modulation is performed by using an inverter that supports the SVM, which minimizes torque ripple by keeping constant switching frequency.

4.2.1 Torque and Flux Error Vector Minimization Strategy

Flux ε_ψ and torque ε_T control errors are the components of complex error vector $\varepsilon_{\psi T}$. This vector should be standardized proportionally to a common reference frame related to current:

$$\varepsilon_{i\psi T} = \varepsilon_{i\psi} + j\varepsilon_{iT} = c_\psi \varepsilon_\psi + j c_T \varepsilon_T \quad (4.14)$$

After standardization of the error vector, the analysis of the influence of the changes of current vector components on error vector $\varepsilon_{i\psi T}$ can be made.

Coefficients c_T and c_ψ are defined as follows [90]:

$$c_T = \frac{i_{qN}}{T_N}, \quad c_\psi = \frac{1}{L_s} \quad (4.15)$$

where

T_N nominal torque,

i_{qN} nominal q-axis stator current.

The predicted error vector in the next sampling period can be written as [90]:

$$\varepsilon_{i\psi T(k+1)} = \varepsilon_{i\psi T(k)} + T_s(-\mathbf{d}_{ixxx}) = \varepsilon_{i\psi T(k)} + T_s \mathbf{d}_{ixxx} \quad (4.16)$$

It can be seen that Eq. (4.16) is similar to (4.6). By using this dependence we can predict the values of the torque and flux errors in the next control step ($k + 1$).

4.2.2 Voltage Vector Selection

The idea of voltage vector selection is the same as in DPC-3V method (described in Sect. 4.1) and is shown in Fig. 56.

Fig. 56 Graphic illustration of voltage vector choice in DTC-3V method

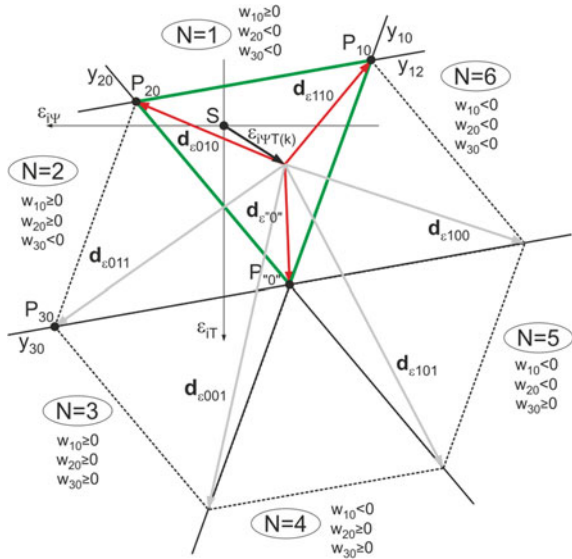


Table 11 Voltage vectors used in corresponding sectors N

w_{10}	w_{20}	w_{30}	Sector N	Used voltage vectors $u_{s1}, u_{s2}, u_{s'0''}$
+	-	-	1	$u_{110}, u_{010}, u_{'0''}$
+	+	-	2	$u_{010}, u_{011}, u_{'0''}$
+	+	+	3	$u_{011}, u_{001}, u_{'0''}$
-	+	+	4	$u_{001}, u_{101}, u_{'0''}$
-	-	+	5	$u_{101}, u_{100}, u_{'0''}$
-	-	-	6	$u_{100}, u_{110}, u_{'0''}$

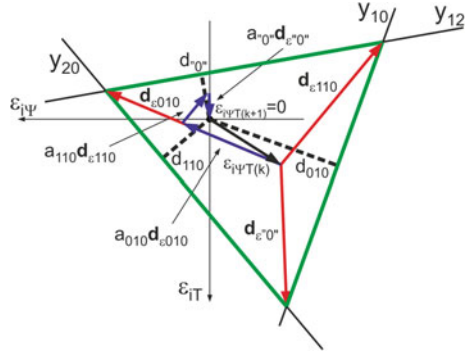
To choose the converter voltage vectors we should determine the equations of three straight lines (y_{10} , y_{20} and y_{30}) containing vertexes and the center of the hexagon. Knowing $d_{\epsilon 110}$, $d_{\epsilon 010}$ and $d_{\epsilon 011}$ (2.28) and the error vector, we can calculate the coordinates of P_{10} , P_{20} , P_{30} and $P_{'0''}$ points, and hence obtain the straight line equations in a general form $Ax + By + C = 0$. After that coefficients w_{xx} are calculated from (4.17):

$$w_{xx} = A_{xx}x_p + B_{xx}y_p + C_{xx} \tag{4.17}$$

where A_{xx} , B_{xx} and C_{xx} are the coefficients of straight line y_{10} , y_{20} and y_{30} equations respectively, x_p and y_p are coordinates of S point (in this case, S is the origin of the reference frame, so its coordinates are equal to zero).

Knowing the signs of w_{xx} coefficients, we can choose from Table 11 sector number N and voltage vectors that provide error vector minimization.

Fig. 57 Compensation concept of torque and flux error vector minimization (steady state)



4.2.3 Calculation of the Voltage Vectors Application Times

Basing on the equations of straight lines containing triangle sides, we should check if the origin of the reference frame lies inside the triangle (Fig. 56). If it does, then the whole procedure can be reduced to the calculation of relative switching-on times (a_{110} , a_{010} and a_{0^0}) of the chosen converter voltage vectors fulfilling the following equation:

$$\epsilon_{i\Psi M(k+1)} = \epsilon_{i\Psi M(k)} + a_{110}d_{e110} + a_{010}d_{e010} + a_{0^0}d_{e^0 0^0} = \mathbf{0} \quad (4.18)$$

The values of the switching-on times of the chosen vectors are described as follows:

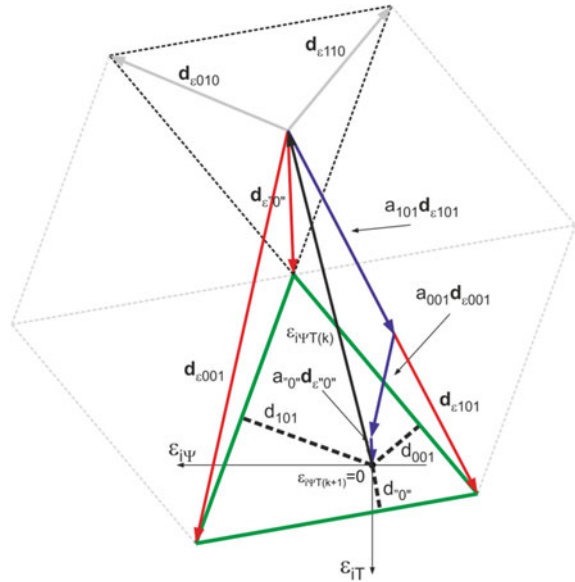
$$t_{110} = a_{110} \cdot T_s, \quad t_{010} = a_{010} \cdot T_s, \quad t_{0^0} = a_{0^0} \cdot T_s \quad (4.19)$$

A graphical illustration of (4.18) is shown in Fig. 57 [102]. In this case (in the steady state, sector $N = 1$) zero vector (\mathbf{u}_{111} or \mathbf{u}_{000}) is used for time t_{0^0} , vector \mathbf{u}_{010} is used for t_{010} and finally vector \mathbf{u}_{110} is used for t_{110} . The sum of the three time periods must be equal to sampling period T_s .

$$t_{110} + t_{010} + t_{0^0} = T_s \quad (4.20)$$

As can be seen from Fig. 57, after T_s sampling period, the torque and flux error vector is equal to zero, which means that the torque and flux errors have been accurately compensated for. Analyzing Fig. 57, it can be theoretically proved by making use of the trigonometric dependences in an equilateral triangle that switching-on times of each voltage vector of the converter are clearly determined by individual lengths of d_{xxx} i.e. the distance of the origin of the reference frame from the straight lines containing triangle sides. These dependences are presented as follows:

Fig. 58 Compensation concept of grid current error vector in transient states, for the origin of the reference frame lying outside the hexagon



$$a_{110} = \frac{d_{110}}{h}, \quad a_{010} = \frac{d_{010}}{h}, \quad a^{v_0r} = \frac{d^{v_0r}}{h} \tag{4.21}$$

where: h is the height of an equilateral triangle and its value is defined as:

$$h = \frac{\sqrt{3}}{2} |U_{sz\beta}| \frac{T_s}{L_s} = \frac{\sqrt{3} 2U_{DC} T_s}{2 \cdot 3 L_s} = \frac{\sqrt{3} U_{DC} T_s}{3L_s} \tag{4.22}$$

Making use of (4.21), the converter output spatial vector is calculated and reproduced using the SVM technique.

Such an approach to torque and flux control will ensure minimization of the torque and flux error vector, and thus reduce both the torque ripples and harmonics content in stator current of the PMSM.

In transient states the origin of the reference frame can be located outside the hexagon presented in Fig. 56, as shown in Fig. 58.

This time, a full compensation of error vector components in a single sampling period T_s is impossible, but even then the control algorithm should be able to minimize the error vector.

In the proposed DTC-3V method one of the active vectors (assigned to sector N from Table 11) remains switched on all the time T_s to ensure the fastest system response to dynamically changing values of the set torque and flux.

The choice of an appropriate vector is determined by the shortest distance of the reference frame origin from the straight lines containing active vectors used in the given sector N . For the presented case ($N = 4$):

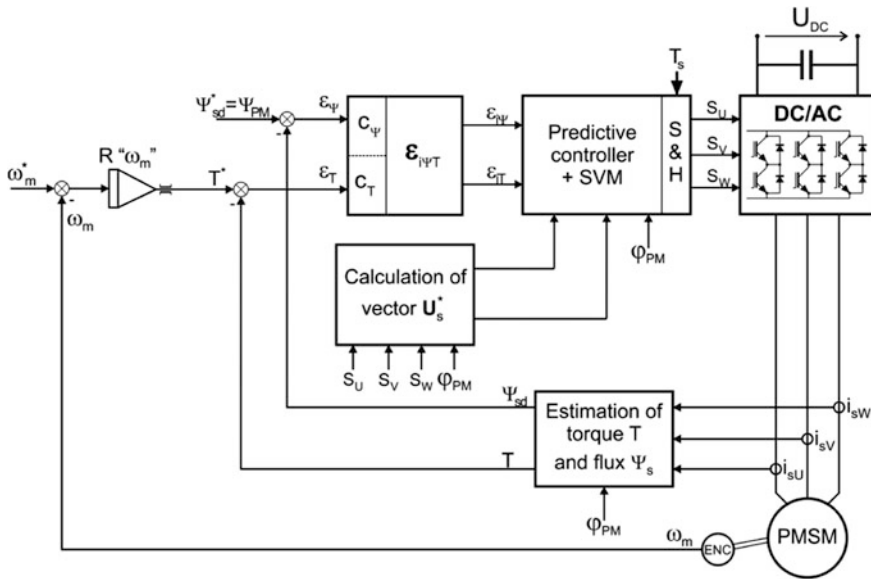


Fig. 59 Control structure of the DTC-3V

$$d_{\min} = \min(d_{001}, d_{101}) \tag{4.23}$$

Two options are possible:

- (a) if $d_{\min} = d_{101}$, then $t_{001} = T_s$, $t_{101} = 0$, $t''_{00'} = 0$
- (b) if $d_{\min} = d_{001}$, then $t_{001} = 0$, $t_{101} = T_s$, $t''_{00'} = 0$

The final schematic diagram of the discussed control method is shown in Fig. 59.

4.2.4 Experimental Results

The effectiveness of the proposed control strategy is experimentally tested with a four-pole 2.8-kW PMSM drive, which is characterized by the nominal parameters: $T_N = 36$ Nm, $n_N = 750$ rpm, $U_{DC} = 350$ V, $R_S = 1.35$ Ω, $L_S = 0.01325$ H, $\Psi_{PM} = 0.56$ Wb.

The control algorithm is programmed in the ADSP-21262 32-bit floating point SHARC DSP. A three phase inverter of IGBT's is used to feed the PM synchronous machine. Hall-effect sensors (LEM LA-55P and LV-25P) are used for current and voltage measurements, respectively. It should be noted that all current waveforms in the figures below show the real currents (not the sampled ones) measured by current probe connected to the scope. The sampling time is equal to $T_s = 200$ μs.

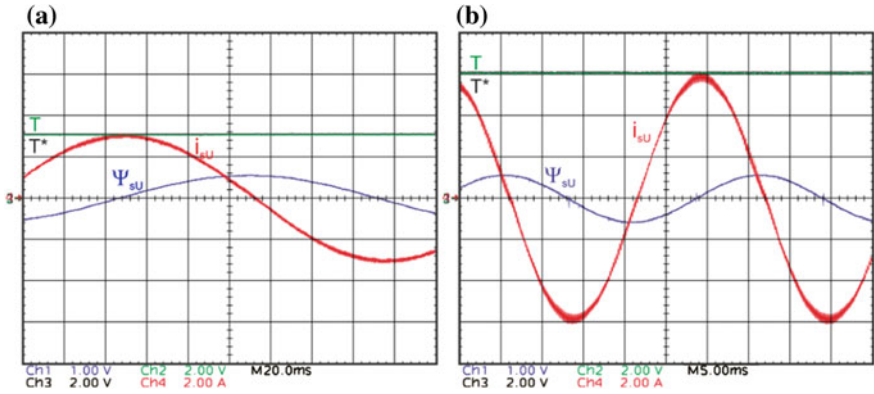


Fig. 60 Steady state operations using DTC-3V: stator current i_{sU} (Ch4—2 A/div), stator flux Ψ_{sU} (Ch1—1 Wb/div), set torque T^* (Ch2—6.67 Nm/div) and torque T (6.67 Nm/div) at angular speed equal to $\omega_m = 15$ rad/s (a) and $\omega_m = 50$ rad/s (b)

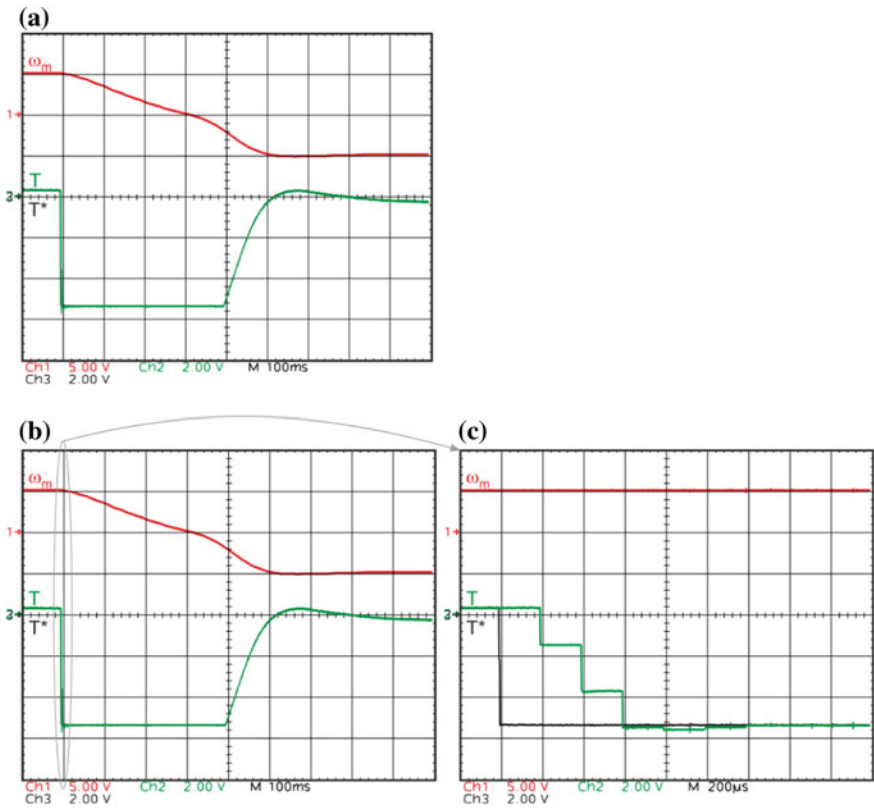


Fig. 61 Transient state operations with the DTC-3V method (speed reversal ± 50 rad/s): i_{sU} —5 A/div, Ψ_{sU} —1 Wb/div, $|\Psi_s|$ —0.2 Wb/div, M^* , M —13.33 N m/div, ω_m —50 rad/s/div

Figure 60a, b show the motor torque, flux and phase current obtained with a rotor angular velocity of 15 and 50 rad/s respectively. It can be seen, especially at low motor speeds, that the proposed predictive strategy brings small current and torque ripples, and the phase current shows a good sinusoidal waveform. The DTC-3V exhibits a very good steady state performance that is needed for servo drives with synchronous motors.

Figure 61 shows the transient state of the system during motor speed reversal from 50 to -50 rad/s. Torque response time in the DTC-3V method is comparable to the fastest nonlinear methods (such as DTC or FOC method with nonlinear hysteresis current controllers). This is due to the fact that each of these control methods identifies a dynamic state during which voltage vectors giving the longest current derivatives are selected. This means that the transient response should be as fast as possible.

Laboratory tests have shown that the new predictive DTC-3V strategy ensures the torque ripple minimization and constant switching frequency. With this proposed control scheme, it is possible to obtain a similar dynamic performance as with the conventional nonlinear methods (such as the DTC). Instead of torque and flux comparators and a standard switching table a new, specific vector modulation is used. This approach allows us to combine the dynamic performance of DTC method with the advantages of the methods based on space vector modulation such as constant switching frequency and low torque ripples.

4.3 Finite Control Set Model Predictive Control— FCS-MPC

The main purpose of the coupling circuit in AC/DC converter connected to the grid is high harmonic suppression of the switching frequency and low attenuation in the band related to the basic harmonic of a grid current. These requirements are met by

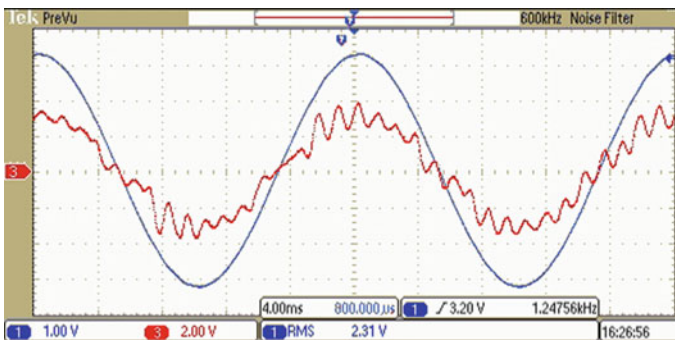


Fig. 62 Grid phase voltage e_{LI} (Ch1, 100 V/div) and grid phase current i_{LI} (Ch3, 4A/div), $THD_i = 18.3\%$

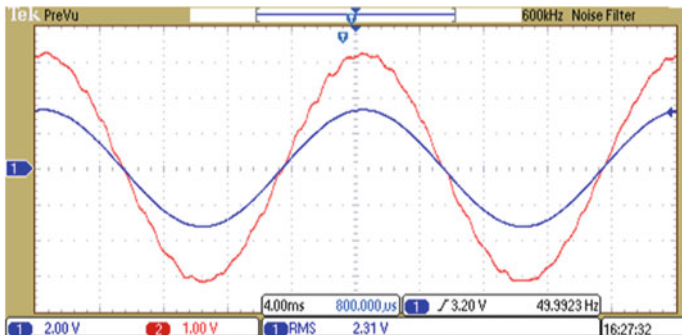


Fig. 63 Grid phase voltage e_{LI} (Ch1, 200 V/div) and capacitor phase voltage u_{cLI} (Ch2, 100 V/div)

the LCL circuit, whose attenuation in the passband is 20 dB/dec and in the stop-band of 60 dB/dec. An important drawback of the LCL circuit is the presence of a filter resonance frequency f_r (4.24). This defect hinders the direct application of the algorithms used in the case of an L filter for an LCL circuit.

$$f_r = \frac{1}{2\pi} \sqrt{\frac{L_1 + L_2}{L_1 L_2 C}} \tag{4.24}$$

Figures 62 and 63 present the results of laboratory tests of AC/DC converter predictive current control based on the L model [9, 45]. The tests were carried out using an LCL filter. Figure 62 shows the course of the grid current i_{LLI} (marked in red) with a high content of harmonics of the filter resonant frequency f_r . The THD_i factor is very high and amounts to 18.3 %. Figure 63 also shows that the voltage on capacitors u_{cLI} is distorted. The algorithm correctly reproduces current i_2 applied from the side of the converter, however, it has no impact on the grid current i_1 and capacitor voltage u_c .

These results confirm that the prediction algorithms FCS-MPC in cooperation with the LCL filter require appropriate modifications. The following section presents some predictive control algorithms that enable a cooperation with an LCL coupling circuit.

4.3.1 Predictive Current Control of an AC/DC Inverter with Active Damping—PCi-AD

An active damping method is used to damp higher harmonics (related to the resonant frequency f_r) of the filtering capacitors voltage. This is executed by emulating the damping resistance connected in parallel (or in series) to the LCL filter capacitors. Most of the known algorithms of this type are based on a change in the modulation index [100]. Due to the absence of the modulator the above is not

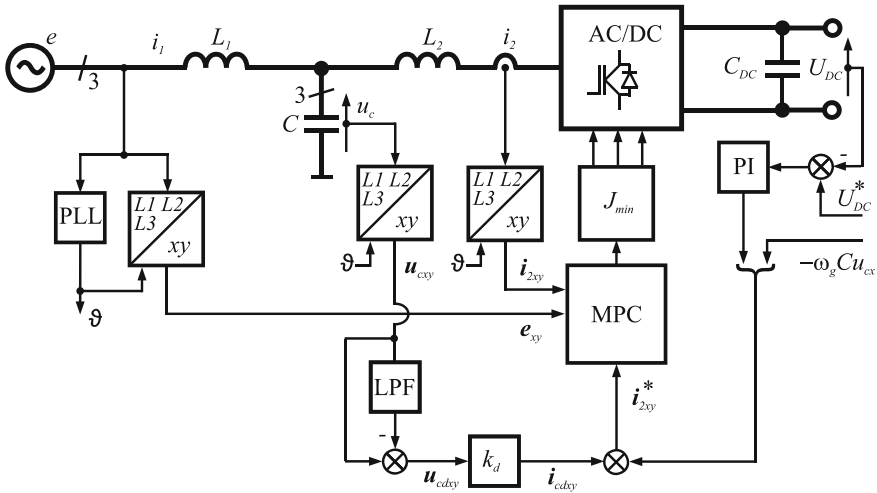


Fig. 64 Control structure of the PCi-AD

possible for the FCS-MPC methods. For this purpose, the active damping algorithm [101] designed for the DPC method was adapted and developed.

A schematic diagram of the PCi-AD method is shown in Fig. 64. Voltages u_{cL1} , u_{cL2} , u_{cL3} of the LCL filter capacitors are transformed into the rotating coordinate system xy and filtered in low-pass filter. Next, subtracting the filter output signal from the voltage u_{cxy} provides higher harmonic voltage u_{cdxy} of the capacitors. Resonant harmonic current i_{cdxy} , which should be suppressed, is calculated according to the equation:

$$i_{cdxy} = k_d u_{cdxy} \tag{4.25}$$

where

k_d is damping factor.

Reference values of converter current vector i_{2xy}^* are calculated according to the following formula:

$$i_{2x}^* = k_p e U_{DC} + k_i \int e U_{DC} dt + i_{cdx} \tag{4.26}$$

$$i_{2y}^* = i_{cdy} - \omega C u_{cx} \tag{4.27}$$

where

$-\omega_g C u_{cx}$ current compensating reactive power of capacitors.

Prediction is the process of choosing the best of all possible control states. This is performed by online minimizing of the specific cost function J . It means that at

each step kT_s , the impact of all converter voltage vectors \mathbf{u}_{xy} on converter current vector \mathbf{i}_{2xy} (proportional to the active and reactive power) is examined.

Prediction process starts with the measurement of currents and voltages (step kT_s). Current vector derivative (2.14) in the digital implementation takes the form:

$$\mathbf{d}_{2i} \approx \Delta \mathbf{i}_{2xy}(k+1)/T_s \quad (4.28)$$

Using Eqs. (4.28) and (2.14), (as shown in Fig. 8) the predicted change of converter current $\Delta \mathbf{i}_{2xy}(k+1)$ which occur at time $(k+1)$ can be determined by:

$$\Delta \mathbf{i}_{2xy}(k+1) = \frac{1}{L_2} \left(\mathbf{u}_{xy}^*(k+1) - \mathbf{u}_{xy}(k+1) \right) T_s \quad (4.29)$$

For sufficiently small sampling times T_s , it can be assumed that:

$$\mathbf{i}_{2xy}^*(k+1) \approx \mathbf{i}_{2xy}^*(k) \quad (4.30)$$

$$\mathbf{u}_{xy}^*(k+1) \approx \mathbf{u}_{xy}^*(k) \quad (4.31)$$

The next step is to calculate the value of the current vector in the next sampling step $(k+1)T_s$.

$$\mathbf{i}_{2xy}(k+1) = \mathbf{i}_{2xy}(k) + \Delta \mathbf{i}_{2xy}(k+1) \quad (4.32)$$

Predicted current error in next sample time $(k+1)T_s$ is calculated using the following equation:

$$\boldsymbol{\varepsilon}_{i2xy}(k+1) = \mathbf{i}_{2xy}^*(k) - \mathbf{i}_{2xy}(k+1) \quad (4.33)$$

The last step of the algorithm is to calculate the cost function J and choose the best inverter voltage vector $\mathbf{u}_{xy}(k+1)$.

$$J = \sqrt{\boldsymbol{\varepsilon}_{i2x}(k+1)^2 + \boldsymbol{\varepsilon}_{i2y}(k+1)^2} \quad (4.34)$$

The cost function determines the properties of the predictive controller. The purpose of the cost index is to minimize the length of the current vector error. The voltage vector whose current prediction is closest to the expected reference current is applied to the load at the next sampling $(k+1)T_s$ period. In other words, the selected vector will be the one that minimizes the quality (cost) function.

The implementation of the active damping algorithm, as shown above, reduces the value of capacitor voltage harmonics \mathbf{u}_{cxy} , which is advantageous for the reduction of grid current distortions.

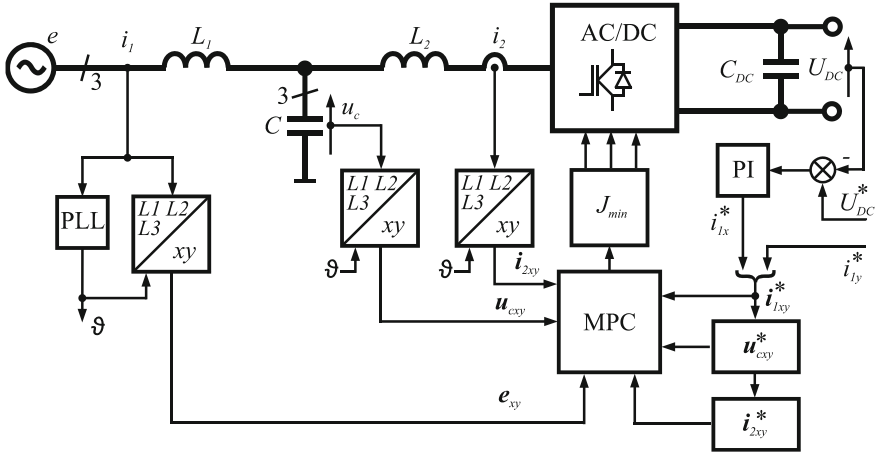


Fig. 65 Control structure of the PCi_{2u_c}

4.3.2 Predictive Current and Capacitor Voltage Control—PCi_{2u_c}

The PCi_{2u_c} method represents a completely new approach to control of AC/DC converters with an LCL filter. The method uses basic advantages of the MPC methods, i.e. multivariable control tasks and elimination of the cascade control structure. A schematic diagram of the method is shown in Fig. 65. Prediction process starts with the measurement of currents and voltages (step k). Then, based on reference value of grid current vector \mathbf{i}_{1xy}^* (proportional to the active and reactive power), reference capacitor voltage vector \mathbf{u}_{cxy}^* is calculated:

$$u_{cx}^* = e_{gx} + \omega_g L_1 i_{1y}^* \quad (4.35)$$

$$u_{cy}^* = e_{gy} - \omega_g L_1 i_{1x}^* \quad (4.36)$$

Next, reference components of inverter current vector \mathbf{i}_{2xy}^* are calculated:

$$i_{2x}^* = i_{1x}^* + \omega_g C u_{cy}^* \quad (4.37)$$

$$i_{2y}^* = i_{1y}^* - \omega_g C u_{cx}^* \quad (4.38)$$

In the following step the predicted converter current vector is obtained from formula:

$$\Delta \mathbf{i}_{2xy}(k+1) = \frac{1}{L_2} \left(\mathbf{u}_{xy}^*(k+1) - \mathbf{u}_{xy}(k+1) \right) T_s \quad (4.39)$$

$$\mathbf{i}_{2xy}(k+1) = \mathbf{i}_{2xy}(k) + \Delta \mathbf{i}_{2xy}(k+1) \quad (4.40)$$

Knowing that $\Delta \mathbf{i}_{1,xy}(k+1) \ll \Delta \mathbf{i}_{2,xy}(k+1)$, we can assume that the grid current change during sampling time is close to zero $\Delta \mathbf{i}_{1,xy} \approx 0$.

By using the previously calculated change of converter current $\Delta \mathbf{i}_{2,xy}(k+1)$, the capacitor voltage vector in the next step can be obtained from the following equations:

$$\Delta \mathbf{u}_{cxy}(k+1) = \frac{\mathbf{i}_{1,xy}(k) - j\omega_g C \mathbf{u}_{cxy}^*(k+1) - (\mathbf{i}_{2,xy}(k) + 0.5\Delta \mathbf{i}_{2,xy}(k+1))}{C} T_s \quad (4.41)$$

$$\mathbf{u}_{cxy}(k+1) = \mathbf{u}_{cxy}(k) + \Delta \mathbf{u}_{cxy}(k+1) \quad (4.42)$$

Equation (4.41) is obtained from Eq. (2.10) assuming linear change of the current vector $\mathbf{i}_{2,xy}$ in time T_s .

The expected errors of controlled variables are calculated from:

$$\boldsymbol{\varepsilon}_{i_{2,xy}}(k+1) = \mathbf{i}_{2,xy}^*(k) - \mathbf{i}_{2,xy}(k+1) \quad (4.43)$$

$$\boldsymbol{\varepsilon}_{u_{cxy}}(k+1) = \mathbf{u}_{cxy}^*(k) - \mathbf{u}_{cxy}(k+1) \quad (4.44)$$

In the last stage of the prediction, optimal inverter voltage vector $\mathbf{u}_{xy}(k+1)$ is selected on the basis of extended cost function J . The calculations are repeated for all of the inverter voltage vectors.

$$J = \sqrt{\left(\boldsymbol{\varepsilon}_{i_{2x}}^2 + \boldsymbol{\varepsilon}_{i_{2y}}^2\right) + w_{uc}^2 \left(\boldsymbol{\varepsilon}_{ucx}^2 + \boldsymbol{\varepsilon}_{ucy}^2\right)} \quad (4.45)$$

The PCi₂u_c method does not have a separate block of active damping. Expanded cost function J , which consists of a component connected with capacitor voltage vector \mathbf{u}_{cxy} , allows the suppression of higher harmonics associated with the resonant frequency of the LCL filter. The value of the weighting factor w_{uc} determines the level of unwanted harmonics suppression.

4.3.3 Experimental Results

The experimental evaluation was performed on a 2-level inverter with the control system implemented on digital signal processor ADSP 21369. The drive signals for the IGBTs were generated by FPGA. Tests were carried out under the following

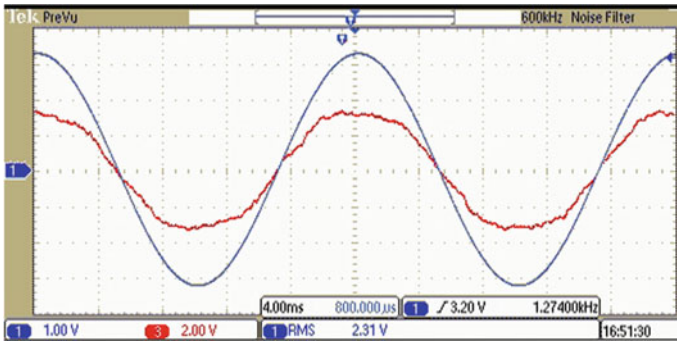


Fig. 66 Experimental results for the PCi-AD. Grid phase voltage e_{L1} (Ch1, 100 V/div) and grid phase current i_{LL1} (Ch3, 4A/div), $\text{THD}_i = 8.5\%$

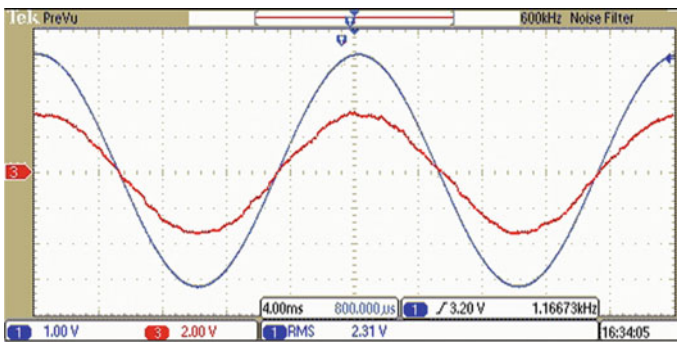


Fig. 67 Experimental results for the PCi₂u_c. Grid phase voltage e_{L1} (Ch1, 100 V/div) and grid phase current i_{LL1} (Ch3, 4 A/div), $\text{THD}_i = 4.6\%$

conditions: $U_{DC} = 650\text{ V}$, $L_1 = 1.8\text{ mH}$, $L_2 = 3.4\text{ mH}$, $C = 20\text{ }\mu\text{F}$, $E_{L1} = E_{L2} = E_{L3} = 230\text{ V}$, $P = 3.1\text{ kW}$, $Q = 0\text{ var}$.

Figure 66 shows grid voltage e_{L1} and grid current i_{LL1} for the PCi-AD method. The THD_i of grid current i_{LL1} is 8.5%. An effect of the active damping control loop is reduction of the harmonic currents allocated in the LCL filter resonance band. However, the reduction of these harmonic currents causes an increase in the low-order harmonics (5th, 7th, 11th) in grid current. Similar behaviour is presented in paper [101]. The solution uses an active harmonic rejection controller.

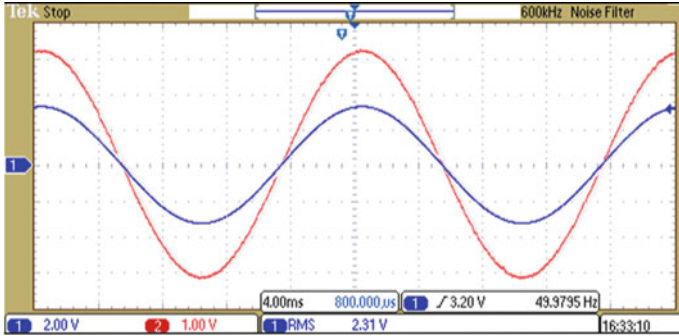


Fig. 68 Experimental results with the PCi_2u_c . Grid phase voltage e_{LI} (Ch1, 200 V/div) and capacitor phase voltage u_{cLI} (Ch2, 100 V/div)

Figure 67 shows grid voltage e_{LI} and grid current i_{LLI} of the PCi_2u_c method. The grid current THD_i is lower and amounts to 4.6 %. A low-order harmonics (5th, 7th, 11th) have a much smaller values than in the $PCi-AD$ method. Extension of the cost function J makes it possible for one predictive controller to regulate the grid current and suppress harmonic resonance without adding the additional harmonics.

As shown in Fig. 68, there is practically no harmonics associated with the resonant frequency of the LCL filter in the capacitor voltage u_{cLI} . This voltage is similar to grid voltage e_{LI} .

4.4 Predictive Control of 2-Level Current Source Rectifier

The presented method selects the best rectifier current vector in order to control the grid current and provide unit power factor. This strategy requires a predictive model of the circuit that is described in the next subsection. The subsequent subsection contains simulation results of the control system.

4.4.1 Predictive Control Strategy

Grid current behavior is described by derivative calculated from (2.31) [82–84].

$$\frac{di_{gxy}}{dt} = \frac{1}{L} (e_{gxy} - u_{cxy} - j\omega_g Li_{gxy}) \tag{4.46}$$

In each sample time T_s the predicted current change can be calculated from Eq. (4.47).

$$\Delta \mathbf{i}_{gxy}(k+1) = \frac{d}{dt} \mathbf{i}_{gxy} T_s = \Delta \mathbf{i}_{gx}(k+1) + j \Delta \mathbf{i}_{gy}(k+1) \quad (4.47)$$

The expected value of the grid current vector is given by (4.48).

$$\mathbf{i}_{gxy}(k+1) = \mathbf{i}_{gxy}(k) + \Delta \mathbf{i}_{gxy}(k+1) \quad (4.48)$$

Analyzing (4.46), the value of the current vector depends on the capacitor voltage vector. In order to control the current prediction of the capacitor voltage vector is needed. Equation (4.49) allows us to describe voltage behavior.

$$\frac{d\mathbf{u}_{cxy}}{dt} = \frac{1}{C} (\mathbf{i}_{gxy} - \mathbf{i}_{xy} - j\omega_g C \mathbf{u}_{cxy}) \quad (4.49)$$

The predicted value of the capacitor voltage vector is given by (4.50).

$$\mathbf{u}_{cxy}(k+1) = \mathbf{u}_{cxy}(k) + \Delta \mathbf{u}_{cxy}(k+1) \quad (4.50)$$

Predicted values are compared to the reference values. The reference value of the grid current vector has only component x while, in order to minimize reactive power, component y equals zero ($i_{gy}^* = 0$). The reference values of capacitor voltage components are described by (2.33) and (2.34).

Cost function is calculated by using Eq. (4.51) [86].

$$J = \sqrt{w_{ix} \varepsilon_{ix}^2 + w_{iy} \varepsilon_{iy}^2 + w_{ux} \varepsilon_{ux}^2 + w_{uy} \varepsilon_{uy}^2} \quad (4.51)$$

where errors are defined as:

$$\varepsilon_{ix} = i_{gx}^* - i_{gx}(k+1) \quad (4.52)$$

$$\varepsilon_{iy} = i_{gy}^* - i_{gy}(k+1) \quad (4.53)$$

$$\varepsilon_{ux} = u_{cx}^* - u_{cx}(k+1) \quad (4.54)$$

$$\varepsilon_{uy} = u_{cy}^* - u_{cy}(k+1) \quad (4.55)$$

and w_{ix} , w_{iy} , w_{ux} , w_{uy} are weighting factors.

Weighting factors decide whether priority is given to those states which minimize the error in the filter voltage or those which improve the grid currents. Basically, they are adjusted empirically to provide unit power factor and eliminate noticeable deviations of the grid current with respect to the reference.

The control algorithm works as follows: at each sampling time, for all possible switching states the predicted values of the filter voltage and grid currents are calculated and then used to calculate cost function J . Next, the switching state with the minimum value of J is applied to the converter.

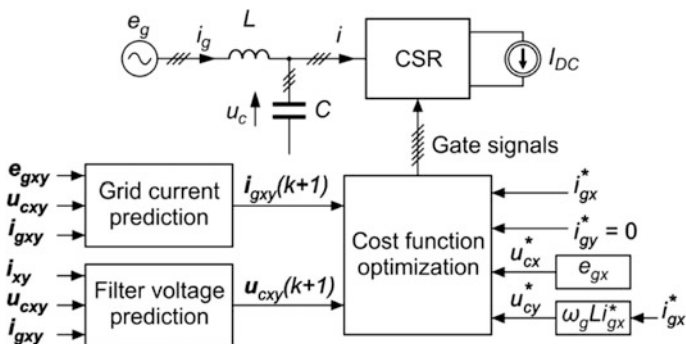
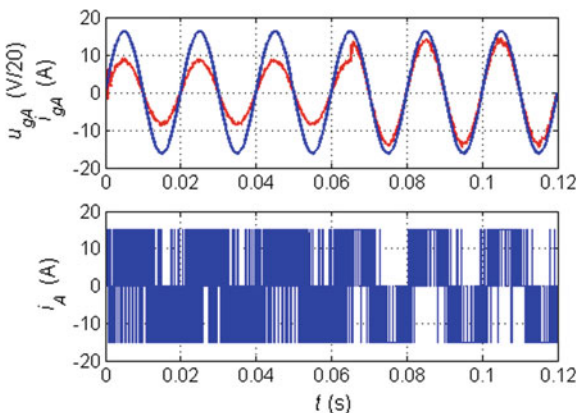


Fig. 69 Proposed predictive control scheme

Fig. 70 Source voltage, grid phase current and rectifier current in steady and transient states. Step change of the grid current applied in 0.065 s



Complete control scheme is shown in Fig. 69.

4.4.2 Simulation Results

In order to validate the proposed method, simulations have been carried out using MATLAB/Simulink. The algorithm operates with a sample time of $T_s = 50 \mu s$. Output current has value $I_{DC} = 15 A$. The results present steady and transient states for various filter parameters and power flow directions.

Figure 70 presents steady and transient operation for $L = 2.5 mH$ and $C = 50 \mu F$. The rectifier starts at 0 s and in the first 0.065 s a value $i_{gx}^* = 7 A$ is applied. A step change of i_{gx}^* is given at time 0.065 s, where reference value increases to 12 A. Figure 71 shows FFT analysis of the grid current in steady state, Figs. 72 and 73 show transient states in details.

Fig. 71 FFT analysis of the grid current for: $i_{gx}^* = 7$ A (a) and $i_{gx}^* = 12$ A (b)

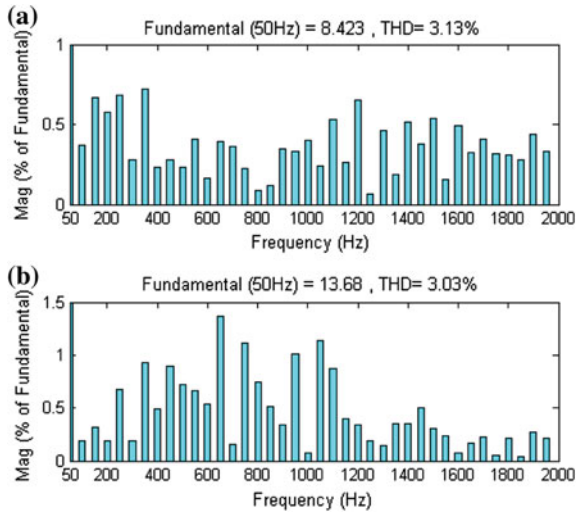


Fig. 72 Grid phase current and rectifier current at start-up

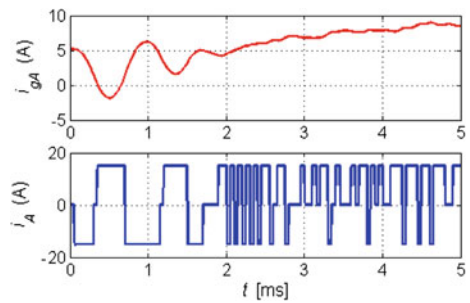
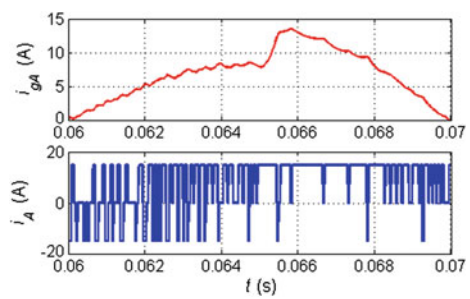


Fig. 73 Grid phase current and rectifier current during step change of reference current i_{gx}^*



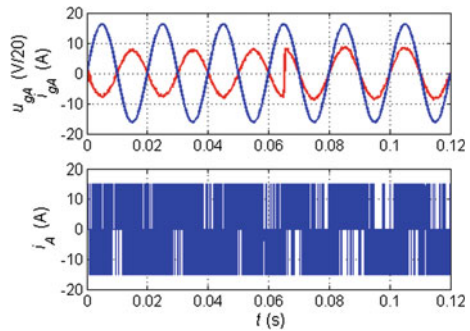
As shown in Fig. 70, the system has a good static performance. The grid current is in phase with the respective source voltage (Fig. 70) and has low distortions (Fig. 71).

The rectifier starts with some oscillations caused by the filter. However, their amplitude decreases quickly, which can be seen in Fig. 72. The method allows us to

Table 12 THD for different currents and filter values

Filter parameters		THD value (%)	
L (mH)	C (μ F)	For $i_{gx}^* = 7$ A	For $i_{gx}^* = 12$ A
1.5	60	4.36	6.09
1.5	83	4.8	5.49
2.5	50	3.13	3.03
2.5	60	3	2.78

Fig. 74 Source voltage, grid phase current and rectifier current in steady and transient state. Step change of the grid current applied in 0.065 s



obtain fast and stable response to the step change of the reference current i_{gx}^* , as in Fig. 73.

The same experiment was performed for different L and C values whose resonant frequency is approximately 10 times higher than the grid frequency. To obtain precise estimation of the filter behavior the sampling frequency was significantly higher than the resonance frequency. In every case unit power factor was obtained. Table 12 shows a comparison of steady state results and presents THD for each reference grid current and filter parameters.

The results given in the Table 12 allow us to conclude that the inductance has a major impact on the THD value. Resonant frequency is the same for the values in the second and the third row of the table and distortions of the grid current are much lower in the third case. Thus, in the case of low grid inductance, better performance is obtained after adding external inductance.

The proposed method has been tested for feeding energy back to the grid. For this reason, a step change of i_{gx}^* is given at time 0.065 s. The reference value changes from -7 to 7 A. The results are shown in Fig. 74. Concluding, predictive control provides feeding the grid without reactive power and with low distorted current.

4.4.3 Conclusion

The predictive control strategy, presented in this paper, works effectively, which has been confirmed by the results. Sample time used in the simulations is long

enough to perform calculations and sufficiently short to predict voltage and current values. Additionally, filtering capacitances and inductances are quite low. In spite of that, FFT analysis indicates very good phase current regulation supported with higher harmonics amplitude lower than 1.5 % of the fundamental (Fig. 71). This result is obtained regardless of the small differences between inductance and capacitance values in the circuit, and inductance and capacitance used by algorithm. Moreover, unit power factor is obtained independently of the reference values and filter values. Furthermore, dynamic response is fast and stable, which can be important for certain types of load, such as the active filter.

5 Conclusions

This chapter is devoted to a modern look-up table and predictive control methods of three phase power electronic converters. The authors discuss voltage source converters in two and three level configurations as well as a two level current source rectifier. Some of the methods deal with DC/AC inverter fed induction and PMSM motors. The other methods presented in the chapter are dedicated to the control of the AC/DC rectifier working as an Active Front End of an AC/DC/AC converter.

The authors focus on the methods with a non-linear look-up table and predictive control due to their excellent dynamic properties (limited only by the physical parameters of controlled systems such as the value of the DC voltage, grid inductance or AC motor leakage inductance). Moreover, non-linear methods, especially the predictive ones, provide very good quality of control in steady states, i.e. lack of active and reactive power steady-state error (AC/DC) or torque error (in the case of DC/AC converters). Look-up table methods are taken into consideration as they also ensure the above mentioned advantages in a relatively short calculation time that results in lower hardware requirements (e.g. less expensive microprocessors can be used in the control system). The selected look-up table and predictive methods are proposed for both 2-level and 3-level converters.

Section 3 of the chapter is preoccupied with both DTC-3L-3A and DPC-3L-3A methods. These methods are characterized by a novel division of the error area into three sectors, which makes it possible to control motor torque and flux (grid currents in the case of DPC-3L-3A) with reduced switching frequency in comparison to the standard DTC and DPC methods. The experimental results have shown excellent performance of the methods in both steady and transient states. In the steady state the DPC 3L3A method is characterized by a close to sinusoidal shape of current, small value of THD coefficient at a relatively small transistor switching frequency. The DTC 3L3A method shows low values of phase current distortions and torque ripples. The flux and current for the DTC 3L3A method has almost a perfect sinusoidal shape. Similarly to all look-up table methods, the proposed algorithms are characterized by short processing time that makes it possible to implement the control algorithms on cheap standard processors. Owing to the

above, the look-up table methods can be an interesting alternative for predictive control.

Section 4 describes selected Model Predictive Control methods for 2-level AC/DC and DC/AC converters. DPC-3V and DTC-3V belong to ICS-MPC methods. They are based on current (torque and flux in the case of DTC-3V) error vector minimization criteria.

The new algorithms minimize the error vector of the grid current (torque and flux errors in the case of DTC-3V) for each and every state of the system. In the steady state the control system uses the SVM modulation that provides all the advantages typical of linear methods, i.e. constant switching frequency, low grid current (torque) ripples. Moreover, they have no limitations arising from the use of linear controllers. In transient states, the proposed solution provides maximum dynamics, comparable to the fastest nonlinear control methods.

The subsequent part of Sect. 4 presents a modern FCS-MPC method of the voltage source rectifier with an input LCL filter. To predict the direction and rate of changes of converter current and capacitor voltage vectors, equations describing voltages and currents have been introduced. The predicted values are used to define errors for every output voltage vector, which allows us to find the minimal value of the cost function. All this results in choosing an optimal voltage vector and error minimization.

The last algorithm discussed in Sect. 4 is dedicated to the current source rectifier. It is based on cost function minimization. Basing on the predicted values of the grid current and the capacitor voltage, the algorithm chooses a proper current vector. The great advantage of the method is grid current harmonics reduction combined with a low sample time.

All the described control methods have been illustrated by the results of simulation and laboratory tests confirming their characteristics.

References

1. Ma K, Blaabjerg F (2014) Modulation methods for neutral-point-clamped wind power converter achieving loss and thermal redistribution under low-voltage ride-through. *IEEE Trans Ind Electron* 61(2):835–845
2. Bae Y, Kim R-Y (2014) Suppression of common-mode voltage using a multicentral photovoltaic inverter topology with synchronized PWM. *IEEE Trans Ind Electron* 61(9):4722–4732
3. Singaravel MR, Daniel SA (2015) MPPT with single DC–DC converter and inverter for grid-connected hybrid wind-driven PMSG–PV system. *IEEE Trans Ind Electron* 62(8):4849–4857
4. Yaramasu V, Wu B (2014) Model predictive decoupled active and reactive power control for high-power grid-connected four-level diode-clamped inverters. *IEEE Trans Ind Electron* 61(7):3407–3416
5. Holtz J (1992) Pulsewidth modulation—a survey. *IEEE Trans Ind Electron* 39(5):410–420
6. Rodriguez J, Dixon J, Espinoza J, Pont J, Lezana P (2005) PWM regenerative rectifiers: state of the art. *IEEE Trans Ind Electron* 52(1):5–22

7. Jacob B, Baiju MR (2015) A new space vector modulation scheme for multilevel inverter which directly vector quantize the reference space vector. *IEEE Trans Ind Electron* 62 (1):88–95
8. Lim CS, Levi E, Jones M, Rahim NA, Hew WP (2014) FCS–MPC-based current control of a five-phase induction motor and its comparison with PI–PWM control. *IEEE Trans Ind Electron* 61(1):149–163
9. Antoniewicz P, Kazmierkowski MP (2008) Virtual-flux-based predictive direct power control of AC/DC converter with online inductance estimation. *IEEE Trans Ind Electron* 55 (12):4381–4389
10. Rodriguez J, Pontt JCA, Silva P, Correa P, Lezana P, Cortés P, Ammann U (2007) Predictive current control of a voltage source inverter. *IEEE Trans Ind Electron* 54(1):496–503
11. Kennel R, Linder A (2005) Model predictive control for electrical drives. Paper presented at the power electronics specialist conference PESC'05, Recife, 16 June 2005
12. Cortez P, Rodriguez H, Antoniewicz P, Kazmierkowski M (2008) Direct power control of an AFE using predictive control. *IEEE Trans Ind Electron* 23(5):2516–2523
13. Cortez P, Rodriguez H (2012) Predictive control of power converters and electrical drives. Wiley, New York
14. Larrinaga SA, Vidal MA, Apraiz JRT, Oyarbide E (2007) Predictive control strategy for DC/AC converters based on direct power control. *IEEE Trans Ind Electron* 54(3):1261–1271
15. Yin H, Dieckerhoff S (2015) Experimental comparison of DPC and VOC control of a three-level NPC grid connected converter. Paper presented at the IEEE international symposium on power electronics for distributed generation systems (PEDG), Aachen, 22–25 June 2015
16. Malinowski M, Kazmierkowski MP, Jasiński M (2004) Simple direct power control of three-phase PWM rectifier using space vector modulation (DPC–SVM). *IEEE Trans Ind Electron* 51(2):447–454
17. Zhi D, Xu L, Williams BW (2009) Improved direct power control of grid-connected DC/AC converters. *IEEE Trans Power Electron* 24(5):1280–1292
18. Reznik A, Simoes MG, Al-Durra A, Muyeen SM (2014) LCL filter design and performance analysis for grid-interconnected systems. *IEEE Trans Ind App* 50(2):1225–1232
19. Khajehodini SA, Karimi-Ghartemani M, Jain PK, Bakhshai A (2011) A control design approach for three-phase grid-connected renewable energy resources. *IEEE Trans Sustain Energy* 2(4):423–432
20. Jovcic D, Lu Z, Hajian M (2013) LCL VSC converter for high-power applications. *IEEE Trans Power Deliv* 28(1):137–144
21. Sikorski A, Korzeniewski M (2013) Improved algorithms of direct torque control method. *Automatika—J Control Meas Electron Comput Commun* 53(2):188–198
22. Xia C, Zhao J, Yan Y, Shi T (2014) A novel direct torque control of matrix converter-fed PMSM drives using duty cycle control for torque ripple. *IEEE Trans Ind Electron* 61 (6):149–163
23. Cortés P, Kazmierkowski MP, Kennel R, Quedo E, Rodriguez J (2008) Predictive control in power electronics and drives. *IEEE Trans Ind Electron* 55(12):4312–4324
24. Rodriguez J, Wu B, Rivera M, Wilson A, Yaramasu V, Rojas C (2010) Model predictive control of three-phase four-leg neutral-point-clamped inverter. Paper presented at the international power electronics conference, IPEC 2010, Sapporo, 21–24 June 2010
25. Calle-Prado A, Alepuz S, Bordonau J, Nicolas-Apruzzese J, Cortés P, Rodriguez J (2015) Model predictive current control of grid-connected neutral-point-clamped converters to meet low-voltage ride-through requirements. *IEEE Trans Ind Electron* 62(3):1503–1514
26. Choi D-K, Lee K-B (2015) Dynamic performance improvement of AC/DC converter using model predictive direct power control with finite control set. *IEEE Trans Ind Electron* 62 (2):757–767

27. Bouafia A, Gaubert J-P, Krim F (2010) Predictive power control of three-phase pulsewidth modulation (PWM) rectifier using space-vector modulation (SVM). *IEEE Trans Power Electron* 25(1):228–236
28. Zhang Z, Xu H, Xue M, Chen Z, Sun T, Kennel R, Hackl CM (2015) Predictive control with novel virtual-flux estimation for back-to back power converters. *IEEE Trans Ind Electron* 62(5):2823–2834
29. Alkorta P, Barambones O, Cortajarena JA, Zubizarreta A (2014) Efficient multivariable generalized predictive control for sensorless induction motor drive. *IEEE Trans Ind Electron* 61(9):5126–5133
30. Ren Y, Zhu ZQ (2015) Enhancement of steady-state performance in direct-torque-controlled dual three-phase permanent-magnet synchronous machine drives with modified switching table. *IEEE Trans Ind Electron* 62(6):3338–3350
31. Zhang YA, Xie W, Li ZC, Zhang Y (2013) Model predictive direct power control of a PWM rectifier with duty cycle optimization. *IEEE Trans Power Electron* 28(11):5343–5351
32. Ren Y, Zhu ZQ, Liu J (2014) Direct torque control of permanent-magnet synchronous machine drives with a simple duty ratio regulator. *IEEE Trans Ind Electron* 61(10):5249–5258
33. Restrepo JA, Aller JM, Viola JC, Bueno A, Habelter TG (2009) Optimum space vector computation technique for direct power control. *IEEE Trans Power Electron* 24(6):1637–1645
34. Eskandari-Torbati H, Khaburi DA (2013) Direct power control of three-phase PWM rectifier using model predictive control and SVM switching. Paper presented at the 4th power electronics, drive systems and technologies conference, PEDSTC 2013, Tehran, 13–14 Feb 2013
35. Zhang Z, Xu H, Xue M, Chen Z, Sun T, Kennel R, Hackl CM (2015) Predictive control with novel virtual-flux estimation for back-to-back power converters. *IEEE Trans Ind Electron* 62(4):2823–2834
36. Vazquez S, Marquez A, Aguilera R, Quevedo D, Leon JI, Franquelo LG (2015) Predictive optimal switching sequence direct power control for grid-connected power converters. *IEEE Trans Ind Electron* 62(4):2010–2020
37. Blaschke F (1972) Das Verfahren der Feldorientierung zur Regelung der Asynchronmaschine. *Siemens Forschungs und Entwicklungsberichte* 1(1):184–193
38. Buja GS, Kazmierkowski MP (2004) Direct torque control of PWM inverter-fed AC motors—a survey. *IEEE Trans Ind Electron* 51(4):744–757
39. Lai YS, Chen JH (2001) A new approach to direct torque control of induction motor drives for constant inverter switching frequency and torque ripple reduction. *IEEE Trans Energy Convers* 16(3):220–227
40. Lascu C, Boldea I, Blaabjerg F (2006) Comparative study of adaptive and inherently sensorless observers for variable-speed induction-motor drives. *IEEE Trans Ind Electron* 53(1):785–792
41. Takahashi I, Noguchi T (1986) A New quick-response and high-efficiency control strategy of an induction motor. *IEEE Trans Ind App* 22(5):820–827
42. Papafotiou G, Kley J, Papadopoulos KG, Bohren P, Morari M (2009) Model predictive direct torque control—part II: implementation and experimental evaluation. *IEEE Trans Ind Electron* 56(6):1906–1915
43. Wang F, Li S, Mei X, Xie W, Rodriguez J, Kennel RM (2015) Model-based predictive direct control strategies for electrical drives: an experimental evaluation of PTC and PCC methods. *IEEE Trans Ind Informatics* 11(3):671–681
44. Rodriguez J, Kazmierkowski MP, Espionza JR, Zanchetta P, Abu-Rub H, Young HA, Rojas CA (2013) State of the art of finite control set model predictive control in power electronics. *IEEE Trans Ind Informatics* 9(2):1003–1016
45. Rodriguez J, Cortes P (2012) Predictive control of power converters and electrical drives. Wiley-IEEE Press, Chichester

46. Kang JK, Sul SK (2004) Analysis and prediction of inverter switching in direct torque control of induction machine based on hysteresis bands and machine parameters. *IEEE Trans Ind Electron* 48(3):545–553
47. Idris NRN, Yatim AHM (2004) Direct torque control of induction machines with constant switching frequency and reduced torque ripple. *IEEE Trans Ind Electron* 51(4):758–767
48. Lascu C, Boldea I, Blaabjerg F (2004) Variable-structure direct torque control—a class of fast and robust controllers for induction machine drives. *IEEE Trans Ind Electron* 51(4):785–792
49. Lai YS, Wang WK, Chen YC (2004) A new approach to direct torque control of induction motor drives for constant inverter switching frequency and torque ripple reduction. *IEEE Trans Ind Electron* 51(4):768–775
50. Ambrozic V, Buja GS, Menis R (2004) Band-constrained technique for direct torque control of induction motor. *IEEE Trans Ind Electron* 51(4):776–784
51. Noguchi T, Yamamoto M, Kondo S, Takahashi I (1999) Enlarging switching frequency in direct torque-controlled inverter by means of dithering. *IEEE Trans Ind App* 35(6):1358–1366
52. Habetler TG, Profumo F, Pastorelli M, Tolbert LM (1992) Direct torque control of induction machines using space vector modulation. *IEEE Trans Ind App* 28(5):1045–1053
53. Bertoluzzo M, Buja G, Menis R (2006) Direct torque control of an induction motor using a single current sensor. *IEEE Trans Ind Electron* 53(3):778–784
54. Beerten J, Verweckken J, Driesen J (2009) Predictive direct torque control for flux and torque ripple reduction. *IEEE Trans Ind Electron* 57(1):404–412
55. Miranda H, Cortés P, Yuz J, Rodríguez J (2009) Predictive torque control of induction machines based on state space models. *IEEE Trans Ind Electron* 56(6):1916–1924
56. Geyer T, Papafotiou G, Morari M (2009) Model predictive direct torque control—part I: concept, algorithm and analysis. *IEEE Trans Ind Electron* 56(6):1894–1905
57. Papafotiou G, Geyer T, Morari M (2009) Model predictive direct torque control—part II: implementation and experimental evaluation. *IEEE Trans Ind Electron* 56(6):1906–1915
58. Casadei D, Serra G, Tani A (2000) Implementation of a direct torque control algorithm for induction motors based on discrete space vector modulation. *IEEE Trans Power Electron* 15(4):769–777
59. Rodríguez J, Lai J-S, Peng FZ (2002) Multilevel inverters: a survey of topologies, controls, and applications. *IEEE Trans Ind Electron* 49(4):724–739
60. Kouro S, Malinowski M, Gopakumar K, Pou J, Franquelo LG, Wu B, Rodríguez J, Perez MA, Leon JI (2010) Recent advances and industrial applications of multilevel converters. *IEEE Trans Ind Electron* 57(8):2553–2580
61. Lee J-S, Lee K-B (2015) Open-switch fault tolerance control for a three-level NPC/T-type rectifier in wind turbine systems. *IEEE Trans Ind Electron* 62(2):1012–1020
62. Chaturvedi P, Jain S, Agarwal P (2014) Carrier-based neutral point potential regulator reduced switching losses for three-level diode-clamped inverter. *IEEE Trans Ind Electron* 61(2):613–624
63. Rivera S, Wu B, Kouro S, Yaramasu V, Wang J (2015) Electric vehicle charging station using a neutral point clamped converter with bipolar DC bus. *IEEE Trans Ind Electron* 62(4):1999–2009
64. Busquets-Monge S, Maheshwari R, Nicolas-Apruzzese J, Lupon E, Munk-Nielsen S, Bordonau J (2014) Enhanced DC-link capacitor voltage balancing control of DC–AC multilevel multileg converters. *IEEE Trans Ind Electron* 62(5):4722–4732
65. Abu-Rub H, Holtz J, Rodríguez J, Baoming G (2010) Medium-voltage multilevel converters—state of the art, challenges, and requirements in industrial applications. *IEEE Trans Ind Electron* 57(8):2581–2596
66. Hartman MT (2005) Space vectors sets of voltage multilevel inverter part I. Classic two-levels, NPC and DCI circuit topologies. Paper presented at IEEE compatibility in power electronics, Gdynia, Poland, 1 June 2005

67. Teichmann R, Malinowski M, Bernet S (2005) Evaluation of three-level rectifiers for low-voltage utility applications. *IEEE Trans Ind Electron* 52(2):471–482
68. Alemi P, Dong-Choon L (2011) Power loss comparison in two- and three-level PWM converters. Paper presented at the IEEE international conference on power electronics and ECCE, Jeju, 30 May–3 June 2011
69. Razali AM, Rahman MA, George G, Rahim NA (2015) Analysis and design of new switching lookup table for virtual flux direct power control of grid-connected three-phase PWM AC–DC converter. *IEEE Trans Ind App* 51(2):1189–1200
70. Zhang Y, Qu C (2015) Table-based direct power control for three-phase AC/DC converters under unbalanced grid voltages. *IEEE Trans Power Electron* 30(12):7090–7099
71. Cuzner R, Drews D, Venkataramanan G (2012) Power density and efficiency of system compatible, sine-wave input/output drives. Paper presented at the IEEE energy conversion conference and exposition (ECCE), Raleigh, 15–20 Sept 2012
72. Fukuda S, Hasegawa H (1988) Current source rectifier/inverter system with sinusoidal currents. Conference record of the 1988 IEEE industry applications society annual meeting, Pittsburgh, 2–7 Oct 1988
73. Espinoza JR, Joos G (1998) State variable decoupling and power flow control in PWM current-source rectifiers. *IEEE Trans Ind Electron* 45(1):78–87
74. Liu F, Wu B, Zargari NR, Pande M (2011) Inductor current feedback control based active damping for high power PWM current source rectifier. Paper presented at the IEEE international electric machines and drives conference (IEMDC), Niagara Falls, 15–18 May 2011
75. Li YW, Wu B, Zargari NR, Wiseman JC, Xu D (2007) Damping of PWM current-source rectifier using a hybrid combination approach. *IEEE Trans on Power Electron* 22(4):1383–1393
76. Tan L, Li Y, Xu W, Wang P, Liu C (2009) An improved control method for PWM current source rectifier with active damping function. Paper presented at the IEEE international conference on industrial technology (ICIT), Gippsland, 10–13 Feb 2009
77. Liu F, Wu B, Zargari NR, Pande M (2011) An active damping method using inductor-current feedback control for high-power PWM current-source rectifier. *Trans Power Electron* 26(9):2580–2587
78. Tomasini M, Feldman R, Wheeler P, Clare J, Klumpner C (2009) dq -control of high-power current source rectifiers utilizing selective harmonic elimination. Paper presented at the 13th European conference on power electronics and applications (EPE), Barcelona, 8–10 Sept 2009
79. Noguchi T, Takeuchi D, Nakatomi S, Sato A (2005) Novel direct power control strategy of current source PWM rectifier. *Int Conf Power Electron Drives Syst* 2:860–865
80. Noguchi T, Sato A, Takeuchi D (2006) Minimization of DC reactor and operation characteristics of direct-power-controlled current-source PWM rectifier. Paper presented at the IEEE 32nd annual conference on industrial electronics, Paris, 6–10 Nov 2006
81. Noguchi T, Sano K (2007) Specific harmonic power suppression of direct-power-controlled current-source PWM rectifier. Paper presented at the 7th international conference on power electronics and drive systems (PEDS), Bangkok, 27–30 Nov 2007
82. Correa P, Rodriguez J (2008) A predictive control scheme for current source rectifiers. Paper presented at the power electronics and motion control conference (EPE-PEMC 2008), Poznan, 1–3 Sept 2008
83. Correa P, Rodriguez J, Lizama I, Andler D (2009) A predictive control scheme for current-source rectifiers. *IEEE Trans Ind Electron* 56(5):1813–1815
84. Lizama I, Rodriguez J, Wu B, Correa P, Rivera M, Perez M (2009) Predictive control for current source rectifiers operating at low switching frequency. Paper presented at the IEEE international conference on power electronics and motion control (IPEMC), Wuhan, 17–20 May 2009
85. Zavala P, Rivera M, Kouro S, Rodriguez J, Wu B, Yaramasu V, Baier C, Munoz J, Espinoza J, Melin P (2013) Predictive control of a current source rectifier with imposed

- sinusoidal input currents. Paper presented at IECON 2013—39th annual conference of the IEEE industrial electronics society, Vienna, 11–13 Nov 2013
86. Falkowski P (2016) Predictive control algorithms of an AC/DC converter with LCL filter. *Przegląd Elektrotechniczny* 92(4):92–97
 87. Grodzki R, Sikorski A (2014) Predictive control of the AC/DC converter. Paper presented at 16th international power electronics and motion control conference and exposition (PEMC 2014), Antalya, Turkey, 21–24 Sept 2014
 88. Sikorski A (2009) Bezpośrednia regulacja momentu i strumienia maszyn indukcyjnych. Oficyna Wydawnicza Politechniki Białostockiej, Białystok
 89. Świerczyński D (2005) Direct torque control with space vector modulation (DTC-SVM) of inverter-fed permanent magnet synchronous motor drive. PhD thesis, Warsaw University of Technology, Warsaw
 90. Grodzki R, Sikorski A (2011) A new DTC control for PMSM with torque ripple minimization and constant switching frequency. *COMPEL* 30(3):1069–1081
 91. Salo M, Tuusa H (2000) A vector controlled current-source PWM rectifier with a novel current damping method. *IEEE Trans Ind Electron* 15(3):464–470
 92. Xiao Y, Wu B, Rizzo SC, Sotudeh R (1998) A novel power factor control scheme for high-power GTO current-source converter. *IEEE Trans Ind App* 34(6):1278–1283
 93. Giglia G, Pucci M, Serporta C, Vitale G (2007) Experimental comparison of three-phase distributed generation systems based on VOC and DPC control techniques. Paper presented at European conference on power electronics and applications, Aalborg, Denmark, 2–5 Sept 2007
 94. Yaramasu V, Wu B, Rivera M, Narimani M, Kouro S, Rodriguez J (2015) Generalized approach for predictive control with common-mode voltage mitigation in multilevel diode-clamped converters. *Power Electron IET* 8(8):1440–1450
 95. Busquets-Monge S, Somavilla S, Bordonau J, Boroyevich D (2007) Capacitor voltage balance for the neutral-point-clamped converter using the virtual space vector concept with optimized spectral performance. *IEEE Trans Power Electron* 22(4):1128–1135
 96. Celanovic N, Voroyevich D (2000) A comprehensive study of neutral-point voltage balancing problem in three-level neutral-point-clamped voltage source PWM inverters. *IEEE Trans Power Electron* 15(2):242–249
 97. Gupta AK, Khambadkone AM (2007) A simple space vector PWM scheme to operate a three-level NPC inverter at high modulation index including over modulation region, with neutral point balancing. *IEEE Trans Ind App* 43(3):751–760
 98. Lei L, Yunping Z, Zhan W, Hongyuan J (2005) A simple neutral-point voltage balancing control method for three-level NPC PWM VSI inverters. Paper presented at the IEEE international conference on electric machines and drives, San Antonio, 15 May 2005
 99. Sikorski A, Kulikowski K, Korzeniewski M (2013) Modern direct torque and flux control methods of an induction machine supplied by three-level inverter. *Bull Pol Acad Sci Tech Sci* 61(4):771–778
 100. Malinowski M, Bernet S (2008) A simple voltage sensorless active damping scheme for three-phase PWM converters with an LCL filter. *IEEE Trans Ind Electron* 55(4):1876–1880
 101. Serpa LA, Ponnaluri S, Barbosa PM, Kolar JW (2007) Modified direct power control strategy allowing the connection of three-phase inverters to the grid through LCL filters. *IEEE Trans Ind App* 43(5):1388–1400
 102. Grodzki R (2013) A new predictive DTC strategy for a DC/AC inverter-fed permanent magnet synchronous machine. Paper presented at the XV international PhD workshop OWD 2013, Wisła, 19–22 Oct 2013

Active Power Filter Based on a Dual Converter Topology

Michał Gwóźdź

Abstract This chapter presents a concept for a shunt active power filter (APF) that is able to more accurately map its input current in a reference signal, when compared to a typical filter solution. This can be achieved by interconnecting two separate converters, such that one of the converters corrects a total output current towards a reference signal. The output power of the auxiliary converter is much lower than power of the main converter, while its frequency response is extended. Thanks to the continuous manner of the operation of the auxiliary converter, among other items, pulse modulation components in the filter input current and the total harmonic distortion (THD) is minimized. These benefits are paid for by a relatively small increase in the system's complexity and cost. This converter concept has been named "dual converter topology" (DCT). In this chapter, APF basics are presented, along with the results of simulation experiments and potential practical arrangements of the active filter.

Keywords Active power filter · Converter control · Converter topology · PWM

1 Introduction

Non-linearity of receivers, limited frequency response of power electronics converters and the wide-band nature of signal sampling and pulse width modulation processes are reasons behind inaccurate mapping of a converter's output current in a reference signal. To achieve accurate mapping, both advanced solutions in hardware and substantial modification of their control algorithms are necessary.

The subject of this chapter is a shunt active power filter with a modified topology. The voltage controlled current source (VCCS), a fundamental component of such a filter, is based on two converters connected in parallel. The advantage of

M. Gwóźdź (✉)
Institute of Control and Information Engineering,
Poznan University of Technology, Poznan, Poland
e-mail: michal.gwozdz@put.poznan.pl

this arrangement is the potential for accurate mapping of the VCCS output current in the reference signal. This proposed converter architecture has been called “dual-converter topology” (DCT).

Systems of interconnected, cooperating converters are already widely used in practical systems, e.g. [1–11], related to electric drives, converters for renewable energy sources and UPS systems. This is particularly true of systems using two converters connected in parallel, where the output power of one is a fraction of the power of the other. This idea is also presented in many studies, e.g. [3, 7, 10–12].

A feature common to some of these solutions is that the auxiliary converter (ACN) is activated only during the transient states of the output current of the main converter (MCN). Usually, the role of the ACN depends on maximization of the system’s dynamics, i.e., extension of its frequency response. As a consequence, the total system output current is better mapped in a reference signal. Unfortunately, system control algorithms, especially in relation to ACNs, are often defined informally. As a result, system potentials are not fully utilized. The DCT conception involves the cooperative work of two converters, connected in parallel, where the ACN operates continuously, rather than only in transient system states. Additionally, the rules of the system’s operation are formally defined. Unlike many other conceptions of this kind, particular attention has been paid to the minimization of pulse-width modulation (PWM) carrier component in the (active power filter) APF output current.

In addition to the APF solution discussed in this chapter, the main expected areas for application of the proposed VCCS solution are:

- FACTS
- Current modulators
- Automated Test Equipment (ATE)
- Special purpose power electronics equipment, especially for magnetotherapy [13].

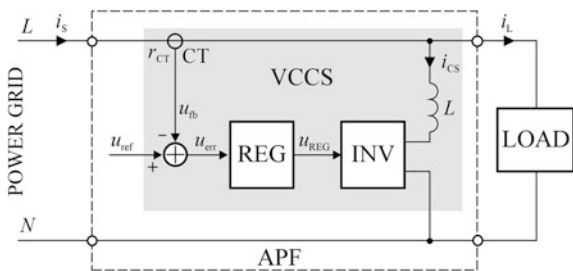
This study presents the first stage of work on the layout of the APF, which includes, among other items, principles of operation of the VCCS based on the DCT and discussion of the APF simulation experiment.

The following text is divided into three sections. The first deals with the structure and principles of the DCT operation. The second section presents the APF simulation model research. Finally, in the third part, conclusions are presented.

2 A Power Electronics Current Source Based on the DCT

Much work has been dedicated to the improvement of power quality, so only a brief outline of the APF system is necessary here for the reader’s convenience. In Fig. 1, a block diagram of a typical shunt APF is shown. The VCCS, a fundamental component of the APF, is an electrical system working in a closed feedback

Fig. 1 Block diagram of a typical single-phase shunt APF



loop. Many factors (e.g., the limited frequency response of the system and the operation of a pulse modulator) lead to the receiver current often being poorly mapped in the reference signal (u_{ref}). Particularly, this happens when the value of the PWM carrier frequency is low, which is enforced by the demands of maximization of converter efficiency.

The VCCS consists of the control module (the output current regulator i.e. the REG block), the power electronics inverter (INV) and the passive filter (the L inductor) at its output. The APF input current i_s is related to the error signal $u_{err} = u_{ref} - r_{CT}i_s$, where r_{CT} is the gain factor of the current transducer (CT), and $r_{CT} = \text{const}$. In such a system, the value of an error signal is relatively large. Taking into account a linear model of APF, the general aim of the VCCS is to fulfil the following theoretical formula:

$$i_s = \frac{1}{r_{CT}} (u_{ref} - u_{err}) \xrightarrow{-\infty < u_{err} < \infty, |u_{err}| \rightarrow 0} \frac{1}{r_{CT}} u_{ref} \tag{1}$$

Fulfilling the Eq. (1) obtains the “ideal case” of APF operation, possible only in theory. In real systems, even modest minimization of the error signal is a difficult task.

The simplified form of the VCCS, based on the proposed DCT concept, is presented in Fig. 2a. The MCN is supplemented with the ACN. The MCN is the high power converter, but its frequency response is limited. The ACN is the low power converter, but its frequency response is significantly extended by comparison with the MCN. In the simplified form, the ACN is equipped with a transconductance amplifier. This amplifier is preceded by a limiter block (LIM), which clips the ACN control signal, i.e., u_{err} . This imposes a maximal value on the ACN output current ($i_{out,A}$). Thus, a relationship between the output power of the ACN and the MCN is established.

In the small-signal model of the system (shown in Fig. 2b), the DELAY block is implemented. This block introduces a τ time delay to reflect delays that occur in real systems due to, for example, a limited signal-sampling period, time required for signal processing and a non-zero period for PWM carrier signals.

The general formula of the VCCS is then modified as follows:

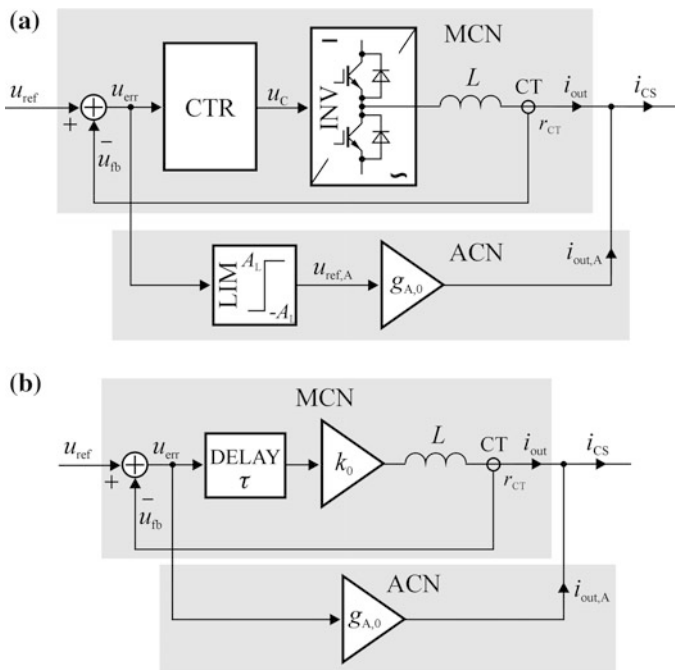


Fig. 2 Block diagram of the VCCS based on the simplified DCT form (a) and its small-signal model (b)

$$i_{CS}(t) = i_{out}(t) + i_{out,A}(t), \quad (2)$$

and, in relation to the linear model of the system:

$$\begin{aligned} i_{CS}(t) &= i_{out}(t) + i_{out,A}(t) = i_{out}(t) + u_{err}(t) * g_A(t) \\ &= i_{out}(t) + [u_{ref}(t) - r_{CT}i_{out}(t)] * g_A(t), \end{aligned} \quad (3)$$

where $g_A(t)$ is the pulse response of the transconductance amplifier.

Assuming the transfer function of the transconductance amplifier has the 0-order form, i.e., $g_A(t) = g_{A,0}\delta(t)$, the general equation to describe the model's operation can be stated as follows:

$$\begin{aligned} i_{CS}(t) &= i_{out}(t) + [u_{ref}(t) - r_{CT}i_{out}(t)] * g_A(t) \\ &= i_{out}(t) + g_{A,0}u_{ref}(t) * \delta(t) - g_{A,0}r_{CT}i_{out}(t) * \delta(t) \\ &= g_{A,0}u_{ref}(t) + (1 - g_{A,0}r_{CT})i_{out}(t) \quad g_{A,0}r_{CT} = 1 \\ &= g_{A,0}u_{ref}(t) \quad | \quad u_{err}(t) | < \langle -A_{LIM}, A_{LIM} \rangle \end{aligned} \quad (4)$$

where $\pm A_{LIM}$ are the values of the signal clipping levels in the LIM block.

The Eq. (4) indicates that a load current can match a reference signal regardless of the degree of mapping in the reference signal of the MCN output current (i_{out}). Under such conditions, the magnitude of the ACN control signal (u_{err}) is not limited by the LIM block.

Figure 3 offers block diagrams of possible practical arrangements of the VCCS based on the DCT and its linear model. This model has been used for system stability analysis based on the Nyquist criterion.

For general cases, the structures of both converters are very similar. However, the parameter values of these systems significantly diverge. For example, to obtain a sufficient frequency response, the PWM carrier frequency in the ACN must be much higher than that in the MCN. Therefore, in the execution module (INV) of the MCN, standard IGBT devices are used, whereas, in the ACN, MOSFET devices are used. In a real system, both converters would be powered from the same DC rails. Thus, the rated voltage of power electronics devices utilized there will be similar, while these devices will differ in their nominal output current values (and, also, their cut-off frequencies). This DCT-based system allows for the avoidance of a specific phenomenon that usually occurs in multi-channel (interleaved) converters—that of

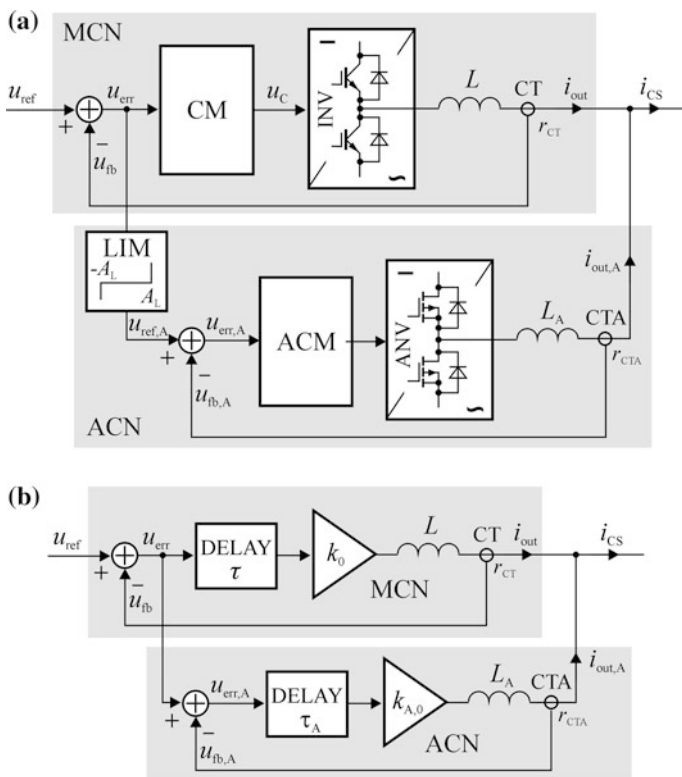


Fig. 3 Block diagram of the VCCS based on the DCT as a real system (a) and its linear model (b)

an unbalanced current flow in particular converter channels, e.g., [6, 14, 15]. This is due to the fact that, in the DCT, output current paths are controlled independently. It is therefore expected that such undesirable interaction between converters will be negligible.

VCCS is a SISO and LTI type model. Thus, it can be expressed in a frequency domain with the following equation:

$$I_{CS} = U_{REF} \frac{1}{r_{CT} j\omega \frac{L}{k_0 r_{CT}} + e^{-j\omega\tau}} + U_{err} \frac{1}{r_{CTA} j\omega \frac{L_A}{k_{A,0} r_{CTA}} + e^{-j\omega\tau_A}} : |u_{err}(t)| \subset \langle -A_L, A_L \rangle \quad (5)$$

where τ_A is the time delay introduced in the linear model of ACN.

Maximal gain values in the controller blocks (k_0 , $k_{A,0}$) are limited by a system stability condition. Assuming the REG block is a P (proportional) type, these values are determined using the following formulas [16]:

$$k_{0,max} < \frac{\pi}{2} \frac{L}{r_{CT}\tau} \quad (6)$$

$$k_{A,0,max} < \frac{\pi}{2} \frac{L_A}{r_{CTA}\tau_A} \quad (7)$$

In light of Eqs. (6) and (7), the Eq. (5) now takes the following form:

$$I_{CS} = U_{ref} \frac{1}{r_{CT} j\omega \frac{2}{\pi} \tau e^{j\omega\tau} + 1} + U_{err} \frac{1}{r_{CTA} j\omega \frac{2}{\pi} \tau_A e^{j\omega\tau_A} + 1} : |u_{err}(t)| \subset \langle -A_L, A_L \rangle, \quad p = \frac{\tau}{\tau_A} \quad (8)$$

Equation (8) expresses the best system for mapping the VCCS output current in the reference signal, given certain operation conditions. Thus, for the system to operate effectively, the following conditions should obtain: $p \gg 1$ (i.e., $f_{c,A} \gg f_c$, where f_c and $f_{c,A}$ are PWM carrier frequencies in the MCN and the ACN respectively), and $L_A \ll L$.

By fulfilling Eq. (8) the VCCS frequency response is approximately p -times extended, as compared to that of the MCN. Thus, a dominant effect on the quality of the VCCS output current (in the sense of minimizing the u_{err} magnitude) is set by both the $f_{c,A}$ value and the u_{err} signal clipping level.

According to the operation of a typical APF, many studies assume that the reference signal is the sinusoidal one, and that this amplitude is equal to U_{ref} . Additionally, it is assumed that the gains of both current transducers are equivalent, i.e., $r_{CT} = r_{CTA} = r$.

The quality of the VCCS output current can be evaluated on the following basis: *THD*, total control error (denoted by ϵ_{tot}), control error related to the first harmonics of this current (denoted by ϵ_1) and the relationship between the PWM component magnitude, $I_{S,PWM}$, in this current and the amplitude of its fundamental harmonics, $I_{S,1}$ (denoted by α). These dependencies are defined by the following formulas:

$$\epsilon_{tot} = \sqrt{\frac{u_{ref} - r(i_{out} + i_{out,A})^2}{|u_{ref}|^2}} 100 \%, \tag{9}$$

$$\epsilon_1 = \left| \frac{U_{ref} - rI_{S,1}}{U_{ref}} \right| 100 \%, \tag{10}$$

$$\alpha = \frac{I_{S,PWM}}{I_{S,1}} 100 \%. \tag{11}$$

3 Simulation Studies

To verify these theoretical assumptions, the simulation model of the 3-phase APF, based on the DCT with the use of the OrCAD/PSpice toolbox, was investigated. The block scheme of this simulation is shown in Fig. 4.

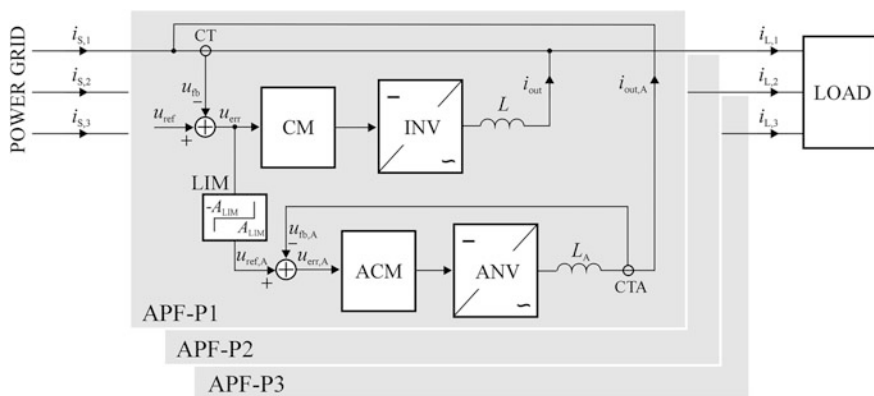


Fig. 4 Simplified block scheme of the APF as a base for its simulation model (single-phase is shown alone for clarity)

Ready-to-use models of power electronics devices, available in the OrCAD/Pspice toolbox, were modified to better approximate real devices. One potential practical arrangement of the VCCS suggested that the IPM/IGBT could be used in the main converter. The L1 series 1200 V [17] family of IPMs manufactured by MITSUBISHI ELECTRIC seems to have been a good choice. For the auxiliary converter, it was determined that a recent device manufactured by CREE, CCS050M12CM2, and a 1200 V SiC MOSFET module [18] could be utilized. Models of these devices were thus used in the APF simulation model.

The basic electrical parameters of the model were as follows:

- Power grid voltage: 3×400 V/50 Hz
- Rated load power: $P_{L,n} = 36$ kW
- PWM carrier frequency: $f_c = 5$ kHz and $f_{c,A} = 100$ kHz
- Current regulator gain factor in the CM block: $k_0 = 30$
- Main converter output inductance: $L = 2$ mH
- Maximal magnitude of the MCN output current (i_{out}): 80 A.

Three different types of APF load were considered:

1. A thyristor-based voltage regulator with a firing angle equal to 90 el. deg., with resistors at the output.
2. A voltage regulator with a resistor and an inductor connected in series at its output.
3. A six-pulse rectifier with a large capacitor in the DC link ($C_{DC} = 330$ μ F). So as to limit input current pulses caused by the capacitor, an inductor was placed at the output of the rectifier ($L_L = 330$ μ F). The value of the resistor in the rectifier DC link was as follows: $R_L = 9$ Ω .

In the case of load No. 1, the $\frac{di_L(t)}{dt}$ value was extremely high, which particularly imposed on the requirements of the APF operation. Additional investigations of the APF were performed as a result. These were designed to determine the values of ε_{tot} and α versus $\frac{P_{ACN}}{P_{MCN}}$ and L_A . The values of the gain factors ($k_0, k_{A,0}$) were set very close to the maximal ones for L and L_A in the given case.

In Fig. 5 graphs of both functions are presented. The “single converter topology” (SCT) was the base of the VCCS structure in this case; neither the ACN nor MCN are present in such system.

The solid lines labelled “SCT-MCN” show the function value for the SCT-based VCCS. The “SCT-ACN” line refers to the case in which the main converter was turned off, adopting the auxiliary role (its output power was enlarged accordingly). The curves of ε_{tot} (Fig. 5a) point to an L_A value in the range 250–1000 μ H as the optimal value for minimization of the ε_{tot} control error, while, for minimization of α

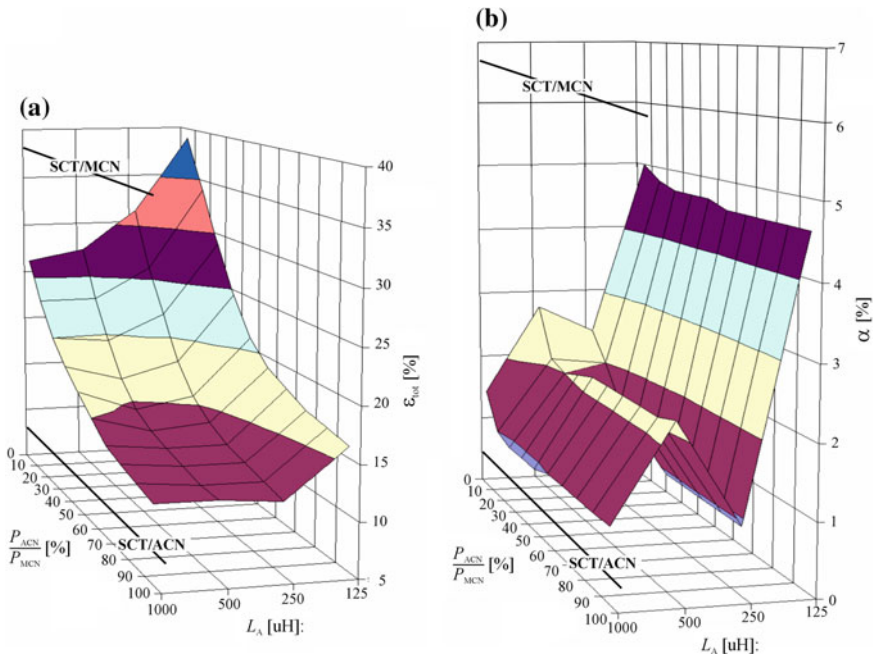


Fig. 5 Graphs of ϵ_{tot} (a) and α (b) versus $\frac{P_{ACN}}{P_{MCN}}$ and L_A

(Fig. 5b), a value of $L_A = 250 \mu\text{H}$ is the best choice. Taking both criteria into account, just this value of L_A was applied in the simulation model. Hence, respecting (7), it was assumed that $k_{A,0} = 70$. Respecting Fig. 5, the rated output power of ACN in the simulation model was set at 25 % of MCN. This value seemed to be a good compromise between the effectiveness of the filter operation and the economic elements of all system implementation. In the following figures, selected signals in the APF simulation model are presented. A single-phase is shown alone for clarity (Figs. 6, 7 and 8).

In Table 1, selected parameters of the load current and the filter input current are presented for the above-mentioned three load types. Both the DCT and the SCT were considered as bases of the VCCS.

These results show a (significantly) more efficient operation of the APF based on the DCT, as compared to the SCT. Depending on the load type, the following relationships obtained:

- THD of the APF input current was reduced 1.6–3.0 times for the SCT and 2.0–4.6 times for the DCT.
- ϵ_{tot} for the DCT was reduced 1.6–2.1 times as compared to the SCT.
- ϵ_1 for the DCT was reduced 1.7–2.7 times as compared to the SCT.

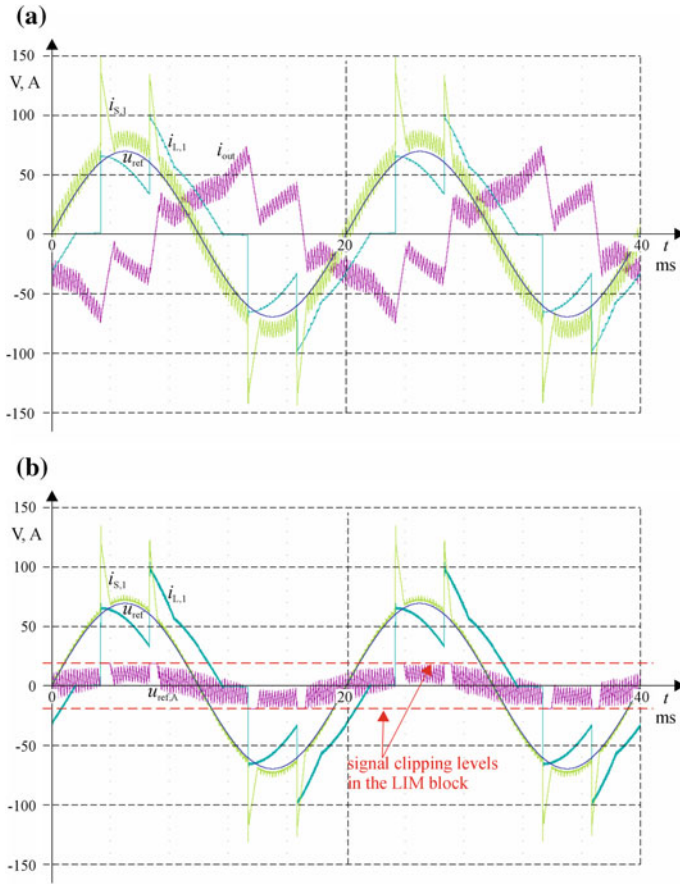


Fig. 6 Waveforms in the simulation model of APF for the load No. 1: **a** receiver current ($i_{L,1}$), reference voltage (u_{ref}), APF input current ($i_{S,1}$) and VCCS output current (i_{out}) while the SCT was used; **b** receiver current, reference voltage, APF input current and reference signal for ACN ($u_{ref,A}$) while the DCT was used

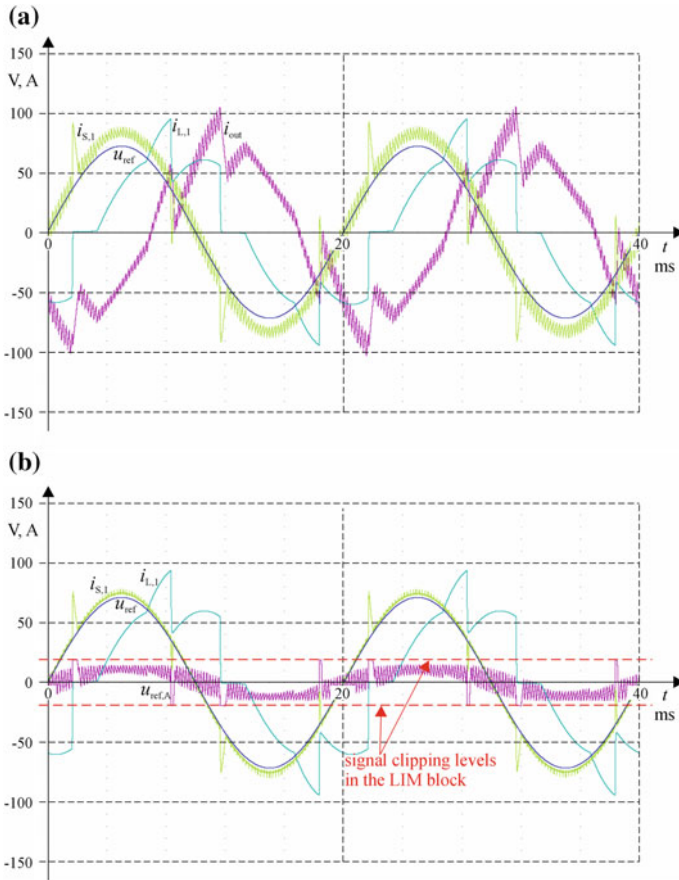


Fig. 7 Waveforms in the simulation model of APF for the load No 2. while the SCT was used (a) and for the DCT (b)

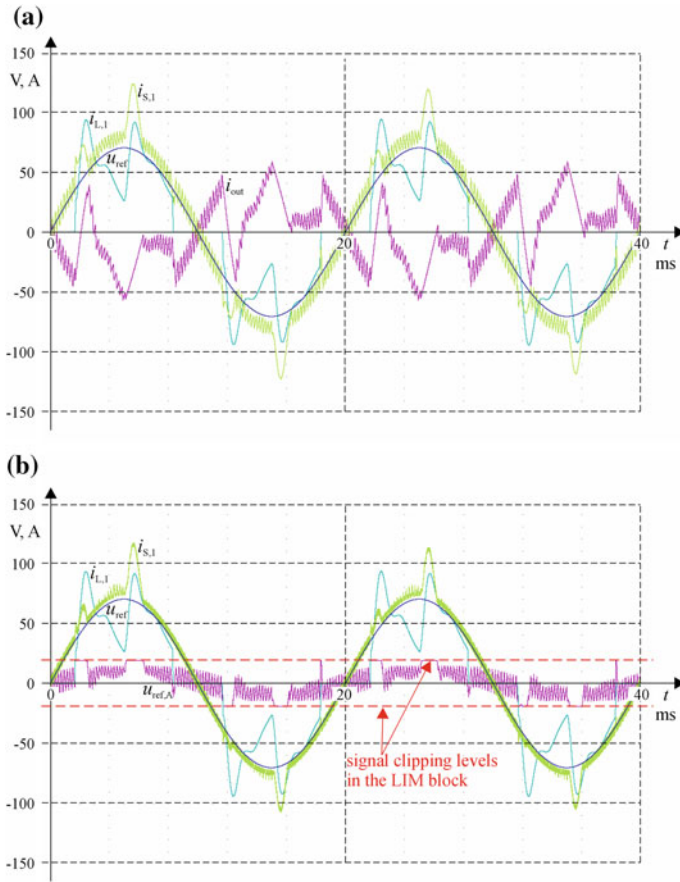


Fig. 8 Waveforms in the simulation model of APF for the load No 3. while the SCT was used (a) and for the DCT (b)

Table 1 The APF simulation model study results

No. of load	THD of $i_{L,1}$ [%]	THD of $i_{S,1}$ [%]		ϵ_{tot} [%]		ϵ_1 [%]	
		SCT	DCT	SCT	DCT	SCT	DCT
1	29.4	17.8	14.8	38.8	24.8	26.2	12.8
2	23.6	8.7	5.1	23.9	11.5	16.0	5.9
3	44.3	14.6	11.8	31.3	20.2	22.6	13.1

4 Conclusions

The power electronics controlled current source, based on the proposed dual-converter topology, is characterized by a much better mapping of its output current in a reference signal, as compared to a typical converter solution. Thanks to the continuous manner of the operation of the auxiliary converter, the pulse width modulation components in this current can also be minimized to the point of practical elimination. Therefore, it is expected that energy transmission loss can be reduced. These benefits are paid for by a relatively small increase in the system's complexity and cost. Shunt power active filters seem to constitute a good example of DCT implementation.

In the author's opinion, there are many potential applications in power electronics equipment for the presented solution of the power electronics system. Thus, this solution will be further developed towards solutions based on the multi-channel (interleaved) converters topology. Finally, a laboratory model of the APF is expected.

References

1. Vásárhelyi et al (2003), Managing transients generated by the reconfiguration process at the tandem inverter fed induction motor. In: Proceedings of IEEE 7th international conference on intelligent engineering systems, pp 388–393
2. Kaneko et al (2005) Analysis of dynamic variation on a combined control strategy for a five-level double converter. In: Proceedings of power electronics specialists conference PESC'05, pp 885–891
3. Imecs et al (2005) Vector control schemes for tandem-converter fed induction motor drives. *IEEE Trans Power Electron* 20(2):493–501
4. Rui et al (2007) The application on active noise cancellation—research on the series-parallel compensated UPS converter. In: International symposium on electromagnetic compatibility EMC 2007, pp 138–141
5. Asiminoaei et al (2008) Shunt active-power-filter topology based on parallel interleaved inverters. *IEEE Trans Ind Electron* 55(3):1175–1189
6. Hirakawa et al (2010) High power density interleaved dc/dc converter using a 3-phase integrated close-coupled inductor set aimed for electric vehicles. In: Proceedings of energy conversion congress and exposition (ECCE), 2010 IEEE, pp 2451–2457
7. Morizane, Kimura (2011) Circulating current control of double converter system for wind power generation. In: Proceedings of the 14th European conference on power electronics and applications (EPE 2011), pp 1–10
8. Tomaszuk, Krupa (2011) High efficiency high step-up DC/DC converters—a review. *Bull Pol Acad Sci Tech Sci* 59(4):475–483
9. Iwazskiewicz et al (2012) Three-phase voltage outages compensator with cascaded multilevel converter. *Arch Electr Eng* 61(3):325–336
10. Sozański (2013) Digital signal processing in power electronics control circuits. Springer, London, ISBN 978-1-4471-5266-5
11. Krystkowiak (2014) Current modulator implemented in modified wideband controlled current source, (in Polish). *Przegląd Elektrotechniczny*, Nr 6:87–90

12. Gwóźdź (2013) Power electronics active shunt filter with controlled dynamics. In: Proceedings. of COMPEL: the international journal for computation and mathematics in electrical and electronic engineering, vol 32, no 4, pp 1337–1344
13. Sieroń et al (2008) Impact of low frequency pulsed magnetic fields on pain intensity, quality of life and sleep disturbances in patients with painful diabetic polyneuropathy. *Diabetes Metab* 34(4):349–354
14. Eirea and Sanders (2008) Phase current unbalance estimation in multiphase buck converters. *IEEE Trans Power Electron* 23:137–143
15. Gwóźdź (2012) Power electronics wideband controlled voltage and current sources on base of interleaved converters, (in Polish). *Przegląd Elektrotechniczny*, Nr 10A:132–134
16. Gwóźdź (2006) Effectiveness of increasing a power grid current by means of a power electronics active compensator, (in Polish). *Przegląd Elektrotechniczny*, Nr 7–8:65–68
17. WWW product page of Mitsubishi electric: http://sem.mitsubishielectric.eu/products/power_semiconductors/ipm. Accessed Nov 2014
18. WWW product page of CREE: <http://www.cree.com/Power/Products/SiC-Power-Modules>. Accessed May 2015

AC/DC/AC Converter with Power Electronics Current Modulator Used in DC Circuit for Renewable Energy Systems

Michał Krystkowiak and Adam Gulczyński

Abstract In this chapter, the elaborated structures of the main circuit and control system of a power electronics AC/DC/AC converter, working as a coupling between the energy grid and a water turbine with an electric machine, are described. In aiming to ensure the high efficiency of this system, input and output converters with sinusoidal current were implemented. The input AC/DC converter is based on a diode rectifier with a power electronics current modulator in the DC circuit, while the output circuit is based on a transistor inverter. This solution is dedicated to high power systems. The chapter also presents an MPPT algorithm, which is elaborated and used to control the DC/DC converter. The chosen simulation and experimental results of the research is analysed.

Keywords Renewable energy · Rectifier · Current modulator · Pulse transformer · Inverter

1 Introduction

This article presents high voltage power and control structures of a developed power electronic AC/DC/AC converter, acting as a coupling between the AC power grid and a renewable energy source (RES). In the presented case, this RES is a hydro generator with a permanent magnet synchronous generator (PMSG). The block scheme of this converter is shown in Fig. 1. The system consists of the following blocks:

M. Krystkowiak (✉) · A. Gulczyński
Institute of Electrical Engineering and Electronics,
Poznan University of Technology, Poznan, Poland
e-mail: mikrystek@poczta.onet.pl

A. Gulczyński
e-mail: adamgulczynski@put.poznan.pl

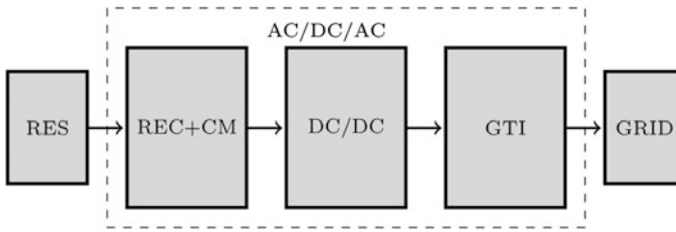


Fig. 1 Structure and control circuit of the current modulator

- REC + CM—rectifier with current modulator
- DC/DC—boost converter
- GTI—grid tied inverter

The solution's ability to correct the waveform of the input (generator) current of diode rectifiers toward a sinusoidal waveform is described.

Additionally, the implemented Maximum Power Point Tracking (MPPT) algorithm, which allows for the achievement of the maximum efficiency of the entire system, is presented.

Furthermore, it is explained how, in order to deliver high-quality energy parameters to the grid, a transistor inverter with a sinusoidal output current was applied.

2 Rectifier with Current Modulator

The circuit for the rectifier stage with the current modulator is shown in Fig. 2. This solution corrects the waveform of the input (generator) current and depends on current modulation in the output DC circuits of the diode rectifiers in parallel connection [1–3]. These converters are built with two six-pulse diode rectifiers (REC1 and REC2), which are supplied by two three-phase transformers with a star-star and star-delta connection. In this way, we achieve a phase shift of about 30 degrees for the voltage sources for each diode rectifier. Additionally, the current modulator (CM) must be placed in the DC output circuit. The CM is a kind of power electronics current source, which is connected to the main output circuit of the rectifiers via a wide-band pulse transformer (PT). With the aid of this transformer, the current of the modulator is added to, or subtracted from, the output currents of each diode rectifier. In this way, we can change the shape of the input currents of these two rectifiers and the resultant source current of all converters. The structure and control circuit of this converter is shown in Fig. 3. The generator of the triangular reference signal (TG) is placed following the block, FI, which is

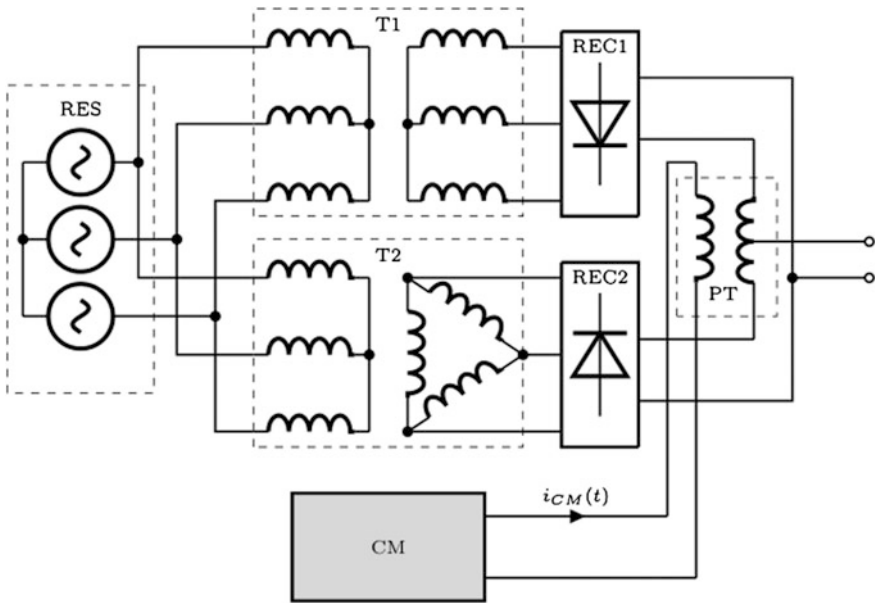


Fig. 2 Circuit of the rectifier stage with a current modulator

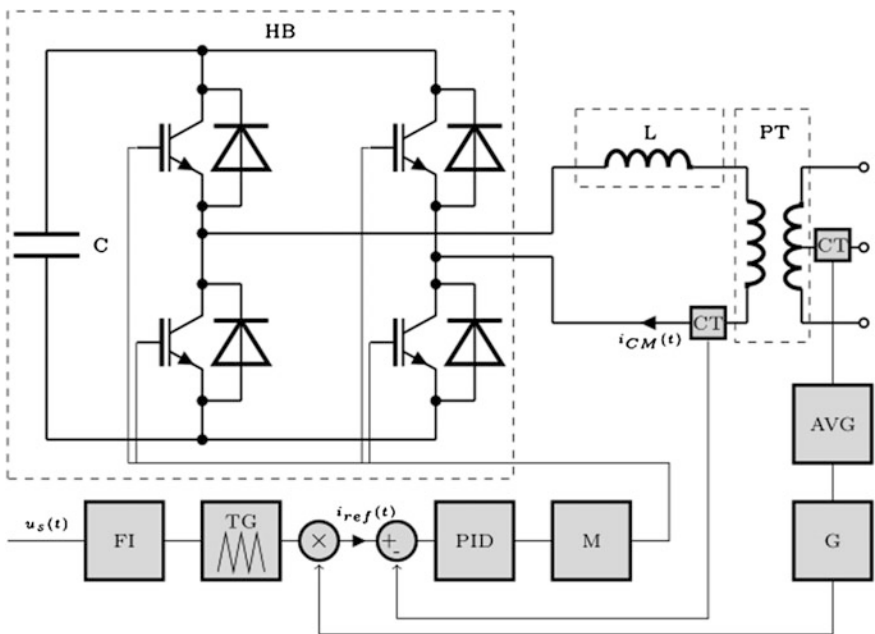


Fig. 3 Structure and control circuit of the current modulator

responsible for the correct detection frequency of the synchronous generator output voltage. The amplitude of the triangular reference signal is equal to one. The reference signal for the power electronics current modulator is calculated by multiplying the output signal of the TG block by the mean value of the output current of the diode rectifier. The G block represents the scale factor, which depends on the transformation ratio. The CT blocks are responsible for currents measurements, while the M and PID blocks represent the PWM modulator and the PID regulator, respectively.

In aiming to achieve an almost sinusoidal current for the generator, the modulator must generate a triangular signal with a frequency equal to six times that of the voltage generator frequency (in this case 300 Hz). The signal generated by the current modulator contains higher harmonics, so the transformer PT should obtain a wide pass band. This magnetic element should also assure the smallest losses of energy and symmetry of both windings of the secondary side. These requirements render this transformer close to the ideal [4].

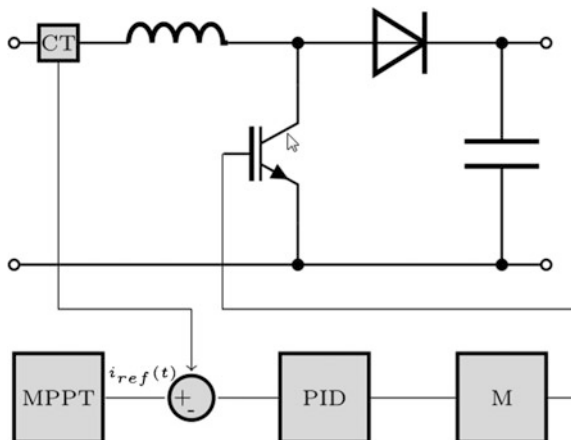
The control system of the presented current source (current modulator) determines the effectiveness of the energy transformation as well as the waveform shape (and quality) of the source current.

The current modulator is built using an IGBT full bridge inverter with a passive serial inductive filter at the output. This converter is connected to the DC output circuits of each diode rectifier via a wide-band pulse transformer [3, 4].

3 Boost Converter

Due to the required minimum value of the DC bus voltage, which should, in this case, be greater than the amplitude of the grid's voltage, the high voltage power part of the DC/DC converter is based on a BOOST converter (Fig. 4) [4].

Fig. 4 Schematic diagram of the DC/DC BOOST converter



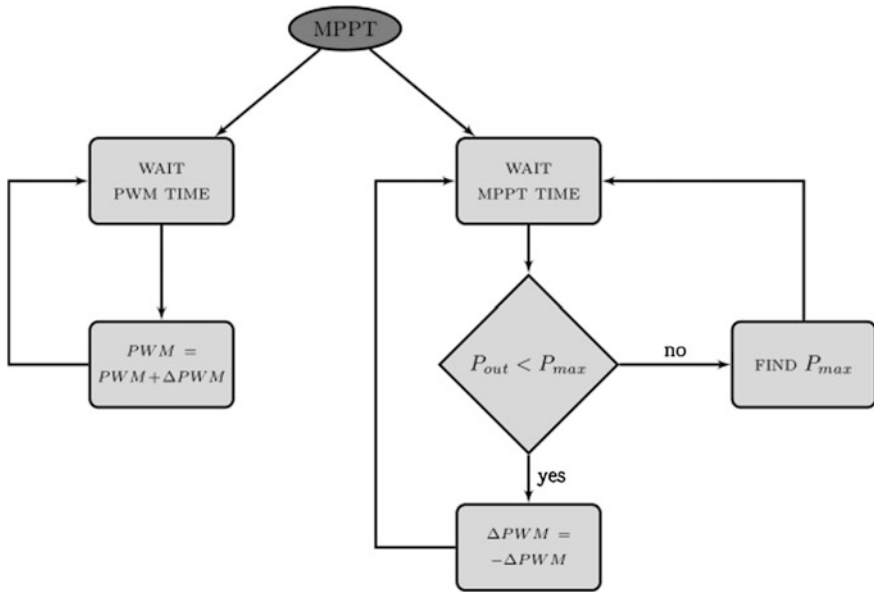


Fig. 5 Structure and control circuit of the current modulator

The purpose of the DC/DC BOOST converter is to increase input voltage and to supply the capacitor group with a mediation DC/DC circuit, from which a grid inverter is powered. In order to achieve the highest possible efficiency of use of energy resources, the MPPT algorithm was elaborated and implemented in the control system of the BOOST converter [5–7]. This block diagram is presented in Fig. 5.

In the developed algorithm, the two main loops were separated. The first loop is responsible for modifying the duty ratio, PWM , which activates a key, T, of the BOOST converter power section (Fig. 4). This process takes place at certain marked intervals, $PWM TIME$, and depends on the second loop, which determines the direction of changes in the duty ratio by a constant value defined as ΔPWM .

The task of the second algorithm’s loop is to search for the maximum power that can be achieved at a certain working point of the system. Depending on the result of comparing the output power (P_{out}) for the current operating at the source point with a predetermined maximum value, the control system determines the direction of changes in the duty cycle and looks for a new maximum power. This comparison is performed in a period defined as $MPPT TIME$.

4 Grid Tied Inverter

The grid inverter (a transistor rectifier operating in inverter mode) is directly responsible for the transfer of energy to the grid and is based on a transistor H-bridge with an inductive output filter. A schematic diagram of this system is presented in Fig. 6 [8].

The system transfers energy from the capacitor battery of the mediation circuit (rechargeable via the BOOST inverter) to the grid, while simultaneously ensuring that it is as close as possible to a sinusoidal signal grid current and that it lacks reactive power generation. It should be noted that the correct operation of this circuit is possible only if the value of the instantaneous voltage in the mediation circuit is greater than the amplitude of the grid voltage. Based on the definition of the active current [9], the grid inverter's control circuit, operating in the current tracking controller, was developed to enable it to adjust and stabilize the voltage on the capacitors of the DC mediation circuit. It should be noted that this function does not comply, in the described case, to a control system of the BOOST converter, and realizes only the MPPT algorithm.

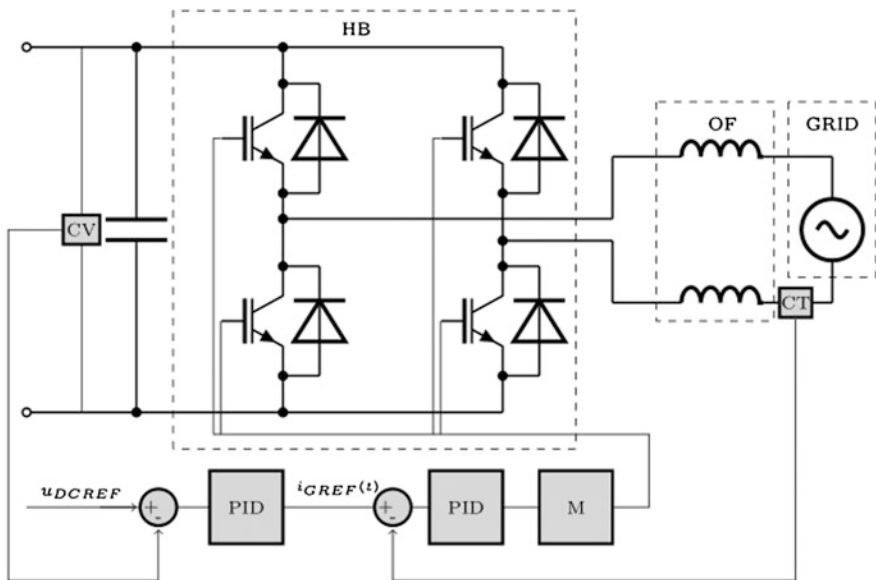


Fig. 6 Schematic diagram of the grid inverter

5 Simulation and Experimental Results

During simulations and experimental research, the effectiveness of the converter was tested. A selection of these results is presented below. Figures 7 and 8 show the output current of the generator. The shape of the generator current was close to sinusoidal (THD = 2.4 %).

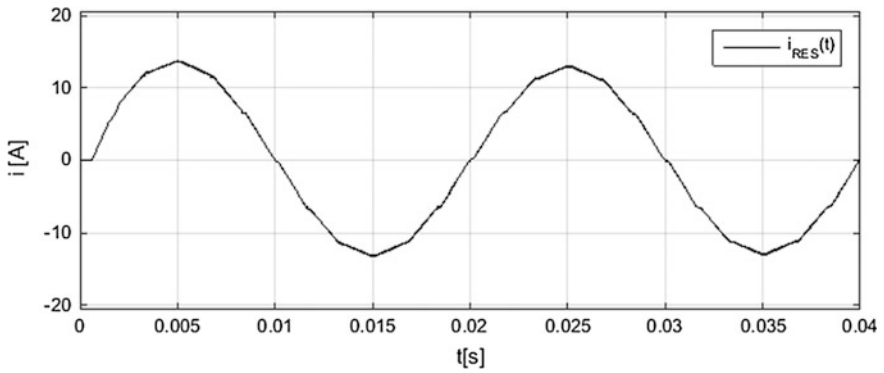


Fig. 7 Simulation results—the waveform of the diode rectifier generator current with current modulation

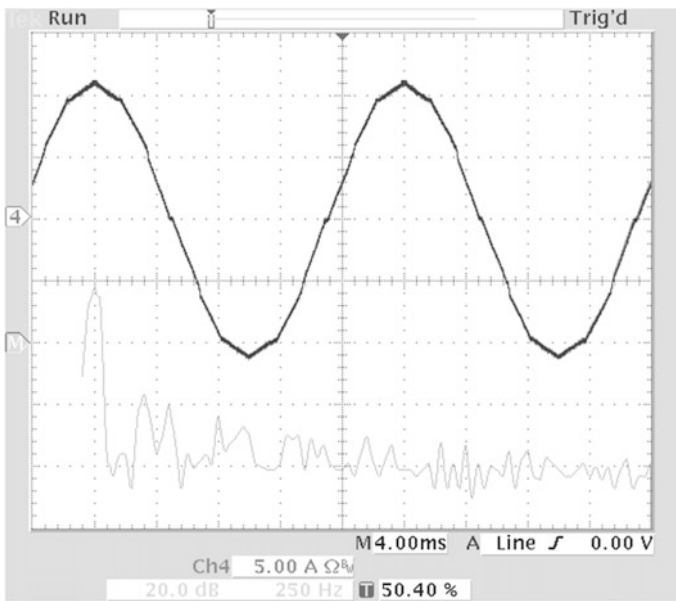


Fig. 8 Experimental results—the waveform and harmonic spectrum of the diode rectifier generator current with current modulation (THD = 2.4 %)

Good mapping of the current modulator within the reference signal was achieved (Figs. 9, 10 and 11).

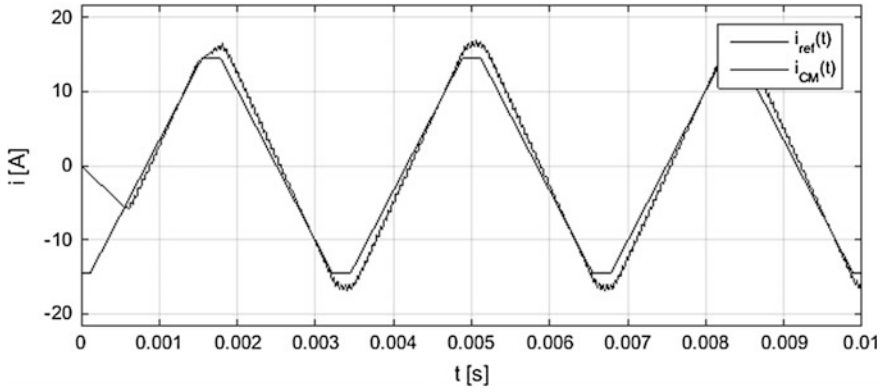


Fig. 9 Simulation results—the output and reference signals of the current modulator

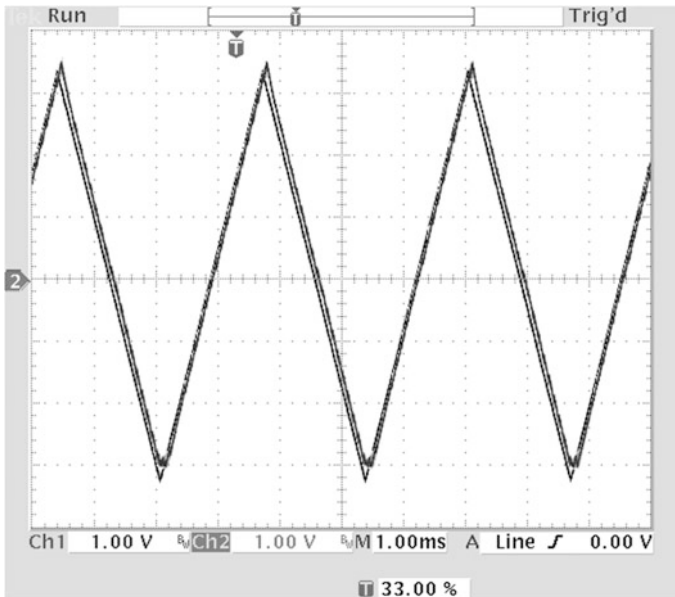


Fig. 10 Experimental results—the output and reference signals of the current modulator

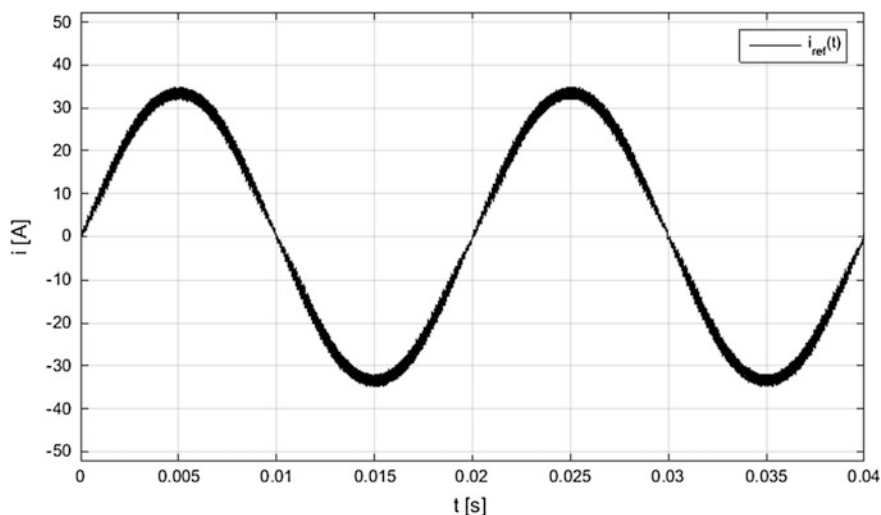


Fig. 11 Simulation results—the grid current trajectory generated by the output inverter of the system

6 Summary

In this chapter, the elaborated structures of the main circuit and control circuit of a power electronics AC/DC/AC system, acting as a coupling between the AC power grid and a renewable energy source (a water turbine with a PMSG generator), were described. The implemented solutions used to obtain the highest possible efficiency of the whole system were presented. In pursuit of this aim, the input and output converters with sinusoidal currents were used and the elaborated MPPT algorithm (to control the BOOST converter) was implemented.

In the proposed solution, the current modulator in a DC output circuit of two six-pulse rectifiers was utilized. As a result, the output current of the generator was almost sinusoidal, which increased the efficiency of the machine. This rectifier solution is very useful for cases of large power loads, as the power of the current modulator is approximately 2–3 % of the total DC load power.

References

1. Strzelecki R, Supronowicz H (2000) The power factor of AC circuits and correction method. OPW, Warsaw
2. Krystkowiak M, Gwózdź M (2008) Control system of power electronics current modulator utilized in diode rectifier with sinusoidal current. Paper presented at 13th international power electronics and motion control conference, Poznan University of Technology, Poznan, 31 Aug–4 Sept 2008

3. Krystkowiak M (2009) Power rectifier with improved indicators working with power electronics current modulator. Dissertation, Poznan University of Technology
4. Gwóźdź M, Krystkowiak M (2008) Calculation of parameters of equivalent circuit of pulse transformer. Paper presented at 20th symposium electromagnetic phenomena in nonlinear circuits, University of Lille, Lille, 2–4 July 2008
5. Krystkowiak M, Gulczyński A (2014) Construction and principle of working of an experimental model of a mini hydroelectric units dedicated to yacht. Paper presented at 9th Conference PES-9, Warsaw University of Technology, Koscielisko, 16–20 June 2014
6. Tan K, Islam S, Optimum control strategies in energy conversion of PMSG wind turbine system without mechanical sensors. *IEEE transactions on energy conversion* 19(2):392–399
7. Krystkowiak M, Gulczyński A (2014) The construction and control algorithm of power electronic converter implemented in unconventional mini-hydroelectric system dedicated to craft marinas. *Poznan University of Technology Academic Journals* 80:27–34
8. Krystkowiak M, Gwóźdź M (2015) Power electronics converter working as a coupling between energetic grid and photovoltaic panels. *Maszyny Elektryczne—Zeszyty Problemowe* 105:57–62
9. Fryze S (1931) The real power, imaginary and apparent power in electrical circuits with distorted waveforms of current and voltage. *Przegląd Elektrotechniczny* 7:193–203

Power Electronics Inverter with a Modified Sigma-Delta Modulator and an Output Stage Based on GaN E-HEMTs

Michał Gwóźdź and Dominik Matecki

Abstract The chapter presents a conception of a power electronics inverter based on a modified sigma-delta modulator (SDM) being used in the inverter's control block. The proposed modulator includes a comparator with dynamic hysteresis instead of a latched comparator, which is typically used in single-bit SDMs. Thanks to this feature, the resolution of the SDM output bit stream is, theoretically, unlimited. As a result, the value of the THD of an inverter output voltage (current) is much lower than that of a typical SDM solution. This benefit is not offset by an increase in the system's complexity. Moreover, the control system is simpler than in the case of a conventional inverter. Due to the very high frequency of an SDM output bit stream, in a power stage of the inverter, the gallium-nitride (GaN)-based E-HEMTs (Enhancement mode High Speed Mobility Transistors) are implemented. However, in the case of a lower value of an inverter output power, an Si-based device is still the proper choice. In the chapter, the inverter control circuit basics, the results of simulation experiments and a possible practical arrangement of this one as a voltage-controlled voltage source (VCVS) are presented.

Keywords Converter control · Gallium nitride transistor · PWM · Sigma-delta modulator

1 Introduction

Delta modulation was first invented at the ITT Laboratories in France by E.M. Deloraine, S. Van Mierlo and B. Derjavitch in 1946. The principle was rediscovered, several years later, at the Phillips Laboratories in Holland, whose engineers

M. Gwóźdź (✉) · D. Matecki
Institute of Control and Information Engineering,
Poznan University of Technology, Poznan, Poland
e-mail: michal.gwozdz@put.poznan.pl

D. Matecki
e-mail: dominik.matecki@put.poznan.pl

published the first extensive studies of both the single-bit and multi-bit concepts. Basically, this technique is used in precision analogue-to-digital converters (ADC) [1–4] for measurement and audio purposes. Following this substantial application area are (audio) amplifiers working in pulse mode, e.g., class-D ones [5]. Nowadays many variants of this type of amplifier designs are recognized and carefully analysed [6–9]. Generally, they use PDM or PWM in a power stage. The interesting solution of a control circuit has been utilized in a class-T amplifier [10]. This class of amplifiers is particularly characterized by the high quality of an output signal. A valuable review of control strategies and topologies of power electronics converters, for a wide range of applications, has been done in the work [11].

In the paper, the SDM is used to direct the control of an output stage of a power electronics voltage-controlled voltage source (VCVS). The basic premise of the proposed SDM conception is obtainment of the precise mapping of a VCVS output voltage in an input signal. Besides this, the structure of the control system is simple, i.e., mostly an analogue one (no “purely” digital components are used in the SDM), and easily implemented in power electronics equipment where high efficiency is necessary. The proposed SDM has been called the *dynamic hysteresis sigma-delta modulator* (DHSDM). The paper presents the initial stage of work on the system layout.

The following text is divided into four sections. The first one deals with the structure and the rule or work of DHSDM. The second one shows the simulation model research for the VCVS. The third part presents the practical arrangements of the output stage of the VCVS. In the last part, conclusions are presented.

2 Dynamic Hysteresis Sigma-Delta Modulator Basics

Sigma-delta modulators’ principles have been the subject of many works. Therefore, only a brief overview of the typical SDM is given here for the reader’s convenience. The basic single-bit SDM architecture is shown in Fig. 1. The integrator operates on the error signal $u_{\text{ERR}} = u_{\text{IN}} - u_{\text{DAC}}$ and the latched comparator produces the output bit stream, whose maximum frequency is equal to the frequency of the sampling clock (f_s).

The basic oversampling sigma-delta modulator increases the overall SNR at low frequencies by shaping the quantization noise such that most of it occurs outside the bandwidth of interest. The digital filter (not shown in the figure) then removes the noise from the bandwidth of interest, and the decimator reduces the output data rate back to the Nyquist rate.

Considering the kind of modulation, the SDM output signal is pulse-duration modulated—Fig. 2. A duration of a single bit is equal to a period of the sampling clock $T_s = 1/f_s$. This one-determines a time resolution, thereby a pass-band, of an SDM (ADC). If an SDM is a part of an ADC architecture, achieving even a high value of a sampling clock is not a technical and technological problem nowadays [12, 13]. Moreover, only multi-bit SDMs are usually implemented in ADC

Fig. 1 Diagram of a basic single-bit SDM with the latched comparator [3]

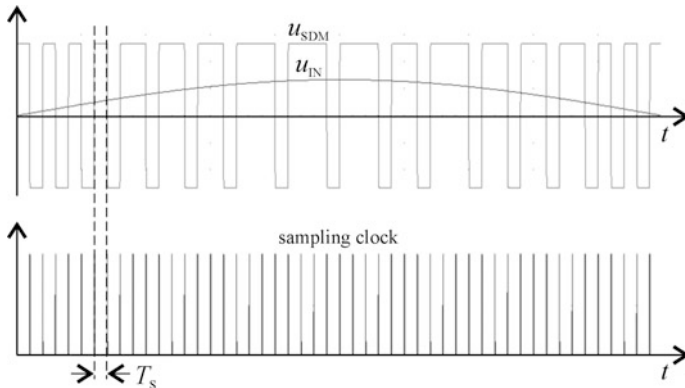
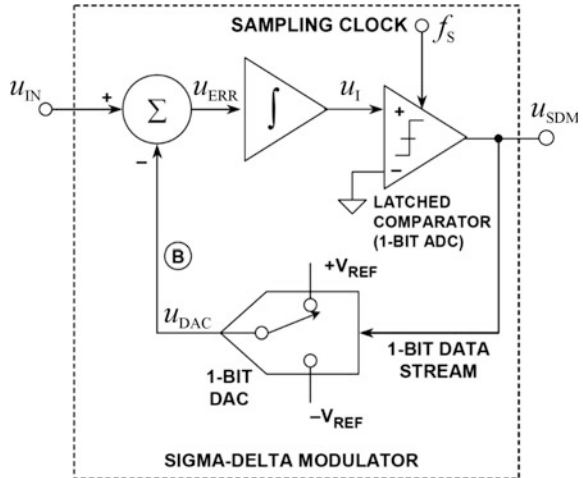
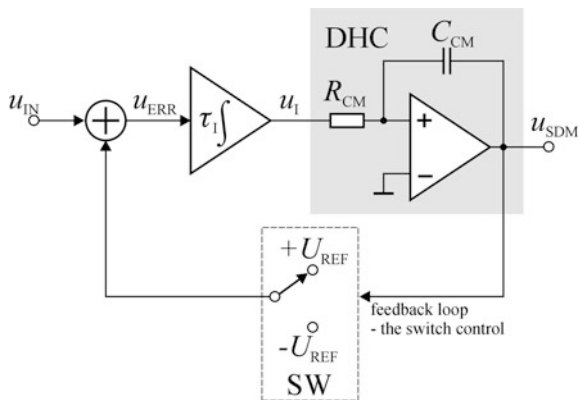


Fig. 2 Signal waveforms in an SDM with the latched comparator

architectures, which allows the increase of an ADC resolution at lower sampling frequencies. This situation rapidly changes if a modulator is used in a structure of a (high-power) class-D amplifier or other power electronics converter. The reason for this limitation is simply the switching time of actual power semiconductor devices. As a result, a THD (SINAD) and other parameters of the amplifier are often unsatisfactory. A solution to this problem can be using a modulator with a pulse-width rather than a pulse-duration modulated by an output signal. There are a number of possible variants of an SDM with such a feature, which have been carefully analysed. One of them was finally selected for further investigations—Fig. 3.

The proposed modulator is similar to a typical single-bit SDM; however, no latched comparator is used in their structure. Instead of this, a comparator with

Fig. 3 Diagram of a single-bit SDM with the dynamic hysteresis comparator



dynamic hysteresis (DHC) has been implemented. The DHC is the subcircuit shown in the shaded box. The particular feature of the proposed SDM solution is that it does not use a sampling signal. It generates the PWM’s similar signal with the “carrier” frequency, which value depends on the time constant of the comparator: $\tau_{CM} = R_{CM}C_{CM}$. A “carrier” frequency value also varies with an SDM input signal magnitude. Thanks to the structure of the SDM being mostly analogue (the SDM is a continuous time circuit), the duration of its output signal can be, theoretically, arbitrarily small. Thus, its time resolution tends to infinity.

The sigma-delta modulator is very difficult to analyse in the time domain because of the apparent randomness of the single-bit data output—the system is both non-linear and time variant. Usually, more or less simplified models of the SDM in a frequency domain are in use, e.g., [1, 2, 4]. These models are also used for a system stability analysis.

By means of heuristic methods, Eq. (1) has been formulated. This specifies the value of the PWM “carrier” frequency of the SDM output signal. However, the equation is valid for small values of the modulation index only, and expresses a maximum value of f_C :

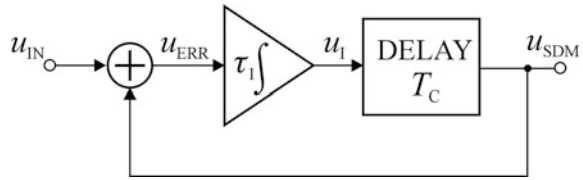
$$f_C = \frac{1}{5\tau_{CM}} = \frac{1}{T_C}. \tag{1}$$

The modulation index m has been determined similarly, as in the case of a “normal” PWM:

$$m = \frac{|u_{IN}|}{|u_{SDM}|}. \tag{2}$$

If τ_I is too small, the system stability can be an issue [1, 2, 14]. The simplified small-signal model of an SDM for the calculation of boundary values of system parameters—for preventing the system stability—is shown in Fig. 4. The model is based on the work [14].

Fig. 4 Small-signal model of the SDM for system stability analysis



The transfer function of this model is given by the following equation:

$$T_{SDM}(j\omega) = \frac{e^{-j\omega T_C}}{j\omega\tau_I + e^{-j\omega T_C}} \tag{3}$$

Taking into account (3), for system stability assurance (using the Nyquist criterion), the value of τ_I can be calculated as:

$$\tau_I > 2T_C \tag{4}$$

By fulfilling the Eq. (4), the integrator is also prevented from entering its output in a saturation state.

The following waveforms in a DHSDM simulation model have been obtained with the aid of the OrCAD/PSPICE toolbox. The model has used only “ideal” components (amplifiers, switches, passive components, etc.), i.e., it does not contain any parasitic elements. Basic model parameters were as follows: $\tau_I = 2 \mu s$, $\tau_{CM} = 200 \text{ ns}$ and u_{IN} is the sinusoidal signal with a fundamental frequency equal to 20 kHz. The modulation index was $m = 0.9$. Selected waveforms in the DHSDM simulation model are shown in Fig. 5.

In the following figure, the spectrum of the DHSDM output signal is shown while the value of the modulation index varies in the range 0.1–1.0 (Fig. 6).

The frequency of the DHSDM switching pattern is spread spectrum in nature; however, while the amplitude of the input signal decreases, this spectrum focuses

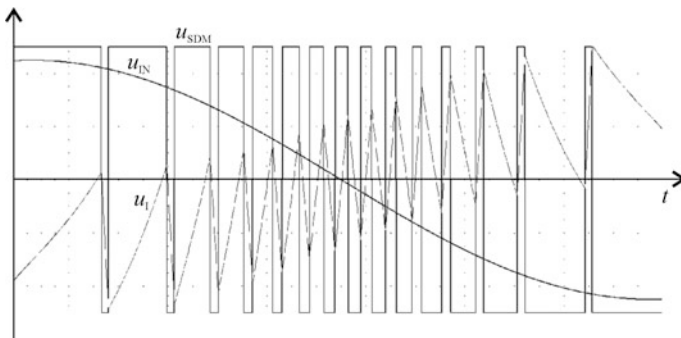


Fig. 5 Waveforms in the DHSDM simulation model: modulator input signal, modulator output signal and signal at the output of the integrator

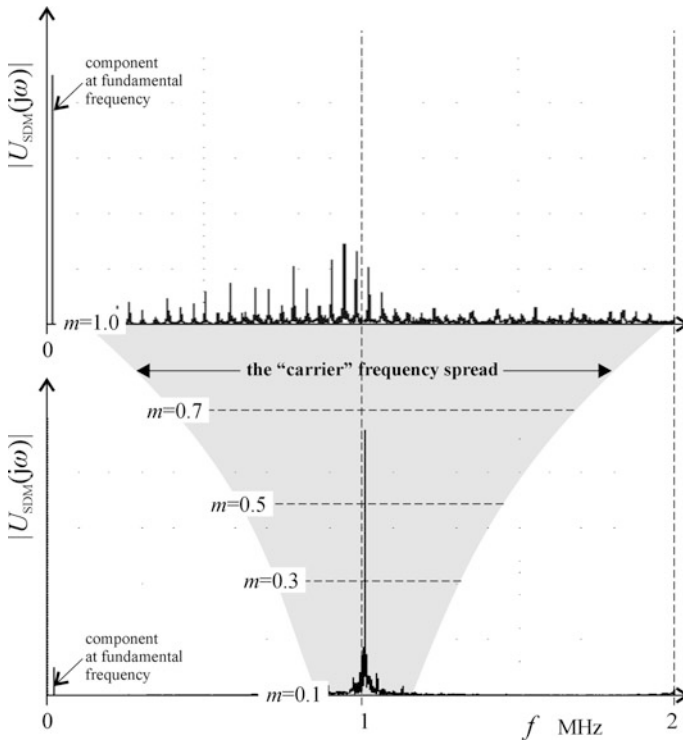


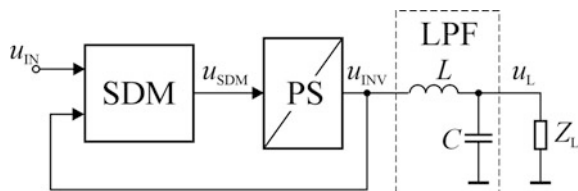
Fig. 6 Spectrum of the DHSDM output signal while the modulation index is in the range 0.1–1.0

more and more on the value given by Eq. (1). The spread-spectrum techniques are often applied to distribute the emissions over a wider frequency range [11, 15]. For actual simulation model parameters, the maximal SDM switching frequency is equal to 1 MHz.

3 Simulation Experiments

In the following figure, the block scheme of a VCVS using the DHC (or the latched comparator) in the SDM is presented. This version has a single-ended structure, i.e., input and output signals are referenced to a common system ground (Fig. 7).

Fig. 7 Block scheme of the VCVS simulation model



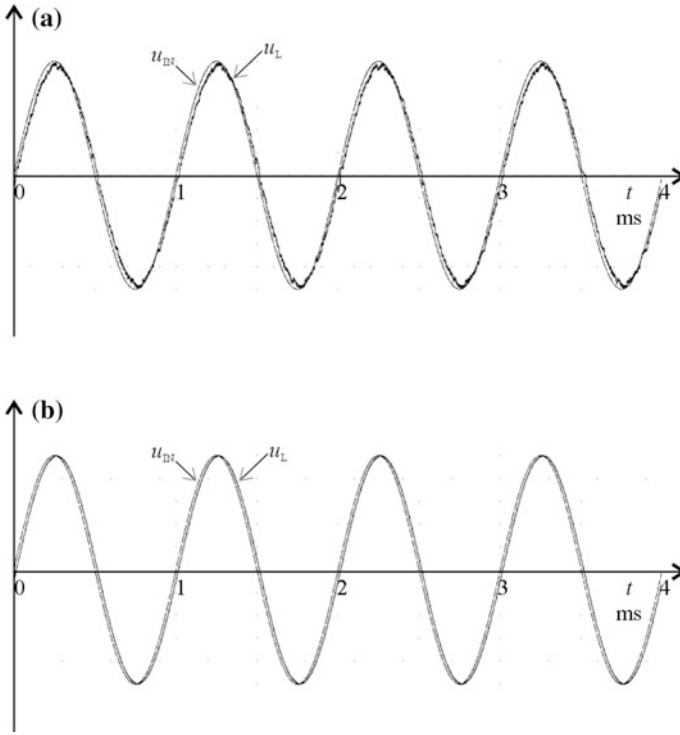


Fig. 8 Waveforms of the input signal and the load voltage in the VCVS simulation model whit using **a** the SDM with a latched comparator and **b** the DHSDM

The amplifier consists of the following elements: an SDM, a power stage (PS) and a second-order low-pass filter (LPF) being loaded by the resistor. The filter is necessary for minimizing the carrier components in the output signal.

Further simulation experiments have also been conducted in an OrCAD environment. In the version of the SDM with a latched comparator, the sampling clock frequency was $f_s = 1$ MHz. Output filter parameters were as follows: $L = 60$ uH, $C = 1$ uF, $m = 0.5$ and the frequency of the input signal (the sinusoidal one) was equal to 1 kHz. The value of the resistor at the output of LPF was set as 4Ω . In Fig. 8, selected waveforms in the simulation model of VCVS are shown, and in Fig. 9, the spectrum of the load voltage is presented.

Investigation results indicate the huge difference in the quality of the VCVS output voltage in favour of the structure DHSDM. The THD of the load voltage (with respect to its 20 harmonics) was equal to 1.5 %, while the latched comparator was used and 0.05 % was the value for the DHSDM.

The following experiments were performed with the VCVS simulation model, based on models of real devices. The diagram of this one is shown in Fig. 10. The most valid functionality elements for the model were AD8042—the 160 MHz

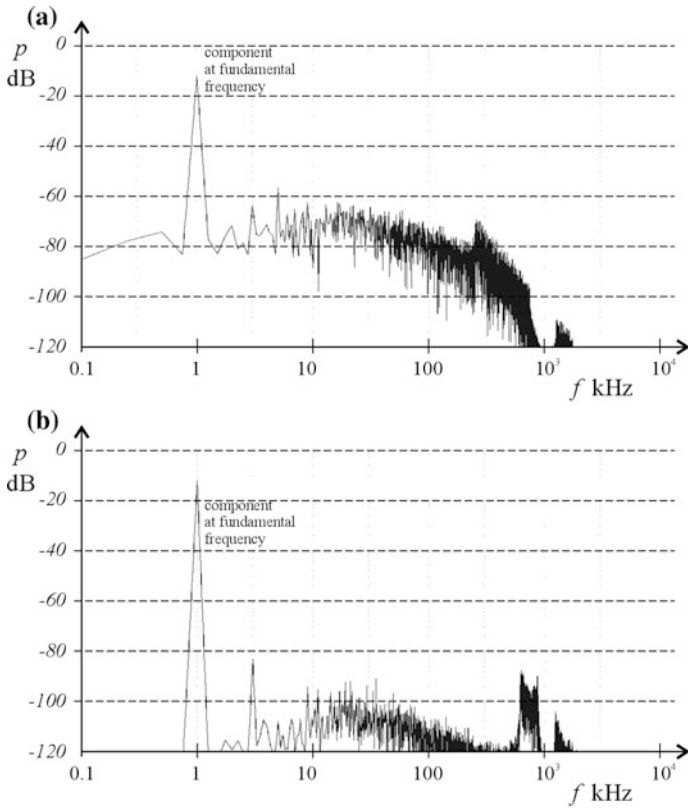


Fig. 9 Spectrum of the load voltage with using **a** the SDM with a latched comparator and **b** the DHSDM

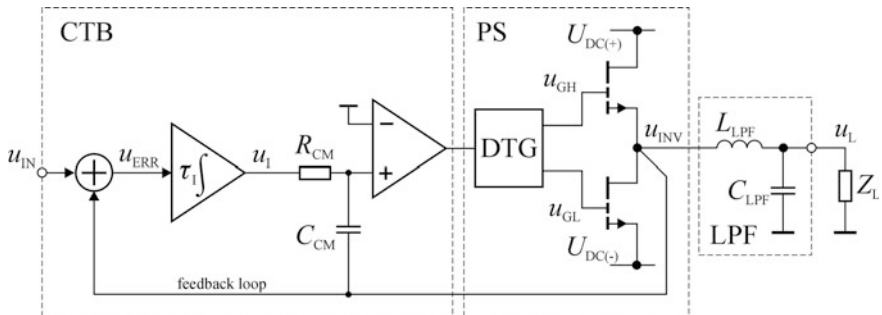


Fig. 10 Arrangement of the VCVS for laboratory tests

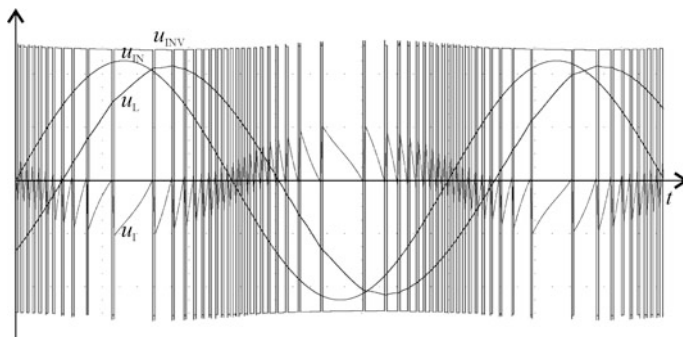


Fig. 11 Waveforms in the VCVS simulation model: modulator input signal, integrator output signal, voltage at the output of the inverter and load voltage

Rail-to-Rail dual operational amplifier (Analog Devices) used in the design of the integrator and comparator, and GS66508P—the 650V/90 A gallium nitride transistor (E-HEMT) [16] (GaN Systems)—used in the power stage of the model. The CTB in Fig. 10 is the control block, while PS is the power stage of the VCVS.

The model parameters were as follows: $\tau_I = 2 \mu\text{s}$, maximum switching frequency of the SDM— $f_C = 2 \text{ MHz}$, dead time for the half-bridge in the power stage—10 ns (dead time was generated in the dedicated DTG block), $L_{\text{LPF}} = 10 \mu\text{H}$, $C_{\text{LPF}} = 1 \mu\text{F}$, $m = 0.1\text{--}0.95$ and the frequency of the input signal (the sinusoidal one)—20 kHz. The voltages of the inverter's DC rails: $\pm 100 \text{ V}$. The value of the resistor at the output of LPF was set at 2Ω , making the inverter's nominal output power equal to 2 kW.

In Fig. 11, selected waveforms in the simulation model of the VCVS are shown, while in Fig. 12, both the THD of the load voltage and the inverter efficiency versus a modulation index are presented.

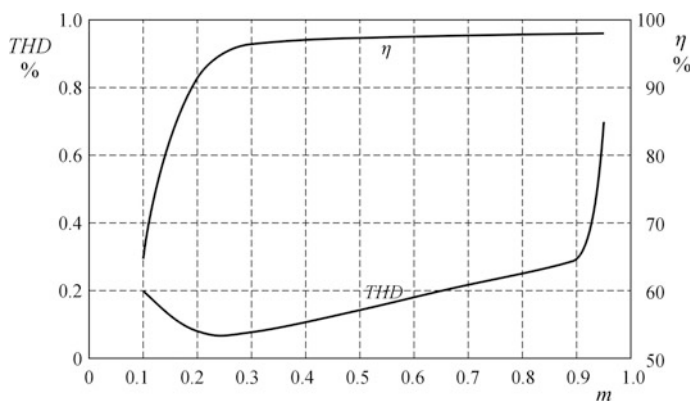


Fig. 12 Calculated curves of the inverter efficiency and THD of the load voltage versus a modulation index

The maximum inverter’s efficiency is equal to 98 %. In the modulation index range of 0.3–0.95, the efficiency curve is very flat, which means that the inverter is highly efficient in the wide range of the output power, i.e., 10–90 % of the nominal one. In the mentioned modulation index range, the THD of the load voltage is lower than 0.3 %. Additional tests—for wide frequency varieties of the input signal—have also been conducted. While this frequency has been lower than 1 kHz, the THD has not exceeded 0.05 %—in a very wide range of m . It points at the high ability of the proposed DHSDM to shape the inverter’s output signal.

4 A Practical Arrangement of the VCVS

For checking theoretical assumptions as well as simulation studies, the laboratory model of the VCVS with DHSDM and GaN transistors was arranged. The diagram of the model output stage is shown in Fig. 13. This diagram does not include a power-supply block.

The main components used in the design are the same as in the VCVS simulation model. For the coupling of the power stage with the control block, isolated precise gate drivers ADuM3123 (Analog Devices) were applied. They obtain both precise timing characteristics of isolator and driver propagation delay (64 ns max.), and a high common-mode transient immunity—over 25 kV/μs. The expected slope time of the inverter’s output voltage is approximately 10 ns. The assumed rated output power of the inverter is equal to 2 kW.

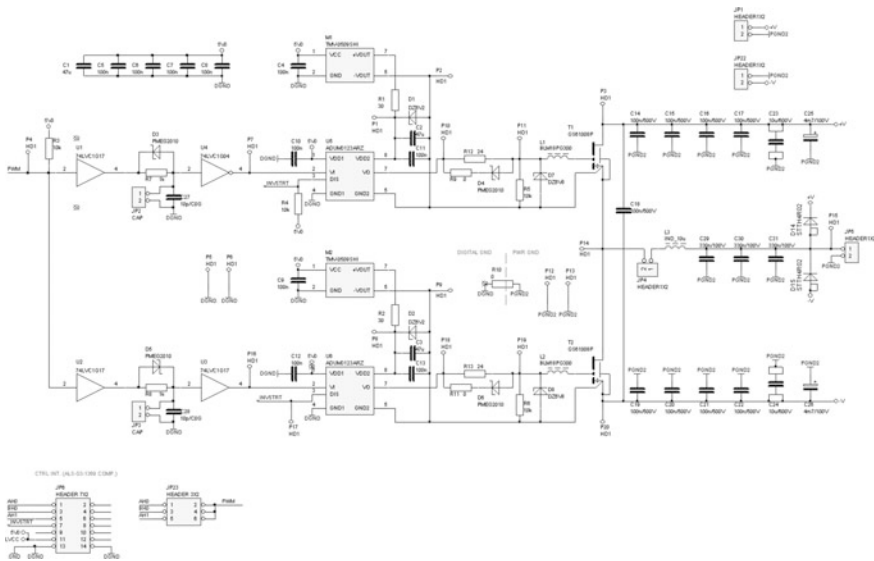


Fig. 13 Diagram of the VCVS power stage for laboratory tests

The laboratory model uses arrangements that, to a certain extent, allow reconfiguration of its structure, as well as chosen power stage properties.

5 Conclusions

Theoretical and simulation studies of the SDM using the dynamic hysteresis comparator have shown crucial advantages of this one when compared to an SDM with a latched comparator. They are characterized by, among other items, theoretically unlimited time resolution of the modulator output signal, as well as simplicity of the SDM—no digital circuitry is implemented in the SDM's structure (as a consequence, perturbations that usually pass from digital tracks to analogue signal paths are limited). Due to the frequency of the output signal being spread across the spectrum, an inverter, in some cases, is able to meet the EMC requirements more easily. The VCVS using the DHSDM provides very good mapping of an output voltage in an input signal; however, it requires confirmation by laboratory tests. Further improvement of the VCVS's features is expected, while this version will be arranged in the fully differential manner.

It seems that the proposed sigma-delta modulator may also find applications in the control circuits of other power electronic equipment, such as active filters, tunable high-power reference current generators and power electronics equipment for renewable energy sources.

References

1. Kester WA et al (2005) The data conversion handbook. Analog Devices Inc, Newnes
2. de la Rosa RM (2011) Sigma-delta modulators: tutorial overview, design guide, and state-of-the-art survey. *IEEE Trans Circuits Syst I: Regul Pap* 58(1):1–21
3. Muthusubramaniam JA, Pavan S (2012) Analysis and design of a high speed continuous time delta sigma modulator using the assisted opamp technique. *IEEE J Solid State Circuits* 47(7):1615–1625
4. Shettigar P, Pavan S (2012) Design techniques for wideband continuous-time delta-sigma modulators with FIR feedback DACs. *IEEE J Solid State Circuits* 47:2865–2879
5. Palmer R (1999) Design considerations for class-D audio power amplifiers. Texas instruments application report (SLOA031)
6. Zhang L et al (2004) Real-time power supply compensation for noise-shaped class D amplifier. In: 117th AES convention, San Francisco, CA
7. Putzeys B (2005) Simple self-oscillating class D amplifier with full output filter control. In: 118th AES convention, Barcelona, Spain
8. Nyboe F et al (2005) Time domain analysis of open-loop distortion in class D amplifier output stages. In: AES 27th international conference, Copenhagen, Denmark
9. Gaalaas E et al (2005) Integrated stereo delta-sigma class D amplifier. *IEEE J Solid-State Circuits* 40(12):2388–2397
10. Tripathi AS et al (1998) Method and apparatus for oversampled, noise-shaping, mixed-signal processing. US Patent 5,777,512. Original Assignee Tripath Technology, Inc

11. Rozanov Y et al (2015) Fundamentals of power electronics: operating principles, design, formulas, and applications. CRC Press, Hardcover, 489 pp. ISBN 97814822987961
12. Sorensen J (2016) Sigma-delta conversion used for motor control. Technical article. In: Analog devices, Inc. <http://www.analog.com/en/products/analog-to-digital-converters/precision-adc-10msps/isolated-ad-converters/ad7405.html#product-reference>. Accessed Jan 2016
13. AD7405: 16-Bit, isolated sigma-delta modulator. In: Analog devices, Inc. Product page <http://www.analog.com/en/products/analog-to-digital-converters/precision-adc-10msps/isolated-ad-converters/ad7405.html#product-overview>. Accessed Jan 2016
14. Gwóźdz M (2011) Stability of discrete time systems on base of generalized sampling expansion. Quarterly "Elektryka". Silesian University of Technology 1(217):29–40
15. Auer M, Karaca T (2016) Spread spectrum techniques for class-D audio amplifiers to reduce EMI. e & i Elektrotechnik und Informationstechnik. Springer, Vienna. ISSN 0932-383X
16. GS66508P, GaN Systems product page. <http://www.gansystems.com/gs66508p.php>. Accessed Jan 2016

FC + TCR-Type Symmetrical Follow-Up Compensator of the Fundamental Harmonic Reactive Power—Analysis and Experiment

Malgorzata Latka

Abstract The chapter presents results of analyses, simulations, and experiments concerning a FC + TCR-type symmetrical follow-up compensator of the fundamental harmonic reactive power in which a three-phase bridge rectifier with two additional thyristors (6T + 2T) was used as the adjustable inductive component. The research pertains to the three-phase 6T + 2T bridge rectifier circuit with the neutral wire led out, where selection and application of the appropriate developed thyristor controlling algorithm (introduction of an additional control angle δ) enables current flow outside supply source phases in those instants of time when output voltages of the star rectifiers have instantaneous negative values. The effect of minimization of rms and the reactive power component of the fundamental harmonic of source currents consists in a reduction of reactive load introduced by 6T + 2T bridge rectifier with respect to 6T bridge with the possibility to control it by choosing an appropriate value of angle δ . To obtain a lower content of harmonics in the power grid current, it has been proposed to couple a 5th and 3rd harmonics filter on the converter. Such a converter, equipped with filters with output terminated with a reactor and stabilizing the direct current value at different values of angle δ , can be used as a FC + TCR-type symmetrical follow-up compensator of reactive power. Regulation of reactive power in such a circuit is instantaneous. The paper ends with a presentation of applications developed in LabVIEW programming environment to visualize the principle of operation, take measurements, and results of laboratory research carried out with the compensator.

Keywords Thyristor bridge rectifier · Reactive power · Filtration · Compensation · Symmetrical follow-up compensator · LabVIEW

M. Latka (✉)

Rzeszow University of Technology, W.Pola 2, 35-959 Rzeszow, Poland
e-mail: mlatka@prz.edu.pl

1 Introduction

Compensation of reactive power in an electric power supply system is an issue of key importance as the reactive power is the cause of, among other things, voltage losses and drops as well as power and energy losses in the system, and first of all, limits the transmission capacity of power supply lines. To compensate slowly-varying receivers, capacitors and/or impedance coils are typically used in the framework of the so-called classic compensation methods. Compensation of fast-varying (turbulent) receivers, such as arc furnaces, electric arc and discharge welding machines, winding engines in mining industry, electric traction etc., requires the use of the so-called follow-up compensators capable to react quickly enough to reactive power changes caused by such receivers. New methods of reactive power compensation and harmonics filtering are still been developed, as are confirmed by the selected literature [1–3].

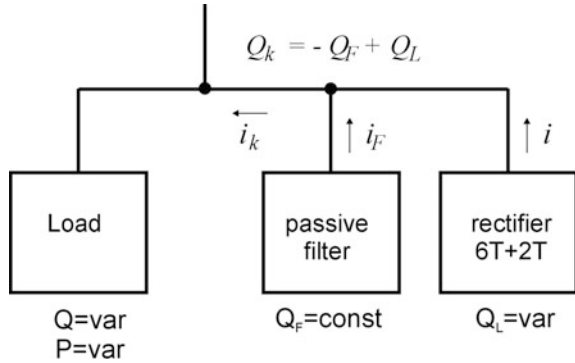
One type of the so-called symmetrical follow-up compensators of the fundamental harmonic reactive power is the reactive power compensator of FC + TCR (Fixed Capacitor + Thyristor Controlled Reactor) type, comprised of a battery of fixed capacitors with properly selected serial reactors and an adjusted induction component of TCR type. Several topologies FC + TCR-type symmetrical follow-up compensator of the fundamental harmonic reactive power have been reported in the literature [4–6].

The present chapter presents results of analyses, simulations, and experiments concerning a FC + TCR-type symmetrical follow-up compensator of the fundamental harmonic reactive power in which, as the adjusted induction element, a three-phase thyristor bridge rectifier with two additional thyristors 6T + 2T was used. Further, the algorithm developed to control a such modified power electronic circuit, which in its classic version (6T bridge) is regarded as a circuit contributing to an increase of reactive power in the system, will be discussed in detail. By upgrading its structure to a 6T + 2T circuit and implementing a specifically developed algorithm, it becomes possible to use it as a component of devices reducing reactive power in electric power supply systems contributing this way to an improvement of electric power quality.

Figure 1 shows a block diagram of a FC + TCR-type symmetrical follow-up reactive power compensator illustrating the principle of compensation. As an adjusted inductive element, three-phase 6T + 2T bridge rectifier was used which it controlled according to specified algorithm, whereas as a capacitive element with constant power, passive LC filter was used to eliminate higher harmonics.

Such a compensator is realized by connecting in parallel a filter of higher harmonics with constant capacitive reactive power Q_F determined in the design development stage and a 6T + 2T bridge rectifier loaded with reactor L_d functioning at a constant average value of load current I_d stabilized in a closed control system, taking up from the supply line an amount of controlled inductive reactive power denoted as Q_L . Then, the compensator supplies to the power supply line a

Fig. 1 A block diagram of FC + TCR type compensator



resultant reactive power Q_k which is the difference between the inductive reactive power and the capacitive reactive power:

$$Q_k = -Q_F + Q_L. \tag{1}$$

Among the merits of a compensating circuit of that type, one should mention the possibility to introduce automated, steady, and immediate control of reactive power output to the supply grid.

2 Thyristor Bridge Rectifier with Two Additional Thyristors (6T + 2T) as an Adjustable Component of an Inductive-Type Compensator

Each modification of either the topology of or the method used to control a rectifier circuit results in a change of its properties and opens a possibility of new applications. Nowadays any change in topology poses neither a technical nor economical problem, and progress in microprocessor technology allows for the realization in practice almost any thyristor controlling algorithm, no matter how complex. This stimulates development of new ideas concerning changes in structure and control algorithms of known and widely used rectifying circuits and new fields for their application.

An example of a modification of the classical bridge rectifier 6T, in scope of both structure and control algorithm, is a three-phase thyristor bridge rectifier with two additional thyristors 6T + 2T with reduced and controlled reactive load. Figure 2 shows a diagram of the resulting 6T + 2T circuit, while Fig. 3 explains the proposed control algorithm in an example of a single pulse of rectified voltage.

The way in which a single output voltage pulse is originated together with the conduction cycle length for individual thyristor T1 is shown for the main thyristors

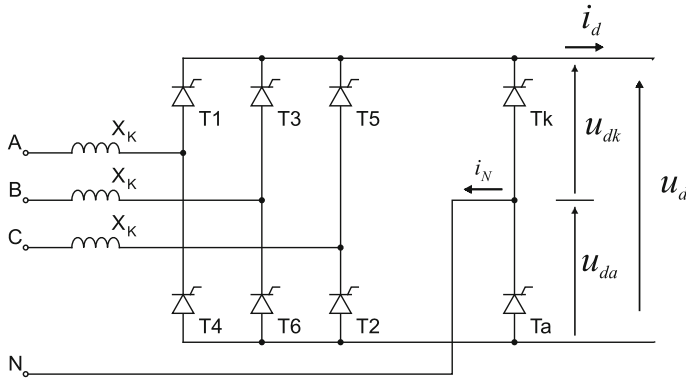


Fig. 2 Schematic diagram of a three-phase thyristor bridge rectifier with two additional auxiliary thyristors 6T + 2T

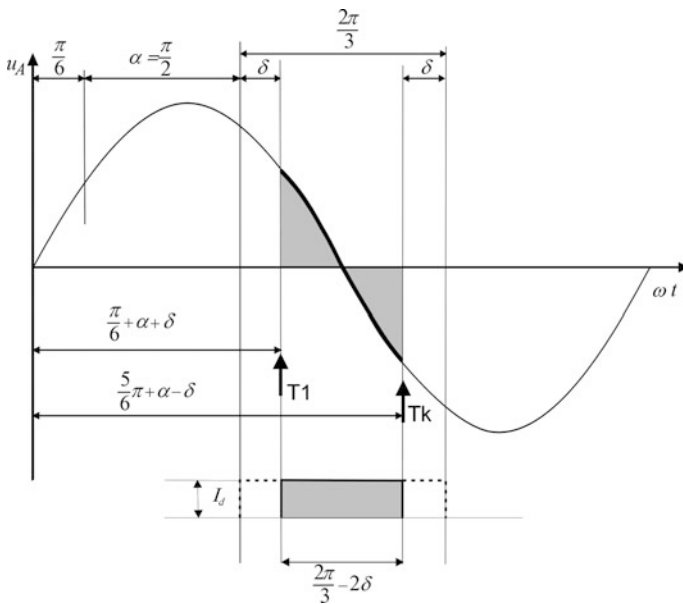


Fig. 3 Illustration of an occurrence of a single cathode star output voltage pulse in a 6T + 2T circuit together with conduction cycle length of an individual thyristor T1 for the main thyristors firing delay angle $\alpha = \pi/2$, arbitrary angle δ , $L_d \rightarrow \infty$, and $L_k = 0$

firing delay angle $\alpha = \pi/2$, at continuous and constant load current I_d ($L_d \rightarrow \infty$) and with commutation in the circuit neglected ($L_k = 0$).

Additional thyristors Tk and Ta added to a 6T circuit in the way shown in Fig. 2 can be fired in instants when output voltages of corresponding star rectifiers are instantaneously negative. Such conditions exist when the main thyristors are fired

with an appropriate thyristor firing delay angle α , i.e. $\alpha > \pi/6$ and at the same time $\alpha \leq \pi/2$, with maintained rectifying mode of operation of the circuit at continuous load current. For angles $0^\circ \leq \alpha \leq \pi/6$, the 6T + 2T circuit behaves as a classic 6T bridge rectifier, as auxiliary thyristors cannot participate in conduction of load current, whereas for angles $\alpha > \pi/2$, at continuous load current, it is absolutely necessary to block pulses firing additional thyristors, as operation of the 6T + 2T circuit in inverter mode is no longer possible. [7–10].

While in a classical 6T bridge rectifier (with $L_k = 0$ and $L_d \rightarrow \infty$), each of the six thyristors conducts for a period of time corresponding to angle $2\pi/3$ and each thyristor is fired at angle α , an angle δ is introduced in the proposed control algorithm, the value of which has an effect on the instant of time on which the additional thyristor is fired. Firing the additional thyristor results, on one hand, in narrowing of the main thyristor conduction cycle, and on the other, taking angle δ into account in firing main thyristors by adding it to angle α results in narrowing of the main thyristor conduction cycle respectively on the other side, to the conduction cycle length equaling in total $2\pi/3 - 2\delta$. Each of the additional thyristors conducts the receiver current for a 2δ -long time interval, 3 times per full cycle.

It is possible to fire the additional thyristor Tk once the condition $5\pi/6 + \alpha - \delta \geq \pi$ is met and at the same time $\alpha > \pi/6$, as at that particular time, the instantaneous value of the load current conducting phase is negative. Algebraic transformation of the conditions leads to the following relationships:

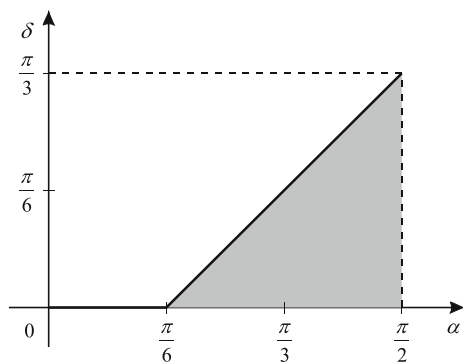
$$\delta \leq \alpha - \frac{\pi}{6} \quad \text{and} \quad \frac{\pi}{6} < \alpha < \frac{\pi}{2}, \tag{2}$$

which determine the dependence of angle δ on angle α presented in Fig. 4. Angle δ may assume values from the shaded area.

A complete diagram of conduction cycles (functions of state) for all thyristors in the 6T + 2T circuit at continuous load current and the commutation effect neglected, for $\alpha = \pi/2$ and selected values of δ is presented in Fig. 5.

As a result of introducing additional thyristors and application of the proposed algorithm to control thyristors in the 6T + 2T circuit with the thyristors' firing time

Fig. 4 A plot of angle δ versus angle α



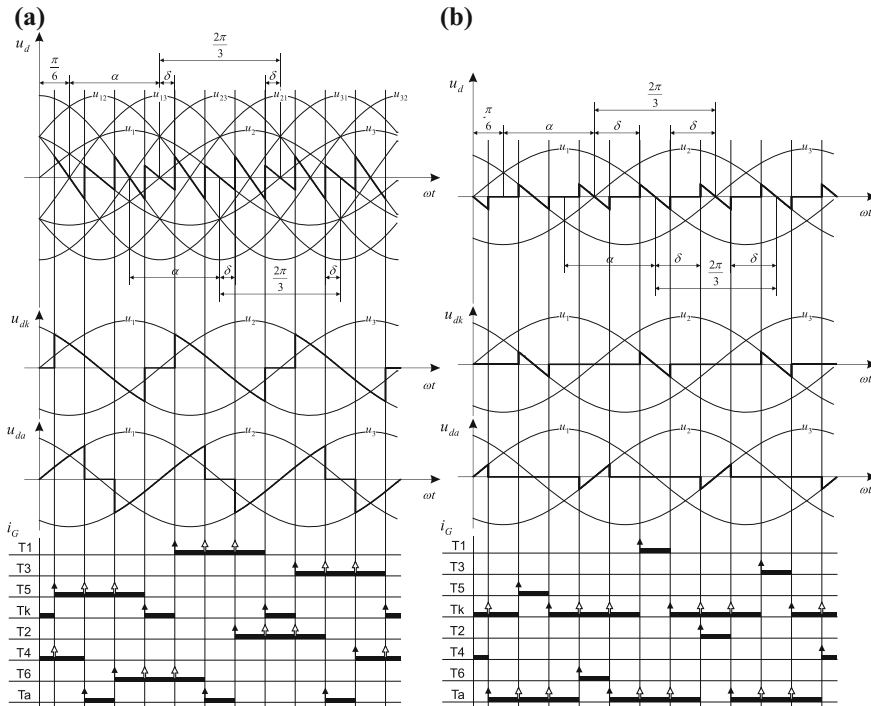


Fig. 5 Waveforms of rectified voltage u_d , star rectifier output voltages u_{dk} and u_{da} , firing pulses i_G , and thyristor conduction cycles in 6T + 2T circuit for **a** $\alpha \approx \pi/2$ and $\delta = \pi/12$, **b** $\alpha \approx \pi/2$ and $\delta = \pi/4$

depending on the value of angle α and additionally on value of angle δ introduced for the purpose of making changes in the control algorithm, the load current flow occurs outside the supply source phases which results in narrowing the source phase current pulses and thus reduces their rms as well as values of reactive power of the fundamental harmonic.

The effect of minimizing of the values of currents flowing through the powers supply grid is a reduction of the reactive load introduced by 6T + 2T bridge rectifier with respect to classic 6T bridge circuit, with an option of controlling it by means of proper selection of angles α and δ determining thyristor firing times. Reactive power of the 6T + 2T bridge rectifier for the fundamental harmonic (phase shift reactive power) can be expressed as:

$$Q_1 = \sqrt{3}U_p I_1 \sin \varphi = U_{d0} I_d \frac{2}{\sqrt{3}} \sin\left(\frac{\pi}{3} - \delta\right) \sin \alpha, \tag{3}$$

where Q_1 is the fundamental harmonic reactive power; U_p —rms value of the supplying source’s inter-phase voltage; I_1 —rms of source phase current fundamental harmonic; I_d —receiver current average value; $Q_{d0} = \frac{3\sqrt{2}}{\pi} U_p$ —average output voltage of 6T-type three-phase thyristor bridge rectifier at $\alpha = 0$.

Some algebra leads to:

$$\frac{Q_1}{U_{d0} I_d} = \sqrt{\frac{2}{\sqrt{3}} \frac{U_d}{U_{d0}} - \left(\frac{U_d}{U_{d0}}\right)^2}, \tag{4}$$

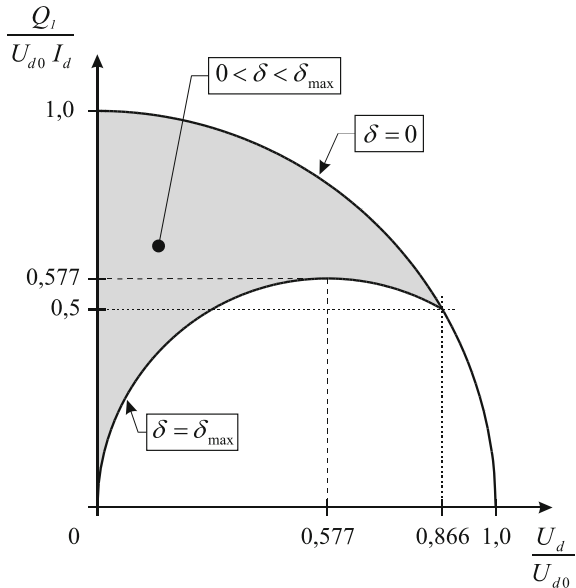
$$U_d = U_{d0} \frac{2}{\sqrt{3}} \cos\left(\alpha - \frac{\delta}{2}\right) \cdot \sin\left(\frac{\pi}{3} - \frac{\delta}{2}\right), \tag{5}$$

U_d is the average voltage value of rectified receiver.

Based on (4) and (5), a plot was drawn showing the relative value of 6T + 2T rectifier fundamental harmonic reactive power as a function of the relative average value of the rectified voltage for the two extreme values of angle $\delta = 0$ and $\delta = \delta_{\max} = \pi/3$. For angles from the interval $0 < \delta < \pi/3$, the obtainable reactive power values are depicted in Fig. 6 by shading the corresponding area.

By modifying both the structure of and the control algorithm for the classic bridge rectifier 6T, it is possible to upgrade it to a one-way controlled three-phase 6T + 2T bridge rectifier with reduced and adjustable reactive load. This creates the possibility to use the circuit as a fast-reacting inductive element in a symmetrical follow-up reactive power compensator.

Fig. 6 Relative value of reactive power vs. relative value of output voltage for 6T + 2T circuit



3 The Commutation Effect in the 6T + 2T Bridge Rectifier Circuit and Its Impact on the Control Algorithm, Restrictions and Control Interval of the Reactive Load Introduced by 6T + 2T Circuit

In an analysis of the 6T + 2T bridge rectifier presented earlier in this chapter, certain simplifying assumptions were adopted allowing up to pass over the commutation effect.

However, due to the occurrence of commutation reactance X_k , the relationships and waveforms shown in Figs. 3, 4, 5 and 6 take the form shown in Figs. 7, 8, 9

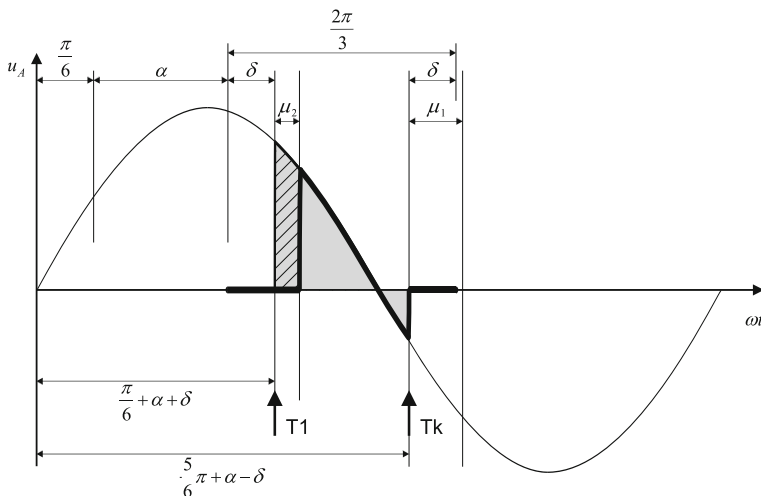
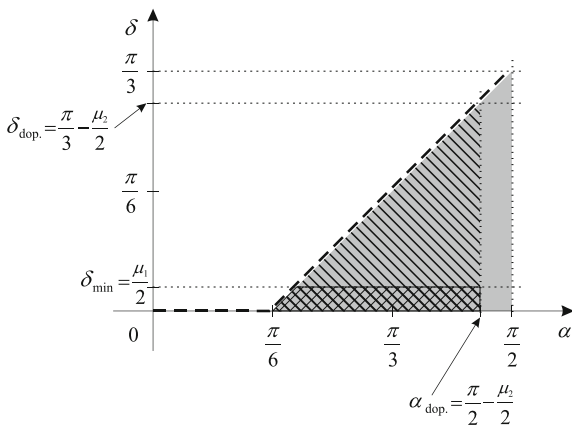


Fig. 7 Waveform of a single continuously repeated output voltage pulse together with commutation points marked for cathode star in 6T + 2T circuit when $X_k \neq 0$

Fig. 8 Graphical interpretation of δ versus α relationship and limits for both angles resulting from commutation effect



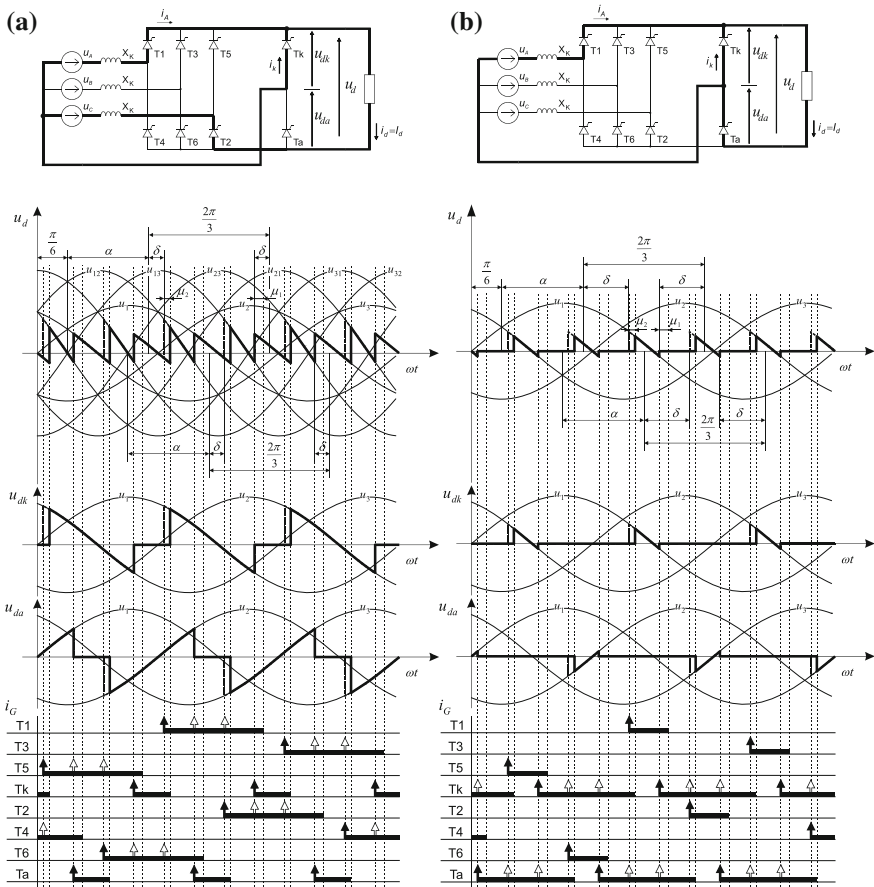


Fig. 9 Schematic diagrams and waveforms of output voltage u_d , star rectifier output voltages u_{dk} and u_{da} , and firing pulses i_G collated with conduction cycles of thyristors in 6T + 2T circuit for **a** arbitrary angle α and angles $\delta < \pi/3$ with commutation processes taken into account; **b** arbitrary angle α and angles $\delta > \pi/3$ with commutation processes taken into account

and 10, respectively. The form of a single, periodically repeated output voltage pulse, with the commutation processes taken into account and with marked commutation angles for the cathode star in three-phase 6T + 2T bridge rectifier, is shown in Fig. 7. The dashed area shows the change of a single pulse shape with respect to the circuit with instantaneous commutation, whereas two types of commutation occur in the 6T + 2T rectifier circuit:

- commutation of the load current from 6T + 2T rectifier’s main thyristor onto an additional thyristor—commutation angle μ_1 ,
- commutation of the load current from an additional thyristor onto the main thyristor—commutation angle μ_2 .

Within one full working cycle equalling the period of voltage supplying $6T + 2T$ bridge rectifier, twelve commutations occur, six for each of the stars. Each commutation is followed by the conduction state of an individual switch which means that the rectifier's circuit operates in a total of 24 of different configurations.

Taking the commutation effect into account it is also necessary to impose a restriction on the thyristor firing delay angle α and angle δ following from the necessity to maintain the rectifying nature of the circuit's operation so that $U_d \geq 0$. Ranges of changes for angles α and δ , after taking into account the commutation effect in the $6T + 2T$ circuit, are as follows:

- angle α change range: $\frac{\pi}{6} \leq \alpha \leq \frac{\pi}{2} - \frac{\mu_2}{2}$,
- angle δ change range: $0 \leq \delta \leq \frac{\pi}{3} - \frac{\mu_2}{2}$,

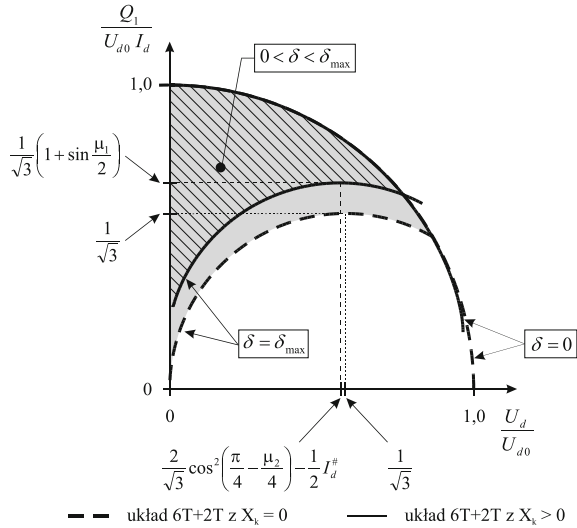
under condition $\delta \leq \alpha - \pi/6$, the same as for the circuit in which the commutation effect is neglected. Graphically, the angle ranges are depicted in Fig. 8 by hatching the corresponding area from Fig. 4, whereas additionally, the area below line δ_{\min} corresponding to the complex commutation occurring in the circuit is dashed with double diagonal lines. The type of commutation (simple or complex) has no effect on the operation of the $6T + 2T$ circuit.

Figure 9a, b show two example diagrams of the $6T + 2T$ circuit with configurations arising in the course of commutation for a specific angle α and two different angles δ and example voltage and current waveforms, as well as the method of controlling main thyristors T1, T2, T3, T4, T5, T6 and additional thyristors Tk and Ta in the discussed $6T + 2T$ bridge rectifier and full diagram of conduction cycles for all thyristors, for a determined angle α and two different angles δ with commutation between the thyristors taken into account. The change with respect to the $6T + 2T$ circuit without commutation consists in different lengths of individual thyristors' conduction cycles. Each of the main thyristors conduct for a period of time corresponding to angle $2\pi/3 - 2\delta + \mu_1$, while each of the additional thyristors—for interval $2\delta + \mu_2$ three times per one working cycle.

The circle diagram of the $6T + 2T$ bridge rectifier fundamental harmonic power with the commutation effect not taken into account presented above in Fig. 6, after analysis carried out with commutation in the circuit taken into account, has been supplemented with corresponding curves and shown in Fig. 10. Dashed lines represent the relationships describing the relative value of the reactive power as a function of the relative value of the voltage rectified in the $6T + 2T$ circuit with commutation neglected, whereas solid lines represent the corresponding relationships for $6T + 2T$ with the effect taken into account. The shaded area in Fig. 10 represents the reactive power change range possible to obtain in the $6T + 2T$ circuit without taking into account the commutation effect, whereas the additionally dashed portion of the shaded area depicts the region of possible reactive power changes in the circuit with commutation taken into account.

The commutation processes result in different restrictions and different intervals available for regulation of reactive load (of inductive nature) introduced by the $6T + 2T$ rectifier, which is possible within a range narrower than this following

Fig. 10 Relative reactive power vs. relative value of rectified voltage for 6T + 2T bridge circuit with the commutation taken into account and neglected



from simplified analysis, the a fact to be unconditionally taken into account in the design of the actual circuit.

4 Passive Filter of Current Higher Harmonics as a Non-adjustable Element of a Symmetrical Capacitive Compensator

It follows from the analysis of the properties of the three-phase 6T + 2T bridge rectifier carrying a continuous and constant load current that reduction of the reactive power introduced by the proposed circuit occurs at the expense of a slight increase in the content of the higher harmonics in phase currents of the source supplying the 6T + 2T rectifier. Amplitudes of individual grid current harmonics in the 6T + 2T rectifier have values larger than those in classic 6T bridge rectifier and additionally, harmonics which are absent in the 6T rectifier, i.e. the 3rd harmonic and its odd multiples, arise in this current. The 3rd harmonic and its odd multiples occur also in current i_N of the 6T + 2T circuit's neutral wire.

That means there is the necessity to filter out these harmonics by means of passive LC filters. This is typically accomplished by connecting a serial LC circuit parallel resonance frequency which is close to that of the unwanted harmonic in parallel with the load generating such a harmonic [11].

To eliminate and suppress harmonics in source phase currents and enable supplying the 6T + 2T rectifier from the transformer's secondary windings without access to the neutral point, the analyzed 6T + 2T rectifier was fitted not only with a passive filter of 5th harmonics used typically in case of the 6T rectifier, but an

additional reactor was connected between the star point of the 5th harmonic filter and the common point of additional thyristors tuning the filter to the 3rd harmonic. The 6T + 2T bridge rectifier with a 3rd and 5th harmonics filter coupled on does not require connection with the neutral wire and at the same time relieves the voltage source (the rectifier's transformer) from the 5th harmonic as well as the 3rd harmonic with all its multiples of the order $3(2n + 1)$.

Moreover, the permanent battery of capacitors being a component of the filter plays the role of the element of compensator with constant value of capacitive reactive power, whereas the reactive power of the higher harmonics filter is larger than the power of the directly connected battery of capacitors in the filter.

Parameters of the filter are selected in the circuit design stage based on forecasted or measured maximum amplitude of the current higher harmonics in the filter's load and with the maximum value of inductive reactive power generated by the inductive element taken into account [11].

Parameters of the 3rd and 5th harmonics filter coupled on to the 6T + 2T circuit were determine based on relationships:

$$X_{L3} = \frac{v_5^2 - v_3^2}{3v_3^2(v_5^2 - 1)} \frac{U_p^2}{Q_{1F}}, \quad (6)$$

$$X_{L5} = \frac{1}{v_5^2 - 1} \frac{U_p^2}{Q_{1F}}, \quad (7)$$

$$X_{C5} = \frac{v_5^2}{v_5^2 - 1} \frac{U_p^2}{Q_{1F}}, \quad (8)$$

where Q_{1F} —filter passive power for the fundamental harmonic, v_3 , v_5 —relative free-running frequency for 3rd and 5th harmonic, respectively [11].

5 Symmetrical Follow-Up Compensator of the Fundamental Harmonic Reactive Power

A diagram of a closed current regulation system for the 6T + 2T bridge rectifier with passive 3rd and 5th harmonics filter coupled on it, operating as a symmetrical follow-up compensator of fundamental harmonic reactive power is presented in Fig. 11.

The 6T + 2T rectifier, supplied from transformer Dy, is loaded with reactor L_d with very small resistance which forces operation of the circuit at the thyristor firing angle $\alpha \approx \pi/2$, or $U_d \approx 0$. The control system comprises a current regulator the role of which is to stabilize receiver current on a predetermined average value, and generators of gate pulses used to fire the rectifier's thyristors according to proposed algorithm under the control of the pulse synchronization and delay system.

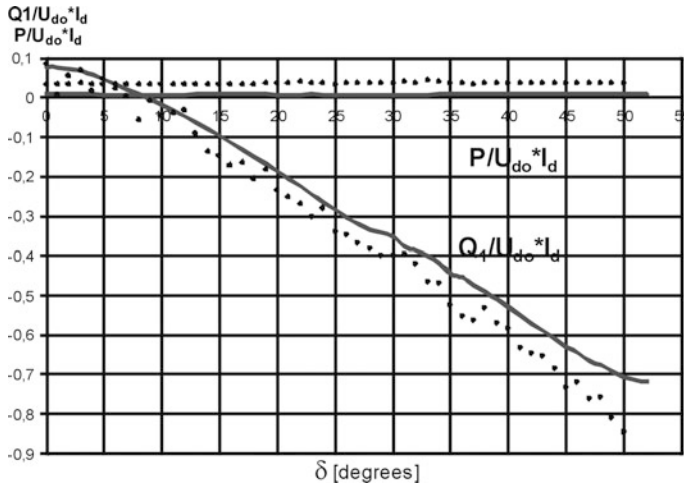


Fig. 12 A comparison of active and reactive power values obtained from simulations and measurements in the 6T + 2T circuit with a passive filter operating as FC + TCR compensator (line symulation results, dot results of measurements)

regulator controlling algorithm may be subject to changes; in this case, the change will involve replacement of the program in one microcomputer only. The current regulator determines angle α based on the measured output current value, predetermined value of the current, and predetermined value of angle δ (as a parameter). Both angles, α and δ , are set on current regulator outputs. Based on these values, the pulse generator produces pulses firing individual thyristors according to the developed algorithm.

Selected results of the measurements, collated with simulation results, as well as oscillograms of voltage and current waveforms in the laboratory 6T + 2T circuit with 3rd and 5th harmonics filter are presented in Figs. 12 and 13.

The experimental portion of the study was carried out by means of the measuring instruments allowing to enabling the correct measurement of distorted waveforms: YOKOGAWA WT1600 power meter and a computer-based measuring system developed in the LabVIEW environment. The use of a computer-based measuring system comprised of a PC-class computer, PCI-6023E measuring card by National Instruments, and LabVIEW software, allowed us to take the measurements automatically and to analyze, visualize, and archive the obtained results.

The following parameters were adopted for the model of the 6T + 2T rectifier with 3rd and 5th harmonics filter (used in both simulations and measuring system):

$U_f = 133 \text{ V}$	$C_5 = 331 \text{ }\mu\text{F}$	$L_d = 20 \text{ mH}$
$L_k \approx 735 \text{ }\mu\text{H}$	$L_5 = 1.275 \text{ mH}$	$R_d = 60 \text{ m}\Omega$
	$L_3 = 0.788 \text{ mH}$	$I_d = 20 \text{ A}$

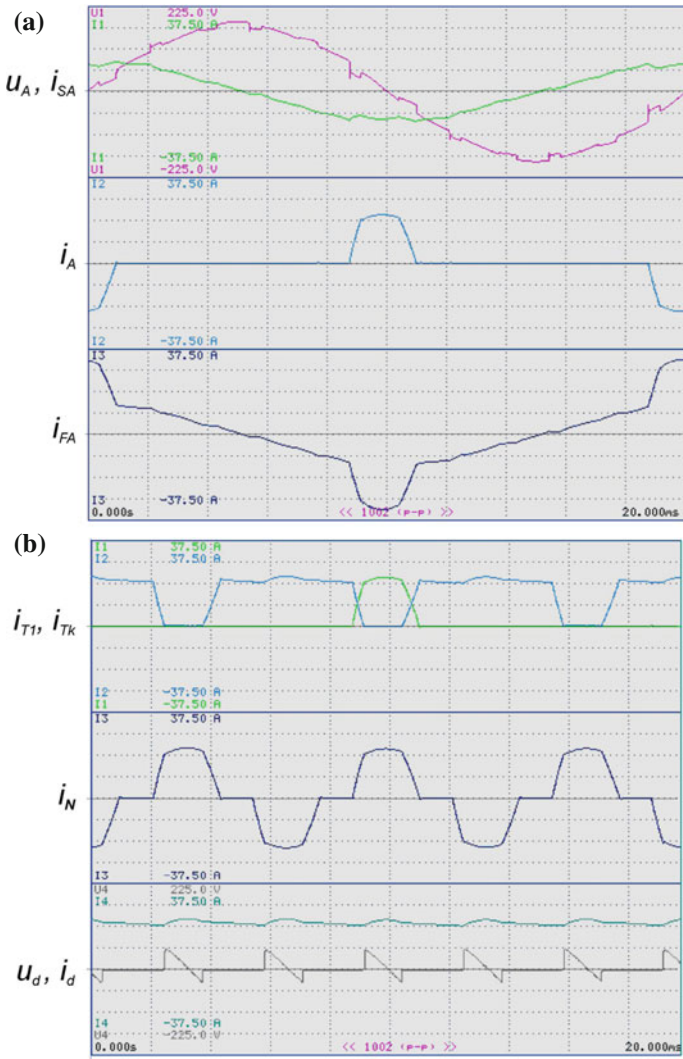


Fig. 13 Example of oscillograms of voltage and current waveforms recorded in the laboratory 6T + 2T circuit with 3rd and 5th harmonics filter for angle $\delta = \pi/2$ operating as FC + TCR compensator

The graph in Fig. 12 contains plots representing the change of the fundamental harmonic reactive power relative value as a function of angle δ . The lines represent the results of simulation and are collated with the results of measurements (dots)

taken on the actual 6T + 2T circuit provided with a filter. The obtained results confirm the possibility to control reactive power in the analyzed 6T + 2T circuit with filter, with the possibility to change the nature of reactive power—from inductive for small angles δ to capacitive with increasing values of the angle. On the other hand, Fig. 13 shows oscillograms of voltage and current waveforms recorded for selected angle $\delta = \pi/2$ in the measuring system for 6T + 2T with a filter of harmonics.

Results from the performed simulations and measurements taken on the laboratory 6T + 2T circuit with the 3rd and 5th harmonics filter confirmed the possibility of using the circuit as a FC + TCR-type symmetrical follow-up compensator of the fundamental harmonic reactive power.

6 Visualization of Selected Measurement Results in the 6T + 2T Circuit with a Passive Filter

The LabVIEW integrated programming environment allows one to design and construct the so-called virtual instruments which accomplish the typical tasks for control-measurement systems used to test power electronic circuits. Equipping a laboratory setup with such virtual instrument offers the possibility to observe and control the operation of an actual power electronic circuit and take measurements of selected quantities. Properly designed windows of the program function as oscilloscopes and meters allowing to observe results of measurements of different quantities taken at selected points at the same time. The so-called virtual instruments developed in LabVIEW for the purpose of laboratory examination of the analyzed FC + TCR represent reflections of actual measuring instruments allowing to acquire, analyze, archive, and interactively present the results of experiments.

The laboratory setup has been designed and constructed comprehensively, which means that in the LabVIEW environment, apart from the laboratory 6T + 2T converter circuit with control and measurement instrumentation, an application has also been developed for the purpose of visualization of the principle of operation of both the 6T + 2T rectifier and the compensator based on it.

Selected measurement results visualized in the LabVIEW environment are shown in Fig. 14, with selected measuring points marked on the schematic diagram of the FC + TCR compensator measuring circuit. The program controls, in the form of windows of the virtual oscilloscope positioned at appropriate points, allow to keep track of several selected waveforms at the same time.

In view of the wide range of executed measurement tasks, the obtained results have been sorted and grouped on separate fields of the program's tabs whose labels describe the type of results presented on them. Figures 15, 16, 17 and 18 show example tabs with controls used to visualize voltage and current waveforms, numerical fields showing average and rms values, selected operating parameters, and the spectrum of harmonics. These example tabs include: input waveforms,

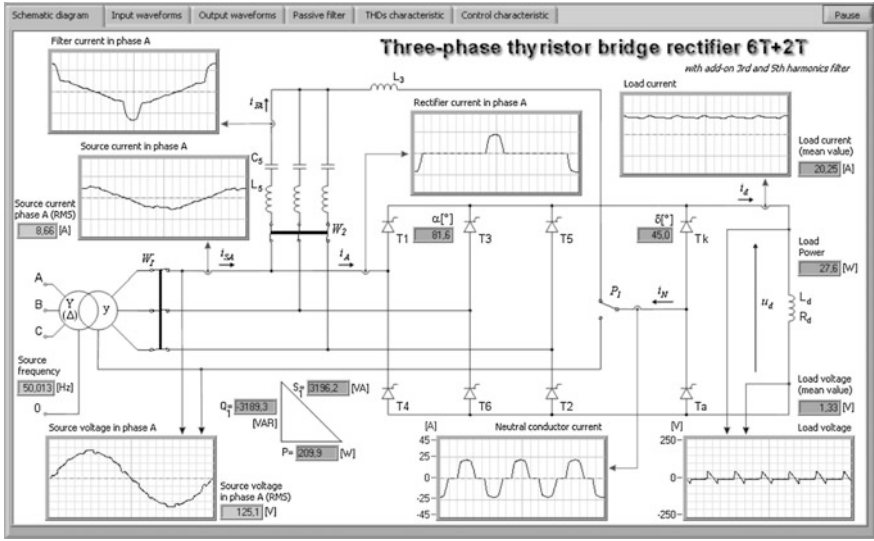


Fig. 14 LabVIEW visualization of the closed measuring setup for the 6T + 2T bridge rectifier with passive 3rd and 5th harmonics filter stabilizing receiver current, operating as a symmetrical follow-up FC + TCR-type reactive power compensator

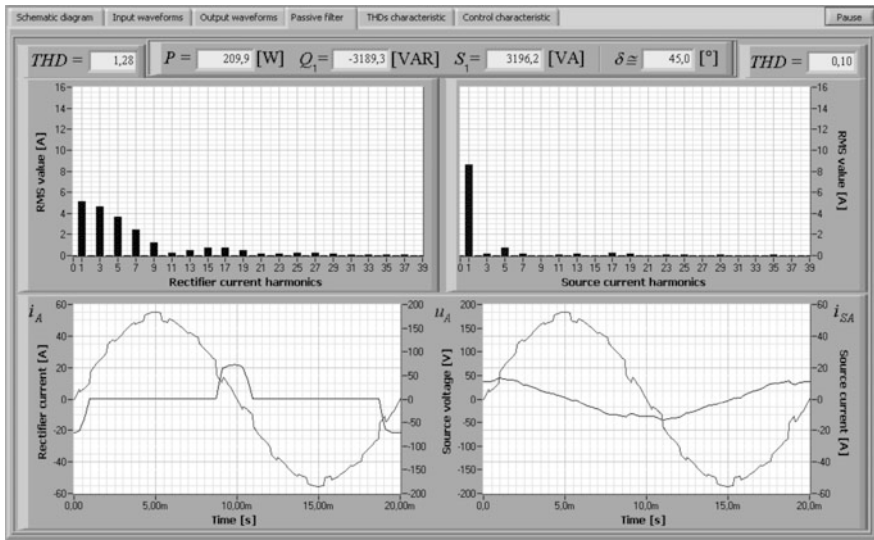


Fig. 15 Results of measurements obtained with the use of LabVIEW program in the laboratory 6T + 2T circuit with 3rd and 5th harmonics filter—waveforms of converter current (left panel) and source current (transformer’s secondary side, left panel) in phase A related to the transformer’s secondary side phase voltage together with spectra of harmonics of these currents

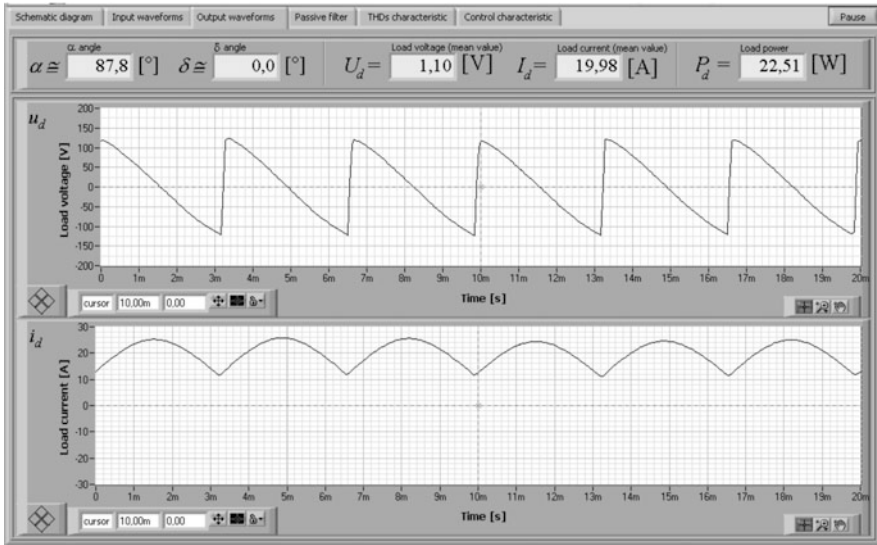


Fig. 16 Results of measurements obtained with the use of LabVIEW program in the laboratory 6T + 2T circuit with 3rd and 5th harmonics filter—voltage and current waveforms and values on the receiver side in the 6T + 2T circuit

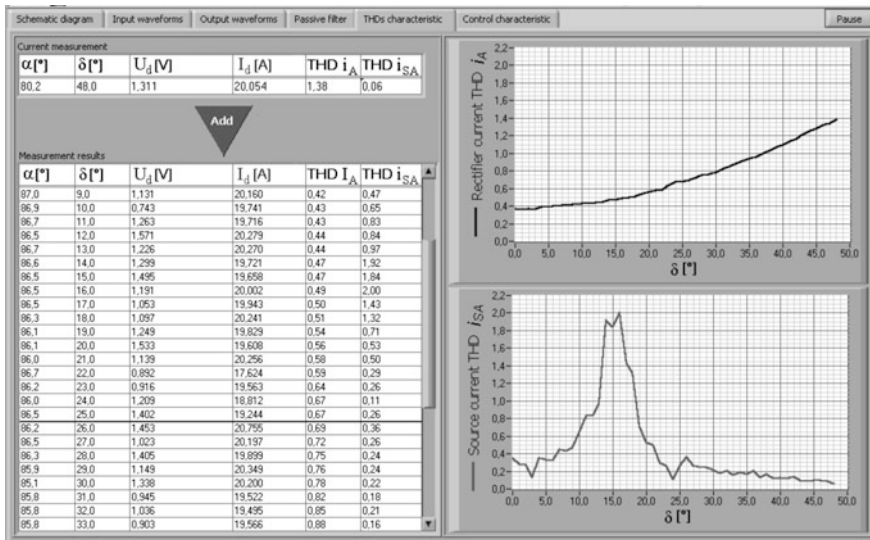


Fig. 17 Table summarizing the results of measurements and widows with THD characteristics of 6T + 2T converter current (upper panel) and source current (lower panel) as functions of angle δ

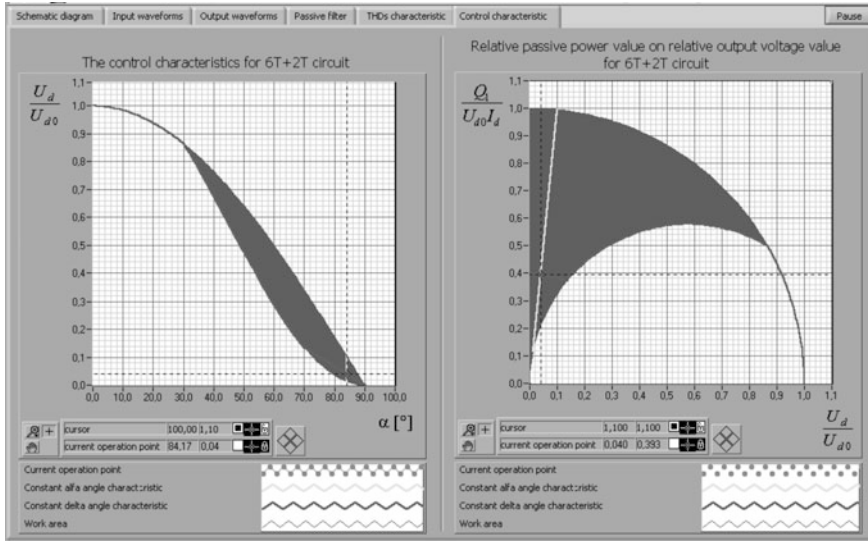


Fig. 18 Presentation of the current operating point against characteristics obtained from theoretical analysis—the control characteristic and relative reactive power versus relative output voltage for the 6T + 2T circuit

output waveforms, passive filter (the tab shows the effect of connecting a passive filter to the circuit), selected characteristics, and the presentation of the selected operating point against selected characteristics.

Features selected for presentation (Fig. 15) include waveforms of: i_A , the converter current in phase A, and i_{SA} , phase A current of the source (transformer’s secondary side), both related to phase voltage on the transformer secondary side u_A , together with the spectra of harmonics contained in the currents. Collation of the harmonic contents illustrates the function of the passive filter employed in the 6T + 2T circuit. Application of passive filters in the 6T + 2T circuit reduces the content of harmonics in the source current supplying the analyzed rectifier as can be seen by comparing the spectra of harmonics before and after integration of the filter. Adding the 3rd and 5th harmonics filter not only eliminated the 5th harmonic and the 3rd harmonic with its odd multiples, but also contributed to a significant decrease of other harmonics rms values. The waveform of the source current i_{SA} reflects its capacitive nature and lends credence to the plausibility of using 6T + 2T with a passive filter as a symmetrical follow-up reactive power compensator.

Figure 16 presents selected voltage and current waveforms and values on the receiver side of the 6T + 2T circuit.

Figure 17 shows a tab allowing to get on-line plots of characteristics in the course of taking the measurements. The measuring program offers also the option of presenting the measured values against the results obtained from theoretical analysis. Figure 18 shows the control characteristic and the plot of relative reactive power vs. relative output voltage for the 6T + 2T circuit, obtained from theoretical

analysis of the examined circuit. On the background of the curves determined this way, it is possible to mark the current circuit's operating point established on the grounds of on-line acquired measurement results.

7 Reactive Power Compensation System

Industrial systems operate numerous devices characterized with high and variable reactive load which makes it necessary to compensate the reactive power in a sufficiently flexible and effective manner. Connecting a FC + TCR-type symmetrical follow-up reactive power compensator based on the 6T + 2T bridge rectifier in parallel to variable load(s) of an inductive nature offers the possibility to develop a compensation system, the structure of which is presented in Fig. 19.

The objective of a compensator with a 6T + 2T rectifier is to generate an appropriate quantity of capacitive reactive power depending on both angle α and angle δ in such a way that the reactive power balance of the grid current fundamental harmonic at a selected point equals a preset value (allowing to the maintenance of required reactive power value).

In the presented compensating circuit, the regulation process occurs as follows: from the preset reactor current value, the measured value of the current is subtracted, and the obtained difference, as an error signal, is used by the PI controller to determine the value of angle α . Similarly, based on the measured value of the grid current reactive component at a determined point, the value of angle δ resulting from the current demand for capacitive reactive power is established. Based on the

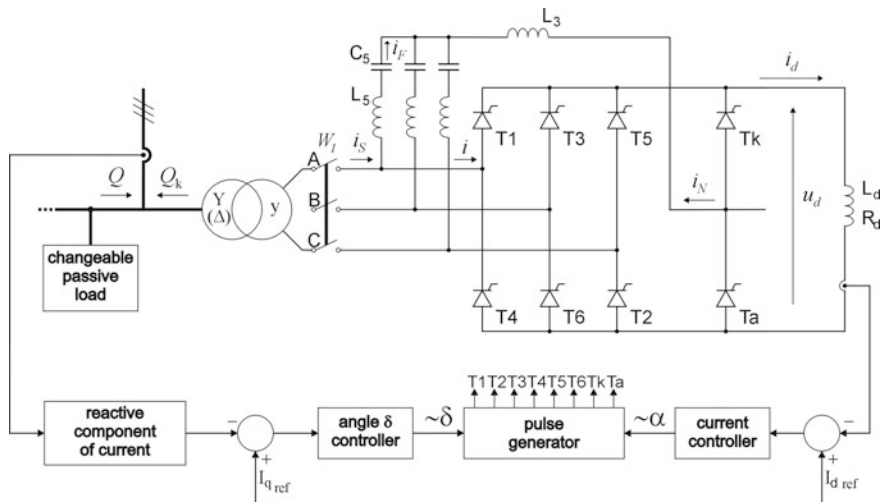


Fig. 19 Structure of the fundamental harmonic reactive power compensation circuit with the use of a symmetrical follow-up reactive power compensator based on the 6T + 2T bridge rectifier

values of angles α and δ obtained from the controllers, the pulse generator produces pulse firing all the thyristors according to an adopted algorithm. A compensation circuit of that type enables automated and immediate control of reactive power.

8 Conclusions

By supplementing a 6T circuit with two additional thyristors as shown in Fig. 2 and controlling properly all the thyristors in the 6T + 2T circuit created this way, it becomes possible to control the reactive power related to the fundamental harmonic by means of the proper selection of values for angles α and δ . Such modification of classic the bridge rectifier 6T leads to realization of a controlled three-phase bridge rectifier with reduced and controlled inductive reactive load.

The 3rd and 5th harmonics filter in 6T + 2T circuit, apart from removing these high-frequency current components and eliminating the neutral wire, plays also the role of a capacitive compensator with constant capacitive reactive power value and together with the circuit (with controlled inductive reactive power) and thus allows enabling a symmetrical follow-up compensator of the fundamental harmonic reactive power of FC + TCR type.

The results obtained from the theoretical analysis and simulations, and above all, from the measurements taken in the laboratory setup, confirm fully the possibility of modifying the classic thyristor rectifier, in scope of both its structure and the method of controlling thyristors in the circuit, for the purpose of reducing the reactive power related to the source current fundamental harmonic. Laboratory tests performed in a closed regulation system with stabilization of the receiver current of the 6T + 2T rectifier with a filter coupled on it and output terminated with a reactor, confirmed also the possibility of using it as a symmetrical follow-up compensator of the fundamental harmonic reactive power.

References

1. Xiong J, Peng Q, Pan H (2012) A novel strategy of harmonic suppression and reactive power compensation. In: Asia-Pacific power and energy engineering conference. doi:[10.1109/APPEEC.2012.6307304](https://doi.org/10.1109/APPEEC.2012.6307304)
2. Chen SX, Eddy XSF, Gooi HB, Wang MQ, Lu SF (2014) A centralized reactive power compensation system for LV distribution networks. In: IEEE transactions on power system, vol 30. doi:[10.1109/TPWRS.2014.2326520](https://doi.org/10.1109/TPWRS.2014.2326520)
3. Gelman V (2013) Thyristor controlled rectifiers (TCR) for traction problems and solutions. In: 3rd international conference on electric power and energy conversion systems, Yildiz Technical University, Istanbul, Turkey, 2–4 Oct 2013
4. Shicheng Z, Gaoyu ZFS (2010) Research on TCR Type SVC System and MATLAB Simulation. In: 5th IEEE conference on industrial electronics and applications. doi:[10.1109/ICIEA.2010.5516668](https://doi.org/10.1109/ICIEA.2010.5516668)

5. Wang D, Yang C, Zhang X, Wang J, Li G (2012) Research on application of TCR + FC typed SVC in power quality integrated management for power traction system, In: international conference on sustainable power generation and supply. doi:[10.1049/cp.2012.1749](https://doi.org/10.1049/cp.2012.1749)
6. Shawon MH, Hanzelka Z, Dziadecki A (2015) Voltage-current and harmonic characteristic analysis of different FC-TCR based SVC. In: IEEE Eindhoven PowerTech. doi:[10.1109/PTC.2015.7232559](https://doi.org/10.1109/PTC.2015.7232559)
7. Trzynadlowski AM (2015) Introduction to modern power electronics, 3rd edn. Wiley, New Jersey. ISBN 978-1-119-00321-2
8. Rozanov Y, Ryvkin SE, Chaplygin E, Voronin P, Hardback PV (2015) Power electronics basics: operating principles, design, formulas, and applications. CRC Press, USA. ISBN 97814
9. Hart DW (2011) Power electronic. McGraw-Hill International Edition, USA
10. Rashid MH (2004) Power electronics: circuits devices and applications, 3rd edn. Pearson Education International, USA, Floryda
11. Das JC (2015) Power system harmonics and passive filter designs, Wiley-IEEE Press, New York. ISBN: 978-1-118-86162-2

Switched Capacitor-Based Power Electronic Converter—Optimization of High Frequency Resonant Circuit Components

Zbigniew Waradzyn, Robert Stala, Andrzej Mondzik
and Stanisław Piróg

Abstract This chapter presents issues of optimization of the resonant circuit components' volume in a switched-capacitor voltage multiplier (SCVM). The SCVM is derived from chip-scale technology but can effectively operate as a power electronic converter in a zero current switching mode when the recharging of switched capacitors occurs in a resonant circuit supported by an inductance. Selection of the passive LC components is not strictly determined, and depends on the optimization strategy according to the volume, efficiency or cost of the converter. Optimization of the volume of LC components is limited by the energy transfer ability via switched capacitors, thus by the rated power of the converter and switching frequency. Depending on the LC values, the converter operates in some specific states that determine the efficiency of the converter and voltage stress on semiconductor switches and diodes. This chapter presents analysis of the converter parameters and operation in the cases of optimization of the resonant circuit components' values. The analytical discussion is also supported by the simulation and experimental results. All the results are provided for the SCVM but can be useful for a variety of switched-capacitor resonant power converters.

Keywords DC-DC converter · Boost converter · Resonant converter · Switched capacitor

Z. Waradzyn (✉) · R. Stala · A. Mondzik · S. Piróg
AGH University of Science and Technology, Kraków, Poland
e-mail: waradzyn@agh.edu.pl

R. Stala
e-mail: stala@agh.edu.pl

A. Mondzik
e-mail: mondzik@agh.edu.pl

S. Piróg
e-mail: pirog@agh.edu.pl

1 Introduction

The switched-capacitor (SC) converter concept can be attractive for a power electronic converter application [1]. The SC power converters can be especially suitable for high voltage gain systems, or the concepts with limited inductive components. Contrary to chip-scale SC circuits, in various concepts of SC power converters the recharging of capacitors is achieved in resonant circuits [1–16]. In this way, the converter operates in the zero current switching (ZCS) mode, which increases its efficiency. Furthermore, inrush currents are limited by oscillatory circuit utilization.

The issues of the components' selection and optimization of the converter, as well as high efficiency design, remain current problems related to SC power converters. They are addressed as major problems of research [1–6] and are related to the concept of the operation of particular topologies [7–17]. The switched-capacitor voltage multiplier (SCVM) [7] is a topology that can be configured as a high voltage gain DC-DC converter using different semiconductor technologies and using different ways of optimizing resonant circuits. Application of suitable switches is determined by voltage ratings in the converter and current stresses. It can be proven that the SCVM can effectively operate as a high frequency Mosfet-based DC-DC [4, 5, 18], but also as a high power and high voltage converter supported by thyristors [14, 15, 17]. The application of suitable LC parameters of SC converter's resonant circuit is determined by the optimization criteria, because it affects the rated power, efficiency, cost, realization technology and stresses on switches. On the other hand, the range of resonant circuit components can be limited, e.g., by feasible switching frequency, available space or the technology of chokes' implementation [16]. It is very important that the results achieved for SCVM can be utilized for the optimization of other ZCS SC converters.

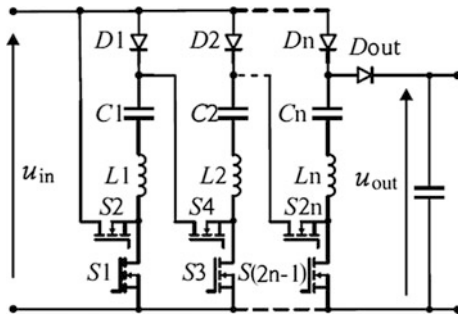
The second section of this chapter introduces the ZCS operation of SCVM, where the resonant operation of the converter and stresses on semiconductor devices are analysed. The resonant circuit optimization problems are also discussed in detail in this section. Experimental results are presented in the following section, to verify the analytical discussion.

2 The Power Electronic Mosfet-Based Switched-Capacitor DC-DC Voltage Multiplier—Configuration and Analysis of Operation

2.1 The Analysed Concept of SCVM

Figure 1 presents a power electronic ZCS voltage multiplier composed of n cells (three cells in this case), where each cell contains two switches, a single diode, an inductance and a capacitor. From the basic concept of the operation of the SCVM it

Fig. 1 The power electronic Mosfet-based SCVM with shared inductances in switching cells



follows that this is a constant ratio boost type converter. The capacitors of the cells are charged from the source in the charging mode, and then discharged in a series connection with the output capacitor. The converter utilizes the switched capacitor concept, in which the capacitors are recharged in parallel and series connections. The topology is adapted to the conversion of power; thus, it must operate with high efficiency. To achieve high efficiency of the power converter, the recharging circuits should have an oscillatory character with an adequate inductance, as well as the quality factor.

The converter that operates with rated power has a determined average value of currents, to which power losses in the diodes are proportional. On the other hand, the converter can effectively operate in a wide range of the capacitance of the switched capacitors C_n , with their partial or full discharge, achieving constant voltage gain. When the minimization possibility of the LC parameters is analysed, the problem of decreasing efficiency can arise.

In the high frequency design, it is assumed that the inductance achieved as PCB air or planar in each switching cell is sufficient for fair ZCS operation. The analysis and operation of the converter differs in such cases from the topology with a central input choke, as presented in [17] for high power designs.

The simplified analysis presented in this section has been carried out by neglecting all parasitic resistances and voltage drops across the power electronic devices, as well as assuming ideal power electronic switches and a constant value of U_{out} . In addition, the value of the converter power is assumed.

The capacitor in each cell is charged during time interval T_{SI} (Fig. 2b) by the current:

$$i_{SI}(t) = \frac{U_{in} - U_{Cmin}}{\rho_1} \sin \omega_{SI}t = I_{SI}m \sin \omega_{SI}t, \tag{1}$$

where:

- U_{in} supply voltage,
- U_{Cmin} minimum voltage across capacitors $C = C1 = \dots = Cn$,
- ρ_1 characteristic impedance of the series LC circuit,
- ω_{SI} angular resonant frequency of the series LC circuit,

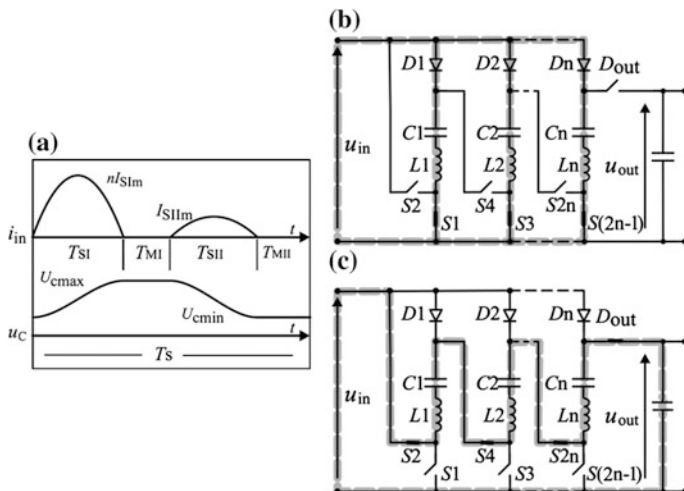


Fig. 2 Stages of operation of the SCVM: **a** input current i_{in} , voltage across switched capacitors u_c , and the definition of time intervals in the switching cycle T_s , **b** charging the capacitors in cells in time interval T_{SI} —path of current, **c** charging the output capacitor in the time interval T_{SII}

I_{SIIm} charging current amplitude.

The charging of the capacitors requires the following time interval:

$$T_{SI} = \frac{\pi}{\omega_{SI}} = \pi\sqrt{L_{SI}C}, \tag{2}$$

where L_{SI} is the overall inductance in each cell capacitor charging circuit.

The voltages across the cell capacitors in time interval T_{SI} are given by the following equation:

$$u_{cSI}(t) = U_{in} - (U_{in} - U_{Cmin}) \cos \omega_{SI}t \tag{3}$$

and achieve their maximum value at $t = T_{SI}$:

$$U_{Cmax} = u_{cSI}(T_{SI}) = 2U_{in} - U_{Cmin}. \tag{4}$$

The output capacitor is charged and all the cell capacitors are discharged during the time interval T_{SII} in the circuit (Fig. 2c) by the current:

$$i_{SII}(t) = -\frac{U_{in} - U_{out} + nU_{Cmax}}{\rho_{II}} \sin \omega_{SII}t = -I_{SIIIm} \sin \omega_{SII}t, \tag{5}$$

where n is number of cells ($n = 3$ in Fig. 1) and:

$$\rho_{II} = \omega_{SII} L_{SII} = \sqrt{\frac{nL_{SII}}{C}}, \quad \omega_{SII} = \sqrt{\frac{n}{L_{SII}C}}. \quad (6)$$

L_{SII} is the overall inductance of the oscillatory circuit in the interval T_{SII} :

$$T_{SII} = \frac{\pi}{\omega_{SII}} = \pi \sqrt{\frac{L_{SII}C}{n}}. \quad (7)$$

The voltages across the cell capacitors in T_{SII} are given by:

$$u_{CSII}(t) = \frac{U_{out} - U_{in}}{n} + \left(U_{Cmax} - \frac{U_{out} - U_{in}}{n} \right) \cos \omega_{SII} t \quad (8)$$

and achieve their minimum value at $t = T_{SII}$:

$$U_{Cmin} = u_{CSII}(T_{SII}) = 2 \frac{U_{out} - U_{in}}{n} - U_{Cmax}. \quad (9)$$

From (4) and (9), it can be deduced that the converter has a constant voltage gain with the theoretical value:

$$U_{out} = (n + 1)U_{in}. \quad (10)$$

The voltage gain of the SCVM does not depend on the capacitance of the switched capacitors as long as the circuit is not overloaded.

In [17] it is proven that, in a high efficiency design, the relation of time intervals T_M to T_S (Fig. 2a) should be minimized, and this can be one of the key points for the proper selection of active and passive components.

2.2 *Semiconductor Switch Technology and Parameters of the SCVM*

All of the conventional switches, as well as WBG-types, can be used for SCVM converters. The selection of switches is determined by the input and output voltage as well as the output power. In the literature, Mosfet-based SC converters are reported for high frequency operations with voltage and current stresses in the range of Mosfet switches (<600 V). Application of SiC switches makes it possible to increase voltage stresses in high-frequency designs. For a larger voltage stress, an IGBT-based converter can be proposed. However, in the resonant SCVM, the turning off control is not demanded; thus, thyristors become an interesting alternative solution for a high voltage and high power SCVM. In [17] the

thyristor-based SCVM concept and results are demonstrated, and in [14] the SC step-down converter is presented. Application of fast turn-off thyristors makes it possible to minimize the relation T_M/T_S . However, in a high power design with sufficiently large capacitors, long periods of resonant oscillation (T_{SI} and T_{SII} intervals) can be achieved to obtain high efficiency using SCR thyristors. The advantages of the thyristor-based SCVM are its high current and voltage ratings, reliability and also simple gate circuits and self turn-off, which protects the switches against hard turn-off by improper control signal management.

The voltage stresses for thyristors in the SCVM are reported in detail in [17]. The case of unidirectional switches is very complicated, because positive as well as negative voltages can occur on thyristors. In the Mosfet-based SCVM (Fig. 1), it is important that the voltage stress on switches depends on the input voltage, but it is also a function of a switch placement (the stress on switches can differ).

The voltage stress on switches responsible for discharging (S_2, S_4, \dots) (Fig. 1) is always equal to U_{in} because they are connected to the input voltage via the charging diodes (D_1, D_2, \dots) and charging switches (S_1, S_3, \dots). For the analysis of voltage stresses on the charging switches (S_1, S_3, \dots) the average capacitor's voltage ($U_{Cavg} = U_{in}$) is taken into account, because each capacitor has series-connected resonant inductance. The voltages on $S_{1,3, \dots}$ switches can then be calculated from the sum of the voltages in loops when $S_{2,4, \dots}$ are turned on and capacitors are charged.

The estimated voltage stresses on switches (Table 1) will be further confirmed by experimental results (Figs. 10 and 11).

It is very important that in the case, in which each capacitor is connected in a series with a resonant inductance, as in Fig. 1, voltage stresses on switches do not depend on the voltage ripple on switched capacitor.

2.3 Resonant Circuit Components of SCVM

The issue of selection of the SCVM parameters presented in this section involves the problems of selection of the semiconductor switches, switched capacitors and the design of resonant inductances.

The voltage u_C across cell capacitors varies between U_{Cmin} (9) and U_{Cmax} (4). U_{Cmin} is equal to:

$$U_{Cmin} = U_{in} - \frac{P_{in}T_S}{2C(n+1)U_{in}}. \quad (11)$$

The limit of the power of the SCVM is determined by the ability of the charge transfer by the recharging of the switched capacitors. Thus, the power of the converter is related to the switched capacitances, switching frequency, number of the cells and the input voltage:

$$P_{\text{in}} \leq 2(n+1)U_{\text{in}}^2 f_S C. \quad (12)$$

From (12) it follows that the switched capacitor's value determines the limit of the converter's power under the fixed switching frequency and the input voltage. For fixed n , P_{in} , U_{in} and f_S , this value should meet the condition:

$$C \geq \frac{P_{\text{in}}}{2(n+1)U_{\text{in}}^2 f_S}. \quad (13)$$

Full discharge operation (minimum voltage across the cell capacitors $U_{C_{\text{min}}} = 0$) occurs at:

$$C = \frac{P_{\text{in}}}{2(n+1)U_{\text{in}}^2 f_S} = \frac{1}{2R_{\text{eq}} f_S}, \quad (14)$$

where

$$R_{\text{eq}} = \frac{(n+1)U_{\text{in}}^2}{P_{\text{in}}} = \frac{U_{\text{out}}^2}{(n+1)P_{\text{in}}}. \quad (15)$$

is an equivalent resistance, introduced to minimize the number of parameters.

A design of the SCVM can be accomplished with minimization of the switched capacitances to the limit described by (13), because the voltage gain of the converter is not affected in this range. This is one of the natural optimization steps; however, it may not be favourable from an efficiency standpoint, as well as problems of the filtering of the input current and selection of components.

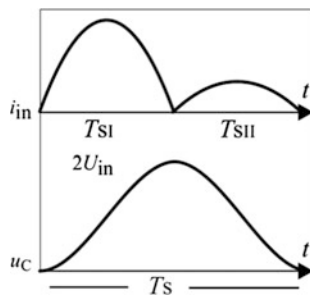
The following specific converter operating states are discussed below:

- operation with full discharge of the switched capacitors at non-interrupted input current,
- operation with full discharge of the switched capacitors at interrupted input current,
- operation with partial discharge of the switched capacitors at non-interrupted input current.

2.3.1 Operation with Full Discharge of the Switched Capacitors in the Case of Non-interrupted Input Current

This is a theoretical case, where T_{MI} and T_{MII} equal zero (the input current is non-interrupted) and the currents have a minimum rms value (Fig. 3). Assuming $T_S = T_{\text{Smin}} = T_{\text{SI}} + T_{\text{SII}}$ in (11), and taking (2) and (7) into account, $U_{C_{\text{min}}}$ can be expressed by the formula:

Fig. 3 Input current i_{in} and voltage across the switched capacitors u_C in the case of their full discharge and non-interrupted input current



$$U_{Cmin} = U_{in} - \frac{\pi P_{in} \left(\sqrt{L_{SI}} + \sqrt{\frac{L_{SII}}{n}} \right)}{2\sqrt{C}(n+1)U_{in}}. \tag{16}$$

At the rated power, the converter with the minimized capacitors C_{min} will operate with full recharging, which means that $U_{Cmin} = 0$. Hence:

$$C_{min} = \left[\frac{\pi P_{in} \left(\sqrt{L_{SI}} + \sqrt{\frac{L_{SII}}{n}} \right)}{2(n+1)U_{in}^2} \right]^2 = \left[\frac{\pi \left(\sqrt{L_{SI}} + \sqrt{\frac{L_{SII}}{n}} \right)}{2R_{eq}} \right]^2. \tag{17}$$

The value of the minimal capacitance C_{min} of the switched capacitors, aside from depending on the power of the converter, the input voltage and the number of the cells, is also dependent on the values of the inductances. Assuming $L_{SI} = L_{SII}/n$ (Fig. 1), the formula (17) becomes the following:

$$C_{min} = \left[\frac{\pi P_{in}}{(n+1)U_{in}^2} \right]^2 L = \frac{\pi^2}{R_{eq}^2} L. \tag{18}$$

Operation with non-interrupted input current, which is assumed here, requires the frequency:

$$f_s = f_{smax} = \frac{1}{T_{SI} + T_{SII}} = \frac{1}{2\pi\sqrt{L_{SI}C}}, \tag{19}$$

which, taking (18) in account, can be expressed in the form:

$$f_{smax} = \frac{R_{eq}}{2\pi^2 L}. \tag{20}$$

Capacitance C_{min} (18) and frequency f_{smax} (20) as functions of L for three values of R_{eq} are shown in Fig. 4. $R_{eq} = 48$ corresponds, e.g., to $n = 3$, $U_{in} = 50$ V, $P_{in} = 208.3$ W. The results obtained show that the frequency in the range of

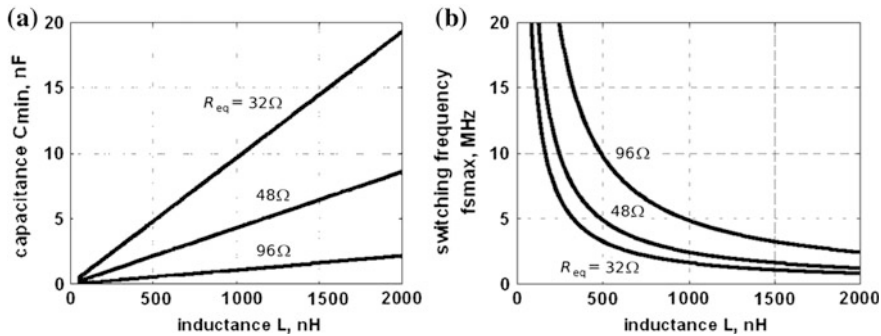


Fig. 4 Dependencies for operation with full discharge of the switched capacitors in the case of non-interrupted input current ($T_S = T_{SI} + T_{SII}$): **a** minimum cell capacitance C_{min} (18), **b** maximum switching frequency f_{smax} (20) versus $L = L_{SI} = L_{SII}/n$ for three values of R_{eq}

megahertz has to be implemented in this converter, which for many reasons may not be applicable in practice.

A criterion for optimizing the volume of the capacitors can lead to selecting capacitances that assure full discharging of the switched capacitors in a switching cycle for the rated power. In addition, it is advantageous to operate the converter with near-zero time intervals T_{MI} and T_{MII} to minimize conduction losses. This kind of operation implies strict dependencies between the operating frequency, the capacitances of the switched capacitors and the power, input voltage and inductances of the converter (18), (20). However, for an inductiveless design, this requires low values of switched capacitors capacitances and very high switching frequencies.

It is assumed in the analysis that the currents are half-sine waves. This assumption can be made if the quality factors Q_I and Q_{II} of charging and discharging series RLC circuits are high enough, e.g., higher than 2.5.

$$Q_I = \frac{1}{r_{SI}} \sqrt{\frac{L}{C_{min}}} = \frac{R_{eq}}{\pi r_{SI}} \tag{21}$$

For the R_{eq} parameters from Fig. 4 and resistance of each charging circuit $r_{SI} = 100 \text{ m}\Omega$, the quality factor Q_I is equal to 101.9, 152.8 and 305.6, respectively. Additionally, if resistance of discharging circuit in each cell $r_{SII} = r_{SI}$ then $Q_{II} = Q_I$, and the currents will be almost ideally sinusoidal.

In conclusion, the analysis results shown in Fig. 4 prove that the converter optimization criterion assuming minimizing the switched capacitors' volume may not be the right one in the case of inductiveless design (small stray inductances or PCB-type ones). The reason is that assuring high efficiency requires, in this case, using high switching frequencies, which may not be applicable in practice. It is also very important that for higher rated power (lower R_{eq} in Fig. 4), the switched capacitances rise, which decreases the frequency of oscillations.

In the case of using larger values of inductance, e.g., of the order of microhenries, lower frequencies are required and the discussed operating state of the converter is acceptable. This is discussed briefly later in the chapter (Fig. 9).

2.3.2 Operation with Full Discharge of the Switched Capacitors in the Case of Interrupted Input Current

Full discharge can take place at maximum recharging frequency f_{Smax} (20) as described above but also at lower frequencies with higher values of capacitors. To achieve this, the switching period T_S has to be increased by introducing time intervals T_{MI} and T_{MII} between current pulses (Fig. 5). At the same time, the capacitances of the switched capacitors have to be increased to fulfil Eq. (14), which will also affect the half periods T_{SI} and T_{SII} . In this case f_S is equal to:

$$f_S = 1/T_S = 1/(T_{SI} + T_{MI} + T_{SII} + T_{MII}), \tag{22}$$

where T_{MI} and T_{MII} are higher than zero.

An advantage of this kind of operation is a possibility of operation with much lower frequencies than f_{Smax} (20), (Fig. 4b). A drawback are higher amplitudes of the current pulses and lower efficiency [17].

2.3.3 Operation with Partial Discharge of the Switched Capacitors in the Case of Non-interrupted Input Current

If the switched capacitors of SCVM have higher capacitances than is required for operation with full discharging (14), the SCVM operates with partial discharge of the switched capacitors and the desired voltage gain; however, the resonant circuits as well as the efficiency should be analysed in this case. This analysis is limited to the case when the converter operates with non-interrupted currents at soft switching (Fig. 6) with frequency given by (19), and with inductances $L_{SI} = L_{SII}/n = L$.

Then, the value of the cell capacitances C meets the condition:

Fig. 5 Input current i_{in} and voltage across the switched capacitors u_C in the case of their full discharge and interrupted input current

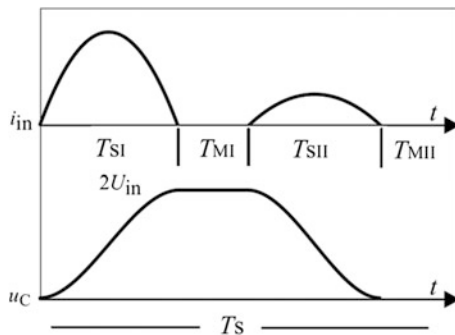
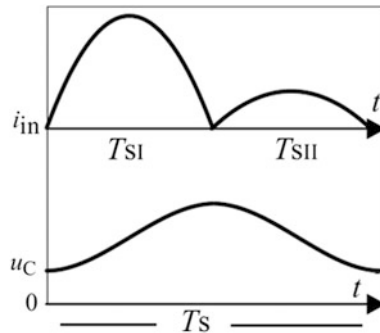


Fig. 6 Input current i_{in} and voltage across the switched capacitors u_C in the case of their partial discharge and non-interrupted input current



$$C = \frac{1}{4\pi^2 f_s^2 L}. \tag{23}$$

At lower values of C there would be time intervals with zero current (the input current would be interrupted) whilst in case of higher values of C , hard switching would occur.

Capacitance C (23) as a function of L for various values of f_s at fixed n , U_{in} and P_{in} [fixed R_{eq} (15)] is shown in Fig. 7a.

The normalized value of the initial voltage across the switched capacitors equals (11), (23):

$$U_{Cminw} = \frac{U_{Cmin}}{U_{in}} = 1 - \frac{2\pi^2 f_s L}{R_{eq}}. \tag{24}$$

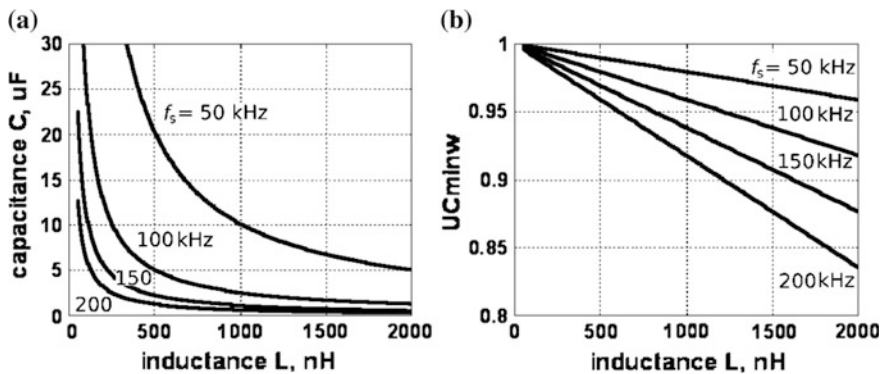


Fig. 7 Dependencies for operation with partial discharge of the switched capacitors in the case of non-interrupted input current ($T_S = T_{SI} + T_{SII}$): **a** capacitance C according to (23), **b** minimum normalized voltage U_{Cminw} (24) versus $L = L_{SI} = L_{SII}/n$ for various values of f_s at $R_{eq} = 48 \Omega$

It can be seen from Fig. 7a that for the used frequencies, the capacitances C are much higher than C_{\min} in Fig. 4a. The capacitors discharge is insignificant and $U_{C_{\min}}$ decreases linearly with an increase of frequency f_s and inductance L (Fig. 7b).

2.3.4 Quality Factor of Resonant Circuits and Inductor Volume Optimization

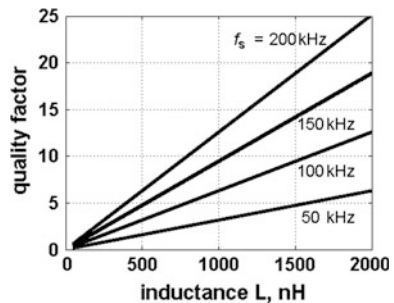
The quality factors Q_I and Q_{II} can be presented in the form:

$$Q_I = \frac{\rho_I}{r_{SI}} = \frac{2\pi f_s L_{SI}}{r_{SI}}, \quad Q_{II} = \frac{\rho_{II}}{nr_{SII}} = \frac{2\pi f_s L_{SII}}{nr_{SII}}. \quad (25)$$

Figure 8 presents Q_I as function of $L_{SI} = L$ for various values of f_s at set values of n , U_{in} and P_{in} ($R_{eq} = 48 \Omega$). The quality factor Q_I (25) is proportional to the inductance L and switching frequency f_s . It results from Fig. 8 that for very small values of L and low frequencies, the quality factor Q_I can even be less than 0.5, which means that the currents do not reach zero (the circuit is not oscillatory) and the ZCS operation is not possible. For higher values of L the circuit becomes oscillatory and the higher the value of L , the less distorted are the currents. For example, for $L = 100 \text{ nH}$ and $r_{SI} = 100 \text{ m}\Omega$, the quality factor $Q_I = 0.94$ at 150 kHz and $Q_I = 0.31$ at 50 kHz. In the former case, the current waveforms will be significantly distorted from sine waves while hard switching would occur in the latter case. However, at $L = 0.7 \text{ }\mu\text{H}$ and the same value of r_{SI} , the quality factor Q_I equals 6.58 and 2.17, respectively.

Hence, the current waveforms will be near sine waves for $L = 0.7 \text{ }\mu\text{H}$ and $f_s = 150 \text{ kHz}$. On the assumption that $L_{SII} = nL_{SI}$ and $r_{SII} = r_{SI}$, the quality factors Q_I and Q_{II} (25) have equal values.

Fig. 8 Quality factor Q_I (25) versus inductance $L = L_{SI}$ for various values of f_s at $R_{eq} = 48 \Omega$, $r_{SI} = 100 \text{ m}\Omega$



In conclusion, to achieve operation with feasible frequencies, the capacitors should be higher than the minimum value resulting from (13), but too high capacitances, required at very low inductances, will make oscillations impossible, due to a quality factor that is too low $Q (<0, 5)$. The converter operation is still possible but its efficiency can decrease.

2.3.5 Limits of the Resonant Inductance

When the switched capacitor is fully recharged, an increase of the resonant inductance can be correct for the minimization of time intervals T_{MI} and T_{MII} . Further increase of the inductance (beyond the ZCS limit) requires the decrease of the switching frequency. In such a case, the power transfer rate falls and the designed capacitance should be increased to maintain the rated power of the converter. These relationships are presented in Fig. 9 based on (18) and (20). From this analysis, it follows that an increase in the inductance may not be favourable.

3 Experimental Results

Experimental measurements make it possible to justify the operation of the SCVM and to analyse the parameters of signals for particular instances of design. The experimental results were achieved for two-stage control presented in Figs. 10 and 11, in the setup described in Table 2 (a 3-cell SCVM with PCB air chokes in each SC cell).

The general operation of the SCVM is confirmed by the experimental waveforms presented in Fig. 10 as well as in Fig. 11. These results make it possible to

Fig. 9 Capacitance C of the switched capacitors and switching frequency f_s versus resonant inductance L under the non-interrupted operation with full discharge of the capacitors. Input voltage is 50 V, number of cells is 3, power of load is 500 W

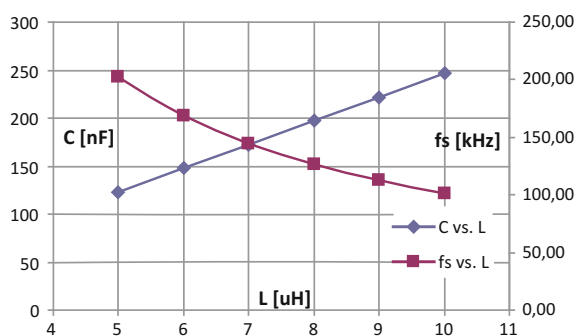


Table 1 Estimated values of voltage stresses on switches in the SCVM configured with inductors in cells for $n = 3$

Switch	S_{out}/D_{out}	$S_{2,4,6}$	S_1	S_2	S_3
Voltage stress	$U_{out} \cdot U_{in}$	U_{in}	U_{in}	$2U_{in}$	$3U_{in}$

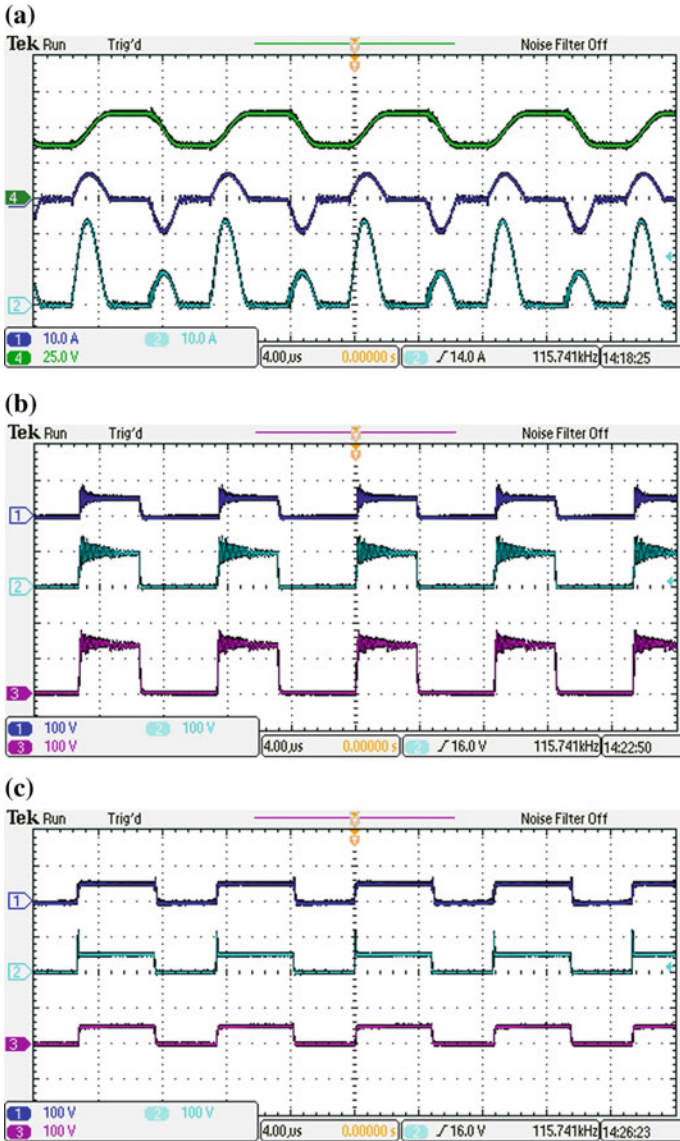


Fig. 10 Waveforms and voltage stresses of tested 3-cell SCVM. Experimental results for $f_s = 115.7$ kHz, $P_{out} = 200$ W with $C_{1,2,3} = 470$ nF. $U_{Cmax} = 59$ V, $I_{inmax} = 24$ A; **a** 1 current of a switched capacitor, 2 input current, 4 voltage on a switched capacitor, **b** voltage on the odd switches: 1 u_{S1} , 2 u_{S3} , 3 u_{S5} , **c** voltage on the even switches: 1 u_{S2} , 2 u_{S4} , 3 u_{S6}

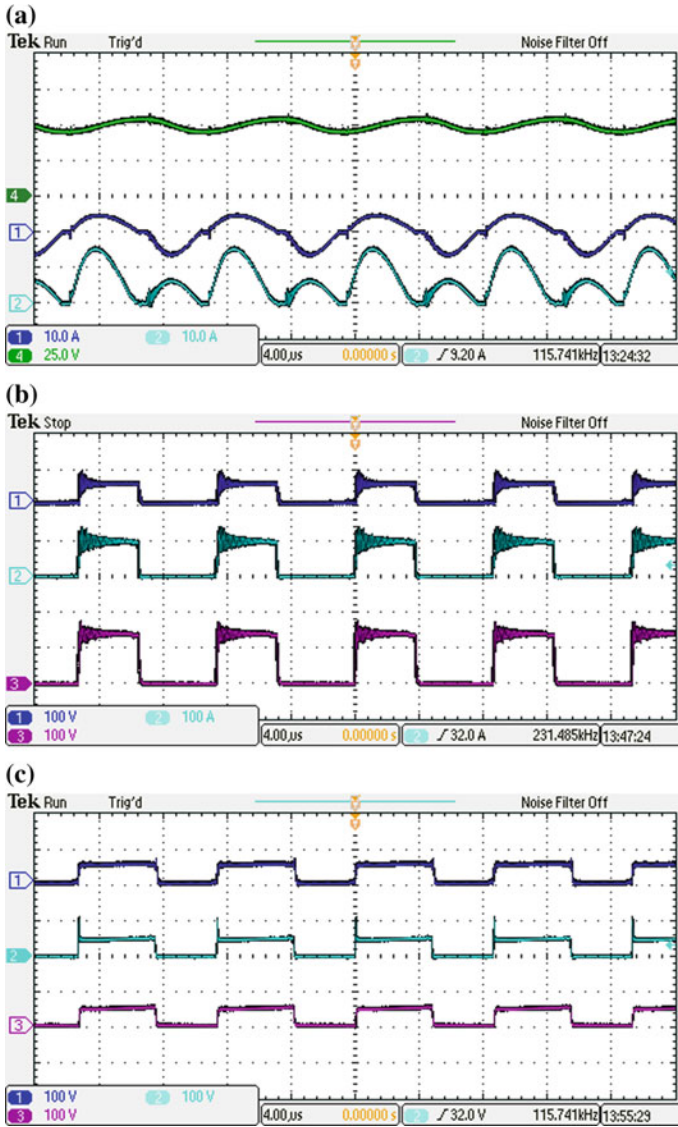
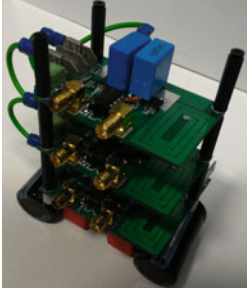


Fig. 11 Waveforms and voltage stresses of tested 3-cell SCVM. Experimental results for $f_s = 115.7$ kHz, $P_{out} = 200$ W with $C_{1,2,3} = 1470$ nF. $U_{Cmax} = 53$ V, $I_{inmax} = 14$ A; **a** I current of a switched capacitor, 2 input current, 4 voltage on a switched capacitor, **b** voltage on the odd switches: 1 u_{S1} , 2 u_{S3} , 3 u_{S5} , **c** voltage on the even switches: 1 u_{S2} , 2 u_{S4} , 3 u_{S6}

Table 2 The laboratory 3-cell Mosfet-based SCVM converter and the parameters of tests

Transistors	SIR872ADP	<p>The 3-cell converter</p> 
Diodes	VB60170G—in cells DPG30C300PC—as D_{out}	
Switched capacitors	470, 1470 nF	
Output capacitor	$C_{out} = 118.3 \mu\text{F}$	
Inductors	$L = 0.7 \mu\text{H}$ air PCB	
Power under the tests	$P_{out} < 200 \text{ W}$	
Input voltage	$U_{in} = 50 \text{ V}$	
Output voltage	$U_{out,theoretical} = 200 \text{ V}$	

compare the operation for two cases of resonant circuit design with different resonant capacitors. For a 200 W load, the switched capacitance can be decreased to the value at which a full discharge occurs. However, for the achieved PCB air choke and feasible switching frequency, the dead time intervals (T_{MI} and T_{MII}) are sizable and can largely decrease the efficiency, as can be observed in Fig. 10, in which deeper discharge of switched capacitors occurs. For the switched capacitances designed to be larger than the optimal capacitors, the maximum capacitor's voltage and current stress, as well as the dead times (T_{MI} , T_{MII}), decrease. This may increase efficiency [17] and the cost of the converter can be lower. Further over-sizing of capacitors will cause a decrease of the quality factor.

From the experimental results of particular cases (for $C = 470$ and $C = 1470$ nF), the voltage stresses on switches remain approximately on the same level (Figs. 10 and 11). The results confirm the analytical estimation (Table 1).

4 Conclusions

Selection of the components of the SCVM and optimization of the converter is a very important and complex issue (which is highlighted in the chapter) in the following aspects:

- the SCVM can be configured using various switches such as Mosfet for high frequency design, but also thyristors, as reported in the literature, for high voltage and high power designs.
- in the selected topology, where resonant inductors are implemented in each cell connected in a series with a switched capacitor, voltage stresses on switches are not increased by voltage ripples on capacitors.
- selection of the switched capacitors is a very complex issue. An optimization of the volume of the capacitors can lead to capacitances that assure full discharging

of the switched capacitors in a switching cycle for the rated power. However, such optimization can stand in opposition to the efficiency demands. The most favourable idea would be to operate the converter at the full discharging of the switched capacitors and with near-zero time intervals between the current pulses of the switched capacitors that are charging and discharging. This kind of operation implies a strict dependence between the operating frequency, the capacitances of the switched capacitors and the inductances of the converter. For an inductiveless design, this requires low values of switched capacitors capacitances, and very high switching frequencies (which may not be applicable in practice). The converter can also be operated at full discharge of the switched capacitors and interrupted input current; however, this requires lower frequencies and higher values of the capacitors. The disadvantages of this kind of operation are higher conduction losses, but switching losses are lower due to a lower switching frequency.

- it is also possible to operate the converter with near-zero time intervals between current pulses of the switched capacitors charging and discharging, and a partial discharge of the switched capacitors. This minimizes conduction losses and switching losses can also be low, due to the possibility of operating the converter at lower frequencies. However, the SCVM converter is not optimized from the capacitance value's standpoint, as it operates at a lower power than its rated power.
- a quality factor should also be analysed for selected *RLC* parameters of the resonant circuits in the SCVM, in order to determine the character of the circuits.

References

1. Ioinovici A (2001) Switched-capacitor power electronics circuits. *Circ Syst Mag* 1(3):37–42. doi:[10.1109/7384.963467](https://doi.org/10.1109/7384.963467) (Third Quarter)
2. Yeung YPB, Cheng KWE, Ho S, Law LKK, Sutanto D (2004) Unified analysis of switched-capacitor resonant converters. *IEEE Trans Ind Electron* 51(4):864–873. doi:[10.1109/TIE.2004.831743](https://doi.org/10.1109/TIE.2004.831743)
3. Cao D, Jiang S, Peng FZ (2013) Optimal design of a multilevel modular capacitor-clamped DC–DC converter. *IEEE Trans Power Electron* 28(8):3816–3826. doi:[10.1109/TPEL.2012.2231438](https://doi.org/10.1109/TPEL.2012.2231438)
4. Stala R, Mondzik A, Kawa A (2016) Resonant-mode switched-capacitor DC-DC converter with inductance on PCB. An analysis and comparison of parameters. *Przegląd Elektrotechniczny*, 04:205–209. doi:[10.15199/48.2016.04.45](https://doi.org/10.15199/48.2016.04.45)
5. Kawa A, Mondzik A, Penczek A, Piróg S, Stala R (2016) Real time, optimal switching frequency calculation for thyristor based DC-DC resonant switched capacitor voltage multiplier. *Przegląd Elektrotechniczny*. 6:25–31. doi:[10.15199/48.2016.06.05](https://doi.org/10.15199/48.2016.06.05) (in Polish)
6. Muller L, Kimball JW (2014) A dynamic model of switched-capacitor power converters. *IEEE Trans Power Electron* 29(4):1862–1869. doi:[10.1109/TPEL.2013.2264756](https://doi.org/10.1109/TPEL.2013.2264756)

7. Cao D, Peng FZ (2010) A family of zero current switching switched-capacitor dc-dc converters. In: Twenty-fifth annual IEEE applied power electronics conference and exposition (APEC), pp 1365–1372
8. Cao D, Peng FZ (2010) Zero-current-switching multilevel modular switched-capacitor DC–DC converter. *IEEE Trans Ind Appl* 46(6):2536–2544. doi:[10.1109/ECCE.2009.5316088](https://doi.org/10.1109/ECCE.2009.5316088)
9. Lee YS, Ko YP, Cheng MW, Liu LJ (2013) Multiphase zero-current switching bidirectional converters and battery energy storage application. *IEEE Trans Power Electron* 28(8):3806–3815. doi:[10.1109/TPEL.2012.2227822](https://doi.org/10.1109/TPEL.2012.2227822)
10. Ye Y, Cheng KWE, Liu J, Xu C (2014) A family of dual-phase-combined zero-current switching switched-capacitor converters. *IEEE Trans Power Electron* 29(8):4209–4218. doi:[10.1109/TPEL.2013.2290733](https://doi.org/10.1109/TPEL.2013.2290733)
11. Hamo E, Cervera A, Peretz MM (2015) Multiple conversion ratio resonant switched-capacitor converter with active zero current detection. *IEEE Trans Power Electron* 30(4):2073–2083. doi:[10.1109/TPEL.2014.2326005](https://doi.org/10.1109/TPEL.2014.2326005)
12. Zotov LG (2011) Two-level DC current power-exchange system based on structures with switched capacitors for autonomous power systems. *Russ Electr Eng* 82(7):388–393. doi:[10.3103/S1068371211070133](https://doi.org/10.3103/S1068371211070133)
13. Parastar A, Seok JK (2015) High-gain resonant switched-capacitor cell-based DC/DC converter for offshore wind energy systems. *IEEE Trans Power Electron* 30(2):644–656. doi:[10.1109/TPEL.2014.2314110](https://doi.org/10.1109/TPEL.2014.2314110)
14. Keiser O, Steimer PK, Kolar JW (2008) High power resonant switched-capacitor step-down converter. In: IEEE power electronics specialists conference, Rhodes, pp 2772–2777. doi:[10.1109/PESC.2008.4592365](https://doi.org/10.1109/PESC.2008.4592365)
15. Mondzik A, Kawa A, Piróg S, Penczek A, Stala R (2016) Optymalizacja kształtu prądu wejściowego tyrystorowego przekształtnika z przełączanymi kondensatorami podnoszącego napięcie stałe o ładowaniu kolejnościowym. *Zagadnienia maszyn, napędów i pomiarów elektrycznych, Prace Naukowe Instytutu Maszyn, Napędów i Pomiarów Elektrycznych Politechniki Wrocławskiej*, nr 71:16–28 (in Polish)
16. Stala R, Mondzik A, Kawa A, Penczek A, Piróg S (2016) An analysis of overload conditions in Mosfet-based power resonant DC-DC step-up converters in switched capacitor voltage multiplier topology. *Przegląd Elektrotechniczny* 05:78–83. doi:[10.15199/48.2016.05.15](https://doi.org/10.15199/48.2016.05.15)
17. Kawa A, Stala R, Mondzik A, Pirog S, Penczek A (2016) High power thyristor-based DC-DC switched-capacitor voltage multipliers. Basic concept and novel derived topology with a reduced number of switches. *IEEE Trans Power Electron* 31(10):6797–6813. doi:[10.1109/TPEL.2015.2505906](https://doi.org/10.1109/TPEL.2015.2505906)
18. Mak O-C, Wong Y-C, Ioinovici A (1995) Step-up DC power supply based on a switched-capacitor circuit. *IEEE Trans Ind Electron* 42(1):90–97. doi:[10.1109/41.345851](https://doi.org/10.1109/41.345851)